Tools for the Characterization of New Modality Drugs Targeting RNA Methyltransferases and Lectins



Dissertation

zur Erlangung des Grades

„Doktorin der Naturwissenschaften“

im Promotionsfach Medizinische Chemie

am Fachbereich Chemie, Pharmazie, Geographie und Geowissenschaften

der Johannes Gutenberg-Universität Mainz

Annabelle Carolin Weldert

geb. in Lahnstein

Mainz
2026

Erste Gutachterin und Betreuerin: [redacted]

Zweiter Gutachter: [redacted]

Zweitbetreuer: [redacted]

Tag der mündlichen Prüfung:

D77 (Dissertation Universität Mainz)

Nachnutzung: Urheberrechtsschutz (in C-1.0)

Declaration of Authorship

I, Annabelle Carolin Weldert, hereby declare that this thesis, titled “Tools for the Characterization of New Modality Drugs Targeting RNA Methyltransferases and Lectins”, was written independently and that I have not used any sources or aids other than those indicated (this also includes AI-based applications or tools*). All verbatim or paraphrased material and quotations have been clearly identified and properly cited (this also applies to texts generated by generative AI, such as ChatGPT). I confirm that I have not used any aids whose use has been explicitly prohibited by the examiner.

In the appendix “Use of AI Tools,” I have documented the AI tools used. By submitting the present work, I accept responsibility for the overall content of the submitted document. This includes responsibility for any AI-generated content that I have incorporated into my thesis. To the best of my knowledge and belief, I have reviewed the accuracy of any adopted (AI-generated) statements and content.

I am aware that any violation of the above points may result in consequences under examination regulations and, in particular, may lead to the doctoral work being graded as “failed.” Enrollment may be revoked for up to two years if students engage in cheating in examinations twice or more frequently (§ 69(4) and (5) HochSchG).

_____

Place, date, and signature

Eigenständigkeitserklärung

Hiermit erkläre ich, Annabelle Carolin Weldert, dass ich die vorliegende Arbeit mit dem Titel:

„Tools for the Characterization of New Modality Drugs Targeting RNA Methyltransferases and Lectins"

selbstständig verfasst und keine anderen als die angegebenen Quellen und Hilfsmittel (dazu zählen auch KI-basierte Anwendungen oder Werkzeuge*) benutzt habe. Sämtliche wörtlichen oder sinngemäßen Übernahmen und Zitate sind kenntlich gemacht und nachgewiesen (dies gilt auch für Texte, die durch generative KI, wie Chat GPT erzeugt wurden). Ich versichere, dass ich keine Hilfsmittel verwendet habe, deren Nutzung die Prüferin oder der Prüfer explizit ausgeschlossen hat.

Im Anhang „Nutzung KI-Tools" habe ich die verwendeten KI-Tools dokumentiert.

Mit Abgabe der vorliegenden Leistung übernehme ich die Verantwortung für das eingereichte Gesamtprodukt. Ich verantworte damit auch jegliche KI-generierten Inhalte, die ich in meine Arbeit übernommen habe. Die Richtigkeit übernommener (KI-generierter) Aussagen und Inhalte habe ich nach bestem Wissen und Gewissen geprüft.

Mir ist bekannt, dass ein Verstoß gegen die genannten Punkte prüfungsrechtliche Konsequenzen hat und insbesondere dazu führen kann, dass die Promotionsleistung als mit „nicht bestanden" bewertet wird. Die Einschreibung kann für bis zu zwei Jahre widerrufen werden, wenn Studierende zweimal oder häufiger bei Prüfungsleistungen täuschen (§ 69 Abs. 4 und 5 HochSchG).

_____

Ort, Datum und Unterschrift





Acknowledgments

[redacted]







Table of Contents

Declaration of Authorship ..... **I**

Eigenständigkeitserklärung ..... **II**

Acknowledgments ..... **V**

Table of Contents ..... **VII**

List of Abbreviations ..... **IX**

Abstract ..... **XIII**

Zusammenfassung ..... **XIV**

1 Introduction **1**

1.1 RNA Methyltransferases in Medicinal Chemistry *1*

1.1.1 RNA Methylation and RNA Methyltransferases as Drug Targets 1

1.1.2 Methyltransferase-like Protein 3 (METTL3) 4

1.1.3 tRNA m^1G37 Methyltransferase (TrmD) 9

1.1.4 DNA Methyltransferase 2 (DNMT2) 15

1.2 New Modalities in Drug Discovery *20*

1.2.1 Proteolysis Targeting Chimeras (PROTACs) 20

1.2.2 Innovative Screening Approaches: DNA-Encoded Libraries and Direct-to-Biology 30

1.3 C-Type Lectins in Drug Delivery *32*

1.3.1 C-Type Lectin Domains and Carbohydrate Interactions 32

1.3.2 Multivalency in Lectine-Carbohydrate Interactions 33

1.3.3 C-Type Lectin Receptors Dendritic Cell-Specific Intercellular Adhesion Molecule-3-Grabbing Non-Integrin (DC-SIGN) and Macrophage Mannose Receptor (MMR) 34

1.3.4 Targeted Drug Delivery via DC-SIGN and the MMR 36

2 Project Overview **39**

2.1 Project 1: Discovery and Characterization of Novel Ligands for RNA Methyltransferases *39*

2.2 Project 2: Binding Characterization of Multivalent Targeting Structures *42*

3 List of Publications **43**

3.1 Publications as Part of this Doctoral Thesis *43*

3.1.1 Project 1: Discovery and Characterization of Novel Ligands for RNA Methyltransferases 43
3.1.2 Project 2: Binding Characterization of Multivalent Targeting Structures 43
3.2 Publications Beyond this Doctoral Thesis 44
4 Discovery and Characterization of Novel Ligands for RNA Methyltransferases 45
4.1 Structure-Guided Design of a Methyltransferase-Like 3 (METTL3) Proteolysis-Targeting Chimera (PROTAC) Incorporating an Indole–Nicotinamide Chemotype 45
4.1.1 Context, Project Summary, and own Contribution 45
4.1.2 Publikation 48
4.2 Nanoscale Direct-to-Biology Optimization and Structural Insights into Selective S. aureus TrmD Inhibitors 77
4.2.1 Context, Project Summary, and own Contribution 77
4.2.2 Publication 80
4.3 DNA-Encoded Library Screening Uncovers Potent DNMT2 Inhibitors Targeting a Cryptic Allosteric Binding Site 115
4.3.1 Context, Project Summary, and own Contribution 115
4.3.2 Publication 118
5 Binding Characterization of Multivalent Targeting Structures 186
5.1 Surface Density of Mono- and Trivalent High-Mannan-Derived Targeting Structures with Different Affinities Impacts Cellular Uptake of Human Serum Albumin-Derived Nanocarriers 186
5.1.1 Context, Project Summary, and own Contribution 186
5.1.2 Publication 189
6 Conclusion and Outlook 218
7 Bibliography 220
8 Appendix 238
8.1 Usage of AI tools 238
8.2 Nutzung KI-Tools 238
9 Curriculum Vitae 1

List of Abbreviations

A	Adenosine
A-to-I	Adenosine-to-inosine
ADME	Absorption, distribution, metabolism, and excretion
AI	Artificial intelligence
AML	Acute myeloid leukemia
APC	Antigen-presenting cell
AR	Androgen receptor
Bcl-2	B-cell lymphoma 2
BRD	Bromodomain
BRET	Bioluminescence resonance energy transfer
BTK	Bruton's tyrosine kinase
C	Cytidine
CADD	Computer-aided drug design
circRNA	Circular RNA
COPD	Chronic obstructive pulmonary disease
CRBN	Cereblon
CRD	Carbohydrate-recognition domain
CTL	C-type lectin
CTLD	C-type lectin domain
CuAAC	Copper-catalyzed azide-alkyne cycloaddition
CUL	Cullin
D2B	Direct-to-biology
DC	Dendritic cells
DC_{50}	Half-maximal degradation concentration
DC-SIGN	Dendritic cell-specific intercellular adhesion molecule-3-grabbing non-integrin
DDB1	DNA damage-binding protein 1
DEL	DNA-encoded library
D_{max}	Maximal level of target degradation
DNA	Deoxyribonucleic acid
DNMT2	DNA Methyltransferase 2
DSF	Differential scanning fluorimetry
ECD	Extracellular domain
E. coli	*Escherichia coli*
ER	Estrogen receptor
FP	Fluorescence polarization
G	Guanosine
HAKAI	E3 ubiquitin ligase CBLL1
HBAs	Hydrogen bond acceptors
HBDs	Hydrogen bond donors

HER2	Human epidermal growth factor receptor 2
HIF-1α	Hypoxia inducible factor 1α
H. inf.	*Haemophilus influenzae*
HIV	Human immunodeficiency viruses
HSA	Human serum albumin
HTS	High-throughput screening
IAP	Inhibitor of apoptosis protein
IC_{50}	Half-maximal inhibitory concentration
ICAM	Intercellular adhesion molecule
ITC	Isothermal titration calorimetry
K_D	Dissociation constant
LBDD	Ligand-based drug design
LYTACs	Lysosome-targeting chimeras
m^1A	N^1-Methyladenosine
m^6A	N^6-Methyladenosine
m^5C	5-Methylcytosine
m^1G	N^1-Methylguanosine
m^7G	N^7-Methylguanosine
MBC	Minimal bactericidal concentration
MD	Molecular dynamics
MDM2	Mouse double minute 2 homolog
METTL	Methyltransferase-like protein
MHC	Major histocompatibility complex
MIC	Minimum inhibitory concentrations
miRNA	Micro RNA
MMR	Macrophage mannose receptor
MPro	SARS-CoV-2 main protease
mRNA	Messenger RNA
MRSA	Methicillin-resistant *S. aureus*
MST	Microscale thermophoresis
MTases	Methyltransferases
MTC	m^6A Methyltransferase complex
MTD	Methyltransferase domain
MTHF	N^5,N^{10} –Methylenetetrahydrofolate
MW	Molecular weight
ncRNA	Non-coding RNA
NSun2	NOP2/Sun RNA methyltransferase 2
PAMPA	Parallel artificial membrane permeability assay
PARP	Poly ADP ribose polymerase
PAR2	Protease-activated receptor-2
PCR	Polymerase chain reaction
PD	Pharmacodynamics

PK	Pharmacokinetic
POI	Protein of interest
PPI	Protein–protein interactions
PRDX1	Peroxiredoxin1
PROTAC	Proteolysis Targeting Chimera
Ψ	Pseudouridine
RBM15	RNA-binding motif protein 15
RBX1	CUL2–RING-box protein 1
RIBOTAC	Ribonuclease targeting chimera
RIP1	Receptor interacting protein 1
RIPTAC	Regulated induced proximity targeting chimera
RNA	Ribonucleic acid
rRNA	Ribosomal RNA
SAH	*S*-adenosyl-L-homocysteine
SAM	*S*-adenosyl-L-methionine
SAR	Structure–activity relationship
SARS-CoV-2	Severe acute respiratory syndrome coronavirus 2
S. aureus	*Staphylococcus aureus*
sEH	Soluble epoxide hydrolase
SERDs	Selective estrogen receptor degraders
S_N2	Bimolecular nucleophilic substitution
SncRNA	Small non-coding RNA
SPA	Scintillation proximity assay
SPR	Surface plasmon resonance
TPD	Targeted protein degradation
tPSA	Topological polar surface area
TR-FRET	Time-resolved fluorescence energy transfer
tRNA	Transfer RNA
Trm5	tRNA methyltransferase 5
TrmD	tRNA m^1G37 Methyltransferase
TrmH	tRNA (Gm18) Methyltransferase
TS	Targeting structure
U	Uridine
UPS	Ubiquitin–proteasome system
UTRs	Untranslated regions
VHL	Von Hippel-Lindau
VIRMA	Vir-like m^6A methyltransferase-associated
WTAP	Wilms' tumor 1-associated protein
ZC3H13	Zinc finger CCCH domain-containing protein 13

Abstract

Human RNA methyltransferases (MTases) are involved in diverse physiological and pathological processes, while inhibition of prokaryotic MTases may provide new antibiotic strategies. Despite this potential, many RNA MTases remain understudied, including limited high-resolution structural information for several targets. Moreover, although inhibitor development has progressed, major challenges persist: many MTase inhibitors are substrate-derived, often suffer from selectivity and permeability limitations, and must compete with high intracellular substrate levels, which can hinder translation from biophysical binding to cellular effects. Addressing these gaps requires both improved ligand discovery strategies and detailed binding characterization to guide optimization. In the context of drug delivery, using nanocarriers offers an approach to overcome limitations such as selectivity and permeability. The design of the targeting structures on these systems is essential to ensure optimal uptake and biodistribution.

This work can be divided into two projects focusing on the characterization of binding interactions between proteins and ligands: the first project addresses novel ligands for RNA methyltransferases (MTases), and the second investigates multivalent targeting structures for receptor-targeted drug delivery.

In the first project, Proteolysis-targeting chimeras (PROTACs) targeting methyltransferase-like 3 (METTL3) were evaluated in terms of binding mechanism. The lead PROTAC incorporated an indole–nicotinamide METTL3-binding moiety, providing design insights for future PROTAC development. Mechanistic investigation showed that the lead compound forms a stable ternary complex with positive cooperativity. In addition, analysis of a literature compound highlighted the importance of cooperativity over binary affinity for productive degradation. Moreover, inhibitors targeting the *Staphylococcus aureus* tRNA m^1G37 methyltransferase (TrmD), identified using a nanoscale synthesis strategy with a direct-to-biology readout, were analyzed, and a prodrug strategy was used to address permeability limitations. Co-crystallization, yielding the first ligand-bound structure of *S. aureus* TrmD, and subsequent structural analyses identified residues that could be addressed to further improve affinity and selectivity. Novel ligands targeting DNA methyltransferase 2 (DNMT2), identified by a DNA-encoded library screening, were analyzed by isothermal titration calorimetry. In conjunction with other biophysical methods and crystallography, these studies indicated binding to an allosteric pocket, dimerization, and a conformational change. Across the MTase projects, lead compounds displayed cellular activity, reflected in changes in RNA modification levels and/or effects on cell viability and growth.

In the second project, interactions between mono- and trivalent carbohydrate structures and lectin receptors were investigated by molecular docking, and a nano differential scanning fluorimetry (nanoDSF) assay was established to measure binding affinities in solution. The study revealed similar millimolar affinities across all investigated structures, independent of valency and epitope type. Subsequent uptake experiments using a human serum albumin-derived nanocarrier provided further insight into how targeting-structure valency, epitope type, and surface density influence uptake.

Zusammenfassung

Menschliche RNA-MTasen sind an unterschiedlichen physiologischen und pathologischen Prozessen beteiligt, während die Hemmung prokaryotischer MTasen zur Entwicklung neuer Antibiotika beitragen könnte. Viele RNA-MTasen sind jedoch unzureichend untersucht (u. a. wegen begrenzter struktureller Informationen), und trotz Fortschritten in der Entwicklung von Inhibitoren bestehen weiterhin Herausforderungen. Viele Inhibitoren sind von Substraten abgeleitet und weisen daher Einschränkungen in Selektivität und Permeabilität auf. Zusätzlich konkurrieren sie mit hohen intrazellulären Substratkonzentrationen, was häufig die zelluläre Wirksamkeit vermindert. Um diese Lücken zu schließen, sind sowohl verbesserte Strategien zur Ligandentdeckung als auch eine detaillierte Charakterisierung der Bindung erforderlich, um die Optimierung zu leiten. Im Kontext von Wirkstofftransport bieten Nanocarrier einen Ansatz, um Einschränkungen wie Selektivität und Permeabilität zu adressieren. Die Gestaltung der Targeting-Strukturen auf solchen Systemen ist dabei entscheidend, um eine optimale Aufnahme und Biodistribution zu gewährleisten.

Diese Arbeit lässt sich in zwei Projekte unterteilen, die sich auf die Charakterisierung von Bindungsinteraktionen zwischen Proteinen und Liganden konzentrieren: Das erste Projekt befasst sich mit neuartigen Liganden für RNA-Methyltransferasen (MTasen), und das zweite untersucht multivalente Targeting-Strukturen für rezeptorvermittelten Wirkstofftransport.

Im ersten Projekt wurden *Proteolysis-targeting chimeras* (PROTACs), welche die *methyltransferase-like 3* (METTL3) adressieren, hinsichtlich Mechanismus und Bindung untersucht. Der *Lead*-PROTAC enthält eine Indol-Nicotinamid-Struktur zur Bindung an METTL3 und lieferte Designinformationen für die zukünftige PROTAC-Entwicklung. Mechanistische Untersuchungen zeigten einen stabilen ternären Komplex mit positiver Kooperativität. Darüber hinaus hob die Analyse eines Literatur-PROTACs die Bedeutung von Kooperativität gegenüber der binären Affinität für eine wirksame Degradation hervor. Außerdem wurden Inhibitoren der tRNA-m^{1}G37-Methyltransferase (TrmD) von *Staphylococcus aureus* analysiert, die mittels einer Nanoskalen-Synthesestrategie mit *Direct-to-Biology-Readout* identifiziert wurden; Permeabilitätslimitierungen wurden durch eine

Prodrug-Strategie adressiert. Co-Kristallisation, die zur ersten liganden-gebundenen Struktur von *S. aureus* TrmD führte, sowie anschließende Strukturanalysen zeigten Optimierungsansätze für Affinität und Selektivität auf. Neuartige Liganden für die DNA-Methyltransferase 2 (DNMT2), identifiziert mittels eines *DNA-encoded library*-Screenings, wurden mit isothermaler Titrationskalorimetrie analysiert. In Verbindung mit weiteren biophysikalischen Methoden und Kristallographie wurden eine allosterische Bindetasche, Dimerisierung und eine Konformationsänderung identifiziert. Über die MTase-Projekte hinweg zeigten *Lead*-Verbindungen zelluläre Aktivität.

Das zweite Projekt befasst sich mit Wirkstofftransport, bei dem Nanocarrier helfen können, Herausforderungen wie Selektivität und Permeabilität zu überwinden. Die Gestaltung der Zielstrukturen auf diesen Systemen ist entscheidend, um eine optimale Aufnahme und Biodistribution zu gewährleisten. Entsprechend wurden die Wechselwirkungen zwischen mono- und trivalenten Kohlenhydratstrukturen und Lektinrezeptoren mittels molekularem Docking untersucht, und ein *Nano-Differential-Scanning-Fluorimetrie*-Assay wurde etabliert, um die Bindungsaffinitäten in Lösung zu messen. Die Studie zeigte ähnliche Affinitäten für alle untersuchten Strukturen, unabhängig von Valenz und Epitop-Typ. Nachfolgende Aufnahme-Experimente mit einem Nanocarrier lieferten weitere Erkenntnisse darüber, wie Valenz, Epitop-Typ und Oberflächendichte der Targeting-Strukturen die Aufnahme beeinflussen.

1 Introduction

1.1 RNA Methyltransferases in Medicinal Chemistry

1.1.1 RNA Methylation and RNA Methyltransferases as Drug Targets

The term epigenetics was coined in the early 1940s by the British biologist Conrad Waddington to describe the processes that influence how genetic information (the genotype) is translated into observable traits (the phenotype).[1] Over time, the definition has narrowed to refer specifically to alterations in gene expression that are not caused by changes in the DNA sequence.[2,3] As gene expression is not only influenced by DNA but also RNA, the field of epitranscriptomics expanded the concept of epigenetics in the past few decades, focusing on post-transcriptional chemical modifications of cellular RNAs.[4–7] Although the first RNA modifications were identified as early as the 1960s, the field mainly began to gain momentum following the 2011 discovery that N^6-methyladenosine (m^6A) can be enzymatically demethylated, prompting widespread efforts to map its distribution, dynamics, and functions across the transcriptome.[6–13] To date, over 170 chemically distinct RNA modifications[14] have been identified across all classes of RNA molecules, with rapid advances in detection methodologies continuously driving progress in the field of epitranscriptomics.[15–19] Biochemical modifications of RNA occur on all four nucleosides, namely adenosine (A), guanosine (G), cytidine (C), and uridine (U), as well as at the 2'-O-position of the ribose. Common types of purine or pyrimidine base modifications include methylation, pseudouridylation (Ψ), and adenosine-to-inosine (A-to-I) editing, among many others.[12,20–22] These modifications can be found in all types of RNA, including transfer RNA (tRNA), ribosomal RNA (rRNA), messenger RNA (mRNA), non-coding RNA (ncRNA), microRNA (miRNA), and circular RNA (circRNA).[23] Collectively, they play an important role in RNA metabolism, including structure formation, stability, splicing, localization, transcription, translation, and RNA–protein interactions.[5,12,24–26]

Among the different RNA modifications, methylation is the most common, and methylation of mRNA and tRNA is essential for regulating various physiological processes. Moreover, abnormal methylation of these RNAs can influence a variety of diseases such as cancers, cardiovascular diseases, and neurological deficits. An overview of some of the best-studied mRNA and tRNA methylations, N^6-methyladenosine (m^6A), 5-methylcytosine (m^5C), N^1-methyladenosine (m^1A), and N^7-methylguanosine (m^7G), as well as the tRNA modification N^1-methylguanosine (m^1G), which is relevant for this thesis, is shown in Figure 1.[14,21,27–29]

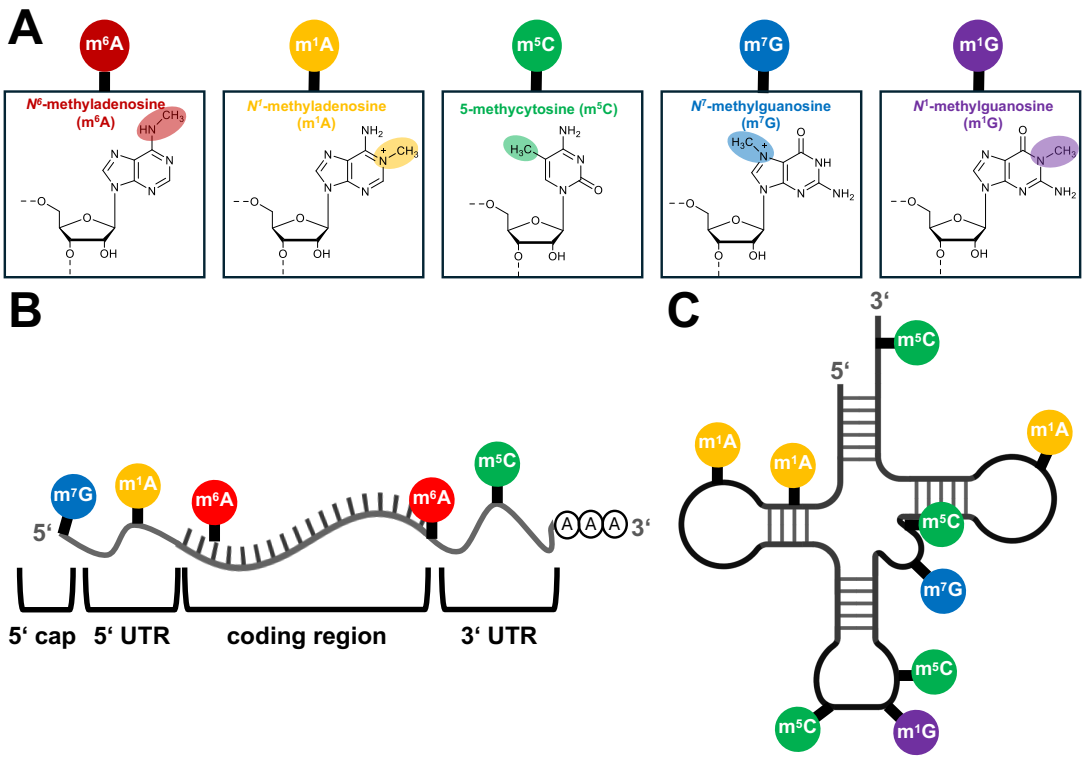


Figure 1: Common messenger ribonucleic acid (mRNA) and transfer RNA (tRNA) methylations. **A** Modifications: N^6-methyladenosine (m^6A), N^1-methyladenosine (m^1A), 5-methylcytosine (m^5C), N^7-methylguanosine (m^7G), and N^1-methylguanosine (m^1G). **B** Example of methylations in a simplified mammalian mRNA molecule consisting of 5′- and 3′-untranslated regions (UTRs), the coding region, a 5′-cap, and a poly-adenosine [poly(A)] tail. **C** Example of methylations in a simplified tRNA molecule. The figure was created with Microsoft PowerPoint, Biorender.com, and ChemDraw. The figure was adapted from Delaunay *et al*.[21] and Cui *et al*.[23]

Methylation is mediated by three classes of effector proteins: writers, which transfer methyl groups to specific target positions; readers, which recognize and bind the modifications; and erasers, which remove them.[30] The writers, called methyltransferases (MTases), generally not only methylate RNA but also other biomolecules like DNA or proteins.[31,32] MTases utilize a cofactor that supplies the methyl group for the transfer reaction and predominantly use *S*-adenosyl-L-methionine (SAM), with only a few using N^5,N^{10}-methylenetetrahydrofolate (MTHF).[33–36] The product of the SAM-dependent methylation, *S*-adenosyl-L-homocysteine (SAH), functions as a non-selective feedback inhibitor for numerous MTases.[37] SAM-dependent MTases are grouped into nine different classes, based on their characteristic structural fold, independent of their phylogenetic origin.[36,38–44] For the purposes of this thesis, only classes I and IV will be discussed in further detail. Class I, referred to as Rossmann-fold MTases, is the most frequently occurring class.[36,43,45] The Rossmann fold features a seven-stranded β-sheet with flanking α-helices forming an αβα-sandwich at the C-terminus. Within this structural motif, glycine-rich regions in the first β-strand are essential for the binding of SAM. Additionally, a highly conserved acidic residue in the β2-strand plays a crucial role in

substrate binding by forming hydrogen bonds with the ribose of the substrate.[36,46,47] The less common class IV is characterized by a unique α/β fold and a deep trefoil knot in the C-terminal half of the catalytic domain.[48–51] This characteristic trefoil knot provides the binding site for SAM, which binds in an unique bent conformation.[48,51] The catalytic domain is referred to as SPOUT domain, a name coined when structural similarities between tRNA-modifying enzymes tRNA (Gm18) methyltransferase (TrmH(SpoU)) and the tRNA m^1G37 methyltransferase (TrmD) were identified.[52]

In drug development, RNA MTases have historically received little attention despite being potential therapeutic targets in a variety of human diseases. For example, in cardiovascular disease, RNA MTases are involved in inflammatory response, fibrosis, and cardiomyocyte turnover.[53–57] Moreover, in cancer, RNA methylation and associated RNA MTases are linked to survival, progression, proliferation, and drug resistance.[58–64] RNA MTases also play essential roles in neurological disorders, where their dysregulation can affect neuronal function and contribute to diseases like Alzheimer's and Parkinson's.[65–68] Beyond human diseases, RNA MTases play critical roles in viral infections. Many flaviviruses and coronaviruses rely on MTases to catalyze RNA cap methylations, which are essential for the viral lifecycle, making these MTases potential targets for antiviral therapy.[69–72] Additionally, targeting prokaryotic MTases has emerged as a promising strategy in the development of novel antibiotics and overcoming resistance to classic antibiotics.[73–76] This relevance across different diseases has led to growing interest and a broad search for selective inhibitors and tool compounds targeting diverse MTases, extensively reviewed elsewhere.[38,70,77,78] A key early milestone was the discovery of the natural product and SAM analog sinefungin as an antibiotic and RNA MTase inhibitor in the 1970s.[79,80] Along with SAH, it is often used as a pan-MTase inhibitor and the use of SAM analogs is a strategy frequently employed to develop MTase inhibitors.[79–83] However, the cellular abundance of SAH and SAM, along with their widespread binding proteins, makes it difficult for small molecules to compete effectively.[84–86] Additionally, the large number of MTases that depend on SAM further complicates the development of selective inhibitors, especially for SAM analogs.[36,87] Moreover, SAM's poor membrane permeability can limit the effectiveness of these inhibitors in cellular contexts.[88,89] As a result, identifying effective and selective small-molecule RNA MTase inhibitors remains a significant challenge, and most candidate compounds for diverse methyltransferases have so far only been evaluated *in vitro*. One promising example is STC-15 (Figure 4B), a methyltransferase-like protein 3 (METTL3) inhibitor, which is the first compound specifically targeting RNA MTases to enter clinical trials.[90,91]

1.1.2 Methyltransferase-like Protein 3 (METTL3)

Among RNA MTases with therapeutic relevance, METTL3 stands out as a central enzyme. It catalyzes the formation of m^{6}A, the most prevalent RNA modification in mammalian cells.[14] However, it does not act alone as the main writer of this modification in mRNA as it is the catalytic core of a writer complex, the m^{6}A-methyltransferase complex (MTC, Figure 2).[92] METTL3 forms a heterodimer with METTL14, which supports METTL3 in recognizing the RNA substrates and is essential for its catalytic activity.[93–95] The dimerization between METTL3 and METTL14 is stabilized by a network of hydrogen bonds and hydrophobic interactions.[93] The METTL3/14 dimer binds to the adaptor protein Wilms' tumor 1-associated protein (WTAP), which, in turn, interacts with several other cofactors, including Vir-like m^{6}A methyltransferase-associated protein (VIRMA), the RNA-binding motif protein 15 (RBM15), the zinc finger CCCH domain-containing protein 13 (ZC3H13), and the E3 ubiquitin ligase CBLL1 (HAKAI), enabling precise regulation of the m^{6}A modification process.[96–98]

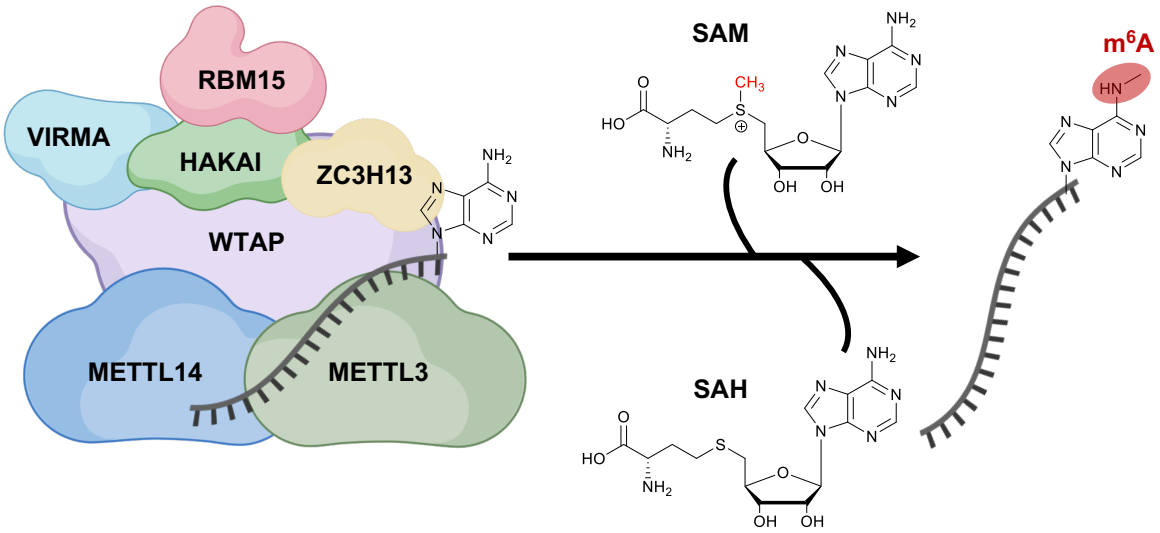


Figure 2: Methylation reaction catalyzed by the *N*^{6}-methyladenosine methyltransferase complex (MTC). The MTC consists of the methyltransferase-like protein 3/14 (METTL3/14) dimer, Wilms' tumor 1-associated protein (WTAP), Vir-like m^{6}A methyltransferase-associated protein (VIRMA), the RNA-binding motif protein 15 (RBM15), the zinc finger CCCH domain-containing protein 13 (ZC3H13), and the E3 ubiquitin ligase CBLL1 (HAKAI). *S*-adenosyl-L-methionine (SAM) functions as a cofactor during the methylation resulting in *S*-adenosyl-L-homocysteine (SAH) as the byproduct. The figure was created with Microsoft PowerPoint, Biorender.com, and ChemDraw.

The m^{6}A modification sites in a wide variety of mRNA substrates of METTL3 are localized in 3′-untranslated regions (UTRs) and near stop codons embedded in specific motifs such as DRACH (D = A/G/U, R = A/G, and H = A/C/U).[11,13,99,100] The addition of the methyl group is critical for regulating various aspects of mRNA metabolism, like stability, translation, splicing, and export.[101–105] The MTC is localized in the nucleus; additionally, METTL3 can localize to the cytoplasm and promote translation independent of m^{6}A catalytical activity.[106–108]

Given the abundance and diverse functions of m^6A, the role of METTL3 in RNA metabolism and its connections to disease are complex and sometimes contradictory, with opposing effects observed in different studies. A comprehensive overview of all these aspects would exceed the scope of this thesis; therefore, only a few key examples will be discussed, with more extensive reviews available elsewhere.[77,109–115]

METTL3 modulates multiple metabolic diseases. In diabetes mellitus, for instance, METTL3 can have harmful effects by inhibiting insulin sensitivity through m^6A modification of fatty acid synthase mRNA.[116] On the other hand, it can also be beneficial by enhancing the expression of insulin secretion-related genes.[116,117] Furthermore, METTL3 plays an important role in the development of obesity and is essential for the occurrence and development of nonalcoholic fatty liver disease.[118–121] In the context of viral infections, such as severe acute respiratory syndrome coronavirus 2 (SARS-CoV-2), increased METTL3 expression modulates viral replication. Similarly, decreased expression helps trigger the immune response and reduces viral replication. Therefore, targeting METTL3 might represent an interesting antiviral strategy.[122–124] METTL3 also plays a central role in cardiovascular disorders, being elevated in ischemic heart disease and cardiac hypertrophy, and contributing to vascular pathologies such as atherogenesis and hypoxic pulmonary hypertension.[125–131]

In cancer, METTL3 has been implicated as both an oncogene and a tumor suppressor. The enzyme influences tumorgenesis, metastasis, proliferation, and drug resistance in malignancies such as colorectal, breast, lung, and gastric cancer.[132–142] Conversely, METTL3 has also been linked to a decrease in metastasis, proliferation, migration, and growth in breast cancer, colorectal cancer, and glioblastoma.[143–145] These contrasting roles highlight the need for a nuanced understanding of METTL3's functions before it can be exploited for cancer therapy. One context in which METTL3 appears particularly interesting is acute myeloid leukemia (AML). Here, it has been identified as an essential gene for cancer cell growth.[146] METTL3 enhances the translation of oncogenes, such as B-cell lymphoma 2 (Bcl-2), and promotes cell survival. While the depletion of METTL3 delays cancer progression, as it leads to differentiation, apoptosis, and cell cycle arrest.[146,147] Beyond its canonical role in methylation, the methyltransferase-independent functions of cytoplasmic METTL3 also have been implicated in the progression of lung cancer, gastric cancer, and ovarian cancer by boosting the translation of oncogenes and epigenetic factors.[106,107,148]

Structurally, METTL3 belongs to the class I of methyltransferases, with the typical Rossmann fold in the methyltransferase domain (MTD) located at the C-terminus (Figure 3A).[93,149] The cofactor SAM binds near a conserved Asp–Pro–Pro–Trp (DPPW) motif and is coordinated by a hydrogen bond system formed by eleven residues in total (Figure 3B). Specifically, the adenine moiety of SAM interacts with the side chain of Asp377 and the main chain of Ile378,

while the hydroxyl groups of the ribose form hydrogen bonds with Gln550, Asn549, and Arg536. The methionine moiety interacts directly with Asp395, Lys513, His538, and Asn539, and indirectly with Glu532 and Leu533 through water-mediated interactions.[95] At the N-terminus of METTL3, a zinc finger domain facilitates binding of the RNA substrate, which is predicted to occur in a positively charged groove at the interface between METTL3 and METTL14.[93,149] The transfer of the electrophilic methyl group from SAM to the nucleophilic N^6 of the adenosine in the RNA substrate proceeds via a bimolecular nucleophilic substitution (S_N2) mechanism, without prior deprotonation of the adenosine-N^6. During the methylation reaction, the N^6 is stabilized by the backbone carbonyl of Pro369 and the side chain of Asp395, which forms an ionic bond with Lys513 (Figure 3C).[150]

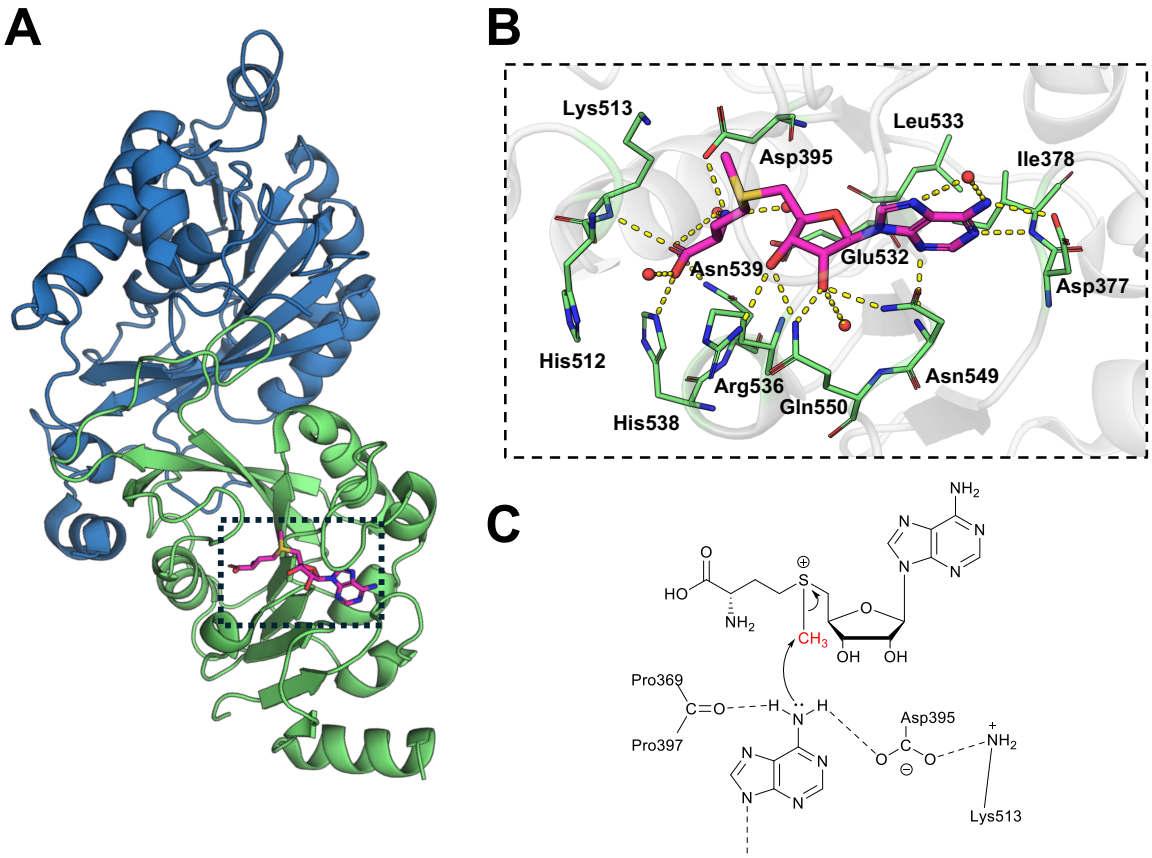


Figure 3: Overall structure, *S*-adenosyl-L-methionine (SAM) binding mode, and catalytic mechanism of the methyltransferase-like protein (METTL)3/14 dimer**. A** The dimer consisting of METTL14 (blue) and METTL3 (green) with cofactor SAM (pink) bound (PDB 5IL1[95]). **B** SAM binding mode in the METTL3 binding site, the METTL3 enzyme is shown as a cartoon (white), selected residues are labeled and shown in stick form (green), polar interactions are shown as dashed lines (yellow), and water as spheres (red). **C** Proposed[150] mechanism of the methyl transfer reaction catalyzed by METTL3. The figure was created with Microsoft PowerPoint, ChemDraw, and PyMOL.

METTL3 represents an attractive therapeutic target due to the involvement in several diseases, and has sparked widespread efforts to develop small-molecule inhibitors. In the scope of this thesis, only some of the most relevant and promising candidates will be discussed, while a

more detailed overview can be found elsewhere.[110,113,151] The first inhibitors discovered for METTL3, identified through a virtual screening, were adenosine and other nucleoside derivatives. However, their affinity was only moderate, with the most promising candidates showing activity in the low micromolar range.[152]

The first non-nucleoside METTL3 inhibitor, UZH1a, was discovered through virtual screening, and a derivative of this compound was further optimized into the first single-digit nanomolar METTL3 inhibitor, UZH2 (Figure 4A). Both UZH compounds exhibited promising cell permeability, selectivity, and m^{6}A level reduction in AML MOLM-13 cells.[153,154] The compounds bind in the SAM-binding pocket of METTL3, with the *N*-methylpyrimidin-4-amine group of UZH2 occupying the same region as the adenosine moiety of SAM and forming polar interactions with Asp377, Ile378, and Asn549. The fluorine atom of the difluorophenyl group engages in a fluorine-π interaction with the nitrogen-containing π-system of Pro397, while the piperidine nitrogen forms a salt bridge with Asp395 in an adjacent region of the binding pocket.

In a high-throughput screening (HTS) of 250,000 diverse drug-like compounds, Storm Therapeutics identified STM1760 as one of only two non-SAM-related hits and optimized it into STM2457 (Figure 4B).[155] The STM compounds bind to the SAM-binding pocket of METTL3, similar to UZH2. In STM2457, the pyridopyrimidone moiety occupies the adenosine region, while the imidazopyridine moiety aligns with the position of the difluorophenyl group in UZH2. Moreover, the secondary amine of STM2457 forms a salt bridge with Asp395, similar to the interaction of the piperidine nitrogen in UZH2 and establishes an additional hydrogen bond with Ser511. While UZH2 and STM2457 possess comparable *in vitro* potency, STM2457 has been more extensively characterized *in vivo*. In various mouse models of AML, STM2457 effectively inhibited leukemia expansion and extended the lifespan of the mice by targeting key stem cell subpopulations of AML.[155] Moreover, STC-15 (Figure 4B), the lead compound of the STM series, has shown promising target engagement and reduction in m^{6}A levels in clinical trials.[90,156] Additionally, the compound has recently entered a study testing combination therapy with the PD-1 inhibitor Toripalimab in patients with advanced cancers.[157]

The biotech company Epics Therapeutics utilized structural information from these previous inhibitors in a ligand-based drug design (LBDD) and an *in silico* modelling approach to identify an initial hit compound with already high METTL3 affinity which was further optimized in a structure–activity relationship (SAR) study to yield the promising inhibitor EP652 (Figure 4C). This compound demonstrated more potent inhibition of AML cell-line viability and reduction of m^{6}A levels in AML cell lines compared to STC-15. The compound also prolonged survival while inhibiting cancer progression in AML mouse models. However, factors such as oral availability still need to be optimized.[158]

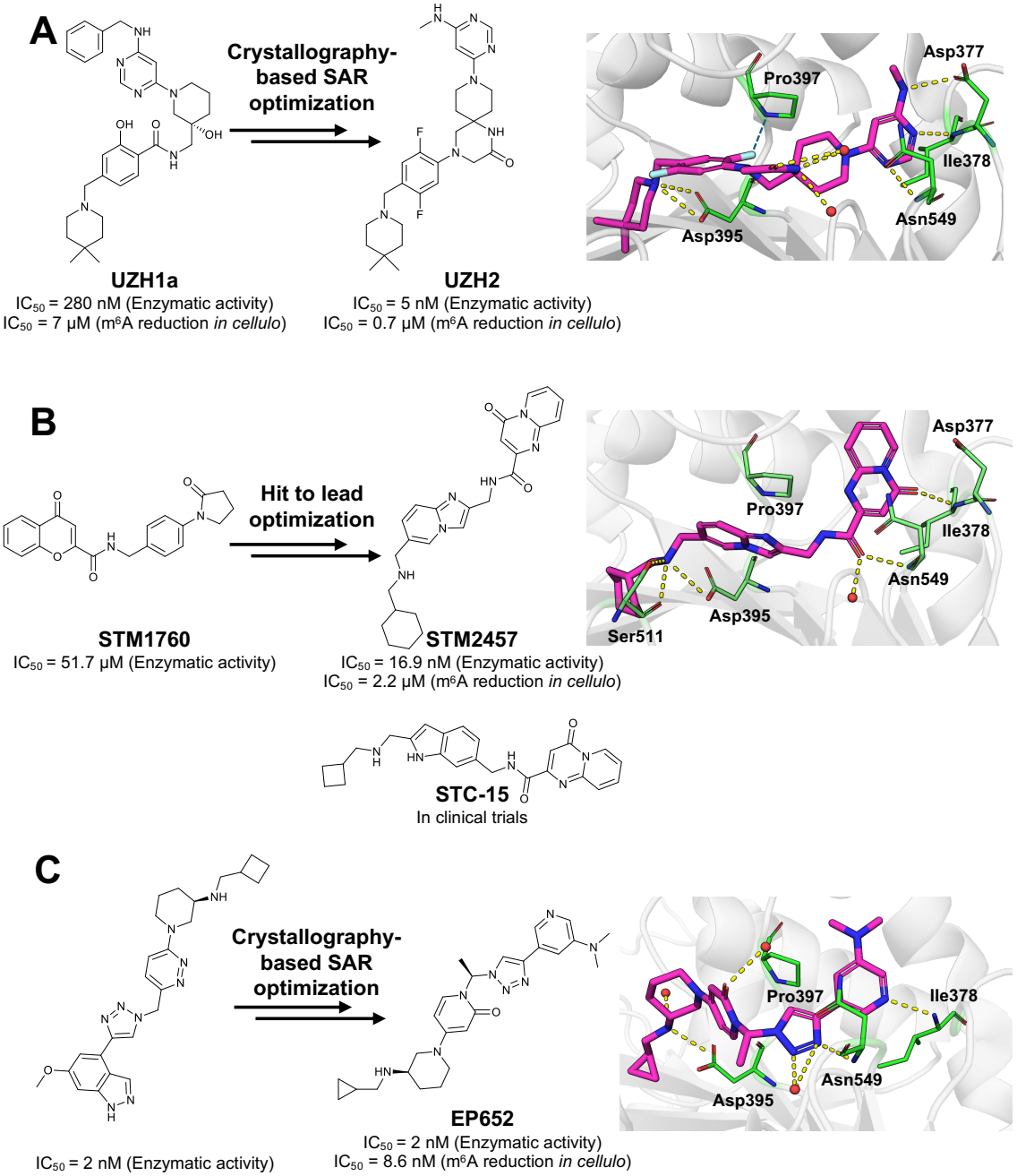


Figure 4: Development and binding mode of potent Methyltransferase-like protein 3 (METTL3) inhibitors. **A** Development of UZH2 (PDB: 7O2F[154]). Half-maximal inhibitory concentration (IC_{50}) values of the METTL3 enzymatic inhibitory activity were determined using a time-resolved fluorescence energy transfer (TR-FRET) assay and m^6A reduction was tested in MOLM-13 cells.[153,154] **B** Development of STM2457 (PDB:7O2I[155]) and STC-15[90,156]. IC_{50} values of the enzymatic inhibitory activity were determined using a RapidFire mass spectrometry methyltransferase assay and m^6A reduction was tested in MOLM-13 cells.[155] **C** Development of EP652 (PDB: 9G4S[158]). IC_{50} values of the enzymatic inhibitory activity were determined using a scintillation proximity assay (SPA) and m^6A reduction was tested in Calu6 cells.[158] Compounds were drawn with ChemDraw or shown in PyMOL as stick form (pink), METTL3 is shown as cartoon (white), selected residues are labeled and shown in stick form (green), polar interactions (yellow) and fluorine-π interactions (light blue) are shown as dashed lines, and water as spheres (red). Further abbreviations: SAR (structure–activity relationship).

In summary, the development of METTL3 inhibitors has progressed from low-affinity nucleoside analogues to potent, selective, and cell-permeable non-nucleoside compounds. One candidate even advanced into clinical evaluation, thereby underscoring the therapeutic potential of METTL3 inhibition in cancer. Despite these developments, limitations remain. There is often a discrepancy between biochemical inhibition and the reduction of m^6A levels in cells, possibly reflecting the high intracellular availability of SAM (Figure 4). Moreover, the non-catalytic functions of METTL3, which also play a role in different cancers, as described above, cannot be addressed by current inhibitors. This highlights the further need to develop alternative strategies to address this highly relevant target.

1.1.3 tRNA m^1G37 Methyltransferase (TrmD)

While METTL3 highlights the therapeutic potential of targeting human RNA MTases in oncology, bacterial RNA MTases represent attractive targets for antibacterial drug discovery. One prominent example is TrmD, which catalyzes the methylation of the N^1-position of guanosine 37 in tRNAs in a variety of bacteria and is a defining member of the unique class IV of methyltransferases.[159,160]

TrmD catalyzes the m^1G37 modification in G36 and G37-containing tRNAs, including all three proline tRNA isoacceptors, the GAG and CAG leucine tRNA isoacceptors, and the CCG arginine tRNA isoacceptor.[161–164] The modification is introduced post-transcriptionally and is essential for maintaining the translational reading frame accuracy in bacteria. Located on the 3′ side of the anticodon, its absence can cause frameshift errors during protein synthesis, resulting in truncated, misfolded, and inactive proteins that are detrimental to cell survival.[161,165–167] Additionally, it has been proposed that growth defects in TrmD mutants can also be attributed to a lack of aminoacylation in m^1G37-unmodified tRNAs.[168] The trmD gene is highly conserved across bacteria, and its essentiality for growth has been demonstrated in phylogenetically diverse species.[161,169–172] Hence, TrmD has long been proposed as a potential antibiotic target.[173] Moreover, in eukaryotes and archaea, the Rossmann-fold tRNA methyltransferase 5 (Trm5) introduces the m^1G37 modification.[161,174] This enzyme differs from TrmD in structure, phylogeny, and catalytic mechanism, indicating that TrmD inhibition could be bacterial-specific and off-target effects on eukaryotic hosts could be minimized.[175–177] Novel ways to target pathogens are desperately needed, as it has been predicted that over 91 million people could die from antibiotic-resistant infections between 2025 and 2050, if no new antibiotics are developed.[178] Structurally, the TrmD enzyme consists of two distinct domains connected by a flexible linker. The N-terminal domain contains the SAM-binding pocket, whereas the C-terminal domain mediates tRNA binding (Figure 5A).[51,164,179]

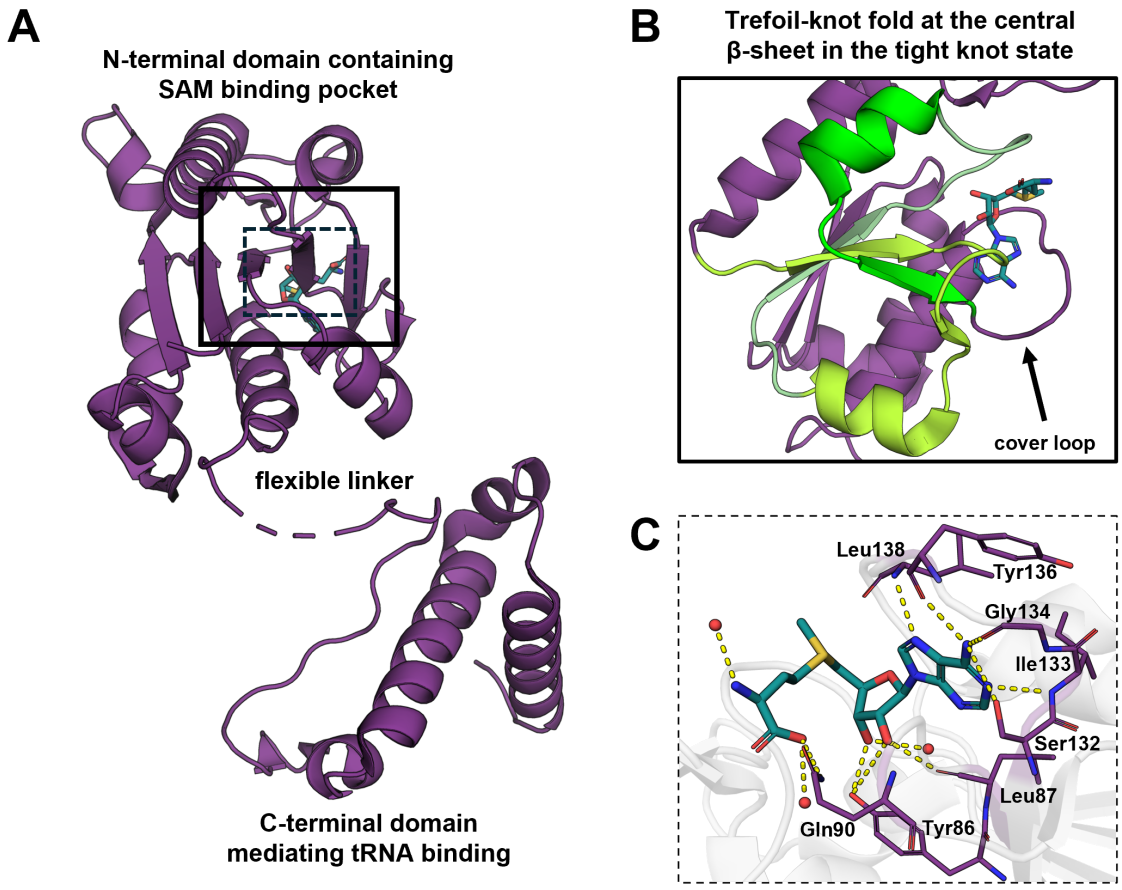


Figure 5: Monomer structure and *S*-adenosyl-L-methionine (SAM)-binding site of the tRNA m^1G37 methyltransferase (TrmD, PDB: 1UAK[51]). Note: the structure is depicted for *Haemophilus influenzae* TrmD; amino-acid numbering may vary in other bacteria. **A** TrmD monomer in complex with SAM, showing the C-and N-terminal domains, connected by a flexible linker. **B** Trefoil-knot structure of the SAM-binding site, with SAM bound in its characteristic bent shape. The three β-sheets forming the knot are highlighted in different shades of green. **C** SAM-binding mode in the monomeric TrmD binding site. TrmD is depicted as a cartoon (white), selected residues are labeled and shown in stick form (purple), SAM is shown in stick form (teal), polar interactions are indicated by dashed lines (yellow), and water molecules are shown as spheres (red). The figure was created with Microsoft PowerPoint and PyMOL.

Multiple sequence alignments of TrmD proteins from various bacterial groups have revealed three highly conserved motifs (A, B, and C) in the active and SAM-binding sites. However, in motif A, the first three amino acids show significant variability, indicating some binding specificity between different bacteria.[160] SAM binds in a deep cleft of a trefoil-knot fold, consisting of three β-strands at a central β-sheet (Figure 5B).[164] This knot structure leads to binding of SAM in an unique bent conformation, essential for methyltransferase activity.[51,180] TrmD binds SAM only in the loose-knot state, in which a cover loop within the trefoil knot moves to accommodate the adenine moiety and then flips back upon binding to retighten the knot (tight-knot state).[164] SAM binding was first described for the TrmD enzyme of *Haemophilus influenzae* (*H. inf.*), where the adenosine moiety forms hydrogen bonds with Ser132 (amino acid enumeration may vary in other bacteria), Ile133, Glu134, Tyr136, and Leu138.

The hydroxyl groups of the ribose form hydrogen bonds with Tyr86 and Leu87, while the methionine moiety, facing toward the adenosine, interacts with Gln90 (Figure 5C).[51]

TrmD is only catalytically functional as a dimer, while each monomer can bind SAM individually; only one tRNA is bound in the active site between the N-terminal domain of subunit A and the C-terminal domain of subunit B (Figure 6A). In the dimer, the methionine moiety of the SAM bound to chain A, additionally interacts with Asp177 and Ser170 from chain B (Figure 6B). Moreover, SAM recognition induces the side chain of Phe171 in chain B to insert between the C-terminal domain of subunit B and the N-terminal domain of subunit A. This causes the C-terminal domain to adopt the tRNA-binding conformation. During the catalytic mechanism, first described for the *Escherichia coli* (*E. coli)* TrmD isoenzyme, Mg^{2+} is required (Figure 6C).[179,181]

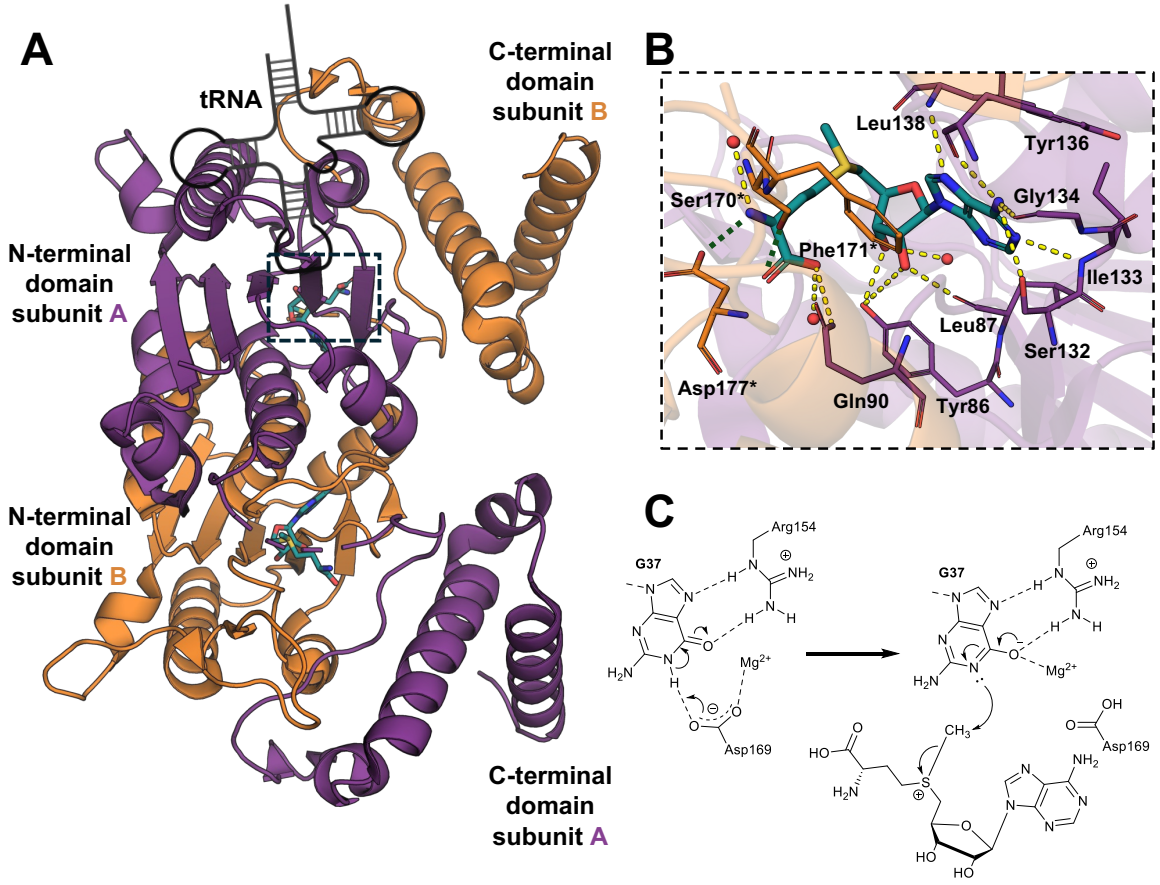


Figure 6: Catalytic activity of the tRNA m^1G37 methyltransferase (TrmD, PDB:1UAK[51]). **A** TrmD in the catalytically active dimeric form, complexed with *S*-adenosyl-L-methionine (SAM) and a transfer ribonucleic acid (tRNA, simplified depiction, not part of the PDB crystal structure). Subunit A is shown in purple and subunit B in orange. **B** SAM binding in the dimeric complex. TrmD is shown as a cartoon (purple subunit A and orange subunit B), selected residues are labeled (residues from subunit B are marked with *) and shown in stick form, SAM is shown in stick form (teal) polar interactions are indicated by dashed lines (yellow subunit A, green subunit B), and water molecules as spheres (red). **C** Proposed[181] mechanism of the methyl transfer reaction catalyzed by TrmD. The figure was created with Microsoft PowerPoint, ChemDraw, and PyMOL.

Asp169, oriented by Mg^{2+}, deprotonates the N^1 of G37, generating a negative charge on O^6 that is stabilized by Mg^{2+} and the side chain of Arg154. The deprotonated N^1 then performs a nucleophilic attack on the methyl group, substituting the sulfonium of SAM. After the methyl transfer, m^1G37-tRNA and SAH are released from the active site, and TrmD returns to the loose-knot state.[164,181]

Given its essential and bacteria-specific role, drug development campaigns against several pathogenic bacteria have focused on identifying novel small-molecule inhibitors of TrmD (Figure 7 and Figure 8).[76,182–186] One of the first studies developing TrmD inhibitors targeted the gram-negative *H. inf.* bacteria, which is associated with a range of infections, including pneumonia, meningitis, and chronic obstructive pulmonary disease (COPD) in adults.[187–189] Several hits for *H. inf.* TrmD were identified by screening of an AstraZeneca fragment collection of 14,000 compounds. Structure-guided optimization of one of those hits led to the development of compound 38 (numbering according to the original study by Hill *et al*.[182]), a potent inhibitor of multiple Gram-negative TrmD isoenzymes (Figure 7A). The thienopyrimidone ring system of this inhibitor occupies the adenine sub-pocket of the SAM-binding site, interacting with Ile133, Tyr136, and Leu138. However, the ring is rotated approximately 90° relative to the adenine ring of SAM. The phenyl moiety of compound 38 occupies the ribose-binding sub-pocket, with the connected amine group forming a hydrogen bond with Glu116. Additionally, the imidazole ring mimics the methionine moiety of SAM by interacting with Asp177 of the opposing TrmD subunit B. Moreover, the authors proposed that a hydrogen bond with Asp169 of subunit B helps to stabilize this flexible region. These interactions mimic structural changes observed during the m^1G37 methylation process, revealing important SAR information. However, despite promising inhibitory activity against a panel of TrmD isoenzymes, the compounds tested in this study showed little or no antibacterial activity.

Subsequently, in an independent study, AZ51 (a potent thienopyrimidinone derivative from the Hill *et al*.[182] series) was co-crystallized with *Pseudomonas aeruginosa* and *Mycobacterium tuberculosis* TrmD.[183] In *Pseudomonas aeruginosa* only, a previously unreported active-site conformational change was observed: while AZ51 binds similarly to other thienopyrimidinones, its piperidine moiety adopts a different orientation, forming an additional polar interaction with Glu121(Figure 7B). Binding of AZ51 induces a 180° flip of the aromatic side chain of Tyr120, which prevents tRNA binding and may explain the high inhibitory potency. Next, the thienopyrimidinone scaffold was further optimized in a structure-based design campaign guided by the crystal structures from *Pseudomonas aeruginosa* and *Mycobacterium tuberculosis* TrmD.

The newly developed thienopyrimidinone derivatives showed nanomolar TrmD binding, tRNA-competitive binding, and micromolar antimicrobial activity against gram-positive and gram-negative bacteria as well as mycobacteria. However, a disconnect between the potency of TrmD binding and antibacterial activity remained (Figure 7B).

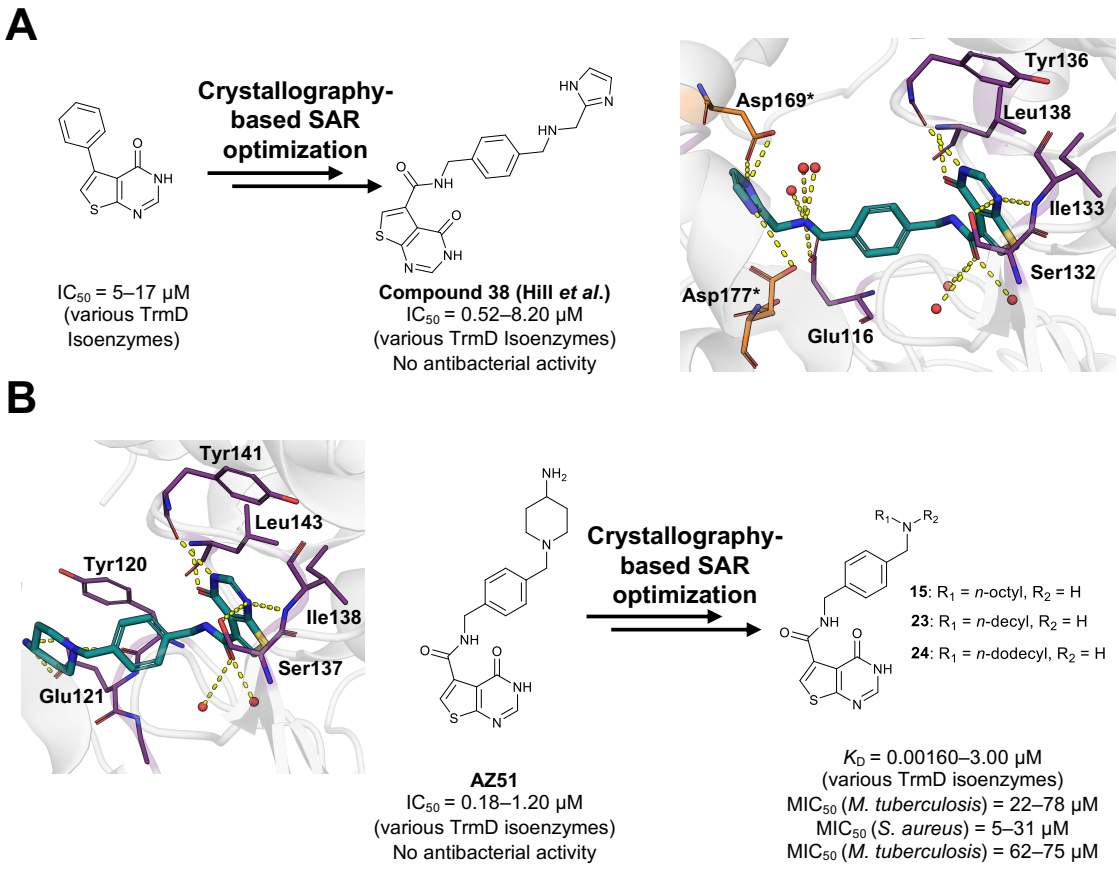
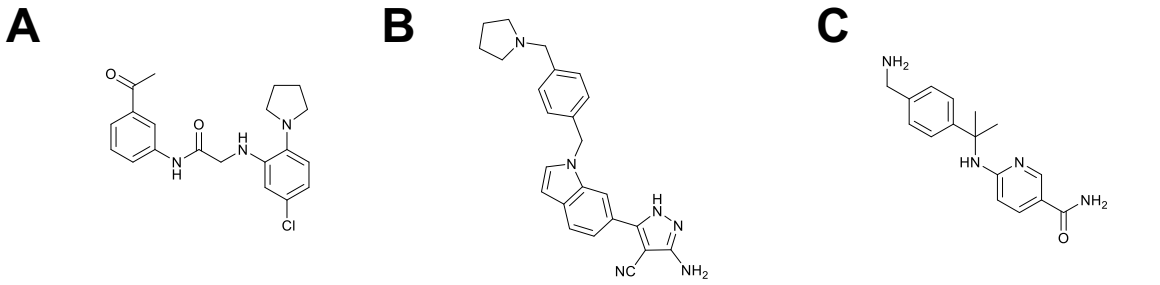


Figure 7: Development and binding mode of potent tRNA m^1G37 methyltransferase (TrmD) inhibitors. **A** Compound 38 binding to *Haemophilus influenzae* TrmD (numbering according to the original study by Hill *et al.*[182], PDB: 4MCB[182]). Half-maximal inhibitory concentration (IC_{50}) values of the TrmD enzymatic inhibitory activity were determined using a scintillation proximity assay (SPA)[182]. **B** Compounds AZ51[182] binding to *Pseudomonas aeruginosa* TrmD (PDB: 6JOE[183]) and 15, 23, and 24 (numbering according to the original study by Zhong *et al.*[183]). IC_{50} values of the TrmD enzymatic inhibitory activity were determined using SPA[182] and the dissociation constants (K_D) for binding to TrmD were determined by surface plasmon resonance (SPR)[183]. Minimum inhibitory concentrations (MIC) were determined against different bacterial strains and are therefore given as ranges. Compounds were drawn with ChemDraw or shown in PyMOL as stick form (tile), TrmD is shown as cartoon (white), selected residues are labeled (residues from subunit B are marked with *) and shown in stick form (purple subunit A and orange subunit B), polar interactions are shown as dashed lines (yellow), and water as spheres (red). Further abbreviations: SAR (structure–activity relationship).

Several other screenings against gram-negative and positive pathogens led to the development of new SAM competitive and non-competitive lead structures and inhibitor classes, with promising micro– nanomolar target affinities (Figure 8). However, like the studies previously mentioned, these compounds frequently failed to translate into efficient antibacterial activity.[76,184–186]



Compound 52 (Zhong *et al.*)
IC_{50} = 4.7 µM in *Pa* TrmD
SAM uncompetitive
MIC_{50} = 23–60 µM
(in various bacterial strains)

Compound 29a (Whitehouse *et al.*)
K_D = 27 nM in *Mab* TrmD
SAM competitive
MIC_{50} (*Mab*) = 50.0 µM
MIC_{50} (*Mtb*) = 12.5 µM

Compound 23 (Wilkinson *et al.*)
IC_{50} = 9 nM in *Mab* TrmD
SAM competitive
MIC_{50} = 256 – >1024 µg/mL
(in various bacterial strains)

Figure 8: Representative literature-known tRNA m^1G37 methyltransferase (TrmD) inhibitors tested against a variety of bacterial strains. **A** Compound 52 (numbering according to the original study by Zhong *et al.*[76]). Half-maximal inhibitory concentration (IC_{50}) values of the enzymatic inhibitory activity against *Pseudomonas aeruginosa* (*Pa*) TrmD were determined by bioluminescent detection of *S*-adenosyl-L-homocysteine (SAH) production[76]. **B** Compound 29a (numbering according to the original study by Whitehouse *et al.*[184]). The dissociation constants (K_D) for binding to *Mycobacterium abscessus (Mab)* TrmD were determined by isothermal titration calorimetry (ITC)[184,185]. **C** Compound 23 (numbering according to the original study by Wilkinson *et al.*[186]). IC_{50} values of the enzymatic inhibitory activity against *Mab* TrmD were determined using an MTase-Glo™ Methyltransferase Assay kit (Promega, WI, USA)[186]. Minimum inhibitory concentrations (MIC) were determined against different bacterial strains.

This gap between potent TrmD inhibition and cellular effects for most TrmD inhibitors is presumably due to poor penetration of the bacterial cell wall. Functional groups that enhance binding affinity, such as dibasic or otherwise charged moieties, often reduce cell wall permeability.[182,183,190] This highlights drug permeability as a major challenge in TrmD inhibitor development. A further shortcoming of current TrmD-focused drug discovery is the lack of investigation on the gram-positive pathogen *Staphylococcus aureus* (*S. aureus*). This organism causes a spectrum of clinical infections ranging from pneumonia and infective endocarditis to sepsis, and it has become a leading cause of antibiotic-associated mortality.[191–193] Deaths attributed to methicillin-resistant *S. aureus* (MRSA), compared to other pathogens, have risen the most in the past 20 years with 130,000 deaths globally in 2021 alone.[178] Despite this urgent need, no inhibitors have been specifically developed against *S. aureus* TrmD, and only a handful of studies have tested inhibitors in this context. Together with the unresolved permeability issues, this shows that TrmD-targeted drug discovery is still in its infancy. Innovative strategies are still required to expand the inhibitor space and translate TrmD inhibition into clinically effective antibacterial agents.

1.1.4 DNA Methyltransferase 2 (DNMT2)

Similarly to TrmD, for certain human methyltransferases, drug development is still at an early stage. One such example is the DNA Methyltransferase 2 (DNMT2), which catalyzes the m^5C modification at the C38 position of tRNA, near the anticodon loop.[194] DNMT2 is often described as an enigmatic enzyme, as many aspects remain unclear or are controversially discussed, including its substrates (other than tRNA), localization, and cellular functions. Among its best-established substrates is the GUC aspartate tRNA isoacceptor.[194] Other RNA substrates of DNMT2 include the GCC glycine, U/CUC glutamate, and A/CAC valine tRNA isoacceptors, which, however, have only been identified in certain species.[195–199] The proposed consensus motif recognized by DNMT2 is a conserved CUXXCAC sequence in the anticodon loop.[196] Interestingly, due to structural similarities to DNA methyltransferases, DNMT2 was initially thought to methylate DNA rather than RNA.[200,201] However, it remains unclear whether DNMT2 possesses DNA methyltransferase activity. The activity is low or undetectable in several organisms, although some studies suggest a contribution of DNMT2 to DNA methylation in specific species.[194,195,202–209] Furthermore, a role for DNMT2 in mRNA and small non-coding RNA (sncRNA) modification has been described in several studies.[210–213] Localization of DNMT2 has been observed both in the nucleus and cytoplasm in different organisms.[214,215]

Although the full spectrum of DNMT2's biological functions is not yet fully understood, a variety of roles have been proposed.[216] For example, the enzyme influences protein translation. It has been demonstrated that DNMT2 prevents specific codon mistranslation, as the C38 modification near the anticodon loop aids discrimination of near-cognate codons.[217] Additionally, DNMT2 influences RNA stability, as the methylation it introduces protects tRNAs against stress-induced ribonuclease cleavage.[198] Furthermore, a double knockout of DNMT2 and NOP2/Sun RNA methyltransferase 2 (NSun2), another m^5C tRNA MTase, has been shown to reduce overall protein synthesis, and an influence on RNA stability was further demonstrated.[218] In addition to its roles in cellular processes, DNMT2 has been implicated in various diseases. In glioblastoma cells, DNMT2 knockdown resulted in loss of DNMT1 levels and activity, leading to decreased DNA methylation levels, which might affect cancer cell fate.[219] Moreover, DNMT2 has been demonstrated to influence the sensitivity of cancer cells to radiotherapy and poly [ADP-ribose] polymerase (PARP) inhibitors by influencing DNA damage repair.[213] Furthermore, knockdown of DNMT2 can sensitize cancer cells to apoptosis induced by doxorubicin-triggered ER stress.[220] These examples highlight the role of DNMT2 as a potential target in cancer treatment and as a diagnostic marker.[221] DNMT2 has also been considered a possible target for preventing and regulating viral diseases, showing antiviral and proviral effects in viruses like *Drosophila* C virus and human immunodeficiency virus 1 (HIV-1)

in different hosts.[216,222,223] Furthermore, DNMT2 has been proposed as part of a defense mechanism against viral infection due to its involvement in the cellular stress response, interacting with several stress-related proteins and relocalizing from the nucleus to cytoplasmic stress granules.[224]

To date, only a few crystal structures of DNMT2 have been solved, including only one human DNMT2 structure bound to SAH and no structure co-crystallized with an RNA substrate.[225–228] Nevertheless, these structures reveal important insights into the overall architecture, cofactor binding, and catalytic mechanism of DNMT2. The enzyme consists solely of a catalytic domain, containing the characteristic motifs I to X of DNA cytosine methyltransferases. SAM is bound via a Rossmann fold, classifying DNMT2 as a class I MTase. The overall structure of the enzyme can be divided into three parts: a large domain and a small domain, each consisting of several β-strands and α-helices, and a hinge region comprising two α-helices (Figure 9A). The cofactor-binding pocket, located in the large domain, involves motifs I and X and a few residues from motifs II–V.[227,228] The adenine moiety of SAH forms polar interactions with Val35, Ile57, Glu58, and a water molecule, while the ribose moiety interacts solely with the side chain of Asp34 and two water molecules. The methionine moiety interacts with Val13, Gly15, Ser76, Ser376, and several water molecules (Figure 9B). During the catalytic methyl group transfer, due to its electron-deficient character, the 5-position of cytosine needs to be activated by the enzyme (Figure 9C).[229] The catalytic Cys79, part of a characteristic Pro-Cys-Gln (PCQ) sequence in motif IV, covalently attaches to position 6 of the cytosine.[230] This leads to an electron shift and activation of the 5-position, aided by protonation of the N^3 nitrogen by Glu119 embedded in a characteristic Glu-Asn-Val (ENV) motif, within motif IV. The resulting protein–RNA complex abstracts the SAM methyl group in a nucleophilic attack. The aromaticity of cytosine is restored after base-catalyzed deprotonation of the 5-position, leading to the breakdown of the covalent bond between RNA and protein, and the release of the methylated tRNA and SAH (Figure 9C).[195,230] The exact binding mode of tRNA has not been determined structurally yet, and has only been modelled, but a surface cleft containing eight basic residues essential for the binding of the GUC aspartate tRNA isoacceptor has been identified.[194,231]

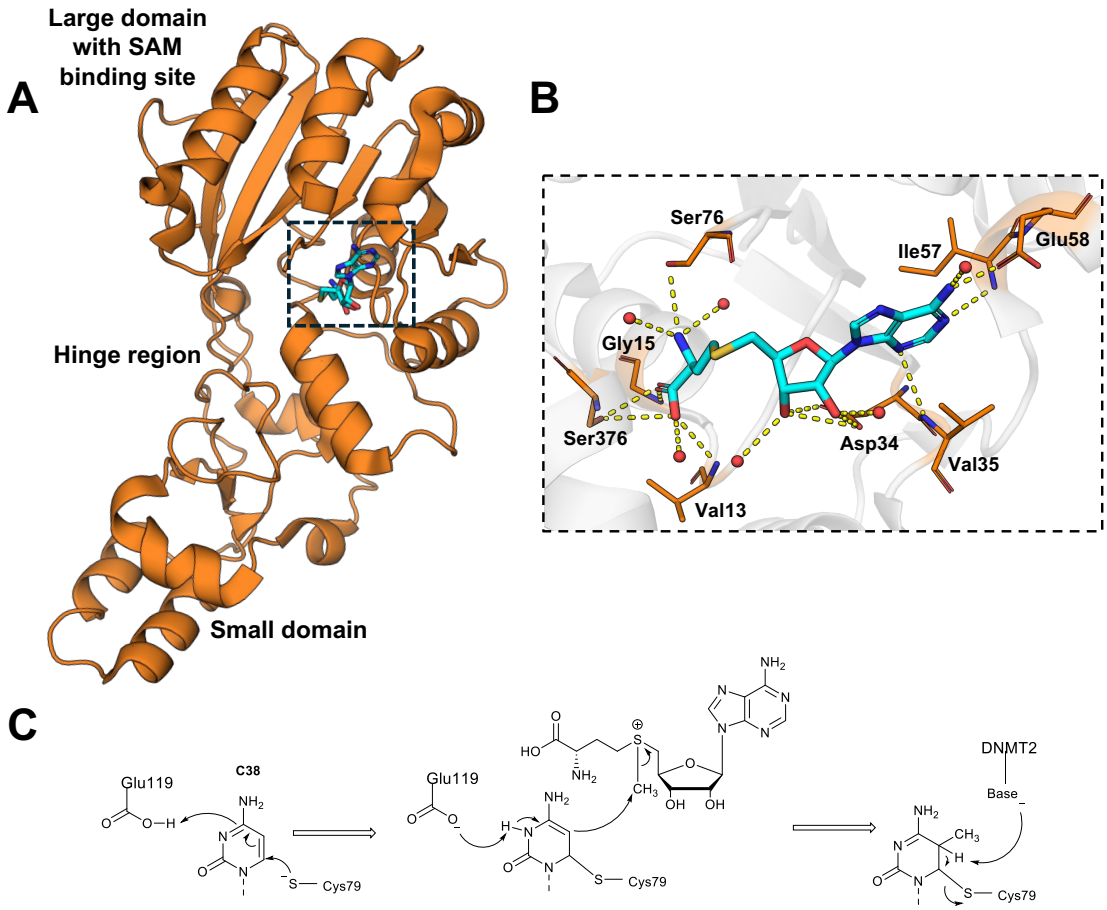


Figure 9: Structure and catalytic mechanism of DNA methyltransferase 2 (DNMT2). **A** Structure of human DNMT2 (orange, PDB: 1G55[228]) in complex with cofactor *S*-adenosyl-L-homocysteine (SAH, cyan). **B** SAH binding mode in the DNMT2 binding site, SAH is shown in stick form (cyan), DNMT2 is shown as a cartoon (white), selected residues are labeled and shown in stick form (orange), polar interactions are shown as dashed lines (yellow), and water as spheres (red). **C** Mechanism[230] of the methyl transfer reaction catalyzed by DNMT2. The figure was created with Microsoft PowerPoint, ChemDraw, and PyMOL.

Due to the potential of modulating a variety of pathological processes by targeting DNMT2, this enzyme is an interesting target for drug development. However, only a few campaigns have developed inhibitors for this enzyme so far, mostly derivatives of the substrate or co-factor. The cytosine analogue azacytidine can bind DNMT2 covalently and suppress aspartate tRNA methylation in human cancer cell lines by being incorporated into RNA.[232,233] Azacytidine, developed for epigenetic cancer therapy, is used in the treatment of leukemia and myelodysplastic syndrome.[234] However, as a general methyltransferase inhibitor, the drug also inhibits other MTases like NSun2.[232,235] Similarly, the pan-MTase inhibitors SAH and sinefungin also inhibit DNMT2 unselectively (Figure 10A,B).

SAH has been derivatized in several studies to develop more effective and selective inhibitors (Figure 10).[236–238] The first approach was to synthesize transition–state analogues based on a 5-methylcytosine-adenosine but, these compounds showed only low activity against DNMT2 (Figure 10C).[237] By systematic side-chain variation of the SAH methionine moiety, Y-shaped

inhibitors based on the structure of *N*-adenosyl-2,4-diaminobutyric acid were developed, showing similar potencies as SAH and SFG (Figure 10D). However, the compounds failed to effectively reduce m^5C levels in HEK-293 cells, probably due to low cell permeability.[236] Through decoration with warheads and selectivity adjustments, these inhibitors were further optimized and confirmed to covalently bind the catalytic Cys79. While the compounds showed stronger inhibition, the reduction of m^5C levels or permeability was not evaluated (Figure 10E).[238] All in all, the SAH-based compounds displayed promising target affinities and some selectivity over a selection of MTases; however, methyltransferasome-wide selectivity was not tested. The development of a dedicated, selective, and cell-active DNMT2 inhibitor still remains a goal and might be achieved by identifying new chemotypes distinct from SAH.

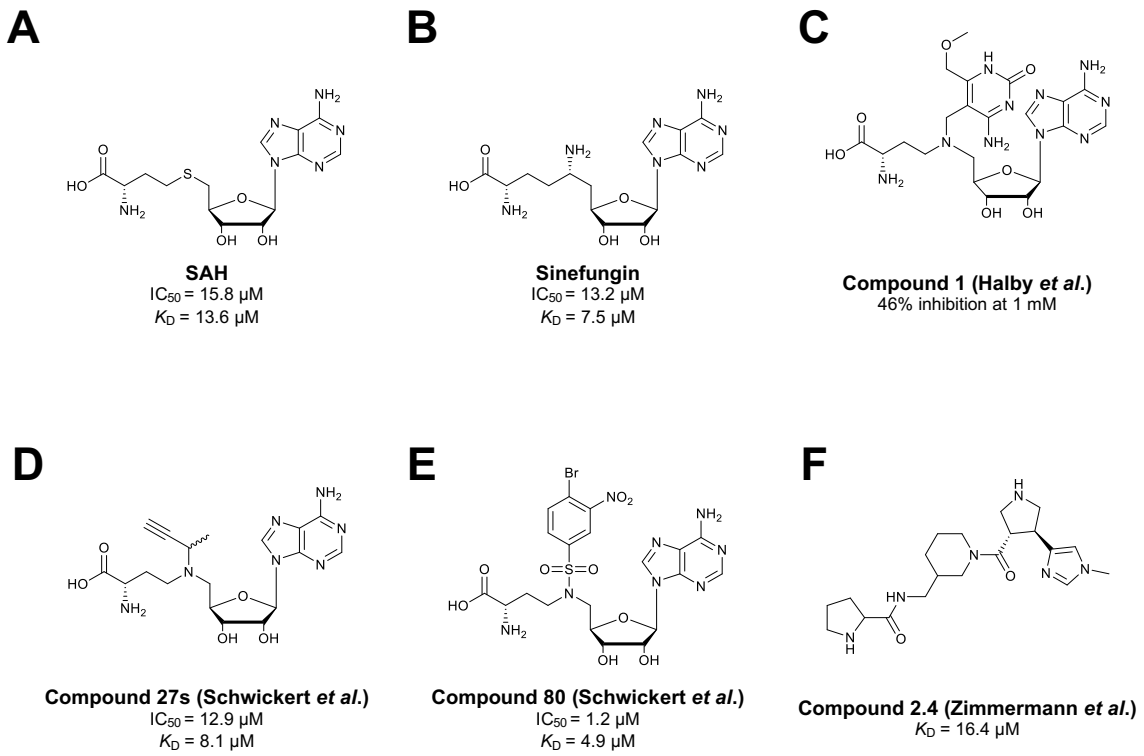


Figure 10: Representative literature-known DNA methyltransferase 2 (DNMT2) inhibitors. **A,B** *S*-adenosyl-L-homocysteine (SAH) and sinefungin. Values determined by Schickert *et al.*[236] IC_{50} value was determined by tritium incorporation assay, and the dissociation constant (K_D) was determined by ITC.[236] **C** Compound 1 (numbering according to the original study by Halby *et al.*[237]). % of inhibition was determined tritium incorporation assay.[237] **D** Compound 27s (numbering according to the original study by Schickert *et al.*[236]). **E** Compound 80 (numbering according to the original study by Schickert *et al.*[238]). IC_{50} value was determined by tritium incorporation assay. K_D value was determined by ITC.[238] **F** compound 2.4 (numbering according to the original study by Zimmermann *et al.*[239]) K_D was determined by Microscale thermophoresis (MST).[239] The figure was created with Microsoft Powerpoint and ChemDraw.

An initial attempt to discover alternative chemotypes was made in a virtual screening. While the hits displayed only moderate binding affinities and were not further tested in cells, they have the potential to serve as starting points in future hit-to-lead optimizations (Figure 10F).[239] Moreover, identifying binders, even outside the active site, that can be developed into chemical probes could greatly aid further analysis of the enigmatic DNMT2 protein.

1.2 New Modalities in Drug Discovery

1.2.1 Proteolysis Targeting Chimeras (PROTACs)

Targeted protein degradation (TPD) has emerged as a new modality over the past 30 years.[240–243] Early examples of protein degraders are selective estrogen receptor degraders (SERDs), which induce proteasomal degradation of the estrogen receptor (ER). SERDs are used to treat ER^+ breast cancer, for example Fulvestrant has been FDA-approved since 2002.[244,245] Building on the concept of pharmacological protein degradation, the first proteolysis-targeting chimera (PROTAC) was described in 2001. PROTACs are heterobifunctional molecules designed to bring a protein of interest (POI) and a ubiquitin ligase (E3) into proximity, leading to the POI's degradation.[246] E3 ligases are part of the ubiquitin–proteasome system (UPS), a mechanism controlling various cellular processes by specific protein degradation. First, ubiquitin, a small regulatory protein, is covalently attached to the target protein by a cascade of enzymes. Ubiquitin-activating enzymes (E1) activate ubiquitin, and ubiquitin-conjugating enzymes (E2) transfer the activated ubiquitin to the protein substrate. E3 ligases finally catalyze the transfer of ubiquitin to the target's N-terminus or ε-NH_2 groups of internal lysine residues, after which a polyubiquitin chain is formed. Next, the polyubiquitinated target is degraded by the 26S proteasome.[247,248] The revolutionary concept of hijacking this UPS to selectively degrade disease-relevant proteins quickly gained interest in academia and industry, as it is poised to target proteins previously deemed undruggable.[240–243] Major milestones in PROTAC development include the identification of small-molecule E3 ligands in 2008, the first *in vivo* proof concept in 2013, the first crystal structure of a ternary POI–PROTAC–E3 complex in 2017, and the first PROTAC entering clinical trials in 2019.[241,249–251]

This rapid and successful development sparked the design of numerous other TPD techniques.[252–254] Some of them also exploit the UPS, such as molecular glues, which are small-molecules that can modulate protein–protein interactions between E3 ligases and the POI.[255,256] Others use alternative degradation systems, e.g., lysosome-targeting chimeras (LYTACs), which hijack the endosomal pathway to degrade extracellular and membrane-associated proteins.[257] Moreover, some new degradation techniques focus on targets other than proteins, such as ribonuclease-targeting chimeras (RIBOTACs), which recruit an RNase for targeted RNA degradation.[258] Additionally, PROTACs have inspired the development of another type of heterobifunctional molecule, namely regulated induced proximity-targeting chimeras (RIPTACs). These molecules are designed to link target proteins selectively expressed in cancer cells to proteins essential for cell survival, resulting in suppression of the essential proteins' function and selective cancer cell death.[258] Halda Therapeutics, a company

focused on RIPTAC development, was recently acquired by Johnson & Johnson in a multibillion-dollar deal, further highlighting the high relevance of these techniques in the pharmaceutical industry.[259]

Mechanism of PROTACs

To facilitate efficient degradation, PROTACs must induce spatial proximity between the POI and the E3 ligase by forming a ternary complex. This complex is reversible and dissociates after ubiquitination, leading to a catalytic mechanism where one PROTAC molecule can initiate multiple rounds of POI degradation (Figure 11A).[260] Degradation efficiency is often monitored via immunoblotting and quantified using the maximal level of target degradation (D_{max}) and the half-maximal degradation concentration (DC_{50}) of the PROTACs.[242,243,260] The affinity of the PROTAC to the POI and E3 ligase in a ternary complex might vary from the individual binary affinities between the components, which is referred to as cooperativity of the ternary complex. The first crystal structure of a ternary complex revealed that this cooperativity, which can impact efficiency and selectivity of target degradation, is influenced by the formation of novel protein–protein interactions (PPIs) within the complex.[251] The PROTAC cooperativity can be described by a cooperativity factor (α), which is defined in equation 1 as the ratio of the binary affinity (K_D^{binary}) to the ternary affinity ($K_D^{ternary}$).

$$\alpha = \frac{K_D^{binary}}{K_D^{ternary}} \qquad \text{Equation 1}$$

If the newly formed PPIs stabilize the complex and thus increase its affinity, the cooperativity is positive (α > 1). Conversely, repulsive interactions or steric clashes between the components can reduce affinity, resulting in negative cooperativity (α < 1). Some ternary complexes also exhibit non-cooperative binding (α = 1).[251,261,262] Mathematical models describe ternary complex formation as bell-shaped curves that depend on the concentration of the bridging species, which can be applied to PROTACs (Figure 11B). Initially, the ternary complex concentration increases with rising PROTAC concentration. However, at saturating concentrations, binary complexes are predominantly formed, and the ternary complex concentration decreases.[261,263] This phenomenon is referred to as the ‘hook effect’ and often results in reduced degradation efficiency at higher PROTAC concentrations.[242,264] Positive cooperativity can counteract this phenomenon, since it can influence the amount of ternary complex formed (Figure 11C).[261,263,265] Moreover, studies have demonstrated that cooperativity can counteract low binary affinities, and conversely, that high binary affinity alone is often insufficient to achieve efficient degradation.[266,267] This has led to the proposition that the induction of a stable ternary complex is more important for predicting degrader efficiency than the binary affinity to either the POI or the E3 ligase and needs to be considered during

PROTAC development.[242,243] Consequently, a variety of methods have been developed to measure cooperativity and ternary complex formation. The cooperativity factor can be determined using biophysical techniques traditionally applied to binary affinity measurements, such as isothermal titration calorimetry (ITC), surface plasmon resonance (SPR), and fluorescence polarization (FP),[251,268,269] while the population of the ternary complex can be monitored using assays such as time-resolved fluorescence energy transfer (Tr-FRET), among others.[270,271]

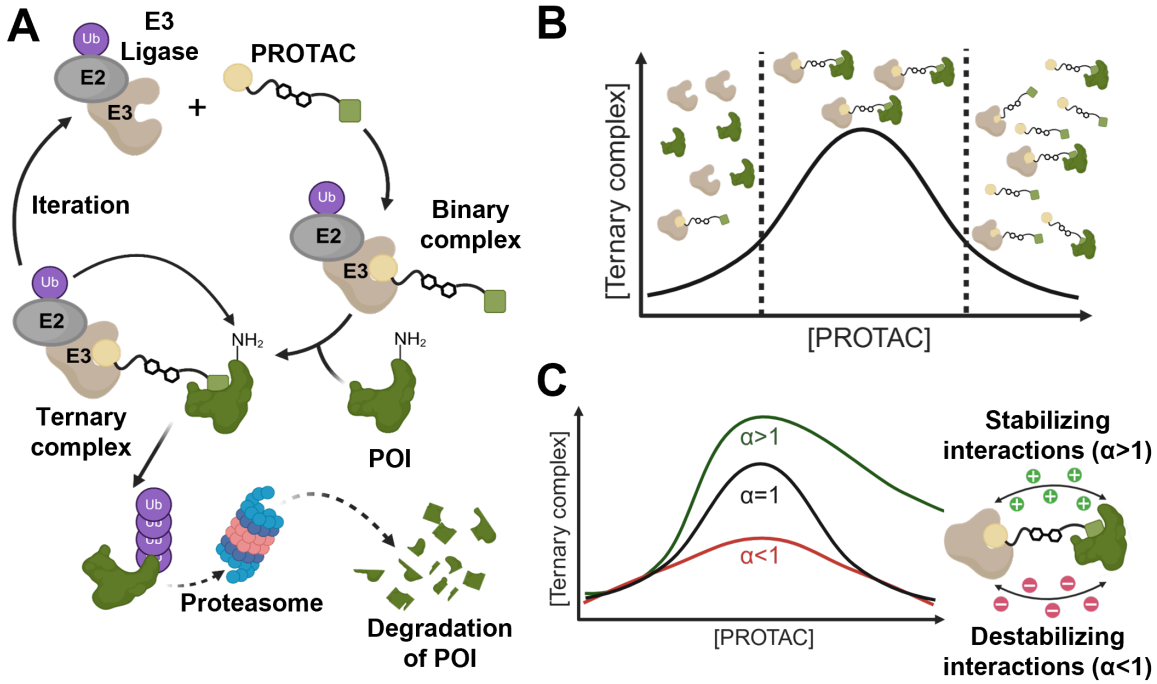


Figure 11: Mechanistic considerations of proteolysis targeting chimeras (PROTACs). **A** PROTAC-mediated degradation of a protein of interest (POI) via the ubiquitin–proteasome system (UPS). **B** Influence of PROTAC concentration on ternary complex formation. **C** Influence of positive (α>1) and negative (α<1) cooperativity on ternary complex formation. The figure was created with Microsoft PowerPoint and Biorender.com.

However, effective degradation in cells is not solely influenced by ternary complex formation, as PROTACs that do not exhibit cooperativity can still lead to effective degradation.[272] Additionally, it has been proposed that multiple ternary complex conformations exist and not all of these conformations lead to productive degradation. Other factors, such as cell-permeability of the PROTAC and accessibility of POI lysins for ubiquitination, are also highly correlated with degradation efficacy.[273–277] Therefore, sufficient ubiquitination induced by the PROTAC is often evaluated during development using methods such as nano bioluminescence resonance energy transfer (nanoBRET) to monitor ubiquitination kinetics.[274] Additionally, it is important to confirm that the POI is degraded via the expected UPS pathway, which can be achieved by competition experiments with different inhibitors of the UPS.[249,278]

Design Considerations for PROTACS

Designing an effective PROTAC involves several challenges. PROTACs are molecules consisting of two binding moieties, one targeting the E3 ligase and the other the POI, connected by a linker. Each component must be optimized specifically to achieve an efficient degrader. Furthermore, some factors that govern the formation of a productive ternary complex remain unclear, complicating structure-based design efforts.

Choosing a suitable E3 ligase ligand is essential in PROTAC design. The human genome encodes over 600 different E3 ligases; however, to date, the vast majority of PROTACs incorporate binders targeting just two E3 ligases, namely von Hippel-Lindau (VHL) and Cereblon (CRBN).[279–281] One key reason is the availability of suitable small-molecule ligands with strong binding affinities, acceptable physicochemical profiles, and structural information available about their binding modes (Figure 12).[282] Early PROTACs often used peptidic E3 ligase ligands. However, peptide-based moieties possess some unfavorable properties for drug development, including low cell permeability and poor metabolic stability.[246,283,284] VHL is a Cullin (CUL) RING ligase and part of the E3 ubiquitin ligase CUL2–RING-box protein 1 (RBX1)–ElonginB–ElonginC–VHL complex.[285–287] The natural substrate of VHL is the transcription factor hypoxia inducible factor 1α (HIF-1α), and the first peptidic PROTACs were based on this substrate.[288] Using co-crystal structure–guided design, several small-molecule VHL ligands with affinities ranging from low micromolar to low nanomolar were developed.[289–293] One prominent example, VH032 (Figure 12A), was employed in the development of the first high-quality, small-molecule PROTACs, representing a major milestone in PROTAC research.[260,290,294]

CRBN is a subunit of the E3 ubiquitin ligase complex CUL4–RBX1–DNA damage-binding protein 1 (DDB1)-CRBN.[295] In 2010, it was discovered that thalidomide, which was famously involved in one of the biggest drug scandals to date due to its strong teratogenicity, binds to CRBN (Figure 12B).[296,297] Thalidomide and its derivatives, such as pomalidomide and lenalidomide, have shown excellent efficacy in the treatment of multiple myeloma.[298–300] However, their mode of action remained unclear until it was discovered that lenalidomide induces the selective degradation of lymphoid transcription factors by functioning as a molecular glue.[301,302] This finding led to the development of potent thalidomide-based PROTACs and established thalidomide-derived degraders as some of the most important in the field.[303,304] One crucial step in the development of thalidomide-based PROTACs was the disclosure of co-crystal structures of CRBN with thalidomide. These structures revealed that part of the phthalimide ring is solvent-exposed, providing suitable linker attachment points, also referred to as exit vectors.[305,306] Identifying suitable exit vectors in E3 ligase ligands is essential, as target binding must be maintained after linker attachment.

Consequently, several exit vectors for the VHL ligand scaffold have been explored, with N-terminal linker attachment via an amide bond being by far the most common (Figure 12A).[307]

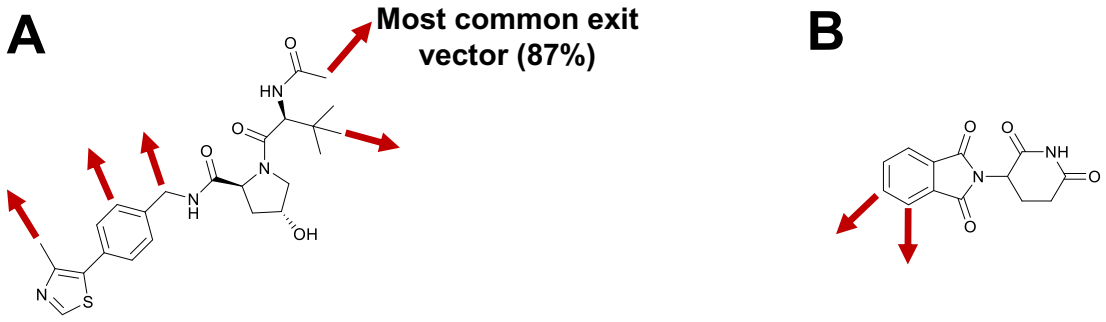


Figure 12: Most frequently used E3 ligands with exit vectors for linker attachment (red arrow). **A** VH032[290]. **B** Thalidomid[297]. The figure was created with ChemDraw.

Various crystal structures of PROTACs targeting VHL or CRBN have demonstrated that the PPIs formed by the E3 ligases within the complex vary depending on the POI, or in some cases even between different PROTACs targeting the same POI. This structural plasticity of E3 ligases may explain why numerous POIs can be targeted by only a few ligases, as well as some of the differences in cooperativity and selectivity observed among different PROTACs.[251,270,271] While VHL- and CRBN-based PROTACs have shown great success, the limited range of E3 ligases currently used also presents certain disadvantages. In oncology, drug resistance can arise as tumor cells might mutate or downregulate CRBN and VHL, which are non-essential for cell survival in some cancer cell lines.[308] Resistance to CRBN- or VHL-based degraders has been observed in preclinical studies.[309,310] Moreover, targeting specific E3 ligases that are overexpressed in tumor tissues could enable more selective cancer treatments.[246] Other E3 ligases, such as inhibitor of apoptosis protein (IAP) and mouse double minute 2 homolog (MDM2), have also been employed in degrader design. Still, most degraders currently in clinical trials still utilize VHL or CRBN, and an active search for new E3 ligases to target is ongoing.[240,278,281,282,311]

When it comes to the choice of suitable POI ligands, PROTACs have advantages over classical small-molecule inhibitors. While high affinity is generally preferred in PROTAC design, their catalytic mechanism might allow efficient degradation even for ligands with moderate binding affinity, especially when positive cooperativity is involved.[260,266] Moreover, as discussed above, the selectivity of a PROTAC depends not only on the choice of the POI binder but also on its ability to form productive ternary complexes and on factors such as the structural plasticity of the E3 ligase. Hence, small molecules with limited intrinsic selectivity but other favorable properties may nonetheless yield highly selective PROTACs.[251,266,270] Furthermore, it is not necessary to impact the target's biological function, hence, binding sites

other than the active site might be addressed. However, drug development campaigns still often utilize known orthosteric binders with readily available information about their binding modes as POI-targeting moieties.[242] The choice of exit vector, similar to that in E3-binding ligands, is highly important, not only to maintain sufficient binding affinity of the POI ligand but also to enable the formation of productive ternary complexes.[267] Other than the attachment point, the length of linkers can influence the selectivity of PROTACs, even between different isoforms of a protein. For example, shorter linkers can lead to higher selectivity by reducing the number of accessible binding conformations.[270,312,313] Another important property is linker rigidity, which can influence the ternary complex formation by constraining the PROTAC in its bioactive conformation.[271,314] In addition, incorporating rigid basic moieties such as piperazinyl or pyridine groups in linker has shown to improve linker solubility.[314]

Computer-aided drug design (CADD) in PROTAC development

Despite valuable knowledge gained on PROTAC mechanisms and design over the past two decades, identifying the right combination of E3 ligase ligand, POI binder, and linker, including the appropriate choice of exit vectors and the discovery of new E3 and POI binders, still often proves highly challenging. The design process is still largely empirical and often time- and labor-intensive. Computer-aided drug design (CADD) is widely used to support classical drug development and represents a powerful tool for exploring large chemical spaces through virtual screening, performing mechanistic analyses via molecular dynamics (MD), and predicting binding modes in the absence of crystal structures to guide structure-based design.[315] These capabilities also have great potential to accelerate PROTAC development, and several *in silico* techniques tailored for PROTAC design have recently been established.[316–325] However, modeling the ternary complex is quite challenging, often referred to as “three-body problem”, since not only the ligand–protein interactions but also PPIs need to be considered. Several structure-based approaches employing traditional docking tools such as MOE and Rosetta have been developed. These approaches have demonstrated the ability to reproduce crystallographic ternary complex structures reliably.[316–319] Further analysis of these docking poses, for example, through (MD) simulations, can be used to gain insights into cooperativity, efficacy, selectivity, and linker optimization.[316,320,321,326] Modern artificial intelligence (AI)-based approaches, including AlphaFold and RosettaFold, could also be used to predict and analyze the PPIs. Although still under development, these methods hold great potential, as they can be used to not only model the POI–E3 complex but also the proteins involved in the ubiquitination process, thereby helping to optimize PROTACs for enhanced ubiquitination efficiency.[322,323,327,328] Similarly, *in silico* models have been developed to distinguish productive from unproductive ternary complexes by predicting the likelihood of ubiquitination of the

POI.[324,325] *In silico* methods have already been successfully applied to aid the design and analysis of selective and effective PROTACs and, although not yet widely used in PROTAC development, they hold considerable promise as computational tools continue to advance.[326,329–331]

Pharmacokinetics and Pharmacodynamics of PROTACs

In terms of physicochemical properties, PROTACs usually fall beyond the classical Lipinski rule-of-five due to their high molecular weight, which results from their bifunctional nature.[332] However, oral administration is generally preferred for drugs over intravenous administration, and PROTACs can still exhibit oral bioavailability beyond the rule-of-five space.[333,334] A survey of drug companies revealed optimal chemical properties for degrader oral bioavailability as follows: topological polar surface area (tPSA) of 100–200 $Å^2$, molecular weight (MW) <900 g/mol, <14 hydrogen bond acceptors (HBAs), <5 hydrogen bond donors (HBDs), and LogD 3–5.[334] Additionally, solubility and permeability can still be achieved in PROTACs with higher PSA due to chameleonic behavior.[335] Fine-tuning the linker in terms of logP and basicity (pKa) is often utilized to balance the PROTAC's permeability, solubility, and metabolic stability.[243,311,334]

In terms of PROTAC metabolism, similar to small molecules, the major mechanisms of elimination are cytochrome P450-mediated metabolism and glucuronidation by UDP-glucuronosyltransferase enzymes. Additionally, hydrolysis by amidases and esterases often occurs, presumably due to the connective nature of PROTACs, where the components are frequently linked by amide or ester bonds. The linker tends to be the most labile moiety for cleavage. This is a major challenge, as it can result in the release of the POI and E3 ligand individually, potentially leading to competition with the degrader.[333,334,336] Non-metabolic clearance can be achieved via biliary and particularly renal routes, despite the high MW and large PSA of PROTACs.[334] Notably, due to challenges such as nonspecific binding, low stability, and poor solubility, classic *in vitro* absorption, distribution, metabolism, and excretion (ADME) assays are unsuitable or need to be adapted for PROTACs, potentially skewing the literature data. For example, several issues have been reported with plasma protein binding assays and parallel artificial membrane permeability assays (PAMPAs). Thus, PAMPA is often not recommended as a suitable method for PROTACs.[278,334]

When it comes to the ideal choice of POI for PROTAC therapy, PROTACs expand the druggable space compared to classical small molecules.[337] PROTACs not only eliminate the catalytic activity of the target but eliminate all biological activities, such as scaffolding functions.[313,338] Moreover, PROTACs can overcome compensatory protein overexpression and degrade mutant proteins that cannot be targeted by inhibitors, thereby reducing drug

resistance.[304,313,339] Additionally, suitable E3 ligases need to be expressed in the same tissue as the POI, which can be exploited to reduce side effects if the E3 expression level is low in cells that should not be targeted.[340] However, there are also certain constraints specific to PROTAC POIs. The binding surface needs to be accessible by E3 ligases, lysine residues suitable for ubiquitination must be present, and structurally disordered segments are needed as degradation initiation sites.[341] Resistance to PROTACs can still arise from mutations that disrupt the formation of the ternary complex.[330] Additionally, as mentioned before, E3 ligase downregulation can lead to resistance.[309,310] The therapeutic window of PROTACs depends not only on the efficacy and pharmacokinetic (PK) properties of the PROTAC but also on the resynthesis rate of the POI. If the turnover rate is relatively slow, after complete depletion of the POI, less PROTAC is required to degrade the resynthesized target. Furthermore, even after the removal of the PROTAC, the resynthesis of the POI takes time. It has been demonstrated that this can lead to a disconnect between pharmacodynamics (PD) and PK. In addition to the catalytic mechanism of PROTACs, this could result in lower dosing and longer dosing intervals for PROTACs compared to small molecules with similar PK profiles.[342–345] Yet, even with potentially low drug doses, there are some safety concerns regarding PROTACs, including their physicochemical properties (e.g., solubility), off-target degradation, and prolonged on-target degradation.[346]

Overall, PROTACs display unique PK and PD properties, offering the potential to address novel drug targets. However, the first wave of PROTACs entering clinical trials was developed for targets with clinically validated roles in disease, serving as an initial proof of concept for the novel technique.[241]

PROTACs currently in clinical trials

The majority of PROTACs in clinical trials are being developed for oncology-related indications, while some address other indications such as autoimmune disorders. Several PROTAC drug candidates have advanced to phase 2 or 3 clinical trials (Table 1).[311,347]

Table 1. Proteolysis Targeting Chimeras (PROTACs) currently in late-stage clinical trials, including the protein of interest (POI), E3 ligase addressed, and the indication. Trial information was obtained from ClinicalTrials.gov; some studies are ongoing and may still be recruiting. If the target E3 ligase was not disclosed, this is marked as n.d. The table was partly adapted form review articles.[311,347] The completeness of this information cannot be guaranteed. Further abbreviations: CRBN (Cereblon), VHL (Von Hippel-Lindau), ER (estrogen receptor)., AR (androgen receptor), BTK (Bruton's tyrosine kinase), BCL (B-cell lymphoma), BRD (bromodomain).

PROTAC	POI	E3 Ligase	Indication	Status
ARV-471	ER	CRBN	Breast cancer	Phase 3[348]
BMS-986365	AR	CRBN	Prostate cancer	Phase 3[349]
BGB-16673	BTK	CRBN	B-cell malignancies	Phase 3[350]
ARV-766	AR	CRBN	Prostate cancer	Phase 2[351]
BMS-986458	Bcl6	CRBN	Lymphoma	Phase 2[352]
DT2216	Bcl-XL	VHL	Cancer	Phase 2[353]
HRS-5041	AR	n.d.	Prostate cancer	Phase 2[354]
HRS-1358	ER	n.d.	Breast cancer	Phase 2[355]
GT-20029	AR	n.d.	Acne/androgenic alopecia	Phase 2[356]
MT-4561	BRD4	n.d.	Cancer	Phase 2[357]
PRT3789	SMARCA2	VHL	Cancer	Phase 2[358]

The first PROTAC to ever enter clinical trials, ARV-110, targets the androgen receptor (AR), which is heavily implicated in driving prostate cancer.[359,360] The compound, developed by Arvinas, consists of an aryloxy cyclohexane-based AR antagonist, a short and rigid piperidine–piperazine linker, and a fluorinated thalidomide derivative that recruits CRBN as the E3 ligase (Figure 13A).[361] ARV-110 is orally bioavailable and was evaluated in pretreated patients with metastatic castration-resistant prostate cancer in clinical trials, demonstrating antitumor activity even in patients harboring AR mutations.[362] This provided clinical proof that PROTACs can function as drugs, although the development of ARV-110 was later discontinued for strategic reasons.[311] Another PROTAC developed by Arvinas, ARV-471, which targets the ER, is currently in phase 3 clinical trials.[348] Structurally, ARV-471 consists of a lasofoxifene-based POI-targeting moiety, the same linker as ARV-110, and lenalidomide to recruit CRBN

(Figure 13B).[301,363,364] Around 70 % of breast cancer cases are ER-positive and human epidermal growth factor receptor 2 (HER2)-negative.[365] ARV-471 has been tested in pretreated patients with $ER^+/HER2^-$ locally advanced or metastatic breast cancer in clinical trials, where the drug demonstrated promising oral pharmacokinetics and degradation activity.[366] The compound has the potential to become the world's first approved PROTAC drug and was recently submitted to the U.S. FDA, based on positive results from the phase 3 trials.[367] Two other PROTACs are currently in phase 3 clinical trials: BMS-986365, which also targets the AR and was developed for prostate cancer, and BGB-16673, which targets Bruton's tyrosine kinase (BTK) and was developed for B-cell malignancies (Figure 13C,D).[350,352,368,369] Both molecules have shown promising results in their respective indications, including activity against mutant forms of their targets.[370,371] As these late-stage candidates approach potential approval, the next major milestone in PROTAC development will soon be reached, demonstrating the therapeutic value of PROTACs for patients.

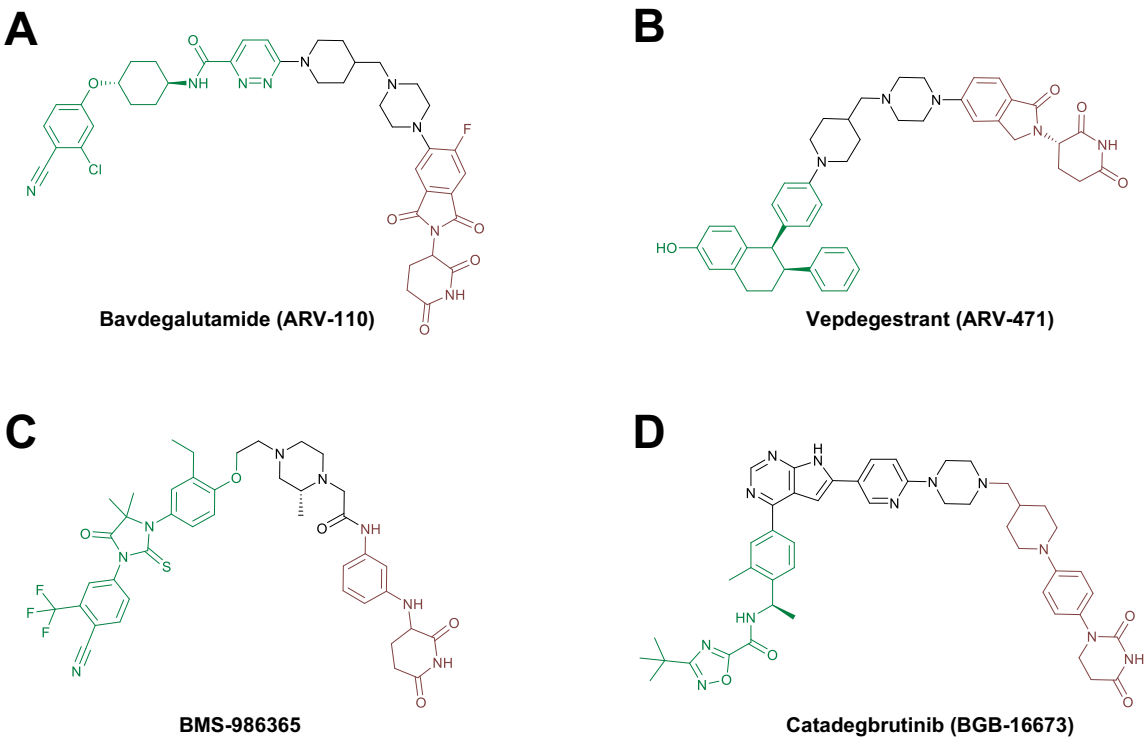


Figure 13: Structures of proteolysis targeting chimera (PROTAC) drug candidates that have entered late-stage clinical trials. **A** Compound ARV110[360,361]. **B** Compound ARV-471[364]. **C** Compound BMS-986365[368]. **D** Compound BGB-16673[369]. The E3 ligase-binding parts are colored in brown, the linker in black and the protein of interest binding parts are colored in green. The figure was created with ChemDraw.

The success of the PROTACs technique over the past 20 years has been remarkable, and it will be exciting to see whether PROTACs can ultimately deliver drugs that tackle novel targets, previously deemed "undruggable", a vision proposed since their inception but not yet realized.

1.2.2 Innovative Screening Approaches: DNA-Encoded Libraries and Direct-to-Biology

While PROTACs represent a novel approach for targeting a wide range of proteins through an unique mechanism, over the past decades, several innovative techniques for screening large libraries of chemically diverse compounds have also emerged.

One such strategy are DNA-encoded libraries (DELs), first described in the 1990s.[372,373] DELs consist of a vast collection of compounds, which can be created by connecting building blocks through diverse chemical approaches such as amine capping reactions, metal-catalyzed cross-couplings, and copper-catalyzed azide-alkyne cycloaddition (CuAAC).[374] Often, a split-and-pool technique is used during library synthesis (Figure 14A). Building blocks are covalently attached to unique DNA barcodes, pooled, and then split into separate reaction pools. New building blocks are added to these pools, and the DNA tag is ligated with an additional DNA barcode encoding the newly appended building block. By repeating this pattern, large libraries can be created in a short time.[374,375] The DNA-barcode allows for testing of all compounds simultaneously in the same vessel, utilizing the concept of affinity selection, usually by employing an immobilized target protein to capture active ligands. The barcodes of these ligands are then amplified by polymerase chain reaction (PCR) and sequenced to identify the ligands' chemical structure (Figure 14B).[375,376]

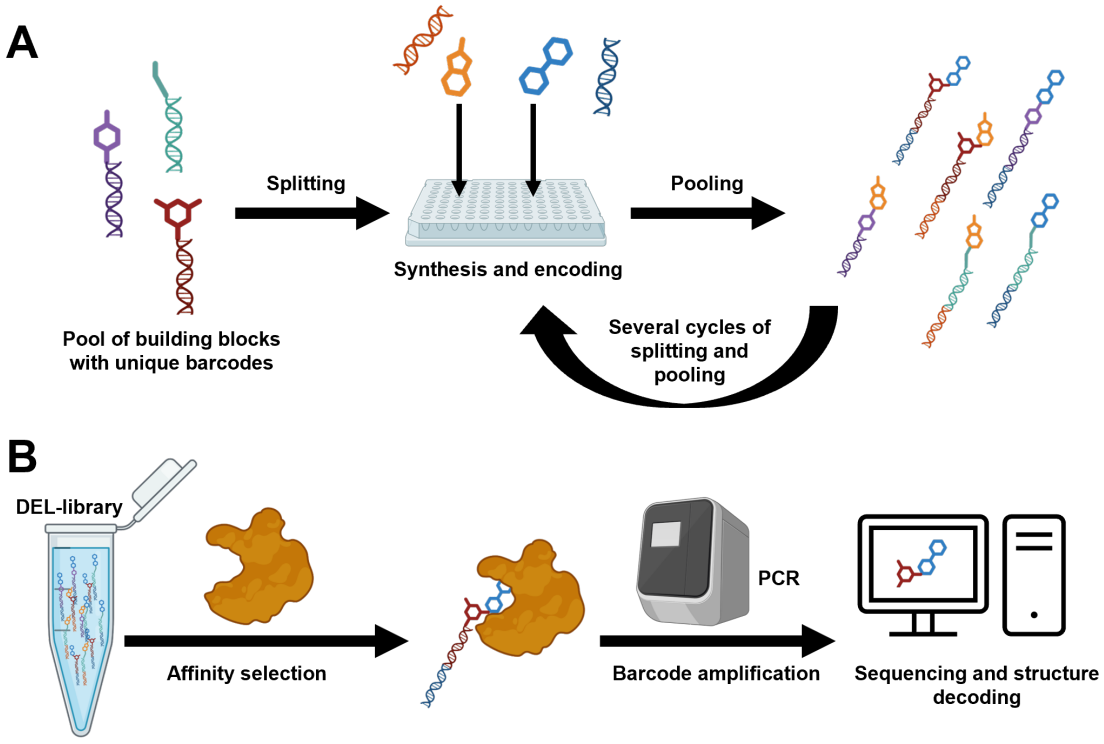


Figure 14: DNA-encoded library (DEL) synthesis and screening. **A** DEL synthesis using a split-and-pool technique. **B** Screening of a DEL and identification of hit structures. Further abbreviations: PCR (polymerase chain reaction).

This technique has several advantages over classical HTS. Consumables such as targets, buffers, and compounds in the library are drastically reduced, as usually only tens of micrograms of target and picomolar quantities of DEL are needed for testing. Moreover, testing can be done in just a few days and with many targets in parallel. Furthermore, it is not necessary to implement and validate new assays for each new target, which also significantly saves time and materials.[375] Due to these advantages, DEL libraries are used in early-stage drug discovery campaigns in both academia and the pharmaceutical industry. Optimization of DEL-derived hits has already led to lead compounds with promising *in vivo* properties, with some even progressing to clinical stages, against a diverse set of targets such as the receptor interacting protein 1 (RIP1) kinase, soluble epoxide hydrolase (sEH), and protease-activated receptor- 2 (PAR2).[376–379] DELs can also be used in PROTAC development and have been successfully employed to identify novel POI binders, E3 ligase binders, and even bifunctional molecules containing both. A key advantage of this method is that the ligands are already presented in a linked format, with a DNA tag that can be replaced by the PROTAC linker moiety. Moreover, DEL screening can also reveal non-active binding sites that may be exploited for degrader design.[380–383]

Another strategy employed in the generation and testing of large compound libraries is the direct-to-biology (D2B) approach. In this method, crude reaction mixtures, synthesized by biologically compatible chemistry are directly used to test compound activity, enabling the rapid identification of novel hits. This approach significantly accelerates empirical optimization by shortening the classical design-make-test cycle, as it eliminates the need to purify the products beforehand.[384–386] The D2B approach has already been used to accelerate drug discovery against targets like the SARS-CoV-2 main protease (MPro) and peroxiredoxin 1 (PRDX1).[386–388] D2B has also been used in PROTAC design to gain insights into linker SAR, exit-vector identification, and the discovery of novel PROTACs for a variety of targets.[389–394]

Novel modalities such as PROTACs, DEL, and D2B are driving innovation in drug discovery, with successful applications in both industry and academia. This makes these techniques attractive options to tackle issues in complex or understudied areas of drug discovery, such as RNA MTases.

1.3 C-Type Lectins in Drug Delivery

1.3.1 C-Type Lectin Domains and Carbohydrate Interactions

C-type lectins (CTLs) are a large family of Ca^{2+}-dependent carbohydrate-binding proteins, and many important biological functions are mediated by lectin-carbohydrate interactions, including cell–cell communication, homeostasis, and modulation of immune responses.[395–398] The domains of these lectins, known as C-type lectin domains (CTLDs), have a characteristic compact globular structure and conserved residue motifs across many different lectins, although the overall organization of these proteins can vary widely.[399–403] Not all of the CTLDs can bind carbohydrates. Therefore, the CTLDs that do bind carbohydrates are often referred to as carbohydrate-recognition domains (CRDs), and this terminology will be used in this thesis.[400] CRDs have multiple Ca^{2+} binding sites but primarily bind carbohydrates by coordinating their vicinal hydroxy groups via a central Ca^{2+} ion (Figure 15). This ion is coordinated by residues with carbonyl side chains that form two characteristic motifs: Glu-Pro-Asn or Gln-Pro-Asp, and Trp-Asn-Asp. These motifs not only coordinate the Ca^{2+} but are also directly involved in monosaccharide binding. The distinction between the two motifs Glu-Pro-Asn and Gln-Pro-Asp dictates carbohydrate specificity.[400,404] Additionally, secondary binding sites can contribute to specificity and affinity in oligosaccharide binding.[405]

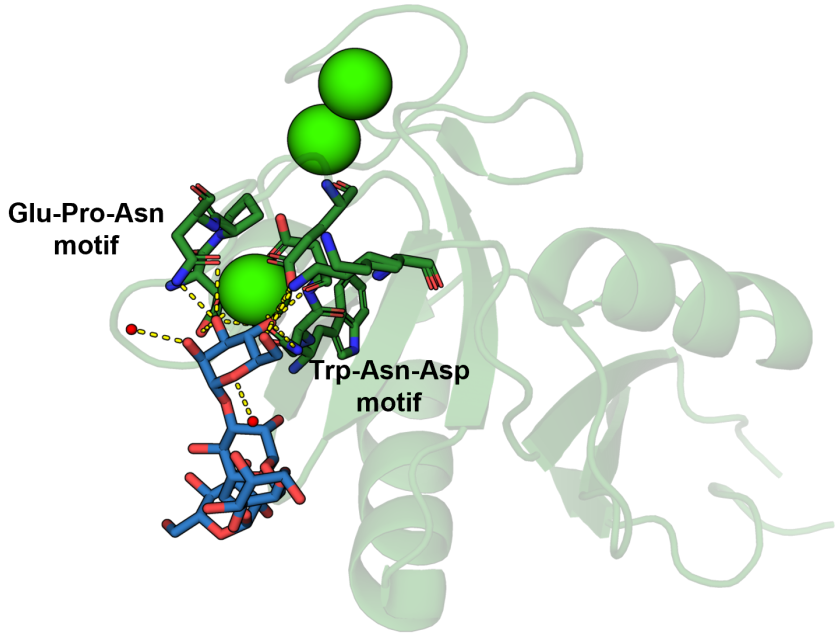


Figure 15: C-type lectin carbohydrate recognition domain containing a high mannose ligand (PDB: 1SL4[405]). The protein is shown as a cartoon, with selected residues, including the characteristic Glu-Pro-Asn and Trp-Asn-Asp motifs depicted as sticks (forest green). Calcium ions are shown as large spheres (light green), the ligand is shown as sticks (blue), and water molecules are represented as spheres (red). The figure was created using Microsoft PowerPoint and PyMOL.

Overall, the interaction of CRDs with carbohydrates, especially monomeric ligands, is often very weak with K_D values in the millimolar or high micromolar range.[406–408] This is partly due to the hydrophilic nature of carbohydrates, which results in enthalpically unfavorable desolvation upon binding.[409] Another issue with carbohydrate-binding is that the CRDs of different lectins often recognize the same minimal binding motif, such as mannose, which further reduces ligand selectivity. In general, targeting lectins is challenging, and ligands must be carefully designed to achieve specific lectin–ligand interactions and to exploit the defined steric and hydrogen-bonding requirements resulting from the multiple hydroxyl groups of the endogenous carbohydrate ligands.[410,411]

1.3.2 Multivalency in Lectine-Carbohydrate Interactions

Multivalency in biological systems, characterized by the simultaneous binding of multiple ligand epitopes to several binding sites on a biological target, is often exploited by nature and drug design to overcome low-affinity binding. It can influence avidity, duration, and selectivity of biomolecular interactions.[412–415] Lectins utilize this to overcome their weak affinity for carbohydrates. The receptors form multimeric structures that cluster their CRDs to recognize natural multivalent carbohydrate ligands, enhancing both avidity and specificity. Similarly, in ligand design, carbohydrates can be presented on suitable scaffolds in a multivalent manner to match the arrangement of CRDs on target lectins.[416–418]

Different types of multivalency effects influence avidity in lectin carbohydrate interactions (Figure 16). Statistical rebinding refers to the proximity of multiple binding epitopes on a multivalent ligand creating a locally increased concentration of ligand epitopes, thereby increasing the probability of (re)binding to the target. The chelating effect refers to the simultaneous binding of one multivalent ligand to multiple CRDs on the same lectin oligomer, while clustering refers to the simultaneous binding of one multivalent ligand to different lectin oligomers.[419–422] Designing ligands in a specific way to utilize these effects is highly complex. Statistical rebinding is more likely to occur if the ligand epitopes are connected by shorter, more flexible linkers, while very large, high-valency scaffolds are more likely to lead to clustering or chelation.[422–425] However, in large, flexible assemblies, the entropic penalty upon binding can lower avidity and binding specificity.[413,426] In contrast, more rigid, smaller linkers need to be precisely matched to the size of the receptor to achieve sufficient multivalent binding. Hence, an appropriate balance between the rigidity and flexibility of the linker, as well as its general composition and length, is necessary to achieve optimal avidity by combining binding effects like statistical rebinding, clustering, and chelation.[423,424,427,428]

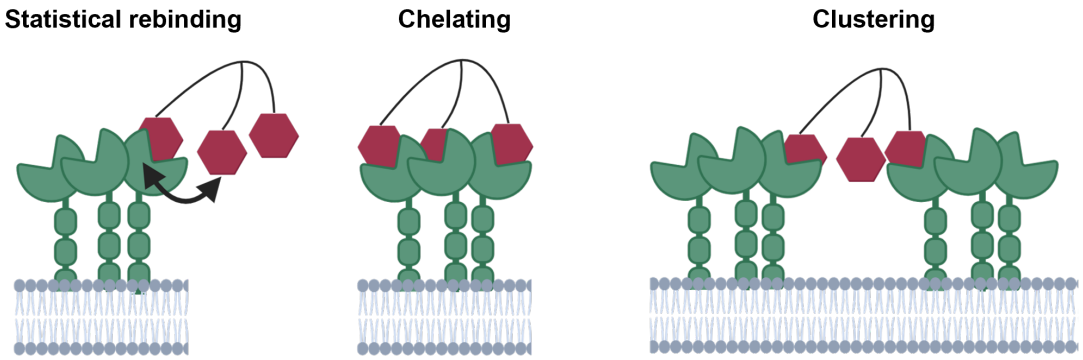


Figure 16: Effects influencing avidity in carbohydrate-lectin interactions, including statistical rebinding, chelating, and clustering. The figure was created using Microsoft PowerPoint and Biorender.com.

Another effect that plays a role in multivalent binding interactions is cooperativity, described by the cooperativity factor α_{multi}, as the first binding event may influence the subsequent ones. This influence can be positive (synergistic), noncooperative (additive), or negative (interfering). For a multivalent interaction with n ligand-receptor interactions, α_{multi} is determined from the association constant of the polyvalent interaction ($K_{\text{n}}^{\text{multi}}$), and the association constant of the corresponding monovalent reaction (K^{mono}) according to equation 2.

$$\alpha_{\text{multi}} = \frac{\lg\left(K_n^{\text{multi}}\right)}{\lg\left(K^{\text{mono}}\right)^n} \qquad \text{Equation 2}$$

For lectin carbohydrate interactions, negative cooperativity is often observed. However, the multivalent interactions are still typically much stronger than their monovalent counterparts. Therefore, the enhancement factor β, defined by equation 3, is generally considered more valuable to describe the effectiveness of multivalent ligands than α_{multi}.[413,429,430]

$$\beta = \frac{K_n^{\text{multi}}}{K^{\text{mono}}} \qquad \text{Equation 3}$$

1.3.3 C-Type Lectin Receptors Dendritic Cell-Specific Intercellular Adhesion Molecule-3-Grabbing Non-Integrin (DC-SIGN) and Macrophage Mannose Receptor (MMR)

One of the most studied CTLs over the last two decades, dendritic cell-specific intercellular adhesion molecule-3-grabbing non-integrin (DC-SIGN), is a strong example of the benefit of multivalency. DC-SIGN is part of the immune system and expressed on a variety of cell types, including monocytes, dermal dendritic cells (DCs), macrophages, and platelets.[431,432] The transmembrane protein consists of three main domains: an N-terminal cytoplasmic region, a transmembrane segment, and an extracellular domain (ECD), which is further organized into an elongated neck region and the CRD.

The DC-SIGN receptor forms tetramers on the cell surface and the neck region is essential for this multimeric CRD presentation (Figure 17A).[406,433] The tetrameric CRDs of DC-SIGN interact with specific carbohydrate structures, such as fucose, Lewis-type, and high-mannose moieties on self-glycoproteins and pathogens. These interactions trigger internalization into compartments with increasing acidity, such as the lysosome, resulting in the separation of the tetramers and ligand release. In the lysosome, the released antigens are processed and presented via the major histocompatibility complex (MHC) to activated $CD4^+$ T cells.[432–436] Additionally, DC-SIGN can bind to intercellular adhesion molecule 2 (ICAM2) and ICAM3, functioning as an adhesion receptor.[435,437] Multiple pathogens have adapted to hijack the DC-SIGN receptor and evade the immune response.[438–440] In response, several carbohydrate ligands targeting the receptor have been developed to either prevent pathogen binding or modulate the immune response.[416] Multivalent presentation is frequently used to enhance the affinity of these ligands, and this strategy has been demonstrated to successfully inhibit the uptake of HIV-1, Dengue virus, and Ebola virus.[416,427,441,442]

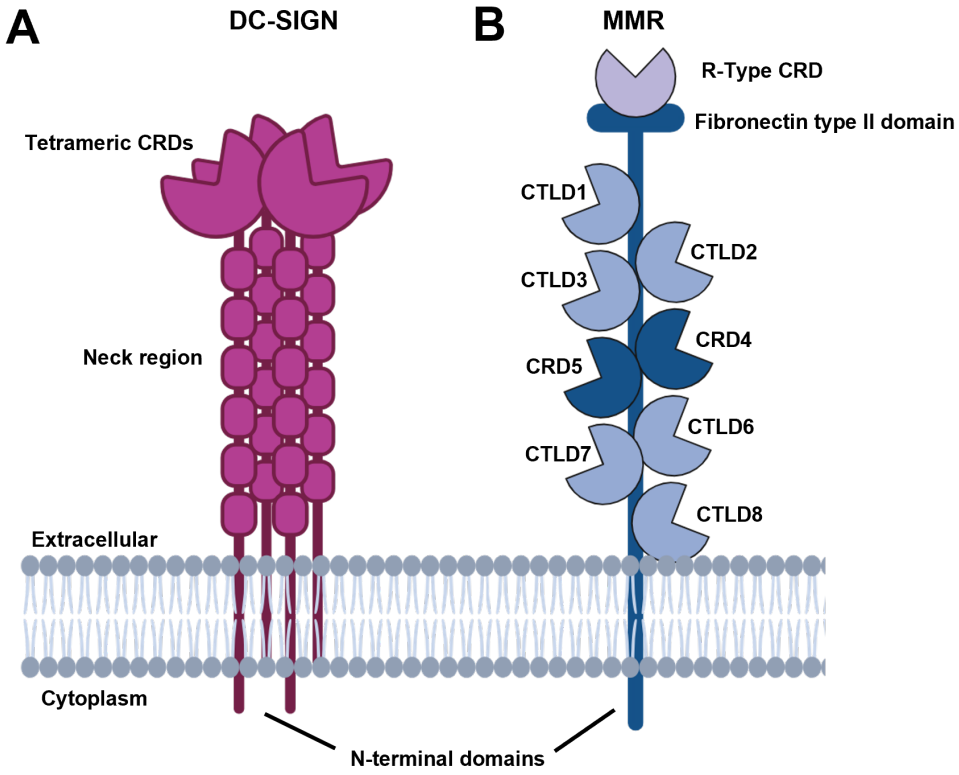


Figure 17: Domain structure of C-type lectines **A** dendritic cell-specific intercellular adhesion molecule-3-grabbing non-integrin (DC-SIGN) and **B** the macrophage mannose receptor (MMR), including carbohydrate recognition domains (CRDs) and C-type lectin domains (CTLDs). The figure was created using Microsoft PowerPoint and Biorender.com.

Another receptor important for immune response and expressed on antigen-presenting cells such as DCs and macrophages, is the transmembrane macrophage mannose receptor (MMR). Like DC-SIGN, the receptor recognizes a range of pathogens, such as viruses and bacteria, which are internalized via receptor-mediated endocytosis and trigger an immune response.[443–

[448] Moreover, by binding and scavenging unwanted glycoproteins and pituitary hormones, the MMR serves as a homeostatic receptor.[449–451] Unlike DC-SIGN, the MMR does not form a tetramer but instead comprises multiple connected domains, which lead to multivalency and can recognize diverse ligands (Figure 17B).[407,452,453] The extracellular C-terminal domain is a CRD binding 4-sulfo-*N*-acetylglucosamine (GalNAc) residues on certain glycoprotein-containing hormones.[454] The adjacent fibronectin type II domain binds collagen fragments, whereas the remainder of the extracellular portion consists of eight CTLDs. Among these CTLDs 4 and 5 account for most of the carbohydrate-binding activity and function as the CRDs. These CRDs bind sugar moieties like fucose, GlcNAc residues, and high-mannose oligosaccharides.[407,452,453,455]

1.3.4 Targeted Drug Delivery via DC-SIGN and the MMR

Decorating drugs or drug carriers with carbohydrates, addressing C-type lectins such as DC-SIGN and the MMR, is an effective strategy for targeted drug delivery to immune cells.[456–459] For example, therapeutic glycoproteins for the treatment of lysosomal storage diseases have been delivered to macrophages by decorating them with high-mannose structures to target the MMR.[458,459] Nanocarriers decorated with targeting structures offer additional benefits. These include protection of the cargo, enhanced lifetime, controlled release, increased efficacy, and reduced toxicity and off-target effects.[456,460–463] A wide range of nanocarriers can be decorated with carbohydrates for drug delivery, including liposomes, proteins, polymeric nanoparticles, and inorganic nanocarriers.[456,457,464] The cargo delivered can include antigens to cause a defined immune response, small molecule drugs that address targets in the immune cells, or genetic material to induce specific cellular effects (Figure 18).

For example, mannose-decorated liposomes or polymers have been used successfully in the delivery of DNA and RNA to antigen-presenting cells (APCs), by addressing the MMR to modulate the immune response.[465,466] Likewise, carbohydrate-modified liposomes and dendrimers targeting both the MMR and DC-SIGN have been utilized in the delivery of antigens to potentiate immunogenicity, functioning as potential vaccines, for example, in cancer therapy.[467–469] Moreover, mannosylated solid lipid nanoparticles, delivering drugs like rifampicin, caused an antibacterial effect in macrophages.[470] In addition to synthetic nanocarriers, endogenous transport proteins such as human serum albumin (HSA) can also be used in carbohydrate-mediated targeting. HSA offers several advantages over other drug delivery systems, such as superior biodegradability and biocompatibility, non-toxicity, and non-immunogenicity. Additionally, it provides multiple functional groups that can be readily used for targeted ligand attachment.[471] HSA decorated with mannose has been shown to deliver

chemotherapeutic agents to cancer cells.[472,473] Moreover, HSA functionalized with trimannose has been demonstrated to deliver drugs relevant for immunotherapy to immune cells.[474]

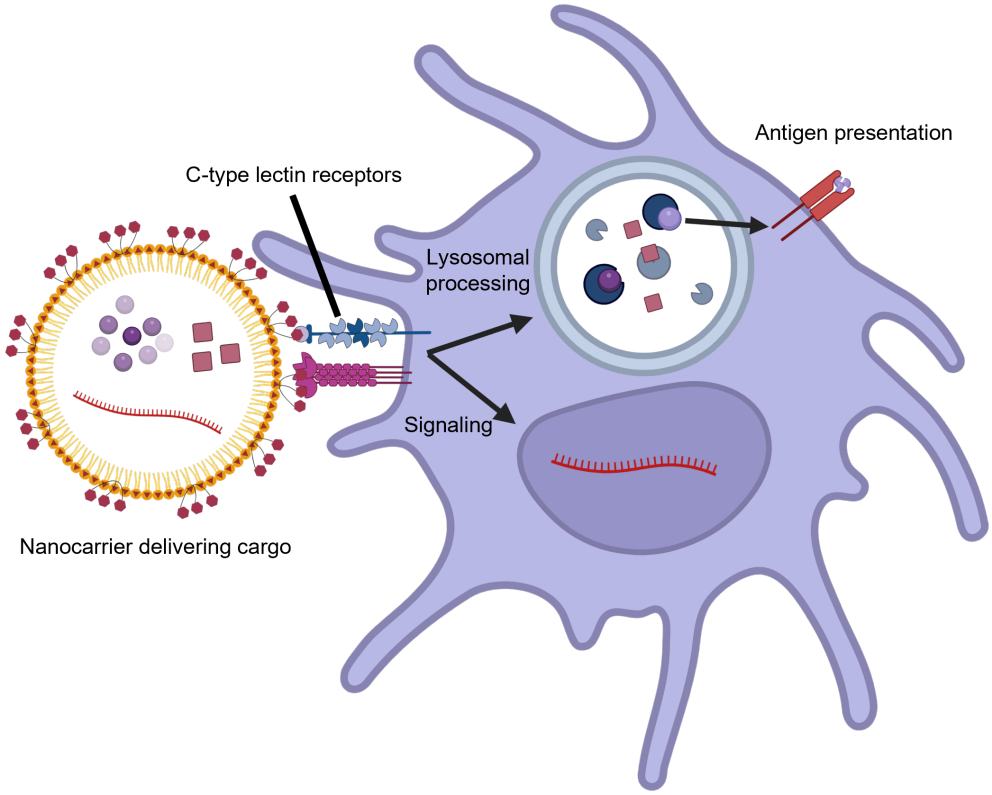


Figure 18: Cargo delivery by a generic nanocarrier decorated with carbohydrates to an antigen-presenting cell (APC). The cargo (antigens, small molecules, and genetic material) is delivered by targeting lectin receptors. Antigens are delivered to a lysosome, where they are processed and trigger an immune response. Small molecules are delivered to a lysosome and interact with lysosomal proteins. Genetic material is delivered to the APC, modulating the immune response. The figure was created using Microsoft PowerPoint and Biorender.com.

In these carrier systems, multivalent carbohydrate presentation is achieved not only by using inherently multivalent ligands but also by arranging numerous targeting structures in close spatial proximity. Consequently, biodistribution and cellular uptake, both factors highly important for targeted drug delivery, are influenced not only by ligand valency and the composition of the binding epitopes but also by ligand density and the overall surface properties of the carrier. These parameters must therefore be considered during the design of the targeting strategy, in addition to the multivalency effects discussed above, such as statistical rebinding.[475–477] Increasing the density of ligands on the carrier surface generally leads to more binding interactions and higher avidity. However, blindly increasing the targeting structure density is not always beneficial. If the density is too high, the targeting structures are sterically hindered, which reduces cell uptake. Flexible targeting structures can reduce this steric hindrance, but, as discussed above, might be entropically unfavorable.[477,478] Moreover, receptor density also affects avidity, and excessively high ligand density may cause unnecessary receptor consumption, reducing receptor availability on the target cell and

slowing the uptake of subsequent carrier systems.[479] Type and density of target structures also influence the size, shape, and charge of the carrier itself, which in turn also influences uptake and distribution. In summary, while an increase in target structure density initially leads to a more effective uptake, usually an optimal density exists after which the uptake efficiency plateaus or even decreases. This optimum depends on targeting structure composition and carrier type.[477]

Overall, targeted drug delivery via lectin carbohydrate interactions can be a useful tool, especially to influence the immune response. To achieve optimal carrier uptake, choosing the optimal type and density of targeting structure is essential. This depends on the type of binding epitope, valency, and flexibility of the targeting structures. However, fine-tuning these factors is highly complicated. Moreover, *in vivo*, the selective biodistribution of the carrier is not clearly linked to increased avidity of the carrier, and the connection is under-researched.[476] Hence, to achieve optimal drug targeting, more research on the design of targeting structures is still essential.

2 Project Overview

The publications included in this thesis are the results of two research projects. The first project focused on the discovery and characterization of novel ligands for disease-relevant RNA methyltransferases (MTases), whereas the second project focused on the characterization of targeting structures for drug delivery. Across both projects, biophysical and computational methods were employed to characterize ligand binding interactions and to derive structure-function relationship information to guide optimization of ligand properties.

2.1 Project 1: Discovery and Characterization of Novel Ligands for RNA Methyltransferases

In the first project, including three publications, new approaches to drug development were employed to target RNA MTases with disease relevance. The first publication focused on the development of proteolysis-targeting chimeras as an alternative to classical small molecules to target METTL3. For biophysical evaluation of binding to the METTL3/14 complex, the purified enzyme complex is required; however, it has predominantly been produced using non-bacterial expression systems (e.g., insect cell/baculovirus).[154,155,158,480,481] Because recombinant expression in *E. coli* is generally faster and more cost-effective than these systems, within this thesis, expression and purification of the METTL3/14 complex was established in *E. coli*. Cooperativity is an important factor in PROTAC design, as it influences phenomena such as the hook effect (see Chapter 1.2.1). To investigate and compare the cooperativity of the developed lead PROTAC **AF151** and the literature compound **WD6305**, two biophysical assays, a fluorescence polarization (FP) assay and a homogeneous time-resolved fluorescence (HTRF) assay, were established. These investigations, supported by a computational approach, revealed that **WD6305** shows reduced binary affinity to the E3 ligase but high ternary complex affinity, resulting in strong positive cooperativity and an efficient degradation profile. This highlights the importance of cooperativity over binary affinity, and the publication was featured in a blog post by the Drug Hunting literature group (55k members on LinkedIn).

In the second publication, a nanoscale synthesis strategy combined with direct-to-biology assays for rapid hit identification against the TrmD of the pathogen *S. aureus* was used. In this thesis, *S. aureus* TrmD was recombinantly expressed in *E. coli* to enable binding studies and crystallization of the screening hits. Additionally, to investigate selectivity against the human m^1G37 methyltransferase Trm5, expression and purification of this enzyme were established. Co-crystallization with literature compound **2** and hit compound **8h** yielded the first crystal

structures of *S. aureus* TrmD in complex with ligands, which are highly valuable for future structure-based design of TrmD inhibitors and were subsequently used in a docking campaign.

In the third publication, a DNA-encoded library screening to identify novel ligand chemotypes for DNMT2 was applied. To investigate the elusive binding mode of the screening hits, ITC experiments were conducted within this thesis, which provided initial evidence for ligand-induced conformational changes. Additionally, displacement titrations with SAH were conducted, hinting at an allosteric mode of inhibition, which was subsequently confirmed by crystallography. Moreover, ITC-derived stoichiometry informed investigations of DNMT2 dimerization in the native state, with one ligand binding per monomer.

The following publications constitute the results obtained for this project (‡ indicates shared first authorship):

(1) **Weldert, A. C.;** Frey, A. F.; Krone, M. W.; Krähe, F.; Kuhn, H.; Kersten, C.; Barthels, F. Structure-Guided Design of a Methyltransferase-like 3 (METTL3) Proteolysis Targeting Chimera (PROTAC) Incorporating an Indole–Nicotinamide Chemotype. *RSC Med Chem* **2025**, *16* (9), 4194–4207. https://doi.org/10.1039/D5MD00359H.

Own contributions: Establishing protein expression and purification of the METTL3/14 complex, protein expression and purification of the VHL–elongin B–elongin C (VCB) complex, binary FP assays (compounds **35–42**), establishing of ternary FP and HTRF assays (partly conducted by [redacted] as part of a supervised research module, compounds **AF151** and **WD6305**), molecular docking of ternary METTL3/14–VCB–ligand complexes (**AF151**, **WD6305**, **KH12**), preparation of docking poses for MD simulations, cell culture (80%), Western blot analysis (50%), writing the main part of the manuscript, writing parts of the supporting information.

Contributions from other authors: Syntheses, binary FP assays (compounds **5–34**), binary HTRF assays, MD simulations, cell culture (20%), Western blot analysis (50%), cell viability assays, RNA m^6A quantification, real-time apoptosis assay, writing parts of the manuscript, and supporting information.

(2) Hübner, A. F.‡; **Weldert, A. C.**‡; Marciniak, T.; Hof, F.; Beck, V. S.; Carien, S.; Mulartschyk, S. N.; Wolf, E.; Ziebuhr, W.; Barthels, F. Nanoscale Direct-to-Biology Optimization and Structural Insights into Selective *S. Aureus* TrmD Inhibitors. *J Med Chem* **2025**, 68 (24), 26246–26262. https://doi.org/10.1021/acs.jmedchem.5c02323.

Own contributions: Protein expression and purification of *S. aureus* TrmD construct, establishing protein expression and purification of Trm5 (as part of the supervised Master's

thesis of [redacted] ITC (compounds **1** and **2** against *S. aureus* and *H. influenzae* TrmD), FP assay for selectivity determination (50%), crystallization condition screening and co-crystallization with compounds **2** and **8h**, crystal structure model building (iterative refinement in Phenix and manual adjustment/validation in Coot to fit the electron density, including correction of artifacts), SeeSAR analysis, writing parts of the manuscript and supporting information.

Contributions from other authors: Syntheses, direct-to-biology screening, protein expression and purification of *H. influenzae* and *E. coli* TrmD constructs, FP assay for selectivity determination (50%), validation of compounds with FP assays, inhibition assays (^{3}H-incorporation and aptamer), bacterial growth inhibition assays, Cell Titer Glo cell viability assay, lysate assay, crystal structure initial model building (molecular replacement to obtain a starting model, followed by initial refinement and manual inspection in REFMAC and Coot), molecular modeling, writing parts of the manuscript, and supporting information.

(3) Frey, A. F.‡; Schwan, M.‡; **Weldert, A. C.**; Kadenbach, V.; Kopp, J.; Nidoieva, Z.; Zimmermann, R. A.; Gleue, L.; Zimmer, C.; Jörg, M.; Friedland, K.; Helm, M.; Sinning, I.; Barthels, F. DNA-Encoded Library Screening Uncovers Potent DNMT2 Inhibitors Targeting a Cryptic Allosteric Binding Site. *iScience* **2025**, *28* (9), 113300. https://doi.org/10.1016/j.isci.2025.113300.

Own contributions: ITC: direct and displacement titrations, cell culture (40%), editing of the manuscript, and supporting information.

Contributions from other authors: DEL screening, syntheses, activity and binding assays (^{3}H-incorporation, MST, FP assay and AS-MS), electrophoretic mobility shift assay, PAMPA, protein and tRNA preparation and purification, protein crystallization, SeeSAR analysis, pull-down assay, cell culture (60%), cell viability assays and tRNA LC/MS assay, writing the manuscript and supporting information.

2.2 Project 2: Binding Characterization of Multivalent Targeting Structures

In the second project, comprising one publication, mannan-derived targeting structures with different valencies and epitope types were characterized. Early characterization within this thesis included molecular docking of the structures to monovalent receptor domains of DC-SIGN and MMR to determine linker influence on binding mode. The affinities of carbohydrate structures to isolated lectin receptors are often weak and in the millimolar range (see Chapter 1.3.1), which makes biophysical characterization challenging. While solution-based methods such as ITC have been employed to measure these interactions, they are material-intensive.[482,483] Initial attempts to measure these interactions using other biophysical methods, such as MST, were unsuccessful, partly because one component needs to be labeled. A nanoDSF setup was therefore established in this thesis as a label-free, in-solution alternative to enable investigation of the millimolar affinities of the targeting structures.

The following publication constitutes the results obtained for this project (‡ indicates shared first authorship):

(4) Forster, R.‡; Lantzberg, B.‡; **Weldert, A.**‡; Rosenberger, L.; Zeyn, Y.; Kowalczyk, D.; Kuan, S. L.; Kersten, C.; Bros, M.; Weil, T.; Schirmeister, T.; Opatz, T. Surface Density of Mono- and Trivalent High-Mannan-Derived Targeting Structures with Different Affinities Impacts Cellular Uptake of Human Serum Albumin-Derived Nanocarriers. *Biomacromolecules* 2025, *26* (11), 8087–8102. https://doi.org/10.1021/acs.biomac.5c01510.

Own contributions: Protein expression and purification of DC-SIGN and MMR, establishment of nanoDSF experiments, *in silico* DC-SIGN model building, molecular docking, writing parts of the manuscript, writing parts of the supporting information.

Contributions from other authors: Syntheses of all targeting structures (**$ManN_3$**, **Man_3N_3**, **$(Man)_3N_3$**, and **$(Man_3)_3N_3$**), synthesis of HSA conjugates, MS of HSA conjugates, dynamic light scattering of HSA conjugates for distribution determination, cell culture, fluorescence-activated cell sorting, writing parts of the manuscript, writing parts of the supporting information.

3 List of Publications

(‡ indicates shared first authorship)

3.1 Publications as Part of this Doctoral Thesis

3.1.1 Project 1: Discovery and Characterization of Novel Ligands for RNA Methyltransferases

(1) **Weldert, A. C.;** Frey, A. F.; Krone, M. W.; Krähe, F.; Kuhn, H.; Kersten, C.; Barthels, F. Structure-Guided Design of a Methyltransferase-like 3 (METTL3) Proteolysis Targeting Chimera (PROTAC) Incorporating an Indole–Nicotinamide Chemotype. *RSC Med Chem* **2025**, *16* (9), 4194–4207. https://doi.org/10.1039/D5MD00359H.

(2) Hübner, A. F.‡; **Weldert, A. C.**‡; Marciniak, T.; Hof, F.; Beck, V. S.; Carien, S.; Mulartschyk, S. N.; Wolf, E.; Ziebuhr, W.; Barthels, F. Nanoscale Direct-to-Biology Optimization and Structural Insights into Selective *S. Aureus* TrmD Inhibitors. *J Med Chem* **2025**, 68 (24), 26246–26262. https://doi.org/10.1021/acs.jmedchem.5c02323.

(3) Frey, A. F.‡; Schwan, M.‡; **Weldert, A. C.**; Kadenbach, V.; Kopp, J.; Nidoieva, Z.; Zimmermann, R. A.; Gleue, L.; Zimmer, C.; Jörg, M.; Friedland, K.; Helm, M.; Sinning, I.; Barthels, F. DNA-Encoded Library Screening Uncovers Potent DNMT2 Inhibitors Targeting a Cryptic Allosteric Binding Site. *iScience* **2025**, *28* (9), 113300. https://doi.org/10.1016/j.isci.2025.113300.

3.1.2 Project 2: Binding Characterization of Multivalent Targeting Structures

(4) Forster, R.‡; Lantzberg, B.‡; **Weldert, A.**‡; Rosenberger, L.; Zeyn, Y.; Kowalczyk, D.; Kuan, S. L.; Kersten, C.; Bros, M.; Weil, T.; Schirmeister, T.; Opatz, T. Surface Density of Mono- and Trivalent High-Mannan-Derived Targeting Structures with Different Affinities Impacts Cellular Uptake of Human Serum Albumin-Derived Nanocarriers. *Biomacromolecules* **2025**, *26* (11), 8087–8102. https://doi.org/10.1021/acs.biomac.5c01510

3.2 Publications Beyond this Doctoral Thesis

(5) Hoba, S. N.‡; Schwickert, M.‡; Kammerer, L.; Sabin, M.; **Weldert, A. C.**; Nidoieva, Z.; Meidner, J. L.; Barthels, F.; Schirmeister, T.; Kersten, C. Parallel Synthesis of 5′-Amino-5′-Deoxy-Adenosine Derivatives for Focused Chemical Space Exploration and Their Application as Methyltransferase Inhibitors. *RSC Med Chem* **2025**, *16* (11), 5395–5418. https://doi.org/10.1039/D5MD00376H.

(6) Nidoieva, Z.‡; Sabin, M. O.‡; Dewald, T.; **Weldert, A. C.**; Hoba, S. N.; Helm, M.; Barthels, F. A Microscale Thermophoresis-Based Enzymatic RNA Methyltransferase Assay Enables the Discovery of DNMT2 Inhibitors. *Commun Chem* **2025**, *8* (1), 32. https://doi.org/10.1038/s42004-025-01439-9.

(7) Meidner, J. L.‡; Frey, A. F.‡; Zimmermann, R. A.‡; Sabin, M. O.; Nidoieva, Z.; **Weldert, A. C.**; Hoba, S. N.; Krone, M. W.; Barthels, F. Nanomole Scale Screening of Fluorescent RNA-Methyltransferase Probes Enables the Discovery of METTL1 Inhibitors. *Angewandte Chemie International Edition* **2024**, *63* (48). https://doi.org/10.1002/anie.202403792.

(8) Previti, S.‡; Ettari, R.‡; Calcaterra, E.; Roggia, M.; Natale, B.; **Weldert, A. C.**; Müller-Ruttloff, C.; Salisch, F.; Irto, A.; Cigala, R. M.; Ziebuhr, J.; Schirmeister, T.; Cosconati, S.; Zappalà, M. Identification of Dual Inhibitors Targeting Main Protease (M pro) and Cathepsin L as Potential Anti-SARS-CoV-2 Agents. *ACS Med Chem Lett* **2024**, *15* (5), 602–609. https://doi.org/10.1021/acsmedchemlett.3c00562.

(9) Medrano, F. J.; de la Hoz-Rodríguez, S.; Martí, S.; Arafet, K.; Schirmeister, T.; Hammerschmidt, S. J.; Müller, C.; González-Martínez, Á.; Santillana, E.; Ziebuhr, J.; Romero, A.; Zimmer, C.; **Weldert, A.**; Zimmermann, R.; Lodola, A.; Świderek, K.; Moliner, V.; González, F. V. Peptidyl Nitroalkene Inhibitors of Main Protease Rationalized by Computational and Crystallographic Investigations as Antivirals against SARS-CoV-2. *Commun Chem* **2024**, *7* (1), 15. https://doi.org/10.1038/s42004-024-01104-7.

(10) Müller, P.; Zimmer, C.; Frey, A.; Holzmann, G.; **Weldert, A. C.**; Schirmeister, T. Ligand-Based Design of Selective Peptidomimetic UPA and TMPRSS2 Inhibitors with Arg Bioisosteres. *Int J Mol Sci* **2024**, *25* (3), 1375. https://doi.org/10.3390/ijms25031375.

(11) Hammerschmidt, S. J.; Barthels, F.; **Weldert, A. C.**; Kersten, C. Advanced Isothermal Titration Calorimetry for Medicinal Chemists with *ITCcalc*. *J Chem Educ* **2024**, *101* (3), 1086–1095. https://doi.org/10.1021/acs.jchemed.3c01133.

(12) Hammerschmidt, S. J.‡; Maus, H.‡; **Weldert, A. C.**‡; Gütschow, M.; Kersten, C. Improving Binding Entropy by Higher Ligand Symmetry? – A Case Study with Human Matriptase. *RSC Med Chem* **2023**, *14* (5), 969–982. https://doi.org/10.1039/D3MD00125C.

4 Discovery and Characterization of Novel Ligands for RNA Methyltransferases

4.1 Structure-Guided Design of a Methyltransferase-Like 3 (METTL3) Proteolysis-Targeting Chimera (PROTAC) Incorporating an Indole–Nicotinamide Chemotype

4.1.1 Context, Project Summary, and own Contribution

The RNA methyltransferase METTL3 is the catalytic core of the major m^6A writer complex and is implicated in a range of disease indications (Chapter 1.1.2).[109–114] Accordingly, several SAM-competitive inhibitors of METTL3 were developed, which show high biochemical potency, and one candidate, STC-15, has recently entered clinical trials. Yet many of these inhibitors display a gap between biochemical activity and cellular efficacy.[90,154,155,158] In addition, methyltransferase-independent functions of METTL3 cannot be addressed by inhibition of the enzyme alone. Consequently, PROTAC candidates targeting METTL3 have been developed. This technique offers a unique catalytic degradation mechanism, and degradation of METTL3 can address catalytic and non-catalytical functions alike. While previous studies demonstrated the therapeutic potential of METTL3 PROTACs, they solely rely on the METTL3 small-molecule inhibitor UZH2-derived METTL3 recruiters, which limits chemotype diversity.[480,481,484,485]

In this study, the METTL3 PROTAC **AF151** (compound **41**) was developed and characterized. **AF151** features a distinct indole–nicotinamide METTL3-binding chemotype. The development was conducted across four design cycles, guided by systematic optimization of METTL3 binding, choice of E3 ligase, exit-vector orientation, and linker properties, while tracking target affinity and degradation efficiency. To enable these studies, expression of the METTL3/14 complex was established in *E. coli* within this thesis, whereas it had previously been performed primarily in non-bacterial expression systems. **AF151** was further characterized mechanistically and exhibited dose- and time-dependent degradation that was dependent on the ubiquitin–proteasome system. Despite similar degradation efficiencies, a difference in the hook effect between **AF151** and the potent literature compound **WD6305**[485], was observed. Hence, biophysical FP and HTRF assays were established within this thesis to investigate the cooperativity of these compounds, supported by computational methods. While both compounds showed positive cooperativity, it was more pronounced for **WD6305**, which may

explain the lack of a hook effect for this compound. Notably, the strong cooperativity was generated by reduced binary affinity for the E3 ligase. In MOLM-13 AML cells, **AF151** reduced cell viability and global m^6A levels, with stronger effects than the parent small-molecule inhibitors. Additionally, the combination with the Bcl-2 inhibitor venetoclax led to slight synergy in cell viability reduction.

Overall, our study expands the chemical diversity of METTL3-targeting PROTACs, provides important mechanistic insights into degrader design, especially regarding the importance of cooperativity over binary affinity, and further highlights METTL3 degradation as a promising therapeutic strategy in acute myeloid leukemia.

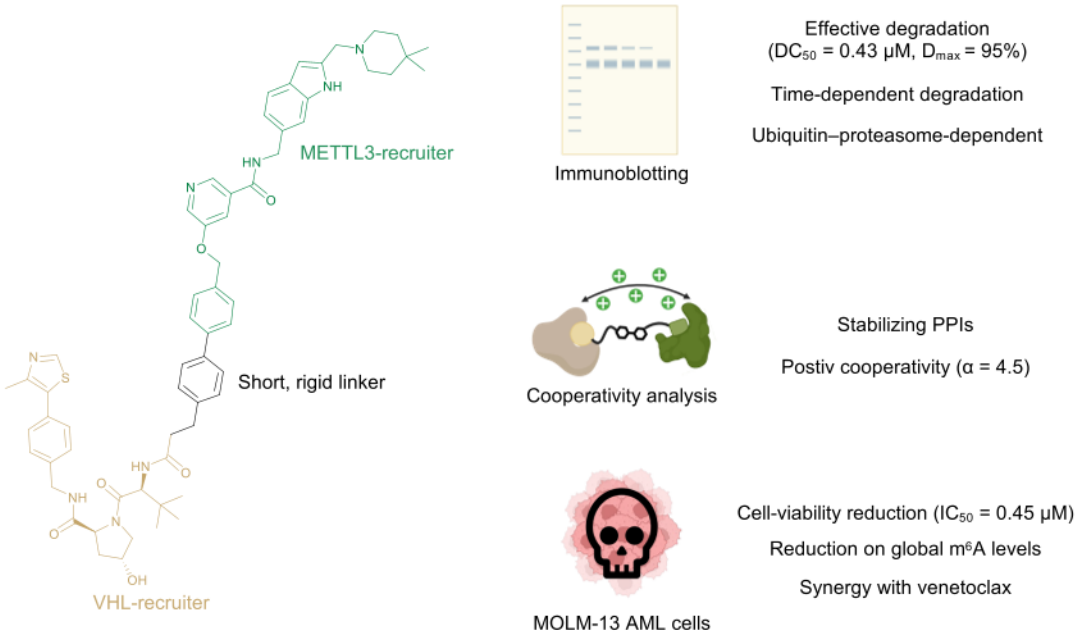


Figure 19: Methyltransferase-like protein 3 (METTL3) proteolysis targeting chimera (PROTAC) **AF151**. The PROTAC contains an METTL3 recruiter (green), a linker (black) and a Von Hippel–Lindau (VHL) recruiter. The PROTAC was evaluated in terms of degradation, cooperativity and effects in the acute myeloid leukemia (AML) cell line MOLM-13. Further abbreviations: PPIs (protein–protein interactions); DC_{50} (half-maximal degradation concentration); D_{max} (maximal level of target degradation). The figure was created with Microsoft PowerPoint, Biorender.com, and ChemDraw.

Own contributions: Establishing protein expression and purification of the METTL3/14 complex, protein expression and purification of the VHL–elongin B–elongin C (VCB) complex, binary FP assays (compounds **35–42**), establishing of ternary FP and HTRF assays (partly conducted by [redacted] as part of a supervised research module, compounds **AF151** and **WD6305**), molecular docking of ternary METTL3/14–VCB–ligand complexes (**AF151**, **WD6305**, **KH12**), preparation of docking poses for MD simulations, cell culture (80%), Western blot analysis (50%), writing the main part of the manuscript, writing parts of the supporting information.

Contributions from other authors: Syntheses, binary FP assays (compounds **5–34**), binary HTRF assays, MD simulations, cell culture (20%), Western blot analysis (50%), cell viability assays, RNA m^6A quantification, real-time apoptosis assay, writing parts of the manuscript, and supporting information.

The work was published in RCS Medicinal Chemistry (impact factor: 3.6) and licensed under a Creative Commons Attribution licence: https://creativecommons.org/licenses/by/3.0/. This publication and the complete supplementary information (SI) are available online at DOI: 10.1039/D5MD00359H. The appended Supporting Information represents an abridged version.

Publication reprinted with permission from RSC Med Chem **2025**, *16*, 4194. „Structure-guided design of a methyltransferase-like 3 (METTL3) proteolysis targeting chimera (PROTAC) incorporating an indole–nicotinamide chemotype. “

© 2025 The Royal Society of Chemistry.

4.1.2 Publikation

The following publication quoted (within “”) from page 48 to page 61 is exactly the same as the manuscript cited on page 47: “

RSC Medicinal Chemistry

ROYAL SOCIETY OF CHEMISTRY

RESEARCH ARTICLE

View Article Online
View Journal | View Issue

Check for updates

Cite this: *RSC Med. Chem.*, 2025, **16**, 4194

Structure-guided design of a methyltransferase-like 3 (METTL3) proteolysis targeting chimera (PROTAC) incorporating an indole–nicotinamide chemotype†

Annabelle C. Weldert, [a] Ariane F. Frey, [a] Mackenzie W. Krone, [b] Franziska Krähe,[a] Hannah Kuhn, [a] Christian Kersten [ac] and Fabian Barthels *[ab]

Methyltransferase-like 3 (METTL3) is the main catalytic subunit of the m^{6}A methyltransferase complex (MTC) and plays an essential role in various disease indications, including acute myeloid leukemia (AML). Here, we describe the structure-guided design and evaluation of METTL3 proteolysis-targeting chimeras (PROTACs), starting from the potent small-molecule inhibitor STM2457. Across four design generations, we highlight key considerations, particularly regarding the exit vector, linker mechanics, and METTL3-binding chemotype composition. Our most effective PROTAC, AF151, forms a stable complex between the E3 ligase von Hippel–Lindau (VHL) and the target-of-interest METTL3, demonstrating efficient METTL3 degradation (DC_{50} = 430 nM) in the AML cell line MOLM-13. This molecule candidate exhibits more pronounced effects on viability inhibition (IC_{50} = 0.45 μM) and more significant m^{6}A level reduction in cancer cells than its non-PRTOAC parent compounds. By incorporating the indole-nicotinamide chemotype as the METTL3-binding recruiter, this PROTAC is structurally distinct from recently published METTL3 PROTACs, expanding the design options for future METTL3 degrader development.

Received 25th April 2025,
Accepted 18th June 2025

DOI: 10.1039/d5md00359h

rsc.li/medchem

Open Access Article. Published on 19 June 2025. Downloaded on 1/15/2026 12:32:17 PM.
This article is licensed under a Creative Commons Attribution 3.0 Unported Licence.

Introduction

RNA modifications are critical for cellular activities, both at the transcriptional and post-transcriptional levels. Among the various RNA modifications, N^6-methyladenosine (m^{6}A) is the most prevalent in mammalian cells,[1] influencing gene expression and cellular processes such as differentiation and stress adaptation.[2–4] m^{6}A is regulated by three key protein groups: writers (methyltransferases), erasers (demethylases), and readers (m^{6}A-binding proteins).[5] The primary writer of m^{6}A in mRNA is the m^{6}A methyltransferase complex (MTC), consisting of methyltransferase-like 3 and 14 (METTL3 and METTL14) and their cofactors, like the Wilms' tumor 1-associating protein (WTAP).[6] As the enzymatic core of the MTC, METTL3 transfers methyl groups from its co-substrate *S*-adenosylmethionine (SAM) to target mRNA, while METTL14 facilitates RNA substrate recognition.[7]

The MTC plays a critical role in numerous diseases, including cardiovascular diseases,[8] viral infections,[9,10] and neurological disorders.[11] Additionally, METTL3 is overexpressed in various cancers, including hematological,[12] lung,[13] and liver cancer.[14] In acute myeloid leukemia (AML), METTL3 enhances the translation of oncogenes like Bcl2, promoting cell survival.[12] Moreover, its depletion leads to cell cycle arrest, differentiation, and apoptosis, delaying leukemia progression.[12,15] Similarly, small-molecule inhibition of METTL3 has been shown to reduce AML growth and increase differentiation and apoptosis, highlighting the pharmacological potential to target METTL3.[16] Several small-molecule METTL3 targeting SAM-competitive inhibitors have been reported, including the selective and highly potent UZH2,[17] EP652,[18] STM2457,[16] and STM3006.[19] The latter two compounds were developed by STORM Therapeutics, whose lead candidate, STC-15, recently entered clinical trials, being the first RNA methyltransferase inhibitor in this class.[20,21]

Despite their low nanomolar potency in biochemical assays, most METTL3 inhibitors require micromolar concentrations to reduce m^{6}A mRNA modification levels in cells,[16,17,19] likely due to competition with the high intracellular concentration of SAM and other

[a] *Institute of Pharmaceutical and Biomedical Sciences, Johannes Gutenberg-University, Staudingerweg 5, 55128 Mainz, Germany. E-mail: barthels@uni-mainz.de*
[b] *Department of Molecular, Cellular, and Developmental Biology, Yale University, 260 Whitney Ave, CT 06520-8103 New Haven, USA*
[c] *Institute for Quantitative and Computational Biosciences, Johannes Gutenberg-University, BioZentrum I, Hanns-Dieter-Hüsch Weg 15, 55128 Mainz, Germany*
† Electronic supplementary information (ESI) available. See DOI: https://doi.org/10.1039/d5md00359h

This journal is © The Royal Society of Chemistry 2025

View Article Online
RSC Medicinal Chemistry Research Article

Open Access Article. Published on 19 June 2025. Downloaded on 1/15/2026 12:32:17 PM.
This article is licensed under a Creative Commons Attribution 3.0 Unported Licence.

pharmacokinetic effects.[22] Furthermore, m^{6}A-independent mechanisms for METTL3, which cannot be captured by competitive SAM inhibition, have been demonstrated to promote tumorigenesis and translation as well.[13,23] Hence, an alternative approach to target catalytic and non-catalytic functions of METTL3 at the same time is selective degradation using proteolysis-targeting chimeras (PROTACs). PROTACs are an emerging class of new modalities in drug discovery, with recent candidates entering late-stage clinical trials.[24,25] These heterobifunctional small molecules contain a protein of interest (POI) ligand, an E3 ligase ligand, and a linker connecting both. PROTACs form ternary complexes with the E3 ligase and POI, leading to ubiquitination and subsequent degradation of the POI *via* the ubiquitin–proteasome system (UPS). This targeted protein degradation impairs both enzymatic and structural functions, thereby expanding therapeutic applications.[26–29]

During the preparation of this manuscript (2024–2025), the first reports of heterobifunctional degraders targeting METTL3 have been published, highlighting the current interest in this specific target class.[30–33] Yet, all reported METTL3 PROTACs are based on the METTL3 recruiting chemotype of UZH2, limiting their structural diversity. Errani *et al.* developed degrader molecules that achieved approximately 50% degradation of METTL3 in multiple AML cell lines.[30] Almost simultaneously, Du *et al.* published the potent (D_{max} ~ 91%) METTL3 degrader WD6305.[31] Soon after, Hwang *et al.* further highlighted the therapeutic potential of METTL3 degradation in gastric cancer cells by targeting its non-catalytic function.[32] Meanwhile, Nar *et al.* demonstrated the synergistic effects of their METTL3 degraders with other anti-cancer agents.[33] While all these studies confirm the therapeutic potential of METTL3 degraders, particularly against AML, the METTL3 PROTACs developed so far lack structural diversity, as all of them use UZH2 (ref. 17) as the METTL3-recruiting chemotype.

In this study, we report the development of **AF151** (compound **41**), a potent METTL3 degrader with an indole-nicotinamide METTL3 binding chemotype based on a series of METTL3 ligands developed by STORM Therapeutics[16] and EPICS Therapeutics.[18] **AF151** exhibits efficient METTL3 degradation and reduces viability in AML cells, offering a structurally distinct alternative to previously reported UZH2-based PROTACs. Here, our synthesis and testing of over 40 PROTAC candidates will support the continued development of METTL3 PROTACs.

Experimental section

Synthesis

The synthetic procedures of all compounds, including NMR and LC-MS data, are detailed in the ESI.†

Reference compounds

WD6305, MLN4924, and elvitegravir were purchased from MedChemExpress. Venetoclax, STM3006, and bortezomib were purchased from BLDpharm. STM2457 was purchased from Cayman Chemicals. VH032 (ref. 34) was synthesized according to reported procedures. Crystal structures of ligand complexes were taken from the Protein Data Bank (PDB).[35]

Recombinant protein expression and purification

METTL3/14. A METTL3/14 expression plasmid was used as described previously.[36] In brief, a pETDuet-1 vector containing the MTase domains of human METTL3 (UniProt: Q86U44, aa 252–580) and METTL14 (UniProt: Q9HCE5, aa 108–444) was introduced into *E. coli* BL21 (DE3) cells. The METTL3 construct carried a C-terminal Strep-tag II, while METTL14 was fused to an N-terminal hexahistidine (His_6) tag. The cells were grown in LB medium containing 100 μg mL^{-1} ampicillin at 37 °C and 160 rpm until they reached an optical density (OD_{600}) of ~0.6. Protein overexpression was induced by adding 0.1 mM isopropyl-β-D-1-thiogalactopyranoside (IPTG) and 0.1 mM $ZnCl_2$, followed by incubation for ~16 h at 18 °C. Cells were harvested by centrifugation and suspended in cold lysis buffer (10 mM potassium phosphate, pH 7.5, 300 mM KCl, 20 mM imidazole, 10% glycerol, 0.1 mM TCEP). Lysozyme, one tablet of protease inhibitor (cOMPLETE), and DNAse I were added. After a 30 minute incubation on ice, the cells were lysed by sonication, and the cell debris was removed by centrifugation. The resulting clear supernatant was kept on ice. The pellet was resuspended in lysis buffer, subjected to a second round of sonication, and centrifuged again to remove insoluble components. The clarified lysates were applied to a HisTrap HP column for affinity purification, pre-equilibrated in binding buffer (10 mM potassium phosphate, pH 7.5, 300 mM KCl, 20 mM imidazole). After washing with several column volumes of wash buffer (10 mM potassium phosphate, pH 7.5, 500 mM KCl, 20 mM imidazole), the protein was eluted with elution buffer (10 mM potassium phosphate, pH 7.5, 300 mM KCl, 250 mM imidazole). Finally, METTL3/14 was purified *via* size-exclusion (SEC), on a Superdex 16/60075 pg SEC column equilibrated with SEC buffer (25 mM Tris HCl, pH 7.5, 100 mM NaCl). METTL3/14 was flash-frozen in liquid nitrogen and stored at −80 °C.

VHL, elongin B, and elongin C (VCB)

VHL (UniProt: P40337, aa 1–213), elongin B (UniProt: Q15370, aa 1–118), and elongin C (UniProt: Q15369, aa 17–112) were expressed as a complex (VCB) as described previously with slight modifications.[37] Briefly, a pCDFDuet-1 vector containing elongin B and C and a pET28a vector containing VHL, harboring a hexahistidine (His_6) tag at the N-terminus, were co-transformed in *E. coli* BL21 (DE3) cells. The cells were grown in LB medium containing 50 μg mL^{-1} kanamycin and 50 μg mL^{-1} streptomycin sulfate at 37 °C and 160 rpm until they reached an OD_{600} of ~0.7. Overexpression was induced by adding 0.3 mM IPTG for ~16 h at 24 °C. After harvesting the cells by centrifugation, the pellet was resuspended in cold lysis buffer (50 mM HEPES, pH 8.0,

Open Access Article. Published on 19 June 2025. Downloaded on 1/15/2026 12:32:17 PM.
This article is licensed under a Creative Commons Attribution 3.0 Unported Licence.

500 mM NaCl, 20 mM imidazole, 5 mM mercaptoethanol). One tablet of protease inhibitor and DNAse I were added, and the cells were lysed by sonication. After removing the cell debris with centrifugation, the supernatant was filtered and applied to a HisTrap HP column for affinity purification, pre-equilibrated in lysis buffer. Unbound sample was washed with 10 CV lysis buffer, and the VCB complex was eluted in a linear gradient of elution buffer (50 mM HEPES, pH 8.0, 500 mM NaCl, 500 mM imidazole, 5 mM mercaptoethanol) from 0 to 100% over 20 CV. The pooled fractions were combined and dialyzed against 20 mM HEPES, pH 8.0, 20 mM NaCl, and 1 mM DTT at 4 °C overnight. Afterwards, the VCB complex was subjected to anion exchange chromatography (AEX) on a HiTrap HP column, preequilibrated in dialysis buffer. The protein complex was eluted in a linear gradient of elution buffer 2 (20 mM HEPES, pH 8.0, 500 mM NaCl, 1 mM DTT) from 0 to 100% over 20 CV. Lastly, the VCB complex was purified by SEC on a Superdex 16/600 75 pg SEC column equilibrated with SEC buffer (20 mM HEPES, pH 7.5, 100 mM NaCl, 1 mM TCEP). The VCB complex was flash-frozen in liquid nitrogen and stored at −80 °C.

Fluorescence polarization (FP) assays

Fluorescence polarization (FP) displacement assays with METTL3/14 (ref. 36) and VCB[38–40] were performed following previous protocols with slight adaptations. All experiments were conducted in black Greiner 96-well half-area plates using a Tecan Spark 10 M plate reader, equipped with polarization filters coupled to a monochromator setup (λ_{ex} = 480 nm, λ_{em} = 530 nm). Reaction mixtures for METTL3/14 contained 300 nM recombinant enzyme, 20 nM FAM-labelled displacement tracer (STM-FL[36]), and the test compounds at varying concentrations in 25 mM Tris HCl, pH 7.5, 100 mM NaCl, and 10% DMSO. For VCB, the mixtures contained 40 nM recombinant enzyme, 10 nM FAM-labelled probe (FAM-DEALAHypYIPMDDDFQLRSF, Tocris Bioscience), and the tested compounds, at varying concentrations, in 50 mM Tris, pH 7.5, 200 mM NaCl, 2 mM DTT, and 10% DMSO. For the ternary K_D determinations, METTL3/14 was added at 12 μM, corresponding to approximately a 30- to 100-fold excess of binary K_D. All measurements were performed at least as technical triplicates. Polarization values (mP) were determined from polarization-specific parallel and orthogonal fluorescence intensities using the Tecan in-built calculation routine. Using GraphPad Prism 8.0.1, the FP values were normalized, and K_D values were calculated using a 4-parameter Hill equation: y(% probe bound) = bottom + ([ligand]slope) × (top–bottom)/([ligand]slope + K_D slope).

Homogeneous time-resolved fluorescence (HTRF) assays

PROTACs binding to VHL or CRBN were measured using a homogeneous time-resolved fluorescence (HTRF) human VHL or CRBN binding kit (Revvity). Samples were prepared according to the manufacturer's protocol, with compounds diluted in the provided diluent while maintaining a constant DMSO concentration with a final concentration of 1.25%. For the ternary K_D determinations, METTL3/14 was added at 4 μM, corresponding to approximately a 20- to 40-fold excess of binary K_D, while all other component concentrations were kept as specified in the protocol. Measurements were performed in triplicate using a Tecan Spark 10 M plate reader, recording donor and acceptor emissions at λ_{em_donor} = 620 nm and $\lambda_{em_acceptor}$ = 665 nm, respectively, following excitation of the HTRF donor at λ_{ex} = 320 nm. The acceptor-to-donor emission ratio was calculated as ratio = signal 665 nm/signal 620 nm. Using GraphPad Prism 8.0.1, the fluorescence values were normalized, and K_D values were calculated as specified above.

Computational analysis

Docking. Ternary PROTAC docking was performed using method 4B of the degrader modeling tool in the Molecular Operating Environment (MOE) 2022.02.[41–43] Briefly, in this method, two protein–ligand complexes were provided, one for the E3 ligase and one for the target. Additionally, the structure of the entire degrader was provided. Protein–protein docking was conducted between the E3 ligase and target complex, and subsequently, different conformations for the PROTAC compound were generated. Lastly, the protein–protein docked ensemble and the PROTAC conformational ensemble were combined. A cluster number was generated for the protein and PROTAC conformations found across all poses, and a double cluster number was assigned by concatenating the two individual cluster numbers. This double cluster population can then be used to prioritize hit selection.[42] The following specifications were applied: PROTAC structures were protonated using Protonate3D[44] and energy-minimized using the MMFF94x[45] force field, while all other calculations employed the Amber10:EHT force field. For WD6305 (ref. 31) and KH12,[32] METTL3/14 (PDB: 7O2F[17]) and VCB (PDB: 4W9H[34]), crystallographic binding modes of the MTase and VHL ligands were directly used as templates in the docking protocol. For **AF151**, VCB (PDB: 4W9H[34]) was also used directly, whereas for METTL3/14 (PDB: 8BN8 (ref. 19)) a template docking with the METTL3/14-binding moiety of **AF151** was performed before ternary complex docking. Missing residues and loops were reconstructed before docking using MOE's *de novo* loop modeler. For MD simulations, for each ternary complex (VCB–**AF151**–METTL3/14, VCB–KH12–METTL3/14, and VCB–WD6305–METTL3/14), the best-scoring representative structures of the three largest double clusters were selected. All structures were protonated using Protonate3D within MOE to account for changes from the ternary complex formation.

Molecular dynamics (MD) simulations

PROTACS were parameterized using antechamber[46] and parmchk2 from the AmberTools24 (ref. 47) with the generalized amber force field (GAFF2 (ref. 48)) and AM1-BCC

 This journal is © The Royal Society of Chemistry 2025

Open Access Article. Published on 19 June 2025. Downloaded on 1/15/2026 12:32:17 PM.
This article is licensed under a Creative Commons Attribution 3.0 Unported Licence.

charges.[49] Ternary complex structures were built with tleap and minimized using sander over 200 time steps. Complexes were then neutralized using sodium ions (Na^+) and solvated using a TIP3P[50] water box exceeding the complexes by 10.0 Å in every dimension. Equilibration and production were performed with NAMD2.14 (ref. 51) and the AMBER (ff19SB[52]) force field. Equilibration was performed over 1 ns with gradually releasing harmonic constraints on the PROTAC and protein atoms and heating from 100 to 300 K. Production MD simulations were performed over 20 ns (all) and prolonged to 100 ns for selected structures (see below) using time steps of 2 fs with rigid bond lengths and a van-der-Waals cut-off of 14.0 Å using periodic boundary conditions in an NPT ensemble. Simulations were visually inspected and analyzed using VMD-1.9.3.[53] Molecular mechanic-generalized born surface area (MM-GBSA) analysis was performed using the 1-trajectory (1A) method with the ante-MMPBSA.py and MMPBSA.py[54] implementation of AmberTools24 with GB model igb5.[55] Simulations of 20 ns or 100 ns, respectively, were analyzed using an interval of 0.1 ns and a salt concentration of 0.1 M. As described previously,[56] the energetic contributions were dissected into their respective parts from the individual binary and ternary complexes from target (T, here METTL3/14), E3 ligase (E, here VCB), and PROTAC (P) (Tables S2 and S3†).

Cell culture

Human acute myeloid leukemia MOLM-13 cells were cultured in Roswell Park Memorial Institute (RPMI 1640) medium with 10% fetal bovine serum (FBS) and 100 μg mL^{-1} penicillin–streptomycin mix at 5% CO_2 and 37 °C. Cell densities were maintained at 0.3–2 × 10^6 cells per mL. MOLM-13 cells were obtained from DSMZ-German Collection of Microorganisms and Cell Cultures GmbH. All reagents and tissue culture plastics were purchased from Thermo Fisher Scientific.

Immunoblotting

MOLM-13 were seeded in 12-well cell culture plates at a density of 1 × 10^6 cells per mL and treated with DMSO (final: 0.1%) or different concentrations of PROTAC degraders in DMSO at the indicated times. Treatments were conducted in biological triplicate with varying passages of MOLM-13 cells. The cells were harvested by centrifugation at 500*g* for 5 min and washed with PBS. The cells were lysed with RIPA lysis buffer with the addition of protease inhibitor (1× cOMPLETE), and insoluble cellular parts were separated by centrifugation (12 000*g* for 10 min), subsequently, the supernatant was boiled with 1× Laemmli sample buffer (Carl Roth) for 5 min at 95 °C. Proteins were separated by SDS–PAGE on 4–20% Criterion™ TGX™ Precast Protein Gels (Bio-Rad) and transferred to Amersham™ Protean® 0.45 μm nitrocellulose membrane (Cytiva) using semi-dry transfer (25 V, 1 A, Towbin buffer). The membrane was blocked with 5% milk (Carl Roth) in TBST buffer and incubated with the following primary antibodies: Anti-METTL3 (1 : 1000, Abcam, ab195352), anti-METTL14 (1 : 1000, Abcam, ab220030), anti-Bcl2 (1 : 1000, Cell Signaling Technology [CST], EPR16891), anti-Mcl-1 (1 : 1000, CST, 5453 T), anti-Bcl-XL (1 : 1000, CST, 2764 T), anti-vinculin (1 : 1000, CST, 13901) or anti-GAPDH (1 : 5000, CST, D17C4) overnight at 4 °C. Subsequently, the membrane was incubated for 1 h at RT with secondary antibodies: anti-rabbit (1 : 2000, VWR, NA934) or anti-mouse (1 : 2000, VWR, 102646-160). The protein bands were detected *via* chemiluminescence using Pierce™ ECL western blotting substrate and a Fusion FX imaging system (Vilber). The ImageLab software (Bio-Rad) was used for band quantification.

Reverse transcription polymerase chain reaction (RT-qPCR)

To determine mRNA expression levels of METTL3 and METTL14, MOLM-13 cells were treated in triplicate with compound **41** (**AF151**, 2 μM), STM2457 (10 μM), and DMSO for 24 resp. 48 h. Afterward, total RNA was extracted using the TRIzol™ reagent (Thermo Fisher Scientific) and purified with the Monarch® Spin RNA Cleanup Kit (New England Biolabs). RT-qPCR was conducted using the two-step GoTaq® RT-qPCR system (Promega) following the manufacturer's protocol. The data were normalized to the DMSO control and GAPDH housekeeping gene (ΔΔCt) using GraphPad Prism 8.0.1. The primer sequences used for RT-qPCR are listed in Table S4.†

Cell viability assays

To determine cell viability, MOLM-13 cells were treated with the indicated compounds in a 1 : 1 serial dilution, with pure DMSO (final: 0.1%) as the negative control. Briefly, 1000 cells were seeded in black Greiner half-area 96-well plates and incubated for 72 h with inhibitors from DMSO stocks under standard cultivation conditions. Then, Promega CellTiter Glo 2.0 reagent was added to each well according to the manufacturer's protocols, and luminescence was measured using a Tecan Spark 10 M. Experiments were conducted in technical triplicate. Data was normalized to the DMSO control and analyzed with GraphPad Prism 8.0.1 to determine EC_{50} values. Synergistic effects of venetoclax and **AF151** on cell MOLM-13 viability were conducted accordingly, with dilution series of both compounds analyzed using the SynergyFinder+ webtoolkit.[57]

RNA m^6A quantification

Quantification of m^6A levels upon compound treatment was conducted in analogy to the study introducing the WD6305 PROTAC.[31] MOLM-13 cells were treated with **AF151** (2 μM), STM2457 (10 μM), and DMSO in triplicate for 24 and 48 h. Total RNA was isolated as specified above. PolyA mRNA was then isolated using the PolyATtract® mRNA Isolation System (Promega). m^6A levels were quantified using a colorimetric m^6A RNA methylation Assay Kit (Abcam) as specified in the manufacturer's protocol. The data was normalized to the DMSO control and displayed using GraphPad Prism 8.0.1.

View Article Online
Research Article RSC Medicinal Chemistry

Open Access Article. Published on 19 June 2025. Downloaded on 1/15/2026 12:32:17 PM.
This article is licensed under a Creative Commons Attribution 3.0 Unported Licence.

Real-time apoptosis assay

MOLM-13 cells were treated with **AF151** at the indicated concentrations for 48 h, with DMSO (final: 0.1%) as the negative control. Apoptosis of technical triplicate samples was detected in real-time using the RealTime-Glo™ annexin V apoptosis assay kit (Promega), following the manufacturer's protocol. Data were plotted using GraphPad Prism 8.0.1.

Results and discussion

Development and initial evaluation of PROTAC candidates

The development pipeline of our METTL3 PROTACs, spanning four molecular generations, is shown in Fig. 1. In our heterobifunctional designs, we aimed to recruit the E3 ligases von Hippel–Lindau (VHL) or cereblon (CRBN) in a ternary complex with METTL3, since well-established ligands are available for all proteins.[58] For VHL, we chose VH032 (ref. 34) and VL285 (ref. 59) (hereinafter referred to as VHL-LH and VHL-RH, respectively), and for CRBN, 4-hydroxy and 5-hydroxy thalidomide[60] as E3 ligase ligands. For METTL3, we chose the small molecule inhibitor STM2457, developed by STORM Therapeutics, due to its high selectivity and potency.[16] Compounds from the STM series show high *in vitro* potency, favourable ADME properties, and efficient m^{6}A level reduction in cancer cells. Compared to the UZH2-based degraders, the STM-based parent compound has been characterized more extensively in clinically relevant AML models. In this regard, STC-15 has shown a robust average reduction of 63% in m^{6}A levels in peripheral blood in humans in a phase 1 clinical trial.[20]

To identify a suitable attachment point for linker conjugation, we analyzed the X-ray structure of STM2457 bound to METTL3 (PDB: 7O2I[16]). Since the cyclohexyl moiety of STM2457 allows the attachment of a solvent-exposed exit vector (Fig. 1A), we selected this molecular segment for linker attachment. Based on the results of a SAR study reported by STORM Therapeutics,[61] we attached a linker segment directly to the secondary amine instead of the cyclohexyl moiety. Further, the original imidazopyridine scaffold was replaced with a benzimidazole for synthetic reasons, yielding **POI-1** (Fig. 1B). To connect **POI-1** to the E3 ligase ligands, we opted for polyethylene glycol (PEG$_n$, n = 1–5) linkers, yielding our first generation of METTL3 PROTACs (Fig. 1C). Synthesis and detailed structure of all generations are shown in the ESI.†

Next, we evaluate the affinity of the PROTAC candidates for METTL3 binding using a competitive fluorescence polarization (FP) assay (Table S1†). This revealed that VHL-based PROTACs exhibited an overall higher affinity for METTL3 compared to CRBN-based PROTACs. However, in general, the METTL3 affinities of our first-generation PROTACs were relatively low compared to the parent compound STM2457 (K_D = 1.4 nM[16]), with our best compounds showing affinities around K_D ~ 4 μM (Table S1†). We concluded that the cyclohexyl moiety of STM2457 is

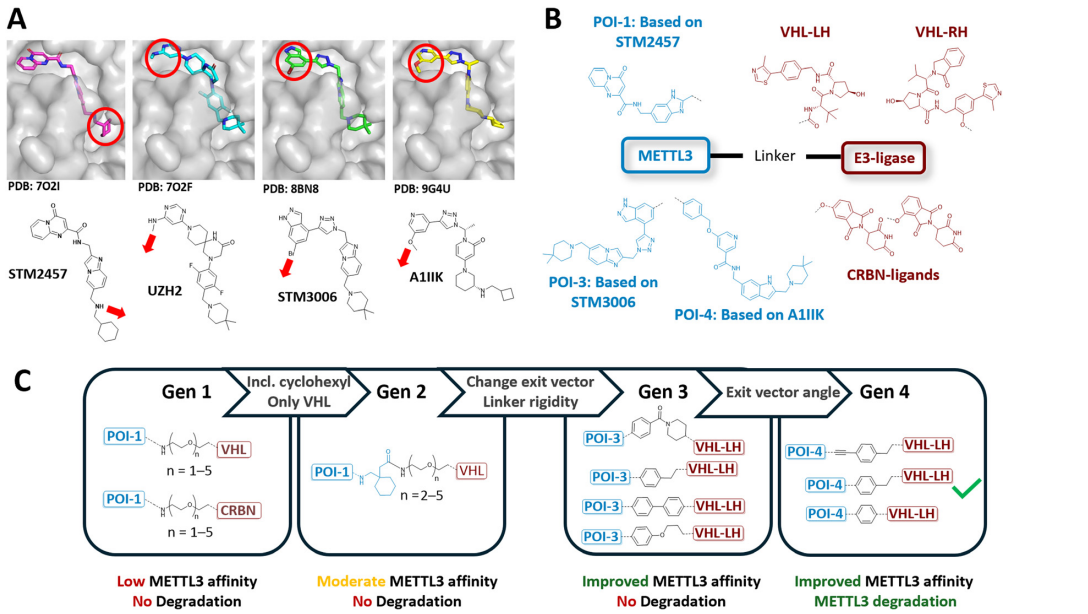


Fig. 1 Development pipeline of PROTACs targeting METTL3. (A) Crystal structures of various METTL3-targeting small-molecule inhibitor complexes: STM2457 (PDB: 7O2I), UZH2 (PDB: 7O2F), STM3006 (PDB: 8BN8), and A1IIK (PDB: 9G4U), showing solvent-exposed regions and thereby possible exit vectors for linker attachment sides. (B) General design and selected structures of our METTL3 PROTAC strategy, including METTL3 and E3 ligase binding moieties used in this study. (C) Structural representation of METTL3 PROTAC development across four generations, specifying changes made between each generation.

 This journal is © The Royal Society of Chemistry 2025

View Article Online
RSC Medicinal Chemistry Research Article

Open Access Article. Published on 19 June 2025. Downloaded on 1/15/2026 12:32:17 PM.
This article is licensed under a Creative Commons Attribution 3.0 Unported Licence.

necessary for high-affinity METTL3 binding. Furthermore, Hwang *et al.* and Errani *et al.* have reported that CRBN-based METTL3 PROTACs exhibit lower degradation activity compared to their VHL-based counterparts.[30,32] Hence, we decided to focus only on the VHL-based PROTACs in the following generations of PROTACs.

Subsequently, we synthesized our second generation of VHL-based PROTACs, including a cyclohexyl motif (Fig. 1C), which demonstrated improved METTL3 affinity (K_D ~ 300 nM, Table S1†). Next, we screened the METTL3 degradation activities of our most promising 2nd-generation PROTACs in MOLM-13 cells. However, none of these molecule candidates showed significant METTL3 degradation activity after treatment (final: 0.1–10 μM) for 16 h (Fig. S4†). Apart from possessing nanomolar affinity to METTL3 and the E3 ligase (Table S1†), PROTACs, in general, need to facilitate the right spatial orientation and alignment of both proteins to achieve efficient target degradation. Linker geometry, length, and rigidity play a crucial role in this process.[28,62,63] Errani *et al.* showed that moving from flexible PEG linkers to more rigid benzyl, piperidine, and piperazine linkers can improve METTL3 degradation; additionally, the increase in lipophilicity enhanced cellular permeability.[30] Furthermore, WD6305 (Fig. 2A), the highly potent PROTAC developed by Du *et al.*, features a relatively rigid and short linker compared to the less potent ones in this study.[31] Based on these findings, we selected a series of shorter and more rigid linkers for our third-generation design (Fig. 1C). Additionally, we theorized that the previously used exit vector of STM2457 (pointing to the RNA binding site) might not be optimal for METTL3–VCB complex formation in cellulo.[6,64,65] All currently published METTL3 degraders base their METTL3-binding functionality on UZH2, with a distinct exit vector away from the RNA binding site (Fig. 1A).

Hence, we changed our METTL3 recruiting ligand from STM2457 to STM3006, which allows us to exit METTL3 at a

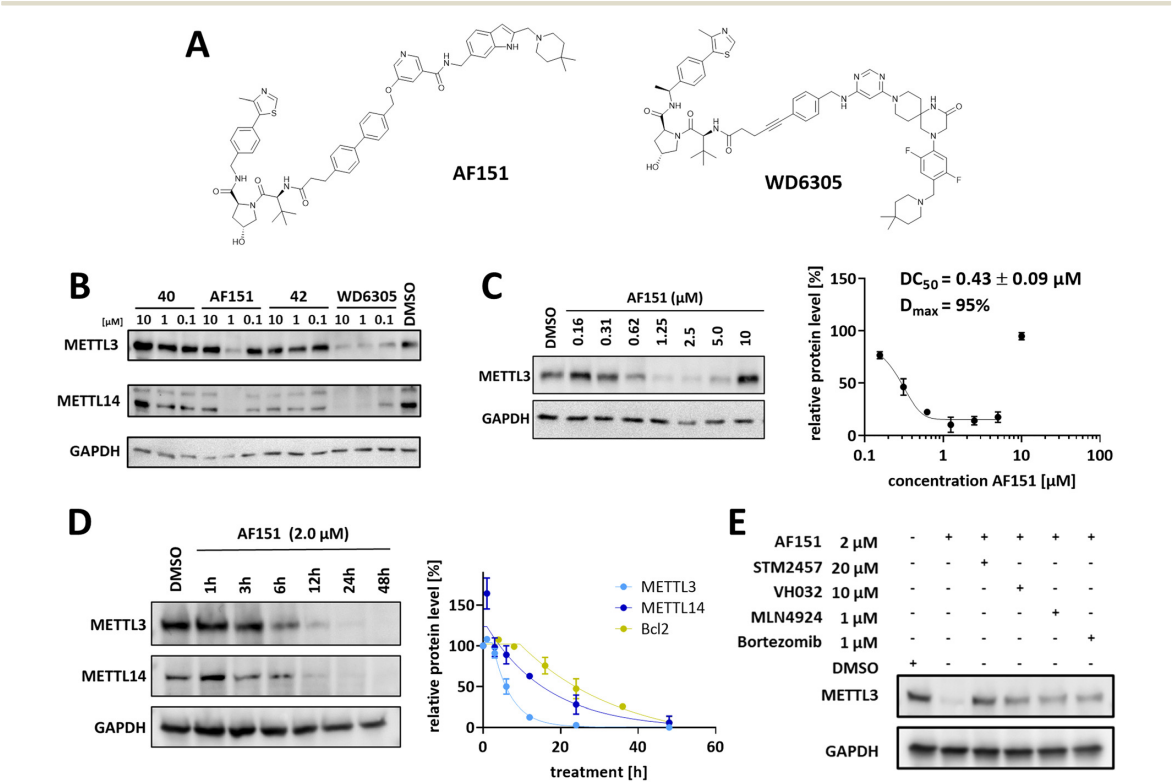


Fig. 2 Cellular characterization of METTL3 PROTAC **AF151**. (A) Structures of **AF151** and reference degrader WD6305, developed by Du *et al.*[31] (B) Western blots of PROTAC screening results analyzing the fourth generation of our PROTAC design. MOLM-13 cells were treated with the indicated compounds at different concentrations (10 μM, 1 μM, and 0.1 μM) for 16 h. WD6305 and DMSO were used as positive and negative controls. (C) Dose–response experiments and DC_{50} determination for **AF151** in MOLM-13 cells. Left: Western blot image after treatment at the indicated concentrations for 16 h. Right: Dose–response curve with different **AF151** concentrations plotted against METTL3 protein levels relative to the DMSO control. (D) Time course treatment experiments. Left: Western blot image after treatment with **AF151** at 2 μM at the indicated time points. Right: Time-response curve with different time points plotted against METTL3, METTL14, and Bcl-2 protein levels relative to the DMSO control. (E) Cellular PROTAC competition assay. MOLM-13 cells were treated with **AF151** in combination with the METTL3 inhibitor STM2457, VH032, MLN4924, or bortezomib at the indicated concentrations. Uncropped Western blot images can be found in Fig. S8–S11.†

Open Access Article. Published on 19 June 2025. Downloaded on 1/15/2026 12:32:17 PM.
This article is licensed under a Creative Commons Attribution 3.0 Unported Licence.

similar position to UZH2 by linker attachment to the indazole ring of **POI-3** (Fig. 1B).[19] Yet, despite these optimizations, cellular degradation analysis still showed little effect on METTL3 protein levels (Fig. S4†). Compared to the potent literature-known WD6305 METTL3 degrader, our **POI-3** geometry differs only slightly by the angle and the rigidity of the exit vector, while linker lengths and position of the linkage are very similar to UZH2-based PROTACs (Fig. 1A). Hence, to further refine the flexibility and the angle of the exit vector, we continued optimizing **POI-3**: the co-crystal structure of EPICS Therapeutics' A1IIK (PDB: 9G4U[18]) showed that replacing STM3006's indazole moiety with a pyridine scaffold will allow an STM-based METTL3 recruiting chemotype but with a UZH2-like exit vector (Fig. 1A),[18] and thus, yielding our 4th generation METTL3 recruiter **POI-4** (Fig. 1B).

Cell-based METTL3 degradation analysis showed that compound **41** (**AF151**, Fig. 2A), a **POI-4**-based PROTAC, led to significant degradation of METTL3 and its heterodimerized partner METTL14 after treatment for 16 h with 1 μM (Fig. 2B). To summarize, while our initial designs showed no METTL3 degradation, optimization efforts, including replacing flexible PEG linkers with more rigid linkers and refining the METTL3 exit vector, led to a functional METTL3 degrader in MOLM-13 cells.

Analysis of AF151's degradation efficiency and mechanism

Encouraged by the initial screening results, we further analyzed compound **41**'s (**AF151**) efficiency in degrading METTL3 in MOLM-13 cells and investigated the underlying molecular mechanisms. The half-degrading concentration (DC_{50}) after 16 h of treatment was determined to be 430 nM (Fig. 2C). Maximal degradation ($D_{max} \sim 95\%$) occurred at 2.5 μM, while we noticed a characteristic "hook effect" >5 μM, where METTL3 degradation decreased. The high concentration of PROTAC leads to saturation of binding sites on both METTL3 and VHL, forming predominantly binary complexes and preventing the formation of ternary complexes and thereby degradation. However, at compound concentrations >5 μM, AF151 still acts as an inhibitor of METTL3, since the catalytic activity of the enzyme is still blocked by the binary complexes.

Time-course analysis revealed that **AF151** induces rapid METTL3 degradation, achieving over 50% METTL3 reduction within the first 6 h of treatment, reaching maximal effect at 24 h, and maintaining it for at least 48 h (Fig. 2D). METTL14 was reduced alongside METTL3, in agreement with prior METTL3 PROTAC studies.[30–33] Of note, treatment with **AF151** led to an initial but transient increase of METTL14 (~150%) after 1 h before inducing METTL14 degradation. Similarly, Errani *et al.* reported elevated levels of METTL3/14 after treatment with the small-molecule inhibitor UZH2. They proposed an unknown cellular compensatory mechanism, which might have led to an increase of METTL14.[30,66] Half-lives for the degradation kinetics of METTL3 and METTL14 were determined at $t_{1/2}$ = 4 h and 11 h, respectively. Thus, the degradation of METTL14 is significantly slower than that of METTL3, which can be explained by the fact that METTL3 occurs not only in complexes with METTL14 but also in a monomeric state and other protein complexes in cells.[67]

Next, we investigated the functional mechanism of **AF151** by confirming the involvement of the UPS. Co-treatment of the degrader with the proteasome inhibitor bortezomib (1 μM),[68] neddylation inhibitor MLN4924 (1 μM),[69] and VH032 (10 μM)[34] suppressed METTL3 degradation, indicating that the process is both proteasome and VHL-dependent. Furthermore, adding a competitive METTL3 ligand STM2457 (20 μM) also inhibited degradation, confirming that **AF151** binds to the SAM-binding site of METTL3 (Fig. 2E).

Interestingly, the dose–response evaluation revealed that **AF151** and WD6305 share DC_{50} values (430 nM for **AF151** *vs.* 140 nM for WD6305 (ref. 31)) in the same order of magnitude, but only **AF151** displays a characteristic hook effect at concentrations up to 10 μM. The relative ternary complex population, and thereby the hook effect, is known to be mainly influenced by the cooperativity of ternary complex formation.[70,71] PROTACs can introduce *de novo* stabilizing or destabilizing protein–protein interactions during ternary complex formation. Hence, the binary binding affinity to METTL3 or the E3 ligase may differ from the ternary affinity in the presence of the second binding partner. This effect is quantified by the cooperativity factor ($\alpha = {K_D}^{binary}/{K_D}^{ternary}$). Positive cooperativity ($\alpha > 1$) indicates stabilizing *de novo* effects during ternary complex formation, while negative cooperativity ($\alpha < 1$) signifies destabilizing *de novo* interactions.[70,72]

To assess the cooperativity of **AF151** and WD6305, we employed a displacement FP assay, previously described to assess PROTAC cooperativity.[38,39] In this assay, the VHL dissociation constants of both METTL3 PROTACs **AF151** and WD6305, with and without near-saturating METTL3 concentrations, were compared (Fig. 3A and B). Here, both PROTACs exhibited overall positive cooperativity (Fig. 3C), facilitating the interaction between METTL3 and VHL. Interestingly, the cooperativity factor of WD6305 (α = 23) is approximately five times higher than that of **AF151** (α = 4.5), which could possibly explain the observed differences in their hook effect characteristics (*i.e.*, lower binary affinity of WD6305 disfavors VHL-PROTAC complex formation in the absence of METTL3).

To validate these findings, we used a homogeneous time-resolved fluorescence (HTRF) assay to assess VHL affinity in the presence and absence of METTL3, confirming positive cooperativity for both PROTACs, with WD6305 displaying a higher α than **AF151** (Fig. S5†). Interestingly, the strong positive cooperativity for WD6305 is not due to an increased ternary affinity. The ternary K_D for **AF151** and WD6305 is very similar at 77 nM and 79 nM, respectively. Instead, the binary affinity of WD6305 for VHL (1.7 μM) is significantly reduced compared to **AF151** (363 nM) or parent compound VH032 (210 nM).

 This journal is © The Royal Society of Chemistry 2025

View Article Online

Open Access Article. Published on 19 June 2025. Downloaded on 1/15/2026 12:32:17 PM.
This article is licensed under a Creative Commons Attribution 3.0 Unported Licence.

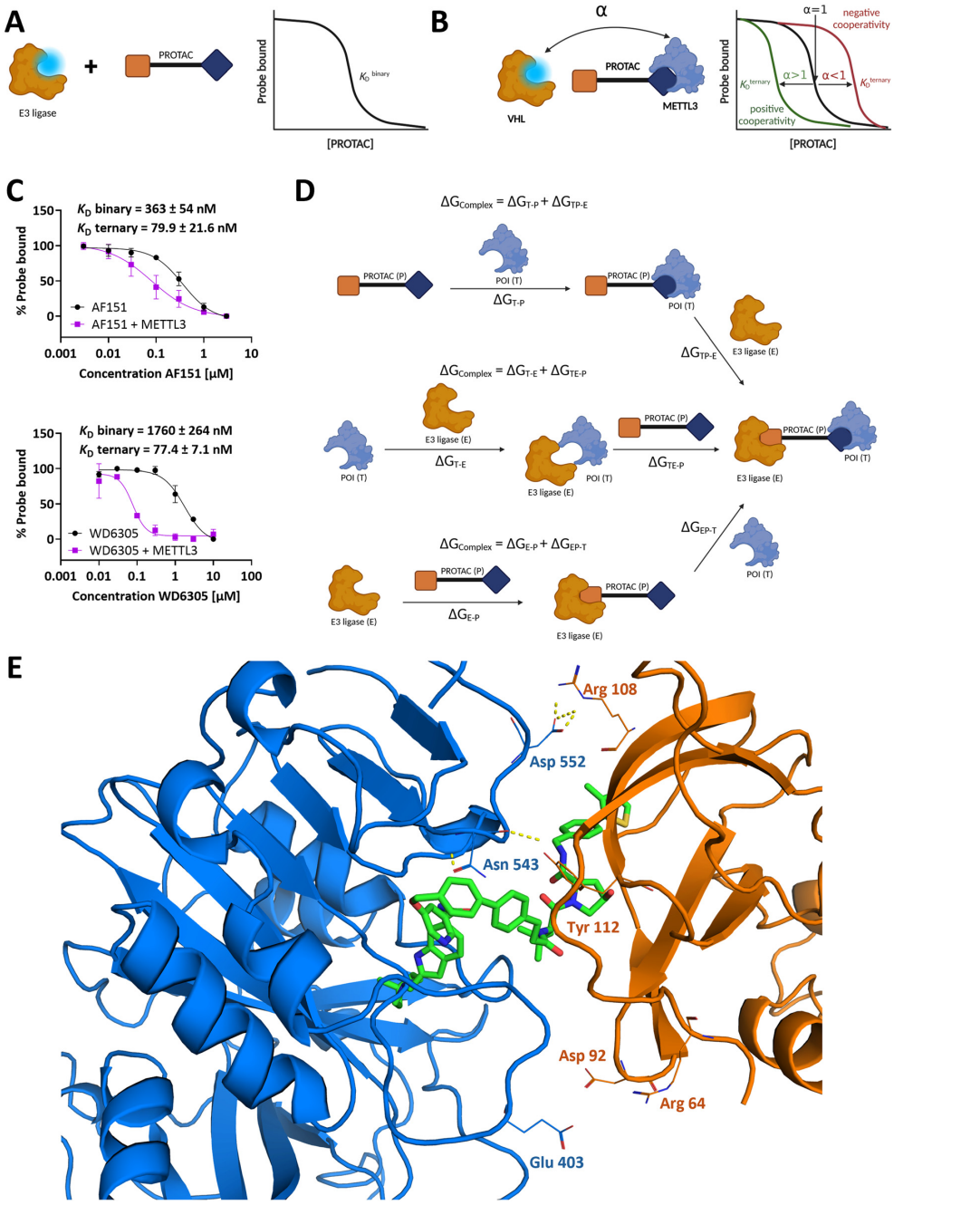


Fig. 3 Investigation of ternary complex formation and cooperativity for **AF151** and WD6305. (A and B) A fluorescent displacement probe binds to the E3 ligase and is displaced upon PROTAC molecule binding. The FP level of the displaced probe was used to determine the dissociation constant of PROTAC binding. Cooperativity is evaluated by comparing the PROTAC's affinity for the E3 ligase in the presence and the absence of METTL3. (C) Cooperativity factor (α) determination for **AF151** and WD6305 binding in the presence (purple) and absence (black) of METTL3 (12 μM). Each data point represents the mean ± SEM from triplicates repeated in two independent experiments. (D) Possible binary and ternary interactions between PROTAC (P), E3-ligase (E), and the protein of interest (target, T) can be described using Gibbs free energy (ΔG) for each interaction. The overall Gibbs free energy change for the formation of the ternary complex can be determined in three equivalent ways: $\Delta G_{complex} = \Delta G_{T-P} + \Delta G_{TP-E} = \Delta G_{E-P} + \Delta G_{EP-T} = \Delta G_{T-E} + \Delta G_{TE-P}$. (E) Most stable predicted binding mode for **AF151** in a ternary METTL3-VCB complex. The proteins are portrayed as cartoons, with the amino acids commonly found in protein–protein interactions across all simulations labeled as lines. Polar protein–protein interactions are shown as dashed yellow lines, and **AF151** is shown as green sticks. METTL3: blue, VHL: orange.

View Article Online
Research Article RSC Medicinal Chemistry

Open Access Article. Published on 19 June 2025. Downloaded on 1/15/2026 12:32:17 PM. This article is licensed under a Creative Commons Attribution 3.0 Unported Licence.

Computational analysis of METTL3 PROTAC complexes

For further investigation of the ternary complex formed by **AF151** and WD6305, the small molecule-induced protein–protein interface was evaluated using *in silico* PROTAC-docking with subsequent molecular dynamics (MD) simulations. Additionally, KH12, the METTL3 PROTAC from Hwang *et al.*, was included in this analysis, since this PROTAC has a comparable structure to WD6305 but exhibits a hook effect similar to **AF151**.[32] While PROTAC-docking provides possible geometries of ternary complexes, this coarse-grained method is not capable of discriminating the correct complex structure from incorrect ones, since the scoring function has insufficient accuracy.

Therefore, for each of the three PROTACs, three ternary complex structures were selected based on clustering and score for subsequent MD simulations. After short MD simulations of 20 ns, complex structures were evaluated based on their overall stability by root-mean-square-deviation (RMSD) analysis and complex stability using MM-GBSA calculations (Fig. S6, Table S2†). MM-GBSA was previously shown to be a good predictor for characterizing cooperativity, including stabilization and hook effects.[56] MD simulations of the most stable complexes per PROTAC, presumably representing the correct complex orientation, were prolonged to 100 ns each prior to MM-GBSA analysis of these effects (Fig. S7, Table S3†). As described previously, simulation times of 50–100 ns were found to be suitable for this analysis.[56] In these ternary complexes, there were only minor differences in MM-GBSA results between 50 ns and 100 ns, indicating sufficient sampling (Table S3†). Only the complex structure of WD6305 diverged from the starting structure after around 53 ns (Fig. S7C†). As the modeling of ternary PROTAC complexes is still in its infancy, some caveats must be raised. While MM-GBSA provides absolute binding free energy values, it should still be considered a coarse-grained method with limited accuracy. Therefore, instead of interpreting absolute ΔG-values, we performed only a qualitative, relative comparison between the ternary complexes. For higher accuracy, computationally more expensive absolute or relative binding free energy calculations (ABFE/RBFE) like free energy perturbations (FEP) or thermodynamic integration (TI) must be performed.[73–76] Likewise, the 1-trajectory (1A) MM-GBSA approach is a simplification assuming the different affinity contributions can be obtained from a single simulation of the ternary complex instead of seven simulations covering ternary and binary complexes and target, ligase, and PROTAC alone (Fig. 3D). Despite these limitations, some observations from MD simulations reveal trends for the molecules under discussion.

Within the 20 ns of simulation, the structurally most stable complexes (Fig. S6†) also showed stronger favorable binding free energies for the ternary complex ($\Delta G_{\text{complex}}$, Table S2†). METTL3/14 and VCB were internally very stable, while structural changes mostly occurred in the whole complex, hence the orientation between target and ligase.

The similar geometry of the complexes with the highest stability used for prolonged MD simulations of 100 ns hints towards the identification of the putatively correct geometry of the complexes (Fig. S7†). MM-GBSA analysis (Table S3†) showed a higher affinity of the PROTAC towards METTL3/14 ($\Delta G_{\text{T–P}}$) than to VCB ($\Delta G_{\text{E–P}}$) in line with FP binding assays. Further, all compounds show a stabilizing effect (positive cooperativity) caused by favorable METTL3/14-VCB (target–E3 ligase, $\Delta G_{\text{T–E}}$) interactions. Without PROTAC, $\Delta G_{\text{T–E}} \sim 0$ kcal mol^{-1}, strong protein–protein interactions should have stabilizing effects for ternary complex formation.

This is reflected in the predicted cooperativity ($\Delta G_{\text{TP–E}} - \Delta G_{\text{E–P}}$, Table S3†). Based on the predicted METTL3/14–**AF151**–VCB complex (Fig. 3E) and $\Delta G_{\text{T–E}}$ contribution from MM-GBSA, mainly hydrophobic contacts contribute to these direct target–ligase interactions. Additionally, some polar interactions are commonly found in the simulations, *e.g.*, Asp552 (METTL3) + Arg108 (VHL), Asn543 (METTL3) + Tyr112 (VHL), and Glu403 (METTL3) + Arg64 (VHL) (Fig. 3E). Hook effects can occur for PROTACs with high affinity to the target or ligase while having low or negative cooperativity. For KH12, the predicted affinity to both METTL3/14 ($\Delta G_{\text{T–P}}$) and VCB ($\Delta G_{\text{E–P}}$) is higher than for **AF151** and WD6305, which might explain the observed hook effect for this compound.[32]

However, this cannot explain the difference between **AF151** (hook effect) and WD6305 (no hook effect at given concentrations), as predicted affinities for METTL3/14 and VCB ($\Delta G_{\text{T–P}}$ and $\Delta G_{\text{E–P}}$, respectively) are similar, while the predicted stabilizing effect for **AF151** ($\Delta G_{\text{T–E}}$) is even higher. Notably, the simulations were performed considering only one possible geometry of the ternary complex, whereas *in vivo* and *in vitro*, different conformations of the complex might form, some of which could lead to less stable interactions.[77] Yet, ternary complex formation is crucial but insufficient by itself for protein degradation since ubiquitination and other cellular mechanisms also play an important role. Some of these alternative conformations possibly result in unproductive complexes.[78,79] Ultimately, the MD simulations reason that the differing degradation profile of **AF151** and WD6305 is not due to overall cooperativity differences and binding mode variation, but raises the hypothesis that one of the other effects influencing cellular degradation might be the reason for **AF151**'s hook effect.

Investigation of cellular response after AF151 treatment

Overall, **AF151** is able to form a stable ternary complex between VHL and METTL3, exhibiting positive cooperativity and effectively reducing METTL3 levels in MOLM-13 cells in a concentration-, time-, and UPS-dependent manner. To assess the cell biological effects of **AF151**, we investigated the cellular downstream responses of MOLM-13 cells following treatment with **AF151**. First, we evaluated METTL3 and METTL14 mRNA levels *via* RT-qPCR and found no significant changes in gene expression following **AF151** or STM2457

 This journal is © The Royal Society of Chemistry 2025

View Article Online

Open Access Article. Published on 19 June 2025. Downloaded on 1/15/2026 12:32:17 PM.
This article is licensed under a Creative Commons Attribution 3.0 Unported Licence.

treatment after 24 h and 48 h (Fig. 4A), thereby verifying that the alteration of METTL3 and METTL14 protein levels by **AF151** is due to degradation rather than inhibited protein expression or feedback stimulation of RNA synthesis. This is in agreement with literature experiments conducted for the WD6305 degrader.[31]

Parent compound STM2457 has been shown to suppress the methyltransferase activity of METTL3, leading to reduced m^{6}A levels and antiproliferative effects on AML cells.[16] Thus, we examined whether the compound-induced degradation of METTL3 similarly resulted in reduced cell viability. For comparison, we determined the reduction in MOLM-13 cell viability caused by **AF151**, WD6305, and STM2457. **AF151** (IC_{50} = 0.45 μM) exhibited a similar reduction in cell viability as WD6305 (IC_{50} = 0.78 μM) and fourfold more efficient cellular inhibition than parent compound STM2457 (IC_{50} = 1.82 μM) (Fig. 4B). This agrees with previous reports that the degradation of METTL3 provides a greater benefit in suppressing cell viability, and METTL3 degraders effectively promote apoptosis in cancer cell lines.[31–33] Next, we compared the effect of **AF151** and STM2457 on global m^{6}A levels in MOLM-13 cell total mRNA, finding that **AF151** caused a more pronounced m^{6}A reduction than the competitive inhibitor STM2457 alone (Fig. 4C).

METTL3 has been shown to regulate the translation of the anti-apoptotic protein Bcl-2 in cancer cells, and METTL3 inhibition using STM2457 leads to a reduction in Bcl-2 protein levels in AML.[16,80] Thus, we evaluated whether the degradation of METTL3 by **AF151** would lead to a decrease in Bcl-2 protein levels. Analysis of the MOLM-13 treatment time course showed that Bcl-2 protein levels decreased alongside METTL3 (Fig. 2D), albeit with slower kinetics ($t_{1/2}$ = 18 h), likely due to a delay in the reduction of METTL3-mediated RNA modifications on Bcl-2 mRNA (Fig. 4E). Recently, Jiao *et al.* demonstrated that inhibition of METTL3 by STM2457 leads to a decrease in Mcl-1 levels in AML cells, another antiapoptotic protein and member of the Bcl-2 family.[81] Thus, we evaluated the impact of METTL3 degradation by **AF151** on Mcl-1 levels. Additionally, we tested the effect on Bcl-XL, another Bcl-2 family member, whose protein levels, however, were not affected by METTL3 inhibition in the study by Jiao *et al.* In summary, we were able to reproduce these results: **AF151** leads to a time-dependent reduction of Bcl-2 and Mcl-1 but not Bcl-XL (Fig. 4E).

Next, we used a homogeneous luminogenic annexin V binding assay to follow MOLM-13 apoptosis levels and progressions in real time, revealing that **AF151** induces apoptosis after approximately 10 h in a dose-dependent manner (Fig. 4D), which is consistent with both the reduction

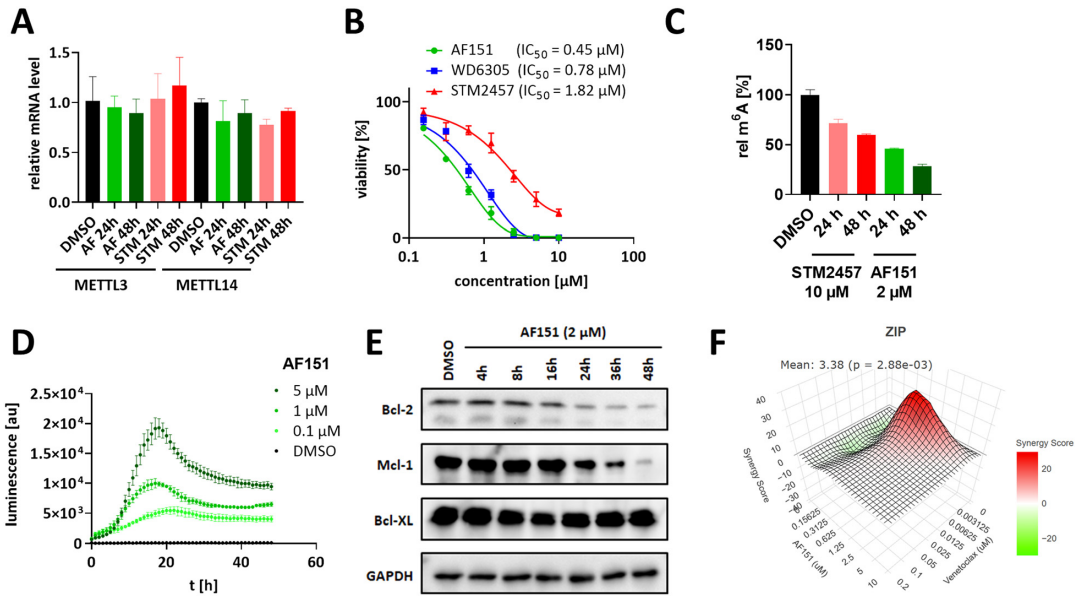


Fig. 4 Evaluation of **AF151** in MOLM-13 cells. (A) Relative METTL3 and METTL14 mRNA levels (ΔΔCt) after treatment with **AF151** (2 μM) or STM2457 (10 μM) for 24 h resp. 48 h. (B) Cell viability inhibition after treatment with varying concentrations of **AF151**, WD6305, and STM2457. (C) m^{6}A quantification of total mRNA isolated from MOLM-13 cells after treatment with **AF151** (2 μM) or STM2457 (10 μM) for the indicated durations. (D) Real-time apoptosis assay (homogeneous luminogenic annexin V binding assay). MOLM-13 cells were treated with **AF151** at the indicated concentrations, and apoptosis was monitored *via* luminescence over 48 h. (E) Time course treatment experiment of Bcl-like proteins performed analogously to Fig. 2D. Western blot image after treatment with **AF151** at 2 μM at the indicated time points. The corresponding time-response plot can be found in Fig. 2D. (F) Zero interaction potency (ZIP) analysis of co-treatment (72 h) with **AF151** and venetoclax in MOLM-13 cells. Quantification and illustration were generated with the SynergyFinder+ webserver.

Open Access Article. Published on 19 June 2025. Downloaded on 1/15/2026 12:32:17 PM.
This article is licensed under a Creative Commons Attribution 3.0 Unported Licence.

in cell viability and the kinetics of Bcl-2 level reduction. Jiao *et al.* showed that STM2457 synergistically enhances the antileukemic efficacy of the Bcl-2 inhibitor venetoclax and can overcome venetoclax resistance in *in vivo* experiments and resistance models. Hence, we hypothesized that co-treatment with a METTL3 degrader and venetoclax could equally lead to synergistic effects on cell viability reduction.

To test this hypothesis, we treated MOLM-13 cells with varying concentrations of **AF151** and venetoclax (Fig. 4F). The matrix of cell viability reduction was analyzed using the zero interaction potency (ZIP) model and quantified with the SynergyFinder method.[57,82] Co-treatment with **AF151** and venetoclax exhibited a slight synergistic reduction in cell viability, predominantly at lower concentrations of venetoclax (mean ZIP = 3.38, maximum ZIP = 28.87; Fig. 4F), *i.e.*, **AF151** is sensitizing MOLM-13 cells for treatment with venetoclax as the apoptosis-inducing effector, possibly by downregulation of Bcl-2 family proteins. Altogether, targeted degradation of METTL3 seems to be an effective strategy against AML and exhibits enhanced efficacy when combined with other agents.

Conclusions

In this work, we developed and characterized **AF151**, a functional METTL3 degrader, in MOLM-13 cells. In-depth characterization proved that **AF151** is an effective and rapid degrader of METTL3, utilizing the UPS. Our PROTAC candidates were developed across four design generations, including the evaluation of target affinities (*via* FP assays) and degradation potency (*via* immunoblotting). In this regard, we explored new chemotypes for METTL3 PROTAC development, offering a structurally distinct alternative to current UZH2-based PROTACs.[30–33] During our development process, we demonstrated that targeting the E3 ligase VHL is preferable to CRBN. Moreover, strategic improvements in METTL3 affinity, exit vector orientation, and linker flexibility were found to be essential. These insights and design guidelines will be a useful resource for following METTL3 PROTAC discovery campaigns.

In the course of this study, we have established an FP-based assay to assess binary METTL3 PROTAC affinities and utilized a literature-reported FP assay for binary and ternary VHL PROTAC interactions. Additionally, we performed MD simulations to analyze the ternary complex formation and cooperativity between METTL3 PROTACs and VHL. In this regard, we noticed the interesting finding that the potent published METTL3 PROTAC WD6305 has a reduced VHL affinity compared to the parent compound VH032, and this generates its strong positive cooperativity and efficient degradation profile.

Overall, we highlighted key design considerations when developing PROTACs targeting METTL3 and proved that an alternative METTL3-binding chemotype, distinct from previously published structures, can lead to the efficient degradation of METTL3. These degradation results, in conjunction with biophysical characterization of the PROTAC-mediated complexes, expand the toolbox for the development of future targeted METTL3 degraders.

Data availability

The data supporting this article have been included as part of the ESI.†

Author contributions

A. C. W.: data curation, formal analysis, investigation, validation, visualization, writing – original draft, A. F. F.: formal analysis, investigation, writing – original draft, M. W. K.: methodology, resources. FK: investigation. HK: investigation. CK: formal analysis, investigation, writing – original draft. FB: conceptualization, methodology, project administration, writing – review & editing.

Conflicts of interest

There are no conflicts of interest to declare.

Acknowledgements

Financial support by the Deutsche Forschungsgemeinschaft (DFG, German Research Foundation) project number 439669440 TRR319 RMaP A01 is gratefully acknowledged. We thank Prof. Craig M. Crews for the helpful discussions and his generosity in allowing us to conduct parts of the study in his laboratory. We thank Dr. Marco Jörg for his support during the Western blot experiments. We thank Axel Guthart for his support in preliminary docking experiments. Some Figures were created with **https://www.biorender.com/** and assisted by Dr. Michael Klein.

References

1 P. Boccaletto, F. Stefaniak, A. Ray, A. Cappannini, S. Mukherjee, E. Purta, M. Kurkowska, N. Shirvanizadeh, E. Destefanis, P. Groza, G. Avşar, A. Romitelli, P. Pir, E. Dassi, S. G. Conticello, F. Aguilo and J. M. Bujnicki, *Nucleic Acids Res.*, 2022, **50**, D231–D235.
2 J. Zhou, J. Wan, X. Gao, X. Zhang, S. R. Jaffrey and S.-B. Qian, *Nature*, 2015, **526**, 591–594.
3 J. Chen, C. Wang, W. Fei, X. Fang and X. Hu, *Am. J. Cancer Res.*, 2019, **9**, 752–764.
4 Y. Wang, Y. Li, J. I. Toth, M. D. Petroski, Z. Zhang and J. C. Zhao, *Nat. Cell Biol.*, 2014, **16**, 191–198.
5 Y. Yang, P. J. Hsu, Y.-S. Chen and Y.-G. Yang, *Cell Res.*, 2018, **28**, 616–624.
6 J. Liu, Y. Yue, D. Han, X. Wang, Y. Fu, L. Zhang, G. Jia, M. Yu, Z. Lu, X. Deng, Q. Dai, W. Chen and C. He, *Nat. Chem. Biol.*, 2014, **10**, 93–95.
7 P. Śledź and M. Jinek, *eLife*, 2016, **5**, e18434.
8 X.-Q. Gao, Y.-H. Zhang, F. Liu, M. Ponnusamy, X.-M. Zhao, L.-Y. Zhou, M. Zhai, C.-Y. Liu, X.-M. Li, M. Wang, C. Shan, P.-P. Shan, Y. Wang, Y.-H. Dong, L.-L. Qian, T. Yu, J. Ju, T.

 This journal is © The Royal Society of Chemistry 2025

Open Access Article. Published on 19 June 2025. Downloaded on 1/15/2026 12:32:17 PM.
This article is licensed under a Creative Commons Attribution 3.0 Unported Licence.

Wang, K. Wang, X.-Z. Chen, Y.-H. Wang, J. Zhang, P.-F. Li and K. Wang, *Nat. Cell Biol.*, 2020, **22**, 1319–1331.
9 N. S. Gokhale, A. B. R. McIntyre, M. J. McFadden, A. E. Roder, E. M. Kennedy, J. A. Gandara, S. E. Hopcraft, K. M. Quicke, C. Vazquez, J. Willer, O. R. Ilkayeva, B. A. Law, C. L. Holley, M. A. Garcia-Blanco, M. J. Evans, M. S. Suthar, S. S. Bradrick, C. E. Mason and S. M. Horner, *Cell Host Microbe*, 2016, **20**, 654–665.
10 N. Li, H. Hui, B. Bray, G. M. Gonzalez, M. Zeller, K. G. Anderson, R. Knight, D. Smith, Y. Wang, A. F. Carlin and T. M. Rana, *Cell Rep.*, 2021, **35**, 109091.
11 A. M. Shafik, F. Zhang, Z. Guo, Q. Dai, K. Pajdzik, Y. Li, Y. Kang, B. Yao, H. Wu, C. He, E. G. Allen, R. Duan and P. Jin, *Genome Biol.*, 2021, **22**, 17.
12 L. P. Vu, B. F. Pickering, Y. Cheng, S. Zaccara, D. Nguyen, G. Minuesa, T. Chou, A. Chow, Y. Saletore, M. MacKay, J. Schulman, C. Famulare, M. Patel, V. M. Klimek, F. E. Garrett-Bakelman, A. Melnick, M. Carroll, C. E. Mason, S. R. Jaffrey and M. G. Kharas, *Nat. Med.*, 2017, **23**, 1369–1376.
13 S. Lin, J. Choe, P. Du, R. Triboulet and R. I. Gregory, *Mol. Cell*, 2016, **62**, 335–345.
14 M. Chen, L. Wei, C.-T. Law, F. H.-C. Tsang, J. Shen, C. L.-H. Cheng, L.-H. Tsang, D. W.-H. Ho, D. K.-C. Chiu, J. M.-F. Lee, C. C.-L. Wong, I. O.-L. Ng and C.-M. Wong, *Hepatology*, 2018, **67**, 2254–2270.
15 I. Barbieri, K. Tzelepis, L. Pandolfini, J. Shi, G. Millán-Zambrano, S. C. Robson, D. Aspris, V. Migliori, A. J. Bannister, N. Han, E. de Braekeleer, H. Ponstingl, A. Hendrick, C. R. Vakoc, G. S. Vassiliou and T. Kouzarides, *Nature*, 2017, **552**, 126–131.
16 E. Yankova, W. Blackaby, M. Albertella, J. Rak, E. de Braekeleer, G. Tsagkogeorga, E. S. Pilka, D. Aspris, D. Leggate, A. G. Hendrick, N. A. Webster, B. Andrews, R. Fosbeary, P. Guest, N. Irigoyen, M. Eleftheriou, M. Gozdecka, J. M. L. Dias, A. J. Bannister, B. Vick, I. Jeremias, G. S. Vassiliou, O. Rausch, K. Tzelepis and T. Kouzarides, *Nature*, 2021, **593**, 597–601.
17 A. Dolbois, R. K. Bedi, E. Bochenkova, A. Müller, E. V. Moroz-Omori, D. Huang and A. Caflisch, *J. Med. Chem.*, 2021, **64**, 12738–12760.
18 G. Dutheuil, K. Oukoloff, J. Korac, F. Lenoir, M. El Bousmaqui, N. Probst, A. Lapin, G. Nakhabina, C. Sorlet, N. Parmentier, D. Karila, N. Ghavtadze, P. Casault, S. Claridge, S. Sapmaz, M. J. Slater and G. L. Fraser, *J. Med. Chem.*, 2025, **68**(3), 2981–3003.
19 A. A. Guirguis, Y. Ofir-Rosenfeld, K. Knezevic, W. Blackaby, D. Hardick, Y.-C. Chan, A. Motazedian, A. Gillespie, D. Vassiliadis, E. Y. N. Lam, K. Tran, B. Andrews, M. E. Harbour, L. Vasiliauskaite, C. J. Saunders, G. Tsagkogeorga, A. Azevedo, J. Obacz, E. S. Pilka, M. Carkill, L. MacPherson, E. N. Wainwright, B. Liddicoat, B. J. Blyth, M. R. Albertella, O. Rausch and M. A. Dawson, *Cancer Discovery*, 2023, **13**, 2228–2247.
20 J. C. Moser, K. P. Papadopoulos, J. Rodon Ahnert, Y. Ofir-Rosenfeld and J.-B. Holz, *J. Clin. Oncol.*, 2024, **42**, 2586.
21 Y. Ofir-Rosenfeld, L. Vasiliauskaitė, C. Saunders, A. Sapetschnig, G. Tsagkogeorga, M. Albertella, M. Carkill, J. Self-Fordham, J. B. Holz and O. Rausch, *Eur. J. Cancer*, 2022, **174**, S123.
22 S. Melnyk, M. Pogribna, I. P. Pogribny, P. Yi and S. J. James, *Clin. Chem.*, 2000, **46**, 265–272.
23 X. Wei, Y. Huo, J. Pi, Y. Gao, S. Rao, M. He, Q. Wei, P. Song, Y. Chen, D. Lu, W. Song, J. Liang, L. Xu, H. Wang, G. Hong, Y. Guo, Y. Si, J. Xu, X. Wang, Y. Ma, S. Yu, D. Zou, J. Jin, F. Wang and J. Yu, *Nat. Cell Biol.*, 2022, **24**, 1278–1290.
24 E. P. Hamilton, C. Ma, M. de Laurentiis, H. Iwata, S. A. Hurvitz, S. A. Wander, M. Danso, D. R. Lu, J. Perkins Smith, Y. Liu, L. Tran, S. Anderson and M. Campone, *Future Oncol.*, 2024, **20**, 2447–2455.
25 D. P. Petrylak, M. McKean, J. M. Lang, X. Gao, R. Dreicer, D. M. Geynisman, T. F. Stewart, M. Gandhi, L. J. Appleman, T. B. Dorff, G. S. Chatta, R. Tutrone, J. de La Cerda, E. Berghorn, J. Gong, T. Yu, E. Dominy, E. Chan and N. D. Shore, *J. Clin. Oncol.*, 2024, **42**, 5011.
26 M. Békés, D. R. Langley and C. M. Crews, *Nat. Rev. Drug Discovery*, 2022, **21**, 181–200.
27 A. C. Lai and C. M. Crews, *Nat. Rev. Drug Discovery*, 2017, **16**, 101–114.
28 D. P. Bondeson, A. Mares, I. E. D. Smith, E. Ko, S. Campos, A. H. Miah, K. E. Mulholland, N. Routly, D. L. Buckley, J. L. Gustafson, N. Zinn, P. Grandi, S. Shimamura, G. Bergamini, M. Faelth-Savitski, M. Bantscheff, C. Cox, D. A. Gordon, R. R. Willard, J. J. Flanagan, L. N. Casillas, B. J. Votta, W. den Besten, K. Famm, L. Kruidenier, P. S. Carter, J. D. Harling, I. Churcher and C. M. Crews, *Nat. Chem. Biol.*, 2015, **11**, 611–617.
29 C. Kim, X.-D. Wang, Z. Liu, S. Zha and Y. Yu, *Biochemistry*, 2023, **62**, 561–563.
30 F. Errani, A. Invernizzi, M. Herok, E. Bochenkova, F. Stamm, I. Corbeski, V. Romanucci, G. Di Fabio, F. Zálešák and A. Caflisch, *JACS Au*, 2024, **4**, 713–729.
31 W. Du, Y. Huang, X. Chen, Y. Deng, Y. Sun, H. Yang, Q. Shi, F. Wu, G. Liu, H. Huang, J. Ding, X. Huang and S. Xu, *Cell Chem. Biol.*, 2024, **31**, 177–183.e17.
32 K. Hwang, J. Bae, Y.-L. Jhe, J. Kim, J.-H. Cheong, H.-S. Choi and T. Sim, *Eur. J. Med. Chem.*, 2024, **279**, 116843.
33 R. Nar, Z. Wu, Y. Li, A. Smith, Y. Zhang, J. Wang, F. Yu, S. Gao, C. Yu, Z. Huo, G. Zheng and Z. Qian, *Genes Dis.*, 2025, **12**, 101452.
34 C. Galdeano, M. S. Gadd, P. Soares, S. Scaffidi, I. van Molle, I. Birced, S. Hewitt, D. M. Dias and A. Ciulli, *J. Med. Chem.*, 2014, **57**, 8657–8663.
35 H. M. Berman, J. Westbrook, Z. Feng, G. Gilliland, T. N. Bhat, H. Weissig, I. N. Shindyalov and P. E. Bourne, *Nucleic Acids Res.*, 2000, **28**, 235–242.
36 J. L. Meidner, A. F. Frey, R. A. Zimmermann, M. O. Sabin, Z. Nidoieva, A. C. Weldert, S. N. Hoba, M. W. Krone and F. Barthels, *Angew. Chem., Int. Ed.*, 2024, **63**, e202403792.
37 A. J. Wijaya, W. Farnaby and A. Ciulli, *Methods Enzymol.*, 2023, **681**, 241–263.

Open Access Article. Published on 19 June 2025. Downloaded on 1/15/2026 12:32:17 PM.
This article is licensed under a Creative Commons Attribution 3.0 Unported Licence.

38 V. Zoppi, S. J. Hughes, C. Maniaci, A. Testa, T. Gmaschitz, C. Wieshofer, M. Koegl, K. M. Riching, D. L. Daniels, A. Spallarossa and A. Ciulli, *J. Med. Chem.*, 2019, **62**, 699–726.
39 I. van Molle, A. Thomann, D. L. Buckley, E. C. So, S. Lang, C. M. Crews and A. Ciulli, *Chem. Biol.*, 2012, **19**, 1300–1312.
40 P. Soares, M. S. Gadd, J. Frost, C. Galdeano, L. Ellis, O. Epemolu, S. Rocha, K. D. Read and A. Ciulli, *J. Med. Chem.*, 2018, **61**, 599–618.
41 M. L. Drummond and C. I. Williams, *J. Chem. Inf. Model.*, 2019, **59**, 1634–1644.
42 M. L. Drummond, A. Henry, H. Li and C. I. Williams, *J. Chem. Inf. Model.*, 2020, **60**, 5234–5254.
43 *Molecular Operating Environment (MOE)*, Chemical Computing Group ULC, 910–1010 Sherbrooke St. W., Montreal, QC H3A 2R7, 2025.
44 P. Labute, *J. Comput. Chem.*, 2008, **29**, 1693–1698.
45 T. A. Halgren, *J. Comput. Chem.*, 1996, **17**, 490–519.
46 J. Wang, W. Wang, P. A. Kollman and D. A. Case, *J. Mol. Graphics Modell.*, 2006, **25**, 247–260.
47 D. A. Case, H. M. Aktulga, K. Belfon, D. S. Cerutti, G. A. Cisneros, V. W. D. Cruzeiro, N. Forouzesh, T. J. Giese, A. W. Götz, H. Gohlke, S. Izadi, K. Kasavajhala, M. C. Kaymak, E. King, T. Kurtzman, T.-S. Lee, P. Li, J. Liu, T. Luchko, R. Luo, M. Manathunga, M. R. Machado, H. M. Nguyen, K. A. O'Hearn, A. V. Onufriev, F. Pan, S. Pantano, R. Qi, A. Rahnamoun, A. Risheh, S. Schott-Verdugo, A. Shajan, J. Swails, J. Wang, H. Wei, X. Wu, Y. Wu, S. Zhang, S. Zhao, Q. Zhu, T. E. Cheatham, D. R. Roe, A. Roitberg, C. Simmerling, D. M. York, M. C. Nagan and K. M. Merz, *J. Chem. Inf. Model.*, 2023, **63**, 6183–6191.
48 D. Vassetti, M. Pagliai and P. Procacci, *J. Chem. Theory Comput.*, 2019, **15**, 1983–1995.
49 A. Jakalian, D. B. Jack and C. I. Bayly, *J. Comput. Chem.*, 2002, **23**, 1623–1641.
50 W. L. Jorgensen, J. Chandrasekhar, J. D. Madura, R. W. Impey and M. L. Klein, *J. Chem. Phys.*, 1983, **79**, 926–935.
51 J. C. Phillips, R. Braun, W. Wang, J. Gumbart, E. Tajkhorshid, E. Villa, C. Chipot, R. D. Skeel, L. Kalé and K. Schulten, *J. Comput. Chem.*, 2005, **26**, 1781–1802.
52 C. Tian, K. Kasavajhala, K. A. A. Belfon, L. Raguette, H. Huang, A. N. Migues, J. Bickel, Y. Wang, J. Pincay, Q. Wu and C. Simmerling, *J. Chem. Theory Comput.*, 2020, **16**, 528–552.
53 W. Humphrey, A. Dalke and K. Schulten, *J. Mol. Graphics*, 1996, **14**, 33–38.
54 B. R. Miller, T. D. McGee, J. M. Swails, N. Homeyer, H. Gohlke and A. E. Roitberg, *J. Chem. Theory Comput.*, 2012, **8**, 3314–3321.
55 R. Anandakrishnan, A. Drozdetski, R. C. Walker and A. V. Onufriev, *Biophys. J.*, 2015, **108**, 1153–1164.
56 K. Xu, Z. Wang, S. Xiang, R. Tang, Q. Deng, J. Ge, Z. Jiang, K. Yang, T. Hou and H. Sun, *J. Chem. Inf. Model.*, 2024, **64**, 7666–7678.
57 S. Zheng, W. Wang, J. Aldahdooh, A. Malyutina, T. Shadbahr, Z. Tanoli, A. Pessia and J. Tang, *Genomics, Proteomics Bioinf.*, 2022, **20**, 587–596.
58 T. Ishida and A. Ciulli, *SLAS Discovery*, 2021, **26**, 484–502.
59 D. L. Buckley, K. Raina, N. Darricarrere, J. Hines, J. L. Gustafson, I. E. Smith, A. H. Miah, J. D. Harling and C. M. Crews, *ACS Chem. Biol.*, 2015, **10**, 1831–1837.
60 J. C. Swartzel, M. J. Bond, A. P. Pintado-Urbanc, M. Daftary, M. W. Krone, T. Douglas, E. J. Carder, J. T. Zimmer, T. Maeda, M. D. Simon and C. M. Crews, *ACS Chem. Biol.*, 2022, **17**, 1789–1798.
61 W. P. Blackaby, D. J. Hardick, E. J. Thomas, F. A. Brookfield, J. Shepherd, C. Bubert and M. P. Ridgill, Storm Therapeutics Ltd (GB) and WIPO (PCT), WO-2021111124-A1, 2021.
62 D. P. Bondeson, B. E. Smith, G. M. Burslem, A. D. Buhimschi, J. Hines, S. Jaime-Figueroa, J. Wang, B. D. Hamman, A. Ishchenko and C. M. Crews, *Cell Chem. Biol.*, 2018, **25**, 78–87.e5.
63 S. Alabi, S. Jaime-Figueroa, Z. Yao, Y. Gao, J. Hines, K. T. G. Samarasinghe, L. Vogt, N. Rosen and C. M. Crews, *Nat. Commun.*, 2021, **12**, 920.
64 R. P. Nowak, S. L. DeAngelo, D. Buckley, Z. He, K. A. Donovan, J. An, N. Safaee, M. P. Jedrychowski, C. M. Ponthier, M. Ishoey, T. Zhang, J. D. Mancias, N. S. Gray, J. E. Bradner and E. S. Fischer, *Nat. Chem. Biol.*, 2018, **14**, 706–714.
65 K.-H. Chan, M. Zengerle, A. Testa and A. Ciulli, *J. Med. Chem.*, 2018, **61**, 504–513.
66 H. Xiao, R. Zhao, W. Meng and Y. Liao, *J. Pharm. Anal.*, 2023, **13**, 625–639.
67 M. Esteva-Socias and F. Aguilo, *NAR Cancer*, 2024, **6**, zcae009.
68 J. Adams, V. J. Palombella, E. A. Sausville, J. Johnson, A. Destree, D. D. Lazarus, J. Maas, C. S. Pien, S. Prakash and P. J. Elliott, *Cancer Res.*, 1999, **59**, 2615–2622.
69 M. L. Hyer, M. A. Milhollen, J. Ciavarri, P. Fleming, T. Traore, D. Sappal, J. Huck, J. Shi, J. Gavin, J. Brownell, Y. Yang, B. Stringer, R. Griffin, F. Bruzzese, T. Soucy, J. Duffy, C. Rabino, J. Riceberg, K. Hoar, A. Lublinsky, S. Menon, M. Sintchak, N. Bump, S. M. Pulukuri, S. Langston, S. Tirrell, M. Kuranda, P. Veiby, J. Newcomb, P. Li, J. T. Wu, J. Powe, L. R. Dick, P. Greenspan, K. Galvin, M. Manfredi, C. Claiborne, B. S. Amidon and N. F. Bence, *Nat. Med.*, 2018, **24**, 186–193.
70 M. S. Gadd, A. Testa, X. Lucas, K.-H. Chan, W. Chen, D. J. Lamont, M. Zengerle and A. Ciulli, *Nat. Chem. Biol.*, 2017, **13**, 514–521.
71 C. Cecchini, S. Pannilunghi, S. Tardy and L. Scapozza, *Front. Chem.*, 2021, **9**, 672267.
72 M. J. Roy, S. Winkler, S. J. Hughes, C. Whitworth, M. Galant, W. Farnaby, K. Rumpel and A. Ciulli, *ACS Chem. Biol.*, 2019, **14**, 361–368.
73 Z. Cournia, B. Allen and W. Sherman, *J. Chem. Inf. Model.*, 2017, **57**, 2911–2937.
74 H. Fu, H. Chen, M. Blazhynska, E. Goulard Coderc de Lacam, F. Szczepaniak, A. Pavlova, X. Shao, J. C. Gumbart, F. Dehez, B. Roux, W. Cai and C. Chipot, *Nat. Protoc.*, 2022, **17**, 1114–1141.
75 C. E. M. Schindler, H. Baumann, A. Blum, D. Böse, H.-P. Buchstaller, L. Burgdorf, D. Cappel, E. Chekler, P. Czodrowski, D. Dorsch, M. K. I. Eguida, B. Follows, T.

 This journal is © The Royal Society of Chemistry 2025

Open Access Article. Published on 19 June 2025. Downloaded on 1/15/2026 12:32:17 PM.
This article is licensed under a Creative Commons Attribution 3.0 Unported Licence.

Fuchß, U. Grädler, J. Gunera, T. Johnson, C. Jorand Lebrun, S. Karra, M. Klein, T. Knehans, L. Koetzner, M. Krier, M. Leiendecker, B. Leuthner, L. Li, I. Mochalkin, D. Musil, C. Neagu, F. Rippmann, K. Schiemann, R. Schulz, T. Steinbrecher, E.-M. Tanzer, A. Unzue Lopez, A. Viacava Follis, A. Wegener and D. Kuhn, *J. Chem. Inf. Model.*, 2020, **60**, 5457–5474.

76 T.-S. Lee, B. K. Allen, T. J. Giese, Z. Guo, P. Li, C. Lin, T. D. McGee, D. A. Pearlman, B. K. Radak, Y. Tao, H.-C. Tsai, H. Xu, W. Sherman and D. M. York, *J. Chem. Inf. Model.*, 2020, **60**, 5595–5623.

77 H. Zhao, *ChemMedChem*, 2024, **19**, e202400171.

78 K. M. Riching, E. A. Caine, M. Urh and D. L. Daniels, *Chem. Soc. Rev.*, 2022, **51**, 6210–6221.

79 B. E. Smith, S. L. Wang, S. Jaime-Figueroa, A. Harbin, J. Wang, B. D. Hamman and C. M. Crews, *Nat. Commun.*, 2019, **10**, 131.

80 Y. Zhang, S. Liu, T. Zhao and C. Dang, *Oncol. Rep.*, 2021, **46**(2), 163.

81 C.-Q. Jiao, C. Hu, M.-H. Sun, Y. Li, C. Wu, F. Xu, L. Zhang, F.-R. Huang, J.-J. Zhou, J.-F. Dai, M. Ruan, W.-C. Wang, Q.-S. Liu and J. Ge, *Cell Death Dis.*, 2025, **16**, 233.

82 B. Yadav, K. Wennerberg, T. Aittokallio and J. Tang, *Comput. Struct. Biotechnol. J.*, 2015, **13**, 504–513.

"

Supplementary Information (SI) for RSC Medicinal Chemistry.
This journal is © The Royal Society of Chemistry 2025

Structure-guided Design of a Methyltransferase-like 3 (METTL3) Proteolysis Targeting Chimera (PROTAC) Incorporating an Indole-Nicotinamide Chemotype

Annabelle C. Weldert[a], Ariane F. Frey[a], Mackenzie W. Krone[b], Franziska Krähe[a], Hannah Kuhn[a], Christian Kersten[a,c], Fabian Barthels[a,b]*

[a]Institute of Pharmaceutical and Biomedical Sciences, Johannes Gutenberg-University, Staudingerweg 5, 55128 Mainz, Germany.

[b]Department of Molecular, Cellular, and Developmental Biology, Yale University, 260 Whitney Ave, CT 06520-8103 New Haven, USA.

[c]Institute for Quantitative and Computational Biosciences, Johannes Gutenberg-University, BioZentrum I, Hanns-Dieter-Hüsch Weg 15, 55128 Mainz, Germany.

* E-Mail: barthels@uni-mainz.de

Table of contents

Biophysical investigation of PROTAC candidates 2

Supplementary FP and HTRF assay dose-response curves 7

Supplementary Western blots (screening results) 9

Supplementary data on biophysical investigation of ternary complexes 10

Molecular dynamics simulations 11

Primer sequences used for RT-qPCR 13

Uncropped Western blot images 14

References 15

Synthesis of E3 ligase recruiters with linker 16

- VHL-RH-based recruiters 16
- VHL-LH-based recruiters 18
- 4-Thalidomide-based recruiters 21
- 5-Thalidomid-based recruiters 23
- VHL-LH building blocks for Suzuki and Sonogashira reactions 26

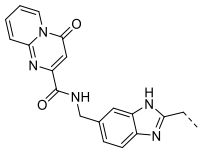
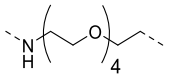
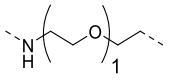
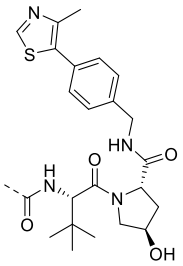
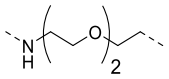
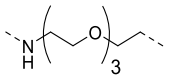
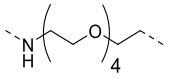
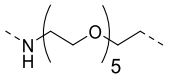
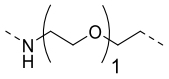
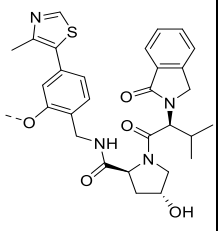
1st and 2nd generation METTL3 recruiter synthesis 28

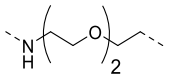
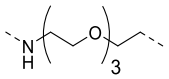
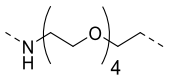
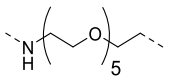
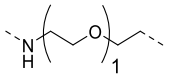
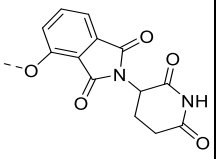
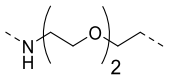
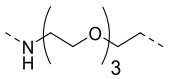
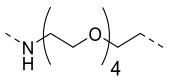
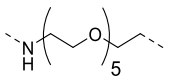
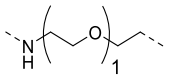
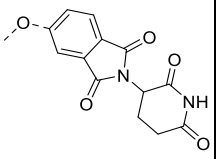
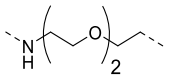
- Synthesis of 1st generation PROTACs 31
- Synthesis of 2nd generation PROTACs 38
- Synthesis of CRBN-based PROTACs 47
- Synthesis of 3rd generation PROTACs 54
- Synthesis of 4th generation PROTACs 57
- Spectral appendix 62

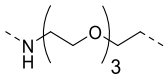
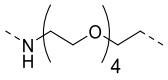
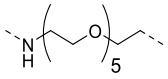
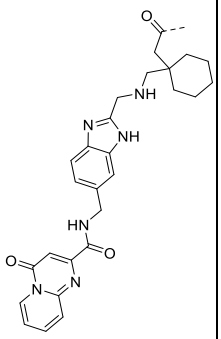
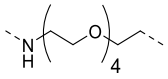
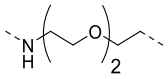
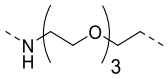
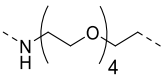
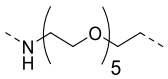
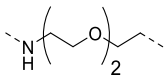
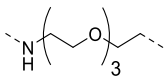
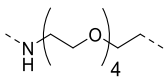
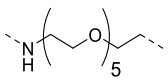
Supporting results & discussion

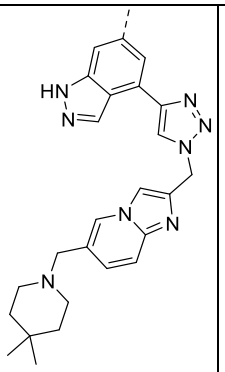
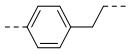
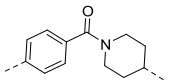
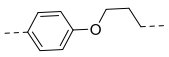
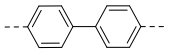
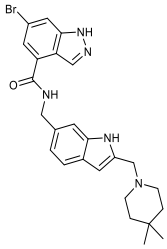
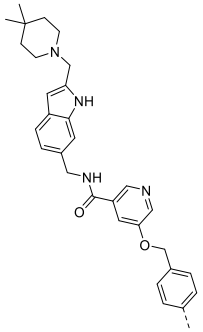
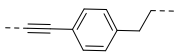
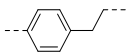
Biophysical investigation of PROTAC candidates

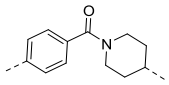
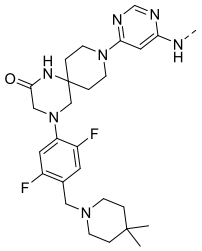
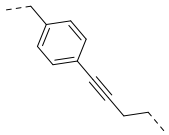
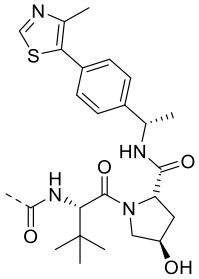
Table S1: Binary affinities to METTL3 were determined for all PROTACs synthesized in this work via FP assays. Selected affinities to the respective E3 ligase were determined via HTRF and FP assays. All K_D values include the mean value and standard deviations from at least technical triplicate measurements. Dose-response curves are depicted in Figures S1–S3 and S5.

Cpd No.	METTL3 recruiter	Linker	E3 ligase recruiter	K_D METTL3 [µM]	K_D E3-ligases [µM]
5	 **POI-1**		none	10.38 ± 0.98	n.d.
6	**POI-1**		 VHL-LH	>100	n.d.
7	**POI-1**		VHL-LH	12.47 ± 1.34	n.d.
8	**POI-1**		VHL-LH	16.07 ± 1.55	n.d.
9	**POI-1**		VHL-LH	37.59 ± 8.73	n.d.
10	**POI-1**		VHL-LH	16.33 ± 1.44	n.d.
11	**POI-1**		 VHL-RH	>100	n.d.

12	**POI-1**		VHL-RH	4.41 ± 1.25	n.d.
13	**POI-1**		VHL-RH	3.94 ± 0.53	n.d.
14	**POI-1**		VHL-RH	7.50 ± 1.07	n.d.
15	**POI-1**		VHL-RH	5.15 ± 0.59	n.d.
16	**POI-1**		 4-Thalidomide	8.06 ± 1.72	n.d.
17	**POI-1**		4-Thalidomide	10.58 ± 1.17	n.d.
18	**POI-1**		4-Thalidomide	26.51 ± 2.05	n.d.
19	**POI-1**		4-Thalidomide	10.58 ± 3.00	n.d.
20	**POI-1**		4-Thalidomide	6.13 ± 1.36	2.98 ± 0.23
21	**POI-1**		 5-Thalidomide	>100	n.d.
22	**POI-1**		5-Thalidomide	6.44 ± 0.54	2.20 ± 0.14

23	**POI-1**		5-Thalidomide	7.27 ± 0.89	n.d.
24	**POI-1**		5-Thalidomide	19.55 ± 2.85	n.d.
25	**POI-1**		5-Thalidomide	31.87 ± 9.06	n.d.
26	 **POI-2**		none	0.433 ± 0.056	n.d.
27	**POI-2**		VHL-LH	0.429 ± 0.046	n.d.
28	**POI-2**		VHL-LH	0.309 ± 0.022	0.145 ± 0.04
29	**POI-2**		VHL-LH	1.53 ± 0.10	n.d.
30	**POI-2**		VHL-LH	0.725 ± 0.079	n.d.
31	**POI-2**		VHL-RH	1.15 ± 0.10	n.d.
32	**POI-2**		VHL-RH	2.05 ± 0.32	0.222 ± 0.05
33	**POI-2**		VHL-RH	2.04 ± 0.46	n.d.
34	**POI-2**		VHL-RH	2.49 ± 0.55	n.d.

35	 **POI-3**		VHL-LH	0.263 ± 0.015	n.d.
36	**POI-3**		VHL-LH	0.223 ± 0.045	n.d.
37	**POI-3**		VHL-LH	2.48 ± 0.392	n.d.
38	**POI-3**		VHL-LH	n.d.*	n.d.
39		none	none	0.0542 ± 0.0066	n.d.
40	 **POI-4**		VHL-LH	0.158 ± 0.019	n.d.
41 (AF151)	**POI-4**		VHL-LH	0.159 ± 0.026	0.363 ± 0.054 (FP) 0.740 ± 0.113 (HTRF)

42	**POI-4**		VHL-LH	0.295 ± 0.050	n.d.
WD6305[1]				0.096 ± 0.001	1.76 ± 0.26 (FP) 2.17 ± 0.28 (HTRF)

*The affinity could not be determined due to fluorescence interference of the biphenyl moiety with FP setup.

Supplementary FP and HTRF assay dose-response curves

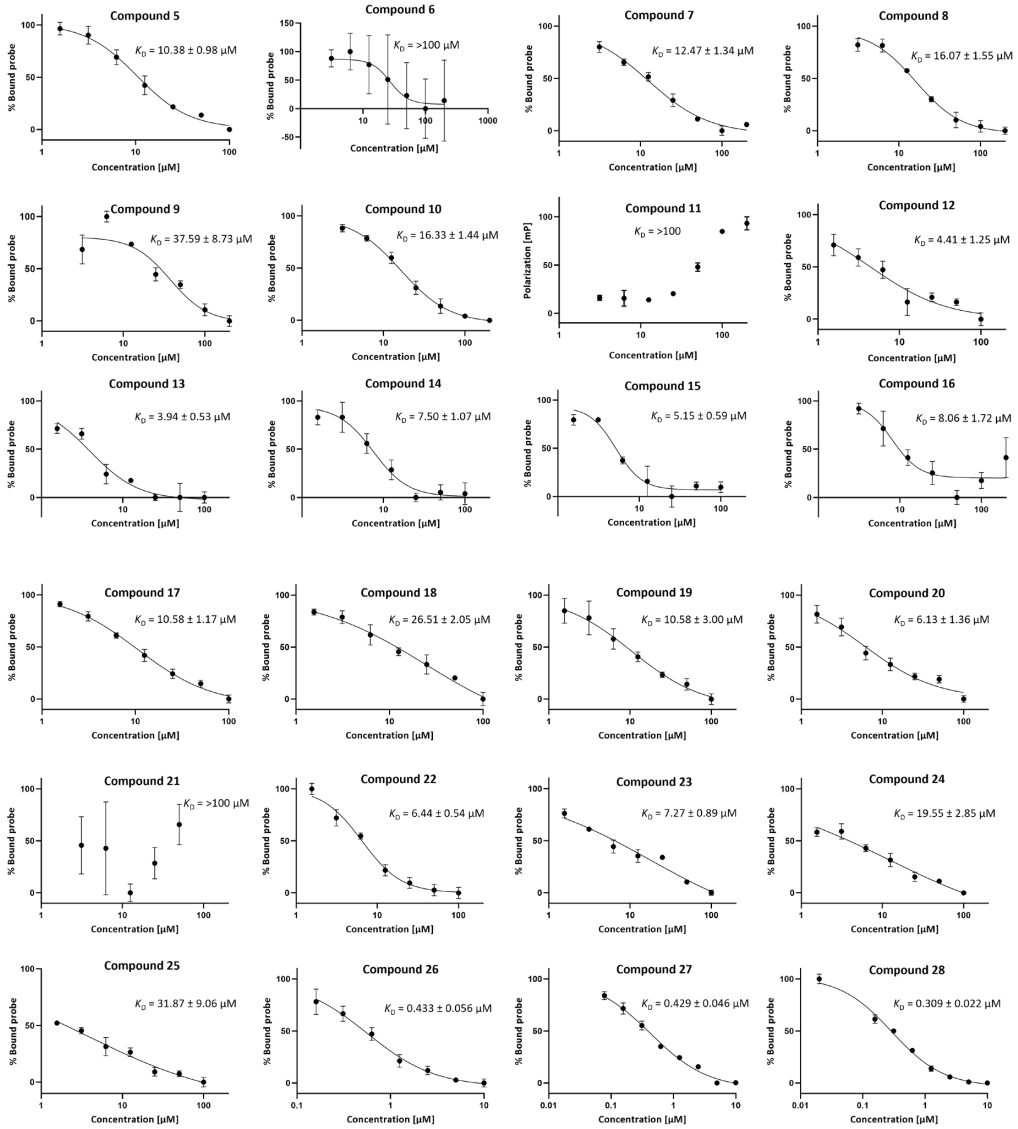


Figure S1: Supplementary FP assay dose-response curves of compounds **5**–**28**. Each experiment was carried out in triplicate. The ligand was titrated to 300 nM METTL3/14 and 20 nM of the displacement probe (STM-FL[2]) to determine the apparent dissociation constant, as specified in the experimental section. Compound **11** led to the visible formation of aggregates; thus, the distorted dose-response curve was not evaluated by non-linear regression.

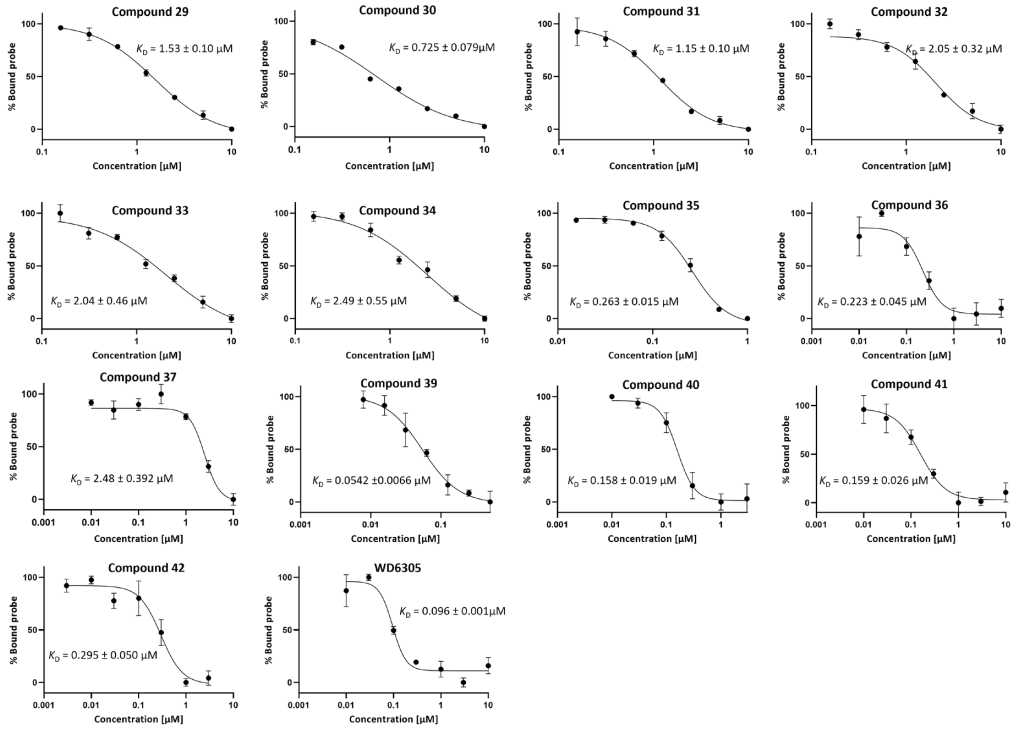


Figure S2: Supplementary FP assay dose-response curves of compounds **29**–**42** and WD6305[1]. Each experiment was carried out in triplicate. The ligand was titrated to 300 nM METTL3/14 and 20 nM of the displacement probe (STM-FL[2]) to determine the apparent dissociation constant, as specified in the experimental section.

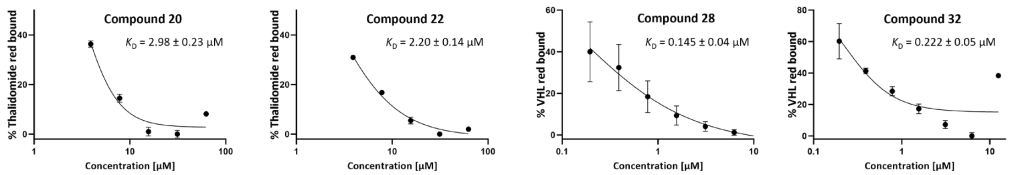


Figure S3: Supplementary Time-Resolved Fluorescence (HTRF) assay results for compounds **20**, **22**, **28**, and **32.** Each experiment was carried out in triplicate. The ligand PROTACs were titrated using an HTRF Human VHL Binding Kit (Revvity) or an HTRF Human Cereblon Binding Kit (Revvity) to determine the apparent dissociation constant, as specified in the experimental section.

Supplementary Western blots (screening results)

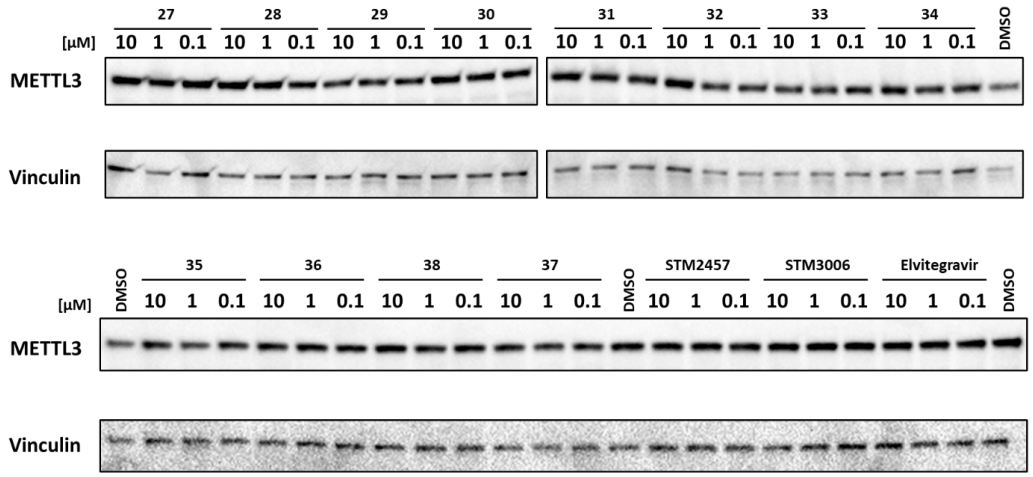


Figure S4: Western blot screening results of PROTAC candidates from the 2nd and the 3rd generation designs. MOLM-13 cells were treated with the indicated compounds at varying concentrations (10 µM, 1 µM, and 0.1 µM) for 16 h. DMSO was used as a negative control. None of the compounds showed significant degradation of METTL3. The METTL3 inhibitors STM2457[3] (Cayman Chemicals), STM3006[4] (BLDpharm), and Elvitegravir[5] (MedChemExpress), were used as conditional controls to prove that competitive METTL3 inhibitors do not function as METTL3 degraders. Shown is a representative Western blot image of two independent experiments.

Supplementary data on biophysical investigation of ternary complexes

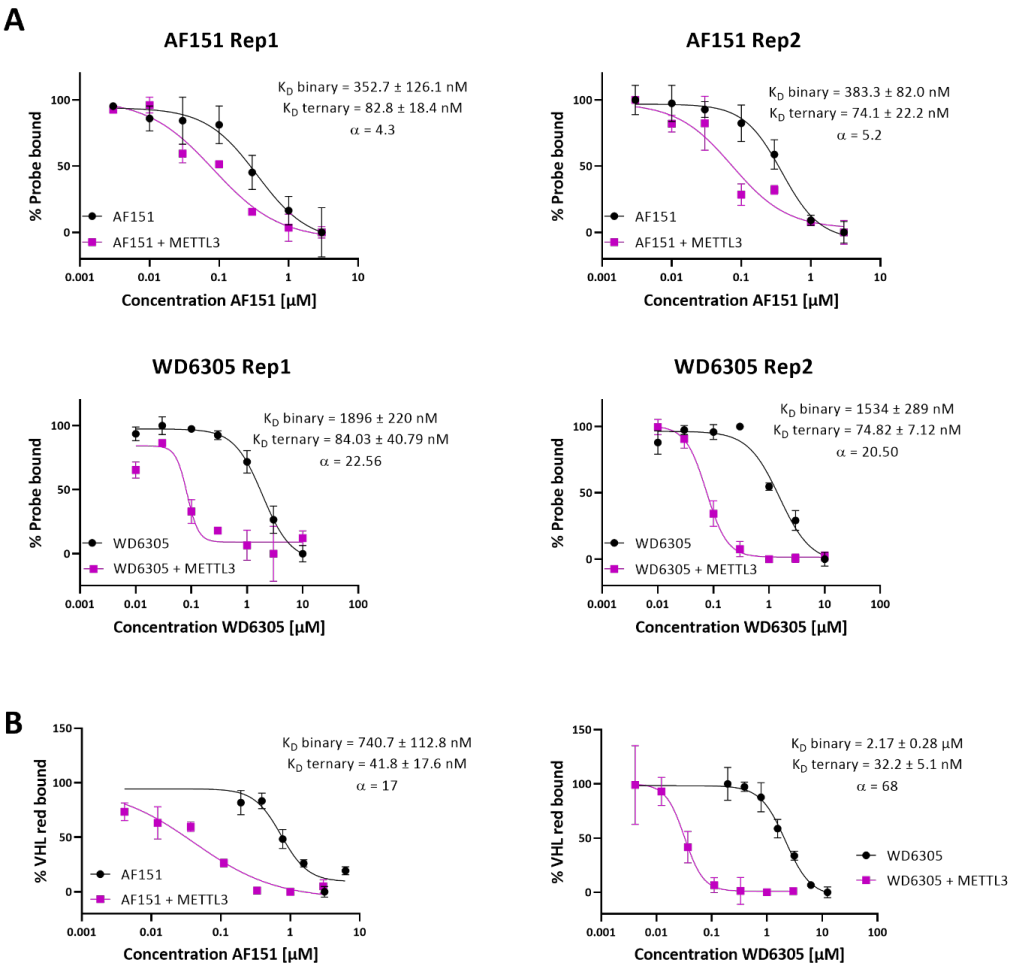


Figure S5. Supplementary data for ternary complex investigation. (**A**) FP dose-response curves for ternary affinity determination of **AF151** and WD6305. Each experiment was carried out in triplicate on two non-consecutive days (Rep1 & Rep2). PROTACs were titrated to 40 nM VCB complex and 10 nM displacement probe to determine the apparent dissociation constant, as specified in the experimental section. For ternary K_D determinations, METTL3/14 was added in near-saturating concentrations relative to the highest PROTAC concentration. (**B**) Homogeneous Time-Resolved Fluorescence (HTRF) assay results for **AF151** and WD6305. Each experiment was carried out in triplicate. The ligand PROTACs were titrated using an HTRF Human VHL Binding Kit (Revvity) to determine the apparent dissociation constant, as specified in the experimental section. For ternary K_D determinations, METTL3/14 was added in near-saturating concentrations relative to the highest PROTAC concentration.

Molecular dynamics simulations

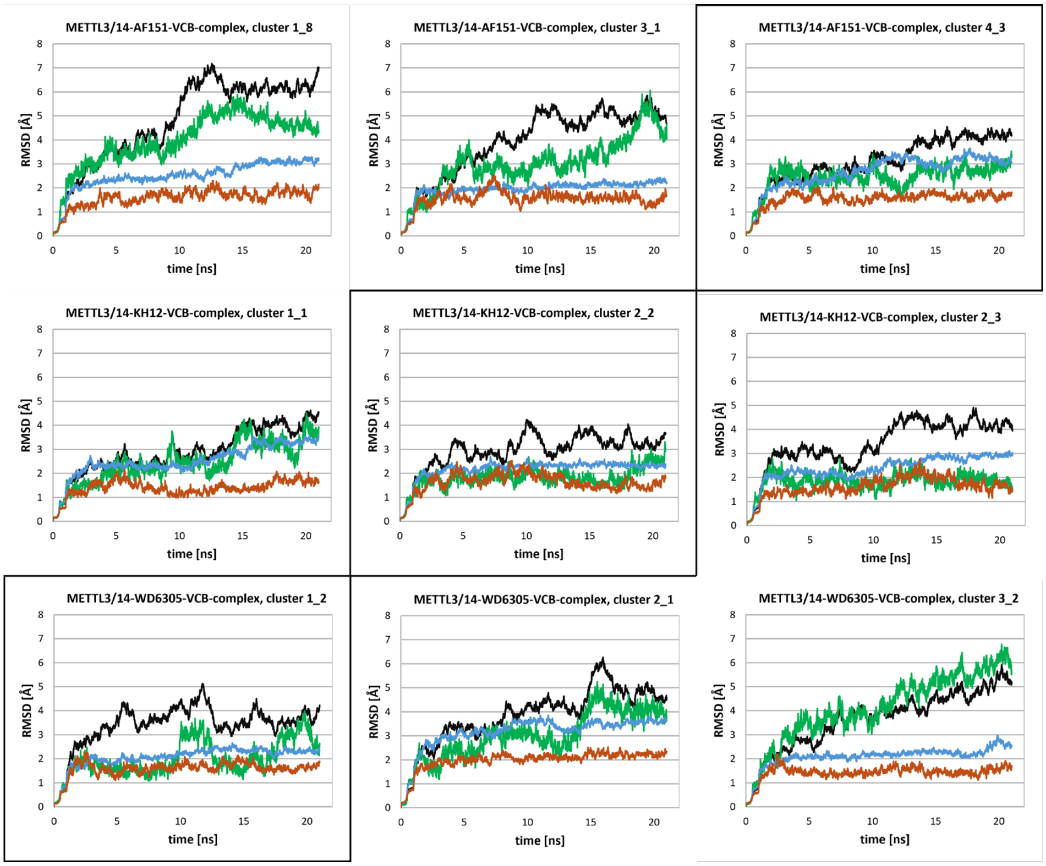


Figure S6: MD simulation RMSD-analysis of ternary METTL3/14-PROTAC-VCB complexes over 1 ns equilibration and 20 ns production. PROTACs **41** (**AF151**), KH12[6] and WD6305[1] were investigated. Complex protein backbone RMSD in Å is depicted in black, METTL3/14 in blue, VCB in orange, and ligand heavy atoms (non-hydrogen) in green. For complex and ligand RMSD, aligned complexes were evaluated, while for internal stability of METTL3/14 and VCB, alignment was performed on the respective target or VCB part. The best-scoring cluster representatives of ternary structures from PROTAC-docking were used as starting structures for MD simulations. In WD6305-complex cluster 1_2, the increased ligand RMSD values are caused by a flip of the phenyl linker. Structures for which MD simulations were prolonged to 100 ns production (Figure S7) are highlighted by a black border.

Table S2: 1A-MM-GBSA analysis of PROTAC-docking generated ternary complexes from 20 ns MD simulations. T: target (METTL3/14), P: PROTAC, E: E3 ligase (VCB). Binding free energy of ternary complex ΔGcomplex = $\Delta G_{T-P} + \Delta G_{TP-E} = \Delta G_{E-P} + \Delta G_{EP-T} = \Delta G_{T-E} + \Delta G_{TE-P}$ according to main manuscript Figure 3D. MM-GBSA scores are in kcal/mol.

	AF151 1_8	**AF151 3_1**	**AF151 4_3**	**KH12 1_1**	**KH12 2_2**	**KH12 2_3**	**WD6305 1_2**	**WD6305 2_1**	**WD6305 3_2**
ΔG_{TE-P}	-129.2	-136.2	-143.1	-150.5	-170.1	-154.7	-152.5	-161.1	-167.1
ΔG_{TP-E}	-68.3	-62.9	-72.3	-66.6	-67.5	-71.9	-70.3	-47.9	-61.6
ΔG_{EP-T}	-89.7	-92.0	-120.0	-123.2	-121.4	-111.6	-116.1	-100.9	-124.9
ΔG_{T-E}	-9.6	-5.5	-18.8	-13.6	-3.6	-9.2	-12.5	+9.7	-6.1
ΔG_{T-P}	-70.5	-62.9	-89.6	-97.5	-106.1	-91.9	-94.7	-103.6	-111.6
ΔG_{E-P}	-49.1	-49.6	-41.9	-41.0	-52.2	-52.2	-48.9	-50.5	-48.3
$\Delta G_{complex}$	-138.8	-141.7	-161.9	-164.1	-173.6	-163.9	-165.0	-151.4	-173.2

Table S3: 1A-MM-GBSA analysis of ternary complexes from 50 ns and 100 ns MD simulations, respectively. T: target (METTL3/14), P: PROTAC, E: E3 ligase (VCB). Binding free energy of ternary complex ΔGcomplex = $\Delta G_{T-P} + \Delta G_{TP-E} = \Delta G_{E-P} + \Delta G_{EP-T} = \Delta G_{T-E} + \Delta G_{TE-P}$ according to main manuscript Figure 3D. MM-GBSA scores are in kcal/mol.

	50 ns			**100 ns**		
	AF151 4_3	**KH12 2_2**	**WD6305 1_2**	**AF151 4_3**	**KH12 2_2**	**WD6305 1_2**
ΔG_{TE-P}	-146.4	-167.1	-146.1	-147.1	-166.6	-147.9
ΔG_{TP-E}	-77.8	-67.9	-64.4	-77.3	-67.5	-70.3
ΔG_{EP-T}	-123.4	-119.7	-105.7	-122.2	-118.1	-111.3
ΔG_{T-E}	-21.5	-4.7	-8.2	-20.3	-4.3	-13.1
ΔG_{T-P}	-90.1	-103.9	-90.0	-90.1	-103.3	-90.7
ΔG_{E-P}	-44.5	-52.1	-48.7	-45.3	-52.7	-49.7
$\Delta G_{TP-E} - \Delta G_{E-P}$	-33.3	-15.8	-15.7	-32.1	-14.8	-20.6
$\Delta G_{complex}$	-167.9	-171.8	-154.4	-167.4	-170.8	-161.0

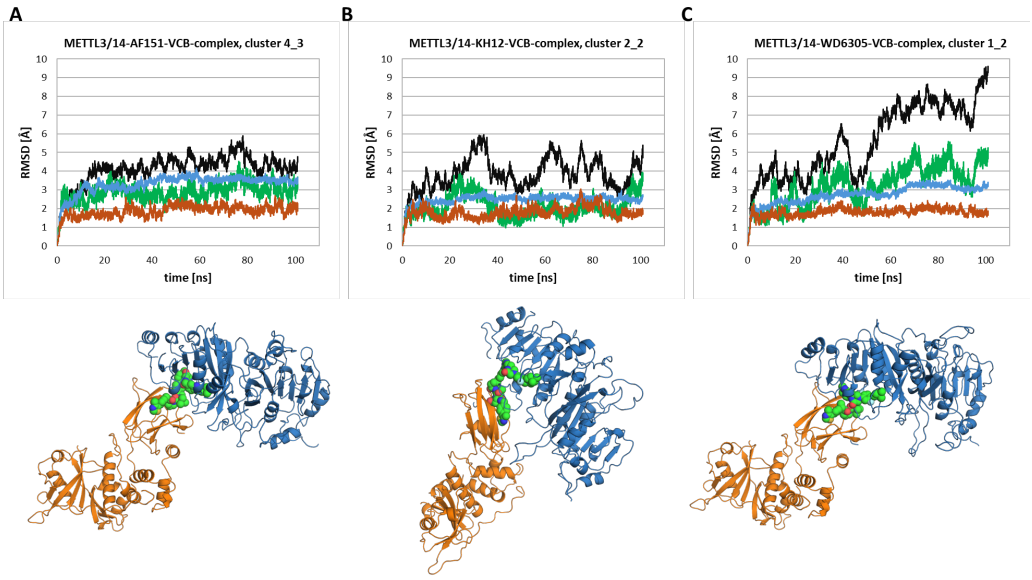


Figure S7: MD-based RMSD-analysis of ternary METTL3/14-PROTAC-VCB complexes over 1 ns equilibration and 100 ns production. Complex protein backbone RMSD in Å is depicted in black, METTL3/14 in blue, VCB in orange, and ligand heavy atoms (non-hydrogen) in green. For complex and ligand RMSD in Å, aligned complexes were evaluated, while for internal stability of METTL3/14 and VCB, alignment was performed on the respective target or VCB part. (**A**) prolonged simulation of **AF151**-complex, cluster 4_3, (**B**) prolonged simulation of KH12-complex, cluster 2_2, (**C**) prolonged simulation of WD6305-complex, cluster 1_2. The starting structures are depicted below the RMSD traces. METTL3/14 blue, VCB orange, and PROTAC carbon atoms green.

Primer sequences used for RT-qPCR

Table S4. Primers used for quantitative reverse transcription polymerase chain reaction.

Gene	Forward Primer	Reverse Primer
METTL3	TTGTCTCCAACCTTCCGTAGT	CCAGATCAGAGAGGTGGTGTAG
METTL14	GAACACAGAGCTTAAATCCCCA	TGTCAGCTAAACCTACATCCCTG
GAPDH	GGAGCGAGATCCCTCCAAAAT	GGCTGTTGTCATACTTCTCATGG

Uncropped Western blot images

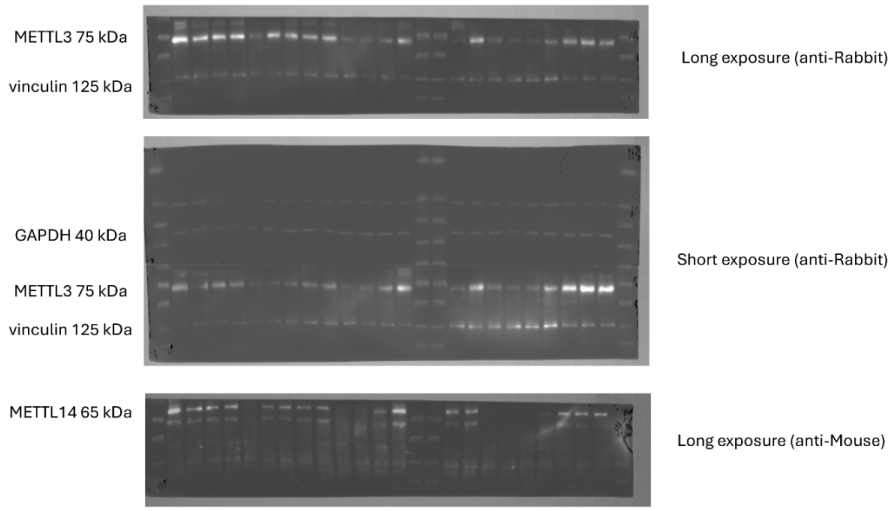


Figure S8: Uncropped images of Figure 2B,C: All data originates from a single blot cut between GAPDH (40 kDa) and METTL3 (75 kDa). For METTL14 ECL detection, the METTL3-detected slice was incubated with mouse anti-METTL14 antibody and anti-Mouse-HRP after the inactivation of anti-Rabbit-HRP with 0.05% sodium azide.

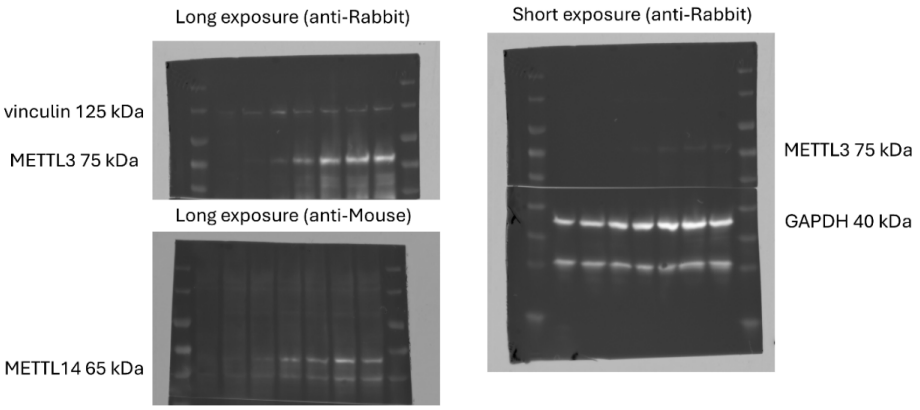


Figure S9: Uncropped images of Figure 2D: All data originates from a single blot cut between GAPDH (40 kDa) and METTL3 (75 kDa). For METTL14 ECL detection, the METTL3-detected slice was incubated with mouse anti-METTL14 antibody and anti-Mouse-HRP after the inactivation of anti-Rabbit-HRP with 0.05% sodium azide.

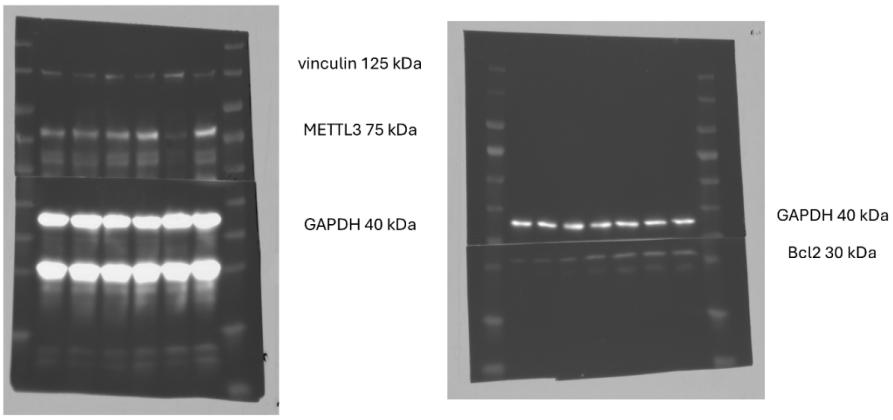


Figure S10: Uncropped images of Figures 2E&4E: Data originates from single blots cut between GAPDH (40 kDa) and METTL3 (75 kDa) for Figure 2E and GAPDH (40 kDa) and Bcl-2 (30 kDa) for Figure 4E.

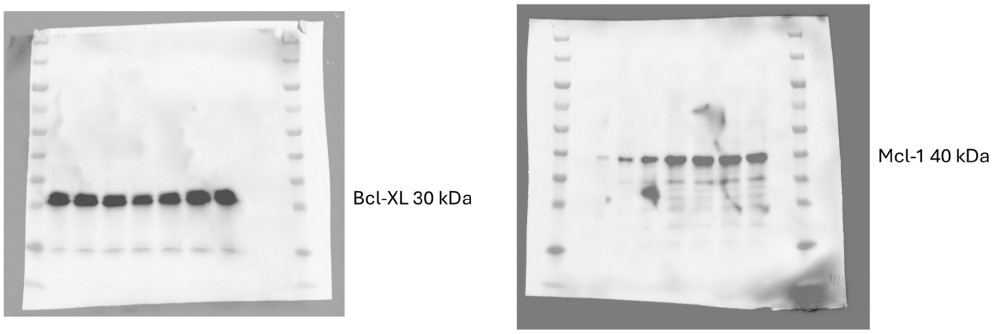


Figure S11: Uncropped images of Figure 4E: Data originates from Bcl-XL (30 kDa) and Mcl-1 (40 kDa) for Figure 4E.

References

1 W. Du, Y. Huang, X. Chen, Y. Deng, Y. Sun, H. Yang, Q. Shi, F. Wu, G. Liu, H. Huang, J. Ding, X. Huang and S. Xu, *Cell chemical biology*, 2024, **31**, 177-183.

2 J. L. Meidner, A. F. Frey, R. A. Zimmermann, M. O. Sabin, Z. Nidoieva, A. C. Weldert, S. N. Hoba, M. W. Krone and F. Barthels, *Angewandte Chemie (International ed. in English)*, 2024, **63**, e202403792.

3 E. Yankova, W. Blackaby, M. Albertella, J. Rak, E. de Braekeleer, G. Tsagkogeorga, E. S. Pilka, D. Aspris, D. Leggate, A. G. Hendrick, N. A. Webster, B. Andrews, R. Fosbeary, P. Guest, N. Irigoyen, M. Eleftheriou, M. Gozdecka, J. M. L. Dias, A. J. Bannister, B. Vick, I. Jeremias, G. S. Vassiliou, O. Rausch, K. Tzelepis and T. Kouzarides, *Nature*, 2021, **593**, 597–601.

4 A. A. Guirguis, Y. Ofir-Rosenfeld, K. Knezevic, W. Blackaby, D. Hardick, Y.-C. Chan, A. Motazedian, A. Gillespie, D. Vassiliadis, E. Y. N. Lam, K. Tran, B. Andrews, M. E. Harbour, L. Vasiliauskaite, C. J. Saunders, G. Tsagkogeorga, A. Azevedo, J. Obacz, E. S. Pilka, M. Carkill, L. MacPherson, E. N. Wainwright, B. Liddicoat, B. J. Blyth, M. R. Albertella, O. Rausch and M. A. Dawson, *Cancer discovery*, 2023, **13**, 2228–2247.

5 L. Liao, Y. He, S.-J. Li, G.-G. Zhang, W. Yu, J. Yang, Z.-J. Huang, C.-C. Zheng, Q.-Y. He, Y. Li and B. Li, *Cancer research*, 2022, **82**, 2444–2457.

6 K. Hwang, J. Bae, Y.-L. Jhe, J. Kim, J.-H. Cheong, H.-S. Choi and T. Sim, *European journal of medicinal chemistry*, 2024, **279**, 116843.

4.2 Nanoscale Direct-to-Biology Optimization and Structural Insights into Selective *S. aureus* TrmD Inhibitors

4.2.1 Context, Project Summary, and own Contribution

S. aureus is a pathogen with a high clinical burden and causes over 100,000 deaths per year worldwide.[178] Due to its essential role in the survival of *S. aureus* and other bacteria, multiple inhibitors for the tRNA methyltransferase TrmD have been developed as potential novel antibiotics. While these inhibitors often show potent *in vitro* inhibitory activity, they frequently lack antibacterial efficacy, likely due to poor permeability across the bacterial cell wall, as many contain di-basic or charged moieties. Moreover, despite the clinical burden of *S. aureus*, it has not been the focus of inhibitor development campaigns.[76,161,165–167,182–186]

In this study, selective inhibitors of the *S. aureus* TrmD were developed. For this purpose, *S. aureus* TrmD was recombinantly expressed within this thesis, and binding of the literature starting points (compounds **1** and **2** reported by Hill *et al*.[182]) was tested by ITC. Consequently, a diverse set of compounds was generated by functionalizing a pyrrolopyrimidone alkyne scaffold with a library of structurally diverse azides (N = 320). Testing in a direct-to-biology assay setup accelerated the development process, leading to the identification of five hits. While these hits showed selective and potent nano–micromolar *in vitro* enzyme inhibition, they lacked antibacterial activity. However, it was discovered that a synthetic intermediate with a Cbz-carbamate of the guanidine-motif-containing hit **8h** showed efficient antibacterial activity. This suggested a prodrug-like mechanism, where the guanidine moiety's polarity is masked, enabling the compound to pass through the bacterial cell wall. Lipophilic tags have been used before in a similar context.[183,486,487] Intracellular cleavage by esterases then releases the active guanidine compound, which was confirmed in a prodrug-lysate assay. The literature compound **2** and hit compound **8h** were subsequently co-crystallized with TrmD within this thesis, resulting in the first ligand-bound crystal structures for *S. aureus* TrmD. The **8h** containing structure was used in a docking campaign to compare the binding modes of the five initial hits in *S. aureus* TrmD to those in *H. influenzae* and *E. coli* TrmDs. These structural investigations revealed that the pyrrolopyrimidone scaffold and triazole linker are critical for selectivity between these bacteria. Additionally, residues unique to the *S. aureus* enzyme were identified close to the inhibitor, which could be targeted to further enhance selectivity in future development.

In summary, our study demonstrated a successful application of a nanomole-scale synthesis campaign combined with direct-to-biology assays for hit identification. We also present a prodrug concept with the potential to address the permeability issues commonly faced by TrmD inhibitors. Moreover, we provide the first *S. aureus* TrmD crystal structure co-crystallized with an inhibitor, offering important structural insights for future structure-based development of selective TrmD inhibitors.

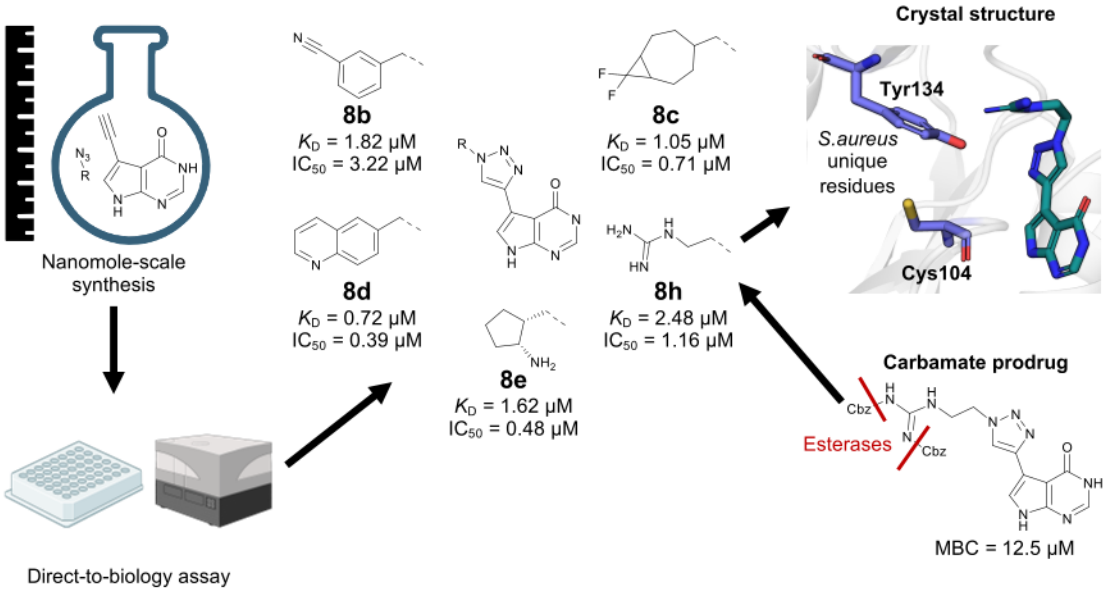


Figure 20: Development and evaluation of inhibitors for the tRNA m¹G37 methyltransferase (TrmD) of *Staphylococcus aureus* (*S. aureus*). Abbreviations: K_D (dissociation constant); IC_{50} (half-maximal inhibitory concentration); MBC (minimal bactericidal concentration). The figure was created with Microsoft PowerPoint, Biorender.com, and ChemDraw.

Own contributions: Protein expression and purification of *S. aureus* TrmD construct, establishing protein expression and purification of Trm5 (as part of the supervised Master's thesis of [redacted], ITC (compounds **1** and **2** against *S. aureus* and *H. influenzae* TrmD), FP assay for selectivity determination (50%), crystallization condition screening and co-crystallization with compounds **2** and **8h**, crystal structure model building (iterative refinement in Phenix and manual adjustment/validation in Coot to fit the electron density, including correction of artifacts), SeeSAR analysis, writing parts of the manuscript and supporting information.

Contributions from other authors: Syntheses, direct-to-biology screening, protein expression and purification of *H. influenzae* and *E. coli* TrmD constructs, FP assay for selectivity determination (50%), validation of compounds with FP assays, inhibition assays (^{3}H-incorporation and aptamer), bacterial growth inhibition assays, Cell Titer Glo cell viability assay, lysate assay, crystal structure initial model building (molecular replacement to obtain a

starting model, followed by initial refinement and manual inspection in REFMAC and Coot), molecular modeling, writing parts of the manuscript, and supporting information.

The work was published in Journal of Medicinal Chemistry (impact factor: 6.8) and licensed under a Creative Commons Attribution licence: https://creativecommons.org/licenses/by/4.0/. This publication and the complete supplementary information (SI) are available online at DOI: 10.1021/acs.jmedchem.5c02323. The appended Supporting Information represents an abridged version.

Publication reprinted with permission from J. Med. Chem. **2025**, *68*, 26246–26262. „Nanoscale Direct-to-Biology Optimization and Structural Insights into Selective *S. aureus* TrmD Inhibitors“
© 2025 The Authors. Published by American Chemical Society.

4.2.2 Publication

The following publication quoted (within “”) from page 80 to page 96 is exactly the same as the manuscript cited on page 79:“

Journal of Medicinal Chemistry

pubs.acs.org/jmc

Open Access

This article is licensed under CC-BY 4.0

Article

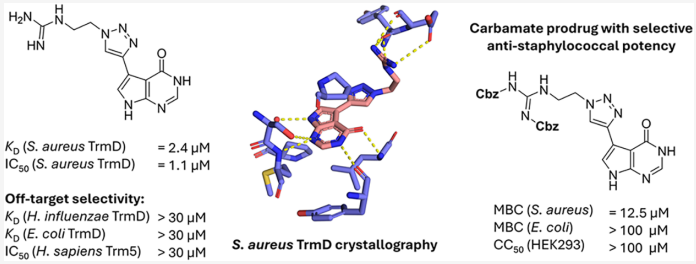
Nanoscale Direct-to-Biology Optimization and Structural Insights into Selective *S. aureus* TrmD Inhibitors

Ariane F. Hübner,[‖] Annabelle C. Weldert,[‖] Tessa Marciniak, Florian Hof, Vivien S. Beck, Samuel Carien, Sophie N. Mulartschyk, Eva Wolf, Wilma Ziebuhr, and Fabian Barthels*

Cite This: *J. Med. Chem.* 2025, 68, 26246−26262

Read Online

ACCESS | Metrics & More | Article Recommendations | Supporting Information



ABSTRACT: The tRNA m^1G37 methyltransferase (TrmD) is considered essential in various bacteria, including *Staphylococcus aureus*, a pathogen responsible for a wide range of diseases. Here, we have performed a high-throughput nanomole-scale synthesis campaign (nanoSAR) by late-stage copper(I)-catalyzed alkyne−azide cycloaddition (CuAAC)-functionalizing a library of structurally diverse azides (N = 320) to a pyrrolopyrimidone alkyne. We have identified selective *S. aureus* TrmD inhibitors with inhibitory activity in the nanomolar to low micromolar range using a direct-to-biology assay read-out. A carbamate-masked guanidine intermediate of the lead structure selectively inhibited *S. aureus* growth at low micromolar concentrations in cell-based assays, while Gram-negative bacteria and an off-target panel of methyltransferases were not affected. Subsequent cocrystallization resulted in a crystal structure of *S. aureus* TrmD bound to an inhibitor, providing detailed insights into its binding mode and enabling future structure-guided optimization.

Downloaded via UNIV MAINZ on January 15, 2026 at 12:33:26 (UTC).
See https://pubs.acs.org/sharingguidelines for options on how to legitimately share published articles.

INTRODUCTION

Staphylococcus aureus is a prevalent bacterial pathogen, causing a broad spectrum of diseases ranging from skin infections to life-threatening conditions such as pneumonia and sepsis.[1] The treatment of *S. aureus* infections is increasingly difficult due to the antibiotic resistance of the pathogen, including the emergence of multidrug-resistant isolates.[2] Particularly, methicillin-resistant *S. aureus* (MRSA) currently represents the deadliest resistance-pathogen pairing globally, causing more than 100,000 deaths in 2019 alone.[3,4] Therefore, the identification of new antimicrobial drugs is strongly desired to overcome resistance issues in *S. aureus*.

One enzyme essential for *S. aureus* among many other bacteria is the tRNA m^1G37 methyltransferase (TrmD), which catalyzes the methyl group transfer from *S*-adenosylmethionine (SAM) to the N^1 position of guanosine 37 in a defined subset of tRNAs.[5−8] Since this modification is located in close proximity to the 3′-side of the anticodon, its absence can lead to tRNA misrecognition during translation and +1-frameshift errors during protein synthesis.[9,10] In eukaryotes and archaea, the m^1G37 modification is introduced by the structurally unrelated tRNA methyltransferase 5 (Trm5).[11,12] Trm5 belongs to class I of methyltransferases, while bacterial TrmD belongs to the unique class IV, also known as SPOUT class.[11] TrmD was identified as a potentially selective antimicrobial drug target, due to its essential role as well as the structural differences from Trm5.[13] Crystal structures of inhibitor-bound TrmD complexes from several organisms, including *Haemophilus influenzae* and *Escherichia coli*, have been solved in the past, offering starting points for drug discovery campaigns.[14−17]

To date, a limited number of TrmD inhibitors targeting diverse bacterial organisms have been reported (15 publications since 2011, according to a PubMed search using the keyword “TrmD Inhibitor”),[14,18−20] but so far, only very few TrmD inhibitors have been effective in targeting *S. aureus*.[16] Despite the urgent need for new antibiotics targeting *S. aureus*,

Received: August 18, 2025
Revised: November 2, 2025
Accepted: December 4, 2025
Published: December 10, 2025



ACS Publications

© 2025 The Authors. Published by American Chemical Society

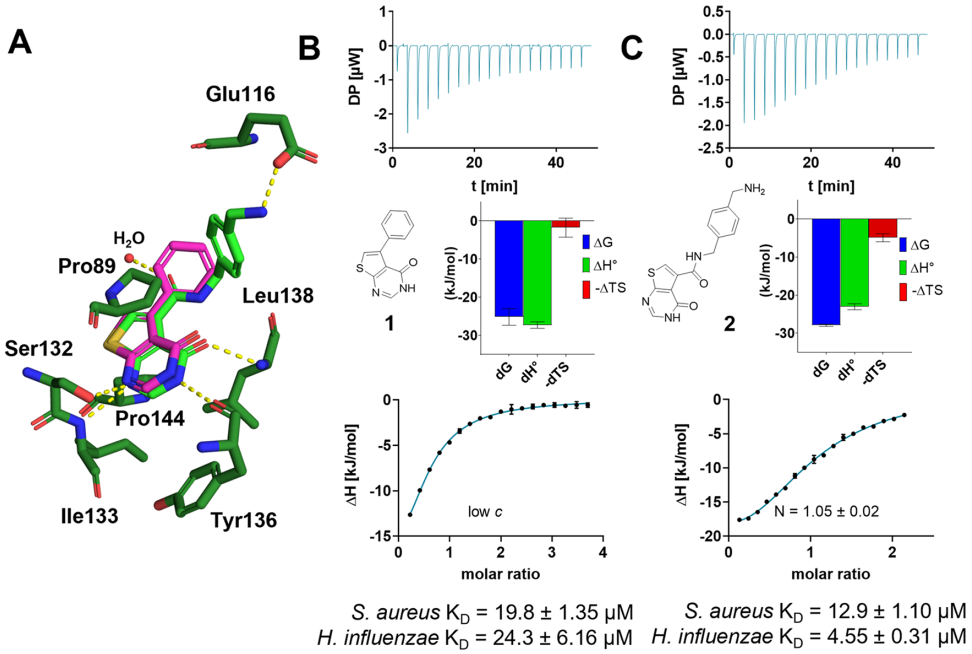


Figure 1. Definition of starting points for the development of *S. aureus* TrmD inhibitors. (A) Crystallographic overlay of literature-known inhibitors **1** (PDB: 4MCD) and **2** (PDB: 4MCC) in the *H. influenzae* SAM-binding pocket. Ligands and amino acids are shown in stick representation; polar interactions are shown as yellow lines, and water as red spheres. The carbon atoms of **1** are shown in pink and those of compound **2** in light green. Interacting residues are displayed in dark green. (B, C) Structures and affinities of inhibitors **1** (B) and **2** (C) binding to *S. aureus* TrmD determined by ITC, incl. thermograms, stoichiometry, and signature plots (data for *H. influenzae* TrmD in Figure S2). Due to low enthalpy signals, a low *c*-titration was performed for inhibitor **1**, resulting in $N < 1$.

previous studies focused mainly on developing TrmD inhibitors for *H. influenzae*, *E. coli*, *Mycobacterium abscessus*, and *Mycobacterium tuberculosis*.[14,18−20] In a development campaign conducted by AstraZeneca, Hill et al. screened a fragment collection to identify *H. influenzae* TrmD inhibitors.[14] They investigated thienopyrimidone-based inhibitors that showed inhibitory activity against a panel of TrmD orthologs (*E. coli*, *H. influenzae*, *Acinetobacter baumanni*, *Klebsiella pneumoniae*, and *Pseudomonas aeruginosa*), offering broadband starting points for drug discovery, but this also suggested only limited interspecies selectivity.[14]

To target this gap, in this present study, we employed the thienopyrimidone scaffold discovered by Hill et al. and optimized the inhibitory profile to develop selective inhibitors targeting *S. aureus* TrmD using a high-throughput nanomole-scale (final: 96 nmol) synthesis strategy. Reactions conducted with less than 300 nmol of starting material are commonly referred to as being performed on the nanomole scale.[21] This miniaturized format offers advantages compared to flask-oriented synthesis campaigns in throughput, development time, and in conserving valuable synthetic intermediates.[22] Notable contributions in this field feature the implementation of a range of standard medicinal chemistry transformations in plate-based formats, including the development of a copper-catalyzed alkyne−azide click reaction (CuAAC) pipeline as described by Gehrtz et al., suitable for our inhibitor development campaign.[21,23−25] If the resulting crude nanomole-scale reaction mixtures are directly analyzed using *in vitro* or *in cellulo* assays to derive structure−activity relationship (SAR) insights, this strategy was coined by several recent reports (2021−) as a *direct-to-biology* (D2B) approach.[26−30]

RESULTS AND DISCUSSION

Definition of an *S. aureus* Targeting Lead Structure.

To date, no dedicated *S. aureus* TrmD inhibitors have been reported. Hence, to define a suitable lead for nanoSAR-based optimization, we analyzed literature-known ligands of TrmD isoenzymes from diverse microorganisms. Hill et al. discovered the thienopyrimidone inhibitor **1** by screening a collection of fragments against *H. influenzae* TrmD, and their subsequent optimization resulted in inhibitor **2** with activities in the nanomolar to micromolar range.[14] X-ray cocrystal structures with *H. influenzae* TrmD were previously solved for inhibitor **1** (PDB: 4MCD) and the optimized *H. influenzae* inhibitor **2** (PDB: 4MCC). Both inhibitors were found to occupy the SAM binding pocket of TrmD (Figure 1A), while the thienopyrimidone moieties targeted the adenine binding pocket, and the phenyl ring of inhibitor **1** extended into the ribose pocket (Figure 1A, Figure S1A). The phenylmethyl-amine moiety of inhibitor **2** reaches further into the methionine part of the SAM pocket (Figure S1B), where an additional interaction with Glu116 can be formed (Figure 1A).[14] Due to the considerable sequence similarity (65%) between *H. influenzae* TrmD and *S. aureus* TrmD, we hypothesized that this thienopyrimidone chemotype might provide a reasonable lead for *S. aureus* drug development. To assess if the thienopyrimidone-based compounds, developed as dedicated *H. influenzae* TrmD inhibitors, are suitable starting points for targeting the *S. aureus* orthologous enzyme, we

https://doi.org/10.1021/acs.jmedchem.5c02323
J. Med. Chem. 2025, 68, 26246−26262

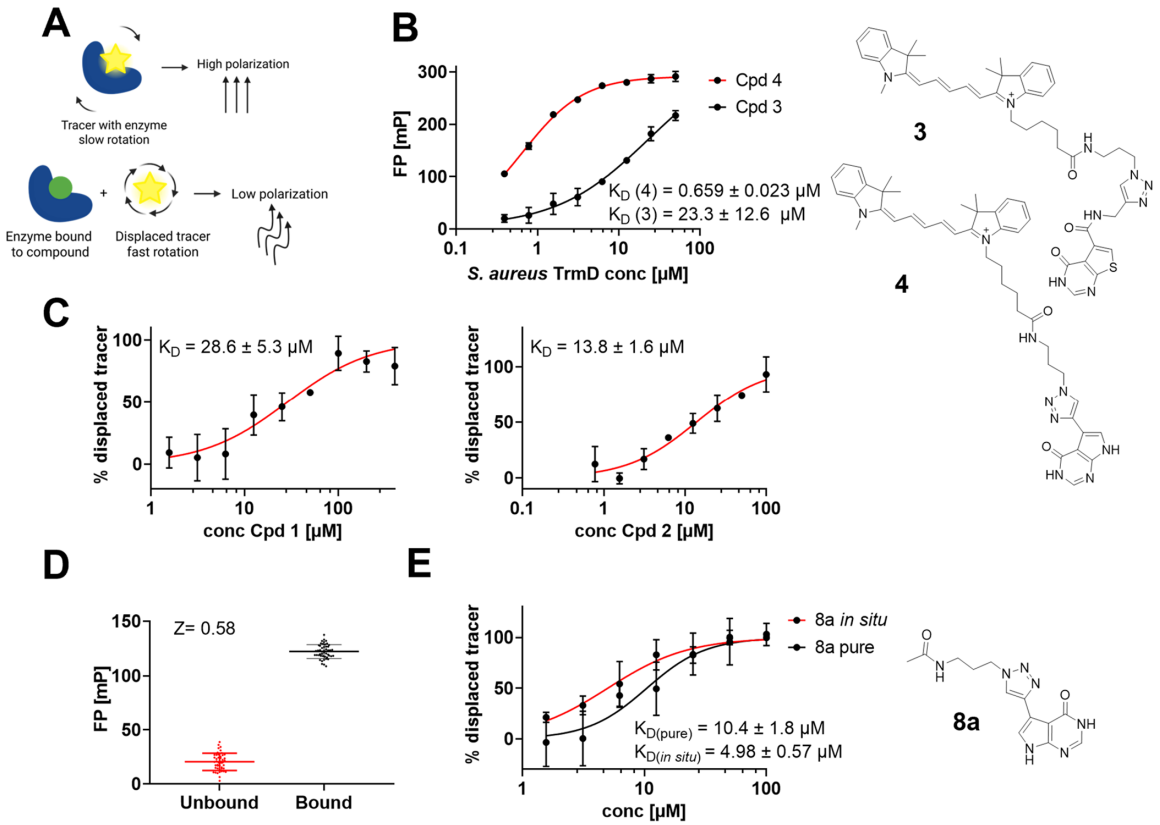


Figure 2. Fluorescence polarization (FP) assays for *S. aureus* TrmD ligand investigation. (A) Concept of the FP displacement assay. (B) Chemical structures and FP-derived affinity of tracers **3** and **4** binding to *S. aureus* TrmD. (C) FP displacement assays for the determination of apparent affinities of parent compounds **1** and **2**. (D) Evaluation of statistical *Z*-factors to assess the high-throughput capability of this FP assay setup. (E) FP displacement assays of nanoSAR test triazole **8a** *in situ* vs chromatographically purified compound.

evaluated the binding thermodynamics of **1** and **2** via isothermal titration calorimetry (ITC) on the recombinant *S. aureus* TrmD enzyme (Figure 1B,C, Figure S2). **1** and **2** showed enthalpy-dominated binding profiles in the micromolar range on both *H. influenzae* and *S. aureus* enzymes, with an unfavorable selectivity toward targeting *S. aureus* TrmD for **2**. The determined dissociation constants were 19.8 and 12.9 μM, respectively, and thus, were deemed suitable as starting points for *S. aureus* targeting ligand optimization.

Development of a Direct-to-Biology Assay Platform for Inhibitor Optimization. To enable the screening of hundreds of nanomole-scale synthesized compounds, the implementation of a high-throughput-capable RNA methyltransferase (MTase) assay is considered fundamental. In a previous publication, we demonstrated the suitability of fluorescence polarization (FP)-based assays as a screening method to identify and characterize MTase inhibitors.[31] In this assay format, a fluorescent, SAM-pocket binding tracer can be displaced by the compound under investigation, and the resulting change in fluorescence polarization defines the readout of the inhibitor compound's affinity (Figure 2A).

Previously, we developed an *H. influenzae* TrmD targeting fluorescent tracer **3**, which we originally intended to adapt for *S. aureus* TrmD.[31] Compared to *H. influenzae* TrmD (K_D = 2.0 μM, Figure S4A), however, this tracer showed only weak affinity for the *S. aureus* orthologous enzyme (K_D = 23.3 μM, Figure 2B). To address this issue, we employed scaffold hopping from a thieno- to a pyrrolopyrimidone, as demonstrated in the study by Hill et al., which resulted in improved binding affinities for *S. aureus* TrmD compared to *H. influenzae* TrmD. Thus, here, we report a new fluorescent tracer **4** dedicated to *S. aureus* TrmD with a pyrrolopyrimidone motif and without the amide linker (Figure 2B). Evaluation of tracer **4** in FP assays confirmed this hypothesis and revealed a K_D-value of 659 nM for *S. aureus* TrmD, suitable for the establishment of a high-throughput-capable assay format (Figure 2B). The structural reason for the preference of the thienopyrimidone motif and an amide-free linker for *S. aureus* TrmD could be rationalized by crystallographic analysis of our *S. aureus* TrmD inhibitor complexes (*vide infra*).

To validate that optimized *S. aureus* tracer **4** is suitable for a direct-to-biology screening of TrmD inhibitors, we investigated dose−response series of parent compounds **1** and **2** by FP displacement assays, yielding apparent binding affinities (K_D = 28.6 and 13.8 μM), and hence, agreeing with the magnitude and relative order determined via ITC (Figure 2C vs Figure 1B,C). Furthermore, we were able to confirm that the assay setup consisting of *S. aureus* TrmD (500 nM) and tracer **4** (10 nM) is suitable as a high-throughput-capable format by determining the assay-specific *Z*-factor (Z = 0.58, Figure

https://doi.org/10.1021/acs.jmedchem.5c02323
J. Med. Chem. 2025, 68, 26246−26262

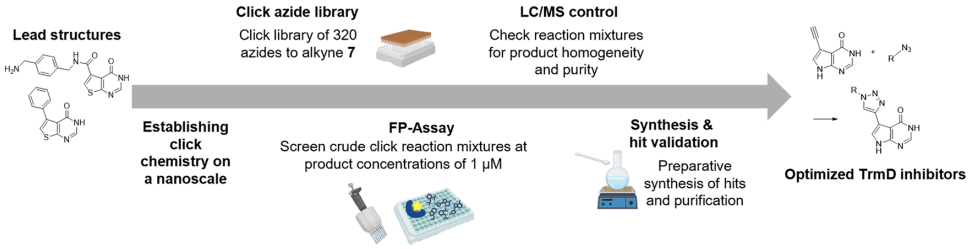
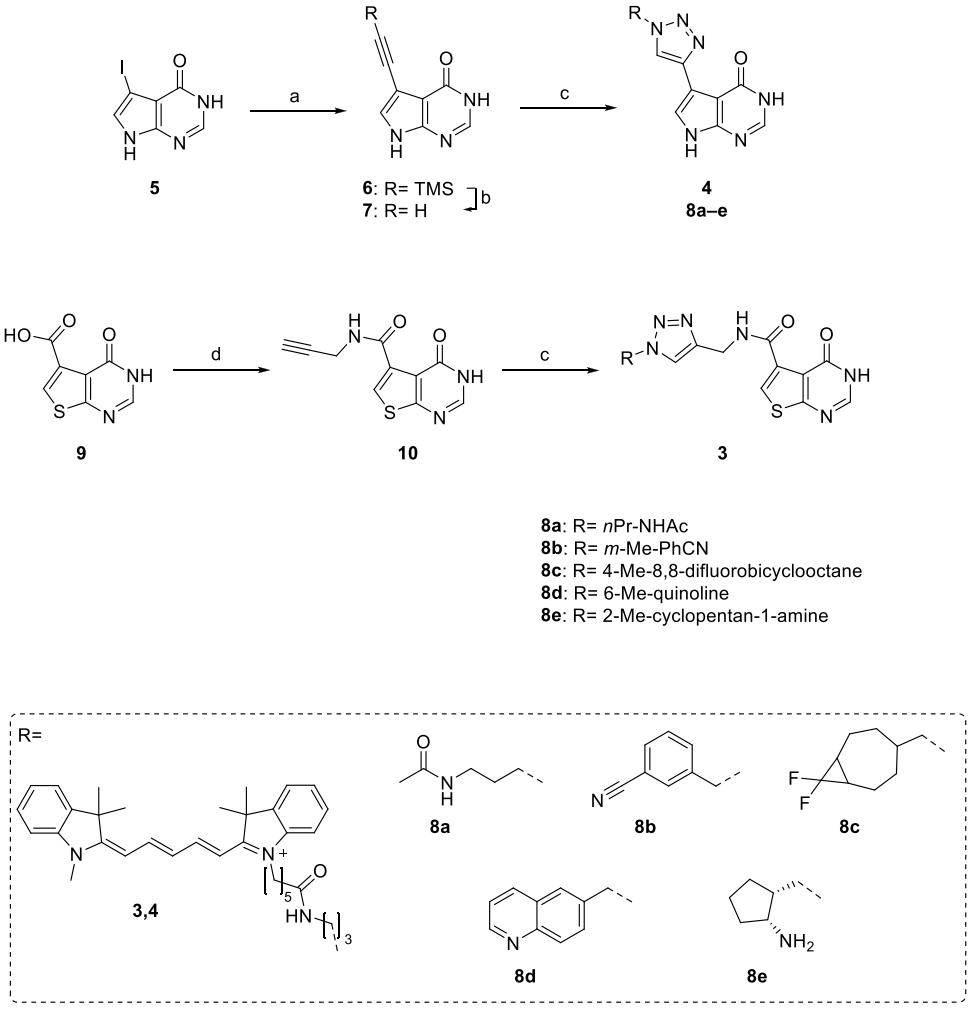


Figure 3. Workflow of the nanoSAR strategy for optimization of *S. aureus* TrmD inhibitors. Reaction of the alkyne precursors **7** with 320 chemically diverse azides resulted in a plate-based library of inhibitor triazoles, which were measured in a direct-to-biology FP displacement assay, followed by an LC/MS confirmation of hit compounds' crude reactions, and subsequently, the preparative synthesis and validation of the selected candidate compounds.

Scheme 1. Overview of Synthetic Procedures[a]

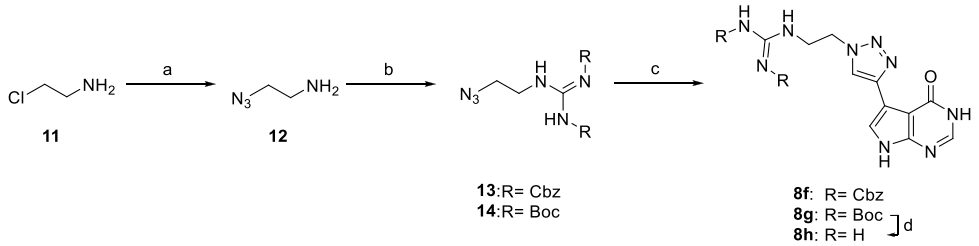


[a]Reagents and conditions: (a) CuI, TMS-acetylene, $Pd(PPh_3)_4$, triethylamine, DMF/THF, rt, 16 h, 29%; (b) 1 M tetra-*n*-butylammonium fluoride, THF/ACN, 0 °C–rt, 1.5 h, 68%; (c) $CuSO_4$×5 H_2O, TBTA, sodium ascorbate, DMSO, H_2O, rt, 16 h, 25–74%; (d) HATU, DIPEA, DCM/DMF, rt, 16 h, 77%–quant.

2D). The *Z*-factor is a statistical parameter that assesses the dynamic range of an assay to determine its suitability for HTS; a *Z*-factor >0.5 is generally considered indicative of an excellent assay.[32] Based on the assay results gleaned from the

https://doi.org/10.1021/acs.jmedchem.5c02323
J. Med. Chem. 2025, 68, 26246–26262

Scheme 2. Overview of the Synthetic Procedure for Compounds 8h−g[a]



[a](a) Sodium azide, water, 90 °C, 16 h, quant.; (b) *N*,*N*′-Bis-Boc- or *N*,*N*′-Bis-Cbz-guanylpyrazole, THF, triethylamine, rt, 72 h, 47−90%; (c) $CuSO_4$×5 H_2O, TBTA, sodium ascorbate, DMSO, H_2O, rt, 16 h, 25−74%; (d) TFA, DCM, 30 min, rt, quant.

tracer experiments, we decided to use the alkyne handle of the compound **4** precursor (cpd **7**) to build a CuAAC-derived nanoSAR triazole library for the development of new *S. aureus* selective TrmD inhibitors. The workflow is illustrated in Figure 3.

To confirm that alkyne **7** (Scheme 1) and the resulting crude nanomole-scale triazoles are compatible with the established direct-to-biology platform, we performed a pilot exploration including the *in situ* synthesis and screening of a representative triazole candidate **8a** (Figure 2E). LC/MS reaction control of pilot alkyne−azide coupling reactions showed consistently >90% conversion rates and no production of side-products; thus, we concluded that this D2B outline is suitable for the generation of a TrmD inhibitor library. The nanomole scale reaction mixture was subsequently tested by FP assay both in crude and after chromatographic purification of this test compound, revealing only slight variation in K_D-values of 4.98 and 10.4 μM, respectively, along with a minimal variation of the Hill slope (Figure 2E). This suggests that crude reactions from the azide library provide a reliable semi-quantitative indication of binding affinities, as the objective of D2B screenings is to rank the potency of substituents in relative order. Also, the FP assay setup using tracer **4** and *S. aureus* TrmD was found to be insensitive toward all components of the *in situ* click reaction, including unreacted alkyne **7** (K_D > 100 μM, Figure S4B).

Chemistry. In this present study, a new alkyne-decorated pyrrolo[2,3-*d*]pyrimidone with similar chemical properties to parent structures **1** and **2** was synthesized (Scheme 1) for the preparation of triazole-based *S. aureus* TrmD inhibitors **8a−e**.

For inhibitor generation, this precursor alkyne **7** was subsequently reacted with diverse aromatic and aliphatic azides via copper(I)-catalyzed azide−alkyne cycloaddition (CuAAC). The thieno-subunit from literature TrmD inhibitors (e.g., **1** and **2**) was substituted with a pyrrolo-unit to facilitate synthesis, without compromising binding affinity. According to Hill et al., replacing the sulfur atom in the thienopyrimidone moiety of the scaffold with a nitrogen was favorable for *S. aureus* selectivity, which allowed us to develop a high-affinity fluorescent tracer **4** (Figure 2).[14] The unoccupied TrmD methionine pocket (Figure S1) leaves space for modifications at the pyrrolo unit, and thus, we synthesized triazole derivatives for both tracer and inhibitor development. The synthetic routes of compounds **6−14**, including the fluorescent tracers and the compounds originating from nanoSAR screening, are described in Schemes 1 and 2.

Literature-known compound **2** was synthesized by a HATU-mediated coupling of *tert*-butyl (4-(aminomethyl)benzyl)-carbamate and 4-oxo-3,4-dihydrothieno[2,3-*d*]pyrimidine-5-carboxylic acid, followed by a Boc-deprotection with TFA in DCM. The synthesis route for alkyne **7** started with a Sonogashira reaction using commercially available 5-iodo-3,7-dihydro-4*H*-pyrrolo[2,3-*d*]pyrimidin-4-one (**5**) and TMS-acetylene, catalyzed by Tetrakis(triphenylphosphine)-palladium(0) and copper(I) iodide, yielding compound **6**. Finally, alkyne **7** was obtained by deprotection of the TMS-group by tetra-*n*-butylammonium fluoride (TBAF). Subsequent CuAAC with alkyne **7** and various azides was performed using $CuSO_4$×5 H_2O, which was reduced *in situ* to copper(I) by sodium ascorbate and stabilized by *tris*((1-benzyl-4-triazolyl)methyl)amine (TBTA) in DMSO and water (1:1).[21] Hit compounds of the nanoSAR study and fluorescent tracers were resynthesized by the same procedure on a preparative scale and purified by reverse-phase flash chromatography.

Preparative synthesis of **8h** started with 2-chloroethylamine (**11**), which was converted to the corresponding azide (**12**) with sodium azide. To introduce the guanidine group, *N*,*N*′-Bis-Boc-1-guanylpyrazole was reacted under basic conditions in THF to afford intermediate **14**. Subsequently, intermediate **14** was reacted with alkyne **7** via CuAAC to yield **8g**. Under similar conditions, compound **8f** was synthesized with *N*,*N*′-Bis-Cbz-1-guanylpyrazole. Final deprotection of the Boc-group of **8g** with TFA and DCM (1:1) yielded lead compound **8h**.

Preparation of a nanoSAR Triazole Library and FP-Based TrmD Screening. Next, we conducted an *S. aureus* TrmD-targeting nanoSAR study. For this, alkyne **7** was reacted on a 96 nmol scale with an in-house diversity-oriented azide library (N = 320, mean pairwise Tanimoto similarity = 0.11) designed to cover a large chemical fragment space, generating a panel of 320 crude triazoles ready for FP assay investigation. The composition of the azide library is designed to be chemically diverse in several categories, including physico-chemical properties such as polar surface area, lipophilicity, and the number of hydrogen bond donors and acceptors, as well as structural features like the number of aromatic rings (Figure S23). A complete list of chemical structures included in the azide library can be found in Table S4. *In situ* reaction conditions for CuAAC were adapted from Gehrtz et al., utilizing $CuSO_4$, which is reduced *in situ* to Cu(I) by sodium ascorbate and stabilized by TBTA.[21] Degassed water and DMSO (1:1) were used as solvents to prevent the oxidation from Cu(I) to Cu(II). For the synthesis of the triazole library, a master mix was prepared, containing all reaction components except the azides. All reactions were started by the addition of the respective azide in 24 μL at a final product concentration

https://doi.org/10.1021/acs.jmedchem.5c02323
J. Med. Chem. 2025, 68, 26246−26262

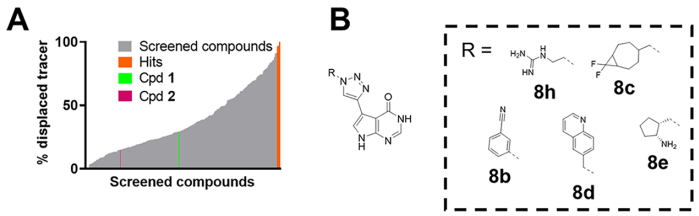


Figure 4. Results, analysis, and hit selection of the nanoSAR TrmD screening. (A) Waterfall plot summarizing the screening of 320 triazole inhibitor candidates at 1 μM. In orange, the five compounds ("hits") with the highest potency (>93% displaced tracer, **8b−e,h**) are shown. (B) Chemical structure representation of the five hits **8b−e,h** that were identified during screening.

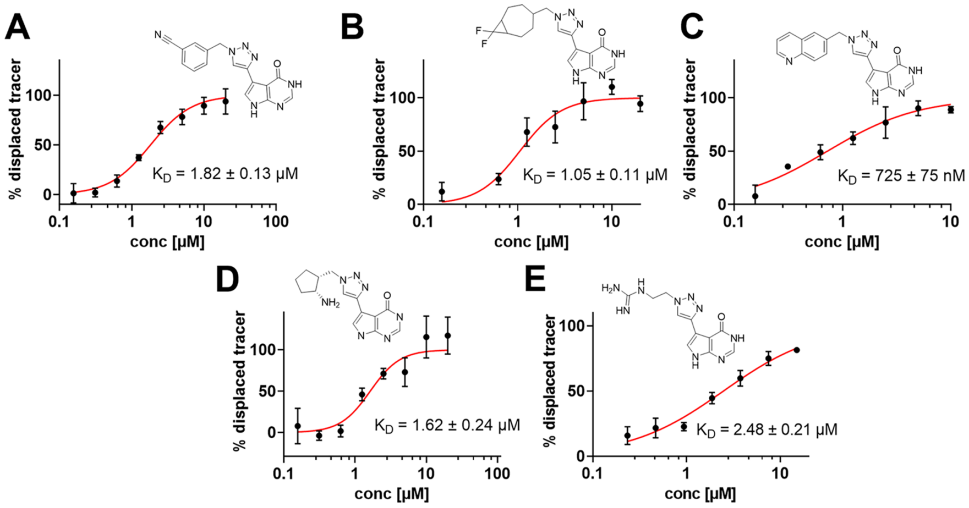


Figure 5. FP-assay of chromatographically purified (A) **8b** (B) **8c** (C) **8d** (D) **8e** (E) **8h** with the respective structures and K_D-values.

of 4 mM (96 nmol). Reaction mixtures were incubated for 16 h at room temperature and under an argon atmosphere in sealed 96-well plates.

Based on the pilot explorations of pyrrolopyrimidine triazoles **4** and **8a** (K_D = 0.66 and 4.98 μM), we adjusted the final concentration of the triazoles for FP screening to 1 μM, assuming full conversion of the click reaction. In this regard, conversion rates were tested for 24 random reaction mixtures by LC/MS and were found consistently to be >90%. For FP assay screening, we used 500 nM of *S. aureus* TrmD and 10 nM of tracer **4** in a total volume of 40 μL in 96-well plates. We performed control measurements and defined 10 nM of tracer **4** in buffer as 100% displacement and the DMSO control as 0% tracer displacement. As primary hits, we intended to select the top 5 compounds that exhibited tracer displacements >93%. The results of the FP screening were visualized in a waterfall plot and plate-based heatmaps (Figure 4, Figure S3).

Five compounds (**8b−e,h**) showed near complete displacement during FP screening at an inhibitor concentration of 1 μM, and consequently, these discovered structures ("hits") were verified for reaction conversion and identity via LC/MS (>90% crude purity). A comprehensive overview of the FP assay results for all compounds generated from the azide library can be found in Table S4. Structurally, hits **8b−e,h** appear to have limited similarity; yet **8b−d** contain hydrophobic, sterically demanding decorations, whereas **8b,e,h** share a basic amine or amidine moiety, and thus, these five hit compounds (**8b−e,h**) were selected for preparative resynthesis and validation. SAR of these enriched ligand features is discussed by crystallography and molecular modeling (*vide infra*).

Resynthesis and Characterization of *S. aureus* TrmD Inhibitors. The five hit compounds identified during the FP screening were subsequently resynthesized on a preparative scale, and binding profiles were validated using the FP assay with >95% chromatographically purified inhibitors. Synthesis procedures of the hits can be found in Schemes 1 and 2. K_D-values and the respective curves for all hit compounds **8b−e,h** were determined by dose−response experiments in the FP assay and can be found in Figure 5 and Table 1. To further investigate the inhibitory efficacy of **8b−e,h**, we utilized a literature-known aptamer-based *S. aureus* TrmD enzyme assay for IC_{50} determination (Table 1) and an orthogonal label-free ^{3}H-scintillation MTase assay (Figures S9, S10).[33] Both K_D and IC_{50} values ranged from 390 nM to 3.22 μM, and in summary, it can be concluded that the nanoSAR strategy has led to a successful optimization of parent compounds **1** and **2** (28.6 and 13.8 μM).

Next, we employed the FP-assay using tracers **3** and **4** to test the selectivity of **8b−e,h** against a panel of TrmD isoenzymes from *S. aureus*, *E. coli*, and *H. influenzae* (Figures S7, S8). Furthermore, we tested the inhibitory potency of **8b−e,h** for the human MTase homologue Trm5 (Figure S6). Since no

https://doi.org/10.1021/acs.jmedchem.5c02323
J. Med. Chem. 2025, 68, 26246−26262

Table 1. Overview of K_D-Values (Determined by FP Assays) and IC_{50}-Values (Determined by Aptamer-Based Enzyme Assays for *S. aureus* TrmD and ^{3}H-Based Enzyme Assay for Trm5) for 8b−e,h[a]

	S. aureus		*E. coli*	*H. influenzae*	Trm5
Cpd	K_D [μM]	IC_{50} [μM]	K_D [μM]	K_D [μM]	IC_{50} [μM]
8a	10.4 ± 1.8	n.d.	n.d.	n.d.	n.d.
8b	1.82 ± 0.13	3.22 ± 1.80	>30	>30	>30
8c	1.05 ± 0.11	0.71 ± 0.10	>30	>30	>30
8d	0.72 ± 0.07	0.39 ± 0.07	>30	>30	>30
8e	1.62 ± 0.24	0.48 ± 0.06	>30	>30	>30
8h	2.48 ± 0.21	1.16 ± 0.12	>30	>30	>30

[a]n.d.: not determined.

suitable fluorescent tracer was available, a functional ^{3}H-based enzyme assay was performed to assess Trm5 selectivity. All hit compounds exhibited at least >10× K_D- or IC_{50}-values for all off-targets compared to the *S. aureus* TrmD, and thus, we conclude that nanoSAR optimization provided not only affine but also selective *S. aureus* TrmD inhibitors (Table 1). In summary, the hit compounds **8b−e,h** demonstrated a significant improvement regarding selectivity and affinity toward the *S. aureus* TrmD compared to the parent compounds **1** and **2**. Also, we investigated mammalian cytotoxicity of the hits **8b−e,h** using CellTiterGlo assays following cell viability in HEK293 cells. In summary, the hit compounds showed no significant effects on cell viability at relevant concentrations up to 100 μM (Figure S11). Slight cytotoxic effects were only observed for compounds **8b** and **8c** at 100 μM, and for **8e** at >10 μM, whereas the identified lead *S. aureus* TrmD inhibitor compound **8h** showed no mammalian cytotoxicity up to 100 μM.

Antibacterial Assays and Potential Prodrug Identification. To assess the antibacterial activity of **8b−e,h**, the effect on *S. aureus* RN4220 was investigated using a dose−response bacterial growth inhibition assay. Also, two synthetic carbamate intermediates (**8f** and **8g**, Figure 6) obtained during the preparation of **8b−e,h** were included in this assay through their similarity with the hit compounds. Here, initial screenings of **8b−h** were conducted at 1, 10, and 100 μM but revealed that the growth of *S. aureus* was not affected by most compounds at concentrations up to 100 μM compared to the untreated controls in bacterial growth inhibition (Figure 6, details for hit compounds from the library **8b-e,h** are shown in Figure S12). Also, none of the compounds showed significant growth inhibition for *E. coli* (Figures S13, S14). As TrmD is an essential protein in *S. aureus*, successful inhibition is expected to lead to cell death and/or growth inhibition, which has been substantiated in numerous literature studies to date.[5,8,34] Yet, it has been observed in similar TrmD drug development campaigns that, despite nanomolar affinity, a majority of TrmD inhibitors fail in terms of antibacterial potency, presumably due to their large polar surface area and insufficient permeability through the bacterial cell wall.[14,18−20,35] Surprisingly, a significant reduction in *S. aureus* growth was observed during treatment of RN4220 with di-Cbz intermediate **8f** (Figure 6A, Figure S15B: MIC = 12.5 μM), while **8f** and **8g** showed no inhibition of Gram-negative *E. coli* (Figures S13, S14). In fact, a slight increase in *E. coli* growth rate at the highest concentration (100 μM) of **8f** could be observed, possibly due to a compensatory effect of this more permeable drug acting on an unknown Gram-negative off-target (Figure S14B).

We hypothesized that the activity of **8f** against *S. aureus* could be attributed to the di-Cbz carbamate moiety, masking the large polar surface area of the guanidine motif of hit **8h**, which itself did not influence bacterial growth, presumably due to the charged nature and limited permeability (Figures S12, S13). The strategy of conjugating a lipophilic tag has previously been shown to improve the permeability of antibacterials.[16,36,37] To determine the minimal bactericidal concentration (MBC) of the substances, bacterial cultures were prepared as in the bacterial growth inhibition assay. While cell growth is not negatively affected by treatment with Boc-carbamate **8g**, and more CFU/mL were observed after incubation, Cbz-carbamate **8f** affects growth starting at 12.5 μM treatment (Figure S16). On average, fewer CFU/mL were determined after 24 h of incubation, but bacteria were not killed completely. This indicates a rather bacteriostatic mode of action.

Subsequently, both synthetic intermediates **8f** (di-Cbz) and **8g** (di-Boc) were evaluated for their *in vitro* TrmD affinity using FP assays. **8g** displayed a K_D-value of 19.8 μM, while **8f** showed no *S. aureus* TrmD binding up to 100 μM (Figure S5A,B), and thus, we concluded that the antistaphylococcal activity of **8f** is not mediated by direct TrmD inhibition. Hence, we developed a mechanistic hypothesis evaluated below: Since carbamates are known to be susceptible to cleavage by esterases, we hypothesized that *in situ* deprotection

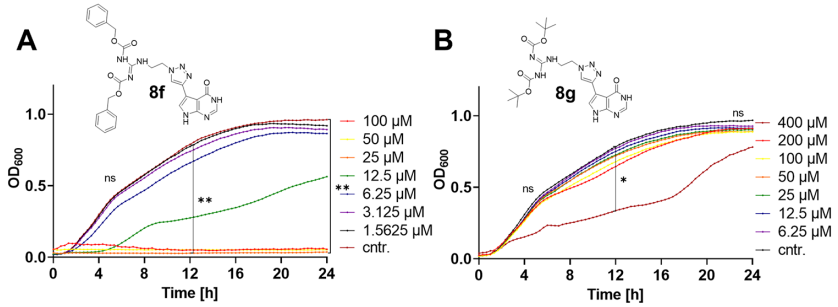


Figure 6. *S. aureus* growth inhibition by **8f** (di-Cbz) and **8g** (di-Boc). (A) *S. aureus* RN4220 treated with **8f** and (B) *S. aureus* RN4220 treated with **8g**. Only **8f** showed a significant effect on *S. aureus* bacteria in lower concentrations. Two-way ANOVA with Dunnett's multiple comparisons test was used for statistical analysis, using a confidence interval of 95% (Time points: 6, 12, and 24 h).

https://doi.org/10.1021/acs.jmedchem.5c02323
J. Med. Chem. 2025, 68, 26246−26262

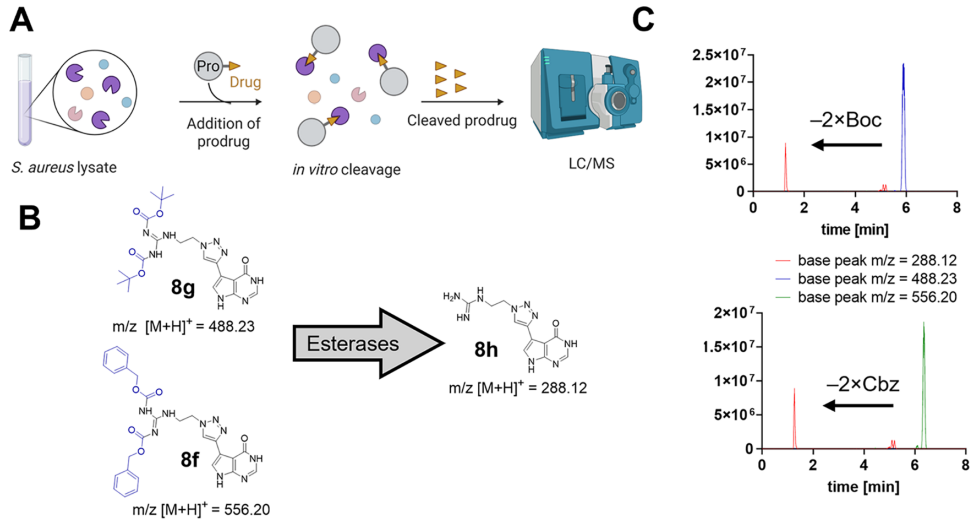


Figure 7. Carbamate-containing synthetic intermediates are readily cleaved by an *S. aureus* cell lysate. (A) Methodology of the conducted prodrug cleavage assay. (B) Structures and calculated masses of carbamates **8f**, **8g**, and for the deprotected hit compound **8h**. (C) LC/MS base-peak chromatograms of *S. aureus* lysates treated with **8f** or **8g** (400 μM) for 16 h. Detailed results of reference and base-peak chromatograms can be found in Figure S17.

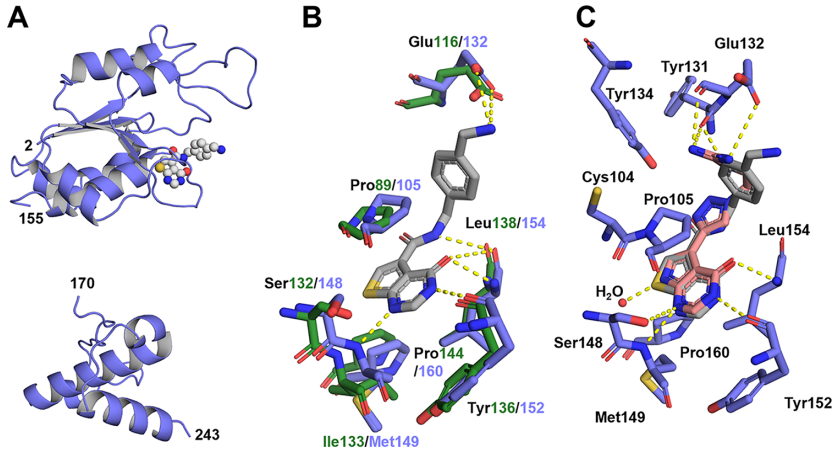


Figure 8. Crystal structures of compounds **2** and **8h** binding to *S. aureus* TrmD. (A) Structure of *S. aureus* TrmD bound to **2**. The protein is depicted as a violet-blue cartoon, and the ligand's carbon atoms as gray spheres. (B) Compound **2** bound to *S. aureus* TrmD (PDB: 9SDV) overlaid with *H. influenzae* TrmD (PDB: 4MCC) binding pocket amino acids. (C) Overlay of **2** (PDB: 9SDV) and **8h** (PDB: 9SDW) in the *S. aureus* binding pocket. Ligands and amino acids are shown in stick representation; polar interactions are shown as yellow lines, and water as red spheres. The carbon atoms of **2** are shown in gray and those of compound **8h** in salmon. Interacting residues are displayed in violet-blue (*S. aureus*) or dark green (*H. influenzae*).

by cytosolic esterases might catalyze the transformation of **8f** (di-Cbz) to **8h** (free guanidine), the potent TrmD inhibitor, suggesting that **8f** might function as a more permeable prodrug.[37−40]

To test this hypothesis, we investigated whether carbamates **8f** and **8g** can be cleaved by total *S. aureus* lysates. A native *S. aureus* RN4220 lysate was prepared and incubated for 16 h with carbamates **8f** and **8g** (c = 400 μM), followed by LC/MS base-peak analysis of the lysate (Figure 7A). Interestingly, both carbamates **8f** and **8g** were readily cleaved in the presence of the lysate, yielding the production of hit compound **8h**, which could be detected in both lysates (Figure 7C). Both di-Boc and di-Cbz prodrugs appeared to be cleaved to a similar degree (~30%) even at the very high concentration of 400 μM.

In this context, single Boc- or Cbz-conjugated guanidines as intermediary deprotection products were not found by LC/MS analysis. Detailed results of reference and base-peak chromatograms can be found in Figure S17. Since carbamate **8g** (di-Boc) was found to be cleaved in the bacterial lysate, too, its lower antistaphylococcal potency in *S. aureus* experiments might be due to lower permeability compared to **8f** (di-Cbz). In summary, we were able to effectively reduce the growth of *S. aureus* cells with **8f**, which was not the primary end point of the nanoSAR optimization, but potentially acts as a *S. aureus*

https://doi.org/10.1021/acs.jmedchem.5c02323
J. Med. Chem. 2025, 68, 26246−26262

carbamate prodrug, which is metabolized by *S. aureus* cells to yield the actual inhibitor **8h** through cleavage of the di-Cbz carbamate.

Previous studies on TrmD inhibitors have also demonstrated that the incorporation of lipophilic moieties enhances antibacterial efficacy compared to analogous compounds lacking such features, which were not effective in the Gram-positive bacterium *S. aureus*.[14,16] Thus, far, lipophilic tags of this Cbz-carbamate type have not been applied as prodrugs in contexts where the differences between IC_{50}-values and MICs were mechanistically explainable. Our findings suggest that, through prodrug strategies, *S. aureus* TrmD can be more effectively targeted, demonstrating that TrmD can, in principle, be targeted with more permeable inhibitors.

To further validate our prodrug hypothesis *in vivo*, we next investigated the intracellular formation of the active TrmD inhibitor **8h** in growing *S. aureus* cells by LC/MS-based quantification. Bacterial cultures were treated with sublethal concentrations (4 μM) of compounds **8f**, **8g**, and **8h**, respectively, followed by cell harvesting and metabolite extraction. Remarkably, only treatment with the di-Cbz carbamate **8f** resulted in detectable intracellular levels of **8h**, while no formation of **8h** could be observed upon treatment with equimolar concentrations of **8g** or **8h** (Figure S18). This finding is in line with our prodrug hypothesis, demonstrating that **8f** undergoes enzymatic cleavage in *S. aureus* cells *in vivo* to release the active TrmD inhibitor **8h**. The absence of measurable intracellular **8h** upon direct treatment with **8h** or **8g** suggests limited uptake of these more polar species, further supporting that the improved antibacterial efficacy of **8f** originates from its enhanced permeability combined with intracellular prodrug activation.

Crystal Structures of TrmD-Inhibitor Complexes. To date, no ligand-bound structure of *S. aureus* TrmD has been reported, with the PDB containing only one apo structure (PDB: 3KY7) of this enzyme.[41] To analyze the binding mode of the compounds identified in the nanoSAR study and to guide future inhibitor optimization, we cocrystallized *S. aureus* TrmD with inhibitor **2** and the new TrmD inhibitor **8h.**

The cocrystal structure of **2** (Figure 8A) was solved at a resolution of 2.5 Å in the space group $P4_332$, containing one protein molecule per asymmetric unit. The structure exhibited a fold similar to that of the apo *S. aureus* TrmD structure (PDB: 3KY7) and other members of the SPOUT-class TrmD enzymes, as reflected by an overall C_α RMSD of 0.50 Å (Figure S19A). The N- and C-terminal domains of the monomer were resolved, but the highly flexible linker connecting the domains could not be resolved, similar to many published TrmD structures.[17,42−44] For the cocrystallized complex, the N-terminal domain showed discrete electron density for inhibitor **2** (Figure 8A, Figure S19). Comparison with the cocrystal structure of inhibitor **2** bound to *H. influenzae* TrmD (PDB: 4MCC) highlights that the structures adopted a similar fold with an overall C_α RMSD of 1.44 Å (Figure S19B). Also, the conformation and ligand interactions of **2** were found to be similar for both *H. influenzae* and *S. aureus* enzymes (Figure 8B). An ionic interaction was formed between the primary amine of **2** and Glu132 in *S. aureus* (Glu116 in *H. influenzae*), a residue highly conserved among TrmD orthologues.[8] The thienopyrimidone ring system displayed interactions with *S. aureus* Met149 (*H. influenzae* Ile133), Tyr152 (Tyr136), Leu154 (Leu138), and Pro105 (Pro89), within the conserved SAM pocket (Figure 8B).

To analyze the differences in binding affinity of parent compound **2** between the *H. influenzae* and *S. aureus* enzymes, we used the HYDE scoring function in the SeeSAR toolkit to predict favorable and unfavorable contributions of individual ligand atoms to the overall binding energy (Figure S20). The computer-aided investigation revealed that the main difference stems from the amide group interactions, which contributed favorably to *H. influenzae* TrmD (HYDE: −3.8 kJ/mol), but unfavorably to the *S. aureus* enzyme (HYDE: +11.0 kJ/mol). This is in line with the observation that fluorescent tracer **3** (K_D = 23.3 μM), containing an amide moiety, showed lower *S. aureus* TrmD affinity to the target than tracer **4** (K_D = 659 nM), where the amide bond was omitted (Figure 2B). Additionally, the terminal amine of inhibitor **2** contributed favorably (HYDE: −3.0 kJ/mol) for the *H. influenzae* enzyme, whereas it resulted in a slightly unfavorable interaction for the *S. aureus* enzyme (HYDE: +0.3 kJ/mol). Also, these two crystallographic findings rationalize the results gleaned from the nanoSAR optimization: the transformation of amide to triazole and the transformation of benzylamine to guanidine were beneficial for *S. aureus* TrmD affinity due to their protein−ligand interactions.

To evaluate the binding interactions and conformation of hit compound **8h**, we cocrystallized this compound with the *S. aureus* TrmD (Figure 8C, Figure S21A). The structure was solved at a resolution of 2.6 Å in the space group $P4_332$. The fold compared to the apo structure (PDB: 3KY7) had an overall RMSD(C_α) of 0.51 Å (Figure S21B), indicating minimal changes in the conformation after ligand binding. For the cocrystallized complex, electron density for **8h** was visible in the SAM-binding N-terminal domain (Figure S21). A comprehensive schematic of ligand-protein interactions for compound **2** and hit compound **8h** was generated with LigPlot + (Figure S22).[45] In the ligand-binding pocket, the pyrrolopyrimidone ring of **8h** occupies a subpocket analogous to the thienopyrimidone ring system of compound **2** (Figure 8C). In both compounds, the pyrimidone N^1 nitrogen formed hydrogen bonds to the backbone of Met149; in **8h**, it additionally formed a hydrogen bond to the Ser148 side-chain hydroxyl. The pyrimidone N^3 nitrogen formed hydrogen bonds to the backbone of Tyr152 in both compounds. Likewise, the pyrimidone carbonyl oxygen interacts with the backbone of Leu154 in each compound. Unique to **8h**, the pyrrole nitrogen atom was found to interact with a water molecule inside the binding pocket, and the guanidine group of **8h** displayed ionic interactions with the side chain of Glu132, analogous to the primary amine of **2**. However, the orientation of the guanidine group differs from that of the amine, extending slightly deeper into the binding pocket and forming additional polar interactions with the backbone of Glu132 and Tyr131, rationalizing the improved affinity and selectivity for *S. aureus* TrmD.

To gain further insights into the selectivity and binding mode of parent compound **2** and compounds **8b−e,h** for the TrmD isoenzymes used in this study, molecular docking was conducted using the Glide algorithm.[46] This analysis compared TrmD structures from *H. influenzae* (PDB: 4MCC), *E. coli* (PDB: 1P9P), and the *S. aureus* structure containing compound **8h** (PDB: 9SDW). Analysis of the docking scores (Table S3) was highly consistent with the ITC and FP assay results: parent compound **2** is predicted with higher binding affinity than compounds **8b−e,h** for *H. influenzae* and *E. coli* isoenzymes, while for *S. aureus* TrmD the triazole-containing

https://doi.org/10.1021/acs.jmedchem.5c02323
J. Med. Chem. 2025, 68, 26246−26262

8b−e,h is preferred over compound **2**. Comparing the predicted poses, in general for compounds **8b−e,h**, we found either ionic interactions between Glu132 and the basic moieties (guanidine and amine) of the inhibitor or hydrophobic interactions between the nonpolar aliphatic and aromatic proportions of the ligand with the binding pocket (Figure S24). The relative affinity differences between TrmD isoenzymes, aside from the scaffold exchange from thienopyrimidone to pyrrolopyrimidone, likely arise from linker-dependent differences in positioning (azide vs amide), which modulate interactions of the azide/amide moiety and the placement of azide-connected substituents within the pocket. This is reflected in both docking scores (Table S3) and predicted poses (Figure S24).

Notably, Tyr134 in *S. aureus* is positioned close to the substituents of the compounds; for example, the side chain oxygen lies only 5.2 Å from the guanidine group carbon of compound **8h**. As this residue is replaced by isoleucine in the *H. influenzae* and *E. coli* isoenzymes, selectivity might be enhanced by targeting this position. In addition, Cys104, which is not conserved in TrmD isoenzymes, is located near the ligands, and addressing this residue with a covalent warhead could further increase selectivity.[8]

CONCLUSION

In this work, we employed a nanoSAR triazole synthesis strategy coupled with a direct-to-biology FP read-out assay to develop affine and selective *S. aureus* TrmD inhibitors. This screening pipeline identified five hit compounds, which exhibited IC_{50}-values and K_D-values in the nanomolar to low micromolar range. In line with previous TrmD drug development campaigns, the identified inhibitors engage the adenine binding subpocket, and the substituents identified by nanoSAR screening expand toward the conserved acidic residue containing TrmD loop.[14,16,18−20] Ionic interactions with Glu132 (or orthologous residues) are a frequently identified interaction fingerprint of previous TrmD inhibitors.[14,16,18−20] Yet, the D2B optimization presented here was able to identify not only potent but also selective *S. aureus* TrmD inhibitors. Yet, during cellular screening, none of these initial inhibitors showed antibacterial activity against *S. aureus*, a property several disclosed TrmD inhibitors with diverse chemotypes share.[14,16,18−20] Surprisingly, one of the synthetic intermediates (**8f**, di-Cbz-masked form of **8h**) showed antimicrobial effects at low micromolar concentrations. We hypothesized that ligand permeability was preventing active inhibitors from engaging cytosolic TrmD target localization, an assumption that has been made in previous TrmD drug discovery campaigns.[14,16,18−20] In a prodrug-lysate assay, we observed that compound **8f** is indeed readily cleaved to form the active inhibitor **8h**, thereby confirming our hypothesis that **8f** might function as a prodrug of **8h**. This concept of Cbz-based prodrug might have broader applicability beyond the presented TrmD inhibitor type, both for other TrmD inhibitors incorporating amine/amidine chemotype and for a broader range of antibiotics.

Subsequently, X-ray crystallography of hit **8h** revealed its binding mode within the SAM-binding pocket of *S. aureus* TrmD, providing structural insights into key interactions. These findings will enable structure-guided optimization of this scaffold to further enhance both the affinity and selectivity of future inhibitors. In this regard, molecular modeling revealed two key targets for selectively increasing the affinity to *S. aureus* TrmD compared to other isoenzymes: Cys104 and Tyr134, which are located in close proximity to the bound ligand **8h** (PDB: 8SDW). These two residues are a unique feature of *S. aureus* TrmD and do not exist in most other TrmD isoenzymes; thus, it is conceivable that future campaigns could address these residues, for example, by covalent warheads.[8]

EXPERIMENTAL PROCEDURES

Protein Preparation and Purification. *Recombinant Expression of H. influenzae TrmD.* TrmD of *H. influenzae* was expressed as described previously.[31] In short, the pET28b(+) plasmid encoding for TrmD of *H. influenzae*, kindly provided by Se Won Suh (Addgene ID: 12665), was used to transform competent BL21 *E. coli* cells. The cells were grown in LB medium containing 50 μg/mL kanamycin at 37 °C and 160 rpm until they reached an OD_{600} of ∼0.7. After reducing the temperature to 16 °C, 0.5 mM isopropyl-β-D-1-thiogalactopyranoside (IPTG) was added to induce overexpression, which was maintained overnight. The cells were harvested by centrifugation and suspended in lysis buffer (20 mM HEPES pH 7.5, 300 mM NaCl, 0.5 mM TCEP, 5% glycerol, 0.1% polysorbate-20). Lysozyme and DNase I were added, and after a 30 min incubation on ice, the cells were lysed by sonication. Cell debris was removed by centrifugation. The supernatant was applied to a HisTrap HP column for affinity purification, pre-equilibrated in binding buffer (20 mM HEPES pH 7.5, 300 mM NaCl, 5 mM imidazole, 0.5 mM TCEP, 5% glycerol, 0.1% polysorbate-20) and washed with several column volumes of binding buffer. Afterward, the protein was eluted in elution buffer (20 mM HEPES pH 7.5, 300 mM NaCl, 500 mM imidazole, 0.5 mM TCEP, 5% glycerol, 0.1% polysorbate-20). Finally, *H. influenzae* TrmD was purified via size-exclusion chromatography (SEC), on a Superdex 16/600 75 pg SEC column equilibrated with SEC buffer (25 mM HEPES pH 7.5, 300 mM NaCl, 1 mM TCEP, 10% glycerol, 0.1% polysorbate-20). The enzyme was flash-frozen in liquid nitrogen and stored at −80 °C until further use.

Recombinant Expression of S. aureus TrmD. Expression and purification were performed similarly to *H. influenzae* TrmD, as described above. The pET28b(+) plasmid encoding for TrmD of *S. aureus*, kindly provided by Angelika Gründling, was used to transform competent BL21 *E. coli* cells. The cells were grown in LB medium containing 50 μg/mL kanamycin at 37 °C and 160 rpm until they reached an OD_{600} of ∼0.7. After reducing the temperature to 16 °C, 0.5 mM IPTG was added to induce overexpression, which was maintained overnight. The cells were harvested by centrifugation and suspended in lysis buffer (20 mM HEPES pH 7.5, 300 mM NaCl, 0.5 mM TCEP, 5% glycerol, 0.1% polysorbate-20). Lysozyme and DNase I were added, and after a 30 min incubation on ice, the cells were lysed by sonication. Cell debris was removed by centrifugation. The supernatant was applied to a HisTrap HP column for affinity purification, pre-equilibrated in binding buffer (20 mM HEPES pH 7.5, 300 mM NaCl, 5 mM imidazole, 0.5 mM TCEP, 5% glycerol, 0.1% polysorbate-20) and washed with several column volumes of binding buffer. Afterward, the protein was eluted in elution buffer (20 mM HEPES pH 7.5, 300 mM NaCl, 500 mM imidazole, 0.5 mM TCEP, 5% glycerol, 0.1% polysorbate-20). Finally, *S. aureus* TrmD was purified on a Superdex 16/600 75 pg SEC column equilibrated with SEC buffer (40 mM Tris pH 7.5, 100 mM NaCl, 10 mM $MgCl_2$, 5% Glycerol). The enzyme was flash-frozen in liquid nitrogen and stored at −80 °C until further use.

Recombinant Expression of E. coli TrmD. Bacterial strains carrying the expression pCA24N plasmid of *E. coli* TrmD were received from the Microbial Physiology Laboratory of the National Institute of Genetics in Japan (National BioResource Project). Expression and purification were performed as described in the original publication with slight adaptations.[47] The cells were grown in LB medium containing 30 μg/mL chloramphenicol at 37 °C and 160 rpm. After the cells reached an OD_{600} of ∼0.7, 1 mM IPTG was added to induce overexpression. After a 2 h incubation, the cells were harvested by centrifugation and suspended in binding buffer (50 mM sodium

https://doi.org/10.1021/acs.jmedchem.5c02323
J. Med. Chem. 2025, 68, 26246−26262

phosphate pH 7.5, 150 mM NaCl, 10 mM imidazole, 0.1% Tween 20). Lysozyme was added, and after a 30 min incubation on ice, the cells were lysed by sonication. Cell debris was removed by centrifugation. The supernatant was applied to a HisTrap HP column for affinity purification, pre-equilibrated in binding buffer, and washed with several column volumes of binding buffer. Afterward, the protein was eluted in elution buffer (50 mM sodium phosphate pH 7.5, 150 mM NaCl, 500 mM imidazole, 0.1% Tween 20). Finally, *E. coli* TrmD was mixed 1:5 with storage buffer (50 mM sodium phosphate pH 8.0, 300 mM NaCl, 2 mM DTT, 1 mM EDTA, 0.1% Tween 20, 60% Glycerol). The enzyme was flash-frozen in liquid nitrogen and stored at −20 °C until further use.

Recombinant Expression of Human Trm5. A pET-28a(+) plasmid encoding a truncated construct of Trm5 (aa 66−475), with flexible termini omitted, carrying the putative RNA and SAH binding sites, was used to transform competent *E. coli* Rosetta2 (DE3) cells. The cells were grown at 37 °C and 160 rpm in LB medium containing 50 μg/mL kanamycin and 25 μg/mL chloramphenicol. After reaching an OD_{600} of ∼0.7. The temperature was reduced to 18 °C. 0.2 mM IPTG was added to induce overexpression, and the cells were incubated overnight. After harvesting the bacteria by centrifugation, these were suspended in lysis buffer (50 mM Tris HCl, 500 mM sodium chloride, 1 mM β-mercaptoethanol, 0.5 mM PMSF, 5% glycerol, pH 7.5). A protease inhibitor tablet (cOmplete) was added, and the cells were lysed by sonication. After removing the cell debris by centrifugation, the supernatant was applied to a HisTrap FF column for affinity purification, pre-equilibrated in binding buffer (20 mM Tris HCl, 500 mM sodium chloride, 1 mM β-mercaptoethanol, 0.5 mM PMSF, 25 mM imidazole, 5% glycerol, pH 7.5). After washing the column with several column volumes of binding buffer, the protein was eluted in elution buffer (20 mM Tris HCl, 500 mM sodium chloride, 1 mM β-mercaptoethanol, 0.5 mM PMSF, 250 mM imidazole, 5% glycerol, pH 7.5). As a final purification step, Trm5 was purified on a Superdex 16/600 75 pg SEC column equilibrated with SEC buffer (20 mM HEPES, 250 mM sodium chloride, 10 mM β-mercaptoethanol, 10% glycerol, pH 7.5). The enzyme was flash-frozen in liquid nitrogen and stored at −80 °C until further use.

Fluorescence Polarization (FP) Assays. Fluorescence polarization (FP) assays were performed as follows. The assays for *H. influenzae* TrmD have been described previously.[31] All assays were conducted in technical triplicate using black 96-well half area plates. For the FP assays, a tracer (20 nM Cy5TPD[31] for *E. coli* and *H. influenzae* TrmD, 10 nM tracer **4** for *S. aureus* TrmD) was mixed with the respective enzyme (2 μM *E. coli* TrmD, 2 μM *H. influenzae* TrmD, 500 nM *S. aureus* TrmD) in buffer (*E. coli* and *H. influenzae* TrmD: 50 mM HEPES, 500 mM NaCl, 5% Glycerol, pH 7.5, *S. aureus* TrmD: 40 mM Tris HCl, 100 mM NaCl, 10 mM $MgCl_2$, 5% Glycerol, pH 7.5). The compounds were added in varying concentrations for K_D-value determination. For K_D-value determination of tracers, the enzyme concentration was varied, and no inhibitory compounds were added (DMSO < 0.5% for TrmDs). The Z-factor for tracer **4** was determined by measuring 48 replicates of the free tracer (positive controls, PC) and 48 replicates of a mixture of enzyme and tracer (negative controls, NC). The *Z*-factor is defined in terms of the means (μ) and standard deviations (σ) of the positive and negative controls and calculated as $Z = 1-(3*(\sigma_{nc} + \sigma_{pc})/(\mu_{nc}-\mu_{pc}))$. Fluorescence polarization was measured using a Spark 10 M plate reader (Tecan) equipped with polarization filters and a monochromator setup (λ_{ex} = 635 nm, λ_{em} = 680 nm). Polarization values (mP) were determined from polarization-specific parallel and orthogonal fluorescence intensities. K_D-values were calculated in GraphPad Prism 8.0.1 using the four-parameter Hill equation: y(% tracer bound) = bottom + ([ligand]slope) × (top−bottom)/([ligand]slope + $K_D$slope).

Aptamer-Based MTase Enzyme Inhibition Assay. For the determination of *S. aureus* TrmD IC_{50}-values, a split aptamer assay according to Nidoieva et al. was employed.[33] The assay was performed in 40 mM Tris HCl, 100 mM NaCl, 10 mM $MgCl_2$, 5% Glycerol, pH 7.5. Enzyme reaction mixtures contained synthetic $tRNA^{LeuCAG}$ substrate (synthetic $tRNA^{Leu}$: 5′-GCGAAGGUGGCGGAAUUGGUAGACGCGCUAGCUUCAGGUGUUAGUGUCCUUACGGACGUGGGGGUUCAAGUCCCCCCCCUCGCACCA-3′, Genscript, final concentration: 2 μM), *S. aureus* TrmD (final concentration: 100 nM), SAM (New England Biolabs, final concentration: 2 μM), and the test compounds in varying concentrations (3% DMSO, final volume 10 μL). Pure DMSO was used as a mock treatment reaction control. The assay was carried out in triplicate in black 384-well plates (Greiner). Enzyme reactions were quenched by the addition of 1 μL SDS (3%) after an incubation time of 60 min at room temperature. Subsequently, the aptamer detection mix described in Nidoieva et al. was added to the reactions, and samples were measured using a Tecan Spark 10 M plate reader equipped with a monochromator setup (λ_{ex} = 485 nm; λ_{em} = 600 nm) exported for statistical analysis and plotting in GraphPad Prism 8.0.1.

^{3}H-based MTase Enzyme Inhibition Assay. ^{3}H-based inhibition assays for TrmD *S. aureus* were performed in 50 mM HEPES, 5 mM $MgCl_2$, 80 mM NaCl, 0.005% Tween-20, 1 mM DTT, pH 7.5 buffer; and for Trm5[48] in 100 mM Tris-HCl, 0.1 mM EDTA, 6 mM $MgCl_2$, 100 mM KCl, 2 mM DTT, pH 7.4. The reaction mixture contained for *S. aureus* TrmD: 1 μM synthetic $tRNA^{Leu}$ (Genscript, see above) and 100 nM *S. aureus* TrmD; For human Trm5:10 μM synthetic $tRNA^{Leu}$ and 1.5 μM Trm5. Compounds were screened for *S. aureus* TrmD at 1 μM and for Trm5 at 30 μM. The enzymatic reactions were started by the addition of SAM as a mixture of ^{3}H-SAM (Hartmann Analytics, *S. aureus* TrmD: 0.5 μM, Trm5: 2 μM) and cold SAM (New England Biolabs, *S. aureus* TrmD: 0.5 μM, Trm5: 98 μM) to a final activity of 0.04 μCi μL^{-1} (TrmD) or 0.16 μCi μL^{-1} (Trm5). The reaction mixtures were incubated in duplicate for 60 min (TrmD)/30 min (Trm5) at 37 °C. As a negative control, the reaction mixture without the enzyme was used, and as a positive control, the reaction mixture without the test compound was used. After the enzyme incubation time, aliquots of 8 μL were taken from the reaction mixture and spotted on Whatman glass microfiber filters (GF/C, 25 mm). The tRNA was precipitated on the filters with 5% ice-cold TCA for 15 min. The filters were washed twice with 5% TCA at room temperature for 20 and 10 min, and once in EtOH for 10 min. After drying, the filters were transferred into scintillation vials with 3 mL of PerkinElmer Gold MV liquid scintillation cocktail. Scintillation was measured with a scintillation counter (TriCarb Liquid Scintillation Analyzer 4810TR; measurement time of 1 min).

Isothermal Titration Calorimetry (ITC). Experiments were conducted in the *S. aureus* TrmD SEC buffer (40 mM Tris, pH 7.5, 100 mM NaCl, 10 mM $MgCl_2$, 5% glycerol) for the *S. aureus* enzyme. The *H. influenzae* enzyme was buffer exchanged into its ITC buffer (50 mM HEPES, pH 7.5; 500 mM NaCl; 5% glycerol) using Amicon Ultra-15 centrifugal filter units (Merck) prior to use. Compound **1** (BLD Pharmatech) and compound **2** were dissolved in DMSO to a final concentration of 20.0 and 11.6 mM, respectively, and diluted in ITC buffer to give ligand solutions at 1 and 0.58 mM, respectively. Due to a low enthalpy signal, a low c-value titration was performed for compound **1**. In this type of experiment, the ligand is typically added at high concentration and in large excess relative to its binding partner, driving more binding events per injection. This causes the equivalence point to be reached after only a few injections and leads to the loss of the characteristic sigmoidal binding curve. TrmD was diluted to a final concentration of 50 μM, and DMSO was added to a final concentration of 5% to match the buffers. ITC measurements were performed using a MicroCal PEAQ-ITC Automated workstation (Malvern Panalytical) equipped with a 200 μL Hastelloy cell and a 40 μL injection syringe. The experiments were conducted in duplicates at 25 °C with a stirring speed of 750 rpm and a reference power of 42 μW. Each titration consisted of 19 injections of 2 μL compound solution, delivered into the cell containing 50 μM TrmD at 0.5 μL/s, with 150 s between injections. Control experiments were performed by titrating ligands into the ITC buffer. Data were analyzed and fitted using the MicroCal PEAQ-ITC Analysis Software 1.21 and plotted in GraphPad Prism 8.0.1.

Bacterial Growth Inhibition Assays. Compounds were dissolved in DMSO to a final concentration of 20 mM. To determine the compound's activity against different bacteria, a bacterial culture

https://doi.org/10.1021/acs.jmedchem.5c02323
J. Med. Chem. 2025, 68, 26246−26262

(*E. coli* ATCC10536, *S. aureus* RN4220) was set up to an optical density at 600 nm (OD_{600}) of 0.05 from an overnight culture in Mueller-Hinton broth (Carl Roth). The compound was added in different concentrations ranging from 400 μM to 1 μM. DMSO concentration was constantly adjusted to be 1% in the final culture. Cultures of 200 μL were incubated for 24 h at 37 °C in flat-bottom 96-well polystyrene culture plates (Greiner) using a BioTek Synergy H1 plate reader. Plates were incubated under constant shaking, and absorbance at 600 nm was measured every 20 min. The experiment was performed in three biological replicates with three technical replicates each. For the statistics, two-way ANOVA with Dunnett's multiple comparisons test was used because results were affected by two factors (time and compound concentration). As all results were compared to an untreated sample, Dunnett's test was used to correct for multiple comparisons using a confidence interval of 95%. Time points 360 min (6 h), 720 min (12 h), and 1440 min (24 h) were chosen and analyzed using GraphPad PRISM (10.4.2).

To determine the minimal bactericidal concentration of the substances, bacterial cultures were prepared as in the bacterial growth inhibition assay but incubated statically at 37 °C. A serial dilution of the initial culture was made and plated on a TSB agar plate to determine the CFU/mL of the original culture. After 24 h, the cultures were diluted again and plated. Bacterial colonies were counted, and the CFU/mL was calculated. The experiment was performed in n = 3 biological replicates. Data evaluation was done using GraphPad Prism. One-way ANOVA with Dunnett's multiple comparisons test was used for statistical analysis, and all samples were compared to the starting CFU/mL.

Cell Titer Glo Cell Viability Assay. Cell viability assays were conducted with HEK293 cells (ATCC) to investigate the compounds' mammalian cytotoxicity. Cells were cultured according to standard protocols (DMEM, 10% FBS, 1× Penicillin/Streptomycin, 37 °C, 5% CO_2). Cell viability was assessed using the Promega CellTiterGlo assay kit. Briefly, 1000 cells were seeded in white half a rea 96-well plates (Greiner) and incubated for 48 h with inhibitors from DMSO stocks (final: 0.1% DMSO) under standard cultivation conditions. Then, the cell titer reagent was added to each well according to the manufacturer's protocols, and luminescence was measured using a Tecan Spark 10 M plate reader.

Bacterial Lysate Carbamate Cleavage Assays. An overnight culture of *S. aureus* RN4220 was set up in TSB medium (BD Bacto Tryptic Soy Broth). The next day, a 150 mL day culture was started at an initial OD_{600} of 0.1. The culture was incubated at 200 rpm shaking at 37 °C. The bacteria were harvested after 3 h and 40 min (OD_{600} = 3.30). A 1 mL aliquot was retained to determine cell number. 150 mL of the culture was centrifuged at 4000 rpm for 10 min at 4 °C. The resulting pellet was resuspended in 10 mL of JB Lysis Buffer (0.1% Triton X-100, 20 mM Tris-HCl, 150 mM KCl, 1 mM $MgCl_2$, 1 mM DTT, and protease inhibitors) and transferred to FastPrep tubes. Cells were mechanically lysed (2 × 30 s, 6.5 m/s) and cooled for 5 min on ice. The samples were centrifuged, and the supernatant was transferred to a new tube. Subsequently, it was centrifuged again at 5000 rpm for 30 min at 4 °C. The pellet was washed three times with 1× PBS, reducing the volume to 1 mL. Protein concentration was determined using the Pierce BCA Protein Assay Kit (Thermo Scientific). The final sample was frozen in liquid nitrogen and stored at −80 °C. 100 μL of this lysate was incubated with **8f−h** (final concentration 400 μM, 2% DMSO) for 16 h at 30 °C. Afterward, 100 μL acetonitrile was added, and the samples were passed through a syringe filter. Ten μL of the samples were injected during LC/MS (Agilent 1100 system, LC/MSD trap) using an Agilent Poroshell 120 EC-C18 150 × 2.10 mm 4 μm column; mobile phase (gradient: acetonitrile/H_2O, 0.1% formic acid). The LC/MS chromatograms and their corresponding mass spectra (base-peak) were analyzed using MestReNova (12.0.4) for prodrug deprotection products.

***S. aureus* Inhibitor Uptake Assay.** An overnight culture of *S. aureus* RN4220 was set up in Müller-Hinton medium. The next day, a 100 mL day culture with 4 μM of compound (**8f**, **8g**, **8h**, or DMSO) was started at an initial OD_{600} of 0.05. The culture was incubated at 200 rpm shaking at 37 °C. The total bacterial culture was harvested after reaching an OD_{600} of 0.3 by centrifugation at 4,000 rpm for 10 min at 4 °C. The resulting pellet was washed twice with 1× PBS, then resuspended in 1 mL of JB Lysis Buffer (0.1% Triton X-100, 20 mM Tris-HCl, 150 mM KCl, 1 mM $MgCl_2$, 1 mM DTT, and protease inhibitors) and transferred to Lysis matrix E tubes. Cells were mechanically lysed by Fast prep (2 × 30 s, 6.5 m/s) and cooled for 5 min on ice. The samples were centrifuged, and the supernatants were transferred to a new tube. Subsequently, they were centrifuged again at 5000 rpm for 30 min at 4 °C. The resulting pellet was washed twice with 1× PBS, reducing the volume to 100 μL, while the resulting supernatant was cleared once more by centrifugation. The samples were frozen in liquid nitrogen and stored at −80 °C. The prepared lysates were loaded on a solid-phase extraction cartridge (C18 Chromabond, Macherey-Nagel) and eluted with 30% ACN in water (1 mL). The collected eluate was lyophilized and resolved in 100 μL ACN/water. 10 μL of the samples were injected during LC/MS (Waters Alliance 2695 coupled to a Waters QDa mass-sensitive detector) using an Agilent Poroshell 120 EC-C18 150 × 2.10 mm 4 μm column; mobile phase (gradient: acetonitrile/H_2O, 0.1% formic acid). The LC/MS chromatograms and their corresponding mass spectra (base-peak) were analyzed using MestReNova (12.0.4) for prodrug deprotection products.

Crystallization, Data Collection, Model Building, and Refinement. Co-crystals of the *S. aureus* TrmD protein and compounds **2** or **8h** were obtained at 20 °C with a hanging drop setup. The protein (271 μM) was incubated with compounds in 7-fold molar excess (2 mM final concentration) for 30 min on ice before crystallization. The reservoir solution contained 1.4 M Na Malonate pH 7.4, 0.1 M Bis-Tris Propane.[42] Crystallization drops consisted of 1 μL reservoir solution and 1 μL of the preincubated protein and compound. Cubic crystals grew within 2 weeks. Crystals were frozen in liquid nitrogen using 25% glycerol as the cryo-protectant. Diffraction data were collected at the Diamond Light Source Beamline I03 (Oxfordshire, U.K.). All data sets were processed with XDS[49] and scaled with AIMLESS within the CCP4[50] cloud.[50−52] The resulting data sets had a maximum resolution of 2.50 Å (Structure with compound **2**) or 2.60 Å (Structure with compound **8h**). The crystals belong to space group $P4_332$ with one TrmD molecule per asymmetric unit. The structures were solved by molecular replacement with PHASER using Apo-TrmD (PDB: 3KY7) as the search model.[53,54] The compounds were parametrized from SMILES using phenix.elbow.[55] Model building and refinement were performed with Coot, Refmac, and phenix.refine.[50,56−58] The quality of the resulting structural models was assessed using MolProbity.[59,60] Due to the high flexibility of the loop between amino acids Val175 and Ser188, this region was not modeled. Additionally, some amino acids with flexible side chains and insufficient electron density to fit the side chain were truncated to alanine residues. In the structure with compound **2**, residues Leu35, Asn36, Lys41, Arg42, Gln44, Lys48, Gln50, Lys63, Glu90, Glu193, and Lys204 were truncated. In the structure with compound **8h**, residues Asn36, Lys41, Arg42, Lys48, and His64 were truncated. The crystallographic data are summarized in Tables S1 and S2. Coordinates and structure factors are deposited at the Protein Data Bank (PDB) under accession codes: 9SDV and 9SDW.

Molecular Modeling. For molecular docking of compounds **2** and **8b−e,h**, a Glide docking protocol was conducted within the Schrödinger Maestro 2020.04 worksuite.[46] The protein structures 4MCC (*H. influenzae* TrmD) and 1P9P (*E. coli* TrmD) were downloaded from the PDB, and 9SDW was used for docking into the *S. aureus* isoenzyme. Receptor preparation was performed with the automated binding site, protonation, and energy minimization routine within Maestro "Protein preparation" and "Receptor grid generation". Energy minimization of ligands was conducted using the "LigPrep" routine. The docking protocol was performed under default parameters with standard precision settings. Ligand binding poses were visualized using PyMol.

General Synthesis Procedures. All reagents and solvents were of analytical grade quality and purchased from standard commercial suppliers. Chemicals were used without further purification unless

https://doi.org/10.1021/acs.jmedchem.5c02323
J. Med. Chem. 2025, 68, 26246−26262

otherwise noted. ^{1}H and ^{13}C spectra were recorded on Bruker Fourier 300 MHz, Bruker Avance Neo 400 MHz, and Bruker Avance III 600 MHz spectrometers. Chemical shifts δ are given in parts per million (ppm) using residual proton peaks of the solvent as the internal standard. HPLC and mass spectra were obtained by LC/MS, consisting of an 1100 series HPLC system from Agilent with an Agilent Poroshell 120 EC-C18 150 × 2.10 mm, 4 μm column. The detection wavelengths were dependent on the specific compound absorbance characteristics: 210 and 254 nm. The MTase tracers (**3** and **4**) were analyzed for their purity at 650 nm (Cy5). The molecular mass of all compounds and intermediates was analyzed by an Agilent 1100 series LC/MSD trap with electron spray ionization (ESI) in positive mode. Preparative column chromatography was performed with silica gel (0.06−0.02 mm) obtained from Macherey-Nagel or prepacked Biotage reverse-phase silica columns for flash chromatography (Biotage Isolera One) eluting with ACN/H_2O. Preparative HPLC was performed on an Agilent 1290 system with an MZ-Aqua Perfect C18 7 μm column. All compounds are >95% pure by HPLC analysis.

Protocol for the Nanomole-Scale Synthesis. A commercial azide diversity library (Enamine) containing 320 azides at a concentration of 100 mM in DMSO in a 96-well tube rack was employed for this nanoSAR study. For the reaction of the azides with alkyne **7** via CuAAC, a master mix was prepared. The master mix contained for one 96-well plate: 600 μL of a 33.33 mM sodium ascorbate solution dissolved in Milli-Q water, 200 μL of a 12.52 mM TBTA solution dissolved in DMSO, 500 μL of a 20 mM alkyne **7** solution dissolved in DMSO, 600 μL of a 4.81 mM $CuSO_4$×5 H_2O solution dissolved in Milli-Q water and 400 μL of pure DMSO. The solvents were degassed with argon to avoid oxidation of the copper(I) during the reaction. To each well of a 96-well PCR plate (Applied Biosystems MicroAmp) were added 23 μL of the master mix and 1 μL of the 100 mM azide stock. The final concentrations in the Mastermix were: 8.7 mM sodium ascorbate (8.3 mM in reaction well), 1.1 mM TBTA (1.0 mM in reaction well), 4.3 mM **7** (4.1 mM in reaction well), 1.3 mM $CuSO_4$×5 H_2O (1.2 mM in reaction well). The 96-well PCR plate was purged with argon, and the implementation of the experiments was conducted under an argon atmosphere. The reactions were mixed, centrifuged, and sealed airtight. The plate was allowed to incubate at room temperature for 16 h before the formed triazoles were investigated via FP-assays.

General Procedure for Preparative CuAAC. Compound **7** (2−5 mg, 0.013−0.031 mmol, 1.0 equiv), the respective azide (0.015−0.037 mmol, 1.2 equiv), TBTA (2−5 mg, 0.004−0.009 mmol, 0.3 equiv), copper(II)sulfate pentahydrate (1−2 mg, 0.004−0.009 mmol, 0.3 equiv), and sodium ascorbate (5−12 mg, 0.026−0.062 mmol, 2.0 equiv) were dissolved in water (500 μL) and DMSO (1.0 mL). The reaction was stirred for 16 h at room temperature under an argon atmosphere before the solvents were removed *in vacuo*. Afterward, the crude product was purified via reverse-phase flash chromatography.

*Compound **2**: N-(4-(Aminomethyl)benzyl)-4-oxo-3,4-dihydrothieno[2,3-d]pyrimidine-5-carboxamide.* 4-Oxo-3,4-dihydrothieno[2,3-*d*]pyrimidine-5-carboxylic acid (22 mg, 0.110 mmol, 1.0 equiv) and *tert*-butyl (4-(aminomethyl)benzyl)carbamate (26 mg, 0.110 mmol, 1.0 equiv) were mixed with HATU (42 mg, 0.110 mmol, 1.0 equiv) and DIPEA (60 μL, 0.343 mol, 3.0 equiv) in 4 mL anhydrous DMF. The mixture was stirred for 16 h at room temperature before the organic solvent was removed *in vacuo*. The residue was dissolved in DCM (1 mL) and TFA (1 mL) and stirred for 30 min at room temperature. The crude product was purified via flash chromatography. Yield: 17 mg, quant. ^{1}H NMR (300 MHz, MeOD) δ [ppm] = 8.40 (s, 1H), 8.18 (s, 1H), 7.52−7.43 (m, 4H), 4.66 (d, J = 2.3 Hz, 2H), 4.13 (s, 2H). ^{13}C NMR (75 MHz, MeOD) δ [ppm] = 168.9, 163.1, 161.2, 146.7, 141.0, 133.4, 132.8, 130.2, 129.4, 121.0, 44.1. LC/MS: m/z calculated for $C_{15}H_{14}N_4O_2S$ $[M + H]^+$: 315.1, found: 315.0.

*Compound **3**: 3,3-Dimethyl-1-(6-oxo-6-((3-(5-((4-oxo-3,4-dihydrothieno[2,3-d]pyrimidine-5-carboxamido)methyl)-1H-1,2,3-triazol-1-yl)propyl)amino)hexyl)-2-((1E,3E)-5-((E)-1,3,3-trimethylindolin-2-ylidene)penta-1,3-dien-1-yl)-3H-indol-1-ium trifluoroacetate.* The compound was synthesized according to the general procedure for preparative click reactions with alkyne **10** (0.63 mg, 0.0027 mmol, 1.5 equiv) and Cy5-azide (1.1 mg, 0.0018 mmol, 1.0 equiv). Yield: 1.5 mg, quant. LC/MS: m/z calculated for $C_{45}H_{52}N_9O_3S^+$ $[M + H]^{2+}$: 399.7, found: 399.6. Purity (HPLC): 98%.

*Compound **4**: 3,3-Dimethyl-1-(6-oxo-6-((3-(4-(4-oxo-4,7-dihydro-3H-pyrrolo[2,3-d]pyrimidin-5-yl)-1H-1,2,3-triazol-1-yl)propyl)amino)hexyl)-2-((1E,3E)-5-((E)-1,3,3-trimethylindolin-2-ylidene)penta-1,3-dien-1-yl)-3H-indol-1-ium trifluoroacetate.* The compound was synthesized according to the general procedure for preparative click reactions with alkyne **7** (0.19 mg, 0.0016 mmol, 1.3 equiv) and Cy5-azide (0.7 mg, 0.0012 mmol, 1.0 equiv). LC/MS: m/z calculated for $C_{43}H_{50}N_9O_2^+$ $[M + H]^{2+}$: 362.7, found: 362.7. Purity (HPLC): 97%.

*Compound **6**: 5-((Trimethylsilyl)ethynyl)-3,7-dihydro-4H-pyrrolo[2,3-d]pyrimidin-4-one.* To a minimum volume flask was added 5-iodo-3,7-dihydro-4*H*-pyrrolo[2,3-*d*]pyrimidin-4-one (232 mg, 0.890 mmol, 1.0 equiv), CuI (34 mg, 0.178 mmol, 0.2 equiv), TMS-acetylene (190 μL, 1.832 mmol, 2.0 equiv), $Pd(PPh_3)_4$ (54 mg, 0.046 mmol, 0.05 equiv), THF (5.0 mL), DMF (2.0 mL), and triethylamine (70 μL). The reaction was stirred for 16 h at room temperature. Subsequently, the solvent was removed *in vacuo*, and the residue was dissolved in DCM (10 mL). The solution was washed with water (3 × 10 mL), and the solvent was removed. The crude product was purified via reverse-phase flash chromatography. Yield: 60 mg, 29%. ^{1}H NMR (300 MHz, DMSO-d_6) δ [ppm] = 12.17 (s, 1H), 11.86 (s, 1H), 7.84 (s, 1H), 7.39 (d, J = 2.6 Hz, 1H), 0.20 (s, 9H). ^{13}C NMR (75 MHz, DMSO) δ [ppm] = 157.5, 147.8, 144.6, 126.4, 107.2, 99.9, 98.4, 93.6, 0.1. LC/MS: m/z calculated for $C_{11}H_{13}N_3OSi$ $[M + H]^+$: 232.1, found: 231.8.

*Compound **7**: 5-Ethynyl-3,7-dihydro-4H-pyrrolo[2,3-d]-pyrimidin-4-one.* Intermediate **6** (30 mg, 0.129 mmol, 1.0 equiv) was dissolved under an argon atmosphere in anhydrous acetonitrile (5.0 mL). Subsequently, TBAF (1 M in THF, 261 μL, 0.261 mmol, 2.0 equiv) was added dropwise at 0 °C. The reaction was stirred for 1.5 h at room temperature before it was terminated by the addition of 2.0 mL of saturated ammonium chloride solution. The solution was lyophilized, and the crude product was purified via reverse-phase flash chromatography. Yield: 14 mg, 68%. ^{1}H NMR (300 MHz, DMSO-d_6) δ [ppm] = 7.85 (s, 1H), 7.38 (s, 1H), 3.90 (s, 1H). ^{13}C NMR (75 MHz, DMSO) δ [ppm] = 157.7, 147.8, 144.6, 126.1, 107.4, 97.7, 80.6, 77.9. LC/MS: m/z calculated for $C_8H_5N_3O$ $[M + H]^+$: 160.0, found: 159.9.

*Compound **8a**: N-(3-(4-(4-Oxo-4,7-dihydro-3H-pyrrolo[2,3-d]-pyrimidin-5-yl)-1H-1,2,3-triazol-1-yl)propyl)acetamide.* The compound was synthesized according to the general procedure for *in situ* click reactions and to general procedure for preparative click reactions with alkyne **7** and azide **15**. Yield (preparative): 2.0 mg, 51%. LC/MS: m/z calculated for $C_{13}H_{15}N_7O_2$ $[M + H]^+$: 302.1, found: 302.0.

*Compound **8b**: 3-((4-(4-Oxo-4,7-dihydro-3H-pyrrolo[2,3-d]-pyrimidin-5-yl)-1H-1,2,3-triazol-1-yl)methyl)benzonitrile.* The compound was synthesized according to the general procedure for preparative click reactions with alkyne **7** and commercially available 3-(azidomethyl)benzonitrile. Yield: 2.5 mg, 25%. ^{1}H NMR (400 MHz, DMSO-d_6) δ [ppm] = 8.76 (s, 1H), 7.84 (d, J = 15.0 Hz, 3H), 7.67−7.53 (m, 3H), 5.75 (s, 2H). ^{13}C NMR (101 MHz, DMSO) δ [ppm] = 143.9, 138.0, 132.8, 131.9, 131.5, 130.1, 122.9, 118.5, 118.1, 117.3, 111.7, 109.5, 104.1, 51.7. LC/MS: m/z calculated for $C_{16}H_{11}N_7O$ $[M + H]^+$: 318.1, found: 317.9. Purity (HPLC): 96%.

*Compound **8c**: 5-(1-((8,8-Difluorobicyclo[5.1.0]octan-4-yl)-methyl)-1H-1,2,3-triazol-4-yl)-3,7-dihydro-4H-pyrrolo[2,3-d]-pyrimidin-4-one.* The compound was synthesized according to the general procedure for preparative click reactions with alkyne **7** and commercially available 4-(azidomethyl)-8,8-difluorobicyclo[5.1.0]-octane. Yield: 3 mg, 28%. ^{1}H NMR (400 MHz, DMSO-d_6) δ [ppm] = 8.64 (t, J = 4.1 Hz, 1H), 7.86 (s, 1H), 7.52 (d, J = 3.0 Hz, 1H), 4.39 (d, J = 8.0 Hz, 2H), 1.96−1.41 (m, 9H), 1.21 (q, J = 13.4, 12.1 Hz, 3H). ^{13}C NMR (101 MHz, DMSO) δ [ppm] = 158.8, 148.7, 143.9, 123.1, 117.1, 109.7, 104.1, 55.4, 50.8, 44.0, 37.1, 32.0, 29.3,

https://doi.org/10.1021/acs.jmedchem.5c02323
J. Med. Chem. 2025, 68, 26246−26262

25.1, 25.0, 24.9, 20.4, 16.7. LC/MS: m/z calculated for $C_{17}H_{18}F_2N_6O$ $[M + H]^+$: 361.2, found: 361.1. Purity (HPLC): 100%.

Compound ***8d****: 5-(1-(Quinolin-6-ylmethyl)-1H-1,2,3-triazol-4-yl)-3,7-dihydro-4H-pyrrolo[2,3-d]pyrimidin-4-one.* The compound was synthesized according to the general procedure for preparative click reactions with alkyne **7** and commercially available 6-(azidomethyl)-quinoline. Yield: 6 mg, 56%. ^{1}H NMR (400 MHz, DMSO-d_6) δ [ppm] = 8.93−8.81 (m, 1H), 8.58 (t, J = 7.2 Hz, 1H), 8.26−7.49 (m, 6H), 5.92 (s, 2H). ^{13}C NMR (101 MHz, DMSO) δ [ppm] = 148.5, 143.9, 137.7, 135.2, 130.0, 129.9, 127.1, 126.9, 117.2, 117.0, 109.6, 52.3, 52.2. LC/MS: m/z calculated for $C_{18}H_{13}N_7O$ $[M + H]^+$: 344.2, found:344.0. Purity (HPLC): 99%.

Compound ***8e****: 5-(1-(((1R,2R)-2-Aminocyclopentyl)methyl)-1H-1,2,3-triazol-4-yl)-3,7-dihydro-4H-pyrrolo[2,3-d]pyrimidin-4-one.* The compound was synthesized according to the general procedure for preparative click reactions with alkyne **7** and commercially available (1*R*,2*R*)-2-(azidomethyl)cyclopentan-1-amine. Yield: 6 mg, 64%. ^{1}H NMR (400 MHz, DMSO-d_6) δ [ppm] = 8.73 (s, 1H), 7.98 (s, 2H), 7.87 (d, J = 3.5 Hz, 1H), 7.56−7.52 (m, 1H), 4.57 (dd, J = 13.7, 5.7 Hz, 1H), 4.41 (dd, J = 13.7, 9.8 Hz, 1H), 3.70−3.66 (m, 1H), 2.61 (dq, J = 13.0, 6.7 Hz, 1H), 2.02 (dh, J = 13.1, 6.1 Hz, 1H), 1.86−1.67 (m, 2H), 1.64−1.46 (m, 3H). ^{13}C NMR (101 MHz, DMSO) δ [ppm] = 158.8, 148.8, 144.0, 122.8, 117.2, 109.6, 104.1, 52.9, 48.6, 42.7, 30.0, 26.6, 20.9. LC/MS: m/z calculated for $C_{14}H_{17}N_7O$ $[M + H]^+$: 300.2, found: 300.1. Purity (HPLC): 96%.

Compound ***8f****: Di-Cbz-1-(3-(4-(4-oxo-4,7-dihydro-3H-pyrrolo-[2,3-d]pyrimidin-5-yl)-1H-1,2,3-triazol-1-yl)propyl)guanidine.* The compound was synthesized according to the general procedure for preparative click reactions with alkyne **7** and azide **13**. Yield: 4 mg, 29%. ^{1}H NMR (400 MHz, DMSO-d_6) δ [ppm] = 8.68 (s, 1H), 8.62 (t, J = 5.7 Hz, 1H), 7.85 (s, 1H), 7.54−7.52 (m, 1H), 7.38 (dd, J = 8.4, 3.5 Hz, 6H), 7.31 (d, J = 3.1 Hz, 4H), 5.19 (s, 2H), 5.00 (s, 2H), 4.59 (t, J = 5.9 Hz, 2H), 3.81 (q, J = 5.8 Hz, 2H). ^{13}C NMR (101 MHz, DMSO) δ [ppm] = 162.9, 158.8, 155.4, 152.4, 148.7, 143.9, 141.3, 136.8, 135.1, 128.6, 128.5, 128.4, 128.3, 128.0, 127.8, 123.0, 117.1, 109.8, 104.2, 67.7, 66.5, 48.1, 40.8. LC/MS: m/z calculated for $C_{27}H_{25}N_9O_5$ $[M + H]^+$: 556.2, found: 556.0. Purity (HPLC): 98%.

Compound ***8g****: Di-Boc-1-(3-(4-(4-oxo-4,7-dihydro-3H-pyrrolo-[2,3-d]pyrimidin-5-yl)-1H-1,2,3-triazol-1-yl)propyl)guanidine.* The compound was synthesized according to the general procedure for preparative click reactions with alkyne **7** and azide **14**. Yield: 9 mg, 74%. ^{1}H NMR (400 MHz, DMSO-d_6) δ [ppm] = 8.68 (s, 1H), 8.49 (t, J = 5.7 Hz, 1H), 7.85 (d, J = 3.3 Hz, 1H), 7.52 (d, J = 2.4 Hz, 1H), 4.58 (t, J = 5.9 Hz, 2H), 3.76 (q, J = 5.9 Hz, 2H), 1.45 (s, 9H), 1.36 (s, 9H). ^{13}C NMR (101 MHz, DMSO) δ [ppm] = 163.0, 158.8, 155.5, 151.7, 148.7, 143.9, 141.2, 123.0, 117.0, 109.8, 104.2, 82.9, 78.3, 48.2, 27.9, 27.6. LC/MS: m/z calculated for $C_{21}H_{29}N_9O_5$ $[M + H]^+$: 488.2, found: 488.0. Purity (HPLC): 96%.

Compound ***8h****: 1-(3-(4-(4-Oxo-4,7-dihydro-3H-pyrrolo[2,3-d]-pyrimidin-5-yl)-1H-1,2,3-triazol-1-yl)propyl)guanidine.* The compound was synthesized according to the general procedure for preparative click reactions with azide **14**. Subsequently, DCM (0.5 mL) and TFA (0.5 mL) were added to the residues, and the mixture was stirred for 30 min at room temperature. Afterward, the solvents were removed *in vacuo*, and the crude product was purified via reverse-phase flash chromatography. Yield: 3 mg, 32%. ^{1}H NMR (400 MHz, DMSO-d_6) δ [ppm] = 12.14 (s, 1H), 11.93 (d, J = 3.8 Hz, 1H), 8.73 (s, 1H), 7.87 (d, J = 3.2 Hz, 1H), 7.54 (m, 1H), 4.54 (t, J = 6.0 Hz, 2H), 3.69−3.63 (m, 2H), 2.54 (s, 1H), 1.39−1.16 (m, 2H). ^{13}C NMR (101 MHz, DMSO) δ [ppm] = 158.8, 156.9, 156.8, 148.8, 143.9, 141.3, 123.0, 117.2, 109.6, 104.1, 48.3, 40.8. LC/MS: m/z calculated for $C_{11}H_{13}N_9O$ $[M + H]^+$: 288.1, found: 288.0. Purity (HPLC): 98%.

Compound ***10****: 4-Oxo-N-(prop-2-yn-1-yl)-3,4-dihydrothieno[2,3-d]pyrimidine-5-carboxamide.* 4-Oxo-3,4-dihydrothieno[2,3-*d*]-pyrimidine-5-carboxylic acid (12 mg, 0.061 mmol, 1.0 equiv), DIPEA (43 μL, 0.244 mmol, 4.0 equiv), and HATU (23 mg, 0.061 mmol, 1.0 equiv) were dissolved in 3 mL anhydrous DCM. The mixture was stirred for 15 min at room temperature before propargylamine (5 μL, 0.073 mmol, 1.2 equiv) was added in one portion. The reaction was stirred for 16 h at room temperature. The reaction mixture was washed with a saturated sodium bicarbonate solution and 1 M HCl. The crude reaction mixture was purified via reverse-phase flash chromatography. Yield: 11 mg, 77%. ^{1}H NMR (300 MHz, DMSO-d_6) δ [ppm] = 8.39 (s, 1H), 8.29 (s, 1H), 4.13 (dd, J = 5.1, 2.5 Hz, 2H), 3.17 (t, J = 2.5 Hz, 1H). ^{13}C NMR (75 MHz, DMSO) δ [ppm] = 167.1, 159.9, 159.6, 146.0, 131.8, 131.6, 119.2, 80.6, 73.5, 28.5. LC/MS: m/z calculated for $C_{10}H_7N_3O_2S$ $[M + H]^+$: 234.0, found: 233.9.

Compound ***12****: 2-Azidoethan-1-amine.* 2-Chloroethylamine hydrochloride (100 mg, 0.862 mmol, 1.0 equiv) was dissolved in water (5.0 mL). Sodium azide (168 mg, 2.586 mmol, 3.0 equiv) was added, and the reaction was allowed to stir for 12 h at 90 °C. Subsequently, a 15% potassium hydroxide solution (8.0 mL) was added, and the product was extracted with diethyl ether. The organic solvent was removed *in vacuo*. Yield: 85 mg, quant. ^{1}H NMR (300 MHz, $CDCl_3$) δ [ppm] = 3.36 (t, J = 5.7 Hz, 2H), 2.87 (t, J = 5.7 Hz, 2H), 1.51 (s, 2H). ^{13}C NMR (75 MHz, $CDCl_3$) δ [ppm] = 77.5, 77.1, 76.6, 54.6, 53.5, 41.4.

Compound ***13****: Benzyl N-[(1Z)-[(2-azidoethyl)amino]-({[(benzyloxy)carbonyl]amino}) methylidene]carbamate.* *N,N′*-Di-Cbz-1*H*-pyrazol-1-carbamidine (380 mg, 1.005 mmol, 1.0 equiv) was dissolved in THF (2.0 mL), and **12** (185 mg, 2.150 mmol, 2.2 equiv) in THF (2.0 mL) was added dropwise. One drop of triethylamine was added, and the reaction was allowed to stir for 16 h at room temperature. The solvent was removed *in vacuo*, and the crude product was purified via reverse-phase flash chromatography. Yield: 357 mg, 90%. ^{1}H NMR (300 MHz, $CDCl_3$) δ [ppm] = 8.54 (s, 1H), 7.34−7.14 (m, 10H), 5.06 (d, J = 11.0 Hz, 5H), 3.43 (dt, J = 33.8, 5.2 Hz, 4H). ^{13}C NMR (75 MHz, $CDCl_3$) δ [ppm] = 163.0, 156.0, 153.6, 136.4, 134.4, 128.8, 128.6, 128.42, 128.35, 128.1, 128.0, 68.3, 67.3, 50.1, 40.3. LC/MS: m/z calculated for $C_{19}H_{20}N_6O_4$ $[M + H]^+$: 397.2, found: 397.1.

Compound ***14****: [N,N′-Bis(tert-butoxycarbonyl)-N″-2-azidoethyl]-guanidine.* *N,N′*-Di-Boc-1*H*-pyrazol-1-carbamidine (310 mg, 1.005 mmol, 1.0 equiv) was dissolved in THF (2.0 mL), and **12** (85 mg, 1.000 mmol, 1.0 equiv) in THF (1.0 mL) was added dropwise. One drop of triethylamine was added, and the reaction was allowed to stir for 72 h at room temperature. The solvent was removed *in vacuo*, and the crude product was purified via reverse-phase flash chromatography. Yield: 153 mg, 47%. ^{1}H NMR (300 MHz, DMSO-d_6) δ [ppm] = 3.49 (s, 4H), 3.37 (s, 2H), 1.48 (d, J = 3.9 Hz, 9H), 1.39 (s, 9H). ^{13}C NMR (75 MHz, DMSO) δ [ppm] = 83.1, 78.3, 49.4, 28.0, 27.6. LC/MS: m/z calculated for $C_{13}H_{24}N_6O_4$ $[M + H]^+$: 329.2, found: 329.0.

Compound ***15****: N-(3-Azidopropyl)acetamide.* 3-Azidopropan-1-amine (20 mg, 0.200 mmol, 1.0 equiv), acetic anhydride (30 mg, 0.249 mmol, 1.5 equiv), and acetic acid (40 μL) were mixed at room temperature. The reaction was left to stand for 3 min, then 1.0 mL acetonitrile was added, and the mixture was lyophilized. Yield: 22 mg, 77%. ^{1}H NMR (300 MHz, $CDCl_3$) δ [ppm] = 3.32 (dt, J = 16.9, 6.6 Hz, 4H), 1.96 (s, 3H), 1.77 (p, J = 6.7 Hz, 2H). ^{13}C NMR (75 MHz, $CDCl_3$) δ [ppm] = 170.6, 49.4, 37.3, 28.8, 23.3. LC/MS: m/z calculated for $C_5H_{10}N_4O$ $[M + H]^+$: 143.1, found: 143.0.

■ ASSOCIATED CONTENT

Supporting Information

The Supporting Information is available free of charge at https://pubs.acs.org/doi/10.1021/acs.jmedchem.5c02323.

Supplementary results, NMR, and LC/MS spectra (PDF)

Supplementary Data set including azide library decoding and SMILES strings (XLSX)

Molecular formula strings and associated biochemical and biological data (CSV)

https://doi.org/10.1021/acs.jmedchem.5c02323
J. Med. Chem. 2025, 68, 26246−26262

Accession Codes

PDB ID Code: Coordinates and structure factors have been deposited at the PDB with PDB codes: 9SDV and 9SDW. The authors will release the atomic coordinates upon article publication.

AUTHOR INFORMATION

Corresponding Author

Fabian Barthels − *Institute of Pharmaceutical and Biomedical Sciences, Johannes Gutenberg-University, 55128 Mainz, Germany*; orcid.org/0000-0001-7950-2158; Email: barthels@uni-mainz.de

Authors

Ariane F. Hübner − *Institute of Pharmaceutical and Biomedical Sciences, Johannes Gutenberg-University, 55128 Mainz, Germany*

Annabelle C. Weldert − *Institute of Pharmaceutical and Biomedical Sciences, Johannes Gutenberg-University, 55128 Mainz, Germany*; orcid.org/0009-0001-5016-0286

Tessa Marciniak − *Institute of Molecular Infection Biology, University of Würzburg, 97080 Würzburg, Germany*

Florian Hof − *Institute of Molecular Physiology, Johannes Gutenberg-University, 55128 Mainz, Germany*; orcid.org/0000-0002-6438-1784

Vivien S. Beck − *Institute of Molecular Infection Biology, University of Würzburg, 97080 Würzburg, Germany*

Samuel Carien − *Institute of Molecular Infection Biology, University of Würzburg, 97080 Würzburg, Germany*

Sophie N. Mulartschyk − *Institute of Pharmaceutical and Biomedical Sciences, Johannes Gutenberg-University, 55128 Mainz, Germany*

Eva Wolf − *Institute of Molecular Physiology, Johannes Gutenberg-University, 55128 Mainz, Germany*

Wilma Ziebuhr − *Institute of Molecular Infection Biology, University of Würzburg, 97080 Würzburg, Germany*

Complete contact information is available at: https://pubs.acs.org/10.1021/acs.jmedchem.5c02323

Author Contributions

‖The authors A.F.H. and A.C.W. contributed equally. The manuscript was written through the contributions of all authors. All authors have approved the final version of the manuscript.

Notes

The authors declare no competing financial interest.

ACKNOWLEDGMENTS

We would like to thank Angelika Gründling (Imperial College London, United Kingdom) for the gift of the *S. aureus* TrmD expression plasmid. The authors would like to thank Diamond Light Source for beamtime and the staff of beamline I03 for assistance with crystal testing and data collection. Further, we thank Dr. Andreas Krämer and Dr. Adarsh Kumar for their support during the measurements at the Diamond Light Source. Also, we would like to thank Dr. Michael Klein for assisting while generating figures with BioRender.com. Wilma Ziebuhr acknowledges financial support by the German Research Foundation (DFG) grant DFG-ZI665-3-2. Fabian Barthels acknowledges financial support by the DFG in the framework of the Transregio Collaborative Research Center RMAP (TRR319 RMaP) seed funding.

ABBREVIATIONS USED

ACN,acetonitrile; ANOVA,analysis of variance; CuAAC,copper-catalyzed alkyne−azide click reaction; D2B,direct-to-biology; DCM,dichloromethane; DIPEA,*N*,*N*-diisopropylethylamine; DMF,dimethylformamide; DMSO,dimethyl sulfoxide; FP,fluorescence polarization; HATU,*O*-(7-azabenzotriazol-1-yl)-*N*,*N*,*N*′,*N*′-tetramethyluronium hexafluorphosphate; HEPES,2-[4-(2-hydroxyethyl)piperazin-1-yl]ethanesulfonic acid; IPTG,isopropyl-*β*-D-1-thiogalactopyranoside; ITC,isothermal titration calorimetry; LB,lysogeny broth; m^1G,N^1-methylguanosine; MBC,minimum bactericial concentration; MTase,methyltransferase; NC,negative control; n. d.,not determined; PC,positive control PMSF, phenylmethylsulfonyl fluoride; quant.,quantitative; rt,room temperature; SAH,*S*-adenosylhomocysteine; SAM,*S*-adenosylmethionine; SEC,size exclusion chromatography; SPOUT,trefoil knot protein fold; TBAF,tetra-*n*-butylammonium fluoride; TBTA,*tris*((1-benzyl-4-triazolyl)methyl)amine; TCEP,*tris*(2-carboxyethyl)-phosphine; TFA,trifluoroacetic acid; THF,tetrahydrofuran; TrmD,tRNA (guanine-N^1-)-methyltransferase

REFERENCES

(1) Cheung, G. Y. C.; Bae, J. S.; Otto, M. Pathogenicity and virulence of *Staphylococcus aureus*. *Virulence* **2021**, *12*, 547−569.

(2) Kourtis, A. P.; Hatfield, K.; Baggs, J.; Mu, Y.; See, I.; Epson, E.; Nadle, J.; Kainer, M. A.; Dumyati, G.; Petit, S.; et al. Vital Signs: Epidemiology and Recent Trends in Methicillin-Resistant and in Methicillin-Susceptible *Staphylococcus aureus* Bloodstream Infections — United States. *MMWR. Morb. Mortal. Wkly. Rep.* **2019**, *68*, 214−219.

(3) Naghavi, M.; Vollset, S. E.; Ikuta, K. S.; Swetschinski, L. R.; Gray, A. P.; Wool, E. E.; Robles Aguilar, G.; Mestrovic, T.; Smith, G.; Han, C.; et al. Global burden of bacterial antimicrobial resistance 1990−2021: a systematic analysis with forecasts to 2050. *Lancet* **2024**, *404*, 1199−1226.

(4) Murray, C. J. L.; Ikuta, K. S.; Sharara, F.; Swetschinski, L.; Robles Aguilar, G.; Gray, A.; Han, C.; Bisignano, C.; Rao, P.; Wool, E.; et al. Global burden of bacterial antimicrobial resistance in 2019: a systematic analysis. *Lancet* **2022**, *399*, 629−655.

(5) Forsyth, R. A.; Haselbeck, R. J.; Ohlsen, K. L.; Yamamoto, R. T.; Xu, H.; Trawick, J. D.; Wall, D.; Wang, L.; Brown-Driver, V.; Froelich, J. M.; et al. A genome-wide strategy for the identification of essential genes in *Staphylococcus aureus*. *Mol. Microbiol.* **2002**, *43*, 1387−1400.

(6) Byström, A. S.; Björk, G. R. Chromosomal location and cloning of the gene (trmD) responsible for the synthesis of tRNA (m1G) methyltransferase in *Escherichia coli* K-12. *Mol. Gen. Genet.* **1982**, *188*, 440−446.

(7) Byström, A. S.; Björk, G. R. The structural gene (trmD) for the tRNA(m1G)methyltransferase is part of a four polypeptide operon in *Escherichia coli* K-12. *Mol. Gen. Genet.* **1982**, *188*, 447−454.

(8) Zhang, Y.; Agrebi, R.; Bellows, L. E.; Collet, J.-F.; Kaever, V.; Gründling, A. Evolutionary Adaptation of the Essential tRNA Methyltransferase TrmD to the Signaling Molecule 3′,5′-cAMP in Bacteria. *J. Biol. Chem.* **2017**, *292*, 313−327.

(9) Gamper, H. B.; Masuda, I.; Frenkel-Morgenstern, M.; Hou, Y.-M. Maintenance of protein synthesis reading frame by EF-P and m1G37-tRNA. *Nat. Commun.* **2015**, *6*, No. 7226.

(10) Bjork, G. R. A primordial tRNA modification required for the evolution of life? *EMBO J.* **2001**, *20*, 231−239.

(11) Christian, T.; Evilia, C.; Williams, S.; Hou, Y.-M. Distinct Origins of tRNA(m1G37) Methyltransferase. *J. Mol. Biol.* **2004**, *339*, 707−719.

(12) Christian, T.; Hou, Y.-M. Distinct Determinants of tRNA Recognition by the TrmD and Trm5Methyl Transferases. *J. Mol. Biol.* **2007**, *373*, 623−632.

https://doi.org/10.1021/acs.jmedchem.5c02323
J. Med. Chem. 2025, 68, 26246−26262

(13) White, T. A.; Kell, D. B. Comparative genomic assessment of novel broad-spectrum targets for antibacterial drugs. *Comp. Funct. Genomics* **2004**, *5*, 304−327.
(14) Hill, P. J.; Abibi, A.; Albert, R.; Andrews, B.; Gagnon, M. M.; Gao, N.; Grebe, T.; Hajec, L. I.; Huang, J.; Livchak, S.; et al. Selective Inhibitors of Bacterial t-RNA-(N ^{1} G37) Methyltransferase (TrmD) That Demonstrate Novel Ordering of the Lid Domain. *J. Med. Chem.* **2013**, *56*, 7278−7288.
(15) Ito, T.; Masuda, I.; Yoshida, K.; Goto-Ito, S.; Sekine, S.; Suh, S. W.; Hou, Y.-M.; Yokoyama, S. Structural basis for methyl-donor−dependent and sequence-specific binding to tRNA substrates by knotted methyltransferase TrmD. *Proc. Natl. Acad. Sci. U.S.A.* **2015**, *112*, E4197−E4205.
(16) Zhong, W.; Pasunooti, K. K.; Balamkundu, S.; Wong, Y. H.; Nah, Q.; Gadi, V.; Gnanakalai, S.; Chionh, Y. H.; McBee, M. E.; Gopal, P.; et al. Thienopyrimidinone Derivatives That Inhibit Bacterial tRNA (Guanine37- N 1)-Methyltransferase (TrmD) by Restructuring the Active Site with a Tyrosine-Flipping Mechanism. *J. Med. Chem.* **2019**, *62*, 7788−7805.
(17) Elkins, P. A.; Watts, J. M.; Zalacain, M.; van Thiel, A.; Vitazka, P. R.; Redlak, M.; Andraos-Selim, C.; Rastinejad, F.; Holmes, W. M. Insights into Catalysis by a Knotted TrmD tRNA Methyltransferase. *J. Mol. Biol.* **2003**, *333*, 931−949.
(18) Whitehouse, A. J.; Thomas, S. E.; Brown, K. P.; Fanourakis, A.; Chan, D.S.-H.; Libardo, M. D. J.; Mendes, V.; Boshoff, H. I. M.; Floto, R. A.; Abell, C.; et al. Development of Inhibitors against *Mycobacterium abscessus* tRNA (m 1 G37) Methyltransferase (TrmD) Using Fragment-Based Approaches. *J. Med. Chem.* **2019**, *62*, 7210−7232.
(19) Thomas, S. E.; Whitehouse, A. J.; Brown, K.; Burbaud, S.; Belardinelli, J. M.; Sangen, J.; Lahiri, R.; Libardo, M. D. J.; Gupta, P.; Malhotra, S.; et al. Fragment-based discovery of a new class of inhibitors targeting mycobacterial tRNA modification. *Nucleic Acids Res.* **2020**, *48*, 8099−8112.
(20) Wilkinson, A. J.; Ooi, N.; Finlayson, J.; Lee, V. E.; Lyth, D.; Maskew, K. S.; Newman, R.; Orr, D.; Ansell, K.; Birchall, K.; et al. Evaluating the druggability of TrmD, a potential antibacterial target, through design and microbiological profiling of a series of potent TrmD inhibitors. *Bioorg. Med. Chem. Lett.* **2023**, *90*, No. 129331.
(21) Gehrtz, P.; Marom, S.; Bührmann, M.; Hardick, J.; Kleinbölting, S.; Shraga, A.; Dubiella, C.; Gabizon, R.; Wiese, J. N.; Müller, M. P.; et al. Optimization of Covalent MKK7 Inhibitors via Crude Nanomole-Scale Libraries. *J. Med. Chem.* **2022**, *65*, 10341−10356.
(22) Mahjour, B.; Zhang, R.; Shen, Y.; McGrath, A.; Zhao, R.; Mohamed, O. G.; Lin, Y.; Zhang, Z.; Douthwaite, J. L.; Tripathi, A.; Cernak, T. Rapid planning and analysis of high-throughput experiment arrays for reaction discovery. *Nat. Commun.* **2023**, *14*, No. 3924.
(23) Nolan, M. D.; Schüttel, M.; Scanlan, E. M.; Nielsen, A. L. Nanomole-scale photochemical thiol-ene chemistry for high-throughput late-stage diversification of peptide macrocycles. *Pept. Sci.* **2024**, *116*, No. e24310.
(24) Plesniak, M. P.; Taylor, E. K.; Eisele, F.; Kourra, C. M. B. K.; Michaelides, I. N.; Oram, A.; Wernevik, J.; Valencia, Z. S.; Rowbottom, H.; Mann, N.; et al. Rapid PROTAC Discovery Platform: Nanomole-Scale Array Synthesis and Direct Screening of Reaction Mixtures. *ACS Med. Chem. Lett.* **2023**, *14*, 1882−1890.
(25) Buitrago Santanilla, A.; Regalado, E. L.; Pereira, T.; Shevlin, M.; Bateman, K.; Campeau, L.-C.; Schneeweis, J.; Berritt, S.; Shi, Z.-C.; Nantermet, P.; et al. Nanomole-scale high-throughput chemistry for the synthesis of complex molecules. *Science* **2015**, *347* (1979), 49−53.
(26) Gesmundo, N. J.; Sauvagnat, B.; Curran, P. J.; Richards, M. P.; Andrews, C. L.; Dandliker, P. J.; Cernak, T. Nanoscale synthesis and affinity ranking. *Nature* **2018**, *557*, 228−232.
(27) Chen, S.; Wang, Z.; Gao, J.; Wang, Y.; Liang, J.; Zhu, Y.; Xu, H.; Chen, K.; Jin, L.; Zhang, H.; et al. Rapid Discovery of Celastrol Derivatives as Potent and Selective PRDX1 Inhibitors via Microplate-Based Parallel Compound Library and In Situ Screening. *J. Med. Chem.* **2025**, *68*, 13609−13627.
(28) Wilders, H.; Biggs, G.; Rowe, S. M.; Cawood, E. E.; Riziotis, I. G.; Rendina, A. R.; Grant, E. K.; Pettinger, J.; Fallon, D. J.; Skehel, M.; et al. Expedited SARS-CoV-2 Main Protease Inhibitor Discovery through Modular 'Direct-to-Biology' Screening. *Angew. Chem., Int. Ed.* **2025**, *64* (6), No. e202418314, DOI: 10.1002/anie.202418314.
(29) Stevens, R.; Bendito-Moll, E.; Battersby, D. J.; Miah, A. H.; Wellaway, N.; Law, R. P.; Stacey, P.; Klimaszewska, D.; Macina, J. M.; Burley, G. A.; Harling, J. D. Integrated Direct-to-Biology Platform for the Nanoscale Synthesis and Biological Evaluation of PROTACs. *J. Med. Chem.* **2023**, *66*, 15437−15452.
(30) Thomas, R. P.; Heap, R. E.; Zappacosta, F.; Grant, E. K.; Pogány, P.; Besley, S.; Fallon, D. J.; Hann, M. M.; House, D.; Tomkinson, N. C. O.; Bush, J. T. A direct-to-biology high-throughput chemistry approach to reactive fragment screening. *Chem. Sci.* **2021**, *12*, 12098−12106.
(31) Meidner, J. L.; Frey, A. F.; Zimmermann, R. A.; Sabin, M. O.; Nidoieva, Z.; Weldert, A. C.; Hoba, S. N.; Krone, M. W.; Barthels, F. Nanomole Scale Screening of Fluorescent RNA-Methyltransferase Probes Enables the Discovery of METTL1 Inhibitors. *Angew. Chem., Int. Ed.* **2024**, *63*, No. e202403792.
(32) Zhang, J.-H.; Chung, T. D. Y.; Oldenburg, K. R. A Simple Statistical Parameter for Use in Evaluation and Validation of High Throughput Screening Assays. *SLAS Discovery* **1999**, *4*, 67−73.
(33) Nidoieva, Z.; Sabin, M. O.; Dewald, T.; Weldert, A. C.; Hoba, S. N.; Helm, M.; Barthels, F. A microscale thermophoresis-based enzymatic RNA methyltransferase assay enables the discovery of DNMT2 inhibitors. *Commun. Chem.* **2025**, *8*, No. 32.
(34) Hou, Y.-M.; Matsubara, R.; Takase, R.; Masuda, I.; Sulkowska, J. I. Chapter Three - TrmD: A Methyl Transferase for tRNA Methylation With m1G37. *Enzymes* **2017**, *41*, 89−115.
(35) Zhong, W.; Koay, A.; Ngo, A.; Li, Y.; Nah, Q.; Wong, Y. H.; Chionh, Y. H.; Ng, H. Q.; Koh-Stenta, X.; Poulsen, A.; et al. Targeting the Bacterial Epitranscriptome for Antibiotic Development: Discovery of Novel tRNA-(N 1 G37) Methyltransferase (TrmD) Inhibitors. *ACS Infect. Dis.* **2019**, *5*, 326−335.
(36) Storck, P.; Umstätter, F.; Wohlfart, S.; Domhan, C.; Kleist, C.; Werner, J.; Brandenburg, K.; Zimmermann, S.; Haberkorn, U.; Mier, W.; Uhl, P. Fatty Acid Conjugation Leads to Length-Dependent Antimicrobial Activity of a Synthetic Antibacterial Peptide (Pep19−4LF). *Antibiotics* **2020**, *9*, 844.
(37) Jubeh, B.; Breijyeh, Z.; Karaman, R. Antibacterial Prodrugs to Overcome Bacterial Resistance. *Molecules* **2020**, *25*, 1543.
(38) Larsen, E. M.; Johnson, R. J. Microbial esterases and ester prodrugs: An unlikely marriage for combating antibiotic resistance. *Drug Dev. Res.* **2019**, *80*, 33−47.
(39) Miller, J. J.; Shah, I. T.; Hatten, J.; Barekatain, Y.; Mueller, E. A.; Moustafa, A. M.; Edwards, R. L.; Dowd, C. S.; Hoops, G. C.; Johnson, R. J.; et al. Structure-guided microbial targeting of antistaphylococcal prodrugs. *eLife* **2021**, *10*, No. e66657.
(40) Masson, P.; Shaihutdinova, Z.; Lockridge, O. Drug and prodrug substrates and pseudo-substrates of human butyrylcholinesterase. *Biochem. Pharmacol.* **2023**, *218*, No. 115910.
(41) Berman, H. M. The Protein Data Bank. *Nucleic Acids Res.* **2000**, *28*, 235−242.
(42) Halavaty, A. S.; Minasov, G.; Winsor, J.; Dubrovska, I.; Shuvalova, L.; See, R.; Zoraghi, R.; Reiner, N.; Anderson, W. F. (2009). 2.35 Angstrom resolution crystal structure of a putative tRNA (guanine-7-)-methyltransferase (trmD) from *Staphylococcus aureus* subsp. aureus MRSA252. Preprint, DOI: 10.2210/pdb3ky7/pdb.
(43) Ahn, H. J. Crystal structure of tRNA(m1G37)-methyltransferase: insights into tRNA recognition. *EMBO J.* **2003**, *22*, 2593−2603.
(44) Carlson, H. A.; Smith, R. D.; Damm-Ganamet, K. L.; Stuckey, J. A.; Ahmed, A.; Convery, M. A.; Somers, D. O.; Kranz, M.; Elkins, P. A.; Cui, G.; et al. CSAR 2014: A Benchmark Exercise Using Unpublished Data from Pharma. *J. Chem. Inf. Model.* **2016**, *56*, 1063−1077.

https://doi.org/10.1021/acs.jmedchem.5c02323
J. Med. Chem. 2025, 68, 26246−26262

(45) Laskowski, R. A.; Swindells, M. B. LigPlot+: Multiple Ligand−Protein Interaction Diagrams for Drug Discovery. *J. Chem. Inf. Model.* **2011**, *51*, 2778−2786.
(46) Friesner, R. A.; Banks, J. L.; Murphy, R. B.; Halgren, T. A.; Klicic, J. J.; Mainz, D. T.; Repasky, M. P.; Knoll, E. H.; Shelley, M.; Perry, J. K.; et al. Glide: A New Approach for Rapid, Accurate Docking and Scoring. 1. Method and Assessment of Docking Accuracy. *J. Med. Chem.* **2004**, *47*, 1739−1749.
(47) Kitagawa, M.; Ara, T.; Arifuzzaman, M.; Ioka-Nakamichi, T.; Inamoto, E.; Toyonaga, H.; Mori, H. Complete set of ORF clones of *Escherichia coli* ASKA library (A Complete Set of *E. coli* K-12 ORF Archive): Unique Resources for Biological Research. *DNA Res.* **2006**, *12*, 291−299.
(48) Brulé, H.; Elliott, M.; Redlak, M.; Zehner, Z. E.; Holmes, W. M. Isolation and Characterization of the Human tRNA-(N ^{1} G37) Methyltransferase (TRM5) and Comparison to the *Escherichia coli* TrmD Protein. *Biochemistry* **2004**, *43*, 9243−9255.
(49) Kabsch, W. XDS. *Acta Crystallogr., Sect. D: Biol. Crystallogr.* **2010**, *66*, 125−132.
(50) Winn, M. D.; Ballard, C. C.; Cowtan, K. D.; Dodson, E. J.; Emsley, P.; Evans, P. R.; Keegan, R. M.; Krissinel, E. B.; Leslie, A. G. W.; McCoy, A.; et al. Overview of the *CCP* 4 suite and current developments. *Acta Crystallogr., Sect. D: Biol. Crystallogr.* **2011**, *67*, 235−242.
(51) Evans, P. Scaling and assessment of data quality. *Acta Crystallogr., Sect. D: Biol. Crystallogr.* **2006**, *62*, 72−82.
(52) Evans, P. R.; Murshudov, G. N. How good are my data and what is the resolution? *Acta Crystallogr., Sect. D: Biol. Crystallogr.* **2013**, *69*, 1204−1214.
(53) McCoy, A. J.; Grosse-Kunstleve, R. W.; Adams, P. D.; Winn, M. D.; Storoni, L. C.; Read, R. J. *Phaser* crystallographic software. *J. Appl. Crystallogr.* **2007**, *40*, 658−674.
(54) Vagin, A.; Teplyakov, A. *MOLREP*: an Automated Program for Molecular Replacement. *J. Appl. Crystallogr.* **1997**, *30*, 1022−1025.
(55) Moriarty, N. W.; Grosse-Kunstleve, R. W.; Adams, P. D. *electronic Ligand Builder and Optimization Workbench* (*eLBOW*): a tool for ligand coordinate and restraint generation. *Acta Crystallogr., Sect. D: Biol. Crystallogr.* **2009**, *65*, 1074−1080.
(56) Emsley, P.; Cowtan, K. *Coot*: model-building tools for molecular graphics. *Acta Crystallogr., Sect. D: Biol. Crystallogr.* **2004**, *60*, 2126−2132.
(57) Afonine, P. V.; Grosse-Kunstleve, R. W.; Echols, N.; Headd, J. J.; Moriarty, N. W.; Mustyakimov, M.; Terwilliger, T. C.; Urzhumtsev, A.; Zwart, P. H.; Adams, P. D. Towards automated crystallographic structure refinement with *phenix.refine*. *Acta Crystallogr., Sect. D: Biol. Crystallogr.* **2012**, *68*, 352−367.
(58) Murshudov, G. N.; Skubák, P.; Lebedev, A. A.; Pannu, N. S.; Steiner, R. A.; Nicholls, R. A.; Winn, M. D.; Long, F.; Vagin, A. A. *REFMAC* 5 for the refinement of macromolecular crystal structures. *Acta Crystallogr., Sect. D: Biol. Crystallogr.* **2011**, *67*, 355−367.
(59) Chen, V. B.; Arendall, W. B.; Headd, J. J.; Keedy, D. A.; Immormino, R. M.; Kapral, G. J.; Murray, L. W.; Richardson, J. S.; Richardson, D. C. *MolProbity*: all-atom structure validation for macromolecular crystallography. *Acta Crystallogr., Sect. D: Biol. Crystallogr.* **2010**, *66*, 12−21.
(60) Williams, C. J.; Headd, J. J.; Moriarty, N. W.; Prisant, M. G.; Videau, L. L.; Deis, L. N.; Verma, V.; Keedy, D. A.; Hintze, B. J.; Chen, V. B.; et al. MolProbity: More and better reference data for improved all-atom structure validation. *Protein Sci.* **2018**, *27*, 293−315.


CAS BIOFINDER DISCOVERY PLATFORM™
CAS BIOFINDER HELPS YOU FIND YOUR NEXT BREAKTHROUGH FASTER
Navigate pathways, targets, and diseases with precision
Explore CAS BioFinder
CAS
A division of the American Chemical Society

https://doi.org/10.1021/acs.jmedchem.5c02323
J. Med. Chem. 2025, 68, 26246−26262

”

Supporting Information

Nanoscale Direct-to-Biology Optimization and Structural Insights into Selective *S. aureus* TrmD Inhibitors

Ariane F. Hübner[‡,a], Annabelle C. Weldert[‡,a], Tessa Marciniak[b], Florian Hof[c], Vivien S. Beck[b], Samuel Carien[b], Sophie N. Mulartschyk[a], Eva Wolf[c], Wilma Ziebuhr[b], Fabian Barthels[*,a]

[a]Institute of Pharmaceutical and Biomedical Sciences, Johannes Gutenberg-University, Staudingerweg 5, 55128 Mainz, Germany.

[b]Institute of Molecular Infection Biology, University of Würzburg, Josef-Schneider-Strasse 2, 97080 Würzburg, Germany.

[c]Institute of Molecular Physiology, Johannes Gutenberg-University, Hanns-Dieter-Hüsch-Weg 17, 55128 Mainz, Germany.

Corresponding Author's email address: barthels@uni-mainz.de

Table of contents

Crystallography of parent compounds....S3
Isothermal titration calorimetry (ITC)....S3
Supplementary results of the nanoSAR screening....S4
Fluorescence polarization (FP) assays and selectivity....S4
S. aureus TrmD inhibition (aptamer-based enzyme assay)....S6
TrmD inhibition (^{3}H incorporation enzyme assay)....S6
Cell viability assay (Cell Titer Glo)....S7
Supplementary results of anti-bacterial experiments....S7
Carbamate cleavage assays (LC/MS lysate assay)....S9
Supplementary crystallographic figures....S11
Physicochemical properties of the azide-library....S17
Docking poses compounds 2 and 8b-e,h....S18
NMR and LC/MS Spectra....S19

Crystallography of parent compounds

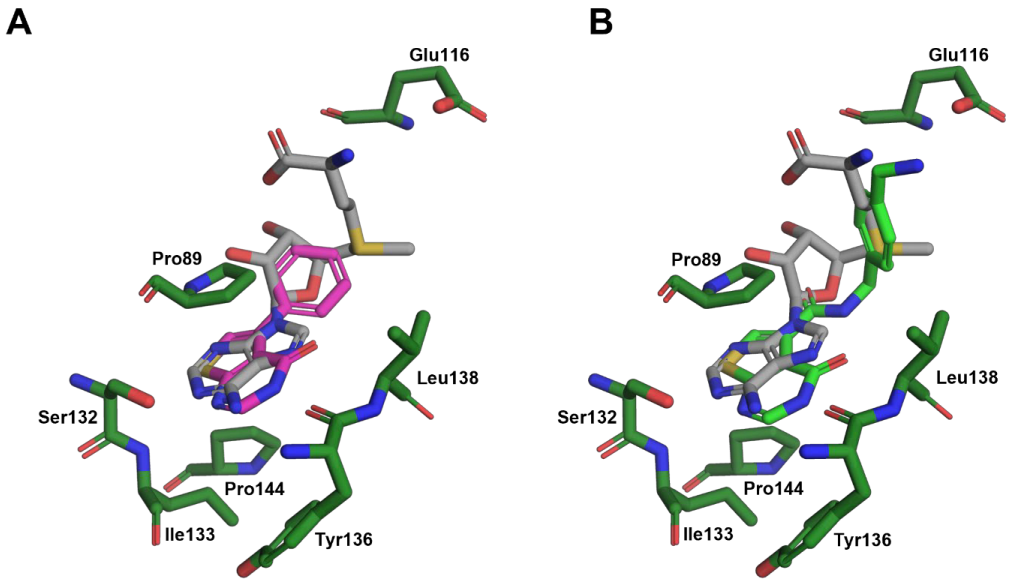


Figure S1: Parent structures for the development of *S. aureus* TrmD inhibitors. Crystallographic overlay with SAM (PDB:1UAK) of literature-known compounds **1** (**A**, PDB: 4MCD) and **2** (**B**, PDB 4MCC) in the *H. influenzae* SAM-binding pocket. Ligands and amino acids are shown in stick representation. The carbon atoms of SAM are shown in grey, those of **1** are shown in pink, and those of compound **2** are shown in lime. Interacting residues are displayed in dark green.

Isothermal titration calorimetry (ITC)

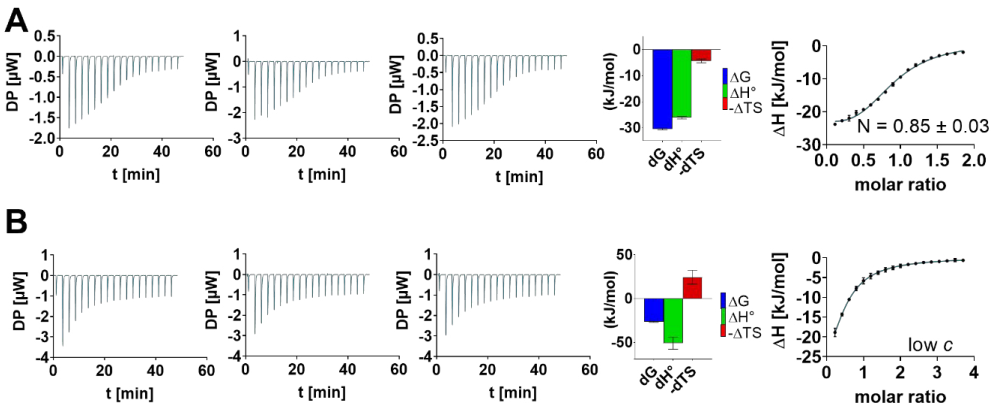


Figure S2. ITC data for the titration of compounds **1** and **2** against *Haemophilus influenzae* TrmD. (**A**) Compound **1** was titrated into *Haemophilus influenzae* TrmD. (**B**) Compound **2** was titrated into *Haemophilus influenzae* TrmD. Note: a low-c titration was performed for compound **2**.

Supplementary results of the nanoSAR screening

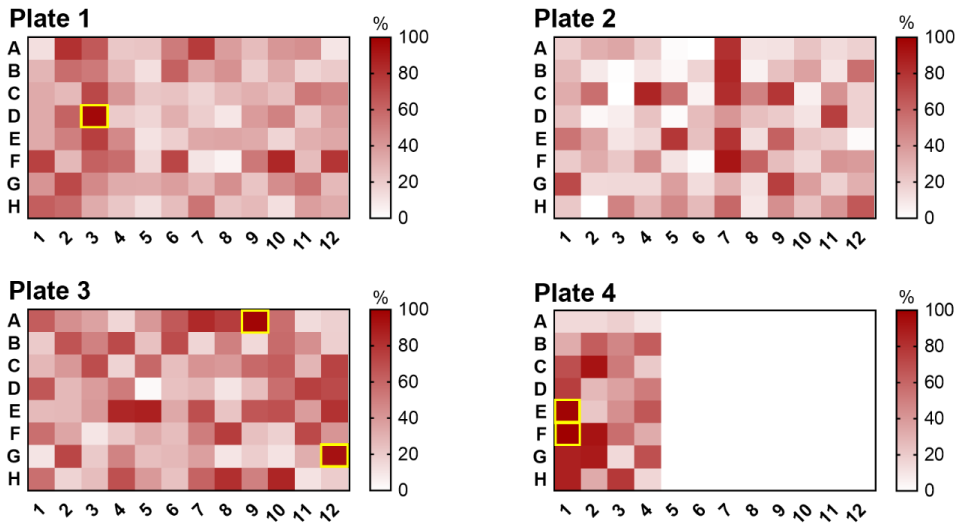


Figure S3. Results of the nanoSAR FP screening are presented in a heat-map format (displaced tracer [%]). The hit compounds **8b–e,h** are highlighted in yellow.

Fluorescence polarization (FP) assays and selectivity

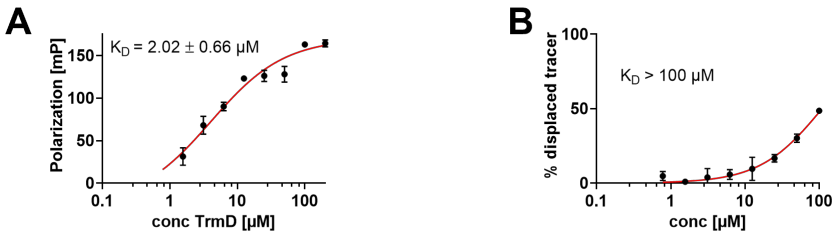


Figure S4. (**A**) Fluorescence polarization assay with tracer **3** titrated against *H. influenzae* TrmD. (**B**) K_D-value determination of alkyne **7** titrated against *S. aureus* TrmD.

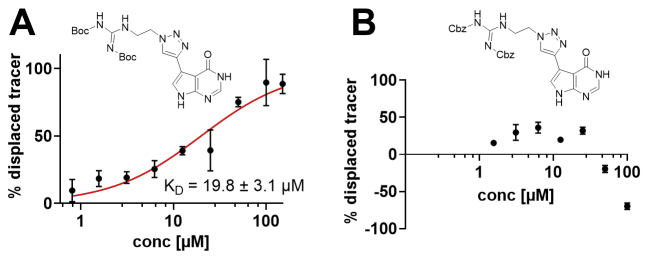


Figure S5. Supplementary FP-assay data on *S. aureus* TrmD. (**A**) **8f** (**B**) **8g.**

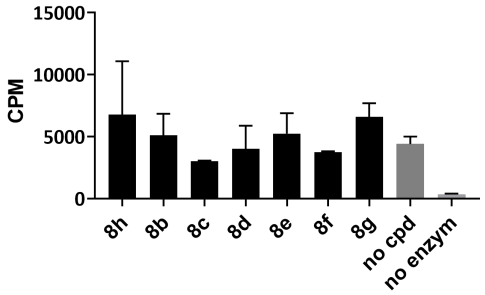


Figure S6. ^{3}H-based enzyme assay for Trm5 selectivity analysis of compound **8b**–**h**. Compounds were assayed at a final concentration of 30 µM, exhibiting no significant inhibition.

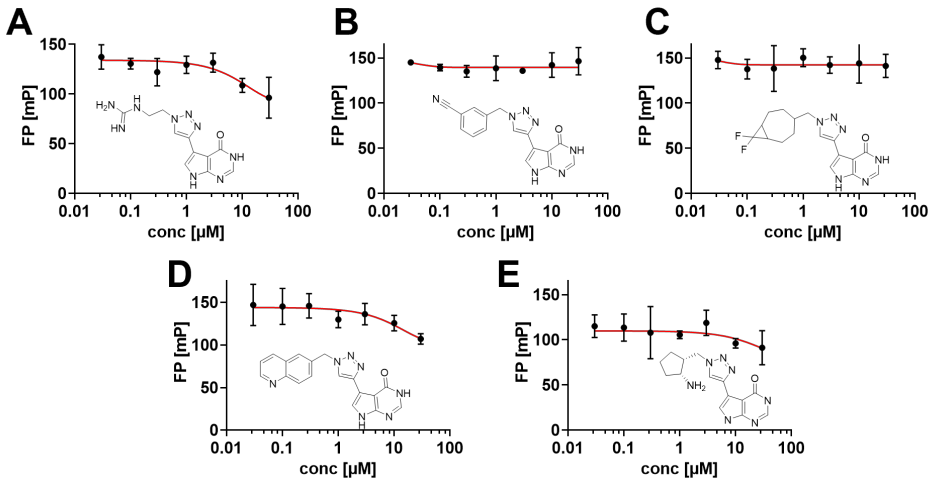


Figure S7. FP selectivity assays on *H. influenzae* TrmD for (**A**) **8h** (**B**) **8b** (**C**) **8c** (**D**) **8d** (**E**) **8e**.

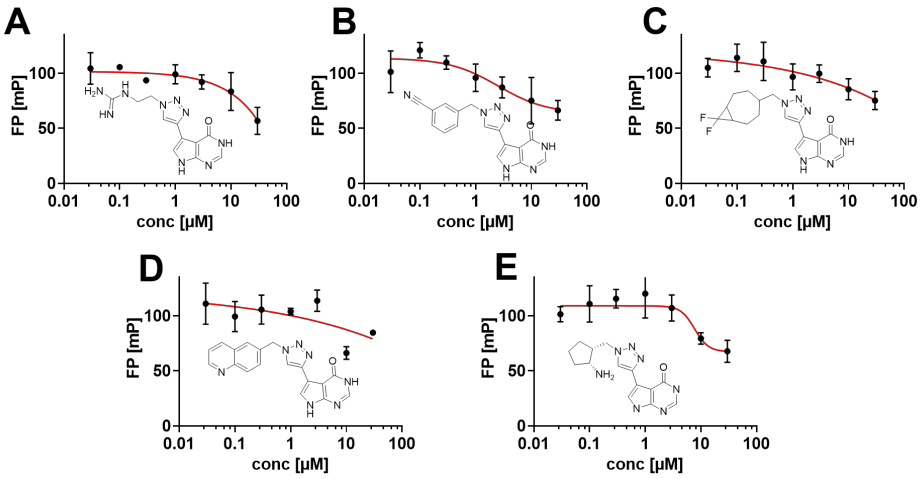


Figure S8. FP selectivity assays on *E. coli* TrmD for (**A**) **8h** (**B**) **8b** (**C**) **8c** (**D**) **8d** (**E**) **8e**.

***S. aureus* TrmD inhibition (aptamer-based enzyme assay)**

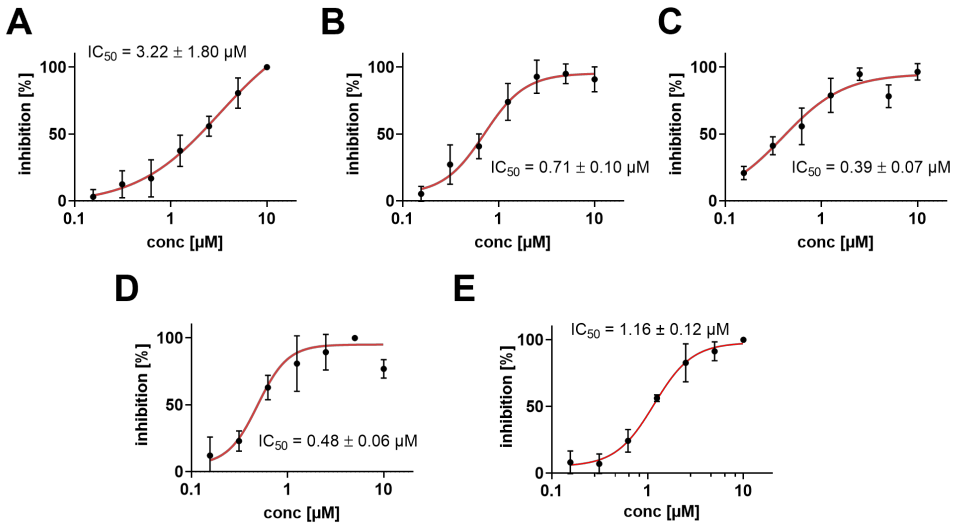


Figure S9. *S. aureus* TrmD inhibition measured by aptamer-based enzyme assay for the determination of IC_{50} values. (**A**) **8b** (**B**) **8c** (**C**) **8d** (**D**) **8e** (**E**) **8h**.

TrmD inhibition (^{3}H incorporation enzyme assay)

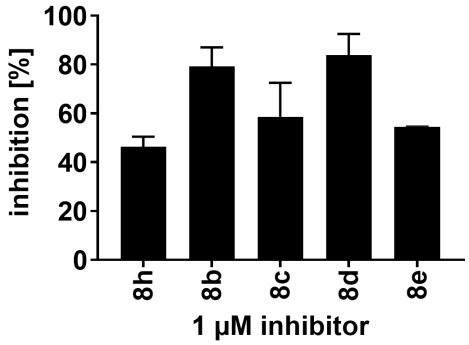


Figure S10. *S. aureus* TrmD inhibition measured by ^{3}H incorporation assay. Compounds were assayed at a final concentration of 1 µM, exhibiting inhibition values between 46% and 84%, confirming the inhibitory potency determined by aptamer-based assays (Figure S9).

Cell viability assay (Cell Titer Glo)

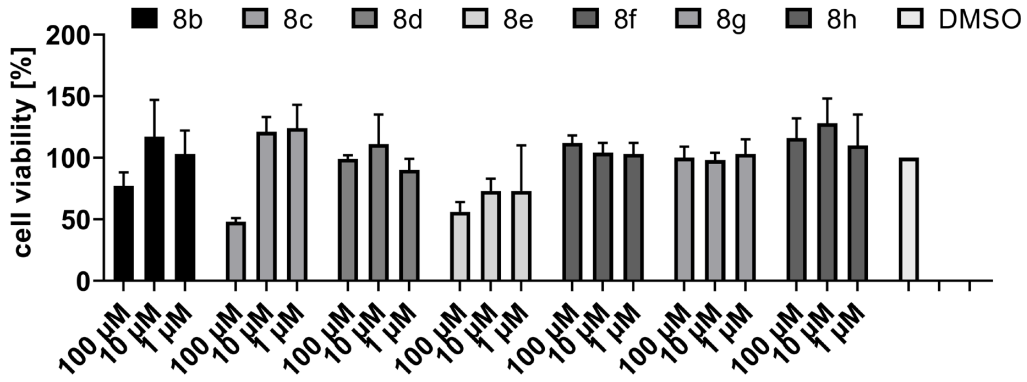


Figure S11. Screening results of the cell viability assay (HEK293). Pure DMSO was used as a control and set to 100% cell viability.

Supplementary results of anti-bacterial experiments

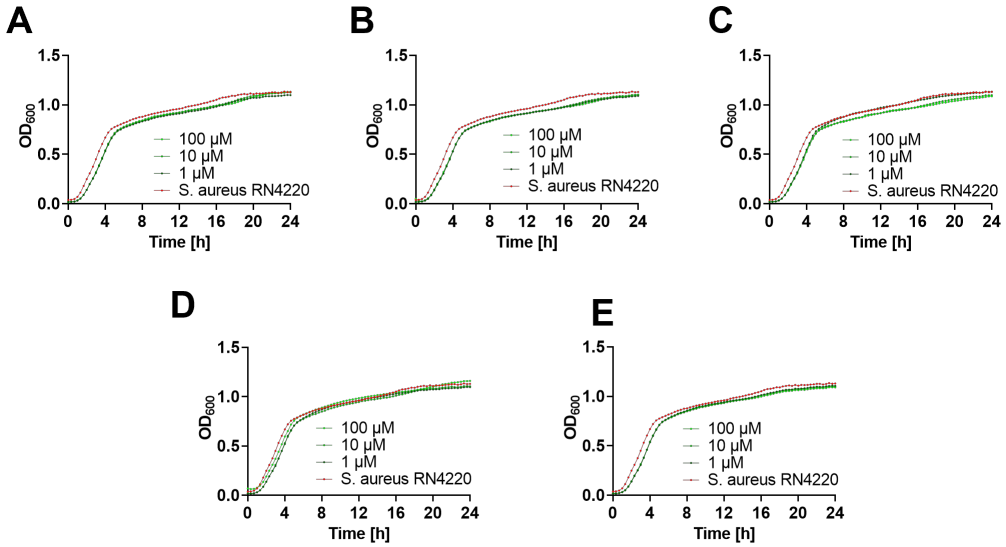


Figure S12. Growth curves of *S. aureus* RN4220 demonstrating the effect of compounds on bacterial growth. Compared to the negative control, no pronounced effect on growth was observed. (**A**) **8h** (**B**) **8b** (**C**) **8c** (**D**) **8d** (**E**) **8e**.

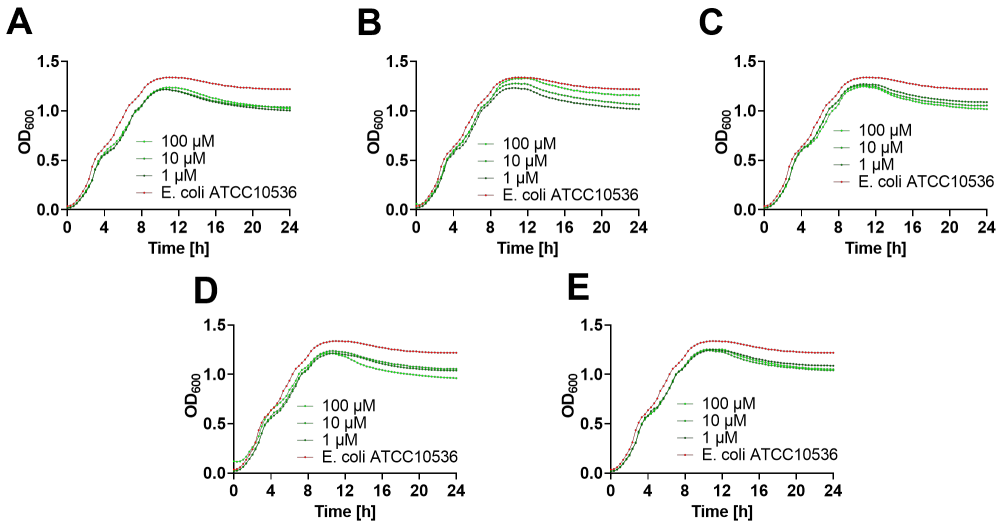


Figure S13. Growth curves of *E. coli* demonstrating the effect of compounds on bacterial growth. Compared to the negative control, no pronounced effect on growth was observed. (**A**) **8h** (**B**) **8b** (**C**) **8c** (**D**) **8d** (**E**) **8e**.

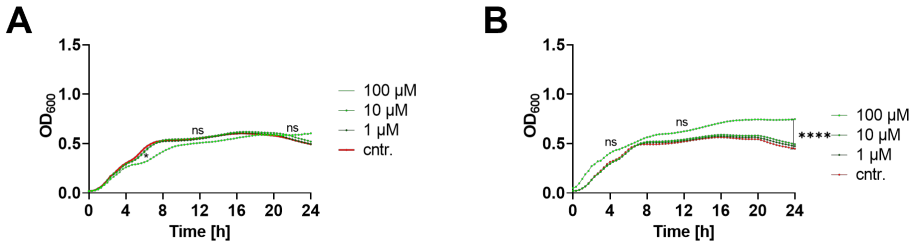


Figure S14. Growth curves of *E. coli* demonstrating the effect of **8g** (**A**) and **8f** (**B**) on bacterial growth. Compared to the negative control, no significant growth inhibition was observed. Two-way ANOVA with Dunnett's multiple comparisons test was used for statistical analysis, using a confidence interval of 95%.

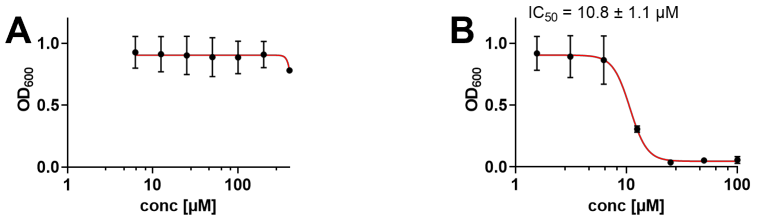


Figure S15. IC_{50} curves of **8g** (**A**) and **8f** (**B**) affecting *S. aureus* growth at 1440 min.

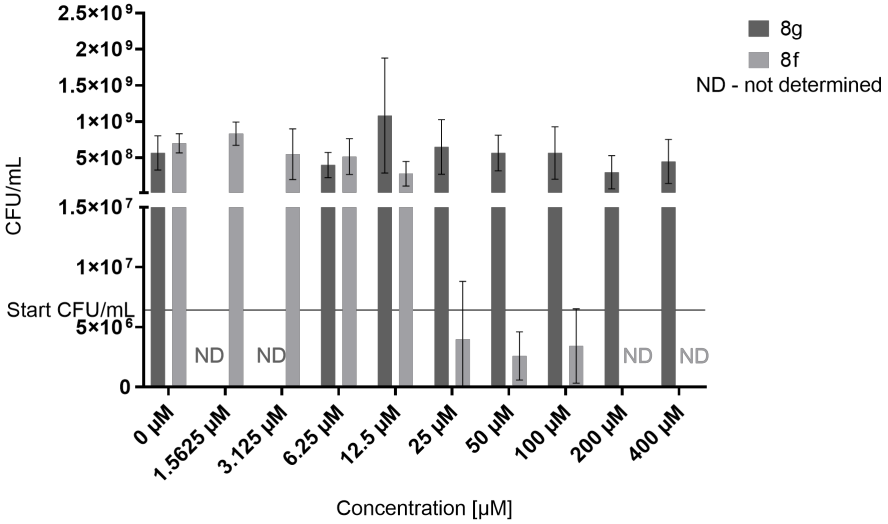


Figure S16. MBC determination of compounds **8f** and **8g**. Only **8f** affects growth starting at 12.5 µM.

Carbamate cleavage assays (LC/MS lysate assay)

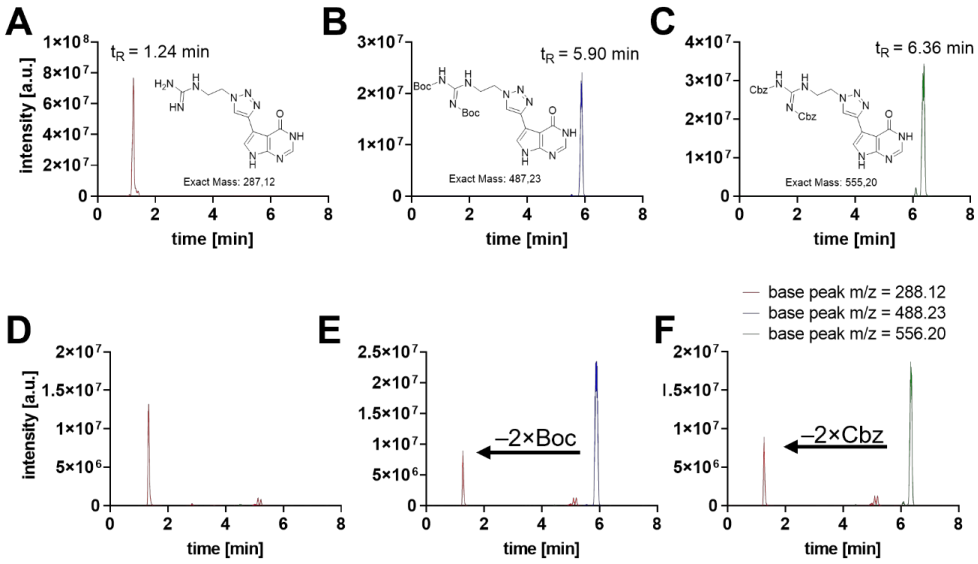


Figure S17. Supplementary results of the in vitro prodrug cleavage assay. (**A**) Basepeak chromatogram of pure reference compound **8h** m/z = 288±0.5. (**B**) Basepeak chromatogram of pure reference compound **8g** m/z = 488±0.5. (**C**) Basepeak chromatogram of pure reference compound **8f** m/z = 556±0.5. (**D**) Basepeak chromatogram of *S. aureus* lysate treated with **8h** m/z = 288±0.5. (**E**) Basepeak chromatogram of *S. aureus* lysate treated with **8g** m/z = 288±0.5; m/z = 488±0.5. (**F**) Basepeak chromatogram of *S. aureus* lysate treated with **8f** m/z = 288±0.5; m/z = 556±0.5.

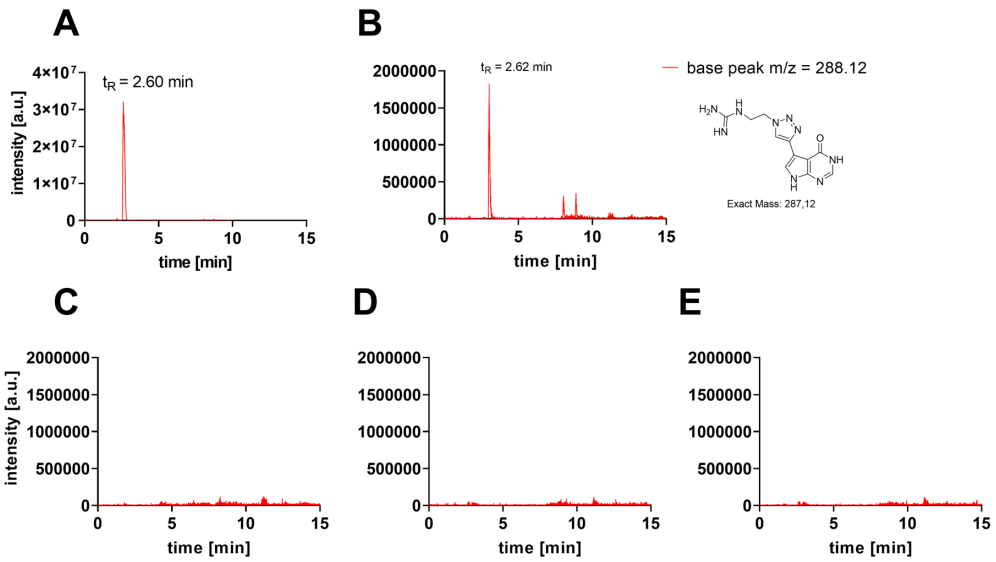


Figure S18. Supplementary results of the in vivo prodrug uptake and cleavage assay. (**A**) Basepeak chromatogram of pure reference compound **8h** m/z = 288±0.5. (**B**) Basepeak chromatogram of the sample derived from growing *S. aureus* culture incubated with compound **8f** and lysed after treatment. (**C**) Basepeak chromatogram of the sample derived from growing *S. aureus* culture incubated with compound **8g** and lysed after treatment. (**D**) Basepeak chromatogram of the sample derived from growing *S. aureus* culture incubated with compound **8h** and lysed after treatment. (**E**) Basepeak chromatogram of the sample derived from growing *S. aureus* culture mock-treated with DMSO and lysed after treatment.

Supplementary crystallographic figures

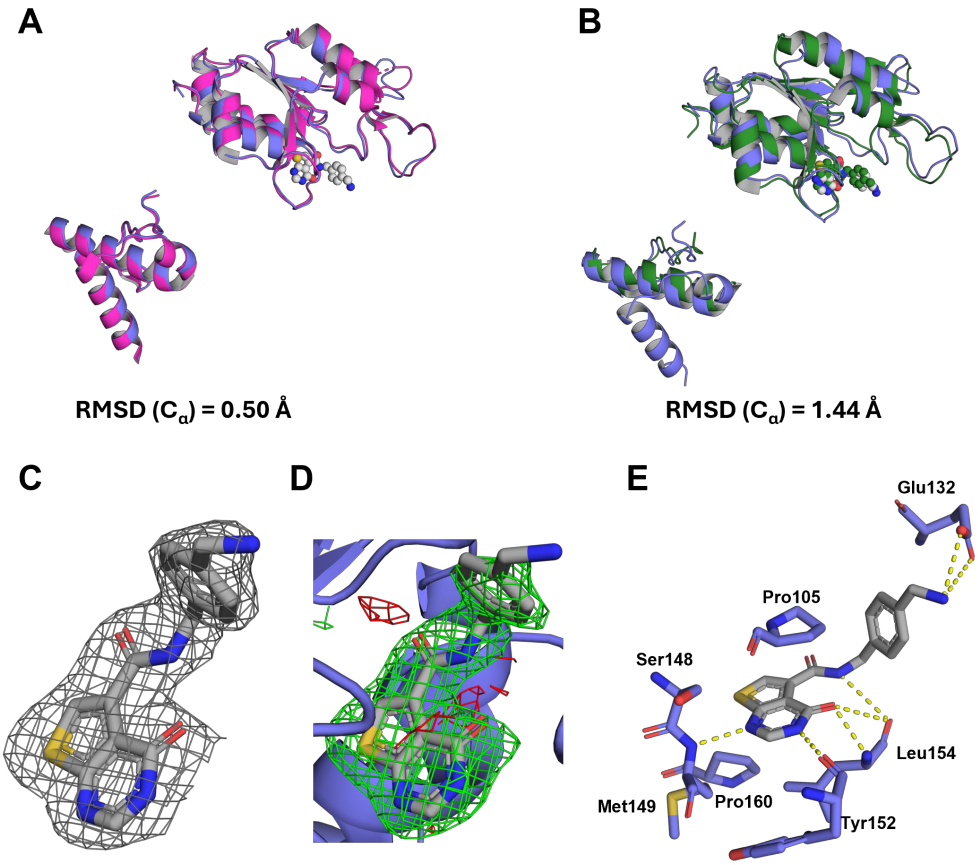


Figure S19. Supplementary crystallographic images for *S. aureus* TrmD co-crystallized with compound **2** (PDB: 9SDV). (**A**) Global superposition of the X-ray structures of *S. aureus* TrmD with compound **2** (violet-blue) and the apo structure (pink, 3KY7). (**B**) Global superposition of the X-ray structures of *S. aureus* TrmD with compound **2** (violet-blue) and *H. influenzae* TrmD with compound **2** (light blue, 4MCC). (**C**) Compound **2** bound *S. aureus* TrmD with $2mF_{obs}$-DF_{calc} electron density map at a contour level of +1σ. (**D**) Compound **2** bound *S. aureus* TrmD with mF_{obs}-DF_{calc} electron density map at a contour level of +3σ. (**E**) Compound **2** in the *S. aureus* SAH binding pocket. Protein structures are depicted as cartoons, interacting residues are shown as sticks, the ligand as spheres or in stick form, and polar interactions as yellow dashed lines.

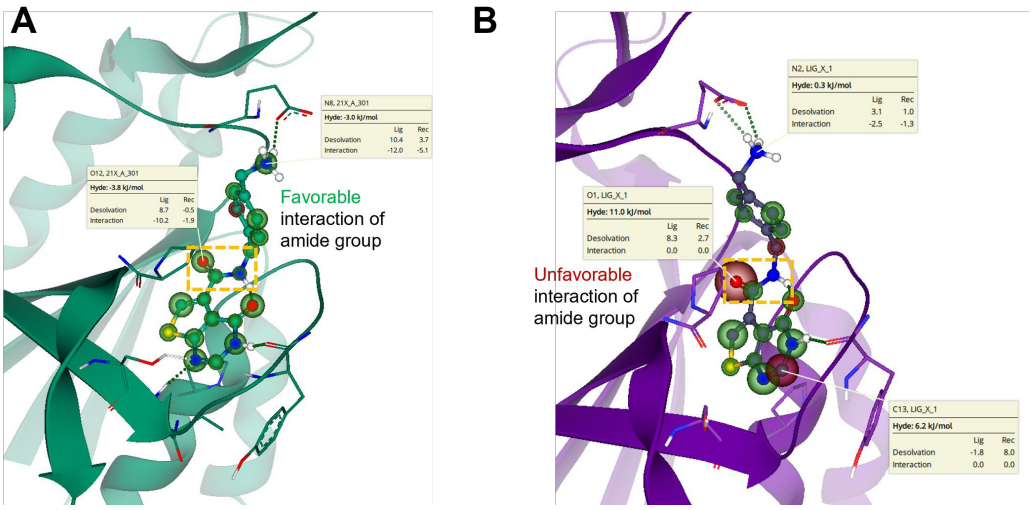


Figure S20. SeeSAR analysis by binding pose inspection of compound **2** bound to *H. influenzae* TrmD (**A**, green, PDB: 4MCC) and *S. aureus* TrmD (**B**, purple, PDB: 9SDV). Proteins are depicted as cartoons with representative binding site amino acids shown as lines. The compound is shown as stick. Hyde coloring enables the identification of favorable resp. unfavorable atom placements (colored spheres; green: favorable, red: unfavored).

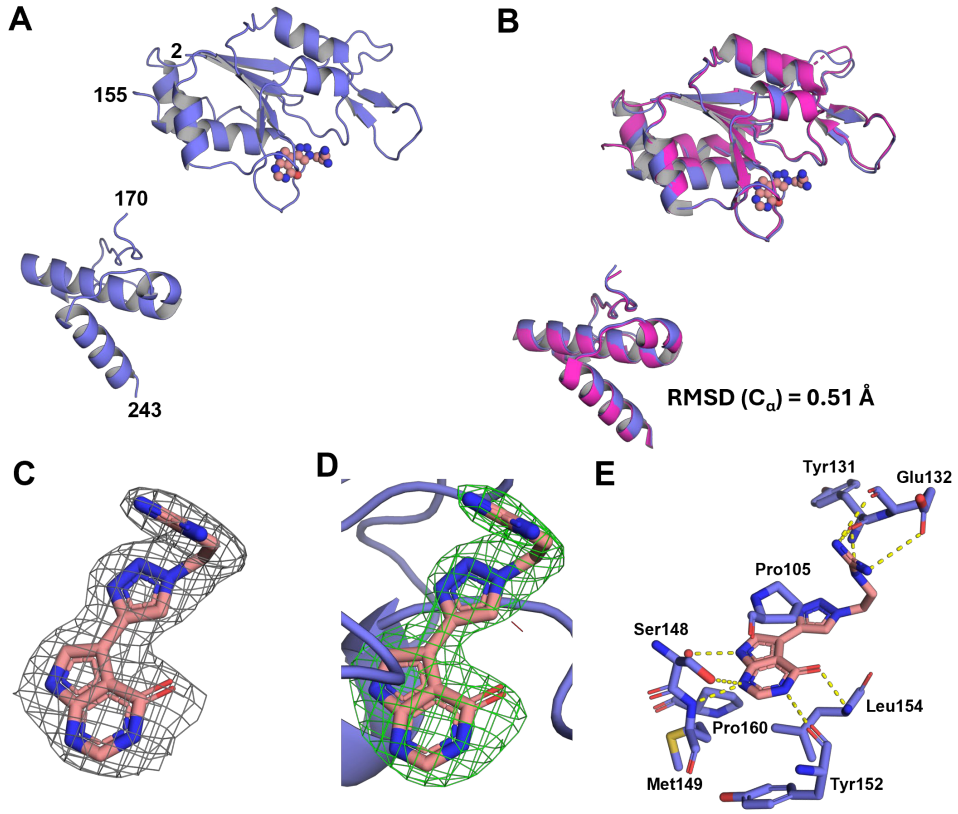


Figure S21. Supplementary crystallographic images for *S. aureus* TrmD co-crystallized with compound **8h** (PDB: 9SDW). (**A**) Structure of *S. aureus* TrmD bound to compound **8h.** (**B**) Global superposition of the X-ray structures of *S. aureus* TrmD with compound **8h** (violet-blue) and the apo structure (pink, 3KYZ). (**C**) Compound **8h** (salmon) bound *S. aureus* TrmD with $2mF_{obs}$-DF_{calc} electron density map at a contour level of +1σ. (**D**) Compound **8h** bound *S. aureus* TrmD with mF_{obs}-DF_{calc} electron density map at a contour level of +3σ. (**E**) Compound **8h** in the *S. aureus* SAH binding pocket. Protein structures are depicted as cartoons, interacting residues are shown as sticks, the ligand as spheres or in stick form, water molecules are shown as spheres, and polar interactions are shown as yellow dashed lines.

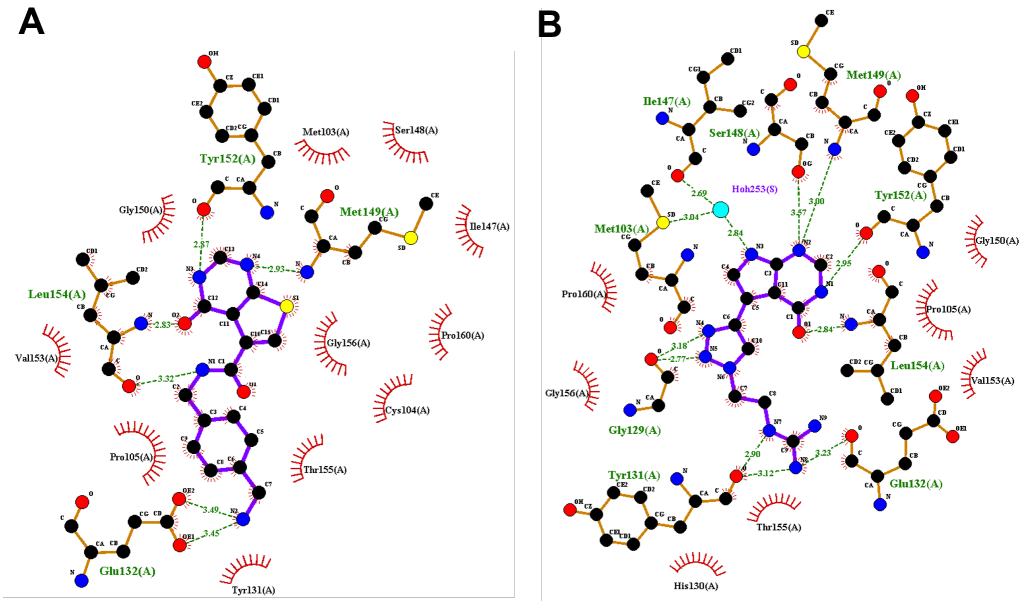


Figure S22. A schematic ligand-protein interaction diagram created with LigPlot+ for compound **2** (**A**) and compound **8h** (**B**). Intermolecular hydrogen bonds are given in green, hydrophobic interaction residues in red, and water as sky blue spheres.

Table S1: X-ray data collection refinement statistics of the structure co-crystalized with compound **2**.

PDB entry 9SDV	
Beamline	Diamond light source I03
Wavelength (Å)	0.976*
Resolution range(Å)	42.23 - 2.5 (2.75 - 2.5)
Space group	P 43 3 2
Unit cell	126.695 126.695 126.695 90 90 90
Total reflections	994338 (101554)*
Unique reflections	12564 (3062)
Multiplicity	78.90 (73.70)*
Completeness (%)	99.98 (99.93)
Mean I/sigma(I)	66.60 (13.10)*
Wilson B-factor (Å^2)	51.86
R-merge	0.06 (0.47)*
R-meas	0.06 (0.47)*
R-pim	0.01 (0.05)*
CC1/2	1.00 (0.99)*
Reflections used in refinement	12564 (3062)
Reflections used for R-free	608 (145)
R-work	0.2226 (0.2594)
R-free	0.2806 (0.3403)
Number of non-hydrogen atoms	1909
macromolecules	1825
Ligands	26
Solvent	58
Protein residues	231
RMS(bonds) (Å)	0.010
RMS(angles) (°)	1.13
Ramachandran favored (%)	95.15
Ramachandran allowed (%)	4.85
Ramachandran outliers (%)	0.00
Rotamer outliers (%)	0.52
Clashscore	8.08
Average B-factor (Å^2)	75.54
Macromolecules (Å^2)	76.10
Ligands (Å^2)	72.08
Solvent (Å^2)	59.51

Statistics for the highest resolution shell are shown in parentheses. * shows data from derived from ccp4.

Table S2: X-ray data collection refinement statistics of the structure co-crystalized with **8h**.

PDB entry 9SDW	
Beamline	Diamond light source I03
Wavelength (Å)	0.976*
Resolution range(Å)	44.86 - 2.6 (2.86 - 2.6)
Space group	P 43 3 2
Unit cell	126.875 126.875 126.875 90 90 90
Total reflections	899457 (112484)*
Unique reflections	11266 (2734)
Multiplicity	79.60 (83.90)*
Completeness (%)	99.97 (99.93)
Mean I/sigma(I)	44.70 (7.00)*
Wilson B-factor (Å^2)	59.97
R-merge	0.10 (0.97)*
R-meas	0.10 (0.98)*
R-pim	0.01 (0.11)*
CC1/2	1.00 (0.97)*
Reflections used in refinement	11266 (2734)
Reflections used for R-free	566 (140)
R-work	0.2275 (0.2534)
R-free	0.2912 (0.3343)
Number of non-hydrogen atoms	1883
macromolecules	1832
Ligands	21
Solvent	30
Protein residues	230
RMS(bonds) (Å)	0.007
RMS(angles) (°)	1.00
Ramachandran favored (%)	97.35
Ramachandran allowed (%)	2.65
Ramachandran outliers (%)	0.00
Rotamer outliers (%)	3.52
Clashscore	14.84
Average B-factor (Å^2)	79.94
Macromolecules (Å^2)	80.47
Ligands (Å^2)	66.73
Solvent (Å^2)	56.82

Statistics for the highest resolution shell are shown in parentheses. * shows data from derived from ccp4.

Physicochemical properties of the azide-library

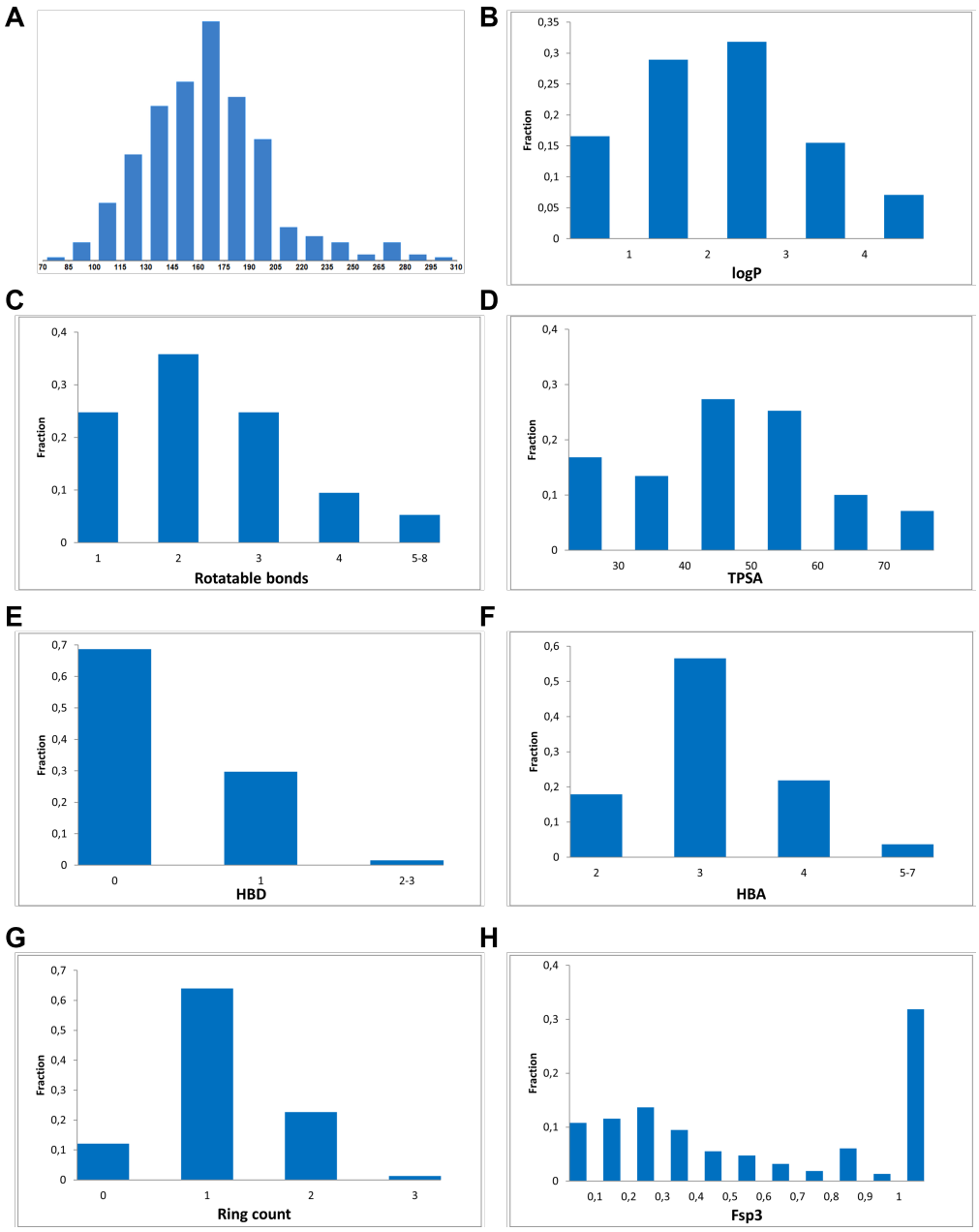


Figure S23. Overview of the physicochemical properties of the azide library purchase from Enamine.net. (**A**) Molecular weight [g/mol], (**B**) log P value, (**C**) Number of rotatable bonds, (**D**) Toplogical polar surface area [Å²], (**E**) Number of H-bond donors, (**F**) Number of H-bond acceptors, (**G**) Number of rings, (**H**) Fraction of sp^3 atoms.

Docking poses compounds 2 and 8b–e,h

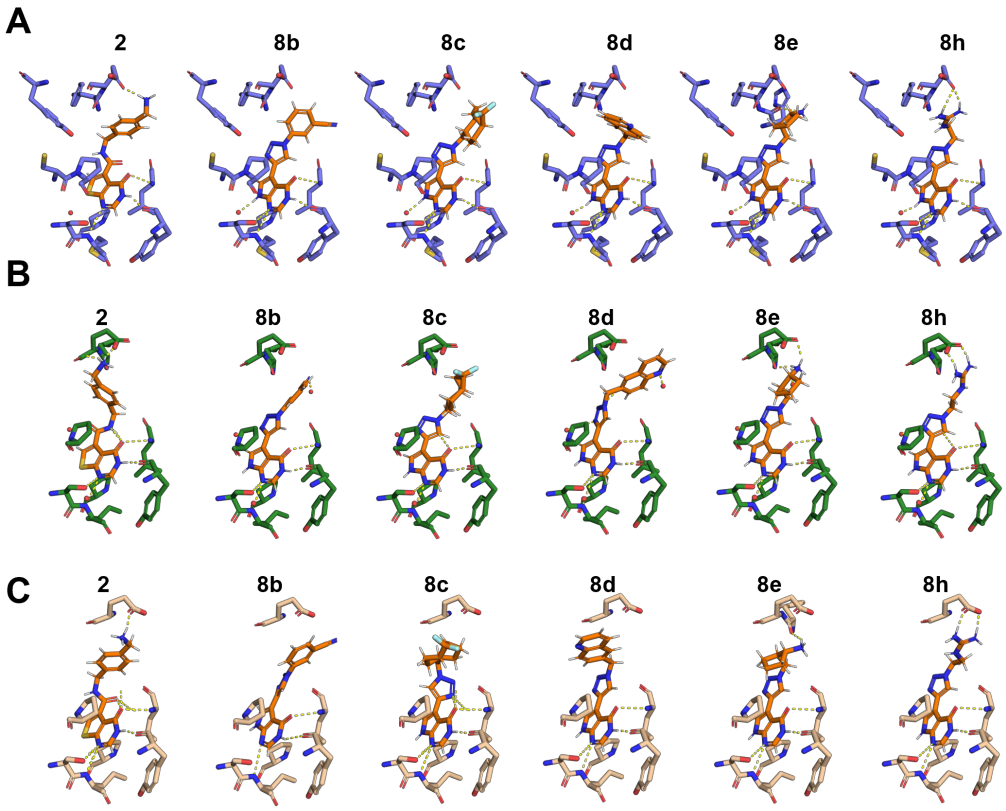


Figure S24: Glide docking poses for compounds **2** and **8b–e,h** after docking to (**A**) *Staphylococcus aureus* (PDB: 9SDW, purple carbons), (**B**) *Haemophilus influenzae* (PDB: 4MCC; green carbons), and (**C**) *Escherichia coli* (PDB: 1P9P, sand carbons). Ligand carbons are shown as sticks in orange, selected amino acids are shown as sticks, and water is shown as red spheres.

Table S3: Glide scores for compounds **2** and **8b–e,h** after docking to *Haemophilus influenzae* (PDB: 4MCC), *Escherichia coli* (PDB: 1P9P), and *Staphylococcus aureus* (PDB: 9SDW).

	2	**8b**	**8c**	**8d**	**8e**	**8h**
Haemophilus influenzae (PDB: 4MCC)	-13.44	-10.78	-11.03	-9.73	-10.74	-11.91
Escherichia coli (PDB: 1P9P)	-12.18	-8.28	-10.61	-11.32	-11.73	-11.38
Staphylococcus aureus (PDB: 9SDW)	-7.95	-11.623	-11.27	-11.80	-12.86	-12.74

4.3 DNA-Encoded Library Screening Uncovers Potent DNMT2 Inhibitors Targeting a Cryptic Allosteric Binding Site

4.3.1 Context, Project Summary, and own Contribution

The RNA MTase DNMT2 has the potential to modulate a variety of pathological processes (Chapter 1.1.4). Current inhibitors targeting DNMT2, mostly SAH derivatives, efficiently inhibit the isolated enzyme *in vitro*, but they fail to reduce m^5C modification levels in cells.[236,238] Moreover, SAH derivatives often lack selectivity, permeability, and must compete with the high amounts of cellular SAM and SAH.[84–86] Consequently, the development of selective, cell-active DNMT2 inhibitors and probes remains a challenge, yet represents an important goal in light of the enzyme's enigmatic nature and the limited understanding of its full range of cellular functions.

In this study, new, selective DNMT2 binders were identified and characterized. A DEL screening yielded five hits, representing new chemotypes: two triazine compounds and three tripeptide compounds. Binding to DNMT2 was assessed using several orthogonal methods, suggesting that these compounds do not bind to the SAM- or tRNA-binding sites. Nevertheless, three of the five ligands showed inhibitory activity, which suggested a unique mode of action. Fluorescent tracers derived from the DEL hits enabled selectivity profiling, revealing selectivity for tripeptide hit **3** over related NSun and DNMT enzymes. ITC experiments with compound **3,** conducted within this thesis suggested a conformational change upon ligand binding and a 1:1 stoichiometry. Additionally, ITC displacement experiments with SAH suggested allosteric binding. The binding mode of compound **3** was further elucidated by crystallography, revealing binding to a previously unrecognized allosteric site. This interaction induces a conformational change that blocks SAH binding and thereby inhibits DNMT2. Moreover, DNMT2 dimerization with one molecule of compound **3** bound per monomer was demonstrated by the crystal structure and size-exclusion chromatography. Structure–activity relationship (SAR) optimization of compound **3** yielded the potent analog **16**, which displayed passive membrane permeability. The cellular activity of compound **16** was assessed across a panel of cancer cell lines, where it reduced tRNA modification levels in the AML cell line MOLM-13. While compound **16** did not reduce cell viability across the tested cell lines, it sensitized MOLM-13 cells to chemotherapeutic treatment with doxorubicin.

In summary, in this publication first-in-class allosteric DNMT2 inhibitors with selectivity over related RNA methyltransferases were identified. Crystallography revealed a cryptic allosteric pocket and a ligand-induced conformational change, providing new structural insight into DNMT2 conformational plasticity and revealing a structural basis for allosteric inhibition. Cell-based assays further suggest that allosteric DNMT2 inhibition synergizes with chemotherapeutic treatment.

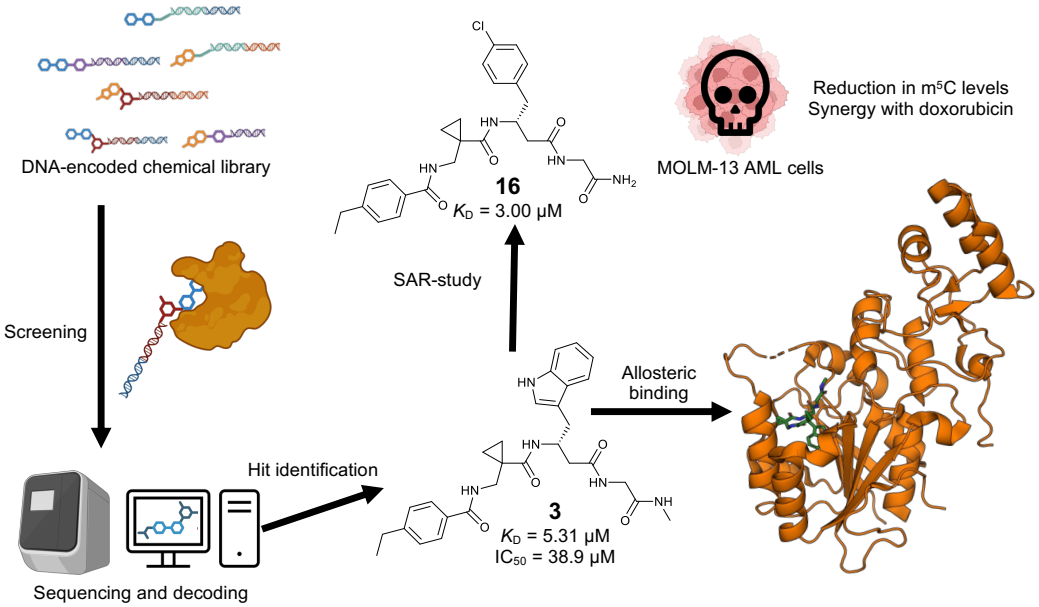


Figure 21: Identification and analysis of novel DNA Methyltransferase 2 (DNMT2) binders. Further abbreviations: PCR (polymerase chain reaction); K_D (dissociation constant); IC_{50} (half-maximal inhibitory concentration); SAR (structure–activity relationship); AML (acute myeloid leukemia). The figure was created with Microsoft PowerPoint, Biorender.com, and ChemDraw.

Own contributions: ITC: direct and displacement titrations, cell culture (40%), editing of the manuscript, and supporting information.

Contributions from other authors: DEL screening, syntheses, activity and binding assays (^{3}H-incorporation, MST, FP assay and AS-MS), electrophoretic mobility shift assay, PAMPA, protein and tRNA preparation and purification, protein crystallization, SeeSAR analysis, pull-down assay, cell culture (60%), cell viability assays and tRNA LC/MS assay, writing the manuscript and supporting information.

The work was published in *iScience* (impact factor: 4.1) and licensed under a Creative Commons Attribution licence: https://creativecommons.org/licenses/by/4.0/. This publication and the complete supplementary information (SI) are available online at DOI: 10.1016/j.isci.2025.113300. The appended Supporting Information represents an abridged version.

Publication reprinted with permission from *iScience* **2025**, *28*, 113300. „DNA-encoded library screening uncovers potent DNMT2 inhibitors targeting a cryptic allosteric binding site.“

© 2025 The Authors. Published by Elsevier Inc.

4.3.2 Publication

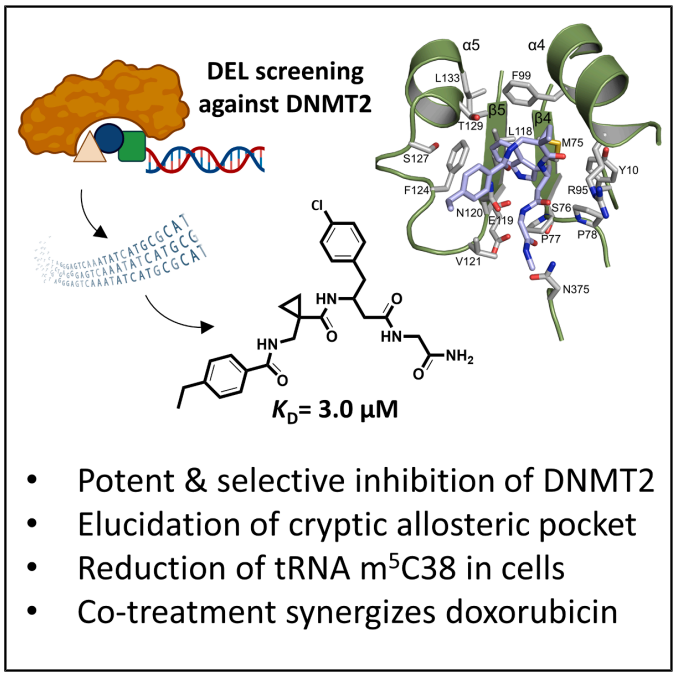
The following publication quoted (within “”) from page 118 to page 158 is exactly the same as the manuscript cited on page 117:“

iScience

Article

DNA-encoded library screening uncovers potent DNMT2 inhibitors targeting a cryptic allosteric binding site

Graphical abstract



Highlights

- DEL screening identifies non-SAH-like, selective DNMT2 inhibitor chemotypes
- Lead compound binds allosterically to a cryptic pocket revealed by X-ray crystallography
- DNMT2 inhibitors reduce m^5C levels and enhance doxorubicin-induced cytotoxicity
- Structural insights enable selective targeting of DNMT2 over related methyltransferases

Authors

Ariane F. Frey, Merlin Schwan, Annabelle C. Weldert, ..., Mark Helm, Irmgard Sinning, Fabian Barthels

Correspondence

barthels@uni-mainz.de

In brief

Biochemistry; Molecular Structure; Properties of biomolecules; Structural biology

Frey et al., 2025, iScience 28, 113300
September 19, 2025 © 2025 The Author(s). Published by Elsevier Inc.
https://doi.org/10.1016/j.isci.2025.113300

CellPress

iScience

CellPress
OPEN ACCESS

Article

DNA-encoded library screening uncovers potent DNMT2 inhibitors targeting a cryptic allosteric binding site

Ariane F. Frey,[1,3] Merlin Schwan,[2,3] Annabelle C. Weldert,[1] Valerie Kadenbach,[1] Jürgen Kopp,[2] Zarina Nidoieva,[1] Robert A. Zimmermann,[1] Lukas Gleue,[1] Collin Zimmer,[1] Marko Jörg,[1] Kristina Friedland,[1] Mark Helm,[1] Irmgard Sinning,[2] and Fabian Barthels[1,4,*]

[1]Institute of Pharmaceutical and Biomedical Sciences (IPBS), 55128 Mainz, Germany
[2]Heidelberg University Biochemistry Center (BZH), 69120 Heidelberg, Germany
[3]These authors contributed equally
[4]Lead contact
*Correspondence: barthels@uni-mainz.de
https://doi.org/10.1016/j.isci.2025.113300

SUMMARY

DNMT2 (TRDMT1) is a human RNA methyltransferase implicated in various disease processes. However, small-molecule targeting of DNMT2 remains challenging due to poor selectivity and low cellular availability of known *S*-adenosylhomocysteine (SAH)-derived ligands. In this study, a DNA-encoded library (DEL) screen identified five non-SAH-like chemotypes that selectively bind DNMT2, including three peptidomimetics. Orthogonal assays confirmed target engagement, and X-ray crystallography revealed a previously unknown allosteric binding pocket formed via active site loop rearrangement. Guided by structural insights, the authors optimized a lead compound with a K_D of 3.04 μM that reduces m^5C levels in MOLM-13 tRNA and synergizes with doxorubicin to impair cell viability. These inhibitors exhibit unprecedented selectivity over other methyltransferases, offering a promising scaffold for future DNMT2-targeting therapeutics. Beyond pharmacological implications, the study provides conceptual advances in understanding allosteric modulation and structural plasticity of DNMT2.

INTRODUCTION

Targeting RNA methyltransferases (MTases) by active site-competitive small-molecule drugs proves challenging due to their universal dependence on *S*-adenosyl-L-methionine (SAM) as a methyl group donating substrate, which is transformed into *S*-adenosylhomocysteine (SAH) during this enzymatic reaction.[1,2] SAH itself presents a pan methyltransferases inhibitor used as a starting point for several RNA MTase drug discovery campaigns.[3–5] A unique representative of this enzyme family is the RNA MTase DNA methyltransferase 2 (DNMT2), also known as TRDMT1, which is structurally related to other DNMTs, but this paralogous enzyme deviates in function and cellular localization.[6–8] Instead of DNA, which is the main target of DNMT1 and DNMT3, DNMT2 introduces the m^5C38 modification in several tRNAs.[6,9] Furthermore, DNMT2 is controversially discussed to be found in both nuclear compartments and the cytoplasm, hinting at its diverse roles and influence in protein biosynthesis.[9–11] Its distinctive catalytic MTase domain, featuring the unique cysteine-phenylalanine-threonine (CFT) motif, underscores its evolutionary and functional uniqueness within the DNMT family.[11] Physiologically, DNMT2 targets various tRNAs, including $tRNA^{Gly}$, $tRNA^{Val}$, and $tRNA^{Asp}$.[9,12] tRNA methylation by DNMT2 plays a role in regulating RNA degradation by ribonucleases, thereby enhancing tRNA stability and overall protein expression.[9,13] Additionally, tRNA m^5C38 methylation improves codon recognition, particularly distinguishing between aspartate and glutamate, thus enhancing translational accuracy.[14] Given DNMT2's role in regulating protein expression and translational accuracy, it is not surprising that DNMT2 misregulation has been implicated in cancer pathogenesis.[15] DNMT2 seems to play a functional role in various cancer cell lines and tumorigenesis, such as cervical or bladder tissue, and leukemia.[15–17] Additionally, DNMT2 silencing was found to correlate with miRNA upregulation which is also related to proliferation and function as tumor suppressor.[18] Also, elevated m^5C levels in small non-coding RNA (sncRNA), introduced by DNMT2, have been linked to metabolic disorders, where these influence the disorders' inheritance induced by high-fat diets in mice.[19] During oxidative stress, a DNMT2 upregulation could be detected, leading to the assumption that DNMT2 also helps cells cope with exogenous stress factors, underscoring DNMT2's multifaceted involvement in disease mechanisms.[20]

Despite its association with various disease mechanisms, DNMT2 remains a challenging target for drug development.[21] This is primarily due to the abundance of SAH and SAM and their ubiquitous binding proteins in cells with which inhibitors must compete.[22–24] Moreover, the fact that over 200 human MTases

This is an open access article under the CC BY license (http://creativecommons.org/licenses/by/4.0/).

CellPress
OPEN ACCESS

iScience
Article

depend on SAM further complicates the discovery of selective inhibitors.[25] Efforts to develop inhibitors targeting DNMT2 have predominantly focused on SAH analogs, which have achieved on-target potency in the micromolar range, but all fail to demonstrate selectivity within the DNMT or NSUN family MTases.[1,3,4] Currently available inhibitors also failed to inhibit DNMT2 within cellular assays, probably due to the low permeability of zwitterionic SAH derivates.[3] The generation of first-in-class selective and cell-active DNMT2 inhibitors is a current requirement to further investigate the function and druggability of DNMT2.

To address the development of cellularly potent DNMT2 inhibitors, we have applied the DNA-encoded library (DEL) screening technology on DNMT2 to identify modulating small molecule chemotypes. The goal was to develop selective chemical tools for DNMT2 investigation, modulation, and inhibition. DEL have gained widespread popularity in both industry and academia as a powerful tool for drug-like hit generation.[26–28] Comprising unique molecular structures tagged with DNA barcodes, DEL enables efficient diverse compound library screening and groundbreaking identification of novel drug scaffolds.[29–32] Since 1992, the DEL technology has undergone continuous development, evolving from initial strategies based on amide bond formation to widely used reactions such as metal-catalyzed cross-couplings, heterocycle synthesis, Diels-Alder cycloaddition, nucleophilic aromatic substitution, and reductions.[32,33] More recently, the methodology has expanded to include advanced transformations like photo-promoted reactions, C–H activation, and functionalization, thereby enabling access to a broad and diverse chemical space.[33] Recently, Wuxi AppTec enabled academic users to open access DEL by providing a DELopen platform containing a library of 4.2 billion unique compounds.[34] Latest DELopen successes include the ligand discovery for diverse proteins such as thrombin, RNase L, E3 ligases, the transcription factor TEAD, and antibacterial drug targets, highlighting its broad utility across various target classes.[30,35–39]

RESULTS AND DISCUSSION

DELopen screening reveals DNMT2 ligand chemotypes

Recombinant human DNMT2 was screened against the fourth-generation DELopen (WuXi AppTec) library (4.2 billion compounds, 27 sub-libraries) to identify small molecule RNA methyltransferase ligands (Figure 1A). DEL pannings were carried out with His-tagged DNMT2 protein stably immobilized on nickel chelate (Tris-NTA) affinity resin (Figure S1B). Selection screens against Tris-NTA resin without protein loading served as a nonspecific binding control. Three successive panning rounds were conducted, while the second round was chosen for deep sequencing based on the total retained DNA conjugates (Figures S1A and S1E). Sequenced hits were decoded and filtered to remove commonly encountered false positives and nonspecific binders to the affinity resin.[40] After affinity enrichment, 1713 unique full-length molecules were identified across three positive selection conditions and their combinations: (**A**) native DNMT2 without additives (n = 28 compounds); (**B**) DNMT2 with SAH (competitor, 100 μM, n = 104 compounds); (**C**) DNMT2 with $tRNA^{Asp}$ (competitor, 10 μM, n = 207 compounds); (**AB**) n = 159 compounds, (**AC**) n = 217 compounds, (**BC**) n = 251 compounds, (**ABC**) n = 747 compounds (Figure 1B).

These post-DEL screening compounds had enrichment scores of at least 100 for DNMT2. The enrichment score was calculated by decoding the DNA tags from next-generation sequencing (NGS) results, considering the corrected copy number, library size, sequencing depth, and other normalization factors (see https://hits.wuxiapptec.com/delopen).[41] A molecule with an enrichment score of 100 is a hundred times more abundant in the sequencing data than the average molecule in the library. Interestingly, DEL sequencing analysis showed that most of the compounds enriched on DNMT2 were found within the condition **ABC**, which may reflect the inability of the low-affinity SAH competitor to completely occlude the active binding site during the panning. The five compounds with the highest confidence (enrichment scores >200 000 and copy number >10, Table S5) and structural diversity (from three sub-libraries in total, see Figure S1F) were selected for further investigation and downstream validation studies (Figures 1C and 1D).

Across the 747 **ABC**-enriched and the five highest-scoring representative molecules (“hits”), recurring patterns were apparent in each of the four building block positions (denoted BB1, BB2, BB3, and BB4), indicating structurally related families: two triazine-based DEL hits (**1**–**2**) and three peptide-based DEL hits (**3**–**5**). Hit molecules **3**–**5** can be described as β-homotripeptides with non-natural side chain groups in building block positions BB2 resp. BB3 and incorporating an N-terminal substituent in BB1. The BB4 C-terminus (corresponding to the DNA tag attachment position) was synthetically amidated with methylamine. These hit compounds were resynthesized without the encoding DNA tag and were studied for DNMT2 active site binding using an MST displacement assay as previously described by Zimmermann et al.[42] For the thermophoretic detection, 5-FAM-triazolyl-adenosyl-diaminobutyric acid (FTAD) was used as a fluorescent probe, which can bind to the DNMT2 SAH binding pocket.[42] When FTAD is bound to DNMT2 versus its unbound state, there is a measurable difference in the F_{norm} value represented by a distinct positive MST shift, and thus, a ligand that can displace the FTAD-DNMT2 interaction can be detected by competitive MST screening assays (Figures S2 and S3).

In this regard, two of the five tested DEL hit compounds, **3** and **5**, induced a quantitative FTAD displacement in the MST assay (Figure 1E). In subsequent dose-response experiments, **3** and **5** showed K_D-values of 48.2 μM and 241 μM, respectively (detailed information in Table 1). Interestingly, **3** and **5** are similar in structure, differing only by the first building block, 4-ethylbenzoic acid for **3** and 4-methylthiophene-2-carboxylic acid for **5** (Figure 1D), while compound **4** features a similar peptidomimetic structure but without β-homo amino acids. In contrast, **1** and **2** share a common triazine core structure due to their origin from the same sub-library (Figure 1C). Notably, compounds **1** and **4** did not lead to FTAD displacement but rather induced a negative MST shift toward a higher FTAD-bound degree thermophoresis resp. strengthened interaction. We speculated about an allosteric binding mode of these compounds, which agrees with the observation that these compounds were identified in the **ABC** panning cluster.

iScience
Article

CellPress
OPEN ACCESS

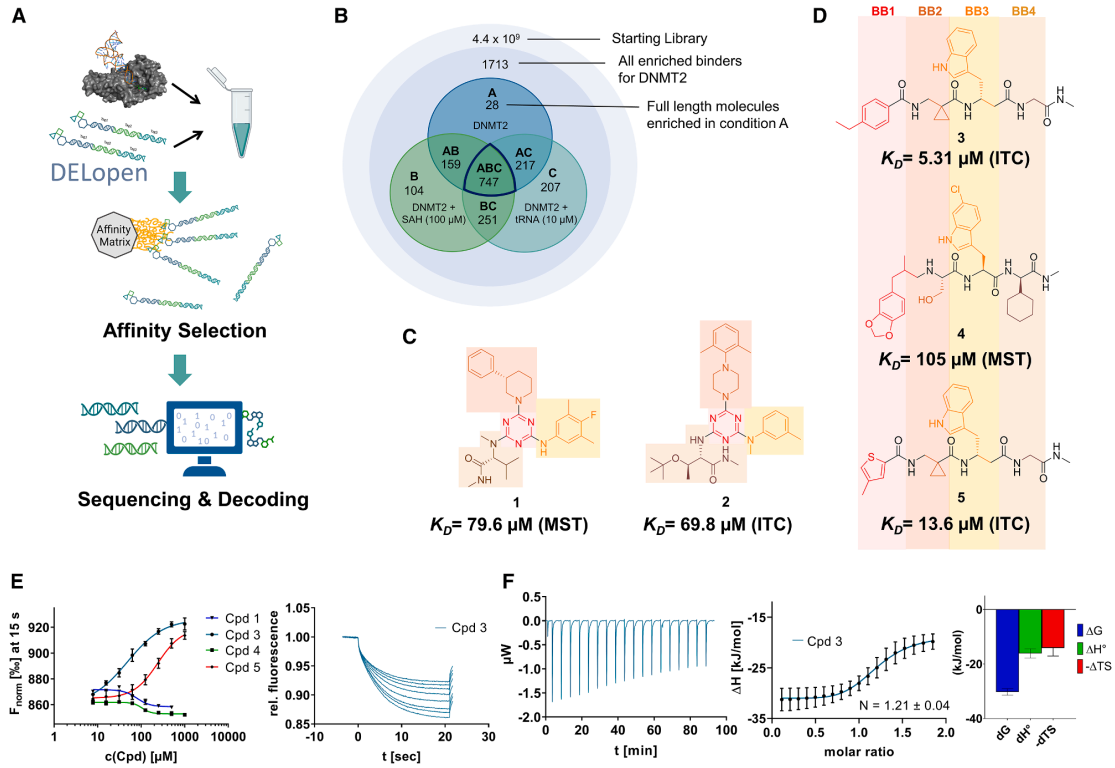


Figure 1. DEL screening reveals DNMT2 ligand chemotypes & biophysical characterization

(A) DELopen screening workflow. DELopen libraries consist of 4.2B compounds encoded by individual DNA barcodes. During affinity selection, small molecule-DNA conjugates are enriched, while non-binders are washed away.

(B) Conditions used during the DELopen screening: In condition A, native DNMT2 without additives was used; condition B: DNMT2 and SAH (100 µM) were mixed to block the SAH binding site; condition C: DNMT2 was incubated with $tRNA^{Asp}$ (10 µM). Most full-length molecules were enriched in condition ABC (unaffected by competitors), from which 5 selected compounds **1**–**5** were chosen for off-DNA synthesis and downstream characterization.

(C) Enriched triazine-based compounds selected from ABC.

(D) Peptidomimetic compounds enriched in ABC and chosen for further study. Building blocks BB1–BB4 are highlighted accordingly.

(E) MST dose-response curves for compounds **1**, **3**, **4**, and **5** with detailed MST traces for compound **3**.

(F) ITC data of compound **3** titrated to DNMT2. From left to right: Titration thermogram, stoichiometry plot, and signature plot. Data are represented as mean ± SEM. A comprehensive overview of the biophysical data for all compounds binding to DNMT2 can be found in the SI.

As an orthogonal biophysical binding experiment, we implemented isothermal titration calorimetry (ITC) ligand binding studies. In these experiments, **2**, **3**, and **5** showed significant binding enthalpy signals when titrated to DNMT2, with K_D-values of 69.8, 5.3, and 13.6 µM, respectively (Figure 1F; Figure S4). Of note, peptidomimetic hits **3** & **5** resulted in particularly long injection equilibration times in the minute magnitude, and thus, we speculated about a conformational change upon ligand binding, which could be confirmed by subsequent crystallography as described below. Interestingly, the thermodynamic profile showed that these hits had different enthalpy and entropy contributions despite their comparable affinity. During the ligand optimization from hit compound **3** to lead structure **16** (see below), this enthalpy contribution to the overall binding affinity increased continuously (Figure 5A). Additionally, an orthogonal and label-free affinity selection-mass spectrometry (AS-MS) assay for top-hit compound **3** was conducted (Figure S6), revealing a K_D-value of 8.40 ± 2.20 µM, which is in agreement with the ITC data.[43] Besides biophysical characterization utilizing DNMT2 binding assays, all five DEL hits were evaluated regarding their inhibitory effects using an enzymatic ^{3}H-incorporation assay, where the tritium-labeled methyl group incorporation from ^{3}H-SAM to the substrate $tRNA^{Asp}$ can be determined.[3,4] Compounds **3**, **4**, and **5** were able to inhibit DNMT2's MTase activity with IC_{50}-values of 38.9, 44.4, and 236 µM, respectively (Figure S7). Data and figures of additional ligand characterization experiments can be found in Figures S2–S7.

Taken together with the data gleaned from the DEL sequencing results, the combined ligand characterization data suggest that the DEL hits identified during this screening campaign are not binding to the DNMT2's active site nor tRNA pockets because hit compounds were enriched in condition

CellPress
OPEN ACCESS

iScience
Article

Table 1. Biophysical data of compounds 1–5 determined by various ligand binding and enzyme inhibition experiments

	^{3}H assay (IC_{50})	MST (K_D)	ITC (K_D)
1	n.i.	79.6 ± 10.0 μM	n.b.
2	n.i.	n.b.	69.8 ± 5.4 μM
3	38.9 ± 6.9 μM	48.2 ± 8.0 μM	5.31 ± 1.67 μM
4	44.4 ± 12.9 μM	105 ± 9 μM	n.b.
5	236 ± 63 μM	241 ± 36 μM	13.6 ± 1.6 μM

All results include the mean value and standard deviations from at least technical triplicate measurements. Raw data and analysis plots are depicted in Figure 1 and Figures S2–S7. n.i. = no inhibition/less than 50% inhibition at 500 μM//n.b. = no enthalpy signal observable (ITC)/no thermophoresis shift observable (MST).

ABC and show only partly competitive behavior during ligand binding experiments. The experimental findings from MST, ITC, and enzymatic ^{3}H-incorporation assay suggest that triazine compounds **1** and **2** act as non-competitive DNMT2 binders without inhibition potency, whereas β-homo-tripeptides **3**–**5** function as DNMT2 enzyme inhibitors. The mode of action resp. their binding site remained elusive from the biophysical investigations but could be finally solved by DNMT2 crystallography (vide infra). We speculated that the minor discrepancies between the enrichment scores' relative order and determined affinities may be due to the DNA tag sequence absence in the off-DNA synthesized hit compounds.

Development of fluorescent tracer molecules and binding site investigation

For further characterization of both triazine- and tripeptide-based DEL hits, fluorophore functionalized tracer compounds **6**–**8** were developed based on their parent compounds for target selectivity determination in fluorescence-based assays and as molecular probes for further investigations (Figure 2A; Figure S3). Three fluorescent probes were designed during this study for both identified DEL chemotypes: Alexa Fluor 488 (AF488) resp. tetramethylrhodamine (TAMRA) labeled β-homo-tripeptides (**6** and **8**), and a Cy5-labeled triazine-based probe (**7**). Apparent binding affinities of fluorescent probes were measured by MST experiments as described above with the modification that the respective probe was used instead of FTAD (Figure 2B; Figures S3E and S3F).[44] By this, probe binding affinities (**6**: 1.65 μM, **7**: 1.36 μM, and **8**: 0.70 μM) were determined which resemble the original DEL hit compounds' magnitude of potency, suggesting that the chosen fluorophores do not significantly interfere with their binding behavior and the probes are suitable for fluorometric MTase investigations.

Next, peptidomimetic probe **6** was utilized to determine MTase binding selectivity toward related DNMT resp. NSUN proteins and to investigate the competitivity of natural DNMT2 substrates (SAH and $tRNA^{Asp}$) by fluorescence polarization (FP) displacement experiments (Figure 2C). Fluorometric assays using DNMT2 revealed that the compound **6**-DNMT2 complex yields high fluorescence polarization (220 mP) compared to enzyme-free buffer conditions (5 mP). By examining whether this effect can be reversed by the addition of natural ligands, we found that SAH (100 μM) is able to displace probe **6**, while $tRNA^{Asp}$ (10 μM) does not show a significant effect, and high fluorescence polarization is retained during the tRNA substrate addition. These results were furthermore confirmed by an ITC displacement experiment, where **3** was able to displace SAH and vice versa (Figure 2D; Figure S5).[45] Interestingly, compound **3** appears to be partly competitive with SAH, although it behaves seemingly non-competitive in the DEL screening. We hypothesize that this discrepancy is due to the low affinity of SAH for DNMT2, and SAH is not retained in DNMT2-bound form during stringent washing steps to remove unspecific DEL-binders.

Probe **6** also enabled the determination of ligand binding selectivity toward other m^5C MTases using the FP assay setup. Since NSUN2, NSUN3, and NSUN6 introduce m^5C in other tRNA and DNMT1 resp. DNMT3A/3L in DNA, these enzymes were selected for the ligand selectivity profile determination. By incubating probe **6** with various related m^5C MTases, it was observed that this probe does not bind to related NSUN and DNMT families' MTase representatives at concentrations up to 20 μM, highlighting its unique DNMT2 binding selectivity (Figure 2C; Figure S3H). Due to the highest potency and excellent selectivity of hit compound **3**, we decided to conduct the following characterizations and further developments using this molecule as a starting point.

To investigate the competition of DEL hit compounds with the $tRNA^{Asp}$ substrate, we conducted an electrophoretic mobility shift assay (EMSA) to analyze the DNMT2-tRNA complex. Here, we found that none of the 5 hit compounds (100 μM) had an influence on the DNMT2-tRNA complex formation (Figure 2E).[46] Analogous MST displacement experiments with *in situ* fluorescently labeled $tRNA^{Asp}$ showed consistently no compound was able to dissociate the nucleic acid-protein complex formed by DNMT2 and $tRNA^{Asp}$ (K_D = 218 nM, Figures S8A and S8B). Furthermore, no compound (100 μM) had a significant influence on the thermophoresis of $tRNA^{Asp}$ in a protein-free solution (Figures S8C and S8D).[47] This finding is supported by our crystal structure of compound **3** with DNMT2 (vide infra). The previously elucidated RNA-binding residues (K122, R160, R162, R275, R289, K295, K367, and R371; mutagenesis study of Jurkowski et al., 2012) are in significant distance to the compound **3** binding pocket, and thus, allow the simultaneous binding of compound **3** and tRNA.[48] The exact binding mode of $tRNA^{Asp}$ to DNMT2 could not be elucidated by crystallography until now, therefore, we have created an Alphafold model illustrating the ternary complex of the SAH resp. compound **3**, and $tRNA^{Asp}$ (Figure S20).

Crystallography unravels an allosteric binding pocket of hit compound 3

For our crystallographic studies, we used a deletion construct of human DNMT2, dubbed DNMT2Δ47, in which residues 191 to 237 were deleted since this region is predicted as intrinsically disordered. A similar construct was successfully used for the only available X-ray structure of human DNMT2 bound to SAH (PDB 1G55[49]). We found that the deletion mutant's catalytical activity is indistinguishable from the full-length wild-type enzyme (Figure S7C), and that hit compound **3** displays medium-range micromolar affinity (48 vs. 102 μM) against both wild-type and DNMT2Δ47 enzymes (Figure 1E vs; Figure S3G).

iScience
Article

CellPress
OPEN ACCESS

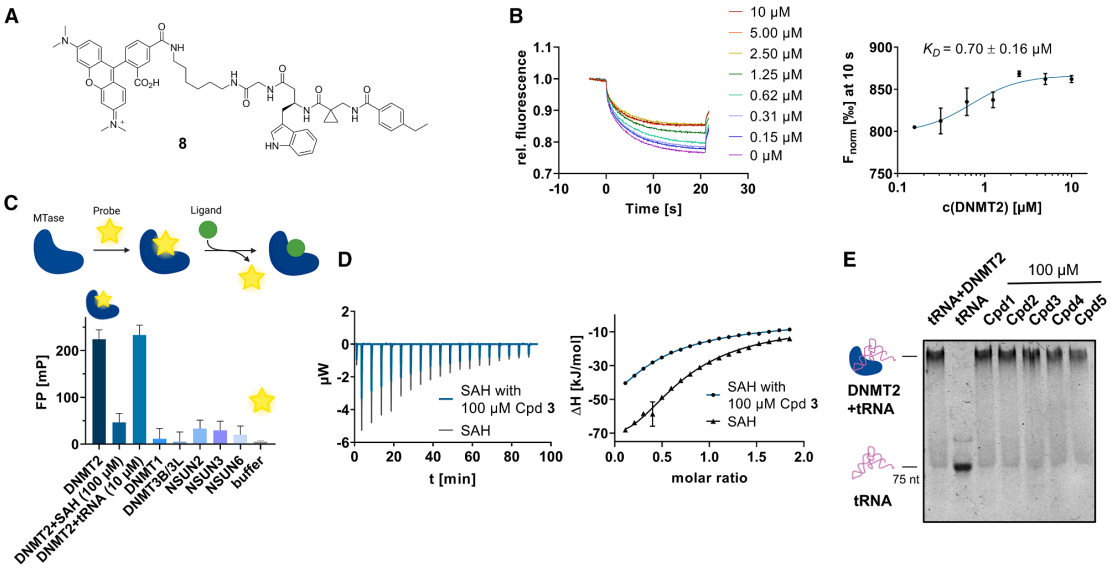


Figure 2. Investigating the ligand binding mode and selectivity with biophysical methods

(A) Chemical structures of probe **8**: TAMRA-labeled β-homo-tripeptide.

(B) MST dose-response curves for probe **8** binding to DNMT2.

(C) Fluorescence polarization assay for probe **6** binding to native DNMT2 (2 µM), DNMT2 (2 µM) preincubated with SAH (100 µM), DNMT2 (2 µM) with $tRNA^{Asp}$ (10 µM), and various related MTase off-targets (all 2 µM).

(D) DNMT2-SAH ITC displacement experiment for compound **3**. SAH was titrated to DNMT2 in the absence resp. presence of compound **3** (100 µM), yielding a significant enthalpy reduction.

(E) EMSA assay investigates the competition of hit compounds **1**–**5** with the tRNA substrate. Positive control: tRNA+DNMT2 (band at high molecular weights); negative control: only tRNA (band at low molecular weights). Hit compounds **1**–**5** (100 µM) were added to the DNMT2-tRNA complex (10 + 5 µM) and analyzed by native PAGE. No compound was able to dissociate the DNMT2-tRNA complex. Data are represented as mean ± SEM. Uncropped PAGE images can be found in Figure S22.

We could obtain an X-ray structure of human DNMT2Δ47 with bound compound **3** at 2.6 Å resolution, which shows an overall fold similar to DNMT2Δ47-SAH (PDB 1G55) as indicated by an overall rmsd (C_α) of 0.69 Å (Figure S17A). The asymmetric unit contains two very similar DNMT2Δ47-compound **3** complexes with an overall rmsd(C_α) of 0.354 Å and the largest differences in the loop region comprising residues 82 to 95 (Figure 3A). A large common surface area of 1685 $Å^2$ is present between these two protein complexes. Interface and packing analysis with PISA[50] supports a stable dimer formed by the two complexes in the asymmetric unit. Therefore, we used analytical size exclusion chromatography to investigate the oligomeric state of DNMT2Δ47-compound **3** in solution. We could show that DNMT2Δ47 with bound compound **3** is indeed dimeric in solution at a high protein concentration of 10 mg/mL (Figure S18), which was also used for crystallization. In contrast, DNMT2Δ47 without ligand is monomeric in solution under the same conditions.

Both complexes in the asymmetric unit show clear electron density for compound **3** (Figure S17C). Most interestingly, compound **3** is bound in a largely hydrophobic pocket adjacent to the active site (Figure 3B). For comparison, the structure with SAH bound in the active site is depicted in Figure 3C, and superpositions of the two different complexes without and with ligands are given in Figures S17A and S17B. Compound **3** is bound by residues mainly from the two regions β4-α4 and β5-α5, which is depicted in Figure 4A for chain A (interacting residues of chain B have been omitted for clarity).

A comprehensive schematic ligand-protein interaction diagram was created with LigPlot+[51] for both DNMT2Δ47-compound **3** complexes in the asymmetric unit (Figure S19). In the following, a detailed description of compound **3** binding to chain A and the differences between both complexes in the asymmetric unit are given. The indole ring of compound **3** is located in a hydrophobic cave formed by Y10, M75, backbone of S76, P77, F99, L118, F124, and L133. Additionally, the amine group of the indole ring forms a hydrogen bond with the backbone carbonyl of E119. The ethylbenzene moiety of compound **3** is bound between V121, F124, S127, T129 and $L279_B$. The ethyl group is also in contact with a glycerol molecule (used for cryo-protection) bound in the dimer interface. The amide group, which connects the ethylbenzene and cyclopropane moieties, is in van der Waals contact with P78 and R95 and forms three hydrogen bonds, namely with the main chain carbonyl of $L278_B$, with the side chain of N120, and an intramolecular H-bond to the amino group connecting the cyclopropane and indole moieties. The cyclopropane moiety is surrounded by the hydrophobic side chains of F99, $L278_B$, and $L279_B$. Finally, the two terminal amide groups of compound

CellPress
OPEN ACCESS

iScience
Article

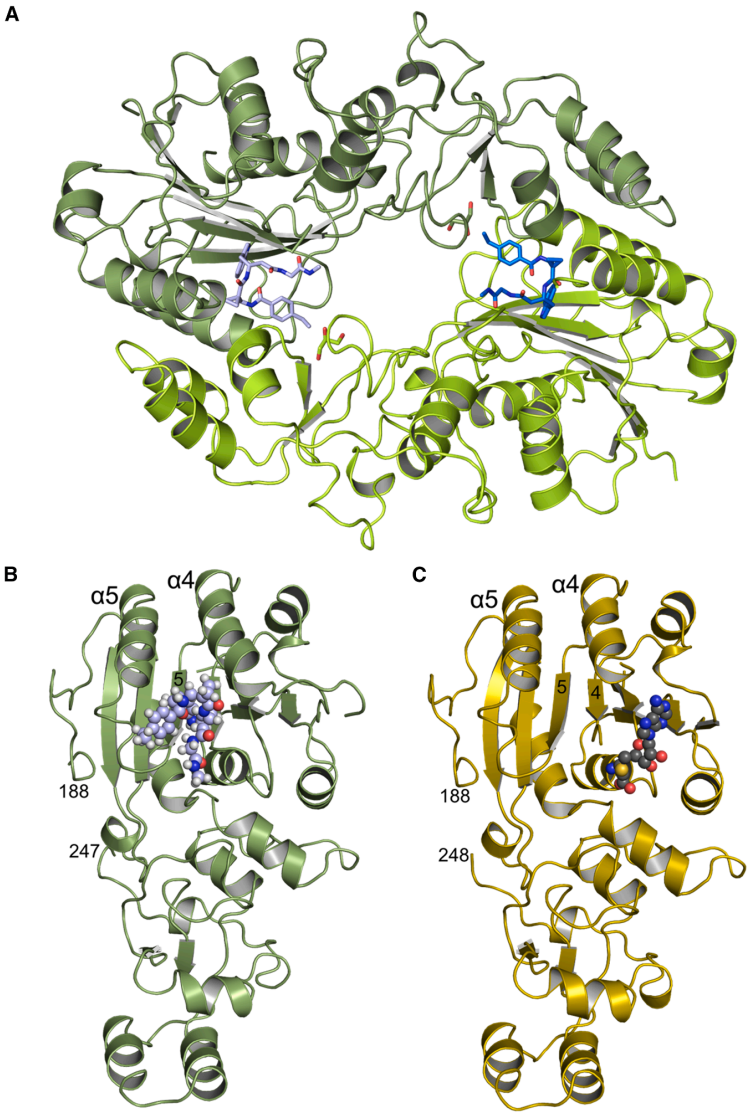


Figure 3. Crystallography unravels an allosteric binding pocket of hit compound 3

(A) X-ray structure of DNMT2Δ47 showing both molecules of the asymmetric unit. Bound compound **3** molecules are represented as sticks. Chain A is shown in green/light blue and chain B in light green/blue.

(B) X-ray structure of DNMT2Δ47-compound **3** chain A depicted as cartoon (green) with compound **3** as spheres (carbon atoms in light blue).

(C) The crystal structure of human DNMT2Δ47 (PDB 1G55) as cartoon (yellow) with bound SAH as spheres (carbon atoms in gray) is given for comparison.

3 form hydrogen bonds with the side chains of N120 and N375. Due to different side chain conformations in chain B, $R95_B$ forms an additional hydrogen bond to this part of compound $\mathbf{3}_B$, and $N281_A$ and $E302_A$ are in non-polar contact with compound $\mathbf{3}_B$. The molecular surface representations of the ligand binding site colored by hydrophobicity (Figure 4B) and electrostatic potential (Figure 4C) show a clear correlation with the properties of the individual moieties of the bound ligand, e.g., the binding of the ethylbenzene moiety to a hydrophobic patch and the interaction of the carbonyl groups with a highly positive patch.

In order to analyze the structural rearrangements induced by compound **3** upon binding to DNMT2Δ47, we created a local superposition with DNMT2Δ47-SAH onto the central β-sheet of the large domain, namely onto β3 to β7. As depicted in Figure 4D, the largest local movement upon binding of compound **3** is observed in the loop following β4 (M75 to P78), where P77 and P78 are rotated and shifted toward the SAH binding site. Additionally, subsequent residues could be built in both complexes with compound **3** (A: C79–F82; B: C79–I87), whereas in DNMT2Δ47-SAH, residues 79 to 96 are not resolved. Binding of compound **3** shifts residues into the SAH binding pocket. Moreover, the active site residue C79 is now resolved and moved into the SAH binding region. The superposition depicted in Figure 4D shows that binding of compound **3** narrows the active site, which prohibits SAH binding due to steric hindrance by P77, P78, and C79. As a consequence, compound **3** acts as an allosteric inhibitor by reshaping the active site.

Structure-activity study leads to structural optimization of hit compound 3

As the next step, we aimed to increase the affinity of the DEL hits to generate a cellularly effective DNMT2 modulator. Compound **3** was chosen for structure-activity-relationship studies (SAR) due to its favorable binding characteristics observed in ITC, MST, and ^{3}H-based enzyme assays. Its suitability for SAR investigation was enhanced by the feasibility of conducting solid-phase peptide synthesis (SPPS) to generate a diverse ligand analog set. A major advantage for compound **3** optimization is given by the elucidated crystal structure, which allows rational considerations for improving ligand interactions in the DNMT2 inhibitors design. First, a computational SeeSAR analysis of the ligand binding pose was performed, which provided information on putative approaches for ligand optimization (Figure S21).[52]

iScience
Article

CellPress
OPEN ACCESS

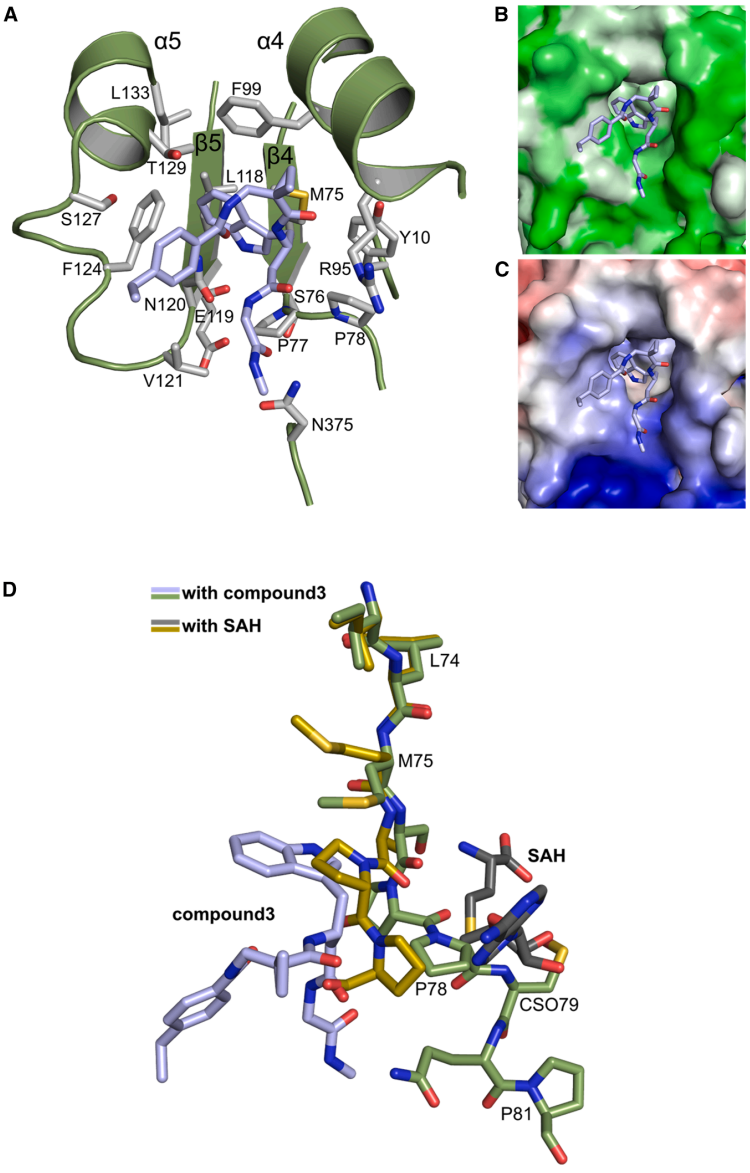


Figure 4. Ligand-protein interactions of compound 3

(A–C) (A) A detailed view of compound **3** (carbon atoms in light blue) bound to DNMT2Δ47 chain A (green cartoon) with interacting protein side chains in light gray. Side chains of chain B are omitted for clarity. Molecular surface representation of the binding site with compound **3** colored by (B) hydrophobicity (white -> green = high -> low) and (C) electrostatic potential from −5 kT/e (red) to +5 kT/e (blue).

(D) Superposition of compound **3**- & SAH-binding protein segments. Local superposition onto the central β-sheet in the large domain of DNMT2Δ47-compound **3** (green/light blue) with DNMT2Δ47-SAH (yellow/gray) showing the end of β4 and following residues with respective ligands. Residues P77, P78, and C79 are shifted toward the SAH binding site upon compound **3** binding.

The following hypotheses on the ligand binding characteristics were derived from this computer-assisted analysis: Most atoms of ligand **3** are already optimally positioned for interaction with the DNMT2 protein (green spheres). A few atoms that are assumed to have an unfavorable effect on the DNMT2 interaction (red spheres of the BB2 and BB3 carbonyl oxygens) cannot be exchanged without the loss of the characteristic U-shaped ligand. In conclusion, we hypothesized that modification to the peptide backbone would lead to a significant loss of binding affinity. The peptide backbone's dihedral angles are mostly in optimal shape for BB3 and BB4 but show minor potential for improvement in BB1 and BB2. Interestingly, there are three regions in the ligand binding pose that allow ligand expansion (gray shading) and thus enable additional potentially beneficial interactions. These regions are localized (1) between BB1 and the C-terminus, which may allow ligand macrocyclization, (2) in the homotryptophan residue 5-position, and (3) near the BB2 cyclopropyl motif. These regions were to be investigated by substitutions and scaffold-hopping strategies in the SAR study. Subsequently, a total of 40 derivatives derived from hit compound **3** were synthesized and screened for DNMT2 binding using the MST assay at a final ligand concentration of 100 μM. If significant binding to DNMT2 was measured (>25% FTAD displacement), the binding affinity was determined by following ITC experiments. A comprehensive overview of compound and assay data can be found in Table S1.

During this SAR study all building block positions (BB1–BB4) were systematically varied: For the BB1 variation (4-ethylbenzoyl), it was observed that the alkyl chain at the phenyl ring's *para* position was replaceable, still resulting in significant binding affinities. Notably, the presence of a (rigidized) alkyne group in this position resulted in the complete DNMT2 binding abolition. Furthermore, substitutions other than the *para* position, as well as the aromatic moiety's absence, failed to sustain ligand affinity. Next, we observed that any BB2 substitution, shortening, or decyclization of cyclopropyl-β-alanine was also not tolerated, highlighting the critical necessity of this special β-amino acid. For the BB3 substitution (β-homo-tryptophan), all attempts to

CellPress
OPEN ACCESS

iScience
Article

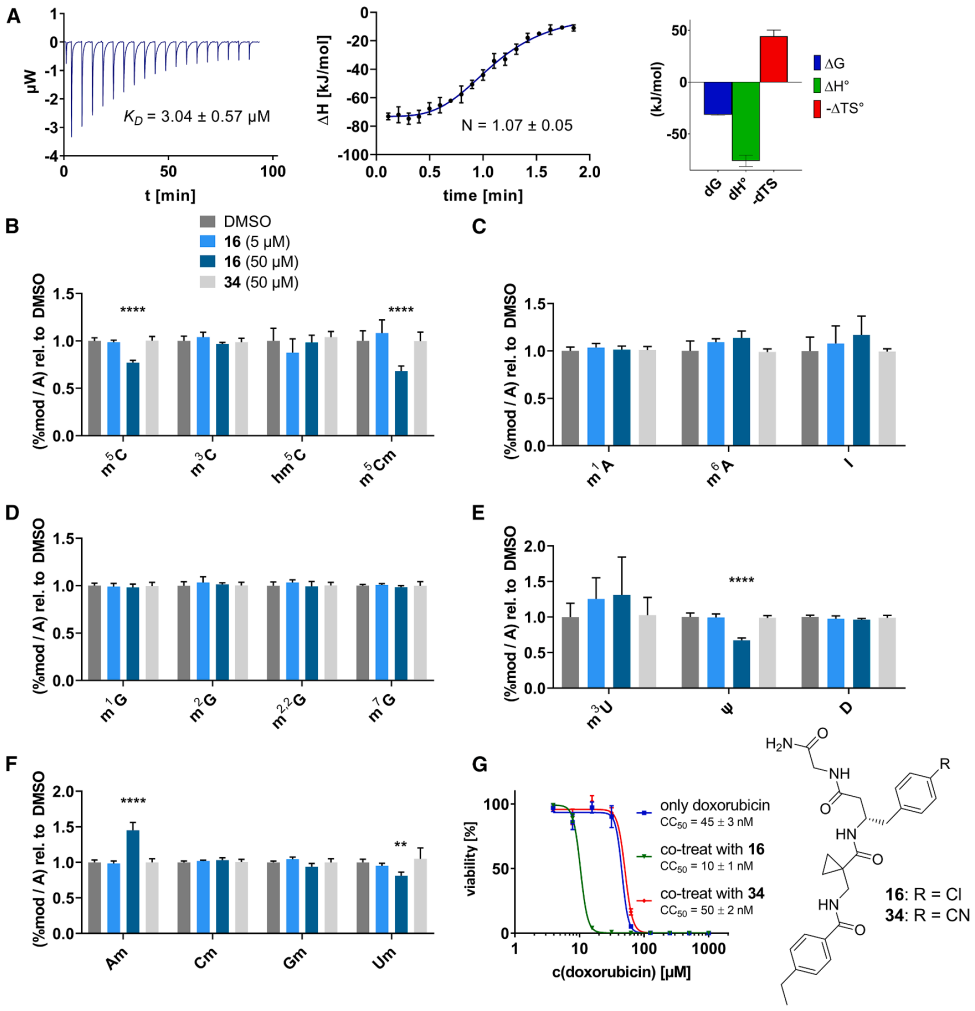


Figure 5. Biophysical and cellular evaluation of SAR study's most potent compound 16

(A) Compound **16** showed a K_D = 3.04 ± 0.57 µM in ITC experiments.

(B) MOLM-13 cells were treated for 72 h with compound **16** (5 and 50 µM) or **34** (50 µM). $tRNA^{Asp-GTC}$, $tRNA^{Val-AAC}$, and $tRNA^{Gly-GCC}$ were enriched by an antisense pull-down strategy. LC-MS/MS-based assay results for cellular tRNA modification changes analysis. Changes in cytosine modifications relative to the DMSO control.

(C) Changes in adenine modifications relative to the DMSO control.

(D) Changes in guanine modifications relative to DMSO control.

(E) Changes in uridine modifications relative to DMSO control.

(F) Changes in 2′*O*-methylations relative to the DMSO control. *$p < 0.05$, **$p < 0.01$, ***$p < 0.001$, ****$p < 0.0001$.

(G) Dose-response curves from cell viability assays of doxorubicin/compound **16** resp. **34** co-treated MOLM-13 cells. Cells were cultured for two passages of each three days in the presence of compound **16** or **34** (50 µM) and subsequently treated with varying concentrations of doxorubicin for 48 h. Data are represented as mean ± SEM. Supplementary cell viability assays can be found in Figure S9.

shorten the peptide backbone, altering the stereochemistry, and most tryptophan ring system replacements yielded no binding to DNMT2. However, replacement with the phenyl-containing analog (β-homo-(*R*)-phenylalanine, (**14**)) resulted in significant binding. Subsequent synthesis of diverse *para*-substituted derivatives showed improved binding affinity compared to parent compound **3**, which could be confirmed by subsequent dose-response MST and ITC experiments (K_D(**16**) = 3.04 ± 0.57 µM, Figure 5A). When substituting BB4 (glycine), extending the peptide backbone, or exchanging with either (*R*)- and (*S*)-alanine,

iScience
Article

CellPress
OPEN ACCESS

BB4 derivates showed significantly lower DNMT2 affinities. Interestingly, amide group methylation between BB1 to BB4, yielded no significant ligand affinity to DNMT2. As an exception, the peptide C-terminus methylation among other modifications (see also probes **6** and **8**) did not disturb the ligand affinity, and thus, represented a potential exit vector from the DNMT2 pocket suitable for ligand conjugation.

In summary, our experimental SAR is a major confirmation of the SeeSAR hypotheses and agrees well with the crystal structure's ligand pose. The BB3 replacement from β-homo-(*R*)-tryptophane (**3**) to β-homo-(*R*)-(4-chloro)phenylalanine (**16**) led to an improvement in ligand affinity, while most other modifications resulted in similar or lower ligand affinities. Since peptidomimetic drugs might be prone to cellular permeability issues, hit compound **3** and the most potent ligands **10**, **14**, **16**, **47**, and **54** were tested for passive membrane transport using a parallel artificial membrane permeation assay (PAMPA). While compounds **3**, **10**, **14**, **47**, and **54** failed to pass through the artificial membrane, compound **16** showed moderate passive permeability (P_{app} = 0.3 10^{-6} cm/s), rendering this compound as the most promising lead structure of this SAR optimization. Detailed PAMPA results can be found in the supporting information (Table S2). Overall, compound **16** showed the best ligand binding properties, and it also demonstrated the ability for passive membrane transport in the PAMPA, making it a promising candidate for cellular studies of DNMT2 inhibition.

Cellular potency of allosteric inhibitors targeting DNMT2

Next, we aimed to investigate whether compound **16** can affect enzymatic DNMT2 activity in a cellular context and is thus able to reduce RNA modification contents in living systems. Previously, DNMT2$^{-/-}$ mice were found to have reduced m^{5}C levels in corresponding tRNAs (tRNA$^{Asp-GTC}$, tRNA$^{Val-AAC}$, and tRNA$^{Gly-GCC}$), while only the double-knockout (DNMT2$^{-/-}$ & NSUN2$^{-/-}$) mutant resulted in a complete m^{5}C elimination in tRNA substrates of DNMT2.[13] Further experiments utilizing siRNA-mediated DNMT2 knockdown and chemical inhibition with the pan-DNMT/NSUN inhibitor azacitidine in leukemia cells demonstrated a total C38 methylation loss.[53,54] Following these observations, we aimed to investigate whether **16** can reduce m^{5}C modification levels in cells through isoacceptor-specific enrichment of DNMT2 tRNA substrates and modification analysis by means of an LC-MS/MS-based assay. In this regard, following previous studies investigating DNMT2's role in leukemia cells,[54,55] we treated MOLM-13 cells with **16** (5 and 50 μM) for 72 h, followed by the isolation of isoacceptor-specific tRNAs using biotinylated antisense DNA oligomers on magnetic beads. LC-MS/MS-based analysis of digested total tRNA isolates was used to determine relative changes in modification levels of 18 abundant tRNA modifications.[56]

As shown in Figure 5, levels of targeted tRNA modifications (m^{5}C and m^{5}Cm) were significantly reduced when MOLM-13 cells were treated with 50 μM of compound **16**. In this regard, the m^{5}C reduction (~25%) is in agreement with previous knock-down experiments, highlighting that 75% of tRNA m^{5}C are mediated by NSUNs.[13] Notably, treatment with 5 μM of compound **16** was found to be too low to stimulate any significant change in RNA modifications, probably due to its moderate cell permeability and proportionally lower cellular concentration. In addition, only minor other modification changes were observed, including mildly reduced pseudouridine and Um levels resp. slightly increased Am levels, highlighting our inhibitor chemotype's DNMT2-selectivity. The origin of those off-target RNA modification alterations remains not entirely solved, but we speculate that RNA-modifying enzymes introducing those modifications are likely to be regulated by DNMT2-mediated m^{5}C modification, rendering them as hierarchical-type modifications.[57] In contrast, treatment of MOLM-13 cells with a tailor-made chemical negative control compound **34**, which does not bind DNMT2, showed, as expected, no reduction of m^{5}C in tRNA (Figures 5B–5F).

To confirm that our lead compound **16** successfully engages DNMT2 in the MOLM-13 cellular environment, we performed cellular thermal shift assays (CETSA) with compounds **16** (cell-active) and **3** (non-permeable control). As expected, we found thermal stabilization of DNMT2 in the CETSA assay after incubation with 50 μM of **16**, whereas no thermal stabilization occurred in a comparable experiment with compound **3** (Figures 6A and 6B). We conclude that our lead structure **16** engaged DNMT2 in MOLM-13 cells and that m^{5}C inhibition is likely mediated by DNMT2 inhibition.

Compound **3**, on the other hand, did not lead to effective DNMT2 engagement due to its lack of passive permeability (Table S2). Based on predictions from Molinspiration and SuperCypPred toolkits, cell-evaluated compounds **3**, **16**, and **34** display highly similar physicochemical profiles, suggesting no significant differences in their expected pharmacokinetic profile (Table S4). The values for molecular weight, topological polar surface area (TPSA), logP, hydrogen bond donors and acceptors, as well as the number of rotatable bonds are all similar. The compounds comply with Lipinski's Rule of Five, except for compound **3**, which violates one parameter (molecular weight >500 Da). According to SuperCypPred predictions, compounds **3** and **16** are inactive against all tested CYP isoforms except CYP3A4, while compound **34** shows no predicted CYP activity (Figure S23). In principle, these findings are in line with our expectations based on research in the literature: The DNMT2 inhibitors presented in this study belong to the class of ''peptidomimetics with non-natural amino acids'', which are known to be limited in their passive permeability, but have good proteolytic and metabolic stability.[58] From the combined results, including the CETSA assay results and the *in vitro* permeability studies (PAMPA), we conclude that only compound **16** but not compound **3** is permeable and that this permeability difference is the reason for the different cellular activities.

Since the genetic DNMT2 knockdown leads only to minor morphological changes in healthy and cancer cells, but the use of the FDA-approved pan-DNMT/NSUN inhibitor azacitidine is an effective cytostatic drug in leukemic cells, the question of whether DNMT2 is a cell viability-affecting drug target for cancer has been discussed for years.[59] We therefore investigated the effect of the DEL hit compounds **1**–**5** and **16** on the cell viability of a diverse panel of cancer cell lines (MOLM-13, HCT, Huh-7, and MDA-MB-231) and one non-cancerous cell line (HEK293)

CellPress
OPEN ACCESS

iScience
Article

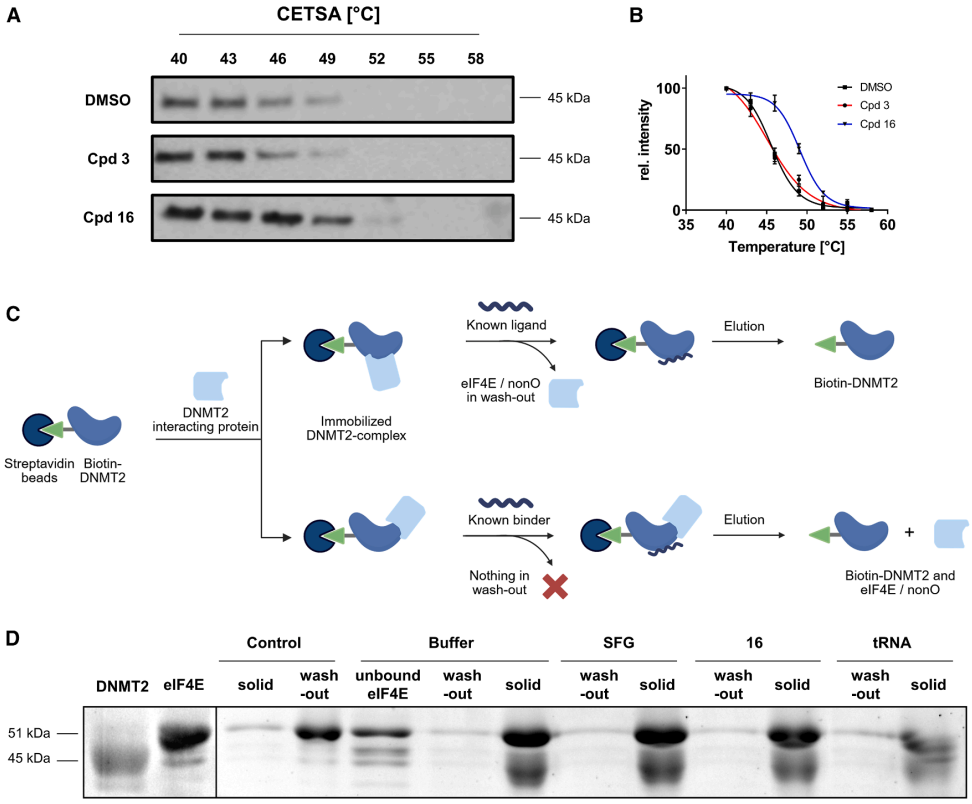


Figure 6. Investigation of allosteric DNMT2 interaction profiles and target engagement

(A) Cellular thermal shift assay (CETSA) to evaluate the DNMT2 target engagement of compounds **3** and **16** in MOLM-13 cells. Uncropped Western blots can be found in Figure S22.

(B) Densitometric analysis of CETSA Western blots highlights the stabilization of DNMT2 in the presence of compound **16** (50 μM) but not compound **3**.

(C) Pull-down competition assay workflow. Biotinylated DNMT2 was immobilized on magnetic streptavidin beads and incubated with recombinant eIF4E protein. Subsequent treatment with the known ligands sinefungin (SFG), compound **16**, or $tRNA^{Asp}$ was used to examine if such ligands can dissociate the DNMT2-eIF4E interaction.

(D) Results of the SDS-PAGE-based analysis. Lane description from left to right: DNMT2/eIF4E: recombinant proteins for size comparison. References were applied at another gel position and merged in this figure; Control: beads without immobilized DNMT2 served as the negative control, i.e., on these beads no binding of eIF4E was observed. Treatment (buffer, SFG, **16**, tRNA): The lane "unbound eIF4E" contains the supernatant after the immobilization of eIF4E, which showed low protein levels, thus, most eIF4E is effectively immobilized on DNMT2 beads. Lanes labeled with (wash-out) contain the supernatant of the respective treatment conditions (buffer, 100 μM SFG, 100 μM **16**, 10 μM $tRNA^{Asp}$), while bands labeled with (solid) contain the solid fraction obtained by boiling the residual beads in Laemmli buffer. Data are represented as mean ± SEM. Uncropped PAGE images can be found in Figure S22.

and compared it with the effect of azacitidine (Figure S9).[54,55] Using an ATP-quantifying cell viability assay, after treatment with varying concentrations of test compounds for 48 h, triazines (**1** and **2**) exhibited cellular toxicity only at concentrations >100 μM, while the peptidomimetic hit compounds (**3**–**5** and **16**) showed only slight reduction in cell viability even at high micromolar concentrations. This suggests that viability is not affected due to DNMT2 inhibition since 50 μM of **16** leads to an efficient m^5C level reduction in MOLM-13 cells. This is further supported by cell viability experiments in HCT mutant cells, including the investigation of HCT DNMT2 knock-down and HCT NSUN2 knock-down cell lines, highlighting low toxicity of all peptidomimetic compounds at 100 μM. From these cell-based investigations, we conclude that the cytotoxic effect of azacitidine (CC_{50} < 10 μM in all cell lines) is not a cause of DNMT2 inhibition but is mediated by DNMT1/3 and NSUNs inhibition. In summary, our DNMT2 inhibitor **16** is well capable of reducing tRNA m^5C levels in a cellular context, but at the same time not reducing the cell viability of cancer cells.

However, it is known from previous publications that a genetic DNMT2 knockdown makes cancer cells more vulnerable to chemotherapeutic treatment with doxorubicin on cancer cell lines.[60] Hence, we exposed selected cell lines to a co-treatment with compound **16** (50 μM) and a variable dose of doxorubicin to

iScience
Article

CellPress
OPEN ACCESS

analyze cell viability using the viability assay described above. Cultivation of MOLM-13, Huh-7 and MDA-MB-231 cells in the presence of 50 μM compound **16** for two passages of three days each led to no observable reduction in cellular viability but made the cells more susceptible to the subsequent treatment with doxorubicin (Figure 5G; Figures S9H and S9I). As expected, co-treatment with the tailor-made negative control **34** (50 μM) did not lead to a synergistic reduction in viability.

Known DNMT2-interacting proteins do not bind to the allosteric pocket

The discovery of allosteric DNMT2 modulators mediating cellular m^5C reduction implicates the question of whether this allosteric pocket may play a role in the cellular regulation of DNMT2 activity. The peptidomimetic structure of the identified hit compounds **3**–**5** might hint at a putative protein-based endogenous ligand, but so far, no allosteric DNMT2 interaction partners have been reported to regulate the enzymatic function. Yet, it was previously found by immunoprecipitation and peptide fingerprinting experiments that human DNMT2 shows interaction with a handful of cellular proteins, which are involved in RNA processing and stress response, including eIF4E, splicing factors NonO resp. SfpQ, and proteins involved in RNA transport.[20] However, it is unknown in which conformation these proteins bind to DNMT2 and whether these can influence DNMT2 activity.

To study a potential connection to our elucidated allosteric pocket, we probed the interaction between recombinant eIF4E resp. NonO proteins and DNMT2 by means of a pull-down competition assay. In this regard, we immobilized biotinylated DNMT2 on streptavidin-coated magnetic beads and incubated with recombinant eIF4E or NonO, which are able to bind to DNMT2. Subsequent treatment with the established DNMT2 ligands sinefungin (100 μM), compound **16** (100 μM), or $tRNA^{Asp}$ (10 μM) was used to analyze if those ligands are able to dissociate the complex between eIF4E/NonO and DNMT2. SDS-PAGE analysis of the pulled-down fractions, including the separated beads (solid) and supernatants (wash-out) revealed that NonO and eIF4E show efficient binding to DNMT2 on magnetic beads but do not bind to the unfunctionalized beads (Figures 6C and 6D; Figure S16), confirming the reports these proteins are in fact DNMT2 interacting proteins. Yet, neither NonO nor eIF4E could be displaced from binding to immobilized DNMT2 by competitive treatment with compound **16**, sinefungin (SFG), or $tRNA^{Asp}$, indicating that both NonO and eIF4E do not bind to the cryptic allosteric binding pocket identified. We hypothesize that both proteins might bind to a distinctive epitope outside of the MTase active site and reject the hypothesis that the identified allosteric pocket is an endogenous binding site at least for these known DNMT2 interacting proteins.

To summarize this study, our DEL screening successfully identified compounds that target a cryptic allosteric pocket of DNMT2, inducing a conformational change that blocks the SAH-binding active site and leads to subsequent DNMT2 inhibition. In-depth characterization of biomolecular interactions and the development of fluorescent DNMT2 probes revealed that this ligand chemotype showed strong selectivity for DNMT2 within the DNMT/NSUN family. The DNMT2-compound **3** crystal structure revealed the unique inhibitor binding mode causing an active site loop displacement. Synthetic structure-activity relationship studies were performed to improve the affinity of the allosteric ligand, which led to the discovery of a lead compound (K_D~3 μM) with improved passive cell permeability and the ability to inhibit DNMT2 in a cellular context, as demonstrated by reduced tRNA m^5C content. By this, we could also confirm that selective chemical DNMT2 inhibition is not affecting cell viability in different DNMT2-insensitive cells, but co-treatment with doxorubicin can inhibit MOLM-13 proliferation synergistically. In summary, allosteric inhibition of DNMT2 could be a potential target for a synergistic cancer treatment strategy.

Limitations of the study

The physiological role of the ligand-induced conformational change remains partly unelucidated and will need further experimentation (e.g., the question of whether this allosteric pocket may play a role in the cellular regulation of DNMT2 activity) and the comprehensive assessment of potential non-m^5C MTase off-targets. Furthermore, the elucidation of ternary DNMT2-tRNA-SAH resp. compound **3** complexes would strengthen the understanding of the catalytic regulation of this conformational change. Whether this type of DNMT2 inhibitor is effective in more advanced cancer assays including *in vivo* treatment should be investigated once the binding affinity to DNMT2 has been further increased and a cellular high-potent tool compound with low nanomolar potency has been achieved. The double-digit micromolar concentrations needed for cellular m^5C reduction will leave room for improvement in future inhibitor designs. This could be attempted in the future by developing a compound **3**-based PROTAC, macrocyclization, or the development of covalent inhibitor conjugates, etc.

RESOURCE AVAILABILITY

Lead contact

Further information and requests for resources and reagents should be directed to and will be fulfilled by the lead contact, Fabian Barthels (barthels@uni-mainz.de).

Materials availability

Molecules generated in this study are available from the lead contact upon request and completion of an MTA. DNMT2Δ47 containing plasmid for recombinant protein expression has been deposited to Addgene: #198382.

Data and code availability

- Coordinates and structure factors of the DNMT2Δ47-compound **3** complex are deposited at the Protein DataBank PDB under accession code 9HGM.
- This paper does not report original code. All software and algorithms are listed in the key resources table.
- Any additional information required to analyze the data reported in this paper is available from the lead contact upon request.

ACKNOWLEDGMENTS

We thank Francesca Tuorto (Heidelberg) for providing NSUN2 knock-down cell lines, Ganna Podoprygorina (Mainz) for support during LC/MS measurements, WuXi AppTec for support during sequencing and data analysis of the

CellPress
OPEN ACCESS

iScience
Article

DEL screenings, Hanna Bodenstaff (Mainz) for support during the synthesis of the inhibitors, Karin Pauly (Mainz) for support during cell viability assays, and Michael Klein (Mainz) for support during the preparation of Biorender illustrations. We acknowledge access to ESRF Grenoble beamline ID30B and thank the ESRF staff for their support. We thank Claudia Siegmann from the CCTP/BZH crystallization platform for excellent technical support. F.B. acknowledges the support from TRR319 (Project-ID 439669440) TP A01. I.S., M.S., and J.K. acknowledge the service SDS@hd supported by the Ministry of Science, Research and Arts Baden-Württemberg and the DFG through grants INST 35/1314-1 FUGG, INST 35/1503-1 FUGG. Financial support by the Deutsche Forschungsgemeinschaft via TRR319 (Project-ID 439669440) B03 to I.S. and TP C01 to M.H. is gratefully acknowledged.

AUTHOR CONTRIBUTIONS

A.F.F. performed DEL panning, analysis of hit clustering data, hit selection, microscale thermophoresis, ^{3}H-assays, FP assays, synthesis of compounds, SeeSAR analysis, and writing of the manuscript; M.S. performed cloning, expression, purification, and characterization of DNMT2Δ47, protein crystallization, data collection, model building, and writing of the manuscript; A.C.W. performed ITC measurements, and cell cultivation; V. K. performed synthesis, MST measurements, AS-MS assay, and pull-down assays; J.K. performed protein crystallization, data collection, model building, and writing of the manuscript; Z.N. performed protein expression and tRNA preparation; R.A.Z. performed protein expression and developed the idea for DNMT2Δ47 mutant; L.G. performed cell viability assays and tRNA LC/MS sample preparation; C.Z. performed PAMPA; M.J. performed cell viability assays; K.F. performed concept of study, supervision, and writing of the manuscript; M.H. performed concept of study, supervision, and writing of the manuscript; I.S. performed concept of study, supervision, data analysis, and writing of the manuscript; F.B. performed concept of study, supervision, and writing of the manuscript. All authors commented on the manuscript.

DECLARATION OF INTERESTS

Mark Helm is a consultant for Moderna Inc.

STAR★METHODS

Detailed methods are provided in the online version of this paper and include the following:

- KEY RESOURCES TABLE
- METHOD DETAILS
  - DEL screening
  - Microscale thermophoresis (MST)
  - Isothermal titration calorimetry (ITC)
  - Fluorescence polarization (FP)
  - ^{3}H-based methyltransferase enzyme activity assays
  - Affinity selection-mass spectrometry (AS-MS)
  - Electrophoretic mobility shift assay (EMSA)
  - *In vitro* permeability assay (PAMPA)
  - Protein and tRNA production
  - DNMT2 cloning, expression, and purification for co-crystallization
  - Analytical size-exclusion chromatography of DNMT2Δ47 with compound **3**
  - Crystallization, data collection, model building, and refinement
  - SeeSAR analysis
  - Pull-down DNMT2 interaction assay
  - tRNA modification analysis by LC/MS
  - Cell viability assays
  - Cellular thermal shift assay (CETSA)
  - Synthesis and characterization of inhibitors and probes
- QUANTIFICATION AND STATISTICAL ANALYSIS

SUPPLEMENTAL INFORMATION

Supplemental information can be found online at https://doi.org/10.1016/j.isci.2025.113300.

Received: April 23, 2025
Revised: June 19, 2025
Accepted: August 1, 2025
Published: August 5, 2025

REFERENCES

1. Fischer, T.R., Meidner, L., Schwickert, M., Weber, M., Zimmermann, R.A., Kersten, C., Schirmeister, T., and Helm, M. (2022). Chemical biology and medicinal chemistry of RNA methyltransferases. Nucleic Acids Res. *50*, 4216–4245. https://doi.org/10.1093/nar/gkac224.
2. Schubert, H.L., Blumenthal, R.M., and Cheng, X. (2003). Many paths to methyltransfer: a chronicle of convergence. Trends Biochem. Sci. *28*, 329–335. https://doi.org/10.1016/S0968-0004(03)00090-2.
3. Schwickert, M., Fischer, T.R., Zimmermann, R.A., Hoba, S.N., Meidner, J. L., Weber, M., Weber, M., Stark, M.M., Koch, J., Jung, N., et al. (2022). Discovery of Inhibitors of DNA Methyltransferase 2, an Epitranscriptomic Modulator and Potential Target for Cancer Treatment. J. Med. Chem. *65*, 9750–9788. https://doi.org/10.1021/acs.jmedchem.2c00388.
4. Schwickert, M., Zimmermann, R.A., Habeck, T., Hoba, S.N., Nidoieva, Z., Fischer, T.R., Stark, M.M., Kersten, C., Lermyte, F., Helm, M., and Schirmeister, T. (2023). Covalent S -Adenosylhomocysteine-Based DNA Methyltransferase 2 Inhibitors with a New Type of Aryl Warhead. ACS Med. Chem. Lett. *14*, 777–787. https://doi.org/10.1021/acsmedchemlett.3c00062.
5. Ahmed-Belkacem, R., Troussier, J., Delpal, A., Canard, B., Vasseur, J.-J., Decroly, E., and Debart, F. (2024). N -Arylsulfonamide-based adenosine analogues to target RNA cap N 7-methyltransferase nsp14 of SARS-CoV-2. RSC Med. Chem. *15*, 839–847. https://doi.org/10.1039/D3MD00737E.
6. Goll, M.G., Kirpekar, F., Maggert, K.A., Yoder, J.A., Hsieh, C.L., Zhang, X., Golic, K.G., Jacobsen, S.E., and Bestor, T.H. (2006). Methylation of tRNAAsp by the DNA methyltransferase homolog Dnmt2. Science *311*, 395–398. https://doi.org/10.1126/science.1120976.
7. Rai, K., Chidester, S., Zavala, C.V., Manos, E.J., James, S.R., Karpf, A.R., Jones, D.A., and Cairns, B.R. (2007). Dnmt2 functions in the cytoplasm to promote liver, brain, and retina development in zebrafish. Genes Dev. *21*, 261–266. https://doi.org/10.1101/gad.1472907.
8. Bohnsack, K.E., Höbartner, C., and Bohnsack, M.T. (2019). Eukaryotic 5-methylcytosine (m5C) RNA Methyltransferases: Mechanisms, Cellular Functions, and Links to Disease. Genes *10*, 102. https://doi.org/10.3390/genes10020102.
9. Schaefer, M., Pollex, T., Hanna, K., Tuorto, F., Meusburger, M., Helm, M., and Lyko, F. (2010). RNA methylation by Dnmt2 protects transfer RNAs against stress-induced cleavage. Genes Dev. *24*, 1590–1595. https://doi.org/10.1101/gad.586710.
10. Muller, S., Windhof, I.M., Maximov, V., Jurkowski, T., Jeltsch, A., Forstner, K.U., Sharma, C.M., Graf, R., and Nellen, W. (2013). Target recognition, RNA methylation activity and transcriptional regulation of the Dictyostelium discoideum Dnmt2-homologue (DnmA). Nucleic Acids Res. *41*, 8615–8627. https://doi.org/10.1093/nar/gkt634.
11. Lyko, F. (2018). The DNA methyltransferase family: a versatile toolkit for epigenetic regulation. Nat. Rev. Genet. *19*, 81–92. https://doi.org/10.1038/nrg.2017.80.
12. Jeltsch, A., Ehrenhofer-Murray, A., Jurkowski, T.P., Lyko, F., Reuter, G., Ankri, S., Nellen, W., Schaefer, M., and Helm, M. (2017). Mechanism and biological role of Dnmt2 in Nucleic Acid Methylation. RNA Biol. *14*, 1108–1123. https://doi.org/10.1080/15476286.2016.1191737.

13. Tuorto, F., Liebers, R., Musch, T., Schaefer, M., Hofmann, S., Kellner, S., Frye, M., Helm, M., Stoecklin, G., and Lyko, F. (2012). RNA cytosine methylation by Dnmt2 and NSun2 promotes tRNA stability and protein synthesis. Nat. Struct. Mol. Biol. *19*, 900–905. https://doi.org/10.1038/nsmb.2357.

14. Tuorto, F., Herbst, F., Alerasool, N., Bender, S., Popp, O., Federico, G., Reitter, S., Liebers, R., Stoecklin, G., Gröne, H.J., et al. (2015). The tRNA methyltransferase Dnmt2 is required for accurate polypeptide synthesis during haematopoiesis. EMBO J. *34*, 2350–2362. https://doi.org/10.15252/embj.201591382.

15. Lewinska, A., Adamczyk-Grochala, J., and Wnuk, M. (2023). TRDMT1-mediated RNA C-5 methylation as a novel target in anticancer therapy. Biochim. Biophys. Acta. Rev. Cancer *1878*, 188964. https://doi.org/10.1016/j.bbcan.2023.188964.

16. Towns, W.L., and Begley, T.J. (2012). Transfer RNA Methytransferases and Their Corresponding Modifications in Budding Yeast and Humans: Activities, Predications, and Potential Roles in Human Health. DNA Cell Biol. *31*, 434–454. https://doi.org/10.1089/dna.2011.1437.

17. Li, L., and Wang, S. (2017). DNA methyltransferase (DNMTs) expression in cervical cancer tissues and its relationship with HPV infection and tumor malignancy. J. Hainan Med. Univ. *23*, 136–139.

18. Lewinska, A., Adamczyk-Grochala, J., Kwasniewicz, E., Deregowska, A., Semik, E., Zabek, T., and Wnuk, M. (2018). Reduced levels of methyltransferase DNMT2 sensitize human fibroblasts to oxidative stress and DNA damage that is accompanied by changes in proliferation-related miRNA expression. Redox Biol. *14*, 20–34. https://doi.org/10.1016/j.redox.2017.08.012.

19. Zhang, Y., Zhang, X., Shi, J., Tuorto, F., Li, X., Liu, Y., Liebers, R., Zhang, L., Qu, Y., Qian, J., et al. (2018). Dnmt2 mediates intergenerational transmission of paternally acquired metabolic disorders through sperm small non-coding RNAs. Nat. Cell Biol. *20*, 535–540. https://doi.org/10.1038/s41556-018-0087-2.

20. Thiagarajan, D., Dev, R.R., and Khosla, S. (2011). The DNA methyltranferase Dnmt2 participates in RNA processing during cellular stress. Epigenetics *6*, 103–113. https://doi.org/10.4161/epi.6.1.13418.

21. Zimmermann, R.A., Fischer, T.R., Schwickert, M., Nidoieva, Z., Schirmeister, T., and Kersten, C. (2023). Chemical Space Virtual Screening against Hard-to-Drug RNA Methyltransferases DNMT2 and NSUN6. Int. J. Mol. Sci. *24*, 6109. https://doi.org/10.3390/ijms24076109.

22. Loenen, W.A.M. (2006). S -Adenosylmethionine: jack of all trades and master of everything? Biochem. Soc. Trans. *34*, 330–333. https://doi.org/10.1042/BST0340330.

23. Fontecave, M., Atta, M., and Mulliez, E. (2004). S-adenosylmethionine: nothing goes to waste. Trends Biochem. Sci. *29*, 243–249. https://doi.org/10.1016/j.tibs.2004.03.007.

24. Grillo, M.A., and Colombatto, S. (2008). S-adenosylmethionine and its products. Amino Acids *34*, 187–193. https://doi.org/10.1007/s00726-007-0500-9.

25. Petrossian, T.C., and Clarke, S.G. (2011). Uncovering the Human Methyltransferasome. Mol. Cell. Proteomics *10*, M110.000976.000976. https://doi.org/10.1074/mcp.M110.000976.

26. Yuen, L.H., and Franzini, R.M. (2017). Achievements, Challenges, and Opportunities in DNA-Encoded Library Research: An Academic Point of View. Chembiochem *18*, 829–836. https://doi.org/10.1002/cbic.201600567.

27. Goodnow, R.A., Dumelin, C.E., and Keefe, A.D. (2017). DNA-encoded chemistry: enabling the deeper sampling of chemical space. Nat. Rev. Drug Discov. *16*, 131–147. https://doi.org/10.1038/nrd.2016.213.

28. Satz, A.L., Brunschweiger, A., Flanagan, M.E., Gloger, A., Hansen, N.J.V., Kuai, L., Kunig, V.B.K., Lu, X., Madsen, D., Marcaurelle, L.A., et al. (2022). DNA-encoded chemical libraries. Nat. Rev. Methods Primers *2*, 3. https://doi.org/10.1038/s43586-021-00084-5.

29. Franzini, R.M., and Randolph, C. (2016). Chemical Space of DNA-Encoded Libraries. J. Med. Chem. *59*, 6629–6644. https://doi.org/10.1021/acs.jmedchem.5b01874.

30. Collie, G.W., Clark, M.A., Keefe, A.D., Madin, A., Read, J.A., Rivers, E.L., and Zhang, Y. (2024). Screening Ultra-Large Encoded Compound Libraries Leads to Novel Protein–Ligand Interactions and High Selectivity. J. Med. Chem. *67*, 864–884. https://doi.org/10.1021/acs.jmedchem.3c01861.

31. Brenner, S., and Lerner, R.A. (1992). Encoded combinatorial chemistry. Proc. Natl. Acad. Sci. USA *89*, 5381–5383. https://doi.org/10.1073/pnas.89.12.5381.

32. Peterson, A.A., and Liu, D.R. (2023). Small-molecule discovery through DNA-encoded libraries. Nat. Rev. Drug Discov. *22*, 699–722. https://doi.org/10.1038/s41573-023-00713-6.

33. Ma, P., Zhang, S., Huang, Q., Gu, Y., Zhou, Z., Hou, W., Yi, W., and Xu, H. (2024). Evolution of chemistry and selection technology for DNA-encoded library. Acta Pharm. Sin. B *14*, 492–516. https://doi.org/10.1016/j.apsb.2023.10.001.

34. Gong, Z., Hu, G., Li, Q., Liu, Z., Wang, F., Zhang, X., Xiong, J., Li, P., Xu, Y., Ma, R., et al. (2017). Compound Libraries: Recent Advances and Their Applications in Drug Discovery. Curr. Drug Discov. Technol. *14*, 216–228. https://doi.org/10.2174/1570163814666170425155154.

35. Proj, M., Bozovičar, K., Hrast, M., Frlan, R., and Gobec, S. (2022). DNA-encoded library screening on two validated enzymes of the peptidoglycan biosynthetic pathway. Bioorg. Med. Chem. Lett. *73*, 128915. https://doi.org/10.1016/j.bmcl.2022.128915.

36. Dawadi, S., Simmons, N., Miklossy, G., Bohren, K.M., Faver, J.C., Ucisik, M.N., Nyshadham, P., Yu, Z., and Matzuk, M.M. (2020). Discovery of potent thrombin inhibitors from a protease-focused DNA-encoded chemical library. Proc. Natl. Acad. Sci. USA *117*, 16782–16789. https://doi.org/10.1073/pnas.2005447117.

37. Meyer, S.M., Tanaka, T., Zanon, P.R.A., Baisden, J.T., Abegg, D., Yang, X., Akahori, Y., Alshakarchi, Z., Cameron, M.D., Adibekian, A., and Disney, M.D. (2022). DNA-Encoded Library Screening To Inform Design of a Ribonuclease Targeting Chimera (RiboTAC). J. Am. Chem. Soc. *144*, 21096–21102. https://doi.org/10.1021/jacs.2c07217.

38. Chana, C.K., Maisonneuve, P., Posternak, G., Grinberg, N.G.A., Poirson, J., Ona, S.M., Ceccarelli, D.F., Mader, P., St-Cyr, D.J., Pau, V., et al. (2022). Discovery and Structural Characterization of Small Molecule Binders of the Human CTLH E3 Ligase Subunit GID4. J. Med. Chem. *65*, 12725–12746. https://doi.org/10.1021/acs.jmedchem.2c00509.

39. Ibrahim, M.T., Verkhivker, G.M., Misra, J., and Tao, P. (2023). Novel Allosteric Effectors Targeting Human Transcription Factor TEAD. Int. J. Mol. Sci. *24*, 9009. https://doi.org/10.3390/ijms24109009.

40. Su, W., Ge, R., Ding, D., Chen, W., Wang, W., Yan, H., Wang, W., Yuan, Y., Liu, H., Zhang, M., et al. (2021). Triaging of DNA-Encoded Library Selection Results by High-Throughput Resynthesis of DNA–Conjugate and Affinity Selection Mass Spectrometry. Bioconjug. Chem. *32*, 1001–1007. https://doi.org/10.1021/acs.bioconjchem.1c00170.

41. Kuai, L., O'Keeffe, T., and Arico-Muendel, C. (2018). Randomness in DNA Encoded Library Selection Data Can Be Modeled for More Reliable Enrichment Calculation. SLAS Discov. *23*, 405–416. https://doi.org/10.1177/2472555218757718.

42. Zimmermann, R.A., Schwickert, M., Meidner, J.L., Nidoieva, Z., Helm, M., and Schirmeister, T. (2022). An Optimized Microscale Thermophoresis Method for High-Throughput Screening of DNA Methyltransferase 2 Ligands. ACS Pharmacol. Transl. Sci. *5*, 1079–1085. https://doi.org/10.1021/acsptsci.2c00175.

43. Prudent, R., Annis, D.A., Dandliker, P.J., Ortholand, J.-Y., and Roche, D. (2021). Exploring new targets and chemical space with affinity selection-mass spectrometry. Nat. Rev. Chem. *5*, 62–71. https://doi.org/10.1038/s41570-020-00229-2.

44. Meidner, J.L., Frey, A.F., Zimmermann, R.A., Sabin, M.O., Nidoieva, Z., Weldert, A.C., Hoba, S.N., Krone, M.W., and Barthels, F. (2024). Nanomole Scale Screening of Fluorescent RNA-Methyltransferase Probes Enables the Discovery of METTL1 Inhibitors. Angew. Chem., Int. Ed. Engl. *63*, e202403792. https://doi.org/10.1002/anie.202403792.

45. Hammerschmidt, S.J., Barthels, F., Weldert, A.C., and Kersten, C. (2024). Advanced Isothermal Titration Calorimetry for Medicinal Chemists with ITCcalc. J. Chem. Educ. *101*, 1086–1095. https://doi.org/10.1021/acs.jchemed.3c01133.

46. Nidoieva, Z., Sabin, M.O., Dewald, T., Weldert, A.C., Hoba, S.N., Helm, M., and Barthels, F. (2025). A microscale thermophoresis-based enzymatic RNA methyltransferase assay enables the discovery of DNMT2 inhibitors. Commun. Chem. *8*, 32. https://doi.org/10.1038/s42004-025-01439-9.

47. Kallert, E., Behrendt, M., Frey, A., Kersten, C., and Barthels, F. (2023). Non-covalent dyes in microscale thermophoresis for studying RNA ligand interactions and modifications. Chem. Sci. *14*, 9827–9837. https://doi.org/10.1039/D3SC02993J.

48. Jurkowski, T.P., Shanmugam, R., Helm, M., and Jeltsch, A. (2012). Mapping the tRNA Binding Site on the Surface of Human DNMT2 Methyltransferase. Biochemistry *51*, 4438–4444. https://doi.org/10.1021/bi3002659.

49. Dong, A., Yoder, J.A., Zhang, X., Zhou, L., Bestor, T.H., and Cheng, X. (2001). Structure of human DNMT2, an enigmatic DNA methyltransferase homolog that displays denaturant-resistant binding to DNA. Nucleic Acids Res. *29*, 439–448. https://doi.org/10.1093/nar/29.2.439.

50. Krissinel, E., and Henrick, K. (2007). Inference of Macromolecular Assemblies from Crystalline State. J. Mol. Biol. *372*, 774–797. https://doi.org/10.1016/j.jmb.2007.05.022.

51. Laskowski, R.A., and Swindells, M.B. (2011). LigPlot+: Multiple Ligand–Protein Interaction Diagrams for Drug Discovery. J. Chem. Inf. Model. *51*, 2778–2786. https://doi.org/10.1021/ci200227u.

52. BioSolveIT GmbH (2024). SeeSAR Version 13.1.1 (BioSolveIT GmbH).

53. Schaefer, M., Hagemann, S., Hanna, K., and Lyko, F. (2009). Azacytidine Inhibits RNA Methylation at DNMT2 Target Sites in Human Cancer Cell Lines. Cancer Res. *69*, 8127–8132. https://doi.org/10.1158/0008-5472.CAN-09-0458.

54. Aumer, T., Gremmelmaier, C.B., Runtsch, L.S., Pforr, J.C., Yeşiltaç, G.N., Kaiser, S., and Traube, F.R. (2022). Comprehensive comparison between azacytidine and decitabine treatment in an acute myeloid leukemia cell line. Clin. Epigenet. *14*, 113. https://doi.org/10.1186/s13148-022-01329-0.

55. Noronha, N., Durette, C., Cahuzac, M., E Silva, B., Courtois, J., Humeau, J., Sauvat, A., Hardy, M.-P., Vincent, K., Laverdure, J.-P., et al. (2024). Autophagy degrades immunogenic endogenous retroelements induced by 5-azacytidine in acute myeloid leukemia. Leukemia *38*, 1019–1031. https://doi.org/10.1038/s41375-024-02250-6.

56. Thüring, K., Schmid, K., Keller, P., and Helm, M. (2016). Analysis of RNA modifications by liquid chromatography–tandem mass spectrometry. Methods *107*, 48–56. https://doi.org/10.1016/j.ymeth.2016.03.019.

57. Huang, S., Wylder, A.C., and Pan, T. (2024). Simultaneous nanopore profiling of mRNA m6A and pseudouridine reveals translation coordination. Nat. Biotechnol. *42*, 1831–1835. https://doi.org/10.1038/s41587-024-02135-0.

58. Lenci, E., and Trabocchi, A. (2020). Peptidomimetic toolbox for drug discovery. Chem. Soc. Rev. *49*, 3262–3277. https://doi.org/10.1039/D0CS00102C.

59. Li, H., Liu, H., Zhu, D., Dou, C., Gang, B., Zhang, M., and Wan, Z. (2024). Biological function molecular pathways and druggability of DNMT2/TRDMT1. Pharmacol. Res. *205*, 107222. https://doi.org/10.1016/j.phrs.2024.107222.

60. Adamczyk-Grochala, J., Bloniarz, D., Zielinska, K., Lewinska, A., and Wnuk, M. (2023). DNMT2/TRDMT1 gene knockout compromises doxorubicin-induced unfolded protein response and sensitizes cancer cells to ER stress-induced apoptosis. Apoptosis *28*, 166–185. https://doi.org/10.1007/s10495-022-01779-0.

61. Winn, M.D., Ballard, C.C., Cowtan, K.D., Dodson, E.J., Emsley, P., Evans, P.R., Keegan, R.M., Krissinel, E.B., Leslie, A.G.W., McCoy, A., et al. (2011). Overview of the CCP 4 suite and current developments. Acta Crystallogr. D Biol. Crystallogr. *67*, 235–242. https://doi.org/10.1107/S0907444910045749.

62. Liebschner, D., Afonine, P.V., Baker, M.L., Bunkóczi, G., Chen, V.B., Croll, T.I., Hintze, B., Hung, L.-W., Jain, S., McCoy, A.J., et al. (2019). Macromolecular structure determination using X-rays, neutrons and electrons: recent developments in Phenix. Acta Crystallogr. D Struct. Biol. *75*, 861–877. https://doi.org/10.1107/S2059798319011471.

63. Emsley, P., Lohkamp, B., Scott, W.G., and Cowtan, K. (2010). Features and development of Coot. Acta Crystallogr. D Biol. Crystallogr. *66*, 486–501. https://doi.org/10.1107/S0907444910007493.

64. Chen, V.B., Arendall, W.B., Headd, J.J., Keedy, D.A., Immormino, R.M., Kapral, G.J., Murray, L.W., Richardson, J.S., and Richardson, D.C. (2010). MolProbity : all-atom structure validation for macromolecular crystallography. Acta Crystallogr. D Biol. Crystallogr. *66*, 12–21. https://doi.org/10.1107/S0907444909042073.

65. Jumper, J., Evans, R., Pritzel, A., Green, T., Figurnov, M., Ronneberger, O., Tunyasuvunakool, K., Bates, R., Žídek, A., Potapenko, A., et al. (2021). Highly accurate protein structure prediction with AlphaFold. Nature *596*, 583–589. https://doi.org/10.1038/s41586-021-03819-2.

66. Banerjee, P., Dunkel, M., Kemmler, E., and Preissner, R. (2020). SuperCYPsPred—a web server for the prediction of cytochrome activity. Nucleic Acids Res. *48*, W580–W585. https://doi.org/10.1093/nar/gkaa166.

67. Simon, R.P., Winter, M., Kleiner, C., Wehrle, L., Karnath, M., Ries, R., Zeeb, M., Schnapp, G., Fiegen, D., Häbe, T.T., et al. (2021). MALDI-TOF-Based Affinity Selection Mass Spectrometry for Automated Screening of Protein–Ligand Interactions at High Throughput. SLAS Discov. *26*, 44–57. https://doi.org/10.1177/2472555220959266.

68. Zimmer, C., Brauer, J., Ferenc, D., Meyr, J., Müller, P., Räder, H.-J., Engels, B., Opatz, T., and Schirmeister, T. (2024). Substitution-Induced Mechanistic Switching in SNAr-Warheads for Cysteine Proteases. Molecules *29*, 2660. https://doi.org/10.3390/molecules29112660.

69. Bogomolovas, J., Simon, B., Sattler, M., and Stier, G. (2009). Screening of fusion partners for high yield expression and purification of bioactive viscotoxins. Protein Expr. Purif. *64*, 16–23. https://doi.org/10.1016/j.pep.2008.10.003.

70. Kabsch, W. (2010). XDS. Acta Crystallogr. D Biol. Crystallogr. *66*, 125–132. https://doi.org/10.1107/S0907444909047337.

71. Evans, P.R., and Murshudov, G.N. (2013). How good are my data and what is the resolution? Acta Crystallogr. D Biol. Crystallogr. *69*, 1204–1214. https://doi.org/10.1107/S0907444913000061.

72. McCoy, A.J., Grosse-Kunstleve, R.W., Adams, P.D., Winn, M.D., Storoni, L.C., and Read, R.J. (2007). Phaser crystallographic software. J. Appl. Crystallogr. *40*, 658–674. https://doi.org/10.1107/S0021889807021206.

73. Moriarty, N.W., Grosse-Kunstleve, R.W., and Adams, P.D. (2009). electronic Ligand Builder and Optimization Workbench (eLBOW): a tool for ligand coordinate and restraint generation. Acta Crystallogr. D Biol. Crystallogr. *65*, 1074–1080. https://doi.org/10.1107/S0907444909029436.

74. Afonine, P.V., Grosse-Kunstleve, R.W., Echols, N., Headd, J.J., Moriarty, N.W., Mustyakimov, M., Terwilliger, T.C., Urzhumtsev, A., Zwart, P.H., and Adams, P.D. (2012). Towards automated crystallographic structure refinement with phenix.refine. Acta Crystallogr. D Biol. Crystallogr. *68*, 352–367. https://doi.org/10.1107/S0907444912001308.

75. Eisenberg, D., Schwarz, E., Komaromy, M., and Wall, R. (1984). Analysis of membrane and surface protein sequences with the hydrophobic moment plot. J. Mol. Biol. *179*, 125–142. https://doi.org/10.1016/0022-2836(84)90309-7.

76. Jurrus, E., Engel, D., Star, K., Monson, K., Brandi, J., Felberg, L.E., Brookes, D.H., Wilson, L., Chen, J., Liles, K., et al. (2018). Improvements to the APBS biomolecular solvation software suite. Protein Sci. *27*, 112–128. https://doi.org/10.1002/pro.3280.

77. Yokogawa, T., Kitamura, Y., Nakamura, D., Ohno, S., and Nishikawa, K. (2010). Optimization of the hybridization-based method for purification of thermostable tRNAs in the presence of tetraalkylammonium salts. Nucleic Acids Res. *38*, e89. https://doi.org/10.1093/nar/gkp1182.

78. Kellner, S., Ochel, A., Thüring, K., Spenkuch, F., Neumann, J., Sharma, S., Entian, K.-D., Schneider, D., and Helm, M. (2014). Absolute and relative quantification of RNA modifications via biosynthetic isotopomers. Nucleic Acids Res. *42*, e142. https://doi.org/10.1093/nar/gku733.

CellPress
OPEN ACCESS

iScience
Article

STAR★METHODS

KEY RESOURCES TABLE

REAGENT or RESOURCE	SOURCE	IDENTIFIER
Bacterial and virus strains		
E. coli Rosetta 2 (DE3) pLysS cells	Merck KGaA	71403
Chemicals, peptides, and recombinant proteins		
Recombinant human DNMT2 (full-length)	Schwickert et al.[3]	N/A
Recombinant human DNMT2Δ47	Schwickert et al.[4]	N/A
Recombinant human DNMT1	ActiveMotif	31404
Recombinant human DNMT3A/3L	Schwickert et al.[3]	N/A
Recombinant human NSUN2	Schwickert et al.[3]	N/A
Recombinant human NSUN3	Schwickert et al.[3]	N/A
Recombinant human NSUN6	Schwickert et al.[3]	N/A
Recombinant human NonO	ActiveMotif	31539
Recombinant human eIF4E	Cayman Chemicals	15137
Anti-DNMT2 (rabbit)	Abcam	ab308120
IRDye 680RD Goat anti-Rabbit	LI-COR	926–68071
TEV protease	New England Biolabs	P8112S
S-adenosylhomocysteine (SAH)	Sigma-Aldrich	A9384
Sinefungin	Sigma-Aldrich	S8559
^{3}H-*S*-adenosylmethionine (SAM)	Hartmann Analytics	ART0288
S-adenosylmethionine (cold)	New England Biolabs	B9003S
L-α-phosphatidylcholine	Sigma-Aldrich	P3556
5-FAM-triazolyl-adenosyl-Dab (fluorescent DNMT2 tracer)	Zimmermann et al.[42]	FTAD
ProteOrange staining	Lumiprobe	10210
Sybr Gold nucleic acid stain	ThermoFisher	S11494
RPMI-1640 medium	ThermoFisher	11875093
McCoys's 5A medium	ThermoFisher	16600082
DMEM medium	ThermoFisher	10564011
Fetal bovine serum	ThermoFisher	12662029
Penicillin/Streptomycin	ThermoFisher	15070063
Doxorubicin	BLDpharm	BD32885
L-Glutamine	ThermoFisher	A2916801
TRIzol reagent	ThermoFisher	15596026
Nuclease P1 from Penicillium citrinum	Sigma-Aldrich	N8630
Snake venom phosphodiesterase from Crotalus adamanteus	Sigma-Aldrich	P3243
Bovine intestine phosphatase	Sigma-Aldrich	A2356
Benzonase	Sigma-Aldrich	70746
Pentostatin	Sigma-Aldrich	SML0508
Milk powder (blotting grade)	Carl-Roth	T145.3
Critical commercial assays		
DELopen screening library	WuXiAppTec	k00000664
Gold MV liquid scintillation cocktail	PerkinElmer	6013151
Cell Titer Glo assay kit	Promega	G7570

(*Continued on next page*)

Continued

REAGENT or RESOURCE	SOURCE	IDENTIFIER
ViaLight Plus Cell Proliferation and Cytotoxicity BioAssay Kit	Lonza	LT07-221
Deposited data		
Crystal structure DNMT2Δ47-compound 3 complex	This paper	PDB 9HGM
Experimental models: Cell lines		
Human MOLM-13 cells	DSMZ	ACC 554; CVCL_2119
Human HCT 116 cells	ATCC	CCL-247; CVCL_0291
Human MDA-MB-231 cells	DSMZ	ACC 732; CVCL_0062
Human Huh-7 cells	DSMZ	PTA-7435; CVCL_0336
Human HEK-293 cells	ATCC	CRL-1573; CVCL_0045
Oligonucleotides		
Human IVT $tRNA^{Asp}$-GUC	Schwickert et al.[3]	N/A
5′-GTGACAGGCGGGGATACTCACCACT-Biotin-3′	GenScript	Custom synthesis
5′-CGTGGCAGGCGAGAATTCTACCACT-Biotin-3′	GenScript	Custom synthesis
5′-CGTGTTAGGCGAACGTGATAACCACT-Biotin-3′	GenScript	Custom synthesis
Recombinant DNA		
pET-Dnmt3A3L-sc27	Addgene	Addgene_71827
pET-28a(+)-DNMT2Δ47	Addgene	Addgene_198382
pET-28a(+)-NSUN2	Addgene	Addgene_188059
pET-28a(+)-NSUN6	Addgene	Addgene_188060
Software and algorithms		
MO.Affinity Analysis 2.3	Nanotemper Technologies	https://nanotempertech.com/
PEAQ-ITC Analysis Software 1.21	MicroCal	https://www.malvernpanalytical.com/
Prism 8.0.1	GraphPad	https://www.graphpad.com/
Unicorn7	Cytiva	https://cytivalifesciences.com
CCP4 software package	Winn et al.[61]	https://ccp4.ac.uk
Phenix software package	Liebschner et al.[62]	https://phenix-online.org
Coot 0.9.8.5	Emsley et al.[63]	https://www2.mrc-lmb.cam.ac.uk/personal/pemsley/coot
MolProbity	Chen et al.[64]	http://molprobity.biochem.duke.edu
PyMol 2.5.7	Schrödinger LLC	https://pymol.org
BioLuminate 5.8	Schrödinger LLC	https://schrodinger.com
SeeSAR 13.0.1	BiosolveIT	https://biosolveit.de
Agilent MassHunter B.05.00	Agilent	https://agilent.com
MestReNova 14.0.1	Mestrelab	https://mestrelab.com
Alphafold 3	Jumper et al.[65]	https://alphafoldserver.com/
Molinspiration property calculation service	Molinspiration Cheminformatics	https://molinspiration.com
SuperCYPsPrep	Banerjee et al.[66]	https://insilico-cyp.charite.de/SuperCYPsPred
ImageLab 6.1	Bio-Rad	https://bio-rad.com
Other		
HisPur Ni-NTA magnetic beads	ThermoFisher	88831
Monolith standard capillaries	Nanotemper Technologies	MO-K022
96-well half-area plates	Greiner Bio-One	675076
Zeba Spin Desalting columns 7K MWCO	ThermoFisher	89882
MAIPNTR10 donor plates	Sigma-Aldrich	MAIPNTR10
Superdex 200 Increase 3.2/300	Cytiva	28990946
EZ-Link Sulfo-NHS-LC-Biotinylation kit	ThermoFisher	21435

(*Continued on next page*)

Continued

REAGENT or RESOURCE	SOURCE	IDENTIFIER
Streptavidin MagBeads	GenScript	L00936
Monarch RNA cleanup (500 μg)	New England Biolabs	T2050S
Whatman glass microfiber filters (GF/C, 25 mm)	Sigma-Aldrich	WHA1822025
Protran nitrocellulose membrane (0.45 μm)	Cytiva	10600003
Criterion TGX Precast Protein Gels (4–20%)	Bio-Rad	5671095

METHOD DETAILS

DEL screening

DEL screening against human DNMT2 protein was performed with the fourth-generation DELopen library (4.2 billion compounds, 27 sub-libraries) by WuXi AppTec. Screening was carried out according to the manufacturer's protocol (available online: https://hits.wuxiapptec.com/assets/pdf/DELopen_Protocol.pdf). Briefly, the DEL panning was performed with recombinant human full-length DNMT2 protein immobilized via the His-tag on ThermoScientific HisPur Ni-NTA magnetic beads. The beads were first washed in a magnetic separation rack with washing buffer (50 mM HEPES, 150 mM NaCl, 5 mM $MgCl_2$, 0.05% polysorbate-20, pH 7.5), and 250 μg beads were transferred for each selection condition to a separate tube. DNMT2 was diluted according to the manufacturer's protocol in selection buffer (50 mM HEPES, 150 mM NaCl, 5 mM $MgCl_2$, 0.05% Polysorbate-20, pH 7.5, 0.1 mg/mL sheared salmon sperm DNA, 1 mM TCEP, and 10 mM imidazole) and successful immobilization on the beads was confirmed by the SDS-PAGE protein capture assay described in manufacturer's protocol. A differential panning procedure was employed with four different selection conditions (A–D): (**A**) Native DNMT2 without additives; (**B**) DNMT2 with SAH (100 μM); (**C**) DNMT2 with $tRNA^{Asp}$ (10 μM); (**D**) No target control with no DNMT2 immobilized.

After three iterative selection rounds, the enriched DNA samples were transferred to WuXi AppTec for further processing, including PCR amplification, quantitation by qPCR, and deep sequencing. All samples passed the DELopen quality control (Figures S1A and S1E) and were forwarded to Illumina NovaSeq deep sequencing. Subsequently, DEL hits selection (Figure S1C) was decided based on enrichment scores, which were calculated by the DELopen unique algorithm described by Kuai et al.[41]

Microscale thermophoresis (MST)

Screening for ligand binding and evaluation of dose-response affinity profiles was performed via microscale thermophoresis (MST) as described previously.[42] The measurements were conducted with a Nanotemper Technologies Monolith NT.115 device. All samples were measured in Monolith standard capillaries at 25 °C. The acquisition mode was set to "Nano-Blue" with an excitation power of 30% and a medium MST power, while the system was controlled using the software MO.Control (version 1.6.1) and for evaluation MO.Affinity Analysis (version 2.3) was used. The samples contained 2 μM DNMT2, 100 nM FTAD (5-FAM-triazolyl-adenosyl-Dab) probe, and 1.3% DMSO in MST buffer (50 mM HEPES, 150 mM NaCl, 1 mM dithiothreitol (DTT), 0.1% PEG-8000, 0.05% polysorbate-20, pH 7.4).[42] All compounds were employed at a final concentration of 100 μM for the initial ligand screening.

For K_D-value determination of the DEL hit-derived fluorescent tracers **6–8**, the respective probe was used at a concentration of 100 nM (instead of FTAD), and the DNMT2 concentration was varied (50 μM–0 μM). All measurements were performed as triplicates. The K_D-value was calculated and plotted in GraphPad Prism 8.0.1. MST experiments with fluorescently labeled tRNA (non-covalent labeling with SybrGold) were used to investigate if hit compounds **1–5** can dissociate the nucleic acid-protein complex formed by DNMT2 and were conducted as described previously.[47] To assess the DEL ligands' effect on the RNA binding, the $tRNA^{Asp}$ substrate (100 nM) was mixed with the DNMT2 enzyme (2 μM) supplemented with 1x SybrGold and 100 μM of the respective ligand.

Isothermal titration calorimetry (ITC)

The DNMT2 protein was purified via size exclusion chromatography eluting in isothermal titration calorimetry (ITC) buffer (50 mM sodium phosphate pH 8.0, 300 mM NaCl, 1 mM EDTA, 2 mM β-mercaptoethanol, 0.1% polysorbate-20) and directly used for measurements.[3] All compounds were dissolved in DMSO to a concentration of 5 mM and were then diluted in ITC buffer to a final concentration of 500 μM. DNMT2 was diluted to a final concentration of 50 μM with 10% DMSO to match the ligand stocks' DMSO concentration. For the ITC measurements, a MicroCal PEAQ-ITC Automated workstation (Malvern Panalytical) with a 200 μL Hastelloy cell and an injection syringe volume of 40 μL was used. All experiments were performed in triplicates at 25 °C unless otherwise noted. For each measurement, 19 compound injections (2 μL each) with an injection speed of 0.5 μL/s were added to the reaction cell containing DNMT2. The spacing time between sequential injections was 300 s, and the stirring speed was set to 750 rpm with a reference power of 42 μW. As control experiments, ligands were titrated into ITC buffer. Data analysis and fitting were carried out using the MicroCal PEAQ-ITC Analysis Software 1.21 and plotted in GraphPad Prism 8.0.1.

Furthermore, displacement ITC experiments were performed as described for the direct titrations above with the following modifications: DNMT2 (50 μM) was preincubated with compound **10** (500 μM, 10% DMSO) or compound **3** (100 μM, 10% DMSO).

iScience
Article

CellPress
OPEN ACCESS

Subsequently, SAH (500 μM, 10% DMSO) was titrated to preincubated protein. During the same sample set, SAH (500 μM) was titrated directly into DNMT2 (50 μM) as a reference titration. Data analysis and displacement curve fitting were accomplished via the MicroCal PEAQ-ITC Analysis Software.

Fluorescence polarization (FP)

Fluorescence polarization (FP) measurements with RNA MTases and small-molecule fluorescent tracers were conducted in black Greiner 96-well half-area plates using a Tecan Spark 10M plate reader as described previously.[44] The reader was equipped with polarization filters coupled to a monochromator setup (λ_{ex} = 480 nm, λ_{em} = 530 nm). For selectivity screening, reaction mixtures contained varying concentrations of recombinant enzyme (DNMT1, DNMT2, DNMT3A/3L, NSUN2, NSUN3, or NSUN6; preparation see below) and 10 nM DEL hit-derived probe **6** in MST buffer. For displacement experiments, 100 μM SAH or 10 μM $tRNA^{Asp}$ were added from buffered stock solutions to the DNMT2-containing mixtures. All measurements were performed as triplicates. Polarization values (in mP) were calculated from polarization-specific parallel and orthogonal fluorescence intensities according to the Tecan in-built calculation routine. K_D-values were calculated and plotted in GraphPad Prism 8.0.1.

^{3}H-based methyltransferase enzyme activity assays

Enzymatic DNMT2 inhibition assays were carried out in 100 mM Tris-HCl, pH 8.0, 100 mM NH_4OAc, 0.1 mM EDTA, 10 mM $MgCl_2$, and 10 mM DTT as described previously.[3,4] First, the $tRNA^{Asp}$ substrate was heated to 75 °C for 5 min and cooled down to room temperature (RT) before it was added to the reaction mixture to a final concentration of 5 μM. The reaction mixture contained 250 nM DNMT2 and the ligand compounds at variable concentrations (5% DMSO). Enzymatic reactions were started by the addition of 0.9 μM SAM as a mixture of ^{3}H-SAM (Hartmann Analytics) resp. cold SAM (NEB) to a final activity of 0.025 μCi μL^{-1}. Enzyme assays were carried out for 30 min at 37 °C. As a negative control served the reaction mixture without DNMT2 and as a positive control the reaction mixture without test compound. After 30 min, aliquots of 8 μL were taken from the reaction mixture and spotted on Whatman glass microfiber filters (GF/C, 25 mm). The RNA was precipitated on the filters with 5% ice-cold TCA for 15 min. The filters were washed twice with 5% TCA at RT for 20 min and 10 min and once in EtOH for 10 min. After drying, the filters were transferred into scintillation vials, and 3 mL of PerkinElmer Gold MV liquid scintillation cocktail was added. Scintillation was measured with a scintillation counter (TriCarb Liquid Scintillation Analyzer 4810 TR; measurement time of 1 min). For IC_{50}-value determination, compounds were analyzed at a minimum of six different concentrations in triplicates. IC_{50}-values were calculated, evaluated, and plotted in GraphPad Prism 8.0.1.

Affinity selection-mass spectrometry (AS-MS)

Orthogonal K_D-value determination for compound **3** was conducted by an affinity selection-mass spectrometry (AS-MS) assay according to Prudent et al.[43] and Simon et al.[67] Compound **3** was dissolved in DMSO (20 mM) and a dilution series in Tris buffer (25 mM Tris, 100 mM NaCl, pH 7.5) was prepared to give final ligand concentrations of 100 μM, 50 μM, 25 μM, 12.5 μM, 6.25 μM, 3.12 μM, 1.56 μM, and 0 μM. DNMT2 was diluted in Tris buffer (130 μM) and added to the dilution series to give a final concentration of 5 μM DNMT2. Zeba Spin Desalting columns 7K MWCO were used for the affinity-based separation. These columns were centrifuged at 2000*g* for 1 min to remove the storage buffer. 20 μL of the prepared samples were loaded to the columns, and the protein-ligand complex was eluted by centrifugation at 2000*g* for 2 min. The centrifuged solutions were diluted with 10 μL ACN and analyzed by LC/MS with an Agilent 1100 Series HPLC system. The data evaluation and subsequent binding affinity determination were performed with MestReNova (version 14.0.1) and GraphPad Prism 8.0.1.

Electrophoretic mobility shift assay (EMSA)

EMSA assays were performed as described previously.[46] DNMT2 (10 μM) was mixed with $tRNA^{Asp}$ (5 μM) and treated with 100 μM of the respective hit compound in DNMT2 assay buffer (100 mM Tris-HCl, pH 8, 100 mM NH_4OAc, 0.1 mM EDTA, 10 mM $MgCl_2$, 10 mM DTT). Subsequently, reaction samples (each 5 μL) were loaded to a native 10% polyacrylamide gel and separated electrophoretically (1 h, 180 V) in 1x TBE. RNA was stained *in situ* with 1x GelRed, and PAGE analysis was conducted by fluorescence scanning at an excitation wavelength of 532 nm (Amersham Typhoon 9400).

In vitro permeability assay (PAMPA)

To determine the passive permeability of selected DNMT2 ligands, a parallel artificial membrane permeation assay (PAMPA) was performed as described previously.[68] The experiment was performed in duplicates with Sigma-Aldrich MAIPNTR10 donor plates with 5 μL of an artificial membrane (1% w/v L-α-phosphatidylcholine in *n*-dodecane) per well. After incubation for 7 h, the acceptor solutions were evaluated by LC/MS (HP Agilent 1100 Series). The peak areas in the UV chromatogram (λ = 210 nm) were used to calculate the areas under the curve (AUCs). The apparent permeability P_{app} was calculated using the following equation with V_D and V_A as volumes of donor and acceptor solutions (0.15 cm^3 and 0.4 cm^3), AUC_{acc} and AUC_{ref} as the area of the analyte signal in the respective chromatogram of sample and reference solutions, A as the porosity-corrected filter area (0.2113 cm^2) and t as the incubation time given in seconds: $P_{app} = -V_D \cdot V_A \cdot \ln(1 - AUC_{acc}/AUC_{ref})/[(V_D + V_A) \cdot A \cdot t]$.

Protein and tRNA production

DNMT2, NSUN2, NSUN6, and DNMT3A/3L were expressed from *E. coli* as described previously, while $tRNA^{Asp}$ was synthesized by *in vitro* transcription as described previously.[3]

DNMT2 cloning, expression, and purification for co-crystallization

For the co-crystallization of DNMT2Δ47 with compound **3**, the coding DNA sequence of human DNMT2 lacking residues 191–237 was amplified by PCR and cloned into a pETHis_1a vector.[69] For this purpose, overhangs for the restriction enzymes NcoI/BamHI were used. The plasmid was transformed in Rosetta II (DE3) *E. coli* (Merck-Novagen) and expressed in ZY autoinduction medium supplemented with trace elements, kanamycin, and chloramphenicol. The cells were grown to OD_{600} = 0.8 at 37 °C (220 rpm shaking) and further cultivated overnight at 20 °C. Harvesting was performed by centrifugation and washing with 1xPBS buffer (0.137 M NaCl, 2.7 mM KCl, 10 mM Na_2HPO_4, 1.8 mM KH_2PO_4). The resulting cell pellet was then resuspended in lysis buffer (20 mM HEPES, pH 7.5, 500 mM NaCl, 20 mM imidazole, 1 M urea, 4 mM β-mercaptoethanol), supplemented with a protease inhibitor mix (Roche) and 1:10000 benzonase. Lysis was performed with a microfluidizer (M1-10L, Microfluidics) followed by clearing the lysate applying centrifugation (40 min at 50,000*g*) and filtering through a 0.45 μm membrane. The supernatant was loaded twice on 4 mL Ni-NTA Agarose (Qiagen) for Ni-IMAC using gravity flow columns (Biorad). The beads were washed with ten column volumes (10 CV) wash buffer (20 mM HEPES, pH 7.5, 150 mM NaCl, 4 mM β-mercaptoethanol), followed by 10 CV high salt buffer (20 mM HEPES, pH 7.5, 2 M NaCl, 4 mM β-mercaptoethanol) and again 10 CV wash buffer. Elution of the His-tagged DNMT2Δ47 was performed with 5 CV elution buffer (20 mM HEPES, pH 7.5, 150 mM NaCl, 300 mM imidazole, 4 mM β-mercaptoethanol). Protein concentration was measured with a NanoPhotometer NP80 (Implen), and TEV protease was added in a 1:75 ratio. Cleavage of the protein by TEV results in two additional residues, namely Gly-Ala, at the N-terminus. The DNMT2Δ47-protease mix was dialyzed overnight against wash buffer using a 6–8 kDa dialysis tube (Spectra/Por). The sample was applied to a reverse Ni-IMAC using 2 mL Ni-NTA Agarose, which was washed with 5 CV wash buffer. The flow-through and wash fractions were pooled, concentrated with an Amicon Ultra concentrator (10 kDa cutoff, Merck KGaA) to 2 mL and loaded for further purification by SEC (size-exclusion chromatography) on a Superdex 75 16/600 gel filtration column (Cytiva) in wash buffer. The peak fractions were pooled, incubated with compound **3** in a 2-fold molar excess, and concentrated with an Amicon Ultra concentrator (10 kDa cutoff, Merck KGaA) to 10 mg/mL for subsequent crystallization.

Analytical size-exclusion chromatography of DNMT2Δ47 with compound 3

To assess the oligomeric state of DNMT2Δ47 upon compound **3** binding, *in vitro* analytical SEC runs were performed on a Superdex 200 Increase 3.2/300 (Cytiva). For the first run, the apo-protein was injected at a concentration of 10 mg/mL; for the second run, it was pre-incubated with a 2-fold molar excess of compound **3**. The resulting chromatograms were analyzed by superposing their 280 nm signals using the Unicorn7 evaluation software (Cytiva).

Crystallization, data collection, model building, and refinement

Crystals were grown at 291 K using sitting drop vapor diffusion. The crystallization reservoir was composed of 0.2 M $MgCl_2$, 0.1 M Tris, pH 8.5, and 12% PEG-8000. Crystallization drops contained 300 nL reservoir solution and 300 nL concentrated protein. Needle-shaped crystals grew within three days. Crystals were frozen in liquid nitrogen using glycerol as the cryo-protectant. Data were collected at ESRF beamline ID30B at cryogenic conditions, integrated using XDS,[70] and scaled using AIMLESS[71] as part of the CCP4 software package.[61] Phases were obtained by molecular replacement with PHASER[72] implemented in the Phenix package[62] using the structure of human DNMT2 (Dong et al.[49]; PDB 1G55) as the search model. The resulting dataset has space group $P2_12_12_1$, a maximum resolution of 2.60 Å, and contains two DNMT2 molecules per asymmetric unit. Compound **3** was parameterized from SMILES description using phenix.elbow.[73] Iterative model building and refinement were performed with Coot[63] and phenix.refine.[74] C24, C79, and C287 side chains show additional electron density in both chains and, therefore, were built as *S*-hydroxycysteine residues (CSO). The quality of the resulting structural models was analyzed with MolProbity.[64] Structure figures were prepared with PyMol 2.5.7 (The PyMol Molecular Graphics System, Schrödinger LLC.). Hydrophobicity of the binding site was visualized by a molecular surface representation colored from high (white) to low (green) hydrophobicity according to the Eisenberg hydrophobicity scale.[75] The electrostatic potential was calculated and visualized using the PyMol APBS plugin.[76] Crystallographic data are summarized in Table S3. Coordinates and structure factors are deposited at the Protein DataBank PDB under accession code 9HGM.

SeeSAR analysis

BiosolveIT SeeSAR (v13.0.1) was used to visualize the estimated binding affinity contributions of the co-crystallized DNMT2 ligand. SeeSAR concedes a semi-quantitative calculation of the thermodynamics using the HYDE algorithm and was used to evaluate torsions, desolvation, and interaction contributions for each ligand's heavy atom.[52] For this, the DNMT2Δ47-binding compound **3** complex (PDB 9HGM) was imported to SeeSAR and evaluated using the "Analyzer" functionalities.

Pull-down DNMT2 interaction assay

For immobilization on streptavidin beads, DNMT2 was biotinylated using the EZ-Link Sulfo-NHS-LC-Biotinylation kit. A 20-fold excess of Sulfo-NHS-LC-Biotin (10 mM in water) was added to DNMT2 and incubated for 2 h on ice. To remove the excess biotin

iScience
Article

CellPress
OPEN ACCESS

reagent, Zeba Spin desalting columns were equilibrated with 1× PBS buffer, and the reaction mixture was loaded and centrifuged for 2 min at 1000*g*. The biotinylation level was estimated using a HABA assay included in the kit according to the manufacturer's protocols. By this, 4.7 biotin molecules were found to be attached per DNMT2 molecule. To confirm that the biotinylation did not affect the binding competence of the SAH and drug binding pockets, MST measurements with FTAD as a fluorescent tracer were performed as described above.

For *in vitro* pull-down assays, biotinylated DNMT2 was immobilized on streptavidin-coated paramagnetic beads (GenScript Streptavidin MagBeads). For this, beads were washed with PBS buffer containing 0.05% Triton X-100, and subsequently, DNMT2 (30 μg per 50 μL beads) was immobilized for 45 min at RT. As a negative control, beads were treated with a protein-free buffered solution. Beads were washed with PBS buffer, and for each sample, 5 μL beads were added to either 1.5 μg of recombinant NonO protein (Active Motif) or 3.0 μg of recombinant eIF4E protein (Cayman). Beads were incubated for 1 h at RT, and subsequently, the supernatant was removed. Afterward, 10 μL PBS-buffered elution solution (containing either 100 μM sinefungin or 100 μM compound **16** or 10 μM tRNA) was added. The samples were incubated for 45 min at RT, and the supernatant was treated with 2 μL 5× Laemmli buffer. For analysis of the proteins still bound to the beads after elution treatment, 10 μL Laemmli buffer supplemented with 10 mM biotin was added to the residual beads. All samples were heated to 95 °C for 10 min and analyzed via SDS-PAGE. Fluorometric protein detection was conducted using ProteOrange staining (Lumiprobe) according to the manufacturer's protocols. Protein bands were visualized using a GE Healthcare Typhoon Trio biomolecular scanner, with laser excitation at 488 nm and fluorescence detection at 580 nm.

tRNA modification analysis by LC/MS

MOLM-13 cells were seeded at a density of 5 × 10^6 cells in 15 mL RPMI-1640 medium (supplemented with 10% FBS) containing DNMT2 inhibitor **16** (5 μM and 50 μM), negative control compound **34** (50 μM), or DMSO as mock treatment. Cells were incubated for 72 h at 37 °C. Post-incubation, cells were harvested and washed with PBS. Cell pellets were lysed in 1.5 mL TRIzol, mixed thoroughly by pipetting, and incubated for 5 min at RT. Subsequently, 150 μL chloroform was added, vortexed, and incubated for 10 min at RT. Samples were centrifuged at 12,000*g* for 15 min at 4 °C. The upper aqueous layer was transferred to new tubes and mixed with 750 μL isopropanol, vortexed, and incubated for 10 min at RT. Following another centrifugation at 12,000*g* for 15 min at 4 °C, the supernatant was discarded. Pellets were washed with 750 μL of 75% ethanol, vortexed, and centrifuged again at 12,000*g* for 15 min at 4 °C. After discarding the supernatant, the pellets were air-dried at 37 °C and dissolved in 50 μL nuclease-free water. Total RNA samples were further purified by New England Biolabs Monarch RNA Cleanup (500 μg) kits according to the manufacturer's instructions (protocol for RNA size fractionation). Small RNA molecules (<100 nt) containing total tRNA were eluted in 50 μL nuclease-free water, and concentrations were determined using a Nanodrop spectrophotometer.

To enrich the DNMT2 tRNA substrates, a literature-known hybridization-based protocol for the purification of thermostable tRNA was adopted.[77] Therefore, three biotin-labeled anti-sense DNA oligonucleotides suitable for tRNA pull-down were designed and purchased from GenScript. Sequences complementary to $tRNA^{Asp-GUC}$: 5′-GTGACAGGCGGGGATACTCACCACT-Biotin-3′, $tRNA^{Gly-GCC}$: 5′-CGTGGCAGGCGAGAATTCTACCACT-Biotin-3′, $tRNA^{Val-AAC}$: 5′-CGTGTTAGGCGAACGTGATAACCACT-Biotin-3'. Next, GenScript streptavidin MagBeads (200 μL) were washed thrice with 1 mL TBST. Biotin-labeled DNA-oligonucleotide solutions were prepared at 7.5 μM in 3 × 400 μL TBST. MagBeads were incubated with 400 μL of each Biotin-oligo for 10 min at RT, then washed with TBST. Unbound oligos were measured by Nanodrop to confirm loading, assuming a theoretical capacity of 3 nmol per 200 μL beads. MagBeads were pooled in 1200 μL TBST and distributed into 12 PCR tubes with 100 μL TBST each. Total tRNA samples (100 μL) were mixed with 100 μL hybridization buffer (20 mM Tris, pH 7.6, 1.8 M NaCl, 0.2 mM EDTA) and added to the prepared MagBeads. The mixture was heated RT to 75 °C over 40 min using a PCR cycler and then cooled to 4 °C. Following centrifugation, supernatants were collected and saved. The beads were washed repeatedly with TBST at 4 °C until the absorbance at 260 nm was less than 0.01. tRNA was eluted by heating the beads in 30 μL Tris buffer (10 mM Tris, pH 7.6) at 75 °C, with the supernatant collected after each elution step, repeated three times. tRNA concentration and purity were determined using a Nanodrop spectrophotometer and 10% denaturing PAGE, respectively.

100 ng of enriched tRNA per sample was enzymatically digested into nucleosides using a mixture of 0.6 U nuclease P1 from *Penicillium citrinum* (Sigma-Aldrich), 0.2 U snake venom phosphodiesterase from *Crotalus adamanteus* (Worthington), 0.2 U bovine intestine phosphatase (Sigma-Aldrich), 10 U benzonase (Sigma-Aldrich), along with 200 ng of Pentostatin (Sigma-Aldrich). This reaction was conducted for 2 h at 37 °C in a buffer containing 5 mM Tris (pH 8) and 1 mM magnesium chloride. Following digestion, the nucleosides were spiked with an internal standard of ^{13}C stable isotope-labeled nucleosides derived from *Saccharomyces cerevisiae* and analyzed. 100 ng of the digested tRNA and 25 ng of the internal standard were analyzed using LC/MS (Agilent 1260 series coupled with an Agilent 6460 Triple Quadrupole mass spectrometer featuring an electrospray ion source). The mobile phase consisted of a 5 mM ammonium acetate buffer (pH 5.3) and LC/MS grade acetonitrile (VWR). The elution process began with 100% ammonium acetate buffer at a flow rate of 0.35 mL/min, transitioning to a linear gradient that reached 8% acetonitrile at 10 min and 40% at 20 min. The initial conditions were restored to 100% ammonium acetate buffer for an additional 10 min. A Synergi Fusion column (4 μm particle size, 80 Å pore size, 250 × 2.0 mm; Phenomenex) was utilized for the separation. The UV signal at 254 nm was monitored using a multiple wavelength detector (MWD) to track the primary nucleosides. The ESI parameters were set as follows: gas temperature at 350 °C, gas flow at 8 L/min, nebulizer pressure at 50 psi, sheath gas temperature at 350 °C, sheath gas flow at 12 L/min, and capillary voltage at 3000 V. The mass spectrometer operated in positive ion mode, employing Agilent MassHunter

CellPress
OPEN ACCESS

iScience
Article

B.05.00 software in dynamic MRM (multiple reaction monitoring) mode for analysis. Quantification was achieved through a combination of external and internal calibration methods, as outlined in Kellner et al.[78]

Cell viability assays

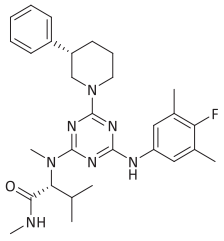
Cell viability assays were conducted with MOLM-13 cells, Huh-7, MDA-MB-231, HEK293, and HCT MTase mutant cell lines (WT, knock-down DNMT2, and knock-down NSUN2) to investigate the DNMT2 inhibiting compounds' cellular effect. Cells were cultured according to standard protocols: MOLM-13 (RPMI, 10% FBS, 1x Penicillin/Streptomycin, 37 °C, 5% CO_2), Huh-7/MDA-MB-231/HEK293 (DMEM, 10% FBS, 1x Penicillin/Streptomycin, 37 °C, 5% CO_2) and HCT (McCoys's 5A Medium, 10% FBS, L-Glutamine, 1x Penicillin/Streptomycin, 37 °C, 5% CO_2). Cell viability was assessed using Promega Cell Titer Glo assay kit (MOLM-13, Huh-7, MDA-MB-231, HEK293) or Lonza ViaLight Plus Cell Proliferation and Cytotoxicity BioAssay Kit (HCT cell lines). Briefly, 1000 cells were seeded in white Greiner half-area 96-well plates and incubated for 48 h with inhibitors/ligands from DMSO stocks (final: 0.1% DMSO) under standard cultivation conditions. Then, the cell titer reagent was added to each well according to the manufacturer's protocols, and luminescence was measured using a Tecan Spark 10M plate reader (MOLM-13, Huh-7, MDA-MB-231, HEK293) or Molecular Devices FlexStation (HCT cell lines). For the co-treatment with doxorubicin/compound **16** or **34**, cells were cultured for two passages of each three days in the presence of compound **16** or **34** (50 μM) and subsequently 1000 cells each in 96-well plates were treated with varying concentrations of doxorubicin for 48 h.

Cellular thermal shift assay (CETSA)

MOLM-13 cells were seeded at a density of 5×10^6 cells in 3 mL RPMI-1640 medium. Subsequently, compound **3** or **16** was added to the MOLM-13 cells to achieve a final concentration of 50 μM, with the same volume of DMSO (final: 0.2%) added as a control. After incubation for 16 h (37 °C, 5% CO_2), the cell suspensions were collected. The cells were washed twice and then counted, followed by the addition of 1 mL PBS. The cell suspension was divided into eight parts, and then heated for 4 min at various temperatures (40, 43, 46, 49, 52, 55, 58 °C) in a PCR thermocycler. The cells were lysed through a freeze-thaw process using liquid nitrogen. The supernatant solutions were used for immunoblotting analysis. Insoluble cellular parts were separated by centrifugation (12,000*g* for 10 min), subsequently, the supernatant was boiled with 1× Laemmli sample buffer for 5 min at 95 °C. Proteins were separated by SDS−PAGE on 4–20% Criterion TGX Precast Protein Gels (Bio-Rad) and transferred to Amersham Protean 0.45 μm nitrocellulose membrane (Cytiva) using semi-dry transfer (25 V, 1 A, Towbin buffer). The membrane was blocked with 5% milk (Carl Roth) in TBST buffer and incubated with anti-DNMT2 antibody (1:1000, Abcam, ab308120) overnight at 4 °C. Subsequently, the membrane was incubated for 3 h at RT with IRDye 680RD Goat anti-Rabbit (1:1000, LICOR, 926–68071). Protein bands were visualized using a GE Healthcare Typhoon Trio biomolecular scanner, with laser excitation at 637 nm and fluorescence detection at 670 nm. The ImageLab software (Bio-Rad) was used for band quantification.

Synthesis and characterization of inhibitors and probes

Rink amide AM resin (loading capacity: 0.6–0.8 mmol/g) or Wang Gly resin (loading capacity: 0.135 mmol/g) was swelled twice for 5 min in DMF. Fmoc-deprotection was performed by treating with 40% piperidine in DMF (2 × 10 min shaking). The resin was rinsed with DCM (3x) and DMF (3x). In the next step, the corresponding building block was coupled to the resin by dissolving the amino acid (3.0 eq. or 1.2 eq.), TBTU (3.0 eq. or 1.2 eq.), and NMM (9.0 eq.) in DMF and shaking for 1.5 h (or 16 h for 1.2 eq.). Subsequently, the resin was rinsed with DCM (3x) and DMF (3x). To couple the next amino acids, the procedure of deprotection and coupling was repeated. When the last amino acid was coupled, the resin was rinsed with DMF (3x) and DCM (3x). To cleave the peptide from the resin, the resin was treated with a mixture of TFA:TIPS:DCM (50:10:40) for 1.5 h. The resin was washed with DCM (3x) and treated again with TFA:TIPS:DCM (50:10:40) for 16 h. All cleavage and wash solutions combined were evaporated under reduced pressure. The crude product was purified by reversed-phase flash column chromatography (Biotage Isolera, ACN/H_2O + TFA), and the product containing fractions were lyophilized. Detailed characterization of the compounds synthesized can be found below:

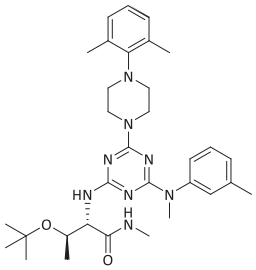


1

Compound **1**: ^{1}H-NMR (400 MHz, DMSO-d_6): δ [ppm] = 8.94 (s, 1H), 7.74–7.16 (m, 6H), 4.76 (s, 2H), 3.32 (d, *J* = 2.8 Hz, 2H), 3.05–2.83 (m, 3H), 2.58 (s, 13H), 2.34–1.90 (m, 6H), 1.79 (d, *J* = 13.0 Hz, 1H), 0.93 (d, *J* = 4.3 Hz, 2H), 0.79 (d, *J* = 6.6 Hz, 2H).

^{13}C-NMR (101 MHz, DMSO): δ [ppm] = 170.7, 170.1, 165.9, 165.8, 143.9, 143.9, 136.0, 128.4, 127.0, 126.4, 123.1, 119.8, 62.6, 49.7, 43.4, 42.2, 31.8, 26.4, 25.7, 25.5, 25.1, 20.0, 19.1, 18.8, 14.5.

LC/MS: m/z calculated for $C_{29}H_{38}FN_7O$ $[M + H]^+$: 520.3, found: 520.3.

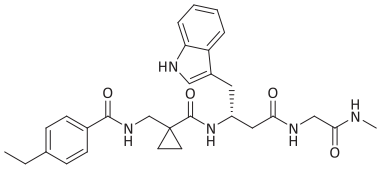


2

Compound **2**: ^{1}H-NMR (400 MHz, DMSO-d_6): δ [ppm] = 7.77–7.68 (m, 1H), 7.27–7.07 (m, 3H), 6.95 (h, *J* = 7.7, 7.1 Hz, 4H), 4.02 (t, *J* = 5.3 Hz, 1H), 3.78–3.68 (m, 3H), 3.38 (s, 3H), 3.32 (s, 3H), 2.97 (d, *J* = 6.0 Hz, 4H), 2.57 (d, *J* = 4.4 Hz, 3H), 2.32–2.23 (m, 9H), 1.06 (dd, *J* = 15.2, 8.3 Hz, 12H).

^{13}C-NMR (101 MHz, DMSO): δ [ppm] = 171.0, 165.6, 165.2, 164.4, 148.0, 144.7, 144.5, 137.6, 137.3, 136.1, 128.9, 128.1, 127.9, 127.0, 126.7, 125.7, 125.4, 124.9, 123.7, 123.0, 73.3, 67.2, 59.2, 49.3, 44.1, 37.3, 28.0, 25.7, 21.0, 20.7, 20.5, 19.4.

LC/MS: m/z calculated for $C_{32}H_{46}N_8O_2$ $[M + H]^+$: 575.3, found: 575.2.

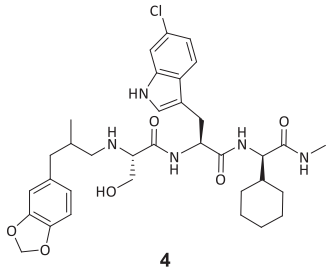


3

Compound **3**: ^{1}H-NMR (600 MHz, DMSO-d_6): δ [ppm] = 10.80–10.76 (m, 1H), 8.58 (t, *J* = 6.1 Hz, 1H), 8.13 (t, *J* = 5.9 Hz, 1H), 8.05 (d, *J* = 7.9 Hz, 1H), 7.76 (d, *J* = 8.2 Hz, 2H), 7.66 (d, *J* = 4.6 Hz, 1H), 7.59 (d, *J* = 7.9 Hz, 1H), 7.29 (t, *J* = 8.2 Hz, 3H), 7.09 (d, *J* = 2.2 Hz, 1H), 7.07–7.01 (m, 1H), 6.98–6.92 (m, 1H), 4.38–4.31 (m, 1H), 3.60 (ddd, *J* = 25.4, 15.6, 6.2 Hz, 2H), 3.48 (dd, *J* = 16.5, 5.7 Hz, 1H), 3.41 (dd, *J* = 14.8, 6.2 Hz, 1H), 2.83 (d, *J* = 6.5 Hz, 2H), 2.64 (q, *J* = 7.6 Hz, 2H), 2.54 (d, *J* = 4.6 Hz, 3H), 2.40–2.30 (m, 2H), 1.18 (t, *J* = 7.6 Hz, 3H), 0.91 (t, *J* = 3.6 Hz, 2H), 0.79 (dd, *J* = 9.4, 3.6 Hz, 2H).

^{13}C-NMR (151 MHz, DMSO): δ [ppm] = 171.6, 170.8, 169.3, 167.2, 147.5, 136.1, 131.4, 127.7, 127.6, 127.5, 123.3, 120.9, 118.6, 118.2, 111.3, 111.2, 47.8, 42.2, 42.1, 29.9, 28.1, 25.5, 25.3, 15.4, 13.2, 12.9.

LC/MS: m/z calculated for $C_{29}H_{35}N_5O_4$ $[M + H]^+$: 518.3, found: 518.2.

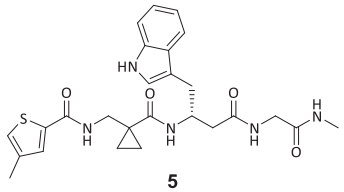


4

Compound **4**: ^{1}H-NMR (400 MHz, DMSO-d_6): δ [ppm] = 10.97 (s, 1H), 8.03 (d, *J* = 8.2 Hz, 1H), 7.90 (d, *J* = 10.1 Hz, 2H), 7.51 (d, *J* = 8.5 Hz, 1H), 7.31 (d, *J* = 6.4 Hz, 1H), 7.09 (s, 1H), 6.92 (d, *J* = 8.5 Hz, 1H), 6.76 (d, *J* = 7.8 Hz, 1H), 6.66 (s, 1H), 6.52 (d, *J* = 7.9 Hz, 1H), 5.94 (s, 2H), 4.92 (s, 1H), 4.62 (q, *J* = 6.9 Hz, 1H), 4.08 (t, *J* = 8.2 Hz, 1H), 3.47 (d, *J* = 11.1 Hz, 1H), 3.03 (ddt, *J* = 37.3, 22.9, 5.8 Hz, 3H), 2.62–2.54 (m, 4H), 2.37–1.94 (m, 4H), 1.58 (dt, *J* = 18.1, 11.0 Hz, 6H), 1.45 (d, *J* = 12.6 Hz, 1H), 1.21–0.77 (m, 6H), 0.63 (d, *J* = 6.4 Hz, 3H).

^{13}C-NMR (101 MHz, DMSO): δ [ppm] = 171.8, 171.0, 170.5, 147.0, 145.1, 136.3, 134.7, 126.4, 125.5, 124.9, 121.7, 120.0, 118.4, 110.7, 109.9, 109.2, 107.8, 100.5, 64.8, 62.1, 57.1, 53.9, 52.6, 35.1, 29.1, 28.3, 27.5, 25.8, 25.5, 25.4, 17.3.

LC/MS: m/z calculated for $C_{34}H_{44}ClN_5O_6$ $[M + H]^+$: 654.3, found: 654.3.

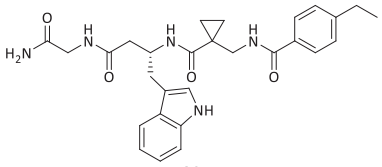


5

Compound **5**: ^{1}H-NMR (400 MHz, DMSO-d_6): δ [ppm] = 10.76 (s, 1H), 8.49 (t, *J* = 7.0 Hz, 1H), 8.10 (d, *J* = 6.6 Hz, 1H), 7.86–7.80 (m, 1H), 7.60 (q, *J* = 8.9, 7.7 Hz, 3H), 7.35 (s, 1H), 7.30 (d, *J* = 8.2 Hz, 1H), 7.09 (s, 1H), 7.07–7.00 (m, 1H), 6.99–6.92 (m, 1H), 4.41–4.30 (m, 1H), 2.82 (t, *J* = 4.7 Hz, 2H), 2.54 (d, *J* = 4.3 Hz, 4H), 2.34 (d, *J* = 7.0 Hz, 2H), 2.21 (d, *J* = 3.2 Hz, 3H), 1.24 (s, 1H), 1.03–0.85 (m, 3H), 0.76 (s, 2H).

^{13}C-NMR (101 MHz, DMSO): δ [ppm] = 172.0, 171.3, 169.7, 162.4, 139.2, 138.3, 136.6, 130.9, 128.0, 126.9, 123.8, 121.3, 119.0, 118.6, 111.7, 111.6, 48.3, 42.6, 30.4, 25.9, 25.6, 23.8, 15.9, 13.4, 13.1.

LC/MS: m/z calculated for $C_{26}H_{31}N_5O_4S$ $[M + H]^+$: 510.2, found: 510.1.



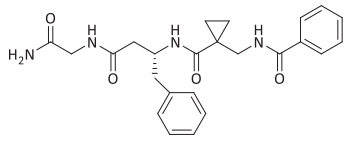
10

Compound **10**: Yield: 2.9 mg (5.80 μmol ≙ 13% of th.), colorless solid.

^{1}H-NMR (600 MHz, DMSO-d_6): δ [ppm] = 10.77 (s, 1H), 8.59 (t, *J* = 6.2 Hz, 1H), 8.07 (t, *J* = 5.9 Hz, 1H), 8.04 (d, *J* = 7.9 Hz, 1H), 7.81–7.71 (m, 2H), 7.59 (d, *J* = 7.9 Hz, 1H), 7.33–7.26 (m, 3H), 7.24 (s, 1H), 7.09 (d, *J* = 2.2 Hz, 1H), 7.04 (t, *J* = 7.3 Hz, 2H), 6.95 (t, *J* = 7.4 Hz, 1H), 4.34 (h, *J* = 6.9 Hz, 1H), 3.61 (dd, *J* = 16.8, 6.0 Hz, 1H), 3.56 (dd, *J* = 14.8, 6.1 Hz, 1H), 3.48 (dd, *J* = 16.8, 5.5 Hz, 1H), 3.41 (dd, *J* = 14.8, 6.1 Hz, 1H), 2.82 (d, *J* = 6.7 Hz, 2H), 2.64 (q, *J* = 7.6 Hz, 2H), 2.33 (d, *J* = 6.8 Hz, 1H), 1.18 (t, *J* = 7.6 Hz, 3H), 0.98–0.72 (m, 4H).

^{13}C-NMR (151 MHz, DMSO): δ [ppm] = 171.6, 171.1, 170.6, 167.2, 147.5, 136.1, 131.4, 127.7, 127.6, 127.5, 123.3, 120.8, 118.6, 118.2, 111.3, 111.2, 47.7, 42.3, 41.9, 40.1, 29.8, 28.1, 25.3, 15.4, 13.3, 12.9.

LC/MS: m/z calculated for $C_{28}H_{33}N_5O_4$ $[M + H]^+$: 504.3, found: 504.1.



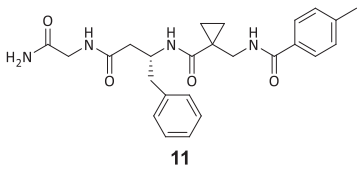
18

Compound **18**: Yield: 15.0 mg (0.034 mmol ≙ 75% of th.), colorless solid.

^{1}H-NMR (300 MHz, DMSO-d_6): δ [ppm] = 8.62 (t, *J* = 6.1 Hz, 1H), 8.10 (t, *J* = 5.9 Hz, 1H), 7.96 (d, *J* = 8.1 Hz, 1H), 7.91–7.75 (m, 2H), 7.67–7.36 (m, 3H), 7.24 (s, 1H), 7.20–7.03 (m, 5H), 7.03 (s, 1H), 4.30 (q, *J* = 7.5 Hz, 1H), 3.74–3.39 (m, 4H), 2.93–2.59 (m, 2H), 2.32 (d, *J* = 6.8 Hz, 2H), 1.04–0.56 (m, 4H).

^{13}C-NMR (75 MHz, DMSO): δ [ppm] = 171.5, 171.1, 170.4, 167.2, 138.8, 134.0, 131.5, 129.2, 128.3, 128.0, 127.4, 126.0, 48.4, 42.3, 41.9, 40.3, 25.2, 13.0.

LC/MS: m/z calculated for $C_{24}H_{28}N_4O_4$ $[M + H]^+$: 437.2, found: 437.2.



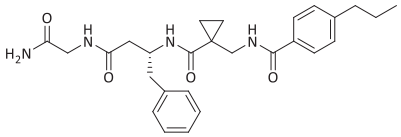
11

Compound **11**: Yield: 15.0 mg (0.033 mmol ≙ 75% of th.), colorless solid.

^{1}H-NMR (300 MHz, DMSO-d_6): δ [ppm] = 8.55 (t, *J* = 6.1 Hz, 1H), 8.09 (t, *J* = 5.9 Hz, 1H), 8.00 (d, *J* = 8.1 Hz, 1H), 7.82–7.69 (m, 2H), 7.32–7.26 (m, 2H), 7.24 (s, 1H), 7.17–7.07 (m, 5H), 7.03 (s, 1H), 4.30 (q, *J* = 7.0 Hz, 1H), 3.72–3.38 (m, 4H), 2.90–2.59 (m, 2H), 2.36 (s, 3H), 2.31 (d, *J* = 6.9 Hz, 2H), 0.96–0.68 (m, 4H).

^{13}C-NMR (75 MHz, DMSO): δ [ppm] = 171.5, 171.1, 170.3, 167.1, 141.4, 138.8, 131.1, 129.2, 128.9, 128.0, 127.4, 126.0, 48.4, 42.3, 41.9, 25.3, 21.0, 13.0.

LC/MS: m/z calculated for $C_{25}H_{30}N_4O_4$ $[M + H]^+$: 451.2, found: 451.1.



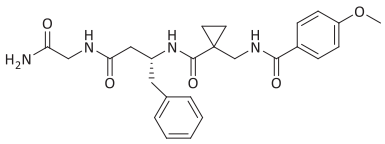
12

Compound **12**: Yield: 5.0 mg (0.010 mmol ≙ 23% of th.), colorless solid.

^{1}H-NMR (400 MHz, DMSO-d_6): δ [ppm] = 8.54 (t, *J* = 6.3 Hz, 1H), 8.08 (t, *J* = 6.0 Hz, 1H), 7.98 (d, *J* = 8.1 Hz, 1H), 7.81–7.73 (m, 2H), 7.33–7.26 (m, 2H), 7.23 (s, 1H), 7.17–7.05 (m, 5H), 7.01 (s, 1H), 4.29 (p, *J* = 7.2 Hz, 1H), 3.70–3.43 (m, 4H), 2.87–2.64 (m, 2H), 2.61 (t, *J* = 7.7 Hz, 2H), 2.31 (d, *J* = 6.9 Hz, 2H), 1.61 (h, *J* = 7.1 Hz, 2H), 0.93–0.72 (m, 7H).

^{13}C-NMR (101 MHz, DMSO): δ [ppm] = 171.5, 171.1, 170.3, 167.2, 145.9, 138.8, 131.4, 129.1, 128.3, 127.9, 127.4, 125.9, 48.4, 42.3, 41.9, 40.3, 37.0, 25.2, 23.9, 13.6, 13.0, 13.0.

LC/MS: m/z calculated for $C_{27}H_{34}N_4O_4$ $[M + H]^+$: 479.3, found: 479.2.



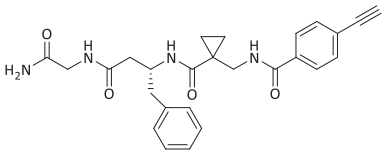
13

Compound **13**: Yield: 18.0 mg (0.040 mmol ≙ 86% of th.), colorless solid.

^{1}H-NMR (300 MHz, DMSO-d_6): δ [ppm] = 8.50 (t, *J* = 6.1 Hz, 1H), 8.16–7.98 (m, 2H), 7.91–7.76 (m, 2H), 7.24 (s, 1H), 7.20–7.07 (m, 4H), 7.06–6.91 (m, 3H), 4.29 (q, *J* = 8.5 Hz, 1H), 3.82 (s, 3H), 3.72–3.40 (m, 4H), 2.90–2.58 (m, 2H), 2.31 (d, *J* = 6.8 Hz, 2H), 0.98–0.61 (m, 4H).

^{13}C-NMR (75 MHz, DMSO): δ [ppm] = 171.5, 171.1, 170.4, 166.8, 161.8, 138.8, 129.3, 129.2, 128.0, 126.1, 126.0, 113.5, 55.4, 48.4, 42.3, 41.9, 25.3, 13.1.

LC/MS: m/z calculated for $C_{25}H_{30}N_4O_5$ $[M + H]^+$: 467.2, found: 467.1.



19

Compound **19**: Yield: 15.0 mg (0.033 mmol ≙ 71% of th.), pale brown solid.

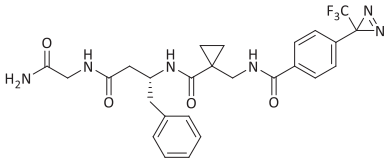
^{1}H-NMR (300 MHz, DMSO-d_6): δ [ppm] = 8.69 (t, *J* = 6.1 Hz, 1H), 8.10 (t, *J* = 5.8 Hz, 1H), 7.96–7.76 (m, 3H), 7.59 (d, *J* = 8.2 Hz, 2H), 7.24 (s, 1H), 7.20–7.06 (m, 5H), 7.03 (s, 1H), 4.39 (s, 1H), 4.30 (q, *J* = 8.2 Hz, 1H), 3.70–3.38 (m, 4H), 2.86–2.57 (m, 2H), 2.32 (d, *J* = 6.8 Hz, 2H), 0.96–0.61 (m, 4H).

^{13}C-NMR (75 MHz, DMSO): δ [ppm] = 171.4, 171.1, 170.4, 166.4, 138.8, 134.0, 131.7, 129.1, 128.0, 127.7, 126.0, 124.7, 83.0, 82.9, 48.4, 42.5, 41.9, 40.2, 25.1, 12.9.

CellPress
OPEN ACCESS

iScience
Article

LC/MS: m/z calculated for $C_{26}H_{28}N_4O_4$ $[M + H]^+$: 461.2, found: 461.1.



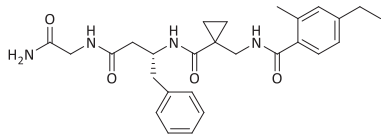
20

Compound **20**: Yield: 17.0 mg (0.031 mmol ≙ 69% of th.), colorless solid.

^{1}H-NMR (300 MHz, DMSO-d_6): δ [ppm] = 8.74 (t, J = 6.0 Hz, 1H), 8.09 (t, J = 5.9 Hz, 1H), 8.01–7.89 (m, 2H), 7.82 (d, J = 8.2 Hz, 1H), 7.39 (d, J = 8.1 Hz, 2H), 7.23 (s, 1H), 7.18–7.03 (m, 4H), 7.03 (s, 1H), 4.29 (p, J = 7.1 Hz, 1H), 3.80–3.39 (m, 4H), 2.94–2.57 (m, 2H), 2.31 (d, J = 6.8 Hz, 2H), 0.99–0.69 (m, 4H).

^{13}C-NMR (75 MHz, DMSO): δ [ppm] = 171.4, 171.1, 170.4, 166.1, 138.8, 135.6, 130.4, 129.1, 128.3, 127.9, 126.4, 125.9, 123.1, 120.4, 48.3, 42.5, 41.9, 40.2, 39.4, 28.3, 27.9, 25.1, 12.8.

LC/MS: m/z calculated for $C_{26}H_{27}F_3N_6O_4$ $[M + H]^+$: 545.2, found: 545.1.



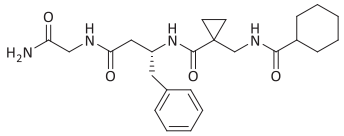
21

Compound **21**: Yield: 10.1 mg (0.021 mmol ≙ 46% of th.), colorless solid.

^{1}H-NMR (300 MHz, DMSO-d_6): δ [ppm] = 8.36 (t, J = 6.2 Hz, 1H), 8.09 (t, J = 5.8 Hz, 1H), 7.93 (d, J = 8.1 Hz, 1H), 7.30–7.11 (m, 7H), 7.11–6.92 (m, 3H), 4.40–4.20 (m, 1H), 3.69–3.45 (m, 3H), 3.43–3.25 (m, 1H), 2.74 (qd, J = 13.5, 6.8 Hz, 2H), 2.58 (q, J = 7.6 Hz, 2H), 2.39–2.16 (m, 5H), 1.17 (t, J = 7.6 Hz, 3H), 0.99–0.62 (m, 4H).

^{13}C-NMR (75 MHz, DMSO): δ [ppm] = 171.6, 171.1, 170.3, 170.0, 145.4, 138.9, 135.3, 134.0, 130.0, 129.2, 128.1, 127.4, 126.0, 124.9, 48.6, 41.9, 40.4, 28.0, 25.2, 19.6, 15.6, 12.9, 12.8.

LC/MS: m/z calculated for $C_{27}H_{34}N_4O_4$ $[M + H]^+$: 479.3, found: 479.2.



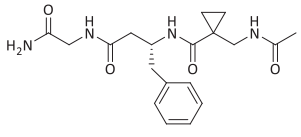
22

Compound **22**: Yield: 16.0 mg (0.036 mmol ≙ 79% of th.), colorless solid.

^{1}H-NMR (300 MHz, DMSO-d_6): δ [ppm] = 8.09 (t, J = 5.8 Hz, 1H), 7.96 (t, J = 6.2 Hz, 1H), 7.86 (d, J = 8.1 Hz, 1H), 7.34–7.09 (m, 6H), 7.02 (s, 1H), 4.38–4.10 (m, 1H), 3.60 (qd, J = 16.8, 5.8 Hz, 2H), 3.45–3.21 (m, 1H), 3.12 (dd, J = 14.7, 6.1 Hz, 1H), 2.89–2.56 (m, 2H), 2.27 (d, J = 6.9 Hz, 2H), 2.19–1.98 (m, 1H), 1.80–1.47 (m, 5H), 1.47–1.02 (m, 5H), 0.91–0.70 (m, 2H), 0.69–0.55 (m, 2H).

^{13}C-NMR (75 MHz, DMSO): δ [ppm] = 176.3, 171.5, 171.1, 170.3, 138.9, 129.2, 128.1, 126.0, 48.4, 43.9, 41.9, 41.3, 40.3, 29.2, 29.1, 25.4, 25.3, 25.1, 12.9, 12.8.

LC/MS: m/z calculated for $C_{24}H_{34}N_4O_4$ $[M + H]^+$: 443.3, found: 443.2.



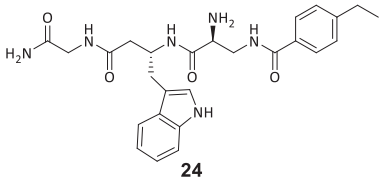
23

Compound **23**: Yield: 7.2 mg (0.018 mmol ≙ 41% of th.), colorless solid.

^{1}H-NMR (300 MHz, DMSO-d_6): δ [ppm] = 8.08 (q, J = 5.9 Hz, 2H), 7.78 (d, J = 8.0 Hz, 1H), 7.42–7.10 (m, 6H), 7.03 (s, 1H), 4.25 (p, J = 6.9 Hz, 1H), 3.80–3.46 (m, 2H), 3.22 (qd, J = 14.8, 6.2 Hz, 2H), 2.93–2.56 (m, 2H), 2.29 (d, J = 6.9 Hz, 2H), 1.80 (s, 3H), 1.01–0.72 (m, 2H), 0.71–0.56 (m, 2H).

^{13}C-NMR (75 MHz, DMSO): δ [ppm] = 171.4, 171.1, 170.3, 170.3, 138.8, 129.2, 128.1, 126.0, 48.3, 41.9, 41.7, 40.0, 39.4, 25.1, 22.5, 12.9.

LC/MS: m/z calculated for $C_{19}H_{26}N_4O_4$ $[M + H]^+$: 375.2, found: 375.2.



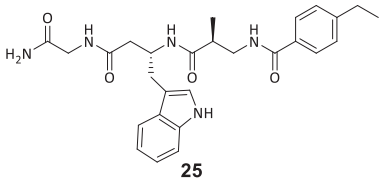
24

Compound **24**: Yield: 5.0 mg (0.010 mmol ≙ 23% of th.), colorless solid.

^{1}H-NMR (400 MHz, DMSO-d_6): δ [ppm] = 10.82 (s, 1H), 8.49 (d, J = 8.0 Hz, 1H), 8.41 (t, J = 5.7 Hz, 1H), 8.21 (s, 3H), 8.02 (t, J = 5.8 Hz, 1H), 7.76 (d, J = 7.9 Hz, 2H), 7.59 (d, J = 7.9 Hz, 1H), 7.43–7.21 (m, 4H), 7.13 (s, 1H), 7.10–7.00 (m, 2H), 6.95 (t, J = 7.4 Hz, 1H), 4.35 (q, J = 7.0 Hz, 1H), 3.94 (t, J = 6.1 Hz, 1H), 3.63 (d, J = 5.7 Hz, 2H), 3.59 (t, J = 5.9 Hz, 2H), 2.83 (m, 2H), 2.65 (q, J = 7.5 Hz, 2H), 2.44–2.29 (m, 2H), 1.18 (t, J = 7.6 Hz, 3H).

^{13}C-NMR (101 MHz, DMSO): δ [ppm] = 171.1, 170.3, 167.1, 166.0, 147.6, 136.2, 131.3, 127.6, 127.5, 127.4, 123.5, 120.9, 118.5, 118.2, 111.3, 110.7, 52.3, 47.8, 41.7, 40.2, 39.0, 29.9, 28.0, 15.4.

LC/MS: m/z calculated for $C_{26}H_{32}N_6O_4$ $[M + H]^+$: 493.3, found: 493.2.



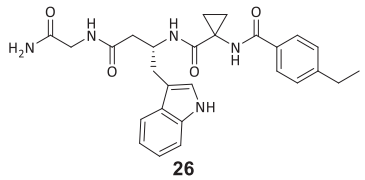
25

Compound **25**: Yield: 1.2 mg (2.520 μmol ≙ 1% of th.), colorless solid.

^{1}H-NMR (400 MHz, DMSO-d_6): δ [ppm] = 10.75 (s, 1H), 8.33 (t, J = 5.8 Hz, 1H), 7.96 (t, J = 5.8 Hz, 1H), 7.78 (d, J = 8.2 Hz, 1H), 7.73 (d, J = 7.9 Hz, 2H), 7.58 (d, J = 7.9 Hz, 1H), 7.31 (d, J = 8.1 Hz, 1H), 7.25 (d, J = 7.5 Hz, 3H), 7.09 (s, 1H), 7.07–6.99 (m, 2H), 6.94 (t, J = 7.4 Hz, 1H), 4.32 (q, J = 7.0 Hz, 1H), 3.69–3.48 (m, 2H), 3.28–3.12 (m, 2H), 2.81 (m, 2H), 2.69–2.53 (m, 3H), 2.38–2.16 (m, 2H), 1.21–1.09 (m, 3H), 0.98 (d, J = 6.8 Hz, 3H).

^{13}C-NMR (101 MHz, DMSO): δ [ppm] = 173.7, 171.1, 170.6, 166.3, 147.0, 136.1, 132.1, 127.6, 127.6, 127.2, 123.3, 120.8, 118.6, 118.2, 111.3, 111.1, 47.1, 42.5, 41.9, 30.2, 28.0, 15.6, 15.4.

LC/MS: m/z calculated for $C_{27}H_{33}N_5O_4$ $[M + H]^+$: 492.3, found: 492.1.



26

Compound **26**: Yield: 5.0 mg (0.010 mmol ≙ 23% of th.), colorless solid.

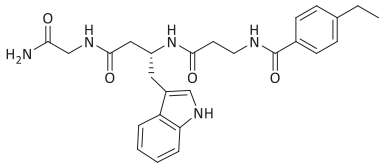
^{1}H-NMR (400 MHz, DMSO-d_6): δ [ppm] = 10.81 (s, 1H), 8.85 (s, 1H), 7.94 (t, J = 5.9 Hz, 1H), 7.87–7.73 (m, 3H), 7.60 (d, J = 7.9 Hz, 1H), 7.42–7.27 (m, 3H), 7.25 (s, 1H), 7.16 (s, 1H), 7.09–6.97 (m, 2H), 6.94 (t, J = 7.4 Hz, 1H), 4.30 (h, J = 6.6 Hz, 1H), 3.61 (t, J = 5.2 Hz, 2H), 2.99–2.71 (m, 2H), 2.66 (q, J = 7.6 Hz, 2H), 2.29 (ddd, J = 48.3, 14.5, 6.2 Hz, 2H), 1.44–1.28 (m, 2H), 1.26–1.10 (m, 3H), 1.06–0.86 (m, 2H).

^{13}C-NMR (101 MHz, DMSO): δ [ppm] = 171.1, 170.8, 170.8, 167.4, 147.4, 136.1, 131.8, 127.8, 127.5, 127.5, 123.6, 120.8, 118.5, 118.2, 111.2, 110.9, 41.8, 38.8, 34.7, 29.7, 28.1, 16.2, 15.5.

CellPress
OPEN ACCESS

iScience
Article

LC/MS: m/z calculated for $C_{27}H_{31}N_5O_4$ [M + H]$^+$: 490.2, found: 490.1.



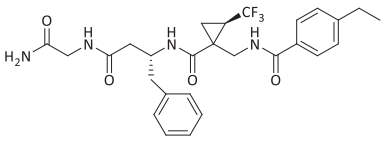
27

Compound **27**: Yield: 11.0 mg (0.023 mmol ≙ 50% of th.), colorless solid.

^{1}H-NMR (300 MHz, DMSO-d_6): δ [ppm] = 10.79 (d, J = 2.4 Hz, 1H), 8.38 (t, J = 5.6 Hz, 1H), 8.03 (t, J = 5.8 Hz, 1H), 7.87 (d, J = 8.2 Hz, 1H), 7.79–7.66 (m, 2H), 7.58 (d, J = 7.8 Hz, 1H), 7.37–7.19 (m, 4H), 7.11 (d, J = 2.2 Hz, 1H), 7.09–7.00 (m, 2H), 7.00–6.90 (m, 1H), 4.33 (q, J = 7.2 Hz, 1H), 3.69–3.50 (m, 3H), 3.49–3.29 (m, 2H), 2.83 (d, J = 6.5 Hz, 2H), 2.64 (q, J = 7.6 Hz, 2H), 2.42–2.18 (m, 3H), 1.18 (t, J = 7.6 Hz, 3H).

^{13}C-NMR (75 MHz, DMSO): δ [ppm] = 171.1, 170.6, 169.9, 166.1, 147.1, 136.1, 132.0, 127.6, 127.2, 123.4, 120.8, 118.6, 118.2, 111.3, 111.1, 47.2, 41.9, 40.0, 36.1, 35.7, 29.8, 28.0, 15.4.

LC/MS: m/z calculated for $C_{26}H_{31}N_5O_4$ [M + H]$^+$: 478.2, found: 478.1.



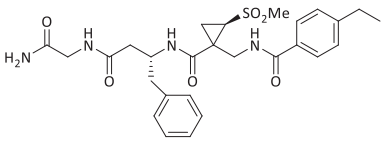
28

Compound **28**: Yield: 23.2 mg (0.040 mmol ≙ 87% of th.), colorless solid.

^{1}H-NMR (300 MHz, DMSO-d_6): δ [ppm] = 8.51 (s, 1H), 8.15 (d, J = 7.5 Hz, 1H), 7.81–7.74 (m, 2H), 7.37–7.13 (m, 6H), 7.07 (s, 4H), 3.70 (s, 4H), 3.63–3.56 (m, 2H), 2.72–2.58 (m, 3H), 2.41–2.29 (m, 2H), 2.05–1.83 (m, 1H), 1.48–1.28 (m, 2H), 1.19 (ddd, J = 7.5, 5.1, 2.7 Hz, 3H).

^{13}C-NMR (75 MHz, DMSO): δ [ppm] = 244.5, 237.0, 214.3, 204.3, 166.2, 148.9, 147.6, 138.2, 131.3, 129.3, 129.1, 128.0, 127.9, 127.7, 127.5, 127.5, 40.3, 40.0, 39.1, 38.8, 38.5, 28.1, 15.4.

LC/MS: m/z calculated for $C_{27}H_{31}F_3N_4O_4$ [M + H]$^+$: 533.2, found: 533.2.



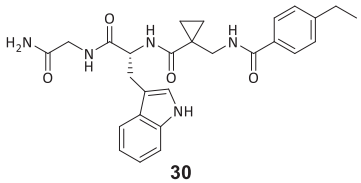
29

Compound **29**: Yield: 19.5 mg (0.036 mmol ≙ 72% of th.), colorless solid.

^{1}H-NMR (300 MHz, DMSO-d_6): δ [ppm] = 8.58–8.41 (m, 1H), 8.26 (t, J = 8.8 Hz, 1H), 8.12 (q, J = 5.8 Hz, 1H), 7.79 (d, J = 7.3 Hz, 2H), 7.36–7.09 (m, 6H), 7.04 (s, 3H), 4.33–4.16 (m, 5H), 3.83 (ddd, J = 30.8, 14.8, 5.2 Hz, 1H), 3.64–3.48 (m, 2H), 3.14 (s, 1H), 3.00–2.80 (m, 1H), 2.66 (qd, J = 7.4, 3.3 Hz, 3H), 2.41–2.26 (m, 2H), 1.73–1.62 (m, 2H), 1.19 (td, J = 7.6, 2.7 Hz, 3H).

^{13}C-NMR (75 MHz, DMSO): δ [ppm] = 171.1, 171.1, 170.3, 170.2, 167.8, 167.6, 167.3, 167.2, 147.8, 147.7, 138.6, 138.5, 131.2, 131.2, 129.3, 129.1, 128.1, 127.9, 127.7, 127.6, 127.5, 42.8, 42.8, 32.9, 32.8, 28.1, 15.4.

LC/MS: m/z calculated for $C_{27}H_{34}N_4O_6S$ [M + H]$^+$: 543.2, found: 543.2.



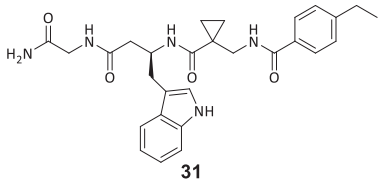
30

Compound **30**: Yield: 24.0 mg (0.049 mmol ≙ quant.), colorless solid.

^{1}H-NMR (300 MHz, DMSO-d_6): δ [ppm] = 10.77 (d, J = 2.4 Hz, 1H), 8.63 (t, J = 6.1 Hz, 1H), 8.44 (d, J = 6.7 Hz, 1H), 8.32 (t, J = 5.9 Hz, 1H), 7.80–7.67 (m, 2H), 7.60 (d, J = 7.7 Hz, 1H), 7.35–7.23 (m, 3H), 7.20 (d, J = 2.3 Hz, 1H), 7.14–7.01 (m, 3H), 6.97 (ddd, J = 8.0, 6.9, 1.1 Hz, 1H), 4.41 (dt, J = 9.4, 6.3 Hz, 1H), 3.74–3.56 (m, 2H), 3.56–3.44 (m, 2H), 3.17 (dd, J = 14.7, 4.8 Hz, 1H), 3.01 (dd, J = 14.7, 9.3 Hz, 1H), 2.65 (q, J = 7.6 Hz, 2H), 1.19 (t, J = 7.6 Hz, 3H), 0.98–0.71 (m, 4H).

^{13}C-NMR (75 MHz, DMSO): δ [ppm] = 172.9, 172.1, 171.1, 167.4, 147.5, 136.1, 131.4, 127.7, 127.5, 127.3, 123.6, 120.9, 118.4, 118.3, 111.4, 110.3, 54.8, 42.3, 42.2, 28.1, 27.1, 25.2, 15.4, 13.6.

LC/MS: m/z calculated for $C_{27}H_{31}N_5O_4$ $[M + H]^+$: 490.2, found: 490.1.



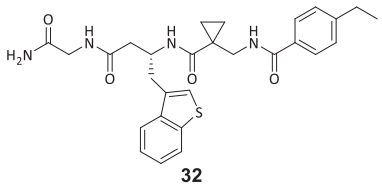
31

Compound **31**: Yield: 8.0 mg (0.016 mmol ≙ 35% of th.), colorless solid.

^{1}H-NMR (300 MHz, DMSO-d_6): δ [ppm] = 10.76 (d, J = 2.4 Hz, 1H), 8.57 (t, J = 6.1 Hz, 1H), 8.16–7.90 (m, 2H), 7.84–7.68 (m, 2H), 7.60 (d, J = 7.8 Hz, 1H), 7.35–7.25 (m, 3H), 7.23 (s, 1H), 7.09 (d, J = 2.2 Hz, 1H), 7.07–6.98 (m, 2H), 6.98–6.88 (m, 1H), 4.34 (q, J = 6.9 Hz, 1H), 3.72–3.36 (m, 4H), 2.83 (d, J = 6.5 Hz, 2H), 2.65 (q, J = 7.6 Hz, 2H), 2.34 (d, J = 6.8 Hz, 2H), 1.19 (t, J = 7.6 Hz, 3H), 1.06–0.59 (m, 4H).

^{13}C-NMR (75 MHz, DMSO): δ [ppm] = 171.5, 171.1, 170.6, 167.2, 147.5, 136.1, 131.5, 127.7, 127.6, 127.4, 123.3, 120.8, 118.6, 118.2, 111.3, 111.2, 47.7, 42.3, 41.9, 39.9, 29.8, 28.1, 25.3, 15.4, 13.2, 12.9.

LC/MS: m/z calculated for $C_{28}H_{33}N_5O_4$ $[M + H]^+$: 504.3, found: 504.1.



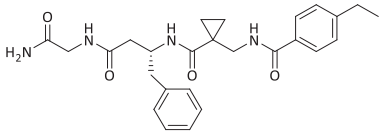
32

Compound **32**: Yield: 10.0 mg (0.019 mmol ≙ 43% of th.), colorless solid.

^{1}H-NMR (300 MHz, DMSO-d_6): δ [ppm] = 8.58 (t, J = 6.1 Hz, 1H), 8.22–8.05 (m, 2H), 8.02–7.93 (m, 1H), 7.93–7.85 (m, 1H), 7.81–7.68 (m, 2H), 7.47–7.18 (m, 6H), 7.03 (s, 1H), 4.42 (q, J = 7.0 Hz, 1H), 3.75–3.43 (m, 4H), 3.00 (qd, J = 14.2, 6.6 Hz, 2H), 2.65 (q, J = 7.5 Hz, 2H), 2.41 (d, J = 6.9 Hz, 2H), 1.19 (t, J = 7.6 Hz, 3H), 0.98–0.68 (m, 4H).

^{13}C-NMR (75 MHz, DMSO): δ [ppm] = 171.7, 171.0, 170.4, 167.2, 147.5, 139.6, 139.0, 133.2, 131.4, 127.7, 127.4, 124.2, 124.0, 123.3, 122.8, 122.1, 46.7, 42.3, 41.9, 40.2, 32.8, 28.1, 25.3, 15.4, 13.1.

LC/MS: m/z calculated for $C_{28}H_{32}N_4O_4S$ $[M + H]^+$: 521.2, found: 521.1.



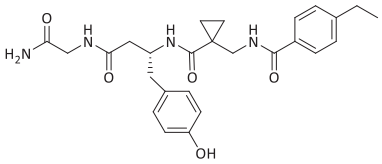
14

Compound **14**: Yield: 16.0 mg (0.034 mmol ≙ 77% of th.), colorless solid.

^{1}H-NMR (600 MHz, DMSO-d_6): δ [ppm] = 8.58 (t, J = 6.2 Hz, 1H), 8.11 (t, J = 5.9 Hz, 1H), 8.01 (d, J = 8.2 Hz, 1H), 7.82–7.74 (m, 2H), 7.32 (d, J = 8.2 Hz, 2H), 7.25 (s, 1H), 7.15–7.12 (m, 4H), 7.12–7.07 (m, 1H), 7.04 (s, 1H), 4.33–4.22 (m, 1H), 3.61 (dd, J = 16.8, 6.0 Hz, 1H), 3.54–3.45 (m, 3H), 2.78 (dd, J = 13.6, 5.1 Hz, 1H), 2.68–2.63 (m, 3H), 2.30 (d, J = 6.9 Hz, 2H), 1.19 (t, J = 7.6 Hz, 3H), 0.92–0.80 (m, 2H), 0.80–0.71 (m, 2H).

^{13}C-NMR (151 MHz, DMSO): δ [ppm] = 171.5, 171.1, 170.4, 167.2, 147.6, 138.9, 131.4, 129.2, 128.0, 127.7, 127.5, 126.0, 48.5, 42.3, 41.9, 40.3, 40.1, 28.1, 25.3, 15.5, 13.1.

LC/MS: m/z calculated for $C_{26}H_{32}N_4O_4$ $[M + H]^+$: 465.3, found: 465.1.



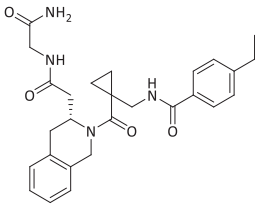
15

Compound **15**: Yield: 15.0 mg (0.031 mmol ≙ 69% of th.), colorless solid.

^{1}H-NMR (600 MHz, DMSO-d_6): δ [ppm] = 9.11 (s, 1H), 8.57 (t, J = 6.1 Hz, 1H), 8.05 (t, J = 5.8 Hz, 1H), 7.95 (d, J = 8.1 Hz, 1H), 7.85–7.71 (m, 2H), 7.41–7.27 (m, 2H), 7.22 (s, 1H), 7.02 (s, 1H), 6.97–6.86 (m, 2H), 6.64–6.49 (m, 2H), 4.21 (h, J = 7.3 Hz, 1H), 3.69–3.44 (m, 4H), 2.74–2.53 (m, 4H), 2.27 (d, J = 6.8 Hz, 2H), 1.19 (t, J = 7.6 Hz, 3H), 0.96–0.60 (m, 4H).

^{13}C-NMR (151 MHz, DMSO): δ [ppm] = 171.5, 171.1, 170.4, 167.2, 155.5, 147.6, 131.4, 130.0, 128.9, 127.7, 127.5, 114.8, 48.7, 42.3, 41.9, 40.2, 38.8, 28.1, 25.2, 15.4, 13.0.

LC/MS: m/z calculated for $C_{26}H_{32}N_4O_5$ $[M + H]^+$: 481.2, found: 481.1.



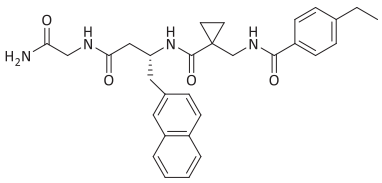
35

Compound **35**: Yield: 11.0 mg (0.023 mmol ≙ 50% of th.), colorless solid.

^{1}H-NMR (400 MHz, DMSO-d_6): δ [ppm] = 8.42 (t, J = 6.1 Hz, 1H), 8.08 (t, J = 6.0 Hz, 1H), 7.70 (d, J = 7.8 Hz, 2H), 7.26 (d, J = 7.9 Hz, 2H), 7.24–7.18 (m, 1H), 7.18–7.08 (m, 4H), 7.00 (s, 1H), 5.39–4.83 (m, 2H), 4.58 (s, 1H), 3.78–3.50 (m, 3H), 2.82–2.67 (m, 1H), 2.63 (q, J = 7.6 Hz, 3H), 2.45–2.23 (m, 2H), 1.18 (t, J = 7.6 Hz, 3H), 0.93–0.49 (m, 4H).

^{13}C-NMR (101 MHz, DMSO): δ [ppm] = 170.9, 170.2, 170.1, 166.5, 147.2, 131.8, 127.6, 127.3, 126.6, 126.0, 41.9, 37.0, 32.0, 28.0, 26.0, 15.4, 9.8, 9.5.

LC/MS: m/z calculated for $C_{27}H_{32}N_4O_4$ $[M + H]^+$: 477.3, found: 477.1.



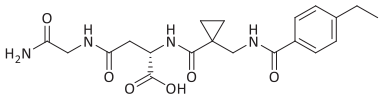
36

Compound **36**: Yield: 19.0 mg (0.037 mmol ≙ 80% of th.), colorless solid.

^{1}H-NMR (300 MHz, DMSO-d_6): δ [ppm] = 8.59 (t, J = 6.1 Hz, 1H), 8.23–8.03 (m, 2H), 7.88–7.72 (m, 3H), 7.69 (d, J = 8.4 Hz, 1H), 7.64–7.49 (m, 2H), 7.50–7.36 (m, 2H), 7.36–7.27 (m, 3H), 7.25 (s, 1H), 7.04 (s, 1H), 4.41 (p, J = 6.9 Hz, 1H), 3.77–3.46 (m, 3H), 3.46–3.26 (m, 1H), 2.98 (dd, J = 13.6, 4.9 Hz, 1H), 2.91–2.75 (m, 1H), 2.67 (q, J = 7.6 Hz, 2H), 2.43–2.28 (m, 2H), 1.21 (t, J = 7.6 Hz, 3H), 0.98–0.66 (m, 4H).

^{13}C-NMR (75 MHz, DMSO): δ [ppm] = 171.5, 171.1, 170.3, 167.2, 147.6, 136.6, 132.9, 131.6, 131.3, 127.9, 127.7, 127.5, 127.4, 127.4, 127.3, 127.2, 125.8, 125.2, 48.4, 42.3, 41.9, 40.5, 39.7, 28.1, 25.3, 15.4, 13.3, 13.0.

LC/MS: m/z calculated for $C_{30}H_{34}N_4O_4$ $[M + H]^+$: 515.3, found: 515.2.



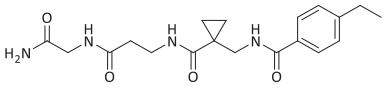
37

Compound **37**: Yield: 5.0 mg (0.012 mmol ≙ 26% of th.), colorless solid.

^{1}H-NMR (600 MHz, DMSO-d_6): δ [ppm] = 8.60 (t, *J* = 6.1 Hz, 1H), 8.26–8.20 (m, 2H), 7.81–7.74 (m, 2H), 7.35 (s, 1H), 7.30 (d, *J* = 8.1 Hz, 2H), 7.08 (s, 1H), 4.49 (q, *J* = 7.0 Hz, 1H), 3.62 (dd, *J* = 16.9, 6.1 Hz, 1H), 3.58–3.50 (m, 2H), 3.47 (dd, *J* = 16.9, 5.6 Hz, 1H), 2.71–2.60 (m, 3H), 1.19 (t, *J* = 7.6 Hz, 4H), 0.99–0.91 (m, 2H), 0.87–0.78 (m, 2H).

^{13}C-NMR (151 MHz, DMSO): δ [ppm] = 173.1, 172.2, 172.1, 171.2, 169.6, 167.3, 147.5, 131.5, 127.7, 127.6, 49.8, 42.1, 42.1, 40.1, 37.1, 28.1, 24.9, 15.5, 13.3, 13.0.

LC/MS: m/z calculated for $C_{20}H_{26}N_4O_6$ $[M + H]^+$: 419.2, found: 419.1.



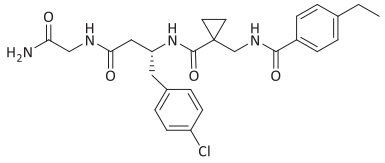
38

Compound **38**: Yield: 5.0 mg (0.013 mmol ≙ 29% of th.), colorless solid.

^{1}H-NMR (600 MHz, DMSO-d_6): δ [ppm] = 8.60 (t, *J* = 6.1 Hz, 1H), 8.10 (dt, *J* = 15.2, 5.6 Hz, 2H), 7.82–7.75 (m, 2H), 7.36–7.26 (m, 3H), 7.05 (s, 1H), 3.58 (d, *J* = 5.8 Hz, 2H), 3.51 (d, *J* = 6.0 Hz, 2H), 3.28 (td, *J* = 7.2, 5.3 Hz, 2H), 2.65 (q, *J* = 7.6 Hz, 2H), 2.30 (t, *J* = 7.3 Hz, 2H), 1.18 (t, *J* = 7.6 Hz, 3H), 0.95 (q, *J* = 3.7 Hz, 2H), 0.81 (q, *J* = 3.7 Hz, 2H).

^{13}C-NMR (151 MHz, DMSO): δ [ppm] = 172.2, 171.2, 170.8, 167.2, 147.6, 131.5, 127.8, 127.5, 42.2, 41.9, 40.1, 36.0, 35.2, 28.1, 25.1, 15.5, 13.1.

LC/MS: m/z calculated for $C_{19}H_{26}N_4O_4$ $[M + H]^+$: 375.2, found: 375.1.



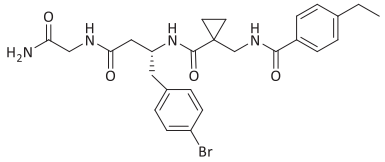
16

Compound **16**: Yield: 21.0 mg (0.042 mmol ≙ 26% of th.), colorless solid.

^{1}H-NMR (300 MHz, DMSO-d_6): δ [ppm] = 8.58 (t, *J* = 6.1 Hz, 1H), 8.11 (t, *J* = 5.8 Hz, 1H), 8.01 (d, *J* = 8.1 Hz, 1H), 7.77 (d, *J* = 8.2 Hz, 2H), 7.31 (d, *J* = 8.2 Hz, 2H), 7.25 (s, 1H), 7.13 (s, 4H), 7.03 (s, 1H), 4.28 (q, *J* = 7.8 Hz, 1H), 3.68–3.40 (m, 4H), 2.82 (dd, *J* = 13.6, 4.8 Hz, 1H), 2.74–2.60 (m, 3H), 2.32 (d, *J* = 6.9 Hz, 2H), 1.20 (t, *J* = 7.6 Hz, 3H), 0.93–0.72 (m, 4H).

^{13}C-NMR (75 MHz, DMSO): δ [ppm] = 171.6, 171.1, 170.3, 167.2, 147.6, 137.8, 131.4, 131.0, 130.6, 127.8, 127.7, 127.5, 54.9, 48.2, 42.3, 41.9, 40.2, 38.6, 28.1, 25.3, 15.4, 13.2, 13.1.

LC/MS: m/z calculated for $C_{26}H_{31}ClN_4O_4$ $[M + H]^+$: 499.2, found: 498.9.



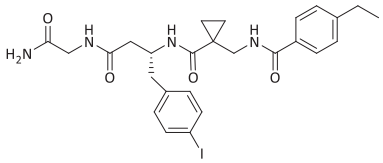
17

Compound **17**: Yield: 29.1 mg (0.053 mmol ≙ 34% of th.), colorless solid.

^{1}H-NMR (300 MHz, DMSO-d_6): δ [ppm] = 8.59 (t, *J* = 6.1 Hz, 1H), 8.12 (t, *J* = 5.9 Hz, 1H), 8.01 (d, *J* = 8.1 Hz, 1H), 7.77 (d, *J* = 8.3 Hz, 2H), 7.35–7.29 (m, 2H), 7.28–7.20 (m, 3H), 7.11–6.99 (m, 3H), 4.28 (td, *J* = 7.8, 4.8 Hz, 1H), 3.69–3.47 (m, 3H), 3.42 (d, *J* = 5.9 Hz, 1H), 2.80 (dd, *J* = 13.6, 4.8 Hz, 1H), 2.65 (p, *J* = 7.6 Hz, 3H), 2.32 (d, *J* = 6.9 Hz, 2H), 1.20 (t, *J* = 7.6 Hz, 3H), 0.95–0.71 (m, 4H).

^{13}C-NMR (75 MHz, DMSO): δ [ppm] = 172.0, 171.5, 170.7, 167.6, 148.0, 138.7, 131.8, 131.2, 128.2, 127.9, 119.6, 48.6, 42.8, 42.4, 28.5, 25.7, 15.9, 13.7, 13.5.

LC/MS: m/z calculated for $C_{26}H_{31}BrN_4O_4$ $[M + H]^+$: 543.1, found: 543.1.



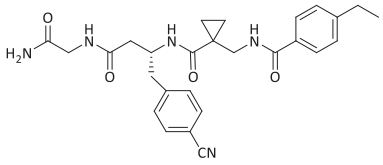
33

Compound **33**: Yield: 32.1 mg (0.054 mmol ≙ 34% of th.), colorless solid.

^{1}H-NMR (300 MHz, DMSO-d_6): δ [ppm] = 8.59 (t, *J* = 6.1 Hz, 1H), 8.11 (t, *J* = 5.9 Hz, 1H), 8.00 (d, *J* = 8.1 Hz, 1H), 7.77 (d, *J* = 8.3 Hz, 2H), 7.46–7.37 (m, 2H), 7.36–7.28 (m, 2H), 7.25 (s, 1H), 7.03 (s, 1H), 6.93 (d, *J* = 8.3 Hz, 2H), 4.27 (q, *J* = 7.2 Hz, 1H), 3.74–3.47 (m, 4H), 2.78 (dd, *J* = 13.7, 4.8 Hz, 1H), 2.72–2.56 (m, 3H), 2.31 (d, *J* = 6.9 Hz, 2H), 1.21 (t, *J* = 7.6 Hz, 3H), 0.95–0.71 (m, 4H).

^{13}C-NMR (75 MHz, DMSO): δ [ppm] = 172.0, 171.5, 170.7, 167.6, 148.0, 139.0, 137.1, 132.0, 131.8, 128.2, 127.9, 92.2, 48.6, 42.8, 42.4, 40.7, 28.6, 25.7, 15.9, 13.7, 13.5.

LC/MS: m/z calculated for $C_{26}H_{31}ClN_4O_4$ $[M + H]^+$: 591.1, found: 591.1.



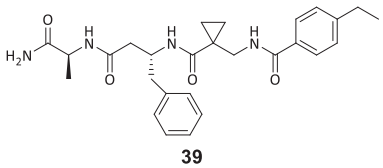
34

Compound **34**: Yield: 26.0 mg (0.044 mmol ≙ 28% of th.), colorless solid.

^{1}H-NMR (300 MHz, DMSO-d_6): δ [ppm] = 8.59 (t, *J* = 6.1 Hz, 1H), 8.15 (t, *J* = 5.9 Hz, 1H), 8.06 (d, *J* = 8.1 Hz, 1H), 7.74 (d, *J* = 8.3 Hz, 2H), 7.50 (d, *J* = 8.3 Hz, 2H), 7.30 (t, *J* = 7.9 Hz, 5H), 7.03 (s, 1H), 4.33 (dq, *J* = 11.7, 6.7 Hz, 1H), 3.68–3.49 (m, 3H), 3.33 (d, *J* = 5.9 Hz, 1H), 2.95 (dd, *J* = 13.6, 4.6 Hz, 1H), 2.81–2.60 (m, 3H), 2.35 (d, *J* = 7.0 Hz, 2H), 1.21 (t, *J* = 7.6 Hz, 3H), 0.94–0.70 (m, 4H).

^{13}C-NMR (75 MHz, DMSO): δ [ppm] = 172.1, 171.5, 170.6, 167.6, 148.1, 145.3, 132.2, 131.7, 130.6, 128.1, 127.9, 119.4, 109.2, 48.3, 42.8, 42.3, 40.7, 28.5, 25.7, 15.8, 13.7, 13.5.

LC/MS: m/z calculated for $C_{27}H_{31}N_5O_4$ $[M + H]^+$: 490.2, found: 490.2.



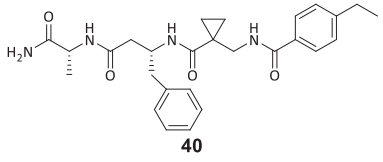
39

Compound **39**: Yield: 14 mg (0.029 mmol ≙ 64% of th.), colorless solid.

^{1}H-NMR (300 MHz, DMSO-d_6): δ [ppm] = 8.53 (t, *J* = 6.1 Hz, 1H), 8.03–7.90 (m, 2H), 7.85–7.69 (m, 2H), 7.39–7.28 (m, 2H), 7.26 (s, 1H), 7.20–7.01 (m, 5H), 6.96 (s, 1H), 4.29 (h, *J* = 7.4 Hz, 1H), 4.16 (p, *J* = 7.1 Hz, 1H), 3.48 (p, *J* = 8.5 Hz, 2H), 2.78 (dd, *J* = 13.5, 5.2 Hz, 1H), 2.72–2.58 (m, 3H), 2.28 (d, *J* = 6.9 Hz, 2H), 1.24–1.11 (m, 6H), 0.92–0.71 (m, 4H).

^{13}C-NMR (75 MHz, DMSO): δ [ppm] = 174.4, 171.5, 169.7, 167.2, 147.6, 138.8, 131.5, 129.1, 128.0, 127.7, 127.5, 126.0, 48.5, 48.0, 42.2, 28.1, 25.2, 18.2, 15.4, 13.0, 12.9.

LC/MS: m/z calculated for $C_{27}H_{34}N_4O_4$ $[M + H]^+$: 479.3, found: 479.2.



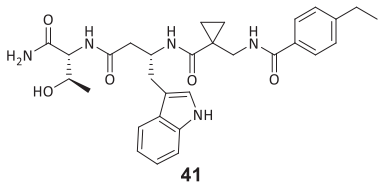
40

Compound **40**: Yield: 3.0 mg (6.263 μmol ≙ 14% of th.), colorless solid.

^{1}H-NMR (400 MHz, DMSO-d_6): δ [ppm] = 8.54 (t, J = 6.0 Hz, 1H), 8.01–7.90 (m, 2H), 7.77 (d, J = 7.8 Hz, 2H), 7.31 (d, J = 7.8 Hz, 2H), 7.25 (s, 1H), 7.18–7.02 (m, 5H), 6.95 (s, 1H), 4.28 (q, J = 7.0 Hz, 1H), 4.16 (p, J = 7.2 Hz, 1H), 3.62–3.51 (m, 1H), 3.44–3.34 (m, 1H), 2.83–2.60 (m, 4H), 2.30 (d, J = 6.9 Hz, 2H), 1.28–1.09 (m, 6H), 0.95–0.67 (m, 4H).

^{13}C-NMR (101 MHz, DMSO): δ [ppm] = 174.3, 171.4, 169.7, 167.2, 147.6, 138.8, 131.4, 129.1, 127.9, 127.7, 127.5, 125.9, 48.4, 48.0, 42.3, 40.2, 28.1, 25.2, 18.2, 15.4, 13.0, 12.9.

LC/MS: m/z calculated for $C_{27}H_{34}N_4O_4$ $[M + H]^+$: 479.3, found: 479.1.



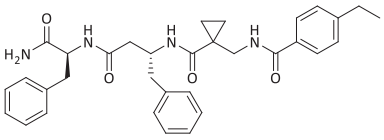
41

Compound **41**: Yield: 7.0 mg (0.013 mmol ≙ 28% of th.), colorless solid.

^{1}H-NMR (300 MHz, DMSO-d_6): δ [ppm] = 10.75 (d, J = 2.4 Hz, 1H), 8.56 (t, J = 6.1 Hz, 1H), 8.00 (d, J = 7.9 Hz, 1H), 7.86 (d, J = 8.6 Hz, 1H), 7.82–7.68 (m, 3H), 7.58 (d, J = 7.8 Hz, 1H), 7.37–7.19 (m, 5H), 7.12–6.98 (m, 3H), 6.98–6.88 (m, 1H), 4.35 (q, J = 6.9 Hz, 1H), 4.21 (dd, J = 8.6, 6.1 Hz, 1H), 3.84 (p, J = 6.3 Hz, 1H), 2.82 (d, J = 6.5 Hz, 2H), 2.65 (q, J = 7.6 Hz, 2H), 2.38 (d, J = 6.9 Hz, 2H), 1.19 (t, J = 7.6 Hz, 4H), 1.03 (d, J = 6.3 Hz, 3H), 0.93–0.86 (m, 2H), 0.81–0.73 (m, 2H).

^{13}C-NMR (75 MHz, DMSO): δ [ppm] = 172.3, 171.6, 170.5, 167.2, 147.5, 136.1, 131.5, 127.7, 127.7, 127.6, 127.4, 127.4, 123.2, 120.8, 118.6, 118.2, 111.3, 111.2, 66.8, 58.1, 47.9, 42.2, 40.2, 29.7, 28.1, 25.3, 19.5, 15.4, 13.3, 13.0.

LC/MS: m/z calculated for $C_{30}H_{37}N_5O_5$ $[M + H]^+$: 548.3, found: 547.8.



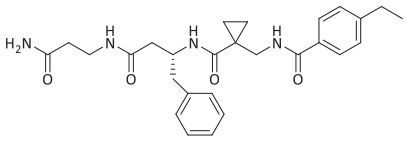
42

Compound **42**: Yield: 15.0 mg (0.027 mmol ≙ 59% of th.), colorless solid.

^{1}H-NMR (300 MHz, DMSO-d_6): δ [ppm] = 8.54 (t, J = 6.1 Hz, 1H), 8.14 (d, J = 8.4 Hz, 1H), 7.98 (d, J = 8.2 Hz, 1H), 7.87–7.71 (m, 2H), 7.39 (s, 1H), 7.31 (d, J = 8.2 Hz, 2H), 7.27–7.22 (m, 3H), 7.22–6.95 (m, 8H), 4.55–4.35 (m, 1H), 4.24 (q, J = 7.3 Hz, 1H), 3.59–3.42 (m, 2H), 3.02 (dd, J = 13.8, 4.7 Hz, 1H), 2.84–2.42 (m, 5H), 2.23 (qd, J = 14.2, 6.9 Hz, 2H), 1.19 (t, J = 7.6 Hz, 3H), 0.97–0.51 (m, 4H).

^{13}C-NMR (75 MHz, DMSO): δ [ppm] = 173.3, 171.5, 170.0, 167.2, 147.6, 138.8, 138.3, 131.5, 129.1, 128.1, 127.9, 127.7, 127.5, 126.2, 125.9, 53.9, 48.4, 42.3, 37.5, 28.1, 25.2, 15.4, 13.0, 13.0.

LC/MS: m/z calculated for $C_{33}H_{38}N_4O_4$ $[M + H]^+$: 555.3, found: 555.2.



43

Compound **43**: Yield: 18.0 mg (0.038 mmol ≙ 82% of th.), colorless solid.

^{1}H-NMR (300 MHz, DMSO-d_6): δ [ppm] = 8.57 (t, J = 6.1 Hz, 1H), 8.05–7.84 (m, 2H), 7.85–7.70 (m, 2H), 7.40–7.24 (m, 3H), 7.22–7.01 (m, 5H), 6.82 (s, 1H), 4.26 (h, J = 7.1 Hz, 1H), 3.61–3.39 (m, 2H), 3.29–3.06 (m, 2H), 2.81–2.57 (m, 4H), 2.32–2.04 (m, 4H), 1.19 (t, J = 7.6 Hz, 3H), 0.98–0.69 (m, 4H).

^{13}C-NMR (75 MHz, DMSO): δ [ppm] = 172.6, 171.4, 169.9, 167.2, 147.6, 138.8, 131.4, 129.2, 128.0, 127.7, 127.5, 125.9, 48.4, 42.2, 40.2, 35.2, 35.0, 28.1, 25.2, 15.4, 13.0.

CellPress
OPEN ACCESS

iScience
Article

LC/MS: m/z calculated for $C_{27}H_{34}N_4O_4$ $[M + H]^+$: 479.3, found: 479.2.



49

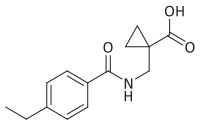
Compound **49**: 1-Cyanocyclopropane-1-carboxylic acid (500 mg, 4.500 mmol, 1.0 eq.) was dissolved in methanol (10 mL), ammonia in methanol (7 M, 1.0 mL), and Raney-nickel (50 mg, 5%) were added. The mixture was stirred under a hydrogen atmosphere (4 bar) for 16 h at RT. The reaction mixture was adjusted to alkaline pH (pH = 8) by adding ammonia in methanol (7 M, 0.5 mL), filtered over Celite S, and the solvent was removed under reduced pressure.

Yield: 574.0 mg (4.986 mmol ≙ quant.), colorless solid.

^{1}H-NMR (300 MHz, Me*O*D): δ [ppm] = 3.06 (s, 2H), 1.36–1.29 (m, 2H), 1.02–0.94 (m, 2H).

^{13}C-NMR (75 MHz, MeOD): δ [ppm] = 177.8, 101.2, 45.2, 15.0.

LC/MS: m/z calculated for $C_5H_9NO_2$ $[M + H]^+$: 116.1, found: 116.0.



50

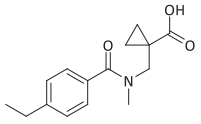
Compound **50**: The crude product **49** (518 mg, 4.500 mmol, 1.0 eq.) was suspended in DCM (10 mL), DMF (0.5 mL), and TEA (620 μL, 4.473 mmol, 1.0 eq.). The mixture was cooled to 0 °C, and a solution of acid 4-ethylbenzoyl chloride (662 μL, 4.500 mmol, 1.0 eq.) in DCM (0.3 mL) was added. The mixture was warmed to RT and stirred for 16 h. The reaction mixture was washed with 1 M hydrochloric acid thrice (5 mL each). The organic phase was separated, dried over sodium sulfate, and the solvents were removed under reduced pressure. The crude product was purified by column chromatography (mobile phase: CH:EtOAc 2:1 with 0.1% TFA)

Yield: 413.0 mg (1.670 mmol ≙ 37% of th.), colorless solid.

^{1}H-NMR (300 MHz, DMSO-d_6): δ [ppm] = 9.99 (s, 1H), 7.80–7.62 (m, 2H), 7.29–7.20 (m, 2H), 7.00 (t, *J* = 6.2 Hz, 1H), 3.62 (d, *J* = 6.1 Hz, 2H), 2.68 (q, *J* = 7.6 Hz, 2H), 1.35 (q, *J* = 4.2 Hz, 2H), 1.24 (t, *J* = 7.6 Hz, 3H), 1.15 (q, *J* = 4.3 Hz, 2H).

^{13}C-NMR (75 MHz, DMSO): δ [ppm] = 181.1, 167.9, 148.5, 131.6, 128.2, 127.3, 42.9, 28.9, 24.8, 16.0, 15.5.

LC/MS: m/z calculated for $C_{14}H_{17}NO_3$ $[M + H]^+$: 248.1, found: 248.0.



51

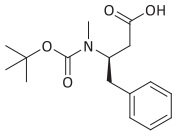
Compound **51**: Compound **50** (50 mg, 0.202 mmol, 1.0 eq.) was dissolved in anhydrous THF (5 mL) and cooled to 0 °C. Sodium hydride (60% suspension, 21 mg, 0.525 mmol, 2.6 eq.) was added and the mixture was stirred for 5 min. Then, methyl iodide (38 μL, 0.610 mmol, 3.0 eq.) was added dropwise. The mixture was warmed to RT and stirred for 16 h. A solution of sodium hydroxide (18 mg, 0.450 mmol, 2.2 eq.) in water (5 mL) was added and the mixture was stirred for 1 h. The mixture was adjusted to acidic pH (pH = 1) with 1 M hydrochloric acid and the solvents were removed under reduced pressure. The crude product was dissolved in sodium hydroxide solution (pH = 12) and was extracted three times with DCM (3 mL each). Then, the aqueous phase was brought to an acidic pH (pH = 1) with 1 M hydrochloric acid and extracted thrice with DCM (3 mL each). The organic phases from the acidic extraction were combined, and dried over sodium sulfate, and the solvent was removed under reduced pressure.

Yield: 44.0 mg (0.168 mmol ≙ 83% of th.), colorless solid.

^{1}H-NMR (300 MHz, *C*D*C*l$_3$, 60 °C): δ [ppm] = 9.87 (s, 1H), 7.30 (d, *J* = 8.2 Hz, 2H), 7.19 (d, *J* = 7.9 Hz, 2H), 3.82 (s, 2H), 3.05 (s, 3H), 2.66 (q, *J* = 7.6 Hz, 2H), 1.39 (q, *J* = 4.1 Hz, 2H), 1.24 (t, *J* = 7.6 Hz, 3H), 1.15–0.94 (m, 2H).

^{13}C-NMR (75 MHz, *C*D*C*l$_3$, 60 °C): δ [ppm] = 179.1, 173.0, 146.2, 133.7, 128.1, 127.9, 127.4, 127.3, 28.8, 23.2, 16.2, 15.3.

LC/MS: m/z calculated for $C_{15}H_{19}NO_3[M + H]^+$: 262.2, found: 262.0.



52

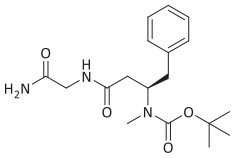
Compound **52**: (*R*)-3-*tert*-butoxycarbonylamino-4-phenylbutyric acid (100 mg, 0.358 mmol, 1.0 eq.) was dissolved in anhydrous THF (7 mL) and cooled to 0 °C. Sodium hydride (60% suspension, 39 mg, 0.975 mmol, 2.7 eq.) was added and the mixture was stirred for 5 min. Then, methyl iodide (67 μL, 1.074 mmol, 3.0 eq.) was added dropwise. The mixture was warmed to RT and stirred for 16 h. Because the reaction was not complete, methyl iodide (46 μL, 0.739 mmol, 2.1 eq.) and sodium hydride (34 mg, 0.850 mmol, 2.4 eq.) were added and the mixture was stirred for an additional 16 h. Water (2 mL) was added, and the pH was confirmed to be > 12. The mixture was stirred for 1 h and all solvents were removed under reduced pressure and the crude product was purified by reversed-phase flash column chromatography (Biotage Isolera, ACN/H_2O + TFA).

Yield: 39.0 mg (0.133 mmol ≙ 37% of th.), colorless solid.

^{1}H-NMR (300 MHz, C*D*Cl$_3$, 60 °C): δ [ppm] = 8.92 (s, 1H), 7.28–6.94 (m, 5H), 4.45 (tt, *J* = 8.9, 6.1 Hz, 1H), 2.93–2.52 (m, 5H), 2.45 (dd, *J* = 15.5 Hz, 5.8 Hz, 1H), 1.27 (s, 9H).

^{13}C-NMR (75 MHz, *C*DCl$_3$, 60 °C): δ [ppm] = 176.1, 155.9, 138.2, 129.2, 128.7, 126.8, 80.3, 55.7, 38.9, 37.6, 30.8, 28.5.

LC/MS: m/z calculated for $C_{16}H_{23}NO_4$ [M-Boc+H]$^+$: 194.1, found: 194.0.



53

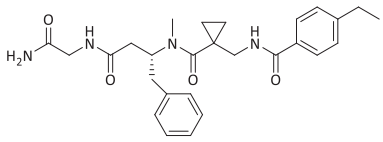
Compound **53**: Compound **52** (35 mg, 0.119 mmol, 1.0 eq.), glycine amide hydrochloride (14 mg, 0.127 mmol, 1.1 eq.), and TBTU (38 mg, 0.119 mmol, 1.0 eq.) were dissolved in anhydrous DMF (1.5 mL), and DIPEA (63 μL, 0.357 mmol, 3.0 eq.) was added. The mixture was stirred for 16 h at RT. All solvents were removed under reduced pressure, and the crude product was purified by reversed-phase flash column chromatography (Biotage Isolera, ACN/H_2O + TFA).

Yield: 33.0 mg (0.094 mmol ≙ 79% of th.), colorless solid.

^{1}H-NMR (300 MHz, C*D*Cl$_3$): δ [ppm] = 7.37–6.99 (m, 6H), 6.85 (s, 1H), 5.92 (s, 1H), 4.62 (s, 1H), 4.17–3.65 (m, 2H), 3.11 (s, 1H), 2.97–2.54 (m, 5H), 2.55–2.34 (m, 1H), 1.33 (s, 9H).

^{13}C-NMR (75 MHz, *C*DCl$_3$): δ [ppm] = 138.0, 129.1, 128.6, 126.7, 80.2, 55.6, 43.0, 38.9, 30.6, 28.4.

LC/MS: m/z calculated for $C_{18}H_{27}N_3O_4$ [M-Boc+H]$^+$: 250.2, found: 250.1.



45

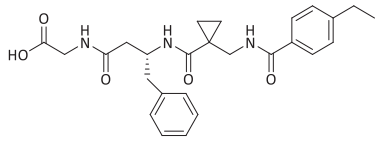
Compound **45**: Compound **53** (26 mg, 0.074 mmol, 1.0 eq.) was dissolved in DCM (1 mL) and TFA (1 mL) was added. The mixture was stirred at RT for 1.5 h. The solvents were removed under reduced pressure. The deprotected crude product (14 mg, 0.127 mmol, 1.1 eq.), **51** (18 mg, 0.074 mmol, 1.0 eq.), and TBTU (25 mg, 0.078 mmol, 1.1 eq.) were dissolved in anhydrous DMF (1.5 mL), and DIPEA (39 μL, 0.224 mmol, 3.0 eq.) was added. The mixture was stirred for 16 h at RT. The solvents were removed under reduced pressure and the crude product was purified by reversed-phase flash column chromatography (Biotage Isolera, ACN/H_2O + TFA).

Yield: 32.0 mg (0.669 mmol ≙ 90% of th.), colorless solid.

^{1}H-NMR (300 MHz, DMSO-d_6): δ [ppm] = 8.34–8.08 (m, 2H), 7.71 (d, *J* = 7.9 Hz, 2H), 7.31–7.08 (m, 8H), 7.03 (s, 1H), 4.82 (s, 1H), 3.60 (s, 2H), 3.35 (s, 2H), 3.08–2.70 (m, 5H), 2.63 (q, *J* = 7.6 Hz, 2H), 2.57–2.33 (m, 2H), 1.18 (t, *J* = 7.6 Hz, 3H), 0.70–0.28 (m, 4H).

^{13}C-NMR (75 MHz, DMSO): δ [ppm] = 171.2, 171.0, 170.5, 166.4, 147.3, 138.6, 131.8, 128.9, 128.1, 127.6, 127.3, 126.1, 41.9, 41.5, 37.4, 37.1, 30.7, 28.0, 26.0, 15.4, 9.5.

LC/MS: m/z calculated for $C_{27}H_{34}N_4O_4$ $[M + H]^+$: 479.3, found: 479.1.



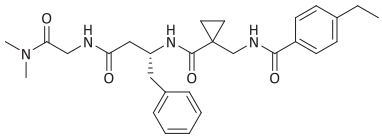
54

Compound **54**: Yield: 48.0 mg (0.103 mmol ≙ 76% of th.): colorless solid.

^{1}H-NMR (300 MHz, DMSO-d_6): δ [ppm] = 12.51 (s, 1H), 8.57 (t, *J* = 6.0 Hz, 1H), 8.24 (t, *J* = 5.9 Hz, 1H), 7.99 (d, *J* = 8.0 Hz, 1H), 7.78 (d, *J* = 7.9 Hz, 2H), 7.32 (d, *J* = 7.9 Hz, 2H), 7.23–6.96 (m, 5H), 4.41–4.10 (m, 1H), 3.88–3.56 (m, 2H), 3.58–3.16 (m, 2H), 2.82 (dd, *J* = 13.5, 5.0 Hz, 1H), 2.66 (q, *J* = 7.6 Hz, 3H), 2.40–2.14 (m, 2H), 1.20 (t, *J* = 7.5 Hz, 3H), 0.97–0.59 (m, 4H).

^{13}C-NMR (75 MHz, DMSO): δ [ppm] = 171.3, 170.4, 167.2, 147.6, 131.4, 138.9, 129.1, 128.0, 125.9, 127.7, 127.5, 48.5, 42.3, 39.8, 39.1, 28.1, 25.2, 15.4, 13.1.

LC/MS: m/z calculated for $C_{26}H_{31}N_3O_5$ $[M + H]^+$: 466.2, found: 466.1.



47

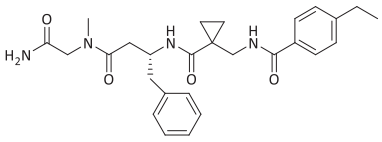
Compound **47**: Compound **54** (10 mg, 0.022 mmol, 1.0 eq.), dimethylamine hydrochloride (2.9 mg, 0.036 mmol, 1.7 eq.), DCC (5.6 mg, 0.027 mmol, 1.3 eq.) and HOBt (3.6 mg, 0.027 mmol, 1.3 eq.) were dissolved in DCM (1 mL). DIPEA (16 μL, 0.092 μmol, 4.3 eq.) was added dropwise and the mixture was stirred for 16 h at RT. More solvent (DCM, 1 mL), dimethylamine hydrochloride (2.6 mg, 0.032 mmol, 1.5 eq.), DCC (5 mg, 0.024 mmol, 1.1 eq.), and DIPEA (11.7 μL, 0.067 mmol, 2.5 eq.) were added and the mixture was stirred for additional 16 h at RT because the reaction was not completed. The solvents were removed under reduced pressure and the crude product was purified by reversed-phase column chromatography (Biotage Isolera, ACN/H_2O + TFA).

Yield: 8.0 mg (0.016 mmol ≙ 76% of th.), colorless solid.

^{1}H-NMR (300 MHz, DMSO-d_6): δ [ppm] = 8.54 (t, *J* = 6.0 Hz, 1H), 8.00–7.89 (m, 2H), 7.81–7.73 (m, 2H), 7.35–7.25 (m, 2H), 7.17–7.06 (m, 5H), 4.25 (p, *J* = 7.1 Hz, 1H), 3.96–3.66 (m, 2H), 3.47 (qd, *J* = 14.8, 6.1 Hz, 2H), 2.89 (s, 3H), 2.80 (s, 3H), 2.74–2.59 (m, 2H), 2.41–2.22 (m, 2H), 1.19 (t, *J* = 7.6 Hz, 3H), 0.95–0.67 (m, 4H).

^{13}C-NMR (75 MHz, DMSO): δ [ppm] = 171.4, 170.1, 168.1, 167.1, 147.5, 138.9, 131.4, 129.2, 128.0, 127.6, 127.5, 125.9, 48.5, 42.3, 40.5, 39.1, 35.6, 35.1, 28.1, 25.2, 15.4, 13.1, 13.0.

LC/MS: m/z calculated for $C_{28}H_{36}N_4O_4$ $[M + H]^+$: 493.3, found: 493.2.



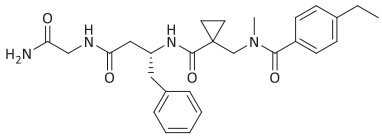
46

Compound **46**: Yield: 16.0 mg (0.033 mmol ≙ 74% of th.), colorless solid.

^{1}H-NMR (300 MHz, DMSO-d_6, 60 °C): δ [ppm] = 8.41–8.23 (m, 1H), 7.93–7.79 (m, 1H), 7.79–7.68 (m, 2H), 7.36–7.25 (m, 2H), 7.24–7.00 (m, 6H), 4.33 (q, *J* = 7.3 Hz, 1H), 4.04–3.69 (m, 2H), 3.62–3.34 (m, 2H), 2.99–2.72 (m, 4H), 2.72–2.60 (m, 2H), 2.60–2.27 (m, 2H), 1.21 (t, *J* = 7.6 Hz, 3H), 1.02–0.63 (m, 4H).

^{13}C-NMR (75 MHz, DMSO, 60 °C): δ [ppm] = 171.3, 170.3, 170.0, 166.9, 147.2, 138.8, 131.4, 128.8, 127.7, 127.3, 127.1, 125.6, 50.0, 48.2, 48.0, 42.2, 37.2, 35.9, 27.7, 25.0, 14.9, 12.6.

LC/MS: m/z calculated for $C_{27}H_{34}N_4O_4$ [M + H]$^+$: 479.3, found: 479.2.



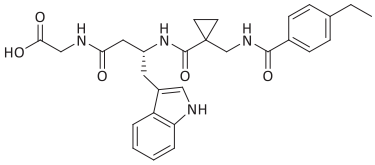
44

Compound **44**: Yield: 17.0 mg (0.036 mmol ≙ 79% of th.), colorless solid.

^{1}H-NMR (300 MHz, DMSO-d_6, 60 °C): δ [ppm] = 7.85 (t, *J* = 5.7 Hz, 1H), 7.53 (s, 1H), 7.28–7.10 (m, 10H), 4.34 (h, *J* = 7.1 Hz, 1H), 3.80–3.45 (m, 4H), 2.88–2.70 (m, 5H), 2.65 (q, *J* = 7.6 Hz, 2H), 2.38–2.28 (m, 2H), 1.21 (t, *J* = 7.6 Hz, 3H), 1.03–0 0.81 (m, 2H), 0.80–0.58 (m, 2H).

^{13}C-NMR (75 MHz, DMSO, 60 °C): δ [ppm] = 170.9, 170.9, 170.7, 170.0, 144.9, 138.5, 133.5, 128.8, 127.7, 127.2, 126.7, 125.7, 47.9, 41.8, 40.0, 39.4, 27.7, 23.7, 14.8, 12.0.

LC/MS: m/z calculated for $C_{27}H_{34}N_4O_4$ [M + H]$^+$: 479.3, found: 479.2.



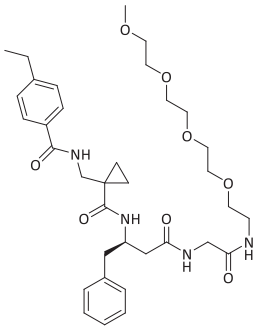
9

Compound **9**: Yield: 1.4 mg (0.028 mmol ≙ 43% of th.), colorless solid.

^{1}H-NMR (400 MHz, MeO*D*): δ [ppm] = 8.24 (d, *J* = 7.6 Hz, 1H), 7.66 (d, *J* = 7.8 Hz, 2H), 7.60 (d, *J* = 7.7 Hz, 1H), 7.25 (d, *J* = 6.5 Hz, 3H), 7.09–6.94 (m, 4H), 6.65 (d, *J* = 7.7 Hz, 1H), 4.56 (d, *J* = 6.4 Hz, 1H), 3.74 (q, *J* = 17.8 Hz, 2H), 3.55 (s, 2H), 3.01 (p, *J* = 7.9 Hz, 2H), 2.69 (q, *J* = 7.5 Hz, 2H), 2.51 (d, *J* = 6.5 Hz, 2H), 2.22 (s, 1H), 1.45 (s, 1H), 1.25 (t, *J* = 7.5 Hz, 3H), 1.10 (q, *J* = 9.8 Hz, 2H), 0.86 (s, 2H).

^{13}C-NMR (101 MHz, MeOD): δ [ppm] = 174.9, 173.8, 170.8, 156.0, 149.9, 138.0, 132.5, 130.8, 129.6, 129.2, 129.0, 128.6, 124.3, 122.2, 119.7, 119.6, 116.0, 112.2, 44.6, 40.9, 30.8, 29.7, 28.0, 26.8, 20.5, 15.8, 14.6, 14.4.

LC/MS: m/z calculated for $C_{28}H_{32}N_4O_5$ [M + H]$^+$: 505.2, found: 504.7.



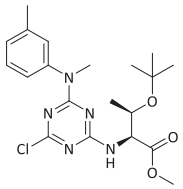
48

Compound **48**: Yield: 5.0 mg (7.641 μmol ≙ 44% of th.), colorless solid.

^{1}H-NMR (400 MHz, DMSO-d_6): δ [ppm] = 8.55 (t, *J* = 6.1 Hz, 1H), 8.13 (t, *J* = 5.9 Hz, 1H), 7.99 (d, *J* = 8.1 Hz, 1H), 7.83 (t, *J* = 5.7 Hz, 1H), 7.80–7.73 (m, 2H), 7.31 (d, *J* = 8.1 Hz, 2H), 7.21–7.02 (m, 5H), 4.29 (q, *J* = 7.1 Hz, 1H), 3.79–3.44 (m, 14H), 3.44–3.27 (m, 4H), 3.26–3.12 (m, 5H), 2.79 (dd, *J* = 13.5, 5.2 Hz, 1H), 2.72–2.58 (m, 3H), 2.31 (d, *J* = 6.8 Hz, 2H), 1.20 (t, *J* = 7.6 Hz, 3H), 0.96–0.66 (m, 4H).

^{13}C-NMR (101 MHz, DMSO): δ [ppm] = 171.5, 170.4, 169.0, 167.2, 147.6, 138.8, 131.4, 129.1, 128.0, 127.7, 127.5, 126.0, 71.3, 69.8, 69.7, 69.6, 69.0, 58.1, 48.4, 42.3, 42.0, 38.6, 30.7, 28.1, 25.2, 15.4, 13.0.

LC/MS: m/z calculated for $C_{35}H_{50}N_4O_8$ $[M + H]^+$: 655.4, found: 655.3.



55

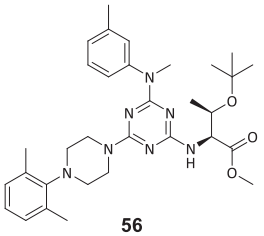
Compound **55**: Cyanuric chloride (195 mg, 1.057 mmol, 1.0 eq.) and methyl *O*-(*tert*-butyl)-L-threoninate (200 mg, 1.057 mmol, 1.0 eq.) were suspended in 2 mL of DCM. The solution was cooled to 0 °C and DIPEA (370 μL, 2.114 mmol, 2.0 eq.) was added. The reaction was allowed to stir for 10 min at 0 °C. Subsequently, *N*,3-dimethylaniline (128 mg, 1.057 mmol, 1.0 eq.), and DIPEA (370 μL, 2.114 mmol, 2.0 eq.) were added at 0 °C and the mixture was stirred for 12 h at 40 °C in a sealed tube. The crude product was purified by column chromatography (mobile phase: CH:EtOAc 20:1–10:1).

Yield: 331.0 mg (0.786 mmol ≙ 74% of th.), colorless oil.

^{1}H-NMR (300 MHz, C*D*Cl$_3$): δ [ppm] = 7.26 (s, 1H), 7.14–6.91 (m, 3H), 6.20–5.73 (m, 1H), 4.41–3.97 (m, 1H), 3.68 (d, *J* = 13.7 Hz, 3H), 3.44 (d, *J* = 7.4 Hz, 3H), 2.36 (d, *J* = 8.2 Hz, 3H), 1.38–0.97 (m, 12H).

^{13}C-NMR (75 MHz, C*D*Cl$_3$): δ [ppm] = 171.6, 165.3, 143.5, 138.8, 129.0, 127.4, 127.0, 124.0, 123.6, 77.4, 74.2, 67.3, 59.6, 52.2, 38.8, 28.4, 21.5.

LC/MS: m/z calculated for $C_{20}H_{28}ClN_5O_3$ $[M + H]^+$: 422.2, found: 422.1.



56

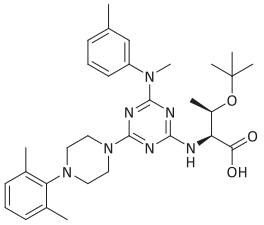
Compound **56**: Compound **55** (80 mg, 0.190 mmol, 1.0 eq.) was dissolved in DMF, 1-(2,6-dimethylphenyl)piperazine (43 mg, 0.228 mmol, 1.2 eq.) and potassium carbonate (65 mg, 0.475 mmol, 2.5 eq.) were added, and the mixture was allowed to stir for 45 min at 100 °C. The solvent was removed in vacuo and the residue was dissolved in DCM, which was washed three times with water. The organic phase was filtered over silica and the product was obtained as an orange oil.

Yield: 103.0 mg (0.179 mmol ≙ 94% of th.), orange oil.

^{1}H-NMR (300 MHz, C*D*Cl$_3$): δ [ppm] = 7.28–7.09 (m, 3H), 6.99 (h, *J* = 4.6, 4.1 Hz, 4H), 4.27–4.11 (m, 1H), 3.81 (d, *J* = 22.4 Hz, 3H), 3.69 (s, 3H), 3.47 (d, *J* = 11.3 Hz, 3H), 3.15–3.00 (m, 4H), 2.95 (s, 1H), 2.88 (s, 1H), 2.34 (dd, *J* = 8.9, 2.4 Hz, 9H), 1.24 (dd, *J* = 9.4, 6.3 Hz, 3H), 1.13 (d, *J* = 4.8 Hz, 9H).

^{13}C-NMR (75 MHz, C*D*Cl$_3$): δ [ppm] = 172.8, 162.6, 161.1, 148.3, 137.9, 136.9, 129.0, 128.0, 127.1, 125.7, 125.2, 123.5, 77.4, 73.9, 67.6, 59.6, 59.4, 51.9, 50.7, 49.8, 47.3, 44.6, 41.6, 36.5, 31.5, 28.4, 21.2, 19.8.

LC/MS: m/z calculated for $C_{32}H_{45}N_7O_3$ $[M + H]^+$: 576.4, found: 576.3.



57

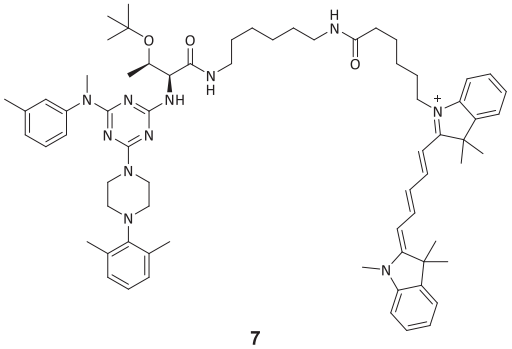
Compound **57**: Compound **56** (88 mg, 0.152 mmol, 1.0 eq.) was dissolved in 1 mL water and 1 mL THF, and sodium hydroxide (30 mg, 0.750 mmol, 5.0 eq.) was added. The mixture was stirred at RT for 48 h. The solvents were removed under reduced pressure and the crude product was purified by reversed-phase column chromatography (Biotage Isolera, ACN/H_2O + TFA).

Yield: 15.0 mg (0.027 mmol ≙ 18% of th.), colorless solid.

^{1}H-NMR (300 MHz, C*D*Cl3): δ [ppm] = 7.39 (t, *J* = 7.5 Hz, 1H), 7.06–6.95 (m, 7H), 4.55 (d, *J* = 7.9 Hz, 1H), 4.21 (dd, *J* = 6.4, 2.3 Hz, 1H), 3.92 (s, 3H), 3.47 (s, 3H), 3.12 (t, *J* = 5.4 Hz, 4H), 2.37 (d, *J* = 8.3 Hz, 3H), 2.33 (s, 7H), 1.16 (d, *J* = 20.0 Hz, 12H).

^{13}C-NMR (75 MHz, C*D*Cl$_3$): δ [ppm] = 184.5, 161.2, 147.6, 137.0, 136.8, 129.3, 129.3, 127.5, 125.9, 123.9, 77.4, 76.9, 75.3, 68.8, 67.0, 49.6, 46.0, 45.9, 39.4, 28.1, 21.4, 20.4, 19.8.

LC/MS: m/z calculated for $C_{31}H_{43}N_7O_3$ $[M + H]^+$: 562.3, found: 562.3.

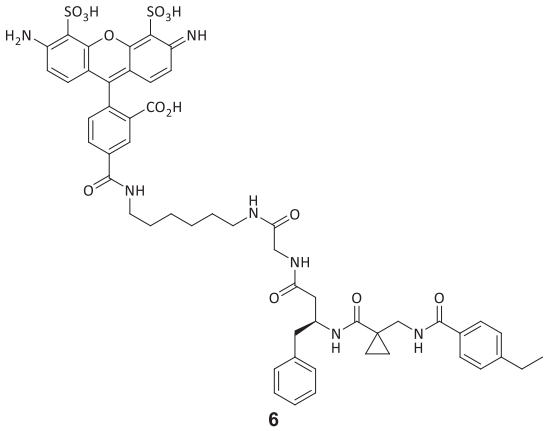


7

Compound **7**: Compound **57** (1.0 mg, 1.700 μmol, 1.0 eq.), Cy5 amine (1.0 mg, 1.700 μmol, 1.0 eq.), HATU (1 mg, 2.000 μmol, 1.2 eq.), and DIPEA (3 μL, 16.000 μmol, 9.5 eq.) were dissolved in 20 μL anhydrous DMF. The reaction was allowed to incubate for 16 h. The crude product was purified by reversed-phase column chromatography (Biotage Isolera, ACN/H_2O + TFA).

Yield: 1.0 mg (0.817 μmol ≙ 48% of th.), blue solid.

LC/MS: m/z calculated for $C_{69}H_{94}N_{11}O_3^+$ $[M + H]^{2+}$: 562.8, found: 562.9.



6

Compound **6**: Compound **54** (0.8 mg, 1.640 μmol, 1.2 eq.), AF 488 amine (1.0 mg, 1.390 μmol, 1.0 eq.), TBTU (0.5 mg, 1.680 μmol, 1.2 eq.), and DIPEA (2.3 μL, 13.200 μmol, 9.5 eq.) were dissolved in anhydrous DMF (0.6 mL) and stirred at RT for 48 h. The crude product was purified by reversed-phase column chromatography (Biotage Isolera, ACN/H_2O + TFA).

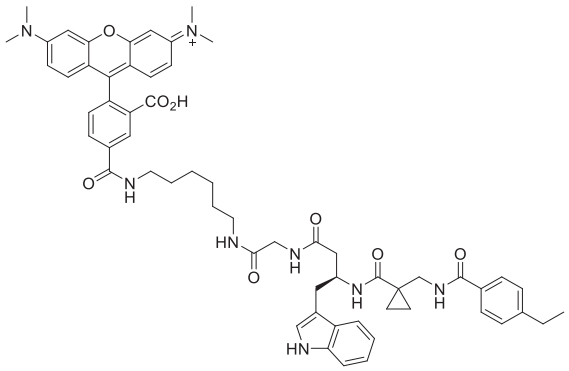
Yield: 0.4 mg (0.37 mmol ≙ 27% of th.), orange solid.

^{1}H-NMR (600 MHz, DMSO-*d*$_6$): δ [ppm] = 9.00 (s, 2H), 8.86 (s, 1H), 8.69 (s, 1H), 8.58 (t, *J* = 6.2 Hz, 1H), 8.50 (s, 2H), 8.26 (dd, *J* = 8.0, 1.8 Hz, 1H), 8.16 (t, *J* = 6.0 Hz, 1H), 8.03 (d, *J* = 8.1 Hz, 1H), 7.81–7.73 (m, 2H), 7.50 (d, *J* = 7.8 Hz, 1H), 7.31 (d, *J* = 8.0 Hz, 1H), 7.15–7.11 (m, 2H), 7.11–7.06 (m, 1H), 7.02–6.88 (m, 3H), 4.28 (dt, *J* = 14.2, 6.9 Hz, 1H), 3.69–3.60 (m, 1H), 3.58–3.50 (m, 1H), 3.50–3.45 (m, 2H), 3.33–3.22 (m, 1H), 3.07–2.99 (m, 2H), 2.78 (dd, *J* = 13.6, 5.2 Hz, 1H), 2.70–2.59 (m, 3H), 2.38 (p, *J* = 1.8 Hz, 1H), 2.31 (d, *J* = 6.9 Hz, 2H), 2.11 (s, 1H), 2.08 (s, 1H), 2.04–1.91 (m, 2H), 1.58–1.48 (m, 2H), 1.38 (q, *J* = 9.4 Hz, 2H), 1.35–1.20 (m, 5H), 1.19 (t, *J* = 7.6 Hz, 2H), 1.13 (s, 1H), 0.91–0.69 (m, 4H).

CellPress
OPEN ACCESS

iScience
Article

LC/MS: m/z calculated for $C_{53}H_{57}N_7O_{14}S_2$ $[M+2H]^{2+}$: 540.7 found: 540.6.



8

Compound **8**: Compound **9** (1.1 mg, 2.112 μmol, 1.2 eq.), TBTU (0.7 mg, 2.112 μmol, 1.2 eq.), and TAMRA-amine (1.0 mg, 1.760 μmol, 1.0 eq.) were dissolved in DMF (3 mL), and DIPEA (0.4 μL, 2.112 μmol, 1.2 eq.) was added. The reaction mixture was shaken for 16 h at RT. Afterward, the solvent was removed under reduced pressure and the crude product was purified by reversed-phase flash column chromatography (Biotage Isolera, ACN/H_2O + TFA).

Yield: 1.9 mg (1.871 μmol ≙ 89% of th.), red solid.

^{1}H-NMR (600 MHz, MeO*D*): δ [ppm] = 8.51 (s, 1H), 8.02 (d, *J* = 7.8 Hz, 1H), 7.88 (d, *J* = 8.2 Hz, 1H), 7.68 (dd, *J* = 8.2, 5.1 Hz, 1H), 7.61 (dd, *J* = 15.0, 8.3 Hz, 2H), 7.50 (d, *J* = 7.9 Hz, 1H), 7.33–7.23 (m, 3H), 7.20–7.12 (m, 3H), 6.98–6.85 (m, 5H), 4.60 (s, 2H), 4.52 (dd, *J* = 14.4, 5.9 Hz, 1H), 3.73 (d, *J* = 16.7 Hz, 1H), 3.66 (s, 1H), 3.63–3.52 (m, 3H), 3.45–3.35 (m, 3H), 3.32 (t, 1H), 3.21 (d, *J* = 2.8 Hz, 6H), 3.17–3.06 (m, 2H), 2.98–2.88 (m, 2H), 2.70–2.60 (m, 4H), 2.52 (dd, *J* = 14.3, 4.9 Hz, 1H), 2.43 (dd, *J* = 14.4, 8.7 Hz, 1H), 1.62–1.54 (m, 2H), 1.49–1.41 (m, 2H), 1.39–1.28 (m, 4H), 1.27–1.16 (m, 6H), 1.06–0.97 (m, 2H), 0.93 (t, *J* = 7.4 Hz, 1H), 0.89–0.76 (m, 3H).

^{13}C-NMR (151 MHz, MeOD): δ [ppm] = 175.0, 174.1, 171.6, 170.7, 169.0, 162.1, 159.0, 158.7, 149.8, 137.9, 132.5, 132.3, 131.0, 129.8, 129.1, 129.0, 128.9, 128.6, 128.5, 128.4, 124.2, 122.2, 119.6, 119.6, 115.1, 114.8, 112.2, 112.1, 97.3, 57.6, 57.5, 57.3, 52.6, 49.9, 49.6, 44.6, 43.7, 41.7, 40.9, 40.7, 40.2, 32.7, 31.1, 30.3, 29.9, 29.8, 27.5, 27.4, 26.9, 21.2, 17.4, 17.3, 17.2, 15.9, 15.9, 14.9, 14.6, 14.6, 14.2.

LC/MS: m/z calculated for $C_{59}H_{67}N_8O_8^+$ $[M + H]^{2+}$: 508.3, found: 508.4.

QUANTIFICATION AND STATISTICAL ANALYSIS

For all experiments, details of quantification, statistical methods, and the software used are described in the corresponding figure legends and methods. All data are expressed as mean ± SEM. *N* values indicate the number of technical or biological replicates per experiment. Each experiment was performed at least in triplicate. The statistical significance of differences of tRNA modification levels was determined by Student's t test with *p* values (*$p < 0.05$, **$p < 0.01$, ***$p < 0.001$, ****$p < 0.0001$). All statistical test methods and analyses were performed using GraphPad Prism 8.05 and are shown in the figure legends. The dose-response curves were fit to four-parameter logistic (4-PL) curve using GraphPad Prism 8 (log[agonist] vs. response – variable slope; Equation: Y = Bottom + (Top–Bottom)/(1 + 10((LogEC$_{50}$-X)*HillSlope)).

”

iScience, Volume *28*

Supplemental information

DNA-encoded library screening uncovers potent DNMT2 inhibitors targeting a cryptic allosteric binding site

Ariane F. Frey, Merlin Schwan, Annabelle C. Weldert, Valerie Kadenbach, Jürgen Kopp, Zarina Nidoieva, Robert A. Zimmermann, Lukas Gleue, Collin Zimmer, Marko Jörg, Kristina Friedland, Mark Helm, Irmgard Sinning, and Fabian Barthels

Supplementary data of DNA encoded library screening

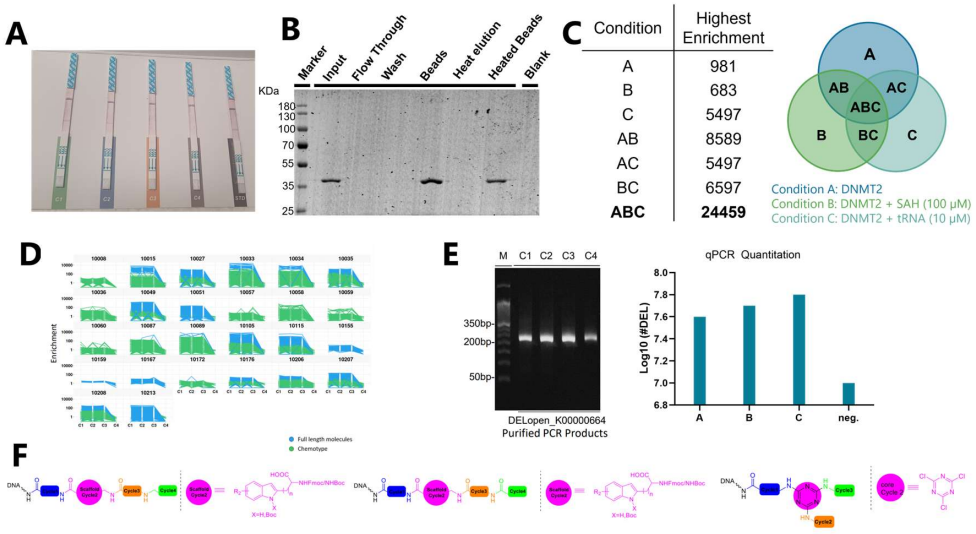
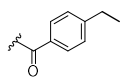
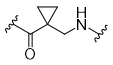
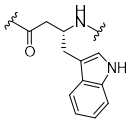
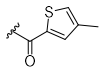
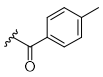
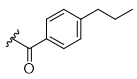
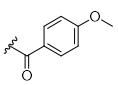
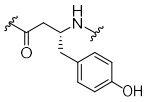
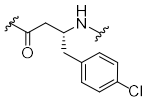
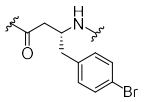
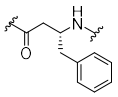
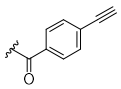
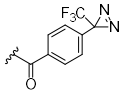
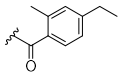


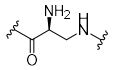
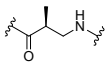
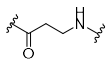
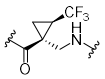
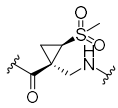
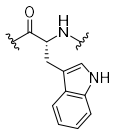
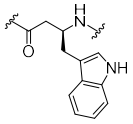
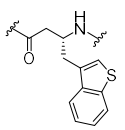
Figure S1: Supplementary data for the DNA encoded library screening on DNMT2. (**A**) Quality control test as provided by Wuxi AppTec. The four tested conditions mentioned in the manuscript are labeled here as C1–C4 (in the manuscript A–D). STD represents the internal standard according to the WuXi protocol (https://hits.wuxiapptec.com/assets/pdf/DELopen_Protocol.pdf). (**B**) DNMT2 capture assay was performed according to the protocol instructions to verify that DNMT2 can be stably immobilized on magnetic beads. The labeling is according to the original protocol. (**C**) Total count of highest enrichment scores for different panning conditions. The conditions are explained in the Venn diagram. (**D**) Overall performance and enrichment scores of the different libraries after the removal of NTC (no target control) binders. Most hits were enriched across C1–C3 equally, meaning neither SAH nor tRNA led to DEL hit displacement. (**E**) Quality control (gel electrophoresis and qPCR) was performed by Wuxi AppTec for all selection conditions after the second panning round. (**F**) Structures of the libraries featuring hit compounds chosen for off-DNA synthesis and further investigations.

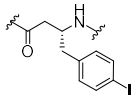
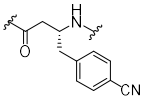
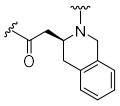
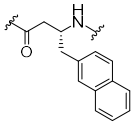
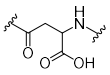
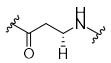
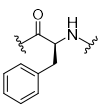
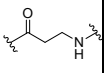
Summary of all synthesized compound 3 analogs

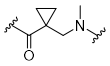
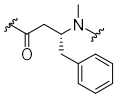
Table S1: Overview of all synthesized compounds during the SAR study around compound 3 and their characterization by MST (F_{norm}) and ITC (K_D). All results include the mean value and standard deviations from at least technical triplicate measurements. Raw data and analysis plots are depicted in Figures S2–S5.

Cpd	BB1	BB2	BB3	BB4	C-Term.	F_{norm} (% displ.)	K_D (ITC) [µM]
3	 (4-ethylbenzoyl)	 (cyclopropyl-β-alanine)	 (β-homo-(*R*)-tryptophane)	 (glycine)	NH-Me	912.1 (53%)	5.31 ± 1.67
5		cyclopropyl-β-alanine	β-homo-(*R*)-tryptophane	glycine	NH-Me	879.3 (13%)	13.6 ± 1.6
9	4-ethylbenzoyl	cyclopropyl-β-alanine	β-homo-(*R*)-tryptophane	glycine	OH	907.7 (46%)	n.d.
10	4-ethylbenzoyl	cyclopropyl-β-alanine	β-homo-(*R*)-tryptophane	glycine	NH_2	903.3 (40%)	n.d.
11		cyclopropyl-β-alanine	β-homo-(*R*)-phenylalanine	glycine	NH_2	891.2 (24%)	n.d.
12		cyclopropyl-β-alanine	β-homo-(*R*)-phenylalanine	glycine	NH_2	890.4 (23%)	n.d.
13		cyclopropyl-β-alanine	β-homo-(*R*)-phenylalanine	glycine	NH_2	897.7 (32%)	n.d.

14	4-ethylbenzoyl	cyclopropyl-β-alanine	β-homo-(*R*)-phenylalanine	glycine	NH_2	896.0 (29%)	3.27 ± 0.97
15	4-ethylbenzoyl	cyclopropyl-β-alanine		glycine	NH_2	862.9 (5%)	n.d.
16	4-ethylbenzoyl	cyclopropyl-β-alanine		glycine	NH_2	928.7 (76%)	3.04 ± 0.57
17	4-ethylbenzoyl	cyclopropyl-β-alanine		glycine	NH_2	924.6 (71%)	n.d.
18		cyclopropyl-β-alanine	 (β-homo-(*R*)-phenylalanine)	glycine	NH_2	868.2 (7%)	n.d.
19		cyclopropyl-β-alanine	β-homo-(*R*)-phenylalanine	glycine	NH_2	871.4 (8%)	n.d.
20		cyclopropyl-β-alanine	β-homo-(*R*)-phenylalanine	glycine	NH_2	876.5 (11%)	n.d.
21		cyclopropyl-β-alanine	β-homo-(*R*)-phenylalanine	glycine	NH_2	862.4 (5%)	n.d.
22		cyclopropyl-β-alanine	β-homo-(*R*)-phenylalanine	glycine	NH_2	864.4 (5%)	n.d.

23		cyclopropyl-β-alanine	β-homo-(*R*)-phenylalanine	glycine	NH_2	864.4 (5%)	n.d.
24	4-ethylbenzoyl		β-homo-(*R*)-tryptophane	glycine	NH_2	860.8 (4%)	n.d.
25	4-ethylbenzoyl		β-homo-(*R*)-tryptophane	glycine	NH_2	855.5 (3%)	n.d.
26	4-ethylbenzoyl		β-homo-(*R*)-tryptophane	glycine	NH_2	861.9 (5%)	n.d.
27	4-ethylbenzoyl		β-homo-(*R*)-tryptophane	glycine	NH_2	863.8 (5%)	n.d.
28	4-ethylbenzoyl		β-homo-(*R*)-phenylalanine	glycine	NH_2	871.9 (8%)	n.d.
29	4-ethylbenzoyl		β-homo-(*R*)-phenylalanine	glycine	NH_2	872.3 (9%)	n.d.
30	4-ethylbenzoyl	cyclopropyl-β-alanine		glycine	NH_2	861.5 (5%)	n.b.
31	4-ethylbenzoyl	cyclopropyl-β-alanine		glycine	NH_2	857.0 (4%)	n.d.
32	4-ethylbenzoyl	cyclopropyl-β-alanine		glycine	NH_2	856.7 (3%)	n.d.

33	4-ethylbenzoyl	cyclopropyl-β-alanine		glycine	NH_2	885.6 (18%)	n.d.
34	4-ethylbenzoyl	cyclopropyl-β-alanine		glycine	NH_2	879.4 (13%)	n.d.
35	4-ethylbenzoyl	cyclopropyl-β-alanine		glycine	NH_2	861.5 (5%)	n.d.
36	4-ethylbenzoyl	cyclopropyl-β-alanine		glycine	NH_2	861.7 (5%)	n.d.
37	4-ethylbenzoyl	cyclopropyl-β-alanine		glycine	NH_2	858.6 (4%)	n.d.
38	4-ethylbenzoyl	cyclopropyl-β-alanine		glycine	NH_2	859.4 (4%)	n.d.
39	4-ethylbenzoyl	cyclopropyl-β-alanine	β-homo-(*R*)-phenylalanine		NH_2	871.4 (8%)	n.d.
40	4-ethylbenzoyl	cyclopropyl-β-alanine	β-homo-(*R*)-phenylalanine		NH_2	870.1 (8%)	n.d.
41	4-ethylbenzoyl	cyclopropyl-β-alanine	β-homo-(*R*)-phenylalanine		NH_2	865.3 (6%)	n.d.
42	4-ethylbenzoyl	cyclopropyl-β-alanine	β-homo-(*R*)-phenylalanine		NH_2	858.8 (4%)	n.d.
43	4-ethylbenzoyl	cyclopropyl-β-alanine	β-homo-(*R*)-phenylalanine		NH_2	874.7 (10%)	n.d.

44	4-ethylbenzoyl		β-homo-(*R*)-phenylalanine	glycine	NH_2	869.7 (7%)	n.d.
45	4-ethylbenzoyl	cyclopropyl-β-alanine		glycine	NH_2	862.6 (5%)	n.d.
46	4-ethylbenzoyl	cyclopropyl-β-alanine	β-homo-(*R*)-phenylalanine		NH_2	868.4 (7%)	n.d.
47	4-ethylbenzoyl	cyclopropyl-β-alanine	β-homo-(*R*)-phenylalanine	glycine	NMe_2	901.0 (36%)	n.d.
48	4-ethylbenzoyl	cyclopropyl-β-alanine	β-homo-(*R*)-phenylalanine	glycine	NH-PEG4	894.1 (27%)	n.d.

MST supplementary data

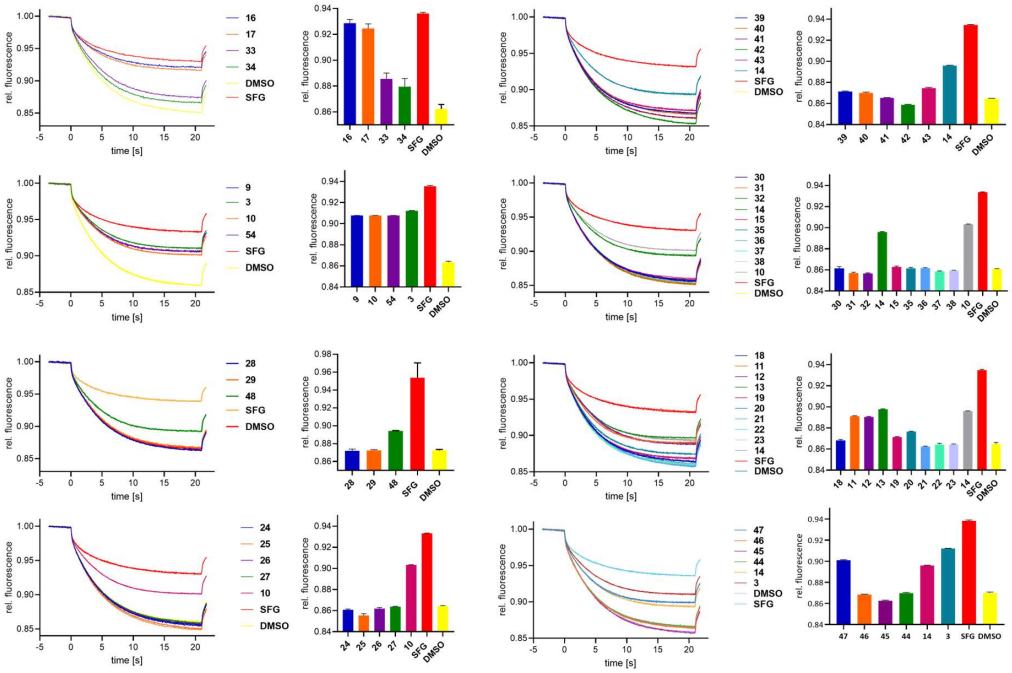


Figure S2: MST screening results of all compounds synthesized during the SAR study. Compounds were measured at a concentration of 100 µM. MST experiments were performed as described in the methods section using the fluorescent FTAD probe.

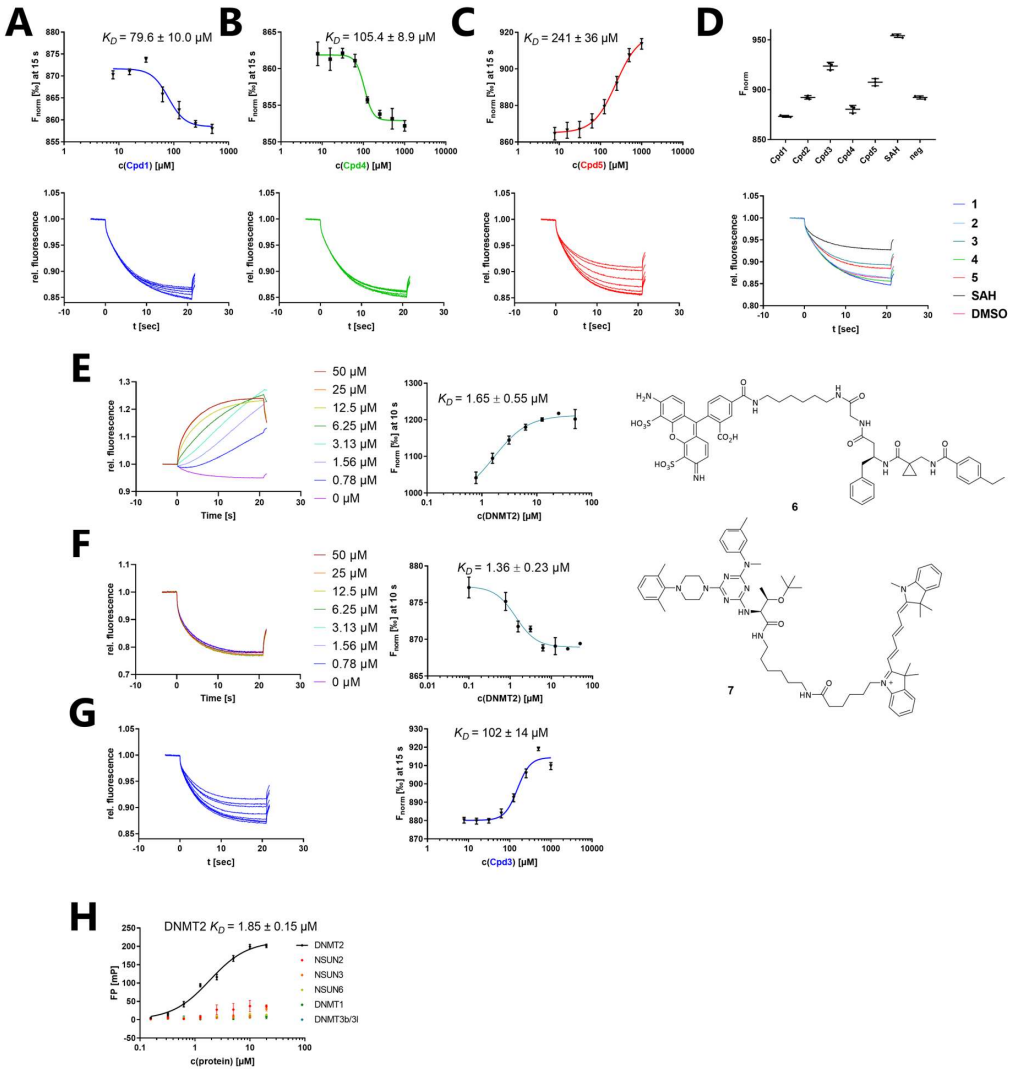


Figure S3: Supplementary MST and FP results for the hit compounds selected from the DEL screening. MST experiments were performed as described in the methods section using the fluorescent FTAD probe. (**A**) K_D-value determination of compound **1**. (**B**) K_D-value determination of compound **4**. (**C**) K_D-value determination of compound **5**. (**D**) Screening of all hit compounds **1–5** from the DEL Screening at 100 µM. (**E**) K_D-value determination of probe **6** by dose-response experiments using variable concentrations of DNMT2. (**F**) K_D-value determination of probe **7** by dose-response experiments using variable concentrations of DNMT2. (**G**) K_D-value determination of compound **3** using the DNMT2 deletion mutant DNMT2Δ47 (2 µM). (**H**) FP assay for probe **6** binding to native DNMT2 and various related MTase off-targets as determined by dose-response experiments.

ITC supplementary data

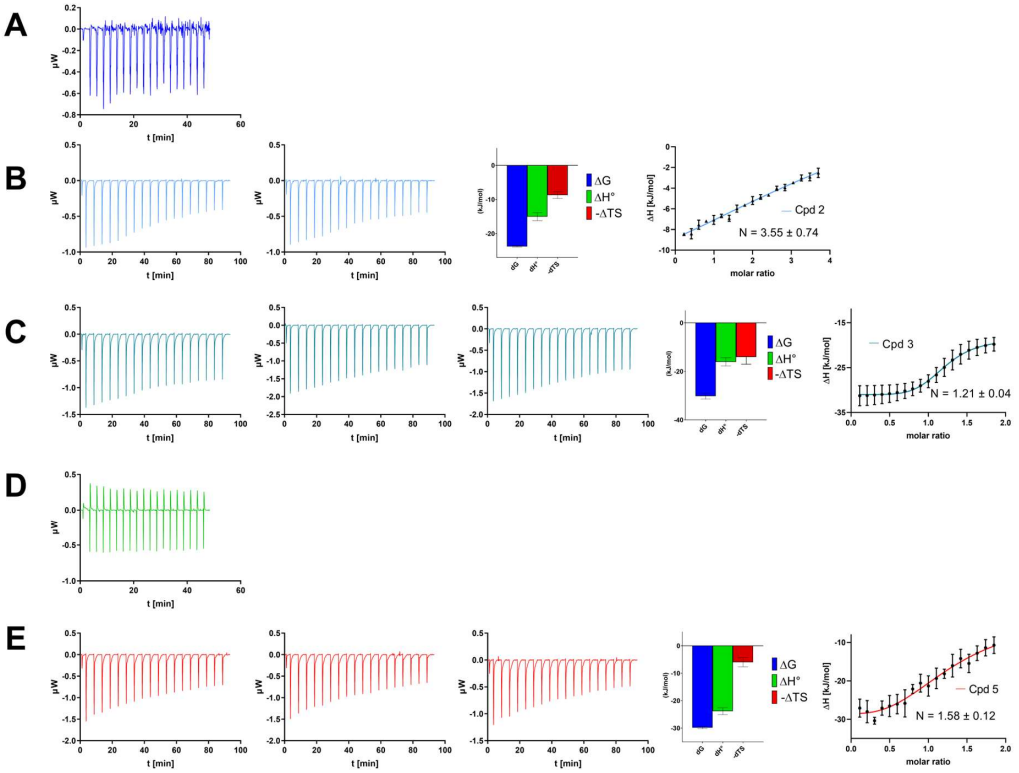


Figure S4: Supplementary ITC data for compounds 1–5. (**A**) Compound **1** was titrated into DNMT2. No enthalpy signal change was observed. (**B**) Compound **2** was titrated into DNMT2. Note: due to low solubility, the upper resp. lower limits of the stoichiometry plot are not reached, and thus, ΔH/ΔS determination might not be accurate. (**C**) Compound **3** was titrated into DNMT2. (**D**) Compound **4** was titrated into DNMT2. No enthalpy signal change was observed. (**E**) Compound **5** was titrated into DNMT2.

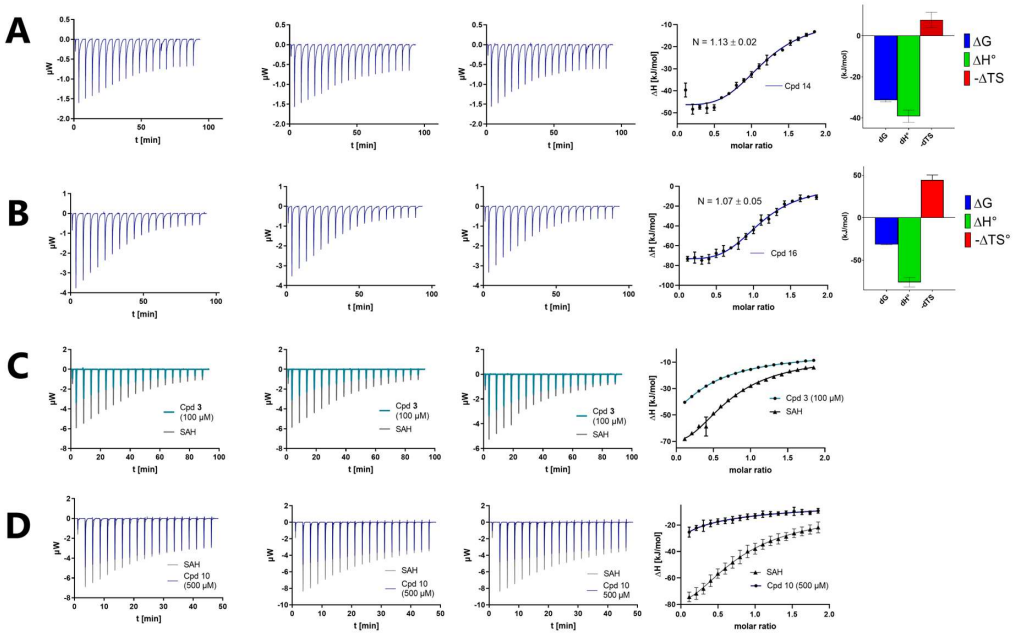


Figure S5: Supplementary ITC data for synthesized compound 3 analogs. (**A**) Compound **14** was determined by direct titration. (**B**) Compound **16** was determined by direct titration. (**C**) Compound **3** measured by SAH displacement. (**D**) Compound **10** measured by SAH displacement.

Affinity selection-mass spectrometry (AS-MS)

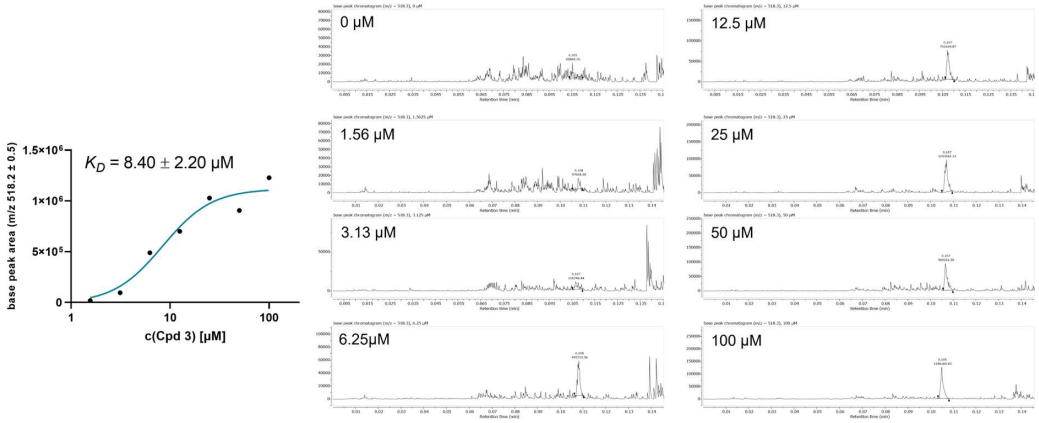


Figure S6: AS-MS-based determination of compound 3 binding affinity to DNMT2. (**left**) Dose-response curve for K_D determination. (**right**) Base peak chromatograms for compound **3** content analysis in the analyzed fractions.

Supplementary data of ^{3}H-based methyltransferase DNMT2 activity assays

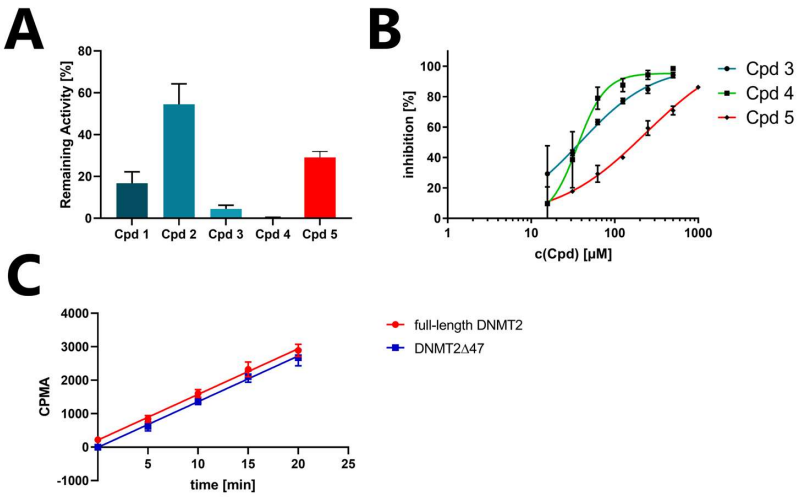


Figure S7: Data from ^{3}H-based methyltransferase enzyme activity assay. (**A**) Screening of compounds **1**–**5**, the remaining DNMT2 activity was determined at 500 µM of the respective compound. (**B**) IC_{50} determination for compounds **3**, **4**, and **5**. (**C**) ^{3}H-based methyltransferase enzyme activity assays with full-length and deletion mutant enzymes (250 nM DNMT2, 5 µM $tRNA^{Asp}$, 0.9 µM SAM), highlighting virtually identical substrate conversion plots (counts per minute [CPMA]) vs. time.

DNMT2-tRNA MST displacement experiments

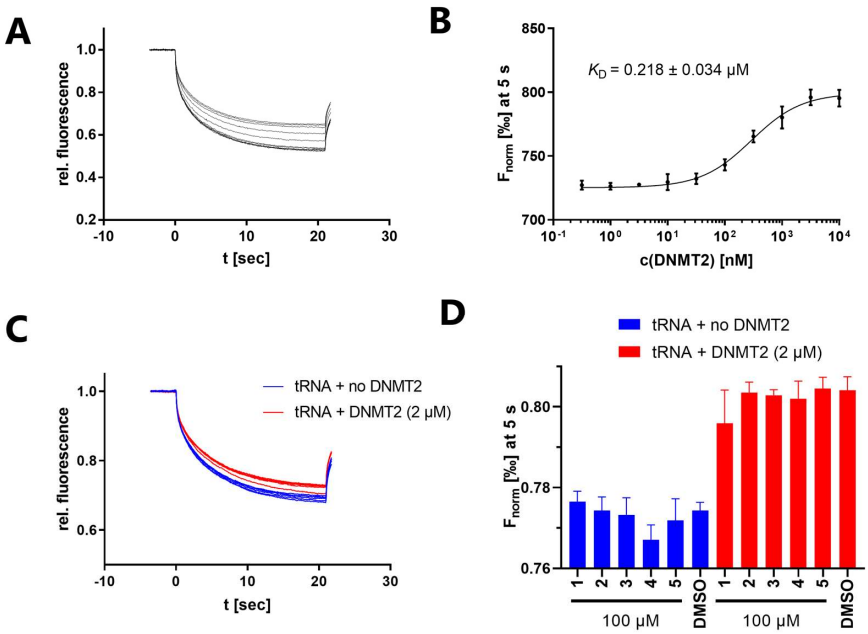


Figure S8: Analysis of DNMT2-RNA interaction by in situ labeling with SybrGold (1×). (**A**, **B**) Dissociation constant (K_D) of $tRNA^{Asp}$ (100 nM, labeled with SybrGold) towards DNMT2 (varying concentrations) was determined by dose-response experiments. (**C**, **D**). Neither the native $tRNA^{Asp}$ samples (blue) nor the DNMT2-tRNA complex (red) showed significant thermophoresis alterations when treated with the hit compounds **1**–**5**.

Cell viability assays

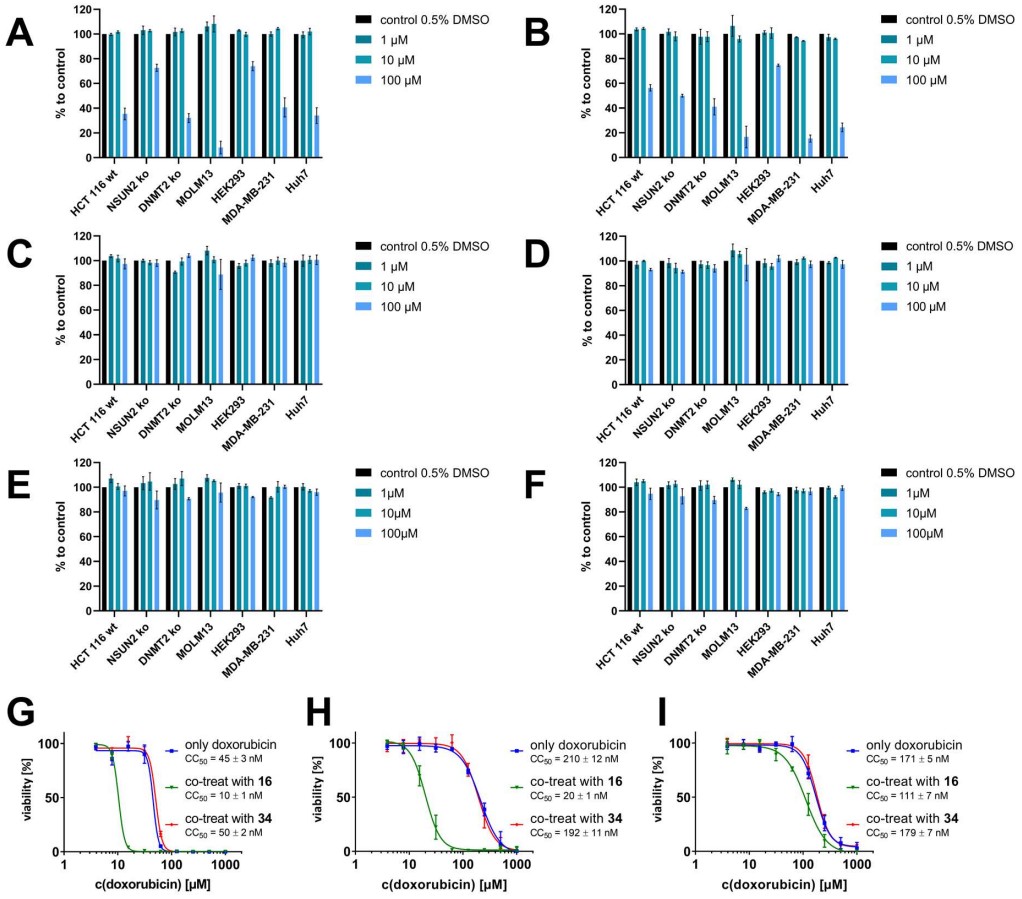
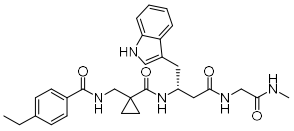
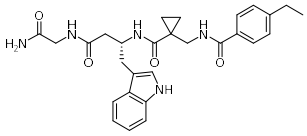
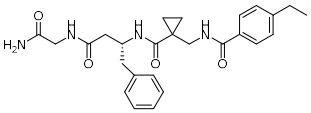
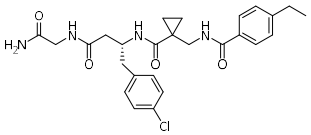
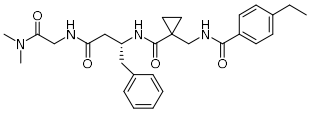
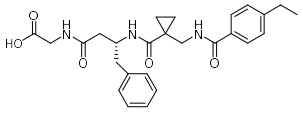


Figure S9: Cell viability assay data for compounds 1–5 and 16 used for the treatment of various cell lines. (**A**) Data for compound **1**. (**B**) Data for compound **2**. (**C**) Data for compound **3**. (**D**) Data for compound **4**. (**E**) Data for compound **5**. (**F**) Data for compound **16**. (**G**) Dose-response curves from cell viability assays of doxorubicin/compound **16** resp. **34** co-treated MOLM-13 cells, (**H**) cotreated MDA-MB-231 cells, and (**I**) cotreated Huh-7 cells.

Parallel Artificial Membrane Permeation Assay (PAMPA)

Table S2: PAMPA results of the investigated compounds determined in duplicates.

Compound	Compound structure	P_{app} [*10^{-6} cm/s]
3		below detection limit
10		below detection limit
14		below detection limit
16		~0.30
47		below detection limit
54		below detection limit

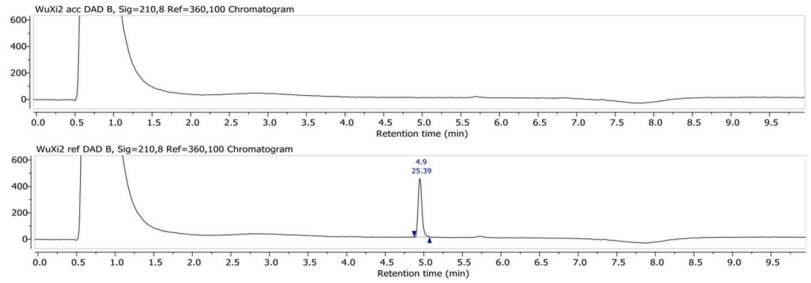


Figure S10: Base peak chromatogram at m/z = 518.3 ± 0.5 of acceptor and reference solution after incubating for compound 3. The peak of compound **3** is marked, and the area under the peak is stated above the peak.

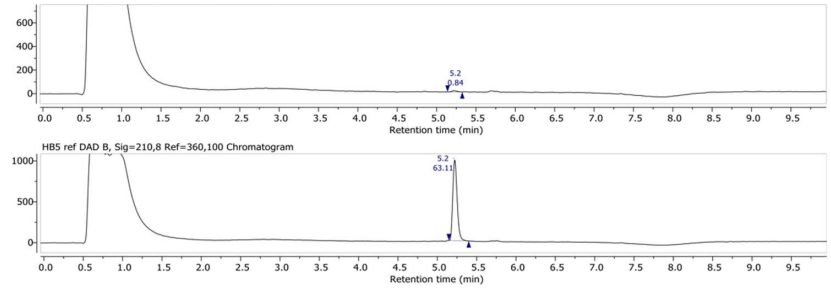


Figure S11: Base peak chromatogram at m/z = 499.2 ± 0.5 of acceptor and reference solution after incubating for compound 16. The peak of compound **16** is marked, and the area under the peak is stated above the peak.

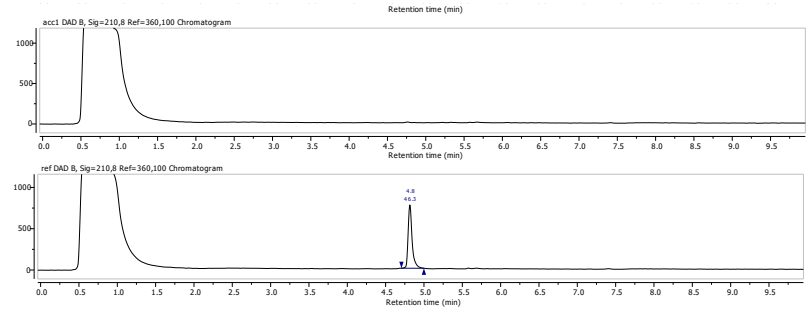


Figure S12: Base peak chromatogram at m/z = 504.3 ± 0.5 of acceptor and reference solution after incubating for compound 10. The peak of compound **10** is marked, and the area under the peak is stated above the peak.

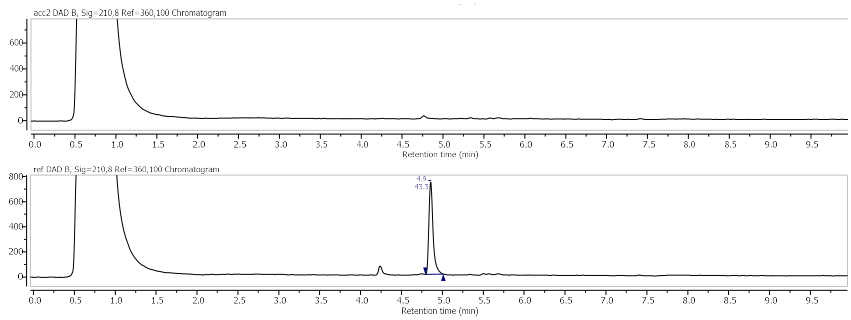


Figure S13: Base peak chromatogram at m/z = 465.3 ± 0.5 of acceptor and reference solution after incubating for compound 14. The peak of compound **14** is marked, and the area under the peak is stated above the peak.

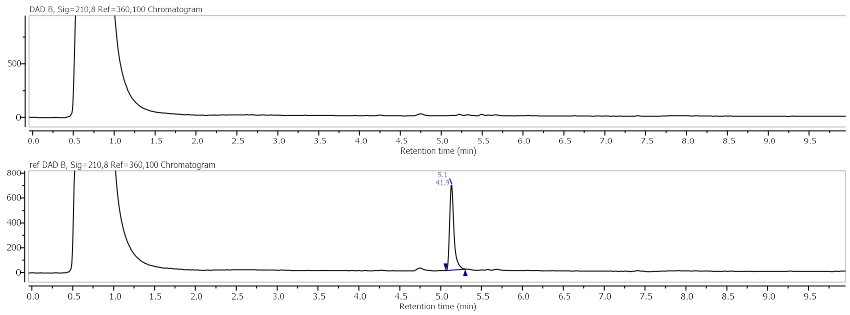


Figure S14: Base peak chromatogram at m/z = 493.3 ± 0.5 of acceptor and reference solution after incubating for compound 47. The peak of compound **47** is marked, and the area under the peak is stated above the peak.

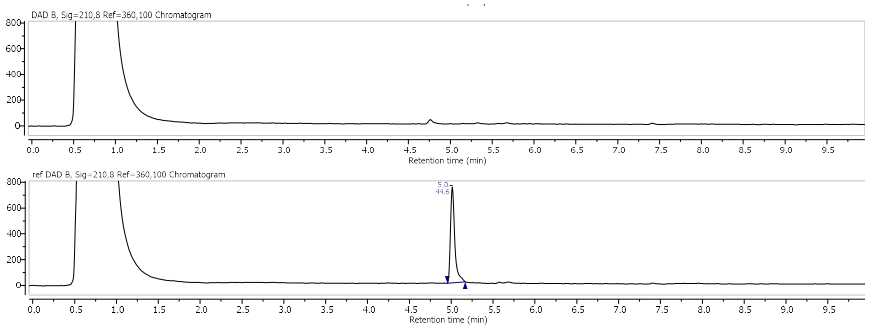


Figure S15: Base peak chromatogram at m/z = 466.2 ± 0.5 of acceptor and reference solution after incubating for compound 54. The peak of compound **54** is marked, and the area under the peak is stated above the peak.

Pull-down interaction assay

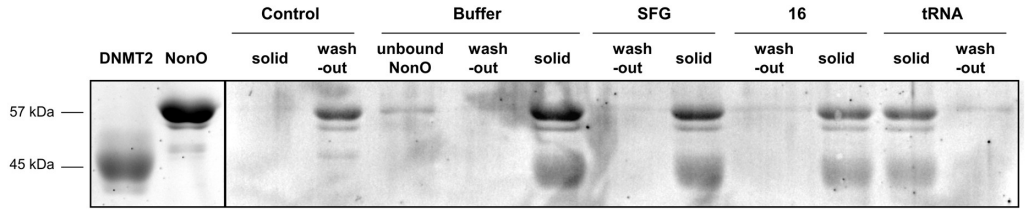


Figure S16: NonO does not bind to the allosteric pocket. Results of the SDS-PAGE-based analysis. Lane description from left to right: DNMT2/NonO: recombinant proteins for size comparison. References were applied at another gel position and merged in this figure; Control: beads without immobilized DNMT2 served as the negative control, i.e. on these beads no binding of NonO was observed. Treatments (buffer, SFG, **16**, tRNA): The lane "unbound NonO" contains the supernatant after immobilization of NonO, which showed low protein levels, thus most NonO is effectively immobilized on DNMT2 beads. Lanes labeled with (wash-out) contain the supernatant of the respective treatment conditions (buffer, 100 µM SFG, 100 µM **16**, 10 µM $tRNA^{Asp}$), while bands labeled with (solid) contain the solid fraction obtained by boiling the residual beads in Laemmli buffer. NonO could not be displaced from binding DNMT2 by competitive treatment with compound **16**, SFG, nor $tRNA^{Asp}$, indicating that NonO does not bind to the allosteric binding pocket identified. Uncropped PAGE images can be found in Figure S22.

Supplementary data for crystallographic investigations

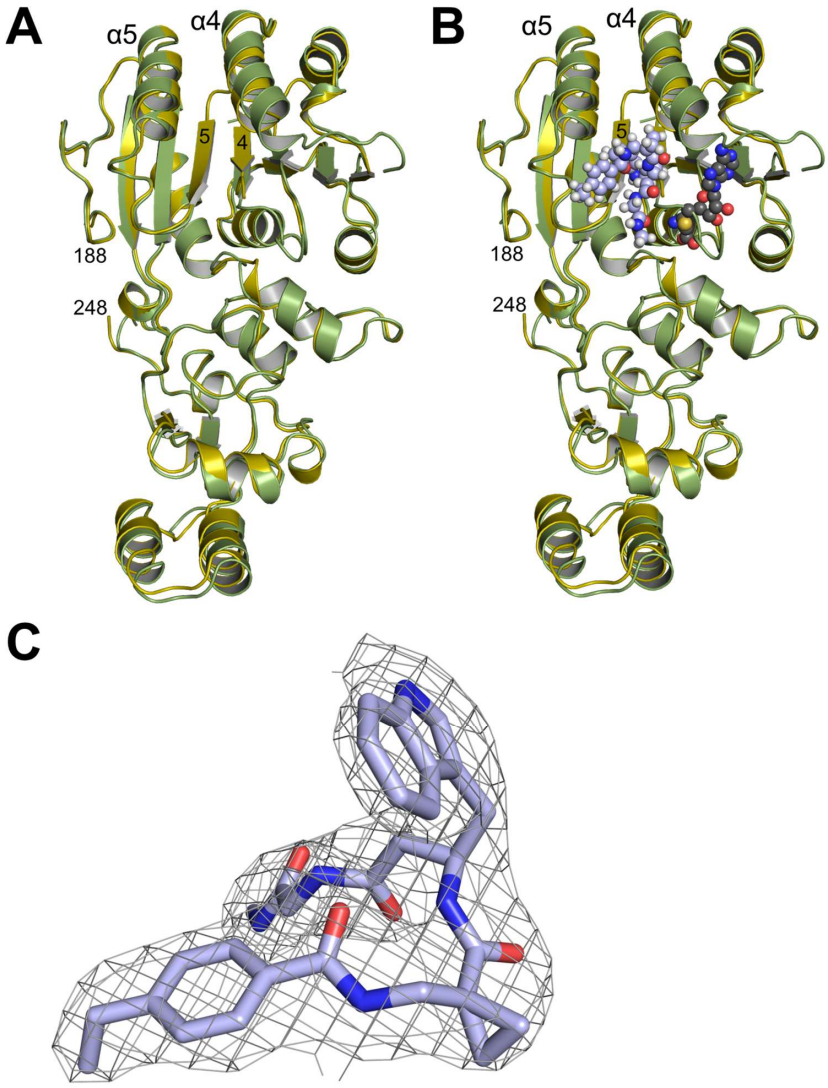


Figure S17: Global superposition of the X-ray structures of human DNMT2Δ47-compound 3 (green / light blue). Human DNMT2Δ47-SAH (yellow / grey) without (**A**) and with (**B**) ligands. (**C**) Compound **3** bound to DNMT2Δ47 (chain A) with $2mF_{obs}$-DF_{calc} electron density map at a contour level of +1σ.

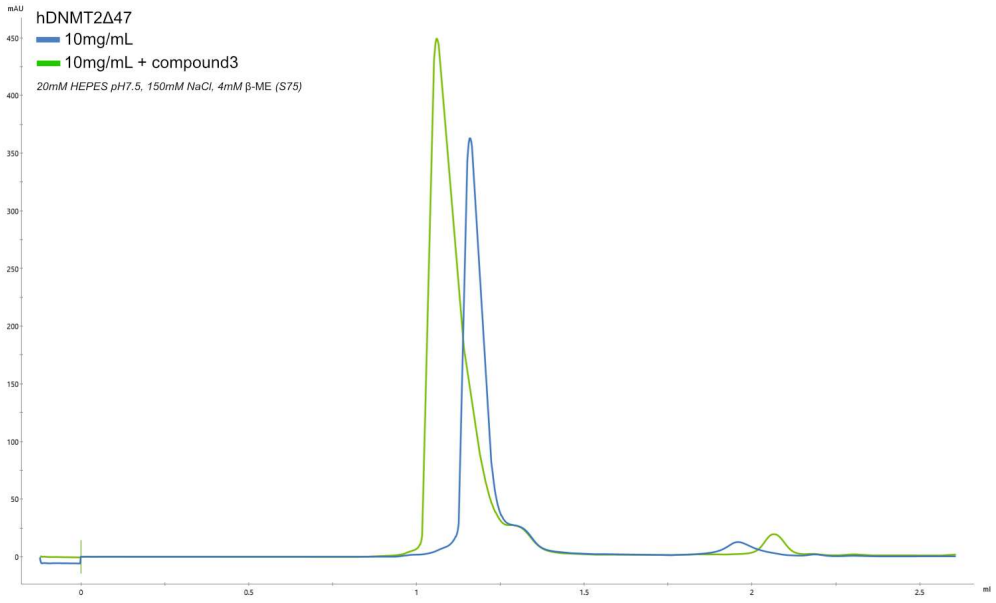


Figure S18: Analytical SEC elution profile of DNMT2Δ47 with and without compound 3. Superposition of two chromatograms showing the 280 nm signal of analytical SEC runs for hDNMT2Δ47 without ligand (blue) and pre-incubated with a 2-fold molar excess of compound **3** (green). For both runs the protein concentration was at 10 mg/mL as used for crystallization. A Superdex S75 3.2/300 column was used with a buffer consisting of 20 mM HEPES pH 7.5, 150 mM NaCl and 4 mM β-mercaptoethanol. The peak shift indicates the dimerization of DNMT2Δ47 upon compound **3** binding.

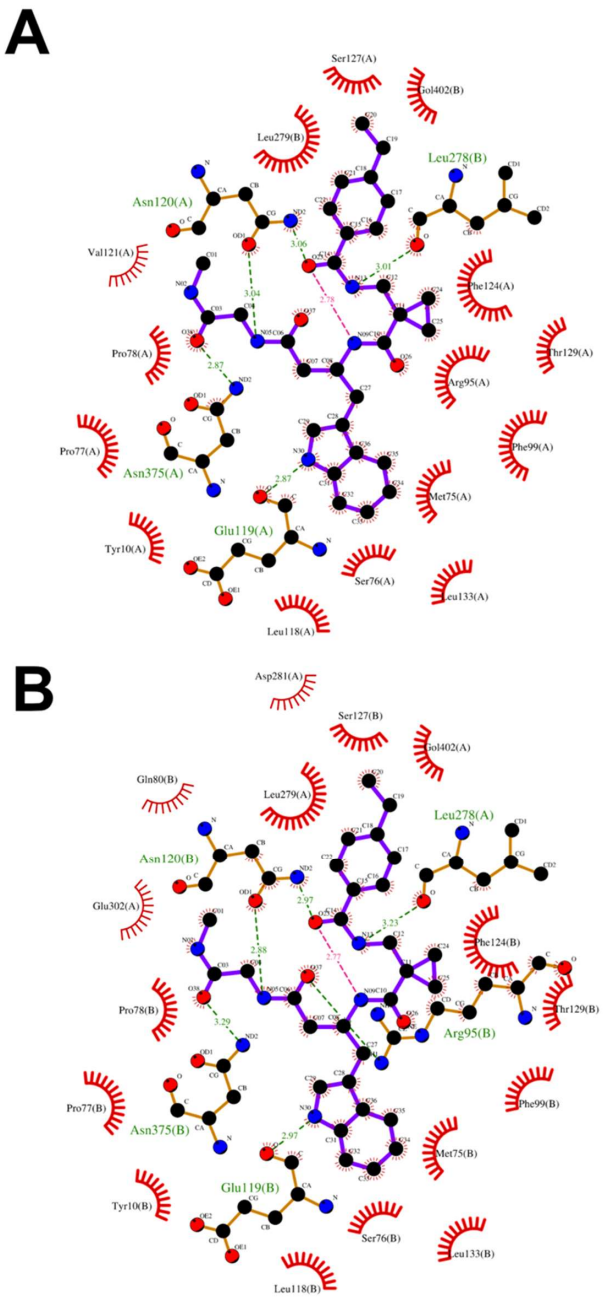


Figure S19: A schematic ligand-protein interaction diagram created with LigPlot+. For compound **3** bound to chain A (**A**) and chain B (**B**). Intermolecular hydrogen bonds are given in green, and the intramolecular hydrogen bond in compound **3** was added to the diagram in magenta.

Table S3: X-ray data collection refinement statistics.

PDB entry 9HGM	
Data Collection	
Beamline	ESRF Grenoble ID30B
Wavelength (Å)	0.8731
Resolution range (Å)	48.67-2.60 (2.72-2.60)
Space group	$P2_12_12_1$
a,b,c (Å)	71.20, 97.35, 125.02
α,β,ɣ (°)	90, 90, 90
Total reflections	263886 (33598)
Unique reflections	27445 (3300)
Multiplicity	9.6 (10.2)
Completeness (%)	100 (100)
Mean I/sigma(I)	10.6 (1.2)
R-merge	0.117 (1.966)
R-pim	0.042 (0.688)
CC1/2	0.999 (0.626)
Refinement	
Resolution range (Å)	48.67-2.60 (2.69-2.60)
Reflections used in refinement	27366 (2667)
Reflections used for R-free	1396 (132)
R-work	0.1995 (0.3377)
R-free	0.2454 (0.3798)
Number of non-hydrogen atoms	5410
Macromolecules	5276
Ligands	88
Solvent	46
Protein residues	656
RMS (bonds) (Å)	0.005
RMS (angles) (°)	0.580

Ramachandran favored (%)	97.4
Ramachandran allowed (%)	2.6
Ramachandran outliers (%)	0
Rotamer outliers (%)	0.84
Clashscore	2.02
Average B-factor (Å^2)	83.3
Macromolecules (Å^2)	83.6
Ligands (Å^2)	68.1
Solvent (Å^2)	74.1

Statistics for the highest-resolution shell are shown in parentheses.

Modeling of a ternary complex consisting of DNMT2-tRNA^{Asp} and small molecules

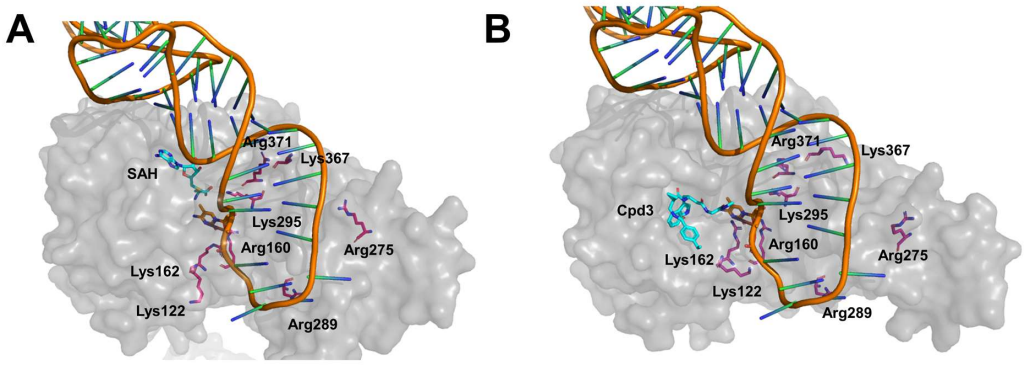


Figure S20: Modelling of ternary DNMT2-tRNA^{Asp} complexes. (**A**) Ternary complex (DNMT2-tRNA-SAH) modeled by AlphaFold, consisting of full-length DNMT2 (sequence from UniProt: O14717), tRNA^{Asp} (sequence: GGGUCGUUAGUAUAGUGGUGAGUAUCCCCGCCUGUCA{m5C}GCGGGAGACCGGGGUUCGAU UCCCCGACGGCCCGCCA), and SAH (relative coordinates from structural alignment with PDB 1G55). (**B**) Ternary complex (DNMT2-tRNA-cpd **3**) modelled by Schrödinger BioLuminate 5.8 consisting of compound **3**-bound DNMT2 (PDB 9HGM) and tRNA^{Asp}. The previously elucidated RNA-binding residues (K122, R160, R162, R275, R289, K295, K367, and R371) are at a significant distance from the allosteric binding pocket, and thus, allow the simultaneous binding of compound **3** and tRNA.

SeeSAR analysis by binding pose inspection of hit compound 3

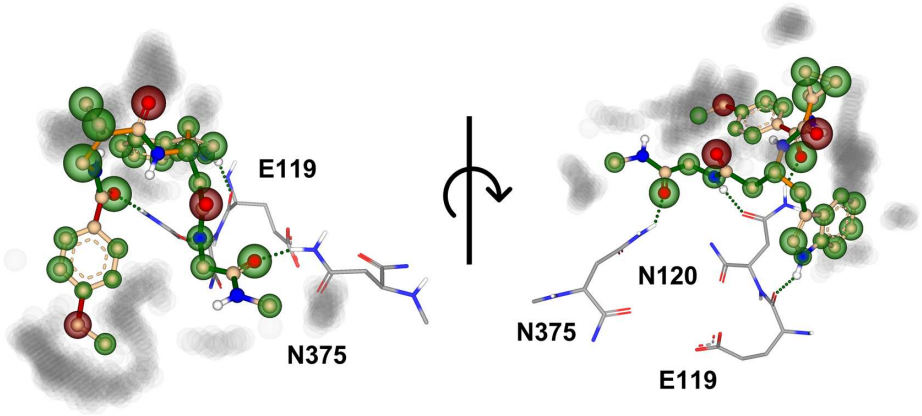


Figure S21: SeeSAR analysis by binding pose inspection of hit compound 3. Hyde coloring enabled the identification of contributing resp. unfavorable atom placements (colored spheres; green: contributing, red: unfavored); the peptide backbone's dihedral angles were evaluated for their torsional free energy (colored sticks). Characteristic hydrogen bonds are formed with the protein residues Glu119, Asn120, and Asn375. Potentially druggable yet unoccupied space in the protein binding pocket is highlighted by grey shadings.

Uncropped gel images

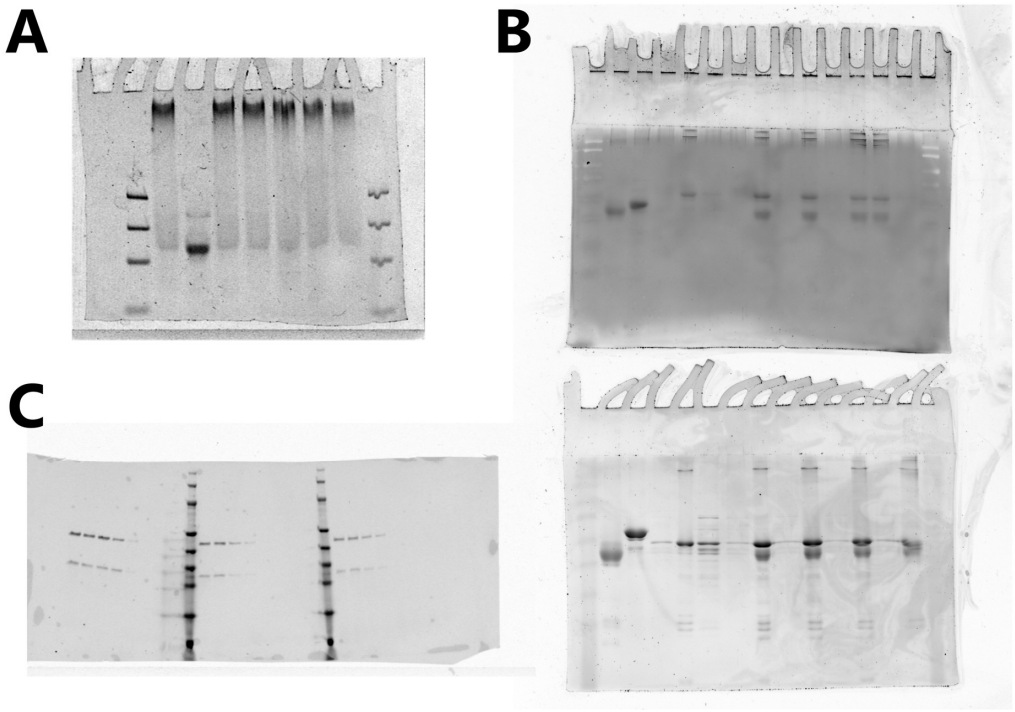


Figure S22: Uncropped PAGE and Western blot images. (**A**) EMSA. (**B**) DNMT2 interaction assays. (**C**) CETSA.

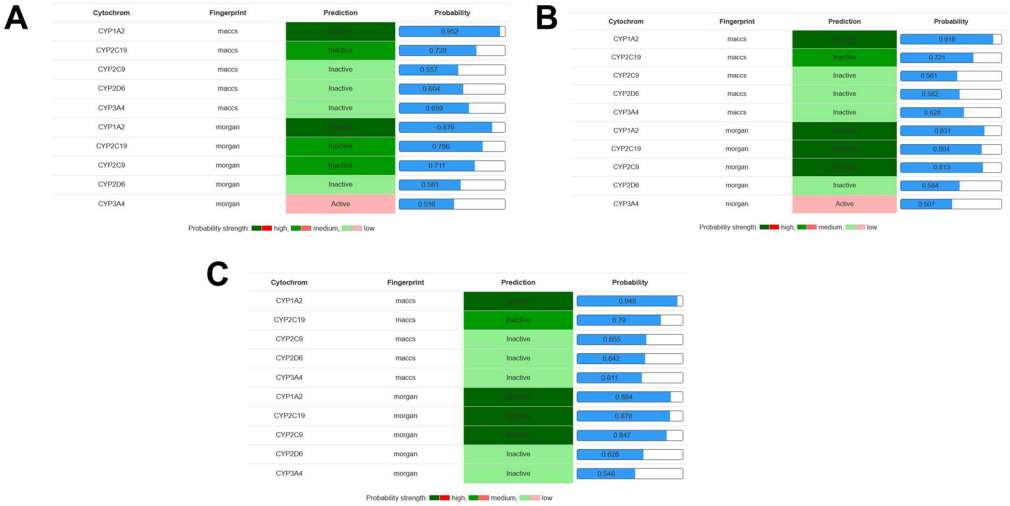
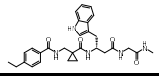
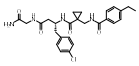
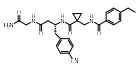


Figure S23: Cyp-enzyme reactivity profiles of compounds. 3 (**A**), **16** (**B**), and **34** (**C**) as determined by SuperCYPsPred.

Table S4: Overview of predicted physicochemical properties of cell evaluated compounds 3 (non-permeable control), 16 (cell-active), and 34 (taylor-made negative control). The values were obtained using the web tools molinspiration.com and SuperCYPsPred. Properties that violate Lipinski's Rule of Five are highlighted in red.

Cpd.	structure	MW [g/mol]	logP	TPSA	#H-acceptors	#H-donors	rotatable bonds
3		517.3	3.75	128.43	9	5	12
16		498.2	3.40	130.39	8	5	12
34		489.2	2.48	154.18	9	5	12

5 Binding Characterization of Multivalent Targeting Structures

5.1 Surface Density of Mono- and Trivalent High-Mannan-Derived Targeting Structures with Different Affinities Impacts Cellular Uptake of Human Serum Albumin-Derived Nanocarriers

5.1.1 Context, Project Summary, and own Contribution

When using nanocarriers for targeted drug delivery, the design of appropriate targeting structures (TS) is crucial, as they influence key factors such as carrier uptake. However, a more comprehensive understanding is still needed to guide the optimal selection of binding epitopes, valency, and density of TSs. Furthermore, the relationship between the biodistribution and avidity of nanocarriers has not been fully explored.[475–477] Recently, Chung *et al.* demonstrated how small changes in the valency of targeting structures could shift the accumulation of HSA-derived nanocarriers from lung metastases to the liver.[488]

In this publication, TSs were investigated in terms of optimal valency, epitope type, and density for cellular uptake and *in vitro* targeting selectivity. Mono- and trivalent TSs, with mono- or trimannose-binding epitopes, were designed with flexible ethylene glycol-based linkers containing azides for functionalization. These TSs were incorporated into an HSA-based nanocarrier system aimed at selectively targeting antigen-presenting cells (APCs), like dendritic cells or macrophages. Targeting was intended to occur via the lectin receptors DC-SIGN and MMR, based on a previous study.[474] Within this thesis, the influence of the linker on the binding mode of these compounds was assessed through molecular docking. To confirm binding to the isolated receptor domains, without multivalency on the receptor side, a nanoDSF study was established within this thesis. This showed weak millimolar binding affinities (K_D) for all structures and highlighted the need for multivalency in both TSs and receptors for efficient binding through avidity effects. The uptake efficiency for a controlled number of TSs per carrier was then investigated in APCs. This showed that for both monovalent and trivalent targeting structures, with increasing numbers, a maximum uptake was reached after which it plateaued or decreased, respectively. Additionally, affinity differences between the binding epitopes and the higher valency of trivalent TSs were only beneficial at lower densities. The selectivity of all TSs for DC-SIGN and MMR-presenting cells in spleen cell populations was confirmed.

Overall, this publicaton provides nanoDSF as an approach to measure carbohydrate−lectin interactions in homogeneous solution and gives insights into the effect of TS type and density on cellular uptake, highlighting that these multivalent ligands may only benefit when few functionalization sites are available on the carrier, which may aid in future design of TSs and carriers.

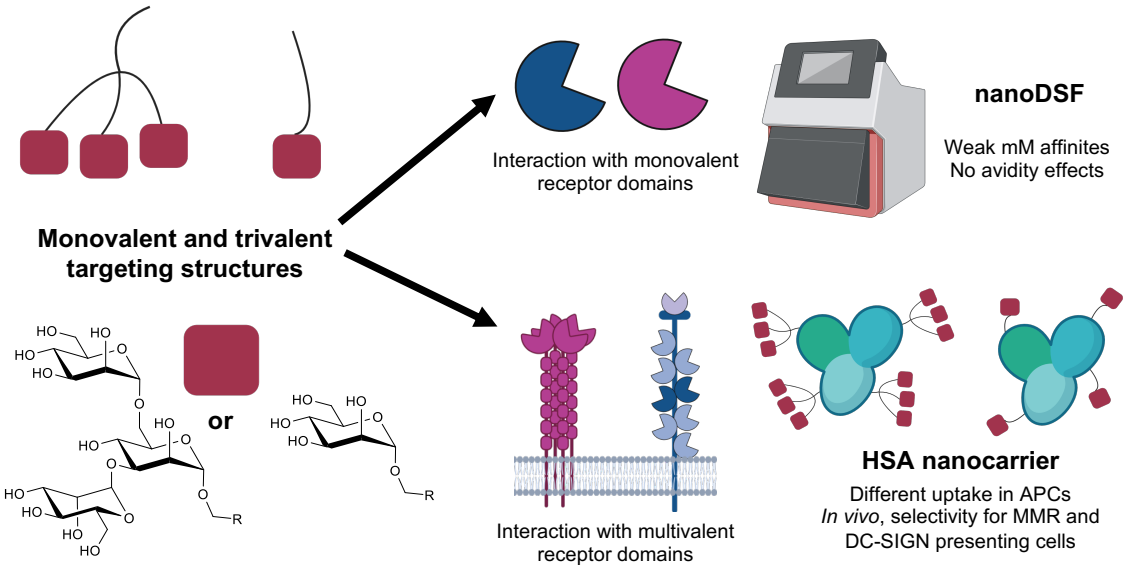


Figure 22: Evaluation of mono and trivalent carbohydrate-targeting structures. Abbreviations: DSF (differential scanning fluorimetry); HSA (human serum albumin); APC (antigen presenting cell); MMR (macrophage mannose receptor); DC-SIGN (Dendritic cell-specific Intercellular adhesion molecule-3-grabbing non-integrin). The figure was created with Microsoft PowerPoint, Biorender.com, and ChemDraw.

Own contributions: Protein expression and purification of DC-SIGN and MMR, establishment of nanoDSF experiments, *in silico* DC-SIGN model building, molecular docking, writing parts of the manuscript, writing parts of the supporting information.

Contributions from other authors: Syntheses of all targeting structures (**$ManN_3$**, **Man_3N_3**, **$(Man)_3N_3$**, and **$(Man_3)_3N_3$**), synthesis of HSA conjugates, MS of HSA conjugates, dynamic light scattering of HSA conjugates for distribution determination, cell culture, fluorescence-activated cell sorting, writing parts of the manuscript, writing parts of the supporting information.

The work was published in Biomacromolecules (impact factor: 5.4) and licensed under a Creative Commons Attribution licence: https://creativecommons.org/licenses/by/4.0/. This publication and the complete supplementary information (SI) are available online at DOI: 10.1021/acs.biomac.5c01510. The appended Supporting Information represents an abridged version.

Publication reprinted with permission from Biomacromolecules **2025**, *26*, 8087. „Surface Density of Mono- and Trivalent High-Mannan-Derived Targeting Structures with Different Affinities Impacts Cellular Uptake of Human Serum Albumin-Derived Nanocarriers.“

© 2025 The Authors. Published by American Chemical Society.

5.1.2 Publication

The following publication quoted (within “”) from page 189 to page 204 is exactly the same as the manuscript cited on page 188:“

BioMACROMOLECULES

Open Access
This article is licensed under CC-BY 4.0

pubs.acs.org/Biomac
Article

Surface Density of Mono- and Trivalent High-Mannan-Derived Targeting Structures with Different Affinities Impacts Cellular Uptake of Human Serum Albumin-Derived Nanocarriers

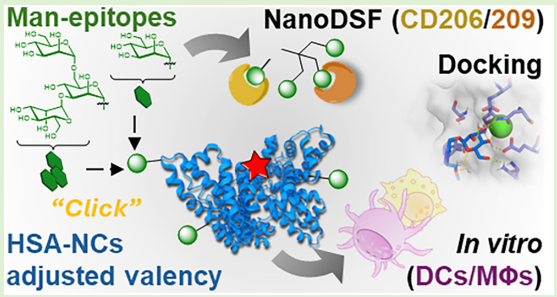
Robert Forster,[#] Bellinda Lantzberg,[#] Annabelle Weldert,[#] Laura Rosenberger, Yanira Zeyn, Danuta Kowalczyk, Seah Ling Kuan, Christian Kersten,[*] Matthias Bros,[*] Tanja Weil,[*] Tanja Schirmeister,[*] and Till Opatz[*]

Cite This: *Biomacromolecules* 2025, 26, 8087−8102

Read Online

ACCESS | Metrics & More | Article Recommendations | Supporting Information

ABSTRACT: Actively targeted delivery of nanocarriers (NC) modified with targeting structures (TS) binding to cell surface receptors, specific to target cells, enables enhanced selectivity and efficacy of cellular uptake. This is influenced by the ligand density on the NC surface. Herein, the impact of type, valency, and surface density of high-mannan derived TS on the C-type lectin receptor (CLR)-mediated uptake of human serum albumin (HSA)-based NCs in immune cell populations was investigated. Monovalent and trivalent TSs were prepared via efficient synthesis protocols and investigated regarding their affinity versus isolated carbohydrate recognition domains (CRD) of CD206 and CD209 within a NanoDSF study. Conjugation to HSA resulted in low valency and saturated NCs with a well-defined mannose epitope count. An *in vitro* study with bone-marrow-derived dendritic cells and splenic immune cells revealed the impact of the NC surface modification on cellular uptake and cell selectivity, allowing insights into the design of TSs and NCs.



Downloaded via UNIV MAINZ on January 15, 2026 at 12:32:29 (UTC).
See https://pubs.acs.org/sharingguidelines for options on how to legitimately share published articles.

1. INTRODUCTION

Actively targeted drug delivery in immunotherapy aims at modulating immune responses by using drug-loaded nanoparticulate carriers (NCs) functionalized with targeting structures (TS).[1−4] Such polymer-, lipid-, or protein-based NCs protect the cargo, improve biodistribution and therapeutic efficacy.[5−9] Mannose-based TS enable selective delivery to antigen-presenting cells (APC) like dendritic cells (DC) or macrophages (MΦ) mediated by C-type lectin receptors (CLR).[10,11] CLR engagement allows internalization and intracellular distribution of NCs prior to the release and processing, as well as presentation of NC-derived antigens and, in the case of sufficient APC activation, downstream T-cell responses. This makes them attractive targets for APC-specific therapies (e.g., tumor immunotherapy).[12−18] Targeting of DCs or M2-polarized MΦs focuses on highly expressed CLRs like CD206 (MMR-1) and CD209 (DC-SIGN), due to involvement of either CLR in antigen internalization and subsequent presentation via major histocompatibility complex (MHC) molecules for T-cell activation.[19−29] CD206 contains eight carbohydrate recognition domains (CRD), with CRD4 being responsible for most of the binding activity.[30−33] CD209 contains one CRD and forms a homotetramer (Figure 1A).[34−36] Glycan array studies revealed binding of epitopes of a nonamannose substructure from naturally occurring high-mannan-type glycans,[37−44] with CD206 preferring shorter, terminally α-(1→2)-linked and CD209 internal α-(1→2)- and α-(1→3)-linked epitopes with canonical binding modes engaging hydroxyl groups 3 and 4 of the mannose units (Man).[45−49] Increased affinity for the α-(1→3)- and α-(1→6)-branched trisaccharide (Man_3) epitopes results from secondary contacts (Figure 1A).[31] CLR targeting thus strongly depends on epitope geometry.[50−52] Singular binding interactions of isolated epitopes and CRDs provide low intrinsic affinity and specificity (K_D in the mM range).[53−56] Presentation of multiple CRDs and formation of oligomers and cell surface clusters by CLRs offer extended binding regions[57−59] and enable multivalent interactions with multimerized epitopes for high functional affinity (avidity) and specificity (K_D in the μM to pM range) due to avidity effects such as clustering, chelation, and statistical rebinding (compare Figure 1C for avidity effects

Received: July 28, 2025
Revised: September 22, 2025
Accepted: September 23, 2025
Published: October 7, 2025



ACS Publications
© 2025 The Authors. Published by American Chemical Society

https://doi.org/10.1021/acs.biomac.5c01510
Biomacromolecules 2025, 26, 8087−8102

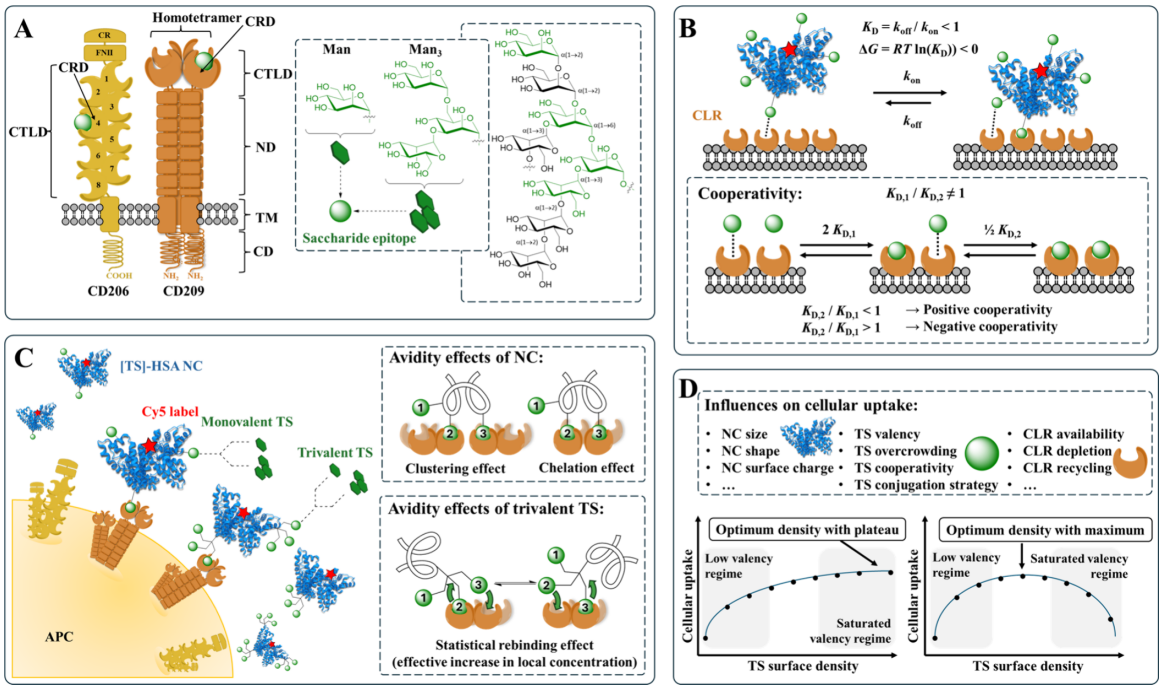


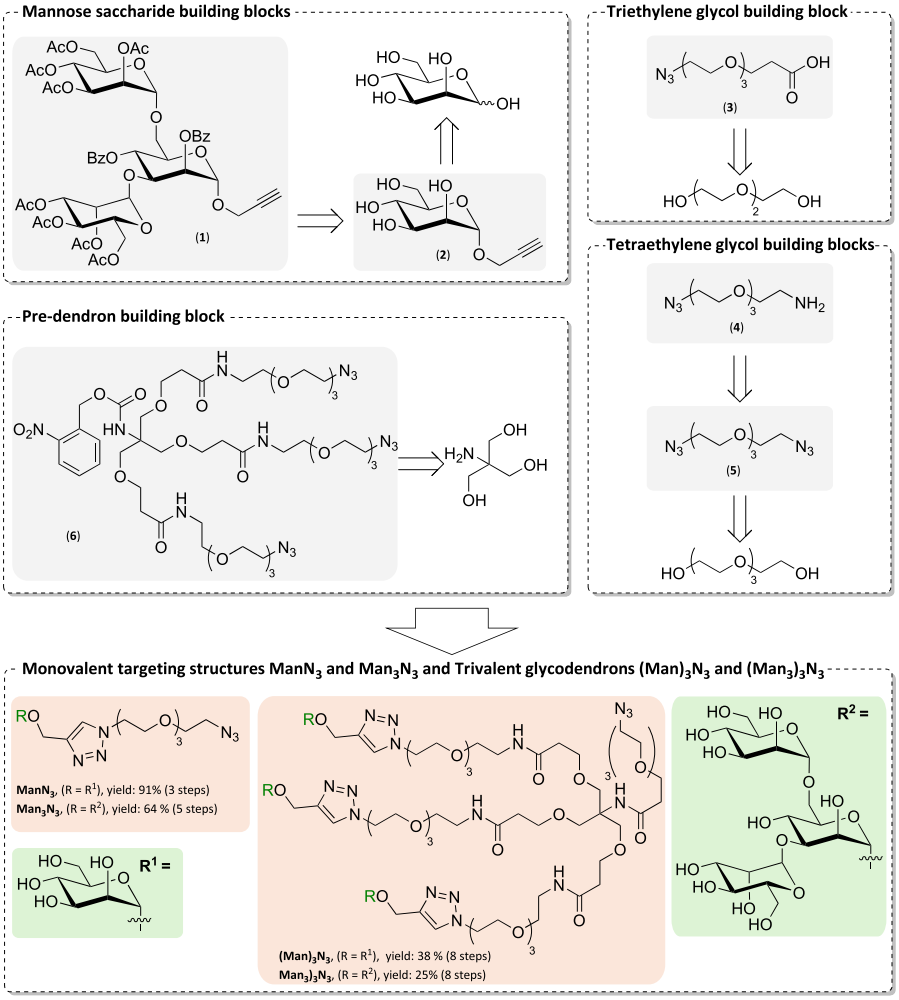
Figure 1. (A) Functional domains of CD206 and CD209: Cysteine-rich (CR), fibronectin type II (FNII), C-type lectin (CTLD), carbohydrate recognition (CRD), neck (ND), transmembrane (TM), and cytoplasmic domain (CD).[11,104,105] Saccharide epitopes Man and Man_3 of the nonasaccharide substructure from high-mannan glycans chosen as TS for CLR binding. (B) Multivalent interactions of NC and cell surface form multiple TS-CRD complexes governed by avidity of NC as a product of intrinsic affinities of individual TS and valency of NC resulting in avidity effects. Formation of initial complex exerts influence on subsequent formations.[81] (C) APC targeting with HSA-NCs presenting mono- and trivalent TSs carrying Man or Man_3 epitopes.[11] Cooperative avidity effects like simultaneous clustering of one CRD of two different CLRs or chelation of two CRDs of one respective CLR (NC multivalency) as well as an effective increase in the local concentration of epitopes by statistical rebinding (TS multivalency) influence uptake.[64−70] (D) Further properties of NCs and TS influencing cellular uptake, with dependency on TS surface density resulting in two trends: (a) increase until constant threshold or (b) increase until maximum, followed by decline.[76]

of potential relevance for the present study). Clustering refers to the ability of multivalent ligands to simultaneously bind to multiple receptors, while chelation enables binding to oligomeric receptors via simultaneous occupation of multiple binding sites. Statistical rebinding refers to the ability of a multivalent ligand to reform individual ligand−receptor bonds upon dissociation using adjacent epitopes, resulting in an increased probability of binding interactions. Acting as an effective increase in local epitope concentration, this leads to a higher apparent binding affinity.[60−70] Similar considerations apply for engagement of CLRs with multivalent NCs presenting mannose TSs, as biodistribution and cellular uptake are markedly influenced not only by size, surface charge and valency of the NC, but also by surface density, conjugation strategy, and orientation of the TSs.[71−82] Formation of TS-CLR complexes (Figure 1B) resulting from multivalent interactions between NCs, presenting multimerized TSs, and cell surfaces, expressing multiple CLRs can be described in thermodynamic terms by the Gibbs free energy, ΔG, which is related to avidity of the system via the dissociation constant, K_D ($\Delta G = RT \ln(K_D)$).[81,83] Models describing ΔG in terms of multivalent binding interactions highlight the number of formed complexes as the main driving force, with each contributing favorable binding enthalpy ΔH to overcompensate the unfavorable decrease in entropy ΔS upon binding ($\Delta G = \Delta H - T\Delta S$).[64,84] Negative values of ΔG describe the equilibrium of the binding process to favor the TS-CRD complex ($\Delta G < 0$ kJ/mol → $K_D < 1$ M). The entropy loss, ΔS, results from the mobility restriction for TSs entering the bound state. Being smaller for TSs already constrained by high surface density or conjugation via rigid linkers, the usage of flexible linkers, which offer the mobility required for adaptation to the target and efficient binding, imparts higher entropic penalties.[85−87] Based on thermodynamic considerations, targeting efficacy of multivalent NCs is assumed to benefit from high TS numbers (TS valency) and CLR expression (receptor availability).[81] On the contrary, targeting efficacy is hampered on the NC level by its size increase inherent to higher surface modification and further impacted by its shape and surface charge.[88] On the cellular level, targeting efficacy is decreased by steric hindrance of closely packed TSs (TS overcrowding), higher consumption of cell membrane receptors per NC binding event (receptor depletion) and slow recycling kinetics of such receptors (receptor recycling).[89] Thus, cellular uptake follows two general trends depending on TSs density: (a) "optimum density with a plateau" and (b) "optimum density with a maximum" (Figure 1D). The underlying mechanisms governing these trends have been comprehensively analyzed by Alkilany et al.[76] Steric hindrance of TSs on NCs with saturated surface also depends on the conjugation strategy employed,[90] with nonoriented TSs experiencing reduced steric hindrance resulting in trend (a) and with oriented, closely packed ligands

https://doi.org/10.1021/acs.biomac.5c01510
Biomacromolecules 2025, 26, 8087−8102

Biomacromolecules pubs.acs.org/Biomac Article

Scheme 1. Retrosynthesis of Building Blocks (Grey Highlight) Involving Mannoses (1) and (2), Linkers (3), (4), and (5), and Predendron (6) for Assembly of Monovalent and Trivalent TSs (Orange Highlight) with Abbreviated Residues (Green Highlight)[a]



[a]Yields and step count are stated for each TS. Synthesis and analytical data are displayed in section 4.1 of the Supporting Information.

experiencing overcrowding effects resulting in trend (b).[76] Ligand density furthermore influences the operating uptake mechanism responsible for internalization of NCs.[91−93] Thus, avidity of NCs represents not a simple "additive" phenomenon summing up intrinsic affinities of TS,[94] as already formed binding interactions influence subsequent formations (Figure 1B), either by positive (first favors second interaction) or negative cooperativity (first hinders second interaction) (TS cooperativity), with avidity effects falling into the first category.[81,83,95] This complex interplay determining biodistribution and cellular uptake of targeted NCs is sensitive to small changes in NC valency and TS surface density with the major contributors summarized in Figure 1D. Chung et al. demonstrated low-valency human serum albumin (HSA)-derived NCs with six Man TSs achieving high uptake in lung metastases via selective CD206-mediated targeting of tumor-associated MΦs, while slightly higher valency of eight TSs shifted accumulation to the liver.[96] Such investigations of targeted delivery approaches are often directed at systemic distribution with limited focus on interactions of multivalent NCs at the cellular level.[81] The latter are often studied in experiments using surface plasmon resonance (SPR)[63,97,98] on artificial or isolated membranes,[99−101] to model the disposition of natural cellular membranes.[81] Given the relevance of low-valency NCs and limited understanding of multivalent interactions occurring at the cellular level, the impact of TS surface density and NC valency on cellular uptake, being a crucial step for targeted delivery approaches, needs to be investigated.[76] Heading out from reported HSA-NCs presenting monovalent TSs with the Man_3-epitope for CLR targeted transport of a toll-like receptor (TLR) 7/8 agonist for APC selective uptake,[102] we used similar systems to present quantifiable amounts of well-defined monovalent and trivalent TSs with Man and Man_3 epitopes at low and high degree of

https://doi.org/10.1021/acs.biomac.5c01510
Biomacromolecules 2025, 26, 8087−8102

functionalization for this study. HSA as basis of NCs enables surface modification with controlled stoichiometry.[103] Quantification of the number of TS per NC was a prerequisite to investigate which effect (i) TS surface density and NC valency, (ii) epitope type, and (iii) epitope clustering have on targeting properties. First, a docking study for both epitopes allowed insights into TS conformation and potential epitope binding modes (sections 3.1 and 3.3). Then, a NanoDSF study revealed binding affinities of all unconjugated TSs for isolated CRDs of CD206 and CD209 (section 3.2). Furthermore, an *in vitro* study of bone marrow-derived DCs (BMDC) allowed the investigation of cellular uptake of TS-HSA conjugates with low degree of functionalization (low valency) and high degree of functionalization (saturated valency) under consideration of influences (i)−(iii) (compare Figure 1D). Cellular uptake levels served as a measure of binding strength to determine the cell targeting ability of NCs within a biologically relevant environment and enabled interpretation in the context of the discussed trends (a) and (b). Finally, an *in vitro* study of splenic immune cells enabled comparisons within a more heterogeneous cell population and indications about APC targeting selectivity in the presence of off-target immune cells.

2. EXPERIMENTAL SECTION

2.1. General Experimental Conditions. For the synthesis of the HSA-based compounds, all reactions were performed without taking precautions to exclude air and moisture, unless stated otherwise. Organic solvents (CH_3CN, HPLC grade; CH_2Cl_2, HPLC grade; DMF, peptide grade; DMSO, analysis grade) were obtained from Thermo Fisher Scientific (Waltham, MA, USA) and used without further purification. Milli-Q water (MQ) was obtained from a Millipore purification system. For the synthesis of carbohydrate-based compounds, reactions involving sensitive and reactive species were conducted under an atmosphere of argon-gas in dried glass ware utilizing the standard Schlenk technique. Dried solvents were used, obtained from a SPS 5 solvent drying system (M. Braun Inertgas-Systeme, Garching, BY, Germany) for toluene and DCM. Further dried solvents were obtained from Acros Organics (Geel, Belgium) in AcroSeal bottles over molecular sieves for DMF, MeOH and pyridine. Glycosylation reactions were conducted in the presence of activated spherical molecular sieve beads (diameter 1−2 mm, pore size 3 Å) supplied from Alfa Aesar (Haverhill, MA, USA). The stated temperatures refer to the temperatures measured with a contact thermometer in the used heating mantle or cooling bath. Heated reactions were conducted in an aluminum block placed on the stirring plate. Glycosylation reactions conducted in a temperature range between −40 °C to −20 °C were placed in an acetone bath, which had its temperature adjusted using a FT902 cryostat (Julabo, Seelbach, BW, Germany). Zemplén-deacylations were neutralized with the ion-exchange resin Amberlite IR 120 (*H*-Form) supplied by Merck Millipore (Burlington, MA, USA). The resin was thoroughly washed with MeOH, H_2O, 1 M HCl, and MeOH in that order prior to use utilizing a glass frit. To remove molecular sieves, ion-exchange resin, and other solids prior to reaction work up, reaction mixtures were filtered through a glass frit using Celite Hyflo Super Cel diatomaceous earth, supplied from Sigma-Aldrich (St. Louis, MO, USA).

2.2. Synthesis of Saccharide Targeting Structures. To present one or three Man or Man_3 epitopes, the clickable monovalent TSs $ManN_3$, Man_3N_3, and the Newkome-type[106] glycodendrons $(Man)_3N_3$, and $(Man_3)_3N_3$ were prepared (Scheme 1). The contained flexible ethylene glycol-based linkers enable conjugation to dibenzocyclooctyne (DBCO)-modified HSA derived NCs via strain-promoted azide alkyne cycloaddition (SPAAC). Their synthesis involves the preparation of saccharide, linker, and predendron building blocks using a set of efficient and scalable synthesis protocols evolving around the copper-catalyzed azide alkyne cycloaddition (CuAAC) reaction for their assembly (Scheme S1 in the Supporting Information for details on the synthesis steps and reaction conditions). The building blocks are summarized in the upper part and the assembled TS in the lower part of Scheme 1. The TSs were obtained with significantly improved yields compared to prior reports (e.g., Man_3N_3: 4% over eight steps).[75] Higher efficiency and robustness of the synthesis route up to the multigram scale results from telescoped reaction protocols (two-step propargylation and Zemplén-deacylation sequence[107] and three-step silylation, benzoylation, desilylation sequence[108]). All building blocks and intermediates were characterized by ^{1}H NMR, ^{13}C NMR, 2D NMR, and high-resolution mass spectrometry (HR-MS). The unconjugated TSs were used in the NanoDSF study and for conjugation to the [DBCO]-HSA precursor.

2.3. Differential Scanning Fluorimetry (NanoDSF) Study of Unconjugated TS. Thermal shift experiments were performed by using a Prometheus NanoDSF instrument (NanoTemper, Munich, Germany). Each sample, containing 12 μM CD209 CRD or CD206 CRD4 (recombinant protein expression and purification displayed in section 6.1 of the Supporting Information) together with varying ligand concentrations in binding buffer (150 mM NaCl, 25 mM Tris-Cl, pH 7.8, and 25 mM $CaCl_2$), was loaded into NanoDSF capillaries. Each ligand concentration was measured in triplicate. Samples were subjected to a controlled temperature increase from 20 to 85 °C at a rate of 1.5 °C per minute. Protein unfolding was monitored by measuring the fluorescence emission ratio at 350 and 330 nm. The FoldAffinity tool developed by Niebling et al.[109] was used to analyze the melting curves (data displayed on section 6.2 of the Supporting Information) and determine the unfolded fraction at each ligand concentration, evaluated at 53 °C for CD206 and at 63 °C for CD209. Data were analyzed according to the vertical slice method developed by Bai et al.[110] The unfolded fraction was plotted against the ligand concentration, and EC_{50} values were determined by fitting the data to the Hill equation using GraphPad Prism 8.0.1. K_D values were calculated using eq 1[110] based on the unfolded fraction in the absence of ligand (f_{uo}) and the total protein concentration ([*P*]). Associated errors were determined according to the standard error propagation rules.

$$K_D = (1 - f_{uo}) \times \left(EC_{50} - \frac{[P]}{2}\right) \quad (1)$$

2.4. Matrix-Assisted Laser Desorption Ionization − Time of Flight Mass Spectrometry (MALDI-ToF-MS). Mass spectra for HSA-based compounds were acquired on a ToF MS rapifleX spectrometer (Bruker Corporation, Ettlingen, BW, Germany) using sinapinic acid as the matrix. The molecular mass for all compounds was calculated as the *m*/*z* value using the peak center representing the singly charged species.

2.5. Agarose Gel Electrophoresis. An 1% agarose gel (0.5 g agarose, 50 mL 1 × TAE buffer) was prepared, and protein (∼1−3 μg) samples were loaded. The gel was run at 150 V for 33 min. The gel was imaged using the Cyanine 5 (Cy5)-channel and stained with coomassie brilliant blue before imaging using a ChemiDoc Imaging system (Bio-Rad Laboratories, Hercules, CA, USA) using the coomassie brilliant blue channel.[111]

2.6. Dynamic Light Scattering (DLS). Measurements of HSA-based compounds (10 μM in MQ) were performed at 25 °C using a Zetasizer Nano S (Malvern Instruments, Malvern, England) equipped with a He/Ne Laser (λ = 633 nm) and a narrow band filter at a fixed scattering angle of 173 °. Volume distribution of DLS measurements of compounds were used to determine the compounds size distribution.

2.7. Synthesis of HSA Conjugates. Synthesis procedures were adapted[102] and modified, as provided in detail in the SI (section 4.2 in the SI). Briefly, native HSA was dye-labeled using Sulfo-Cy5-Maleimide at Cys34 in 50 mM PB, pH 7.4, followed by ring-opening for stabilization in 50 mM borate buffer, pH 9.2 (HSA). The HSA was purified via spin filtration (Vivaspin, 10 kDa cutoff). A fixed number of DBCO-groups (13 or 47, as determined by the average molecular weight from MALDI-ToF-MS analysis) were statistically attached to

https://doi.org/10.1021/acs.biomac.5c01510
Biomacromolecules 2025, 26, 8087−8102

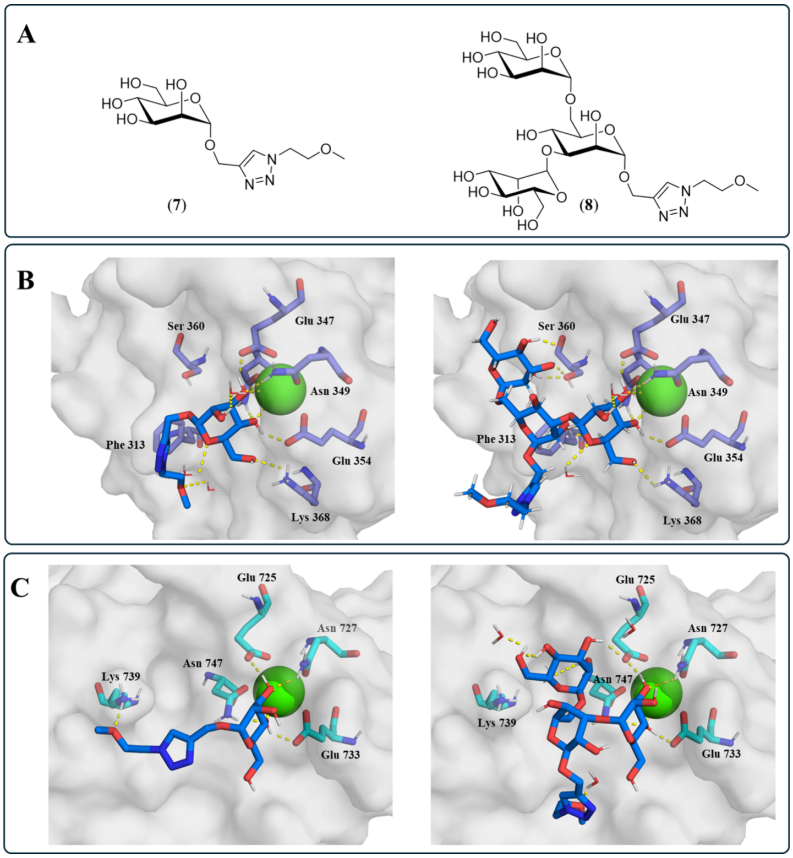


Figure 2. (A) TS Man (**7**) and Man_3 (**8**) with truncated linkers used for the in silico binding mode study. (B) Predicted binding modes for TS Man (**7**) (left) and TS Man_3 (**8**) (right) in complex with CD209 (PDB: 1SL4).[112] (C) Predicted binding mode for TS Man (**7**) (left) and TS Man_3 (**8**) (right) in complex with CD206 (PDB: 7JUF).[31] TS displayed as sticks with blue C-atoms, protein surfaces in light gray, selected amino acid residues inside the CRD as sticks with purple (CD209) or light blue (CD206) C-atoms and label, Ca^{2+}-cations as green spheres, water molecules as lines, and polar interactions as yellow dashed lines.

lysine residues randomly distributed on the NC surface via DBCO-PEG_4-NHS in 50 mM PB, pH 7.4 yielding DBCO-HSA. Subsequently, synthetic azide-functionalized TS ($ManN_3$, Man_3N_3, $(Man)_3N_3$, or $(Man_3)_3N_3$; MQ, 10 mg/mL) was added to DBCO-HSA (1 mg/mL) in 50 mM PB, 8 M urea, 2 mM EDTA. Equivalents of TS and reaction time were strictly controlled and adjusted based on reaction progress monitoring via MALDI-ToF-MS. For conjugates with n(TS) = 1−9, remaining free DBCO groups were capped using excess N_3−PEG_3−OH. All HSA conjugates were purified via spin filtration (Vivaspin, 10 kDa cutoff) and obtained with recovery rates ranging from 38% to quantitative. The degree of modification of HSA with TS was controlled qualitatively via agarose gel electrophoresis (Figure S1 in the Supporting Information) and quantitatively via MALDI-ToF-MS analysis. In total, five groups of NCs were prepared following the described procedure, involving the control group C [C I = Cy5-labeled HSA, C II = DBCO-HSA with 13 DBCO groups attached, and C III = HO-PEG_3-HSA, in which the 13 DBCO groups were saturated with capping reagent], the $ManN_3$ modified group M [M I, M II, M III, M VI, M IX, M_{sat}], the $(Man)_3N_3$ modified group [MD I, MD II, MD III, MD_{sat}], the Man_3N_3 modified group (TM I, TM II, TM III, TM IV, TM IX, TM_{sat}] and the $(Man_3)_3N_3$ modified group [TMD I, TMD II, TMD III, TMD_{sat}], where the Roman numeral always represents the number of TS groups attached. This systematic matrix of NCs with known amounts of epitopes of different structures at variable TS density and NC valency enables the subsequent interpretation of in vitro experiments.

2.8. Cell Culture. Murine bone marrow cells ($2{\cdot}10^5$/mL for GM-CSF supplemented culture) were seeded in 12-well suspension culture plates (Greiner Bio-One, Frickenhausen, BW, Germany) in culture medium (IMDM, 2 mM L-glutamine, 100 U/mL penicillin G, 100 μg/mL streptomycin (Sigma-Aldrich, Deisenhofen, BY, Germany) and 50 μM β-mercaptoethanol (Carl Roth, Karlsruhe, BW, Germany) containing 5% FBS (PAN-Biotech, Aidenbach, BY, Germany)) supplemented with recombinant murine GM-CSF (10 ng/mL) (Miltenyi Biotec, Bergisch Gladbach, NRW, Germany). Cells were kept at 37 °C, 95% relative humidity, and 5% CO_2. Culture media was replenished on day 3 and 6 with GM-CSF supplemented cell culture medium.

2.9. Spleen Cell Isolation. Murine spleens were mechanically disrupted with a pestle and pressed through a cell strainer with a pore size of 40 μm (Greiner Bio-One, Frickenhausen, BW, Germany) to obtain a single-cell suspension. Erythrocytes were lysed using 2.00 mL of Gey's Red Cell Lysis buffer (H_2O dest., 100 μM EDTA, 10.0 mM $KHCO_3$ and 155 mM NH_4Cl) for 1 min at room temperature. Subsequently, cells were washed using an IMDM-based culture medium containing 5% FBS (PAN Biotech, Aidenbach, Germany), 2.00 mM L-glutamine, 100 IU/mL penicillin, 100 μg/mL streptomycin, and 50.0 μM β-mercaptoethanol. Isolated splenocytes

https://doi.org/10.1021/acs.biomac.5c01510
Biomacromolecules 2025, 26, 8087−8102

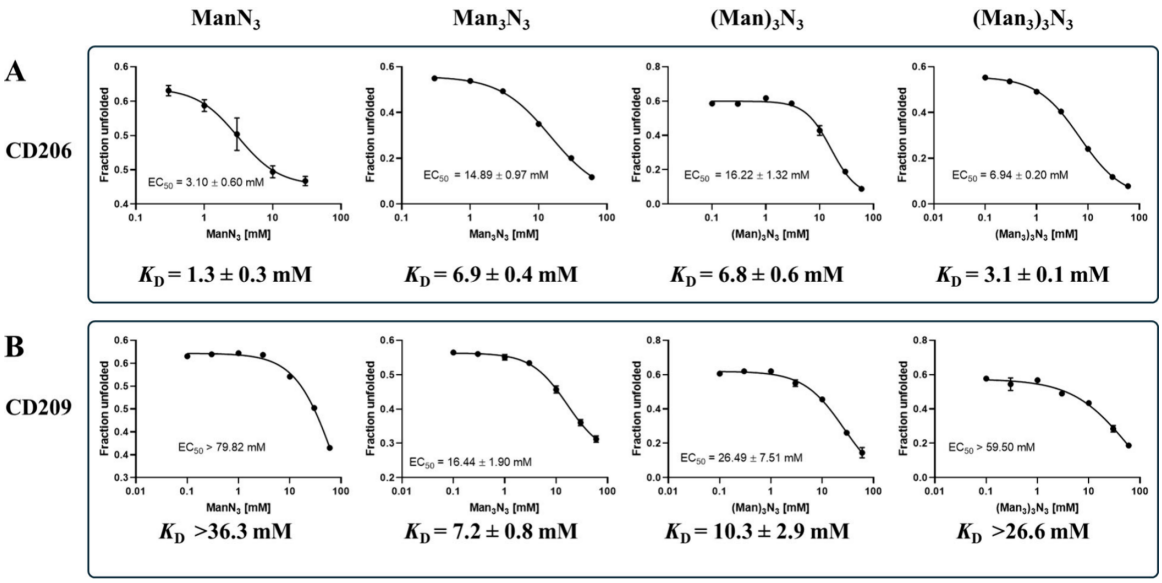


Figure 3. NanoDSF study for binding of mono- and trivalent TSs $ManN_3$, Man_3N_3, $(Man)_3N_3$, and $(Man_3)_3N_3$ to the CRDs of CD206 and CD209. (A) Affinity of mono- and trivalent TSs for CRD4 of CD206. (B) Affinity of mono- and trivalent TSs for CRD of CD209. The unfolded fraction of each CRD at different TS concentrations was determined at 53 °C for CD206 and at 63 °C for CD209. The unfolded fraction was plotted against TS concentration, and EC_{50} values were determined using GraphPad Prism 8.0.1. The respective K_D values were calculated from EC_{50}, as described in section 2.3, and are given for each case.

(2×10^6/500 μL) were used for *in vitro* experiments and stained for FACS analysis.

2.10. Fluorescence Activated Cell Sorting (FACS). After treatment, GM-CSF BMDCs and splenocytes were harvested, washed with staining buffer (PBS, 1% FBS, 0.5 mM EDTA) and incubated with rat antimouse CD16/CD32 antibody (clone 2.4G2; 15 min, 4 °C) to prevent antibody binding to Fcγ receptors. Following this, the samples were incubated with fluorescence-labeled antibodies (20 min, 4 °C). Then, samples were washed with PBS and incubated with a flexible viability dye (FVD, 1:1000 in PBS, 30 min, 4 °C) to identify live/dead cells. Measurements were carried out using an Attune NxT flow cytometer and data were analyzed using Attune NxT software (both are from Thermo Fisher, Waltham, MA, USA).

3. RESULTS AND DISCUSSION

3.1. Prediction of Binding Modes for Monovalent TSs. Predicted binding modes for the TS Man (**7**) and Man_3 (**8**), with a truncated linker unit (Figure 2A), were generated by molecular docking to investigate potential influences of linker placement on binding mode. The molecular docking-predicted binding mode of the TS Man (**7**) to the CRD of CD209 showed polar interactions between the Man epitope and the Ca^{2+}-cation inside the principal Ca^{2+}-binding site, as well as to the surrounding amino acids Glu347, Asn349, Glu354, Lys368, and Asn365 (Figure 2B). The truncated linker is oriented toward the protein surface and interacts with water molecules inside the pocket. The predicted binding mode of the TS Man_3 (**8**) with the CRD of CD209, indicates that the Man_3 epitope predominantly binds through the terminally α-(1→3)-connected mannose residue, with the same interactions as the Man epitope in the prior case. The central mannose moiety forms no additional hydrogen bonds to the CRD, while the terminal α-(1→6)-linked mannose residue forms additional polar interactions with Ser360 in the secondary binding site, consistent with previous crystal structures of similar compounds (Figure 2B).[112] Molecular docking of the TS Man (**7**) to the CRD of CD206, showed that the Man epitope similarly engages in polar interactions with the central Ca^{2+}-cation and surrounding amino acids Glu725, Asn727, Glu733, and Asn747 (Figure 2C). The linker forms a hydrogen bond to Lys739. In the predicted binding mode of the TS Man_3 (**8**) with the CRD of CD206, the characteristic polar interactions again arise from the α-(1→3)-linked mannose residue, with an additional polar interaction between the α-(1→6)-linked mannose and Glu725. The linker interacts with a binding-site water molecule. All linkers are found at the solvent-exposed protein surface, with their orientation pointing away from the primary binding site. Therefore, this attachment point seems to be suitable for linking Man moieties for glycodendrons.

3.2. NanoDSF Binding Study for Mono- and Trivalent TSs. The binding affinity of CRD4 of CD206 to saccharide ligands has been mainly investigated by NMR titration and competition binding assays, yielding high μM to low mM affinities.[31,113] For CD209, surface plasmon resonance (SPR), isothermal titration calorimetry (ITC), and solid-phase competition assays have been employed to measure the affinity of both the tetrameric extracellular domain (ECD) and the monomeric carbohydrate recognition domain (CRD) toward different mannose variations, with reported values ranging from the low millimolar range to being too weak to detect.[35,50,63,114−117] Notably, the isolated CRD is known to have weaker affinities to its ligands than the tetrameric ECD.[36] A growing body of literature has demonstrated that (Nano)-DSF can be utilized to obtain affinity values even in the mM range, which is challenging for other biophysical methods, while having a relatively low sample consumption.[109,110,118,119] The method has previously been used to screen possible ligands of CD209.[115]

https://doi.org/10.1021/acs.biomac.5c01510
Biomacromolecules 2025, 26, 8087−8102

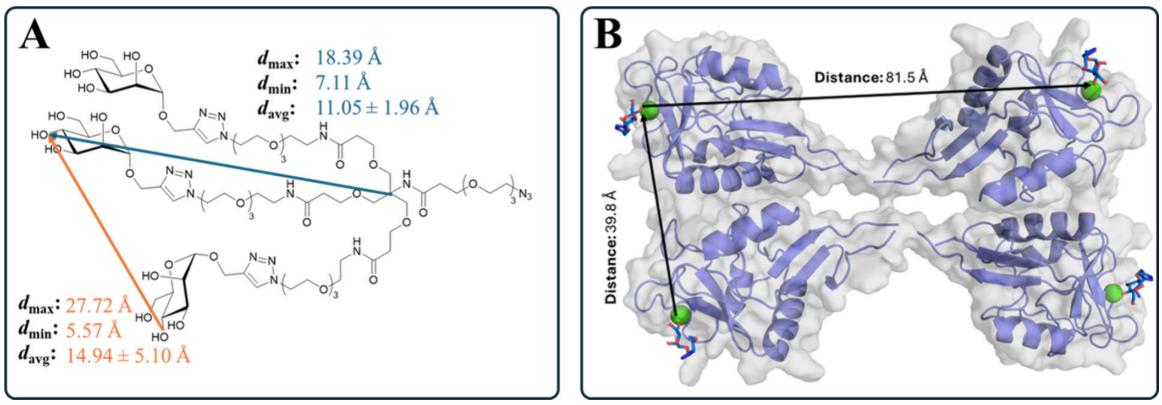


Figure 4. (A) Minimal, maximal, and average distances spanned by two Man epitopes measured between hydroxy groups at C-4 (orange line), as well as minimal, maximal, and average distances of one epitope from the focal point of the glycodendron measured between central carbon and hydroxy groups at C-4 (blue line) obtained from a set of conformers (n = 1000) of TS $(Man)_3N_3$. (B) Model of tetrameric CD209 using CD209 monomers (PDB: 1SL4)[112] aligned on tetrameric DC-SIGNR (PDB: 1XAR, C_α RMSD: 0.41 Å).[104]

In this study, NanoDSF was used to investigate the binding affinity of unconjugated monovalent TSs $ManN_3$ and Man_3N_3, as well as the trivalent TSs $(Man)_3N_3$ and $(Man_3)_3N_3$ for isolated CRDs of CD206 and CD209. Utilization of isolated CRDs instead of the complete tetrameric and octameric receptors allowed an investigation of the affinity without the potential occurrence of avidity effects taking place on the receptor side. For the interaction of $ManN_3$ and $(Man_3)_3N_3$ with the CRD of CD209, only a lower affinity estimate could be obtained, as the tested concentrations of TSs did not achieve sufficient saturation to determine a definitive EC_{50} value. The observed binding affinities to the isolated CRDs were in the low millimolar range, with all ligands showing stabilizing effects. This confirms that the presence of linkers does not prevent interactions between the mannose epitopes and the CRD. For the monovalent TSs, CD206 showed a slight preference for the Man over the Man_3 epitope (1.3 mM vs 6.9 mM; Figure 3), with the affinity of the TS $ManN_3$ being in accordance with K_i values measured via binding competition and NMR assays.[31,113] Notably, the K_D value of the TS Man_3N_3 is slightly higher than what was determined in a solid phase competition assay for a similar structure (K_i = 0.3 mM).[31,113] The difference might originate from differences in the methods. In the solid-phase assay, the biotinylated CRDs were immobilized on streptavidin-coated plates in a defined orientation, likely enhancing the effective presentation of the binding site.[113] In contrast, NanoDSF measurements were conducted with isolated, solubilized monomeric CRDs without surface- or orientation-related effects. Additionally, steric effects and interactions arising from the linker moiety may also impact binding affinity.[115]

For binding to CD209, the opposite trend compared to CD206 could be observed, favoring Man_3N_3 over $ManN_3$ (>36.3 mM vs 7.2 mM), which is consistent with previous publications.[114,117] The preference of CD209 for Man_3N_3 might result from the additional interactions formed by the α-(1→6)-connected mannose unit in Man_3 observed in the docking studies (Figure 2). The multivalent presentation of carbohydrate residues did not lead to a large increase in the affinity. For CD206, the affinities of the trivalent TSs were in the same range as for the monovalent TSs, with $(Man)_3$ having slightly lower affinity than $(Man_3)_3$ (6.8 mM vs 3.1 mM, Figure 3). For CD209, there was a slight trend indicating an increase in affinity of the trivalent $(Man)_3$-TS compared to the monovalent Man-TS (10.3 mM vs >36.3 mM, Figure 3). However, for the Man_3 epitope, the trivalent $(Man_3)_3$-TS exhibited reduced affinity compared to the monovalent Man_3-TS (>26.6 mM vs 7.2 mM, Figure 3). Li et al. reported comparable, monovalent Man and Man_3-TSs involving a triazole moiety used for an SPR assay with tetrameric extracellular domains (ECDs) of CD209 immobilized and all four CRDs oriented toward the solvent, thus mimicking the natural presentation on cell surfaces.[117] The affinities determined for the monovalent TSs were in a similar range to those measured by NanoDSF (Man too weak to detect and Man_3 with IC_{50} = 1.5 mM). However, when the TSs were presented in a trivalent manner, an increase in binding affinity was observed (e.g.: 1.5 mM monovalent vs 2.4 μM trivalent for trimannose),[117] which was not the case in the NanoDSF experiments. Overall, these results suggest that the multivalent presentation of the receptors is crucial to benefit from avidity effects that cannot result from the multivalent ligand presentation alone (Figure 1C). Additionally, in solution, steric hindrance between individual CRDs may limit their simultaneous engagement with a multivalent ligand. The binding interaction between a CRD and a carbohydrate epitope could reduce the accessibility of the remaining epitopes for binding to additional CRDs, also constricted by an increased entropy penalty in comparison to immobilized or preorganized tetrameric CRDs. Intramolecular interactions between the carbohydrate moieties could further interfere with receptor recognition or present key epitopes in suboptimal orientations. In summary, all tested TSs demonstrated measurable binding to the isolated CRDs, confirming that overall, the mannose epitopes remained accessible and functional despite linker modifications and multivalent presentation.

3.3. Prediction of Distances of Mannose Epitopes of a Trivalent TS. As initial prediction for the avidity effects expected of the trivalent TSs (Figure 1C) interacting with the tetrameric CD209 receptor, a set of conformers (n = 1000) of the TS $(Man)_3N_3$ was generated using Omega.[120,121] This set of conformers allowed measurement of the possible distances spanned by two of the involved mannose epitopes (measured

https://doi.org/10.1021/acs.biomac.5c01510
Biomacromolecules 2025, 26, 8087−8102

between hydroxy groups at C-4) as well as minimal and maximal distance of one epitope from the focal point of the glycodendron (measured between central carbon and hydroxy groups at C-4) within the set of conformers (Figure 4, overall distribution shown in Figure S8 in the Supporting Information). Calculation of average distances, for all epitopes, enabled a comparison with the average distance between two Ca^{2+}-ions within the two closest CRDs of the CD209 homotetramer. For chelation effects to originate from the trivalent TS, the distance of about 40 Å needs to be spanned by the glycodendron to enable interaction of two mannose epitopes at two CRDs at the same time, based on a model of the CD209 tetramer (Figure 4B), which is in line with SAXS and MD studies.[98] With the conformers of the TS $(Man)_3N_3$ spanning shorter distances on average (Figure 4A), the glycodendrons should not be capable of engaging in chelating effects. The occurrence of clustering effects involving multiple CD209 homotetramers originating from trivalent TS is highly unlikely. In line with this, NanoDSF, with isolated, monomeric CRDs did not reveal a pronounced affinity gain for trivalent ligands (Figure 3). While this experiment cannot provide a direct test of chelation, because only single-site binding events per CRD are monitored, the NanoDSF data do not contradict the modeling prediction. Therefore, potential increases in binding strengths in a biological setting with correctly immobilized full receptors are most likely a result of increased local concentration of mannose epitopes at one CRD via statistical rebinding (Figure 1C).[87] Avidity effects originating from NCs cannot be predicted within this simplified model and could possibly involve clustering or chelation effect (Figure 1C). Within a biological setting, cellular uptake of NCs could benefit from avidity effects originating from the TSs boosting the effects resulting from the NCs themselves.[98]

3.4. Targeting Capability of TS-Decorated NCs *In Vitro*. To investigate the influence of the designed TSs in a more application-focused setting, we proceeded with *in vitro* experiments using receptors organized in their natural form. For this purpose, we synthesized different HSA-based NCs decorated with all tested TSs (section 4.2 in the Supporting Information) either within the low-valency regime carrying one to three mono- and trivalent TSs (TS I–III), six and nine monovalent TSs (TS VI, TS IX) per NC or within the saturated valency regime saturated with the maximum possible number of TSs per NC (38–45, TS_{sat}). The resulting systems thus contain comparable amounts of Man and Man_3 epitopes per NC, either monovalent or clustered within the glycodendrons, statistically distributed on the surface. The low degrees of modification are supposed to allow a systematic study of potential contributions of avidity effects of the trivalent TSs to receptor interaction and cellular uptake, which would be otherwise superimposed by avidity effects originating from NCs with high valency. Untreated cells (UT) or cells treated with the TLR7/8 agonist R848 as well as cells treated with control conjugates, which are Cy5-labeled only (C I), DBCO-modified (13 groups, C II) or DBCO-modified and capped via SPAAC with triethylene glycol residues (C III), were used as controls for comparison. An *in vitro* study comprising overnight incubation of Granulocyte macrophage colony-stimulating factor (GM-CSF) BMDCs together with the Cy5-labeled TS-HSA conjugates and following FACS analysis was conducted (Figure 5 and Figure 6). Generally, cellular uptake of TS-HSA conjugates resulted from the attachment of TSs, with the untargeted HSA-derived NCs

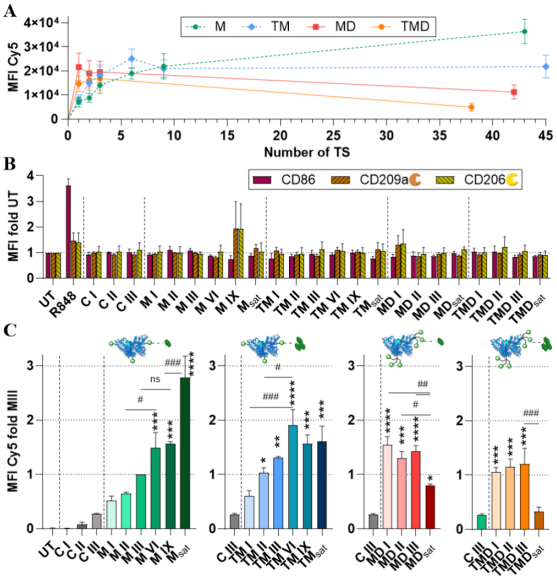


Figure 5. FACS analysis of cellular uptake in GM-CSF BMDCs after incubation overnight with different HSA conjugates (50 nM). (A) Linear plot of the cellular TS-HSA conjugate uptake versus the number of ligands attached. (B) Receptor expression of targeted CLRs (CD206, CD209) and activation marker CD86 upon treatment. (C) Normalized cellular TS-HSA conjugate uptake comparing the NC valency and surface density within each TS type. Data represented as mean ± SEM, $n = 3$; statistical differences are indicated between conjugates #, and vs control conjugate C III* (one-way ANOVA, Tukey test). *,# $p < 0.05$, **,# $p < 0.01$, ***,# $p < 0.001$, ****,# $p < 0.0001$. UT = Untreated control.

providing only limited unspecific uptake, as seen from controls C I, C II, and C III (Figure 5C). Cellular uptake of the TS-HSA conjugates does not induce changes in expression levels of the CLRs CD206 and CD209, as well as of the activation marker CD86 (Figure 5B), ensuring consistent receptor availability upon treatment and supporting NCs potential immunocompatibility. Observed effects on uptake levels thus are assumed not to be impacted by receptor availability. Also, an influence of slow receptor recycling, which affects their availability, is unlikely for CD206 and CD209 due to the reported rapid recycling kinetics and the long incubation time overnight.[122,123] Additionally, receptor depletion, which is most relevant for nano rods and large NCs (>60 nm), is supposed to be neglectable as well due to the size (~7 nm) and globular shape of the HSA-NCs.[76,124−126] In the following, the cellular uptake as a measure of targeting capability and thus indirectly also binding strength of the four groups of TS-HSA conjugates (M, TM, MD, TMD, Figure 5C) is analyzed and evaluated regarding their general uptake trend and the influence of (i) TS surface density and NC valency, (ii) the epitope type, and (iii) epitope clustering. The general uptake trends of NCs in BMDCs functionalized with increasing numbers of statistically attached TSs are visualized with a linear plot of the cellular uptake against the number of TSs per NC for all conjugates (Figure 5A) and by plots grouping respective conjugates to enable comparison of NC valency and surface density within each TS type (Figure 5C). For Man-decorated NCs, the addition of statistically distributed TS

https://doi.org/10.1021/acs.biomac.5c01510
Biomacromolecules 2025, 26, 8087−8102

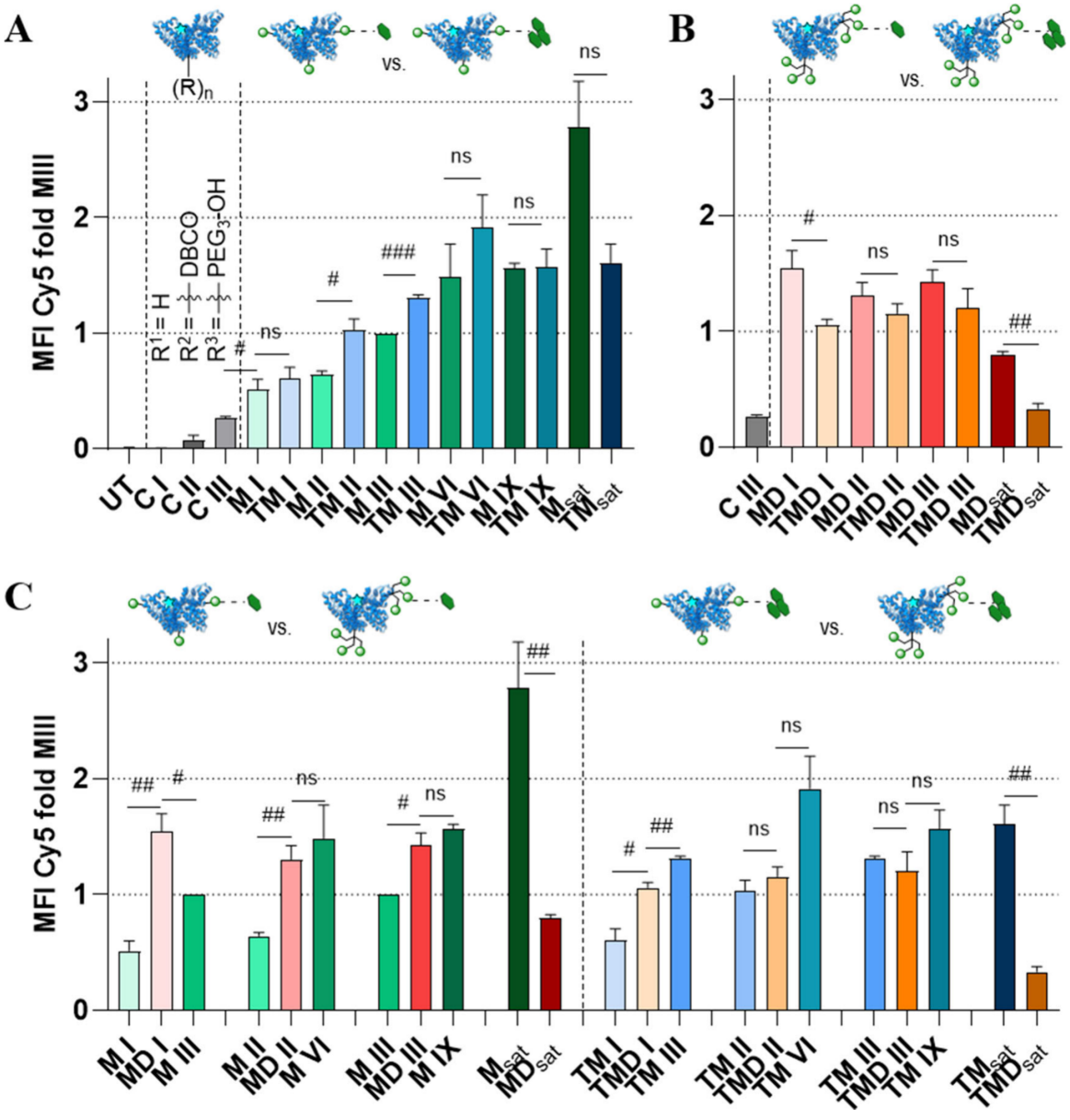


Figure 6. FACS analysis of cellular uptake in GM-CSF BMDCs after incubation overnight with different HSA conjugates (50 nM). Normalized cellular TS-HSA conjugate uptake was calculated by comparing epitope type in (A) M/TM conjugates and (B MD/TMD conjugates and (C) epitope clustering. Data are presented as mean ± SEM, $n = 3$; statistical differences are indicated between conjugates # (*t* test). # $p < 0.05$, # $p < 0.01$, # $p < 0.001$, # $p < 0.0001$. UT = Untreated control.

increases the surface density and leads to an approximately logarithmic increase in cellular uptake at the beginning of the low-valency regime with a significant benefit from M VI onward compared to control conjugate C III. However, the benefit of each additional Man decreases as the total number increases, and the uptake rate slows down. Although a significant increase continues into the saturated valency regime, it becomes less pronounced relative to the TS number and eventually approaches a plateau. For the herein tested Man-decorated NCs, M_{sat} showed the highest cellular uptake. For Man_3-decorated NCs, increasing surface density is also accompanied by an increase in cellular uptake with a significant benefit for TM II. However, a plateau in cell uptake is already reached at a lower TS number from conjugate TM VI onward with no additional significant increase afterward. The onset of this plateau was suggested to occur around a modification rate of 9 TM groups in similar conjugates in GM-CSF BMDC at the same applied concentration prior to this study.[102] In summary, increased surface density of our monovalent TSs results in increased cellular uptake, with the greatest gain in the

https://doi.org/10.1021/acs.biomac.5c01510
Biomacromolecules 2025, 26, 8087−8102

low valency regime and maximum cellular uptake being achieved from conjugate TM VI onward. The observed situation resembles the trend of "optimum density with plateau" (Figure 1D). For NCs decorated with our trivalent TS $(Man)_3$ and $(Man_3)_3$, there is a significantly enhanced cell uptake compared with unmodified NCs for the conjugates MD I and TMD I, respectively. The further increase in the number of TS in the low-valency regime is not accompanied by any significant changes in cellular uptake. At the transition into the saturated valency regime, both conjugate MD_{sat} and conjugate TMD_{sat} show a significant decrease in cellular uptake; in the case of TMD even to the same level as control conjugate C III. Since no visual precipitation or signs of increased aggregation via DLS (Table S2 and Table S4 in the Supporting Information) could be detected, this strong decrease in cellular uptake could reflect the decline in the trend "optimum density with maximum" (Figure 1D) triggered by effects discussed above, like steric overcrowding or negative cooperativity of TSs, superimposing potential avidity effects by clustering or by the NC itself. However, the precise occurrence of the optimum surface density cannot be determined due to the minimal variation in uptake within the low-valency regime and the possibility that the optimum is already reached with the attachment of a single trivalent TS in the form of the conjugates MD I and TMD I.

The difference in cellular uptake mediated by epitope type (Man vs Man_3) is evident from the direct comparison of the respective conjugates decorated with these NCs, as plotted in Figure 6A. Within the low-valency regime, there is a consistent trend that the structurally more complex Man_3 epitope induces a slightly higher cellular uptake, which is statistically significant in a direct comparison of conjugates M II/TM II and M III/TM III, respectively. This is in accordance with literature reports attributing higher affinity to Man_3[31,S1] and with our docking studies (Figure 2). These differences in cellular uptake are attenuated for conjugates M IX/TM IX and the ones with a higher degree of functionalization, with TM conjugates reaching the onset of the observed plateau already within the low-valency regime and at lower MFI levels (Figure 5A and C). This earlier onset of negative effects, like overcrowding, for the TM conjugates could be due to the higher steric demands of the larger epitope. This is also supported by a comparison of the conjugates carrying the different epitope types in their trivalent form (Figure 6B). Conjugates from the TMD group tend to have lower cellular uptake compared with the MD group throughout both regimes of valency, with statistically significant differences between MD I/TMD I and MD_{sat}/TMD_{sat}, respectively. This is presumably due to the higher steric hindrance for the larger Man_3-epitopes when clustered within the glycodendrons, thereby superimposing the inherently higher binding affinity of the Man_3 epitope. The effects of epitope clustering become apparent when conjugates carrying the glycodendron are compared with conjugates carrying the same number of monovalent TS or the same overall number of epitopes presented (Figure 6C). With increasing TS surface density, the ratio of presented epitopes per NC between the groups M vs MD and TM vs TMD remains the same (1:3), but the absolute difference in epitope number increases from 2 to 4 to 6. The conjugate MD I, with one trivalent TS, thus presenting three clustered Man epitopes, shows significantly higher cellular uptake than M I, which has one monovalent TS and thus a single Man epitope. Compared to conjugate M III, which carries three randomly distributed monovalent TSs and thus the same number of epitopes, MD I still achieves higher uptake. This suggests that clustering of epitopes enhances uptake through avidity effects here.

However, while the trivalent Man is superior to the monovalent Man in the subsequent low-valency regime with equivalent TS modification rate (e.g., MD II > M II), this does not apply to conjugates with equivalent epitope count (e.g., MD II vs M VI). And since the conjugates with clustered Man (MD) do not show a significant increase in the cell uptake trend with increasing TS density (Figure 5A), the conjugates with monovalent Man prove to be more effective from a modification rate of two to three onward and especially in the saturated valency regime. For the Man_3 epitope, e.g., when comparing conjugates TM I vs TMD I vs TM III, enhancing cellular uptake comes with epitope count (e.g., TM I vs TMD I), but not with clustering of the epitopes (e.g., TMD I vs TM III) until TM conjugates enter the region of saturated cellular uptake from TM VI onward. In the saturated valency regime, TM_{sat} outperforms TMD_{sat} because of the above-mentioned negative effects, hampering cellular uptake. In summary, when evaluating the targeting capability of the four investigated TSs on our HSA-based NCs in BMDCs, monovalent TSs lead to a general cellular uptake trend "optimum density with plateau", with TM conjugates reaching cellular uptake saturation within the low-valency regime and M conjugates demonstrating the overall highest absolute cellular uptake within the saturated regime. Trivalent TSs on our NCs appear to induce negative effects, which increasingly outweigh the intended avidity benefits of epitope clustering early on and with increasing modification rate. Since this trend appears for both trivalent TSs independent of the type of epitope attached, the design of the dendron backbone may be the cause, potentially a result of excessive flexibility, spatially unfavorable arrangement of epitopes, or a too limited span of dendron arms to enable avidity effects. This results in a general trend of "optimum density with a maximum". Regarding the epitope type, TM conjugates show a higher uptake at the beginning of the low valency regime, but this advantage diminishes with increasing TS count and reverses in the saturated regime.

To test the robustness of the general uptake trends derived for the tested TS-decorated NCs as well as the cell-type selectivity, we performed an additional *in vitro* experiment using a more heterogeneous cell population. We incubated spleen cells derived from murine spleens with TS-conjugates (50 nM) overnight, followed by FACS analysis (Figure 7). In general, the data reveals a higher variability, as expected, and a higher cellular uptake of the control conjugate C III. Among nontargeted splenic immune cells, comprising PMN-, NK-, B-, and T-cells, PMNs exhibit some uptake of TS-conjugates, presumably due to their role as rapid-acting phagocytes in innate immunity. This tendency is slightly more pronounced in M conjugates than in TM/MD/TMD conjugates. However, the absolute cellular uptake among nontargeted splenic immune cells remains low compared to targeted cells. For targeted APCs (DCs and MΦ), the mono- and trivalent TS-conjugates show uptake trends similar to those of BMDCs. It is noteworthy that slight variations occur during the onset of the saturated regime. MD conjugates show a decreased uptake into target cells, whereas M, TM, and TMD conjugates show a similar relative efficiency as in BMDCs.

https://doi.org/10.1021/acs.biomac.5c01510
Biomacromolecules 2025, 26, 8087−8102

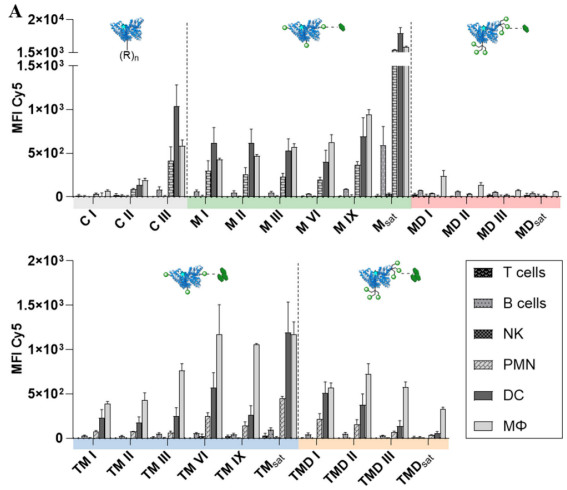


Figure 7. FACS analysis of cellular uptake in spleen cells after overnight incubation with different HSA conjugates (50 nM, (top) M/MD- and (bottom(TM/TMD-HSA conjugates) differentiated into cell types (target cells: macrophages MΦ, DCs; nontarget immune cells: T cells, B cells, NK, and PMN). Data are presented as mean ± SEM, n = 3.

4. CONCLUSION

Within the present study, mono- and trivalent TSs, presenting the Man- and Man_3-epitopes, were synthesized using robust and high yielding procedures. Successful conjugation using SPAAC reactions allowed the preparation of HSA-derived NCs presenting a defined number of randomly dispersed TSs. A NanoDSF investigation provided an approach to measure carbohydrate−lectin interactions in homogeneous solution, revealing binding interactions of unconjugated TSs and isolated CRDs of CD206 and CD209, with affinities in the millimolar range, consistent with earlier reports.[17,55,56] Due to the absence of multivalent CRD presentation, no increase in avidity was observed for the trivalent TSs, stressing the requirement of membrane-like CRD presentation for the investigation of avidity effects.[127] Thus, investigating cellular uptake of HSA conjugates using *in vitro* studies provided a realistic, biological environment to test immunocompatibility and to measure cellular uptake efficiency of the NCs under the influences of epitope type, TS surface density, clustering of epitopes, and overall valency. TS-mediated cellular uptake revealed a strong dependency from respective surface density following two trends as a result of the interplay between additional epitopes favorably contributing to and negative steric or cooperativity effects hindering binding interactions. Growing numbers of monovalent TSs lead to an increase in cellular uptake leveling out into a plateau. Growing numbers of trivalent TSs lead ultimately to a decrease in cellular uptake. Within the design of the studied conjugates, exploitation of the higher intrinsic affinity of the Man_3- over the simpler Man-epitope is beneficial only at low surface densities, providing slight improvements in cellular uptake, with the situation reversed at saturated surface densities, due to mitigation by negative effects, potentially steric overcrowding. Furthermore, trivalent TSs cannot improve cellular uptake of the employed HSA-based NCs by induction of avidity effects due to being hampered by negative effects, especially in the saturated valency regime. To dissect the contributions of either steric overcrowding, negative cooperativity, or other unfavorable effects, which may be the cause of hampered cellular uptake upon using trivalent targeting structures, will require further investigation. Avidity effects originating from a trivalent TS carrying the Man-epitope can only be observed in the low-valency regime. Thus, utilization of these trivalent TSs seems to be beneficial in combination with low valency NCs, which offer only a few connection sites for chemical surface functionalization. In spleen cell populations, all tested TS-HSA conjugates show selectivity for CD206 and CD209 expressing target cells, namely, DCs and macrophages,[19−29] over nontargeted splenic immune cells, with the monovalent Man showing a slightly higher off-target uptake. On a general note, for the design of targeted NCs, the optimization of TSs and surface density always needs to account for the specificities, such as size and flexibility of the NC, impacting steric hindrance and cooperativity effects. Thus, spatially demanding, multivalent TSs seem to be better adapted for use on surfaces of larger NCs, and less demanding, monovalent TSs on the surfaces of smaller NCs.[75] A better understanding of the complex interplay between NC valency and TS surface density *in vitro* may improve the efficacy of targeted delivery approaches by providing means to influence biodistribution and cellular uptake. Thus, this investigation sheds some light on the impact of incremental changes in NC surface modification on cellular uptake and cell selectivity, allowing insights into the design of TSs and NCs.

■ ASSOCIATED CONTENT

Data Availability Statement

Additional information is available from the corresponding authors on request.

Supporting Information

The Supporting Information is available free of charge at https://pubs.acs.org/doi/10.1021/acs.biomac.5c01510.

General conditions and purification methods, analytical methods, synthesis procedures, and analytical data for all steps of saccharide TS preparation and HSA conjugate preparation; Binding modes for monovalent TSs; Recombinant protein expression and purification; NanoDSF melting curves; Histograms for distance distribution of mannose epitopes in a trivalent TS; ^{1}H and ^{13}C NMR spectra of carbohydrate compounds; MALDI spectra of HSA conjugates (PDF)

■ AUTHOR INFORMATION

Corresponding Authors

Till Opatz − *Department of Chemistry, Johannes Gutenberg-University Mainz, 55128 Mainz, Germany*; orcid.org/0000-0002-3266-4050; Email: opatz@uni-mainz.de

Tanja Schirmeister − *Department for Pharmaceutical and Biomedical Sciences, Johannes Gutenberg-University Mainz, 55128 Mainz, Germany*; Email: schirmei@uni-mainz.de

Tanja Weil − *Max Planck Institute for Polymer Research, 55128 Mainz, Germany*; Email: weil@mpip-mainz.mpg.de

Matthias Bros − *Department of Dermatology, University Medical Center of the Johannes Gutenberg-University Mainz, 55131 Mainz, Germany*; Email: mbros@uni-mainz.de

Christian Kersten − *Department for Pharmaceutical and Biomedical Sciences, Johannes Gutenberg-University Mainz,*

https://doi.org/10.1021/acs.biomac.5c01510
Biomacromolecules 2025, 26, 8087−8102

55128 Mainz, Germany; orcid.org/0000-0001-9976-7639; Email: kerstec@uni-mainz.de

Authors

Robert Forster − *Department of Chemistry, Johannes Gutenberg-University Mainz, 55128 Mainz, Germany;* orcid.org/0009-0008-7954-5711

Bellinda Lantzberg − *Max Planck Institute for Polymer Research, 55128 Mainz, Germany;* orcid.org/0009-0006-9323-5897

Annabelle Weldert − *Department for Pharmaceutical and Biomedical Sciences, Johannes Gutenberg-University Mainz, 55128 Mainz, Germany;* orcid.org/0009-0001-5016-0286

Laura Rosenberger − *Department of Dermatology, University Medical Center of the Johannes Gutenberg-University Mainz, 55131 Mainz, Germany*

Yanira Zeyn − *Department of Dermatology, University Medical Center of the Johannes Gutenberg-University Mainz, 55131 Mainz, Germany*

Danuta Kowalczyk − *Department of Chemistry, Johannes Gutenberg-University Mainz, 55128 Mainz, Germany*

Seah Ling Kuan − *Max Planck Institute for Polymer Research, 55128 Mainz, Germany;* orcid.org/0000-0003-3945-4491

Complete contact information is available at: https://pubs.acs.org/10.1021/acs.biomac.5c01510

Author Contributions

[#]These authors contributed equally to this work (R.F., B.L., and A.W.). R.F.: Investigation, Formal analysis, Methodology, Data Curation, Writing - Original Draft, Visualization; B.L.: Investigation, Formal analysis, Methodology, Data Curation, Writing - Original Draft, Visualization; A.W.: Investigation, Formal analysis, Methodology, Data Curation, Writing - Original Draft, Visualization; L.R.: Investigation, Formal analysis; Y.Z.: Investigation, Formal analysis; D.K.: Investigation, Formal analysis; S.L.K.: Supervision, Writing - Review and Editing; C.K.: Supervision, Writing - Review and Editing; M.B.: Resources, Supervision, Funding acquisition; T.W.: Resources, Supervision, Funding acquisition, Writing - Review and Editing; T.S.: Resources, Supervision, Funding acquisition, Writing - Review and Editing; T.O.: Resources, Conceptualization, Project administration, Supervision, Funding acquisition, Writing - Review and Editing. The manuscript was written through contributions of all authors. All authors have given approval to the final version of the manuscript.

Funding

The authors would like to thank the Max Planck Society and the Deutsche Forschungsgemeinschaft (DFG, German Research Foundation) project number 213555243 − SFB 1066 (Q05, B16, B05) for financial support.

Notes

The authors declare the following competing financial interest(s): B.L., Y.Z., R.F., S.L.K., M.B., T.O., and T.W. are coinventors of a pending patent that claims to use mannosylated human serum albumin-based NCs for targeted immunotherapy.

■ ACKNOWLEDGMENTS

The authors would like to thank Dr. Maureen Taylor for providing the plasmid for the CRD4 of CD206, Professor Franck Fieschi for providing the plasmid for the CRD of CD209 and the Group of Professor Heermann for access to the NanoDSF instrument. The authors are grateful to Dr. David Y. W. Ng for valuable discussions regarding analysis of the *in vitro* experiments. We thank the JGU NMR spectroscopy and mass spectrometry department as well as the MPI-P mass spectrometry department for the conducted measurements. OpenAI ChatGPT (GPT-4o) and Grammarly were used for text editing and proofreading purposes. Responsibility for the content rests solely with the authors.

■ ABBREVIATIONS

NC, nanocarrier; TS, targeting structure; CLR, C-type lectin receptor; HSA, human serum albumin; CRD, carbohydrate recognition domain; CD206, cluster of differentiation 206; CD209, cluster of differentiation 209; NanoDSF, Nano differential scanning fluorimetry; APC, antigen-presenting cell; DC, dendritic cell; MΦ, macrophage; MMR-1, macrophage mannose receptor; DC-SIGN, dendritic cell specific ICAM-3 grabbing nonintegrin; MHC, major histocompatibility complex; Man, terminal mannose-monosaccharide; Man_3, α-(1→3)- and α-(1→6)-branched trimannose; SPR, surface plasmon resonance; UT, untreated cells; TLR, toll-like receptor; BMDC, bone marrow-derived dendritic cell; CR, cysteine-rich domain; FNII, fibronectin type II domain; CTLD, C-type lectin domain; ND, neck domain; TM, transmembrane domain; CD, cytoplasmic domain; HPLC, high performance liquid chromatography; SPAAC, strain-promoted azide alkyne cycloaddition; DBCO, dibenzocyclooctyne; CuAAC, copper-catalyzed azide alkyne cycloaddition; TRIS, tris(hydroxymethyl)aminomethane; HRMS, high-resolution mass spectrometry; MALDI-ToF, matrix assisted laser desorption ionization − time of flight mass spectrometry; DLS, dynamic light scattering; C, control conjugate; M, mannose conjugate; TM, trimannose conjugate; MD, mannose glycodendron conjugate; TMD, trimannose glycodendron conjugate; FACS, fluorescence-activated cell sorting; ITC, isothermal titration calorimetry; ECD, tetrameric extracellular domain; NMR, nuclear magnetic resonance; EC_{50}, half maximal effective concentration; Cy5, cyanine 5 dye; GM-CSF, Granulocyte macrophage colony-stimulating factor; MFI, mean fluorescence intensity; PMN-cell, polymorphonuclear neutrophil; NK-cell, natural killer cell

■ REFERENCES

(1) Wang, F.; Ullah, A.; Fan, X.; Xu, Z.; Zong, R.; Wang, X.; Chen, G. Delivery of nanoparticle antigens to antigen-presenting cells: from extracellular specific targeting to intracellular responsive presentation. *J. Controlled Release* **2021**, *333*, 107−128.

(2) Nahar, U. J.; Toth, I.; Skwarczynski, M. Mannose in vaccine delivery. *J. Controlled Release* **2022**, *351*, 284−300.

(3) Suvarna, V.; Sawant, N.; Desai, N. A Review on Recent Advances in Mannose-Functionalized Targeted Nanocarrier Delivery Systems in Cancer and Infective Therapeutics. *Crit. Rev. Ther. Drug Carrier Syst.* **2023**, *40* (2), 43−82.

(4) Zhao, Y.; Guo, Y.; Tang, L. Engineering cancer vaccines using stimuli-responsive biomaterials. *Nano Research* **2018**, *11* (10), 5355−5371.

(5) Feng, X.; Xu, W.; Li, Z.; Song, W.; Ding, J.; Chen, X. Immunomodulatory Nanosystems. *Adv. Sci.* **2019**, *6* (17), No. 1900101.

(6) Kim, C. G.; Kye, Y.-C.; Yun, C.-H. The Role of Nanovaccine in Cross-Presentation of Antigen-Presenting Cells for the Activation of CD8+ T Cell Responses. *Pharmaceutics* **2019**, *11* (11), 612.

(7) Li, S.; Feng, X.; Wang, J.; He, L.; Wang, C.; Ding, J.; Chen, X. Polymer nanoparticles as adjuvants in cancer immunotherapy. *Nano Research* **2018**, *11* (11), 5769−5786.
(8) Wang, J.; Li, Z.; Wang, Z.; Yu, Y.; Li, D.; Li, B.; Ding, J. Nanomaterials for Combinational Radio−Immuno Oncotherapy. *Adv. Funct. Mater.* **2020**, *30* (30), No. 1910676.
(9) Prabahar, K.; Alanazi, Z.; Qushawy, M. Targeted drug delivery system: Advantages, carriers and strategies. *Indian J. Pharm. Educ. Res.* **2021**, *55*, 346−353.
(10) Patil, T. S.; Deshpande, A. S. Mannosylated nanocarriers mediated site-specific drug delivery for the treatment of cancer and other infectious diseases: A state of the art review. *J. Controlled Release* **2020**, *320*, 239−252.
(11) Paurević, M.; Šrajer Gajdošik, M.; Ribić, R. Mannose Ligands for Mannose Receptor Targeting. *Int. J. Mol. Sci.* **2024**, *25* (3), 1370.
(12) Banchereau, J.; Steinman, R. M. Dendritic cells and the control of immunity. *Nature* **1998**, *392*, 245.
(13) Sancho, D.; Reis e Sousa, C. Signaling by Myeloid C-Type Lectin Receptors in Immunity and Homeostasis. *Annu. Rev. Immunol.* **2012**, *30* (1), 491−529.
(14) Tacken, P. J.; de Vries, I. J. M.; Torensma, R.; Figdor, C. G. Dendritic-cell immunotherapy: from ex vivo loading to in vivo targeting. *Nat. Rev. Immunol.* **2007**, *7* (10), 790−802.
(15) Lang, R.; Schoenen, H.; Desel, C. Targeting Syk-Card9-activating C-type lectin receptors by vaccine adjuvants: Findings, implications and open questions. *Immunobiology* **2011**, *216* (11), 1184−1191.
(16) Tang, C.-K.; Sheng, K.-C.; Apostolopoulos, V.; Pietersz, G. A Protein/peptide and DNA vaccine delivery by targeting C-type lectin receptors. *Expert Rev. Vaccines* **2008**, *7* (7), 1005−1018.
(17) Lepenies, B.; Lee, J.; Sonkaria, S. Targeting C-type lectin receptors with multivalent carbohydrate ligands. *Adv. Drug Delivery Rev.* **2013**, *65* (9), 1271−1281.
(18) Rosenblum, D.; Joshi, N.; Tao, W.; Karp, J. M.; Peer, D. Progress and challenges towards targeted delivery of cancer therapeutics. *Nat. Commun.* **2018**, *9* (1), 1410.
(19) Apostolopoulos, V.; Thalhammer, T.; Tzakos, A. G.; Stojanovska, L. Targeting Antigens to Dendritic Cell Receptors for Vaccine Development. *J. Drug Delivery* **2013**, *2013*, No. 1.
(20) Apostolopoulos, V.; Mckenzie, I. f. c. Role of the Mannose Receptor in the Immune Response. *Curr. Mol. Med.* **2001**, *1* (4), 469−474.
(21) East, L.; Isacke, C. M. The mannose receptor family. *Biochim. Biophys. Acta - Gen. Subj.* **2002**, *1572* (2), 364−386.
(22) Reddy, S. T.; Swartz, M. A.; Hubbell, J. A. Targeting dendritic cells with biomaterials: developing the next generation of vaccines. *Trends Immunol.* **2006**, *27* (12), 573−579.
(23) Wilson, D. S.; Hirosue, S.; Raczy, M. M.; Bonilla-Ramirez, L.; Jeanbart, L.; Wang, R.; Kwissa, M.; Franetich, J.-F.; Broggi, M. A. S.; Diaceri, G.; Quaglia-Thermes, X.; Mazier, D.; Swartz, M. A.; Hubbell, J. A. Antigens reversibly conjugated to a polymeric glyco-adjuvant induce protective humoral and cellular immunity. *Nat. Mater.* **2019**, *18* (2), 175−185.
(24) Wang, F.; Xiao, W.; Elbahnasawy, M. A.; Bao, X.; Zheng, Q.; Gong, L.; Zhou, Y.; Yang, S.; Fang, A.; Farag, M. M. S.; Wu, J.; Song, X. Optimization of the Linker Length of Mannose-Cholesterol Conjugates for Enhanced mRNA Delivery to Dendritic Cells by Liposomes. *Front. Pharmacol.* **2018**, *9*, na.
(25) van Kooyk, Y. C-type lectins on dendritic cells: key modulators for the induction of immune responses. *Biochem. Soc. Trans.* **2008**, *36* (6), 1478−1481.
(26) McKenzie, E. J.; Taylor, P. R.; Stillion, R. J.; Lucas, A. D.; Harris, J.; Gordon, S.; Martinez-Pomares, L. Mannose Receptor Expression and Function Define a New Population of Murine Dendritic Cells1. *J. Immunol.* **2007**, *178* (8), 4975−4983.
(27) Engering, A.; Geijtenbeek, T. B. H.; van Vliet, S. J.; Wijers, M.; van Liempt, E.; Demaurex, N.; Lanzavecchia, A.; Fransen, J.; Figdor, C. G.; Piguet, V.; van Kooyk, Y. The Dendritic Cell-Specific Adhesion Receptor DC-SIGN Internalizes Antigen for Presentation to T Cells1. *J. Immunol.* **2002**, *168* (5), 2118−2126.
(28) Tacken, P. J.; de Vries, I. J. M.; Gijzen, K.; Joosten, B.; Wu, D.; Rother, R. P.; Faas, S. J.; Punt, C. J. A.; Torensma, R.; Adema, G. J.; Figdor, C. G. Effective induction of naive and recall T-cell responses by targeting antigen to human dendritic cells via a humanized anti−DC-SIGN antibody. *Blood* **2005**, *106* (4), 1278−1285.
(29) Geijtenbeek, T. B. H.; Torensma, R.; van Vliet, S. J.; van Duijnhoven, G. C. F.; Adema, G. J.; van Kooyk, Y.; Figdor, C. G. Identification of DC-SIGN, a Novel Dendritic Cell−Specific ICAM-3 Receptor that Supports Primary Immune Responses. *Cell* **2000**, *100* (5), 575−585.
(30) Stahl, P. D.; Ezekowitz, R. A. B. The mannose receptor is a pattern recognition receptor involved in host defense. *Curr. Opin. Immunol.* **1998**, *10* (1), 50−55.
(31) Feinberg, H.; Jégouzo, S. A. F.; Lasanajak, Y.; Smith, D. F.; Drickamer, K.; Weis, W. I.; Taylor, M. E. Structural analysis of carbohydrate binding by the macrophage mannose receptor CD206. *J. Biol. Chem.* **2021**, *296*, No. 100368.
(32) Taylor, M. E.; Bezouska, K.; Drickamer, K. Contribution to ligand binding by multiple carbohydrate-recognition domains in the macrophage mannose receptor. *J. Biol. Chem.* **1992**, *267* (3), 1719−1726.
(33) Taylor, M. E.; Drickamer, K. Structural requirements for high affinity binding of complex ligands by the macrophage mannose receptor. *J. Biol. Chem.* **1993**, *268* (1), 399−404.
(34) Švajger, U.; Anderluh, M.; Jeras, M.; Obermajer, N. C-type lectin DC-SIGN: An adhesion, signalling and antigen-uptake molecule that guides dendritic cells in immunity. *Cell. Signal.* **2010**, *22* (10), 1397−1405.
(35) Mitchell, D. A.; Fadden, A. J.; Drickamer, K. A novel mechanism of carbohydrate recognition by the C-type lectins DC-SIGN and DC-SIGNR: subunit organization and binding to multivalent ligands. *J. Biol. Chem.* **2001**, *276* (31), 28939−28945.
(36) Tabarani, G.; Thépaut, M.; Stroebel, D.; Ebel, C.; Vivès, C.; Vachette, P.; Durand, D.; Fieschi, F. DC-SIGN Neck Domain Is a pH-sensor Controlling Oligomerization: SAXS and Hydrodynamic studies of extracellular domain. *J. Biol. Chem.* **2009**, *284* (32), 21229−21240.
(37) Azad, A. K.; Rajaram, M. V.; Schlesinger, L. S. Exploitation of the macrophage mannose receptor (CD206) in infectious disease diagnostics and therapeutics. *JCMB* **2014**, *1* (1), No. 1000003.
(38) Nguyen, D. G.; Hildreth, J. E. K. Involvement of macrophage mannose receptor in the binding and transmission of HIV by macrophages. *Eur. J. Immunol.* **2003**, *33* (2), 483−493.
(39) Monteiro, J. T.; Lepenies, B. Myeloid C-Type Lectin Receptors in Viral Recognition and Antiviral Immunity. *Viruses* **2017**, *9* (3), 59.
(40) Martinez-Pomares, L.; Linehan, S. A.; Taylor, P. R.; Gordon, S. Binding Properties of the Mannose Receptor. *Immunobiology* **2001**, *204* (5), 527−535.
(41) Martinez-Pomares, L. The mannose receptor. *J. Leukocyte Biol.* **2012**, *92* (6), 1177−1186.
(42) Osorio, F.; Reis e Sousa, C. Myeloid C-type Lectin Receptors in Pathogen Recognition and Host Defense. *Immunity* **2011**, *34* (5), 651−664.
(43) van Kooyk, Y.; Unger, W. W. J.; Fehres, C. M.; Kalay, H.; García-Vallejo, J. J. Glycan-based DC-SIGN targeting vaccines to enhance antigen cross-presentation. *Mol. Immunol.* **2013**, *55* (2), 143−145.
(44) Valverde, P.; Martínez, J. D.; Cañada, F. J.; Arda, A.; Jiménez-Barbero, J. Molecular recognition in C-type lectins: the cases of DC-SIGN, Langerin, MGL, and L-sectin. *ChemBioChem.* **2020**, *21* (21), 2999−3025.
(45) Chatterjee, D.; Khoo, K. H. The surface glycopeptidolipids of mycobacteria: structures and biological properties. *Cell. Mol. Life Sci.* **2001**, *58* (14), 2018−2042.
(46) Shibata, N.; Ikuta, K.; Imai, T.; Satoh, Y.; Satoh, R.; Suzuki, A.; Kojima, C.; Kobayashi, H.; Hisamichi, K.; Suzuki, S. Existence of Branched Side Chains in the Cell Wall Mannan of Pathogenic Yeast,

https://doi.org/10.1021/acs.biomac.5c01510
Biomacromolecules 2025, 26, 8087−8102

Candida albicans: Structure-antigenicity relationship between the cell wall mannans of candida albicans and candida parapsilosis. *J. Biol. Chem.* **1995**, *270* (3), 1113−1122.
(47) Feinberg, H.; Mitchell, D. A.; Drickamer, K.; Weis, W. I. Structural Basis for Selective Recognition of Oligosaccharides by DC-SIGN and DC-SIGNR. *Science* **2001**, *294* (5549), 2163−2166.
(48) Adams, E. W.; Ratner, D. M.; Bokesch, H. R.; McMahon, J. B.; O'Keefe, B. R.; Seeberger, P. H. Oligosaccharide and Glycoprotein Microarrays as Tools in HIV Glycobiology: Glycan-Dependent gp120/Protein Interactions. *Chem. Biol.* **2004**, *11* (6), 875−881.
(49) Reina, J. J.; Díaz, I.; Nieto, P. M.; Campillo, N. E.; Páez, J. A.; Tabarani, G.; Fieschi, F.; Rojo, J. Docking, synthesis, and NMR studies of mannosyl trisaccharide ligands for DC-SIGN lectin. *Org. Biomol. Chem.* **2008**, *6* (15), 2743−2754.
(50) van Liempt, E.; Bank, C. M. C.; Mehta, P.; Garcí'a-Vallejo, J. J.; Kawar, Z. S.; Geyer, R.; Alvarez, R. A.; Cummings, R. D.; Kooyk, Y. v.; van Die, I. Specificity of DC-SIGN for mannose- and fucose-containing glycans. *FEBS Lett.* **2006**, *580* (26), 6123−6131.
(51) Holla, A.; Skerra, A. Comparative analysis reveals selective recognition of glycans by the dendritic cell receptors DC-SIGN and Langerin. *Protein Eng., Des. Sel.* **2011**, *24* (9), 659−669.
(52) van Montfort, T.; Eggink, D.; Boot, M.; Tuen, M.; Hioe, C. E.; Berkhout, B.; Sanders, R. W. HIV-1 N-glycan composition governs a balance between dendritic cell-mediated viral transmission and antigen presentation. *J. Immunol.* **2011**, *187* (9), 4676−4685.
(53) Lee, R. T.; Lee, Y. C. Affinity enhancement by multivalent lectin−carbohydrate interaction. *Glycoconjugate J.* **2000**, *17* (7), 543−551.
(54) Monsigny, M.; Mayer, R.; Roche, A.-C. Sugar-lectin interactions: sugar clusters, lectin multivalency and avidity. *Carbohydr. Lett.* **2000**, *4*, 35−52.
(55) Lepenies, B.; Seeberger, P. H. The promise of glycomics, glycan arrays and carbohydrate-based vaccines. *Immunopharmacol. Immunotoxicol.* **2010**, *32* (2), 196−207.
(56) Lepenies, B.; Yin, J.; Seeberger, P. H. Applications of synthetic carbohydrates to chemical biology. *Curr. Opin. Chem. Biol.* **2010**, *14* (3), 404−411.
(57) Drickamer, K. Multiplicity of lectin-carbohydrate interactions. *Nat. Struct. Mol. Biol.* **1995**, *2* (6), 437−439.
(58) Brewer, C. F. Multivalent lectin-carbohydrate cross-linking interactions. *Chemtracts-Biochem. Mol. Biol.* **1996**, *6*, 165−179.
(59) Lundquist, J. J.; Toone, E. J. The Cluster Glycoside Effect. *Chem. Rev.* **2002**, *102* (2), 555−578.
(60) Sharon, N. Lectins: past, present and future. *Biochem. Soc. Trans.* **2008**, *36* (6), 1457−1460.
(61) Sharon, N.; Lis, H. *Lectins*; Springer: Dordrecht, 2003. DOI: 10.1007/978-1-4020-6953-6.
(62) Sharon, N.; Lis, H. History of lectins: from hemagglutinins to biological recognition molecules. *Glycobiol.* **2004**, *14* (11), 53R−62R.
(63) Porkolab, V.; Pifferi, C.; Sutkeviciute, I.; Ordanini, S.; Taouai, M.; Thépaut, M.; Vivès, C.; Benazza, M.; Bernardi, A.; Renaudet, O.; Fieschi, F. Development of C-type lectin-oriented surfaces for high avidity glycoconjugates: towards mimicking multivalent interactions on the cell surface. *Org. Biomol. Chem.* **2020**, *18* (25), 4763−4772.
(64) Kitov, P. I.; Bundle, D. R. On the Nature of the Multivalency Effect: A Thermodynamic Model. *J. Am. Chem. Soc.* **2003**, *125* (52), 16271−16284.
(65) Müller, C.; Despras, G.; Lindhorst, T. K. Organizing multivalency in carbohydrate recognition. *Chem. Soc. Rev.* **2016**, *45* (11), 3275−3302.
(66) Fasting, C.; Schalley, C. A.; Weber, M.; Seitz, O.; Hecht, S.; Koksch, B.; Dernedde, J.; Graf, C.; Knapp, E.-W.; Haag, R. Multivalency as a Chemical Organization and Action Principle. *Angew. Chem., Int. Ed.* **2012**, *51* (42), 10472−10498.
(67) Jayaraman, N. Multivalent ligand presentation as a central concept to study intricate carbohydrate−protein interactions. *Chem. Soc. Rev.* **2009**, *38* (12), 3463−3483.
(68) Kiessling, L. L.; Gestwicki, J. E.; Strong, L. E. Synthetic multivalent ligands in the exploration of cell-surface interactions. *Curr. Opin. Chem. Biol.* **2000**, *4* (6), 696−703.
(69) Kiessling, L. L.; Gestwicki, J. E.; Strong, L. E. Synthetic Multivalent Ligands as Probes of Signal Transduction. *Angew. Chem., Int. Ed.* **2006**, *45* (15), 2348−2368.
(70) Vorup-Jensen, T. On the roles of polyvalent binding in immune recognition: Perspectives in the nanoscience of immunology and the immune response to nanomedicines. *Adv. Drug Delivery Rev.* **2012**, *64* (15), 1759−1781.
(71) Bellato, F.; Feola, S.; Dalla Verde, G.; Bellio, G.; Pirazzini, M.; Salmaso, S.; Caliceti, P.; Cerullo, V.; Mastrotto, F. Mannosylated Polycations Target CD206+ Antigen-Presenting Cells and Mediate T-Cell-Specific Activation in Cancer Vaccination. *Biomacromolecules* **2022**, *23* (12), 5148−5163.
(72) Chae, J.; Kang, S. H.; Kim, J.; Choi, Y.; Kang, S. H.; Choi, J. Targeted and efficient delivery of rifampicin to macrophages involved in non-tuberculous mycobacterial infection via mannosylated solid lipid nanoparticles. *Nanoscale Adv.* **2023**, *5* (17), 4536−4545.
(73) Heck, A. G.; Schwiertz, D.; Lantzberg, B.; Nguyen, H.-C.; Forster, R.; Scherger, M.; Opatz, T.; Van Ginderachter, J. A.; Nuhn, L. Introducing Targeting Units or pH-Releasable Immunodrugs into Core-Clickable Nanogels. *Eur. Polym. J.* **2024**, *214*, No. 113150.
(74) Kvakova, K.; Ondra, M.; Schimer, J.; Petrik, M.; Novy, Z.; Raabova, H.; Hajduch, M.; Cigler, P. Visualization of Sentinel Lymph Nodes with Mannosylated Fluorescent Nanodiamonds. *Adv. Funct. Mater.* **2022**, *32* (23), No. 2109960.
(75) Krumb, M.; Frey, M.-L.; Langhanki, J.; Forster, R.; Kowalczyk, D.; Mailänder, V.; Landfester, K.; Opatz, T. Multivalency Beats Complexity: A Study on the Cell Uptake of Carbohydrate Functionalized Nanocarriers to Dendritic Cells. *Cells* **2020**, *9* (9), 2087.
(76) Alkilany, A. M.; Zhu, L.; Weller, H.; Mews, A.; Parak, W. J.; Barz, M.; Feliu, N. Ligand density on nanoparticles: A parameter with critical impact on nanomedicine. *Adv. Drug Delivery Rev.* **2019**, *143*, 22−36.
(77) Gao, J.; Chen, P.; Singh, Y.; Zhang, X.; Szekely, Z.; Stein, S.; Sinko, P. J. Novel Monodisperse PEGtide Dendrons: Design, Fabrication, and Evaluation of Mannose Receptor-Mediated Macrophage Targeting. *Bioconjugate Chem.* **2013**, *24* (8), 1332−1344.
(78) Herrera-González, I.; González-Cuesta, M.; Thépaut, M.; Laigre, E.; Goyard, D.; Rojo, J.; García Fernández, J. M.; Fieschi, F.; Renaudet, O.; Nieto, P. M.; Ortiz Mellet, C. High-Mannose Oligosaccharide Hemimimetics that Recapitulate the Conformation and Binding Mode to Concanavalin A, DC-SIGN and Langerin. *Chem.—Eur. J.* **2024**, *30* (2), No. e202303041.
(79) Herrera-González, I.; Thépaut, M.; Sánchez-Fernández, E. M.; di Maio, A.; Vivès, C.; Rojo, J.; García Fernández, J. M.; Fieschi, F.; Nieto, P. M.; Ortiz Mellet, C. Mannobioside biomimetics that trigger DC-SIGN binding selectivity. *Chem. Commun.* **2022**, *58* (86), 12086−12089.
(80) Sedaghat, B.; Stephenson, R. J.; Giddam, A. K.; Eskandari, S.; Apte, S. H.; Pattinson, D. J.; Doolan, D. L.; Toth, I. Synthesis of Mannosylated Lipopeptides with Receptor Targeting Properties. *Bioconjugate Chem.* **2016**, *27* (3), 533−548.
(81) Zimmer, O.; Goepferich, A. On the uncertainty of the correlation between nanoparticle avidity and biodistribution. *Eur. J. Pharm. Biopharm.* **2024**, *198*, No. 114240.
(82) Tjandra, K. C.; Thordarson, P. Multivalency in Drug Delivery−When Is It Too Much of a Good Thing? *Bioconjugate Chem.* **2019**, *30* (3), 503−514.
(83) Erlendsson, S.; Teilum, K. Binding Revisited—Avidity in Cellular Function and Signaling. *Front. Mol. Biosci.* **2021**, *7*, No. 615565.
(84) Krishnamurthy, V. M.; Estroff, L. A.; Whitesides, G. M. Multivalency in Ligand Design. *Fragment-Based Approaches in Drug Discovery*, 2006; pp 11−53.
(85) Dam, T. K.; Oscarson, S.; Roy, R.; Das, S. K.; Pagé, D.; Macaluso, F.; Brewer, C. F. Thermodynamic, Kinetic, and Electron

https://doi.org/10.1021/acs.biomac.5c01510
Biomacromolecules 2025, 26, 8087−8102

Microscopy Studies of Concanavalin A and Dioclea grandiflora Lectin Cross-linked with Synthetic Divalent Carbohydrates. *J. Biol. Chem.* **2005**, *280* (10), 8640−8646.
(86) Maslanka Figueroa, S.; Fleischmann, D.; Beck, S.; Goepferich, A. The Effect of Ligand Mobility on the Cellular Interaction of Multivalent Nanoparticles. *Macromol. Biosci.* **2020**, *20* (4), No. 1900427.
(87) Ordanini, S.; Varga, N.; Porkolab, V.; Thépaut, M.; Belvisi, L.; Bertaglia, A.; Palmioli, A.; Berzi, A.; Trabattoni, D.; Clerici, M.; Fieschi, F.; Bernardi, A. Designing nanomolar antagonists of DC-SIGN-mediated HIV infection: ligand presentation using molecular rods. *Chem. Commun.* **2015**, *51* (18), 3816−3819.
(88) Reuter, K. G.; Perry, J. L.; Kim, D.; Luft, J. C.; Liu, R.; DeSimone, J. M. Targeted PRINT Hydrogels: The Role of Nanoparticle Size and Ligand Density on Cell Association, Biodistribution, and Tumor Accumulation. *Nano Lett.* **2015**, *15* (10), 6371−6378.
(89) Elias, D. R.; Poloukhtine, A.; Popik, V.; Tsourkas, A. Effect of ligand density, receptor density, and nanoparticle size on cell targeting. *Nanomedicine: Nanotechnology, Biology and Medicine* **2013**, *9* (2), 194−201.
(90) Tang, P. S.; Sathiamoorthy, S.; Lustig, L. C.; Ponzielli, R.; Inamoto, I.; Penn, L. Z.; Shin, J. A.; Chan, W. C. W. The Role of Ligand Density and Size in Mediating Quantum Dot Nuclear Transport. *Small* **2014**, *10* (20), 4182−4192.
(91) Akhter, A.; Hayashi, Y.; Sakurai, Y.; Ohga, N.; Hida, K.; Harashima, H. Ligand density at the surface of a nanoparticle and different uptake mechanism: Two important factors for successful siRNA delivery to liver endothelial cells. *Int. J. Pharm.* **2014**, *475* (1), 227−237.
(92) Dalal, C.; Saha, A.; Jana, N. R. Nanoparticle Multivalency Directed Shifting of Cellular Uptake Mechanism. *J. Phys. Chem. C* **2016**, *120* (12), 6778−6786.
(93) Song, X.; Li, R.; Deng, H.; Li, Y.; Cui, Y.; Zhang, H.; Dai, W.; He, B.; Zheng, Y.; Wang, X.; Zhang, Q. Receptor mediated transcytosis in biological barrier: The influence of receptor character and their ligand density on the transmembrane pathway of active-targeting nanocarriers. *Biomaterials* **2018**, *180*, 78−90.
(94) Wang, J.; Tian, S.; Petros, R. A.; Napier, M. E.; DeSimone, J. M. The Complex Role of Multivalency in Nanoparticles Targeting the Transferrin Receptor for Cancer Therapies. *J. Am. Chem. Soc.* **2010**, *132* (32), 11306−11313.
(95) Hunter, C. A.; Anderson, H. L. What is Cooperativity? *Angew. Chem., Int. Ed.* **2009**, *48* (41), 7488−7499.
(96) Chung, H.; Park, J. Y.; Kim, K.; Yoo, R. J.; Suh, M.; Gu, G. J.; Kim, J. S.; Choi, T. H.; Byun, J. W.; Ju, Y. W.; Han, W.; Ryu, H. S.; Chung, G.; Hwang, D. W.; Kim, Y.; Kang, H.-R.; Na, Y. R.; Choi, H.; Im, H.-J.; Lee, Y.-S.; Seok, S. H. Circulation Time-Optimized Albumin Nanoplatform for Quantitative Visualization of Lung Metastasis via Targeting of Macrophages. *ACS Nano* **2022**, *16* (8), 12262−12275.
(97) Silpe, J. E.; Sumit, M.; Thomas, T. P.; Huang, B.; Kotlyar, A.; van Dongen, M. A.; Banaszak Holl, M. M.; Orr, B. G.; Choi, S. K. Avidity Modulation of Folate-Targeted Multivalent Dendrimers for Evaluating Biophysical Models of Cancer Targeting Nanoparticles. *ACS Chem. Biol.* **2013**, *8* (9), 2063−2071.
(98) Porkolab, V.; Lepšík, M.; Ordanini, S.; St John, A.; Le Roy, A.; Thépaut, M.; Paci, E.; Ebel, C.; Bernardi, A.; Fieschi, F. Powerful Avidity with a Limited Valency for Virus-Attachment Blockers on DC-SIGN: Combining Chelation and Statistical Rebinding with Structural Plasticity of the Receptor. *ACS Cent. Sci.* **2023**, *9* (4), 709−718.
(99) Cuellar-Camacho, J. L.; Bhatia, S.; Reiter-Scherer, V.; Lauster, D.; Liese, S.; Rabe, J. P.; Herrmann, A.; Haag, R. Quantification of Multivalent Interactions between Sialic Acid and Influenza A Virus Spike Proteins by Single-Molecule Force Spectroscopy. *J. Am. Chem. Soc.* **2020**, *142* (28), 12181−12192.
(100) Di Iorio, D.; Verheijden, M. L.; van der Vries, E.; Jonkheijm, P.; Huskens, J. Weak Multivalent Binding of Influenza Hemagglutinin Nanoparticles at a Sialoglycan-Functionalized Supported Lipid Bilayer. *ACS Nano* **2019**, *13* (3), 3413−3423.
(101) Jung, H.; Robison, A. D.; Cremer, P. S. Multivalent ligand−receptor binding on supported lipid bilayers. *J. Struct. Biol.* **2009**, *168* (1), 90−94.
(102) Lantzberg, B.; Zeyn, Y.; Forster, R.; Jian, L.; Schauenburg, D.; Hieber, C.; Nuhn, L.; Zhou, T.; Silva, M. J. S. A.; Koynov, K.; Jiang, H.-L.; Kuan, S. L.; Bros, M.; Opatz, T.; Weil, T. Glycogen-inspired trimannosylated serum albumin nanocarriers for targeted delivery of toll-like receptor 7/8 agonists to immune cells and liver. *J. Controlled Release* **2025**, *382*, No. 113705.
(103) Karimi, M.; Bahrami, S.; Ravari, S. B.; Zangabad, P. S.; Mirshekari, H.; Bozorgomid, M.; Shahreza, S.; Sori, M.; Hamblin, M. R. Albumin nanostructures as advanced drug delivery systems. *Expert Opinion on Drug Delivery* **2016**, *13* (11), 1609−1623.
(104) Feinberg, H.; Guo, Y.; Mitchell, D. A.; Drickamer, K.; Weis, W. I. Extended Neck Regions Stabilize Tetramers of the Receptors DC-SIGN and DC-SIGNR. *J. Biol. Chem.* **2005**, *280* (2), 1327−1335.
(105) Khoo, U.-S.; Chan, K. Y. K.; Chan, V. S. F.; Lin, C. L. S. DC-SIGN and L-SIGN: the SIGNs for infection. *J. Mol. Med.* **2008**, *86* (8), 861−874.
(106) Cardona, C. M.; Gawley, R. E. An improved synthesis of a trifurcated newkome-type monomer and orthogonally protected two-generation dendrons. *J. Org. Chem.* **2002**, *67* (4), 1411−1413.
(107) Krabicová, I.; Dolenský, B.; Řezanka, M. Selectivity of 1-O-Propargyl-d-Mannose Preparations. *Molecules* **2022**, *27* (5), 1483.
(108) Ramos-Soriano, J.; de la Fuente, M. C.; de la Cruz, N.; Figueiredo, R. C.; Rojo, J.; Reina, J. J. Straightforward synthesis of Man9, the relevant epitope of the high-mannose oligosaccharide. *Org. Biomol. Chem.* **2017**, *15* (42), 8877−8882.
(109) Niebling, S.; Burastero, O.; Bürgi, J.; Günther, C.; Defelipe, L. A.; Sander, S.; Gattkowski, E.; Anjanappa, R.; Wilmanns, M.; Springer, S.; Tidow, H.; García-Alai, M. FoldAffinity: binding affinities from nDSF experiments. *Sci. Rep.* **2021**, *11* (1), 9572.
(110) Bai, N.; Roder, H.; Dickson, A.; Karanicolas, J. Isothermal Analysis of ThermoFluor Data can readily provide Quantitative Binding Affinities. *Sci. Rep.* **2019**, *9* (1), 2650.
(111) Mesapogu, S.; Jillepalli, C. M.; Arora, D. K. Agarose Gel Electrophoresis and Polyacrylamide Gel Electrophoresis: Methods and Principles. In *Analyzing Microbes: Manual of Molecular Biology Techniques*; Arora, D. K., Das, S., Sukumar, M., Eds.; Springer: Berlin; Heidelberg, 2013; pp 73−91.
(112) Guo, Y.; Feinberg, H.; Conroy, E.; Mitchell, D. A.; Alvarez, R.; Blixt, O.; Taylor, M. E.; Weis, W. I.; Drickamer, K. Structural basis for distinct ligand-binding and targeting properties of the receptors DC-SIGN and DC-SIGNR. *Nat. Struct. Mol. Biol.* **2004**, *11* (7), 591−598.
(113) Hitchen, P. G.; Mullin, N. P.; Taylor, M. E. Orientation of sugars bound to the principal C-type carbohydrate-recognition domain of the macrophage mannose receptor. *Biochem. J.* **1998**, *333* (3), 601−608.
(114) Feinberg, H.; Castelli, R.; Drickamer, K.; Seeberger, P. H.; Weis, W. I. Multiple modes of binding enhance the affinity of DC-SIGN for high mannose N-linked glycans found on viral glycoproteins. *J. Biol. Chem.* **2007**, *282* (6), 4202−4209.
(115) Cramer, J.; Lakkaichi, A.; Aliu, B.; Jakob, R. P.; Klein, S.; Cattaneo, I.; Jiang, X.; Rabbani, S.; Schwardt, O.; Zimmer, G.; Ciancaglini, M.; Abreu Mota, T.; Maier, T.; Ernst, B. Sweet Drugs for Bad Bugs: A Glycomimetic Strategy against the DC-SIGN-Mediated Dissemination of SARS-CoV-2. *J. Am. Chem. Soc.* **2021**, *143* (42), 17465−17478.
(116) Sutkeviciute, I.; Thépaut, M.; Sattin, S.; Berzi, A.; McGeagh, J.; Grudinin, S.; Weiser, J.; Le Roy, A.; Reina, J. J.; Rojo, J.; Clerici, M.; Bernardi, A.; Ebel, C.; Fieschi, F. Unique DC-SIGN Clustering Activity of a Small Glycomimetic: A Lesson for Ligand Design. *ACS Chem. Biol.* **2014**, *9* (6), 1377−1385.
(117) Li, R.-J. E.; Hogervorst, T. P.; Achilli, S.; Bruijns, S. C.; Arnoldus, T.; Vivès, C.; Wong, C. C.; Thépaut, M.; Meeuwenoord, N. J.; van den Elst, H.; Overkleeft, H. S.; van der Marel, G. A.; Filippov, D. V.; van Vliet, S. J.; Fieschi, F.; Codée, J. D. C.; van Kooyk, Y.

https://doi.org/10.1021/acs.biomac.5c01510
Biomacromolecules 2025, 26, 8087−8102

Systematic Dual Targeting of Dendritic Cell C-Type Lectin Receptor DC-SIGN and TLR7 Using a Trifunctional Mannosylated Antigen. *Front. Chem.* **2019**, *7*, 650.
(118) Khan, M. F.; Rahman, M. M.; Xin, Y.; Mustafa, A.; Smith, B. J.; Ottemann, K. M.; Roujeinikova, A. Determination of Protein−Ligand Binding Affinities by Thermal Shift Assay. *ACS Pharamcol. Transl. Sci.* **2024**, *7* (10), 3096−3107.
(119) Niesen, F. H.; Berglund, H.; Vedadi, M. The use of differential scanning fluorimetry to detect ligand interactions that promote protein stability. *Nat. Protoc.* **2007**, *2* (9), 2212−2221.
(120) OMEGA 5.0.0.3: OpenEye, Cadence Molecular Sciences, Santa Fe, NM, http://www.eyesopen.com.
(121) Hawkins, P. C. D.; Skillman, A. G.; Warren, G. L.; Ellingson, B. A.; Stahl, M. T. Conformer Generation with OMEGA: Algorithm and Validation Using High Quality Structures from the Protein Databank and Cambridge Structural Database. *J. Chem. Inf. Model.* **2010**, *50* (4), 572−584.
(122) Schetters, S. T. T.; Kruijssen, L. J. W.; Crommentuijn, M. H. W.; Kalay, H.; Ochando, J.; den Haan, J. M. M.; Garcia-Vallejo, J. J.; van Kooyk, Y. Mouse DC-SIGN/CD209a as Target for Antigen Delivery and Adaptive Immunity. *Front. Immunol.* **2018**, *9*, No. 990.
(123) Mastrotto, F.; Pirazzini, M.; Negro, S.; Salama, A.; Martinez-Pomares, L.; Mantovani, G. Sulfation at Glycopolymer Side Chains Switches Activity at the Macrophage Mannose Receptor (CD206) In Vitro and In Vivo. *J. Am. Chem. Soc.* **2022**, *144* (50), 23134−23147.
(124) Zhang, S.; Gao, H.; Bao, G. Physical Principles of Nanoparticle Cellular Endocytosis. *ACS Nano* **2015**, *9* (9), 8655−8671.
(125) Behzadi, S.; Serpooshan, V.; Tao, W.; Hamaly, M. A.; Alkawareek, M. Y.; Dreaden, E. C.; Brown, D.; Alkilany, A. M.; Farokhzad, O. C.; Mahmoudi, M. Cellular uptake of nanoparticles: journey inside the cell. *Chem. Soc. Rev.* **2017**, *46* (14), 4218−4244.
(126) Hoshyar, N.; Gray, S.; Han, H.; Bao, G. The Effect of Nanoparticle Size on In Vivo Pharmacokinetics and Cellular Interaction. *Nanomedicine* **2016**, *11* (6), 673−692.
(127) Budhadev, D.; Poole, E.; Nehlmeier, I.; Liu, Y.; Hooper, J.; Kalverda, E.; Akshath, U. S.; Hondow, N.; Turnbull, W. B.; Pöhlmann, S.; Guo, Y.; Zhou, D. Glycan-Gold Nanoparticles as Multifunctional Probes for Multivalent Lectin−Carbohydrate Binding: Implications for Blocking Virus Infection and Nanoparticle Assembly. *J. Am. Chem. Soc.* **2020**, *142* (42), 18022−18034.



https://doi.org/10.1021/acs.biomac.5c01510
Biomacromolecules 2025, 26, 8087−8102

”

Supporting Information

Surface Density of Mono- and Trivalent High-Mannan Derived Targeting Structures with Different Affinity Impacts Cellular Uptake of Human Serum Albumin Derived Nanocarriers

Robert Forster[†,#], Bellinda Lantzberg[‡,#], Annabelle Weldert[§,#], Laura Rosenberger[ǁ], Yanira Zeyn[ǁ], Danuta Kowalczyk[†], Seah Ling Kuan[‡], Christian Kersten[§,], Matthias Bros[ǁ,*], Tanja Weil[‡,*], Tanja Schirmeister[§,*], Till Opatz[†,*]*

[†] Department of Chemistry, Johannes Gutenberg-University Mainz, Duesbergweg 10 – 14, 55128 Mainz, Germany.

[‡] Max Planck Institute for Polymer Research, Ackermannweg 10, 55128 Mainz, Germany.

[§] Department for Pharmaceutical and Biomedical Sciences, Johannes Gutenberg-University Mainz, Staudingerweg 5, 55128 Mainz, Germany.

[ǁ] Department of Dermatology, University Medical Center of the Johannes Gutenberg-University Mainz, Obere Zahlbacher Straße 63, 55131 Mainz, Germany.

[#] Equal contribution

[*] E-mail: opatz@uni-mainz.de; schirmei@uni-mainz.de; weil@mpip-mainz.mpg.de; mbros@uni-mainz.de; kerstec@uni-mainz.de.

Supporting Information

1 Table of contents

1 Table of contents 2
2 General conditions and purification methods 3
3 Analytical methods 4
4 Synthesis procedures 6
4.1 Synthesis of the mono- and trivalent targeting structures 6
4.2 Synthesis of the TS_n-HSA neoglycoalbumins 49
5 Prediction of binding modes for monovalent TSs 56
6 NanoDSF binding study for mono- and trivalent TSs 56
6.1 Recombinant protein expression and purification. 56
6.2 Differential Scanning Fluorimetry (NanoDSF). 58
7 Prediction of distances of mannose epitopes of a trivalent TS 60
8 Appendix 61
8.1 List of references 61
8.2 List of abbreviations 65
8.3 NMR spectra 67
8.4 MALDI-ToF-MS spectra 98

Supporting Information

5 Prediction of binding modes for monovalent TSs

TS Man (**7**) and Man_3 (**8**) with a truncated linker were docked into the primary carbohydrate-recognition site (CRD) of either CD209 (PDB: 1SL4)[49] or CRD4 of CD206 (PDB: 7JUF)[50] using SeeSAR 13.01.1.[51-53] To recreate experimentally observed mannose-binding modes for CD209, the template docking mode was employed, while for CD206, a constraint to include any oxygen was applied to two oxygen atoms (Figure S 3A). For each ligand, ten poses were generated, ranked by the estimated binding affinity,[53] and the highest-ranked pose was selected for binding mode analysis. The crystallographic binding mode of the reference ligand was visually compared to the predicted pose to assess pose prediction accuracy (Figure S 3B, C). The root mean square deviation (RMSD) values were calculated as 0.41 Å for CD206 and 1.27 Å for CD209.

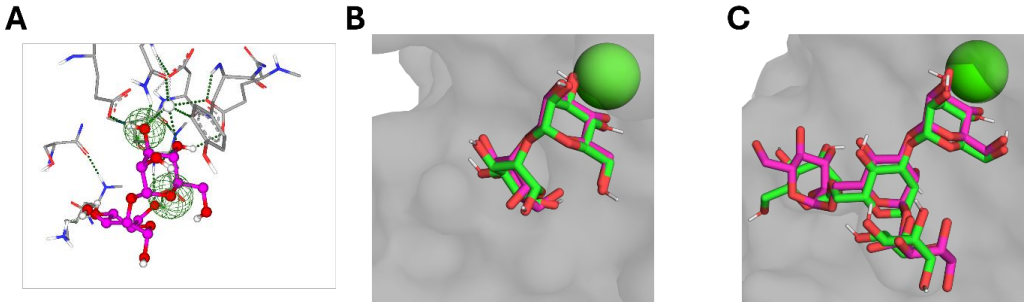


Figure S 3: **A)** Constraints (green spheres) put on reference ligand oxygen atoms for CD206 CRD4. **B)** Redocking the reference TSs for CD206 CRD4 (PDB: 7JUF, RMSD: 0.41 Å). **C)** Redocking the reference TSs for CD209 CRD (PDB: 1SL4, RMSD: 1.27 Å). The poses from the crystal structures are shown with pink carbon atoms, and the docking poses generated by SeeSAR 13.01.1 are shown with green carbon atoms. The protein surfaces are depicted in grey, and the Ca^{2+}-cation inside the binding pocket is represented as a green sphere.

6 NanoDSF binding study for mono- and trivalent TSs

6.1 Recombinant protein expression and purification.

6.1.1 Carbohydrate recognition domain 4 of CD206

CRD 4 of CD206 was expressed as described previously.[50] Briefly, a pT5T expression vector containing CRD4 of CD206 was transformed into competent *Escherichia coli* (E. coli) BL21 (DE3) cells. The cells were grown in LB medium containing 100 µg/mL ampicillin at 37 °C and 160 rpm until they reached an optical density (OD_{600}) of approximately 0.7. Overexpression was induced by adding 0.4 mM Isopropyl-β-D-thiogalactopyranoside (IPTG) for approximately 2.5 hours at 37 °C. Cells were harvested by centrifugation (10.000 × g at 4 °C for 15 minutes) and resuspended in cold buffer A (10 mM Tris-Cl, pH 7.8). Lysis was performed by thoroughly sonicating the cell pellets. Cell debris and inclusion bodies were collected by centrifugation (18,000 × g at 4 °C for 15 minutes), and the supernatant was discarded. The inclusion bodies were then solubilized in 100 mL of denaturing buffer B (6 M guanidine-HCl, 100 mM Tris-Cl, pH 7.0). After adding 2-mercaptoethanol (10 µL), the suspension was incubated at 4 °C on ice for 30 minutes. Insoluble impurities were removed by centrifugation (18,000 × g at 4 °C for 30 minutes). The supernatant was refolded by three-step dialysis against 2 L of buffer C (0.5 M NaCl, 25 mM Tris-Cl, pH 7.8, 25 mM $CaCl_2$) at 4 °C overnight. After centrifugation (18,000 × g at 4 °C for 30 minutes), the renatured CRD4 was purified using a 10 mL column of mannose-conjugated Sepharose prepared by divinyl sulfone coupling.[54] Finally, after washing with one column volume (CV) of buffer

D (150 mM NaCl, 25 mM Tris-Cl, pH 7.8, 25 mM $CaCl_2$), the bound protein was eluted with buffer E (150 mM NaCl, 25 mM Tris-Cl, pH 7.8, 2.5 mM EDTA).

6.1.2 Carbohydrate recognition domain of CD209

The recombinant CRD of CD209 was expressed as described previously.[55] Briefly, a pET-30 expression vector containing the CRD of CD209 was transformed into competent *Escherichia coli* (E. coli) BL21 (DE3) cells. The cells were grown in LB medium containing 100 µg/mL kanamycin at 37 °C and 160 rpm until they reached an optical density (OD_{600}) of approximately 0.7. Overexpression was induced by adding 0.5 mM IPTG for approximately 3 hours at 37 °C. Cells were harvested by centrifugation (10.000 × g at 4 °C for 15 minutes) and resuspended in cold buffer A (25 mM Tris-Cl, 150 mM NaCl, pH 8) supplemented with lysozyme, one tablet of protease inhibitor (cOmplete™, Roche), and DNase I. Lysis was performed by thoroughly sonicating the resuspended cell pellets. Cell debris and inclusion bodies were collected by centrifugation (20,000 × g at 4 °C for 1 hour), and the supernatant was discarded. The inclusion bodies were resuspended in buffer A supplemented with 2 M urea and 1% Triton X-100. After a second centrifugation step, the inclusion bodies were solubilized in buffer A supplemented with 6 M guanidine hydrochloride and 0.01 % 2-mercaptoethanol. Insoluble impurities were removed by centrifugation (20.000 × g at 4 °C for 1 hour). The resulting supernatant was dialyzed against 2 L of buffer B (25 mM Tris, pH 8) at 4 °C overnight. Next, refolding was performed by three-step dialysis against 2 L of buffer C (25 mM Tris-Cl, 150 mM NaCl, pH 8, 4 mM $CaCl_2$) at 4 °C overnight. After centrifugation (20.000 × g at 4 °C for 1 hour), the renatured CRD was purified using a HisTrap HP column pre-equilibrated with buffer D (150 mM NaCl, 25 mM Tris, pH 8, 4 mM $CaCl_2$, 10 mM imidazole). Unbound material was washed with 10 CV of buffer D, and the protein was eluted with buffer E (150 mM NaCl, 25 mM Tris, pH 8, 4 mM $CaCl_2$, 500 mM imidazole). Finally, functional protein was separated from non-functional protein by a 10 mL mannose-agarose column equilibrated with buffer C.

Supporting Information

6.2 Differential Scanning Fluorimetry (NanoDSF).

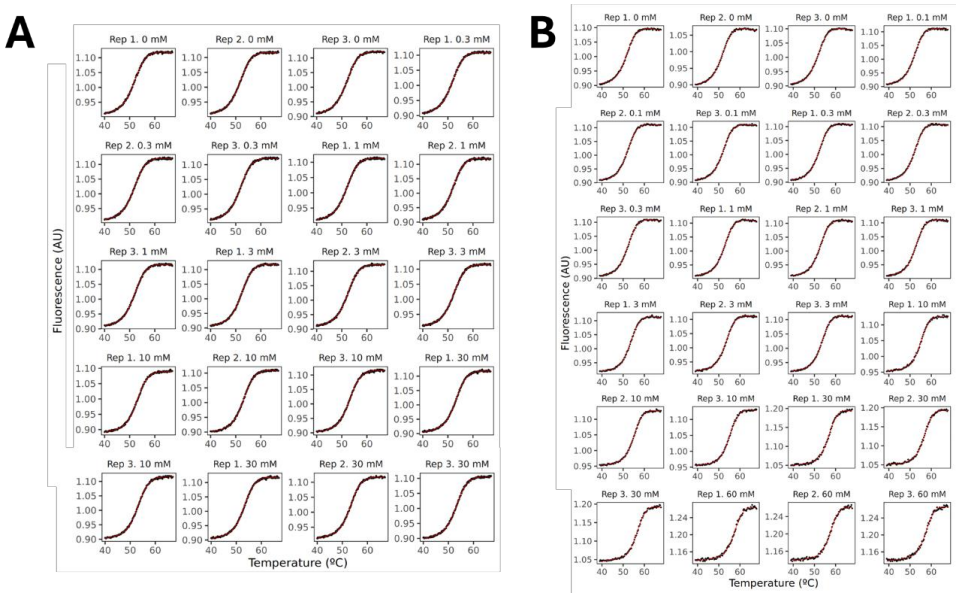


Figure S 4: **A)** Fitting of the fluorescence-based melting curves of protein CD206 CRD4 at different concentrations of the TS $ManN_3$. **B)** Fitting of the fluorescence-based melting curves of protein CD206 CRD4 at different concentrations of the TS Man_3N_3. Plot created by FoldAffinity (spc.embl-hamburg.de).[56]

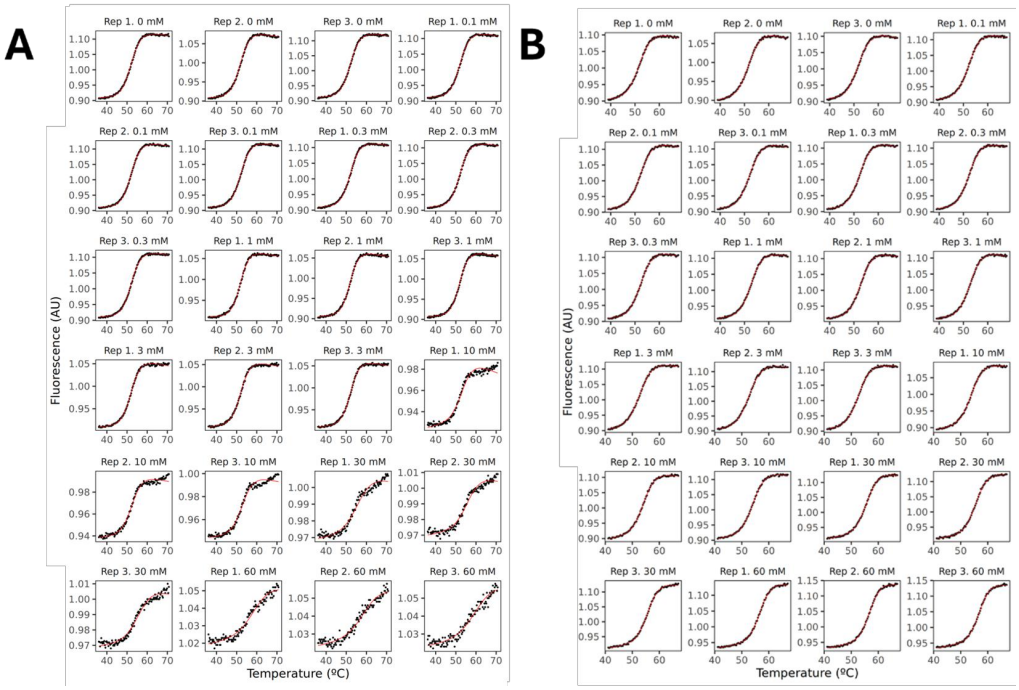


Figure S 5: **A)** Fitting of the fluorescence-based melting curves of protein CD206 CRD4 at different concentrations of the TS $(Man)_3N_3$. **B)** Fitting of the fluorescence-based melting curves of protein CD206 CRD4 at different concentrations of the TS $(Man_3)_3N_3$. Plot created by FoldAffinity (spc.embl-hamburg.de).[56]

Supporting Information

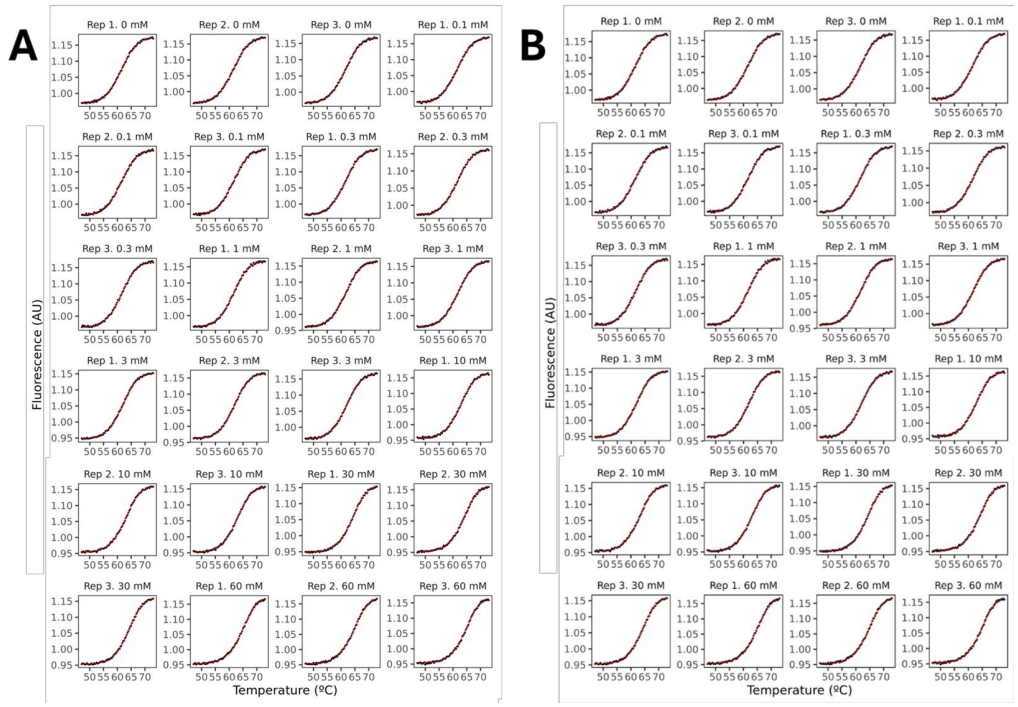


Figure S 6: **A)** Fitting of the fluorescence-based melting curves of protein CD209 CRD at different concentrations of the TS $ManN_3$. **B)** Fitting of the fluorescence-based melting curves of protein CD209 CRD at different concentrations of the TS Man_3N_3. Plot created by FoldAffinity (spc.embl-hamburg.de).[56]

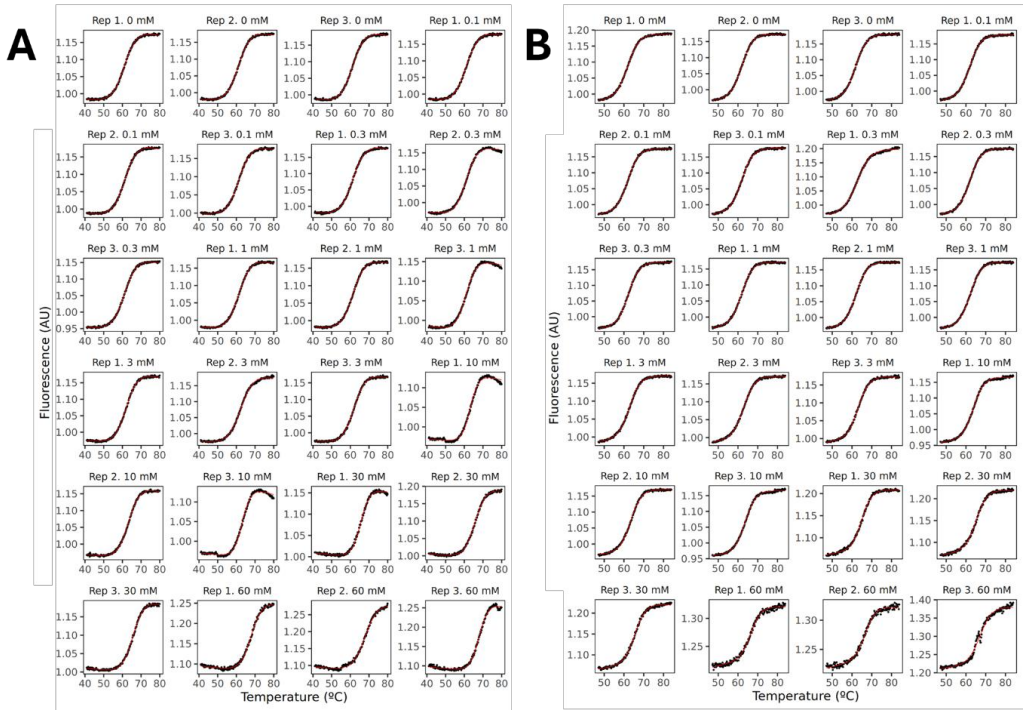


Figure S 7: **A)** Fitting of the fluorescence-based melting curves of protein CD209 CRD at different concentrations of the TS $(Man)_3N_3$. **B)** Fitting of the fluorescence-based melting curves of protein CD209 CRD at different concentrations of the TS $(Man_3)_3N_3$. Plot created by FoldAffinity (spc.embl-hamburg.de).[56]

Supporting Information

7 Prediction of distances of mannose epitopes of a trivalent TS

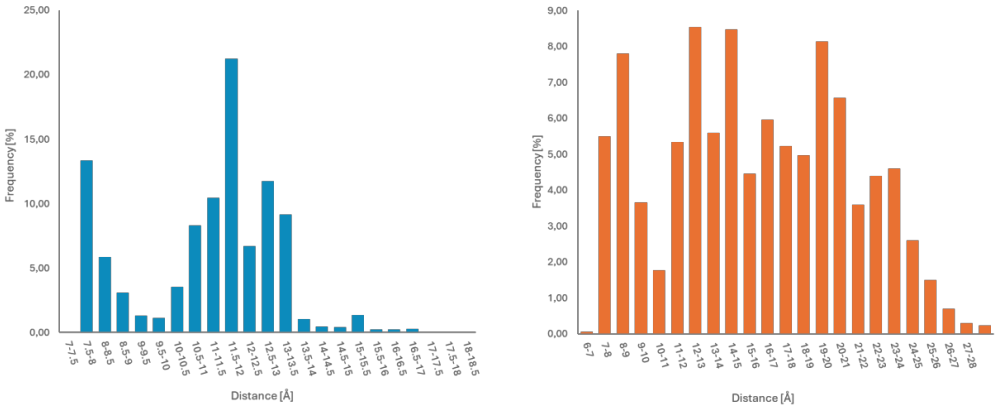


Figure S 8: Distribution of distances between one epitope and the focal point of the glycodendron measured between central carbon and hydroxy groups at *C*-4 (left). Distribution of distances spanned by two Man epitopes measured between hydroxy groups at *C*-4 (right).

Supporting Information

8 Appendix

8.1 List of references

(1) Still, W. C.; Kahn, M.; Mitra, A. Rapid chromatographic technique for preparative separations with moderate resolution. *J. Org. Chem.* **1978**, *43* (14), 2923-2925. DOI: 10.1021/jo00408a041.

(2) Cavalli, E. S.; Mies, T.; Rzepa, H. S.; White, A. J. P.; Parsons, P. J.; Barrett, A. G. M. Pyrimidine Nucleosides Syntheses by Late-Stage Base Heterocyclization Reactions. *Org. Lett.* **2022**, *24* (49), 8931-8935. DOI: 10.1021/acs.orglett.2c03152.

(3) Kramer, J. R.; Deming, T. J. Glycopolypeptides via Living Polymerization of Glycosylated-l-lysine N-Carboxyanhydrides. *J. Am. Chem. Soc.* **2010**, *132* (42), 15068-15071. DOI: 10.1021/ja107425f.

(4) Ekholm, F. S.; Poláková, M.; Pawłowicz, A. J.; Leino, R. Synthesis of divalent 2, 2'-linked mannose derivatives by homodimerization. *Synth.* **2009**, *2009* (4), 567-576. DOI: 10.1055/s-0028-1083283.

(5) Nielsen, M. M.; Holmstrøm, T.; Pedersen, C. M. Stereoselective O-Glycosylations by Pyrylium Salt Organocatalysis. *Angew. Chem. Int. Ed.* **2022**, *61* (6), e202115394. DOI: 10.1002/anie.202115394.

(6) Kramer, S.; Langhanki, J.; Krumb, M.; Opatz, T.; Bros, M.; Zentel, R. HPMA-Based Nanocarriers for Effective Immune System Stimulation. *Macromol. Biosci.* **2019**, *19* (6), 1800481. DOI: 10.1002/mabi.201800481.

(7) León, E. I.; Martín, Á.; Pérez-Martín, I.; Quintanal, L. M.; Suárez, E. C–C Bond Formation by Sequential Intramolecular Hydrogen Atom Transfer/Intermolecular Radical Allylation Reaction in Carbohydrate Systems. *Eur. J. Org. Chem.* **2012**, *2012* (20), 3818-3829. DOI: 10.1002/ejoc.201200300.

(8) Schibilla, F.; Voskuhl, J.; Fokina, N. A.; Dahl, J. E. P.; Schreiner, P. R.; Ravoo, B. J. Host–Guest Complexes of Cyclodextrins and Nanodiamonds as a Strong Non-Covalent Binding Motif for Self-Assembled Nanomaterials. *Chem. Eur. J.* **2017**, *23* (63), 16059-16065. DOI: 10.1002/chem.201703392.

(9) Tanzi, L.; Robescu, M. S.; Marzatico, S.; Recca, T.; Zhang, Y.; Terreni, M.; Bavaro, T. Developing a Library of Mannose-Based Mono- and Disaccharides: A General Chemoenzymatic Approach to Monohydroxylated Building Blocks. *Molecules* **2020**, *25* (23), 5764. DOI: 10.3390/molecules25235764.

(10) Poláková, M.; Beláňová, M.; Mikušová, K.; Lattová, E.; Perreault, H. Synthesis of 1,2,3-Triazolo-Linked Octyl (1→6)-α-d-Oligomannosides and Their Evaluation in Mycobacterial Mannosyltransferase Assay. *Bioconjugate Chem.* **2011**, *22* (2), 289-298. DOI: 10.1021/bc100421g.

(11) Percec, V.; Leowanawat, P.; Sun, H.-J.; Kulikov, O.; Nusbaum, C. D.; Tran, T. M.; Bertin, A.; Wilson, D. A.; Peterca, M.; Zhang, S.; Heiney, P. A. Modular synthesis of amphiphilic Janus glycodendrimers and their self-assembly into glycodendrimersomes and other complex architectures with bioactivity to biomedically relevant lectins. *J. Am. Chem. Soc.* **2013**, *135* (24), 9055-9077. DOI: 10.1021/ja403323y.

(12) Reintjens, N. R. M.; Tondini, E.; Vis, C.; McGlinn, T.; Meeuwenoord, N. J.; Hogervorst, T. P.; Overkleeft, H. S.; Filippov, D. V.; van der Marel, G. A.; Ossendorp, F.; Codée, J. D. C. Multivalent, Stabilized Mannose-6-Phosphates for the Targeted Delivery of Toll-Like Receptor Ligands and Peptide Antigens. *ChemBioChem* **2021**, *22* (2), 434-440. DOI: 10.1002/cbic.202000538.

(13) Krabicová, I.; Dolenský, B.; Řezanka, M. Selectivity of 1-O-Propargyl-d-Mannose Preparations. *Molecules* **2022**, *27* (5), 1483. DOI: 10.3390/molecules27051483.

(14) Arias-Pérez, M.; Santos, M. An efficient approach to partially O-methylated α-D-mannopyranosides using bis-tert-butyldiphenylsilyl ethers as intermediates. *Tetrahedron* **1996**, *52* (32), 10785-10798. DOI: 10.1016/0040-4020(96)00600-X.

(15) Du, Y.; Zhang, M.; Kong, F. Highly efficient and practical synthesis of 3, 6-branched oligosaccharides. *Org. Lett.* **2000**, *2* (24), 3797-3800. DOI: 10.1021/ol000243w.

(16) Halmos, T.; Montserret, R.; Filippi, J.; Antonakis, K. Studies of the selective silylation of methyl α- and β-d-aldohexopyranosides: stability of the partially protected derivatives in polar solvents. *Carbohydr. Res.* **1987**, *170* (1), 57-69. DOI: 10.1016/0008-6215(87)85005-X.

(17) Mark, E.; Zbiral, E.; Brandstetter, H. H. Strukturelle Abwandlungen an partiell silylierten Kohlenhydraten mittels Triphenylphosphan/Azodicarbonsäurediethylester, 4. Mitt.: Transformationen an Mannose und Galaktose. *Monatsh. Chem.* **1980**, *111* (1), 289-307. DOI: 10.1007/BF00938735.

(18) Ramos-Soriano, J.; de la Fuente, M. C.; de la Cruz, N.; Figueiredo, R. C.; Rojo, J.; Reina, J. J. Straightforward synthesis of Man9, the relevant epitope of the high-mannose oligosaccharide. *Org. Biomol. Chem.* **2017**, *15* (42), 8877-8882. DOI: 10.1039/C7OB02286G.

(19) Teumelsan, N.; Huang, X. Synthesis of branched Man5 oligosaccharides and an unusual stereochemical observation. *J. Org. Chem.* **2007**, *72* (23), 8976-8979. DOI: 10.1021/jo7013824.

(20) Traboni, S.; Bedini, E.; Iadonisi, A. Orthogonal protection of saccharide polyols through solvent-free one-pot sequences based on regioselective silylations. *Beilstein J. Org. Chem.* **2016**, *12* (1), 2748-2756. DOI: 10.3762/bjoc.12.271.

(21) van den Bos, L. J.; Dinkelaar, J.; Overkleeft, H. S.; van der Marel, G. A. Stereocontrolled synthesis of β-D-mannuronic acid esters: synthesis of an alginate trisaccharide. *J. Am. Chem. Soc.* **2006**, *128* (40), 13066-13067. DOI: 10.1021/ja064787q.

(22) Zhang, Y.; Chen, C.; Jin, L.; Tan, H.; Wang, F.; Cao, H. Synthesis of unsymmetrical 3,6-branched Man5 oligosaccharide: a comparison between one-pot sequential glycosylation and stepwise synthesis. *Carbohydr. Res.* **2015**, *401*, 109-114. DOI: 10.1016/j.carres.2014.09.010.

(23) Kanaya, T.; Mashio, R.; Watanabe, T.; Schweizer, F.; Hada, N. Synthesis of glycosphingolipids from the fungus Hirsutella rhossiliensis. *Tetrahedron* **2017**, *73* (49), 6847-6855. DOI: 10.1016/j.tet.2017.10.034.

(24) Bakleh, M. E.; Sol, V.; Estieu-Gionnet, K.; Granet, R.; Déléris, G.; Krausz, P. An efficient route to VEGF-like peptide porphyrin conjugates via microwave-assisted 'click-chemistry'. *Tetrahedron* **2009**, *65* (36), 7385-7392. DOI: 10.1016/j.tet.2009.07.028.

(25) Davila, J.; Chassepot, A.; Longo, J.; Boulmedais, F.; Reisch, A.; Frisch, B.; Meyer, F.; Voegel, J.-C.; Mésini, P. J.; Senger, B.; Metz-Boutigue, M.-H.; Hemmerlé, J.; Lavalle, P.; Schaaf, P.; Jierry, L. Cyto-mechanoresponsive Polyelectrolyte Multilayer Films. *J. Am. Chem. Soc.* **2012**, *134* (1), 83-86. DOI: 10.1021/ja208970b.

(26) Krumb, M.; Frey, M.-L.; Langhanki, J.; Forster, R.; Kowalczyk, D.; Mailänder, V.; Landfester, K.; Opatz, T. Multivalency Beats Complexity: A Study on the Cell Uptake of Carbohydrate Functionalized Nanocarriers to Dendritic Cells. *Cells* **2020**, *9* (9), 2087. DOI: 10.3390/cells9092087.

(27) Tavernaro, I.; Hartmann, S.; Sommer, L.; Hausmann, H.; Rohner, C.; Ruehl, M.; Hoffmann-Roeder, A.; Schlecht, S. Synthesis of tumor-associated MUC1-glycopeptides and their multivalent presentation by functionalized gold colloids. *Org. Biomol. Chem.* **2015**, *13* (1), 81-97, 10.1039/C4OB01339E. DOI: 10.1039/C4OB01339E.

(28) Tsakama, M.; Shang, Y.; He, Y.; Fan, B.; Wang, F.; Chen, W.; Dai, X. Synthesis and optical properties of a novel sugar coated poly(p-phenyleneethynylene) effectively quenched by concanavalin A. *Tetrahedron Lett.* **2016**, *57* (16), 1739-1742. DOI: 10.1016/j.tetlet.2016.01.102.

(29) Landeros, J. M.; Silvestre, H. A.; Guadarrama, P. Synthesis of branched cores by poly-O-alkylation reaction under phase transfer conditions. A systematic study. *J. Mol. Struct.* **2013**, *1037*, 412-419. DOI: 10.1016/j.molstruc.2013.01.034.

(30) Newkome, G. R.; Lin, X. Symmetrical, four-directional, poly (ether-amide) cascade polymers. *Macromolecules* **1991**, *24* (6), 1443-1444. DOI: 10.1021/ma00006a042.

(31) Appel, R.; Fuchs, J.; Tyrrell, S. M.; Korevaar, P. A.; Stuart, M. C.; Voets, I. K.; Schonhoff, M.; Besenius, P. Steric Constraints Induced Frustrated Growth of Supramolecular Nanorods in Water. *Chemistry* **2015**, *21* (52), 19257-19264. DOI: 10.1002/chem.201503616.

(32) Cardona, C. M.; Gawley, R. E. An improved synthesis of a trifurcated newkome-type monomer and orthogonally protected two-generation dendrons. *J. Org. Chem.* **2002**, *67* (4), 1411-1413. DOI: 10.1021/jo0161678.

(33) Baldoli, C.; Rigamonti, C.; Maiorana, S.; Licandro, E.; Falciola, L.; Mussini, P. R. A New Triferrocenyl-tris(hydroxymethyl)aminomethane Derivative as a Highly Sensitive Electrochemical Marker of Biomolecules: Application to the Labelling of PNA Monomers and Their Electrochemical Characterization. *Chem. Eur. J.* **2006**, *12* (15), 4091-4100. DOI: 10.1002/chem.200501466.

(34) Odaka, M.; Furuta, T.; Kobayashi, Y.; Iwamura, M. Synthesis, Photoreactivity and Cytotoxic Activity of Caged Compounds of L-Leucyl-L-Leucine Methyl Ester, an Apoptosis Inducer. *Photochem. Photobiol.* **1996**, *63* (6), 800-806. DOI: 10.1111/j.1751-1097.1996.tb09633.x.

(35) Spitzer, D.; Rodrigues, L. L.; Straßburger, D.; Mezger, M.; Besenius, P. Tuneable Transient Thermogels Mediated by a pH- and Redox-Regulated Supramolecular Polymerization. *Angew. Chem. Int. Ed.* **2017**, *56* (48), 15461-15465. DOI: 10.1002/anie.201708857.

(36) André, S.; Cañada, F. J.; Shiao, T. C.; Largartera, L.; Diercks, T.; Bergeron-Brlek, M.; el Biari, K.; Papadopoulos, A.; Ribeiro, J. P.; Touaibia, M.; Solís, D.; Menéndez, M.; Jiménez-Barbero, J.; Roy, R.; Gabius, H.-J. Fluorinated Carbohydrates as Lectin Ligands: Biorelevant Sensors with Capacity to Monitor Anomer Affinity in 19F-NMR-Based Inhibitor Screening. *Eur. J. Org. Chem.* **2012**, *2012* (23), 4354-4364. DOI: 10.1002/ejoc.201200397.

(37) Hellmuth, I.; Freund, I.; Schlöder, J.; Seidu-Larry, S.; Thüring, K.; Slama, K.; Langhanki, J.; Kaloyanova, S.; Eigenbrod, T.; Krumb, M.; Röhm, S.; Peneva, K.; Opatz, T.; Jonuleit, H.; Dalpke, A. H.; Helm, M. Bioconjugation of Small Molecules to RNA Impedes Its Recognition by Toll-Like Receptor 7. *Front. Immunol.* **2017**, *8*, Original Research. DOI: 10.3389/fimmu.2017.00312.

(38) Lu, W.-Y.; Sun, X.-W.; Zhu, C.; Xu, J.-H.; Lin, G.-Q. Expanding the application scope of glycosidases using click chemistry. *Tetrahedron* **2010**, *66* (3), 750-757. DOI: 10.1016/j.tet.2009.11.044.

(39) Yamamoto, S.; Nakahama, S.; Yamaguchi, K. A Heterobifunctional Linker Bearing Azide-reactive Alkyne and Thiol-reactive Maleimide Connected with N-(2-Nitrobenzyl)imide to Synthesize Photocleavable Diblock Copolymers. *Chem. Lett.* **2013**, *42* (8), 791-793. DOI: 10.1246/cl.130235 (acccessed 2/11/2025).

(40) Lindhorst, T. K.; Bruegge, K.; Fuchs, A.; Sperling, O. A bivalent glycopeptide to target two putative carbohydrate binding sites on FimH. *Beilstein J. Org. Chem.* **2010**, *6*, 801-809. DOI: 10.3762/bjoc.6.90.

(41) Reina, J. J.; Rioboo, A.; Montenegro, J. Glycosyl Aldehydes: New Scaffolds for the Synthesis of Neoglycoconjugates via Bioorthogonal Oxime Bond Formation. *Synth.* **2018**, *50* (04), 831-845. DOI: 10.1055/s-0036-1591082.

(42) Amit, B.; Hazum, E.; Fridkin, M.; Patchornik, A. A photolabile protecting group for the phenolic hydroxyl function of tyrosine. *Int. J. Pept. Protein Res.* **1977**, *9* (2), 91-96. DOI: 10.1111/j.1399-3011.1977.tb03468.x.

(43) Amit, B.; Zehavi, U.; Patchornik, A. Photosensitive protecting groups of amino sugars and their use in glycoside synthesis. 2-Nitrobenzyloxycarbonylamino and 6-nitroveratryloxycarbonylamino derivatives. *J. Org. Chem.* **1974**, *39* (2), 192-196. DOI: 10.1021/jo00916a015.

(44) Cheng, S.; Feng, Y.; Li, W.; Liu, T.; Lv, X.; Tong, X.; Xi, G.; Ye, X.; Li, X. Development of novel antivrial agents that induce the degradation of the main protease of human-infecting coronaviruses. *Eur. J. Med. Chem.* **2024**, *275*, 116629. DOI: 10.1016/j.ejmech.2024.116629.

(45) Krumb, M.; Lucas, T.; Opatz, T. Visible Light Enables Aerobic Iodine Catalyzed Glycosylation. *Eur. J. Org. Chem.* **2019**, *2019* (28), 4517-4521. DOI: 10.1002/ejoc.201900143.

(46) Chakraborti, A. K.; Gulhane, R. Perchloric acid adsorbed on silica gel as a new, highly efficient, and versatile catalyst for acetylation of phenols, thiols, alcohols, and amines. *Chem. Commun.* **2003**, (15), 1896-1897. DOI: 10.1039/B304178F.

(47) Dyer, R. G.; Turnbull, K. D. Hydrolytic Stabilization of Protected p-Hydroxybenzyl Halides Designed as Latent Quinone Methide Precursors. *J. Org. Chem.* **1999**, *64* (21), 7988-7995. DOI: 10.1021/jo991085t.

(48) Zhou, K.; Li, G.; Pan, R.; Xin, S.; Wen, W.; Wang, H.; Luo, C.; Han, R. P. S.; Gu, Y.; Tu, Y. Preclinical evaluation of AGTR1-Targeting molecular probe for colorectal cancer imaging in orthotopic and liver metastasis mouse models. *Eur. J. Med. Chem.* **2024**, *271*, 116452. DOI: 10.1016/j.ejmech.2024.116452.

(49) Guo, Y.; Feinberg, H.; Conroy, E.; Mitchell, D. A.; Alvarez, R.; Blixt, O.; Taylor, M. E.; Weis, W. I.; Drickamer, K. Structural basis for distinct ligand-binding and targeting properties of the receptors DC-SIGN and DC-SIGNR. *Nat. Struct. Mol. Biol.* **2004**, *11* (7), 591-598. DOI: 10.1038/nsmb784.

(50) Feinberg, H.; Jégouzo, S. A.; Lasanajak, Y.; Smith, D. F.; Drickamer, K.; Weis, W. I.; Taylor, M. E. Structural analysis of carbohydrate binding by the macrophage mannose receptor CD206. *J. Biol. Chem.* **2021**, *296*, 100368. DOI: 10.1016/j.jbc.2021.100368

(51) SeeSAR, version 13.01.1 BioSolveIT GmbH, St. Augustin, Germany, https://www.biosolveit.de/SeeSAR.

(52) Rarey, M.; Kramer, B.; Lengauer, T.; Klebe, G. A Fast Flexible Docking Method using an Incremental Construction Algorithm. *J. Mol. Biol.* **1996**, *261* (3), 470-489. DOI: 10.1006/jmbi.1996.0477.

(53) Reulecke, I.; Lange, G.; Albrecht, J.; Klein, R.; Rarey, M. Towards an Integrated Description of Hydrogen Bonding and Dehydration: Decreasing False Positives in Virtual Screening with the HYDE Scoring Function. *ChemMedChem* **2008**, *3* (6), 885-897. DOI: 10.1002/cmdc.200700319.

(54) Fornstedt, N.; Porath, J. Characterization studies on a new lectin found in seeds of Vicia ervilia. *FEBS Lett.* **1975**, *57* (2), 187-191. DOI: 10.1016/0014-5793(75)80713-7.

(55) Thépaut, M.; Guzzi, C.; Sutkeviciute, I.; Sattin, S.; Ribeiro-Viana, R.; Varga, N.; Chabrol, E.; Rojo, J.; Bernardi, A.; Angulo, J.; Nieto, P. M.; Fieschi, F. Structure of a Glycomimetic Ligand in the Carbohydrate Recognition Domain of C-type Lectin DC-SIGN. Structural Requirements for Selectivity and Ligand Design. *J. Am. Chem. Soc.* **2013**, *135* (7), 2518-2529. DOI: 10.1021/ja3053305.

(56) Bai, N.; Roder, H.; Dickson, A.; Karanicolas, J. Isothermal Analysis of ThermoFluor Data can readily provide Quantitative Binding Affinities. *Sci. Rep.* **2019**, *9* (1), 2650. DOI: 10.1038/s41598-018-37072-x.

8.2 List of abbreviations

$(HF)_X \cdot Pyr$	Hydrogen fluoride pyridine complex
Ac_2O	Acetic anhydride
AgOTf	Silver triflate
Ar-atm.	Argon atmosphere
ATR	Attenuated total reflection
$BF_3 \cdot OEt_2$	Boron trifluoride diethyl etherate
BzCl	Benzoyl chloride
C_{18}	C_{18}-alkyl chains modified silica for RP chromatography
CDXX	Cluster of differentiation (number = XX)
CD_3CN	Deuterated Acetonitrile
CD_3OD	Deuterated methanol
$CDCl_3$	Deuterated Chloroform
^{c}Hex	Cyclohexane
COSY	Correlated spectroscopy
CRD	Carbohydrate recognition domain
CuBr	Copper(I)bromide
Cy5	Cyanine 5 dye
DC	Dendritic cell
D_2O	Deuterium oxide
DAD	Diode array detector
DBCO	Dibenzocyclooctyne
DCM	Dichloromethane
DIPEA	*N,N*-Diisopropylethylamine
DMAP	*N,N*-Dimethylpyridin-4-amine
DMF	Dimethylformamide
DMSO	Dimethyl sulfoxide
DoM	Degree of modification
EDTA	Ethylenediaminetetraacetic acid
ELS	Evaporative light scattering
Eq.	Equivalent
ESI	Electrospray ionization
Et_2O	Diethylether
EtOAc	Ethyl acetate
EtOH	Ethanol
FCC	Flash column chromatography
H_2O (MQ)	Ultrapure water
H_2SO_4	Sulfuric acid
HCl	Hydrochloric acid
HCOOH	Formic acid
HMBC	Heteronuclear multiple bond correlation
HOPrg	Propargyl alcohol
HPLC	High performance liquid chromatography
HR	High resolution
HSA	Human serum albumin
HSQC	Heteronuclear Single Quantum Coherence
HSQC-NoDec	HSQC without decoupling
I_2	Molecular iodine
ICAM-3	Intercellular adhesion molecule 3 (CD50)
IR	Infra-red
$KMnO_4$	Potassium permanganate
M	Molar mass
MALDI-ToF-MS	Matrix assisted laser desorption ionization with time-of-flight MS
MeOH	Methanol
MS	Mass spectrometry
MsCl	Mesylchloride
MS 3 Å	Molecular sieves (Pore size 3 Å)
$Na_2S_2O_3$	Sodium thiosulfate
Na_2SO_4	Sodium sulfate
NaCl	Sodium chloride
$NaHCO_3$	Sodium bicarbonate
NaN_3	Sodium azide
NanoDSF	Nano differential scanning fluorimetry
NaOH	Sodium hydroxide
NaOMe	Sodium methoxide
NEt_3	Triethylamine
NHS	*N*-Hydroxysuccinimide

Supporting Information

NIS	*N*-Iodosuccinimide
NMR	Nuclear magnetic resonance
NOESY	Nuclear Overhauser enhancement spectroscopy
NP	Normal phase chromatography
OVA	Ovalbumin
PEG	Polyethylene glycol
pH	Potentia hydrogenii
PhSH	Thiophenol
PMDTA	N^1-[2-(Dimethylamino)ethyl]-N^1,N^2,N^2-trimethylethane-1,2-diamine
Pyr.	Pyridine
R_f	Ratio of fronts
RP	Reversed phase chromatography
TBAI	Tetrabutylammonium iodide
TBDMS	*tert*-Butyldimethylsilyl
TFA	Trifluoromethanesulfonic acid
THF	Tetrahydrofuran
TLC	Thin layer chromatography
TM	Trimannose
TOCSY	Total correlation spectroscopy
t_R	Retention time
TRIS	Tris(hydroxymethyl)amin
TS	Targeting structure
TsCl	Tosyl chloride

6 Conclusion and Outlook

Within this thesis, methods for characterizing novel ligands for RNA methyltransferases were established and apllied, providing starting points for further optimization and evaluation. In addition, characterization of multivalent targeting structures provided design insights for receptor-targeted drug delivery.

To target the RNA methyltransferase METTL3, novel PROTACs were developed and extensively characterized. The findings and design insights from this publication support further development of METTL3 degraders based on an indole–nicotinamide recruiter. Moreover, investigation of the literature compound **WD6305**[485] highlighted the importance of cooperativity over binary affinity. Deliberately designing PROTACs with weak binary affinity but high ternary affinity could reduce the hook effect, which often hinders degrading efficiency. This could be achieved if the PROTAC adopts an unfavorable conformation for binding in solution, for example due to intramolecular interactions, but becomes favorable after binding to the first protein. While the effects in MOLM-13 cells were promising, broader testing in cancer and non-malignant cell models will be important to assess efficacy and selectivity. Notably, METTL3 degraders have been reported to reduce growth more strongly in non-malignant cells than in cancer cell lines.[481] Moreover, the effect on the non-catalytic functions of METTL3 could be explored, as the ability to target those is one major advantage of PROTACs compared to classical small-molecule inhibitors.[106,107,148,242] Lastly, the parent compounds of the indole–nicotinamide chemotype developed by STORM Therapeutics and EPICS Therapeutics show promising *in vivo* results in mouse models.[155,158] One compound, STC-15, has entered clinical trials, highlighting the clinical relevance of targeting METTL3.[90,91] Hence, the *in vivo* potency of **AF151** should be evaluated in upcoming studies.

The bacterial RNA methyltransferase TrmD from the pathogen *S. aureus* was targeted using a nanomole-scale synthesis campaign in combination with a direct-to-biology assay readout. Permeability limitations were addressed by using a prodrug strategy, which could be applied to target other pathogens in future studies.[183,486,487] While selectivity of the *S. aureus* TrmD inhibitors was promising against the tested isolated enzymes and in *E. coli*, evaluation across a broader panel of gram-positive and gram-negative pathogens will be important to comprehensively assess selectivity. In addition, resistance liability should be evaluated, by long time exposure of bacteria to the compounds. The structural information gained by the crystal structure could be used to further improve selectivity and affinity, as residues Cys104 and Tyr134, unique to the *S. aureus* TrmD, are positioned in proximity to the inhibitor.[160] The inhibitors could be modified to specifically target these residues, for example, by the addition of covalent warheads. Moreover, the crystal structures could be used in a virtual screening campaign to discover new chemotypes binding to TrmD.

By using a DNA-ecoded library screening, new binding chemotypes targeting the RNA MTase DNMT2 were identified. Extensive biophysical evaluation and crystallography of the most promising hit revealed a new allosteric binding pocket and a conformational change leading to inhibition. Future studies could explore downstream cellular consequences of allosteric DNMT2 inhibition, including effects on global protein synthesis and the DNA methylome, as both have been reported to be affected in DNMT2 knockdown models.[218,219] Moreover, the physiological function of the allosteric pocket remains unknown. While binding of the known DNMT2 interaction partners NonO and eIF4E to this pocket was ruled out, a potential endogenous ligand for the allosteric site remains elusive and could be the focus of future studies.[224] While the inhibitors showed promising *in cellulo* activity, micromolar concentrations were required to reduce tRNA methylation. Future studies could therefore focus on potency optimization, for example via macrocyclization or PROTAC design. Additionally, as compound **16** showed promising permeability and selectivity, it might be developed into a chemical probe to study DNMT2 localization.

Mannose-based mono- and trivalent ligands designed to target APCs for drug delivery were investigated with respect to binding and uptake properties. While nanoDSF binding studies using monovalent receptor domains provided insight into intrinsic receptor affinity in solution, a more accurate assessment of avidity will require studies with multivalent receptor presentations (e.g., membrane-like displays via SPR[489]). In addition, the linker of the structures could be optimized in terms of length and rigidity, as the *in vitro* DC-SIGN model suggested them being too short for chelating effects. Although uptake experiments revealed clear density-dependent trends, the underlying mechanisms (e.g., steric constraints or cooperative effects) could not be fully resolved and should be addressed in future work. Moreover, immunomodulators with pH-cleavable groups (e.g cathepsin S inhibitors, which have been described before[490]) could be attached to the HSA carrier, and uptake and release in APCs could be evaluated with targeting mediated by the structures described in this study.

7 Bibliography

[1] C. H. Waddington, *Endeavour* **1942**, 18.

[2] E. R. Gibney, C. M. Nolan, *Heredity (Edinb).* **2010**, *105*, 4.

[3] S. L. Berger, T. Kouzarides, R. Shiekhattar, A. Shilatifard, *Genes Dev.* **2009**, *23*, 781.

[4] G. Bove, N. Del Gaudio, L. Altucci, *Clin. Epigenetics* **2024**, *16*, 121.

[5] D. Sanoudou, K. K. Gkouskou, A. G. Eliopoulos, C. S. Mantzoros, *Metabolism* **2022**, *132*, 155219.

[6] J. Cerneckis, G.-L. Ming, H. Song, C. He, Y. Shi, *Trends Pharmacol. Sci.* **2024**, *45*, 24.

[7] Y. Saletore, K. Meyer, J. Korlach, I. D. Vilfan, S. Jaffrey, C. E. Mason, *Genome Biol.* **2012**, *13*, 175.

[8] H. Amos, M. Korn, *Biochim. Biophys. Acta* **1958**, *29*, 444.

[9] W. E. Cohn, *J. Biol. Chem.***1960**, *235*, 1488.

[10] G. Jia, Y. Fu, X. Zhao, Q. Dai, G. Zheng, Y. Yang, et al., *Nat. Chem. Biol.* **2011**, *7*, 885.

[11] D. Dominissini, S. Moshitch-Moshkovitz, S. Schwartz, M. Salmon-Divon, L. Ungar, S. Osenberg, et al., *Nature* **2012**, *485*, 201.

[12] I. A. Roundtree, M. E. Evans, T. Pan, C. He, *Cell* **2017**, *169*, 1187.

[13] K. D. Meyer, Y. Saletore, P. Zumbo, O. Elemento, C. E. Mason, S. R. Jaffrey, *Cell* **2012**, *149*, 1635.

[14] A. Cappannini, A. Ray, E. Purta, S. Mukherjee, P. Boccaletto, S. N. Moafinejad, et al., *Nucleic Acids Res.* **2024**, *52*, D239.

[15] M. Helm, Y. Motorin, *Nat. Rev. Genet.* **2017**, *18*, 275.

[16] K. Ron, J. Kahn, N. Malka-Tunitsky, A. Sas-Chen, *FEBS Lett.* **2025**, *599*, 19.

[17] K. Li, J. Peng, C. Yi, *Fundam. Res.* **2023**, *3*, 738.

[18] Y. Zhang, L. Lu, X. Li, *Exp. Mol. Med.* **2022**, *54*, 1601.

[19] M. Helm, M. C. Schmidt-Dengler, M. Weber, Y. Motorin, *Adv. Biol.* **2021**, *5*, 2100866.

[20] J.-J. Xuan, W.-J. Sun, P.-H. Lin, K.-R. Zhou, S. Liu, L.-L. Zheng, et al., *Nucleic Acids Res.* **2018**, *46*, D327.

[21] S. Delaunay, M. Helm, M. Frye, *Nat. Rev. Genet.* **2024**, *25*, 104.

[22] R. J. Ontiveros, J. Stoute, K. F. Liu, *Biochem. J.l* **2019**, *476*, 1227.

[23] L. Cui, R. Ma, J. Cai, C. Guo, Z. Chen, L. Yao, et al., *Signal Transduct. Target. Ther.* **2022**, *7*, 334.

[24] S. H. Boo, Y. K. Kim, *Exp. Mol. Med.* **2020**, *52*, 400.

[25] C. J. T. Lewis, T. Pan, A. Kalsotra, *Nat. Rev. Mol. Cell Biol.* **2017**, *18*, 202.

[26] S. B. Shelton, C. Reinsborough, B. Xhemalce, *PLoS Genet.* **2016**, *12*, e1006139.

[27] M. Zhang, J. Song, W. Yuan, W. Zhang, Z. Sun, *Front. Immunol.* **2021**, *12*, 641507.

[28] K. Wang, Y. Wang, Y. Li, B. Fang, B. Li, W. Cheng, et al., *iScience* **2024**, *27*, 110524.

[29] L. Liu, Y. Zhao, F. Zhang, *J. Adv. Res.* **2025**, *77*, 535.

[30] Y. Chen, Z. Jiang, Y. Yang, C. Zhang, H. Liu, J. Wan, *Int. J. Biol. Macromol.* **2023**, *253*, 126773.

[31] F. Lyko, *Nat. Rev. Genet.* **2018**, *19*, 81.

[32] P. A. Boriack-Sjodin, K. K. Swinger, *Biochemistry* **2016**, *55*, 1557.

[33] C. W. Carreras, D. V. Santi, *Annu. Rev. Biochem.* **1995**, *64*, 721.

[34] J. Urbonavicius, *Nucleic Acids Res.* **2005**, *33*, 3955.

[35] A. S. Delk, D. P. Nagle, J. C. Rabinowitz, *J. Biol. Chem.* **1980**, *255*, 4387.

[36] H. L. Schubert, R. M. Blumenthal, X. Cheng, *Trends Biochem. Sci.* **2003**, *28*, 329.

[37] V. M. Richon, D. Johnston, C. J. Sneeringer, L. Jin, C. R. Majer, K. Elliston, et al., *Chem. Biol. Drug Des.* **2011**, *78*, 199.

[38] T. R. Fischer, L. Meidner, M. Schwickert, M. Weber, R. A. Zimmermann, C. Kersten, et al., *Nucleic Acids Res.* **2022**, *50*, 4216.

[39] J. Mosquera-Rendón, S. Cárdenas-Brito, J. D. Pineda, M. Corredor, A. Benítez-Páez, *BMC Res. Notes* **2014**, *7*, 440.

[40] K. L. Tkaczuk, S. Dunin-Horkawicz, E. Purta, J. M. Bujnicki, *BMC Bioinformatics* **2007**, *8*, 73.

[41] Y. I. Wolf, S. E. Brenner, P. A. Bash, E. V Koonin, *Genome Res.* **1999**, *9*, 17.

[42] C. Zubieta, J. R. Ross, P. Koscheski, Y. Yang, E. Pichersky, J. P. Noel, *Plant Cell* **2003**, *15*, 1704.

[43] T. Wlodarski, J. Kutner, J. Towpik, L. Knizewski, L. Rychlewski, A. Kudlicki, et al., *PLoS One* **2011**, *6*, e23168.

[44] J. Martin, *Curr. Opin. Struct. Biol.* **2002**, *12*, 783.

[45] M. Schapira, *ACS Chem. Biol.* **2016**, *11*, 575.

[46] Q. Sun, M. Huang, Y. Wei, *Acta Pharm. Sin. B* **2021**, *11*, 632.

[47] R. Gana, S. Rao, H. Huang, C. Wu, S. Vasudevan, *BMC Struct. Biol.* **2013**, *13*, 6.

[48] K. Lim, H. Zhang, A. Tempczyk, W. Krajewski, N. Bonander, J. Toedt, et al., *Protein Struct. Funct. Bioinform.***2003**, *51*, 56.

[49] O. Nureki, M. Shirouzu, K. Hashimoto, R. Ishitani, T. Terada, M. Tamakoshi, et al., *Acta Crystallogr. D Biol. Crystallogr.* **2002**, *58*, 1129.

[50] G. Michel, V. Sauvé, R. Larocque, Y. Li, A. Matte, M. Cygler, *Structure* **2002**, *10*, 1303.

[51] H. J. Ahn, *EMBO J.* **2003**, *22*, 2593.

[52] V. Anantharaman, E. V Koonin, L. Aravind, *J. Mol. Microbiol. Biotechnol.* **2002**, *4*, 71.

[53] X. Han, L. Liu, S. Huang, W. Xiao, Y. Gao, W. Zhou, et al., *Nat. Commun.* **2023**, *14*, 7328.

[54] K. Wang, F. Li, L. Zhou, X. Zhao, X. Gao, C. Liu, et al., *Adv. Sci* **.2023**, *10*, e2304329.

[55] L. Wang, J. Zhou, L. Kong, G. Ying, J. Sha, D. Yi, et al., *Life Sci.* **2023**, *329*, 121926.

[56] X.-Z. Chen, X.-M. Li, S.-J. Xu, S. Hu, T. Wang, R.-F. Li, et al., *Cell Death Differ.* **2023**, *30*, 1786.

[57] Y. Wang, T. Jiang, J. Xu, Y. Gu, Y. Zhou, Y. Lin, et al., *Front. Cell Dev. Biol.* **2021**, *9*, 623394.

[58] Y. Zhao, Q. Zhao, P. J. Kaboli, J. Shen, M. Li, X. Wu, et al., *Transl. Oncol.* **2019**, *12*, 1323.

[59] Y. Wang, J. Wang, X. Li, X. Xiong, J. Wang, Z. Zhou, et al., *Nat. Commun.* **2021**, *12*, 6314.

[60] V. Ortiz-Barahona, M. Soler, V. Davalos, C. A. García-Prieto, M. Janin, F. Setien, et al., *Mol. Cancer* **2023**, *22*, 83.

[61] Z. Lu, B. Liu, D. Kong, X. Zhou, D. Pei, D. Liu, *Med. Princ. Pract.* **2024**, *33*, 56.

[62] Y. Hu, C. Chen, X. Tong, S. Chen, X. Hu, B. Pan, et al., *Cell Death Dis.* **2021**, *12*, 842.

[63] M. Janin, V. Ortiz-Barahona, M. C. de Moura, A. Martínez-Cardús, P. Llinàs-Arias, M. Soler, et al., *Acta Neuropathol.* **2019**, *138*, 1053.

[64] H. Weng, H. Huang, H. Wu, X. Qin, B. S. Zhao, L. Dong, et al., *Cell Stem Cell* **2018**, *22*, 191.

[65] Z. Yu, L. Huang, Y. Xia, S. Cheng, C. Yang, C. Chen, et al., *Neurosci. Lett.* **2022**, *791*, 136907.

[66] X. Gong, M. Huang, L. Chen, *CNS Neurosci. Ther.* **2024**, *30*, e14441.

[67] M. Han, Z. Liu, Y. Xu, X. Liu, D. Wang, F. Li, et al., *Front. Neurosci.* **2020**, *14*, 98.

[68] A. M. Shafik, H. Zhou, J. Lim, B. Dickinson, P. Jin, *Hum. Mol. Genet.* **2022**, *31*, 1673.

[69] E. J. Snijder, E. Decroly, J. Ziebuhr, In *Adv Virus Res.*, 2016, Vol. 96, pp. 59–126.

[70] T. Delgado-Maldonado, A. Moreno-Herrera, G. Pujadas, L. K. Vázquez-Jiménez, A. González-González, G. Rivera, *Eur. J. Med. Chem.* **2023**, *252*, 115290.

[71] S. S. Bradrick, *Front. Microbiol.* **2017**, *8*, 2374.

[72] F. Ferron, E. Decroly, B. Selisko, B. Canard, *Antiviral Res.* **2012**, *96*, 21.

[73] I. A. Osterman, O. A. Dontsova, P. V. Sergiev, *Biochemistry (Moscow)* **2020**, *85*, 1335.

[74] Clancy Joanna, B. J. Schmieder, J. W. Petitpas, Manousos MARY, J. A. Williams, Faiella JAMES A., et al., *J. Antibiot. (Tokyo).* **1995**, *48*, 1273.

[75] M. Liu, S. Douthwaite, *Antimicrob. Agents Chemother.* **2002**, *46*, 1629.

[76] W. Zhong, A. Koay, A. Ngo, Y. Li, Q. Nah, Y. H. Wong, et al., *ACS Infect. Dis.* **2019**, *5*, 326.

[77] H. Chen, H. Liu, C. Zhang, N. Xiao, Y. Li, X. Zhao, et al., *Clin. Transl. Med.* **2024**, *14*, e1644.

[78] Y. Gao, X. Liu, J. Li, *Sci. China Life Sci.* **2025**, *9*, 2550.

[79] C. S. Pugh, R. T. Borchardt, H. O. Stone, *J. Biol. Chem.* **1978**, *253*, 4075.

[80] R. L. HAMILL, M. M. HOEHN, *J. Antibiot. (Tokyo).* **1973**, *26*, 463.

[81] J. Zhang, Y. G. Zheng, *ACS Chem. Biol.* **2016**, *11*, 583.

[82] E. Abdelraheem, B. Thair, R. F. Varela, E. Jockmann, D. Popadić, H. C. Hailes, et al., *ChemBioChem* **2022**, *23*, e202200212.

[83] A. Yu. Rudenko, S. S. Mariasina, P. V. Sergiev, V. I. Polshakov, *Mol. Biol.* **2022**, *56*, 229.

[84] M. A. Grillo, S. Colombatto, *Amino Acids* **2008**, *34*, 187.

[85] M. Fontecave, M. Atta, E. Mulliez, *Trends Biochem. Sci.* **2004**, *29*, 243.

[86] W. A. M. Loenen, *Biochem. Soc. Trans.* **2006**, *34*, 330.

[87] T. C. Petrossian, S. G. Clarke, *Mol. Cell. Proteomics* **2011**, *10*, M110.000976.

[88] Y. Sun, J. W. Locasale, *Cell Stress* **2021**, *6*, 1.

[89] J. M. McMillan, U. K. Walle, T. Walle, *J. Pharm. Pharmacol.* **2005**, *57*, 599.

[90] J. C. Moser, K. P. Papadopoulos, J. Rodon Ahnert, Y. Ofir-Rosenfeld, J.-B. Holz, *J. Clin. Oncol.* **2024**, *42*, 2586.

[91] Y. Ofir-Rosenfeld, L. Vasiliauskaitė, C. Saunders, A. Sapetschnig, G. Tsagkogeorga, M. Albertella, et al., *Eur. J. Cancer* **2022**, *174*, S123.

[92] J. Liu, Y. Yue, D. Han, X. Wang, Y. Fu, L. Zhang, et al., *Nat. Chem. Biol.* **2014**, *10*, 93.

[93] P. Śledź, M. Jinek, *Elife* **2016**, *5*, e18434.

[94] P. Wang, K. A. Doxtader, Y. Nam, *Mol. Cell* **2016**, *63*, 306.

[95] X. Wang, J. Feng, Y. Xue, Z. Guan, D. Zhang, Z. Liu, et al., *Nature* **2016**, *534*, 575.

[96] S. Su, S. Li, T. Deng, M. Gao, Y. Yin, B. Wu, et al., *Cell Res.* **2022**, *32*, 982.

[97] Y. Yue, J. Liu, X. Cui, J. Cao, G. Luo, Z. Zhang, et al., *Cell Discov.* **2018**, *4*, 10.

[98] P. Knuckles, T. Lence, I. U. Haussmann, D. Jacob, N. Kreim, S. H. Carl, et al., *Genes Dev.* **2018**, *32*, 415.

[99] J. E. Harper, S. M. Miceli, R. J. Roberts, J. L. Manley, *Nucleic Acids Res.* **1990**, *18*, 5735.

[100] B. Linder, A. V Grozhik, A. O. Olarerin-George, C. Meydan, C. E. Mason, S. R. Jaffrey, *Nat. Methods* **2015**, *12*, 767.

[101] X. Wang, B. S. Zhao, I. A. Roundtree, Z. Lu, D. Han, H. Ma, et al., *Cell* **2015**, *161*, 1388.

[102] J. Zhou, J. Wan, X. Gao, X. Zhang, S. R. Jaffrey, S.-B. Qian, *Nature* **2015**, *526*, 591.

[103] X. Wang, Z. Lu, A. Gomez, G. C. Hon, Y. Yue, D. Han, et al., *Nature* **2014**, *505*, 117.

[104] I. A. Roundtree, G.-Z. Luo, Z. Zhang, X. Wang, T. Zhou, Y. Cui, et al., *Elife* **2017**, *6*, e31311.

[105] W. Xiao, S. Adhikari, U. Dahal, Y.-S. Chen, Y.-J. Hao, B.-F. Sun, et al., *Mol. Cell* **2016**, *61*, 507.

[106] X. Wei, Y. Huo, J. Pi, Y. Gao, S. Rao, M. He, et al., *Nat. Cell Biol.* **2022**, *24*, 1278.

[107] S. Lin, J. Choe, P. Du, R. Triboulet, R. I. Gregory, *Mol. Cell* **2016**, *62*, 335.

[108] J. Choe, S. Lin, W. Zhang, Q. Liu, L. Wang, J. Ramirez-Moya, et al., *Nature* **2018**, *561*, 556.

[109] Y. Yang, P. J. Hsu, Y.-S. Chen, Y.-G. Yang, *Cell Res.* **2018**, *28*, 616.

[110] L. Qiu, Q. Jing, Y. Li, J. Han, *Mol. Biomed.* **2023**, *4*, 25.

[111] M. Esteva-Socias, F. Aguilo, *NAR Cancer* **2024**, *6*, zcae009.

[112] N. Li, X. Wei, J. Dai, J. Yang, S. Xiong, *Mol. Cell. Biochem.* **2025**, *480*, 3429.

[113] F. Fiorentino, M. Menna, D. Rotili, S. Valente, A. Mai, *J. Med. Chem.* **2023**, *66*, 1654.

[114] C. Xue, Q. Chu, Q. Zheng, S. Jiang, Z. Bao, Y. Su, et al., *Signal Transduct. Target. Ther.* **2022**, *7*, 142.

[115] Y. Li, H. Jin, Q. Li, L. Shi, Y. Mao, L. Zhao, *Mol. Cancer* **2024**, *23*, 130.

[116] W. Xie, L. L. Ma, Y. Q. Xu, B. H. Wang, S. M. Li, *Biochem. Biophys. Res. Commun.* **2019**, *518*, 120.

[117] X. Li, Y. Jiang, X. Sun, Y. Wu, Z. Chen, *Metabolism* **2021**, *116*, 154702.

[118] W. Cheng, M. Li, L. Zhang, C. Zhou, S. Yu, X. Peng, et al., *Front. Pharmacol.* **2022**, *13*, 973116.

[119] T. Rønningen, M. B. Dahl, T. G. Valderhaug, A. Cayir, M. Keller, A. Tönjes, et al., *Front. Endocrinol. (Lausanne).* **2021**, *12*, 778875.

[120] Y. Qin, B. Li, S. Arumugam, Q. Lu, S. M. Mankash, J. Li, et al., *Cell Rep.* **2021**, *37*, 109968.

[121] G. Luo, J. Chen, Z. Ren, *Diabetes Metab. Syndr. Obes.* **2021**, *Volume 14*, 4843.

[122] X. Zhang, H. Hao, L. Ma, Y. Zhang, X. Hu, Z. Chen, et al., *mBio* **2021**, *12*, e0106721.

[123] H. M. Burgess, D. P. Depledge, L. Thompson, K. P. Srinivas, R. C. Grande, E. I. Vink, et al., *Genes Dev.* **2021**, *35*, 1005.

[124] N. Li, H. Hui, B. Bray, G. M. Gonzalez, M. Zeller, K. G. Anderson, et al., *Cell Rep.* **2021**, *35*, 109091.

[125] Y. Qin, Y. Qiao, L. Li, E. Luo, D. Wang, Y. Yao, et al., *Life Sci.* **2021**, *274*, 119366.

[126] J. Chen, K. Lai, X. Yong, H. Yin, Z. Chen, H. Wang, et al., *Cardiovasc. Drugs Ther.* **2023**, *37*, 471.

[127] C.-S. Chien, J. Y.-S. Li, Y. Chien, M.-L. Wang, A. A. Yarmishyn, P.-H. Tsai, et al., *PNAS* **2021**, *118*, e2025070118.

[128] M. Fang, J. Deng, Q. Zhou, Z. Hu, L. Yang, *Aging* **2022**, *14*, 2548.

[129] T. Li, Y. Zhuang, W. Yang, Y. Xie, W. Shang, S. Su, et al., *The FASEB Journal* **2021**, *35*, e21162.

[130] H. Shen, K. Xie, M. Li, Q. Yang, X. Wang, *Cell Death Discov.* **2022**, *8*, 322.

[131] X. Wang, Y. Li, J. Li, S. Li, F. Wang, *Cardiovasc. Drugs Ther.* **2023**, *37*, 435.

[132] T. Yu, J. Liu, Y. Wang, W. Chen, Z. Liu, L. Zhu, et al., *Biochem. Biophys. Res. Commun.* **2022**, *614*, 9.

[133] M. Li, M. Xia, Z. Zhang, Y. Tan, E. Li, Z. Guo, et al., *Int. J. Oncol.* **2022**, *61*, 106.

[134] Y. Wang, B. Zhang, Y. Zhu, Y. Zhang, L. Li, T. Shen, et al., *Oncol. Lett.* **2022**, *23*, 186.

[135] Y. Liu, E. Zhai, J. Chen, Y. Qian, R. Zhao, Y. Ma, et al., *Cancer Commun.* **2022**, *42*, 327.

[136] N. Wang, X. Huo, B. Zhang, X. Chen, S. Zhao, X. Shi, et al., *Front. Oncol.* **2022**, *12*, 861807.

[137] S. Li, F. Jiang, F. Chen, Y. Deng, X. Pan, *J. Biochem. Mol. Toxicol.* **2022**, *36*, e22922.

[138] H. Li, C. Wang, L. Lan, L. Yan, W. Li, I. Evans, et al., *Cell. Mol. Life Sci.* **2022**, *79*, 135.

[139] X. Cai, X. Wang, C. Cao, Y. Gao, S. Zhang, Z. Yang, et al., *Cancer Lett.* **2018**, *415*, 11.

[140] F. Cheng, L. Peng, D. Luo, *Clin. Exp. Pharmacol. Physiol.* **2022**, *49*, 748.

[141] S. Li, X. Lu, D. Zheng, W. Chen, Y. Li, F. Li, *J. Cancer Res. Clin. Oncol.* **2022**, *148*, 3485.

[142] H. Zhang, S.-Q. Wang, L. Wang, H. Lin, J.-B. Zhu, R. Chen, et al., *Cell Death Dis.* **2022**, *13*, 657.

[143] Y. Shi, C. Zheng, Y. Jin, B. Bao, D. Wang, K. Hou, et al., *Front. Oncol.* **2020**, *10*, 1126.

[144] R. Deng, Y. Cheng, S. Ye, J. Zhang, R. Huang, P. Li, et al., *Onco. Targets. Ther.* **2019**, *Volume 12*, 4391.

[145] Q. Cui, H. Shi, P. Ye, L. Li, Q. Qu, G. Sun, et al., *Cell Rep.* **2017**, *18*, 2622.

[146] I. Barbieri, K. Tzelepis, L. Pandolfini, J. Shi, G. Millán-Zambrano, S. C. Robson, et al., *Nature* **2017**, *552*, 126.

[147] L. P. Vu, B. F. Pickering, Y. Cheng, S. Zaccara, D. Nguyen, G. Minuesa, et al., *Nat. Med.* **2017**, *23*, 1369.

[148] W. Hua, Y. Zhao, X. Jin, D. Yu, J. He, D. Xie, et al., *Gynecol. Oncol.* **2018**, *151*, 356.

[149] J. Huang, X. Dong, Z. Gong, L.-Y. Qin, S. Yang, Y.-L. Zhu, et al., *Protein Cell* **2019**, *10*, 272.

[150] I. Corbeski, P. A. Vargas-Rosales, R. K. Bedi, J. Deng, D. Coelho, E. Braud, et al., *Elife* **2024**, *12*, RP92537.

[151] G. Li, W. Chen, D. Liu, S. Tang, *Eur. J. Med. Chem.* **2025**, *290*, 117560.

[152] R. K. Bedi, D. Huang, S. A. Eberle, L. Wiedmer, P. Śledź, A. Caflisch, *ChemMedChem* **2020**, *15*, 744.

[153] E. V. Moroz-Omori, D. Huang, R. Kumar Bedi, S. J. Cheriyamkunnel, E. Bochenkova, A. Dolbois, et al., *ChemMedChem* **2021**, *16*, 3035.

[154] A. Dolbois, R. K. Bedi, E. Bochenkova, A. Müller, E. V. Moroz-Omori, D. Huang, et al., *J. Med. Chem.* **2021**, *64*, 12738.

[155] E. Yankova, W. Blackaby, M. Albertella, J. Rak, E. De Braekeleer, G. Tsagkogeorga, et al., *Nature* **2021**, *593*, 597.

[156] W. P. Blackaby, D. J. Hardick, E. J. Thomas, F. A. Brookfield, J. Shepherd, C. Bubert, et al., *WIPO - World Intellectual Property Organization.* Polyheterocyclic compounds as mettl3 inhibitors **2021**. WO2021111124A1

[157] STORM Therapeutics LTD, STC-15 as a Part of Combination Therapy With Toripalimab in Selected Advanced Cancers, 2025. *Bethesda (MD): National Library of Medicine (US), ClinicalTrials.gov [Internet], ID: NCT06975293*.

[158] G. Dutheuil, K. Oukoloff, J. Korac, F. Lenoir, M. El Bousmaqui, N. Probst, et al., *J. Med. Chem.* **2025**, *68*, 2981.

[159] A. S. Byström, G. R. Björk, *Mol. Gen. Genet.* **1982**, *188*, 440.

[160] Y. Zhang, R. Agrebi, L. E. Bellows, J.-F. Collet, V. Kaever, A. Gründling, *Journal of Biological Chemistry* **2017**, *292*, 313.

[161] G. R. Bjork, *EMBO J.* **2001**, *20*, 231.

[162] Y.-M. Hou, R. Matsubara, R. Takase, I. Masuda, J. I. Sulkowska, In *Enzymes*, **2017**, pp. 89–115.

[163] M. Redlak, C. Andraos-Selim, R. Giege, C. Florentz, W. M. Holmes, *Biochemistry* **1997**, *36*, 8699.

[164] T. Ito, I. Masuda, K. Yoshida, S. Goto-Ito, S. Sekine, S. W. Suh, et al., *PNAS* **2015**, *112*, E4197.

[165] H. B. Gamper, I. Masuda, M. Frenkel-Morgenstern, Y.-M. Hou, *Nat. Commun.* **2015**, *6*, 7226.

[166] G. R. Björk, P. M. Wikström, A. S. Byström, *Science (1979).* **1989**, *244*, 986.

[167] H. B. Gamper, I. Masuda, M. Frenkel-Morgenstern, Y.-M. Hou, *Int. J. Mol. Sci.* **2015**, *16*, 14866.

[168] B. E. Clifton, M. A. Fariz, G.-I. Uechi, P. Laurino, *Nucleic Acids Res.* **2021**, *49*, 12467.

[169] S. E. Thomas, A. J. Whitehouse, K. Brown, S. Burbaud, J. M. Belardinelli, J. Sangen, et al., *Nucleic Acids Res.* **2020**, *48*, 8099.

[170] J. Jaroensuk, Y. H. Wong, W. Zhong, C. W. Liew, S. Maenpuen, A. E. Sahili, et al., *RNA* **2019**, *25*, 1481.

[171] K. O'Dwyer, J. M. Watts, S. Biswas, J. Ambrad, M. Barber, H. Brulé, et al., *J. Bacteriol.* **2004**, *186*, 2346.

[172] A. S. Byström, G. R. Björk, *Mol. Gen. Genet.* **1982**, *188*, 447.

[173] T. A. White, D. B. Kell, *Comp. Funct. Genomics* **2004**, *5*, 304.

[174] T. Christian, C. Evilia, S. Williams, Y.-M. Hou, *J. Mol. Biol.* **2004**, *339*, 707.

[175] T. Christian, Y.-M. Hou, *J. Mol. Biol.* **2007**, *373*, 623.

[176] R. Sakaguchi, A. Giessing, Q. Dai, G. Lahoud, Z. Liutkeviciute, S. Klimasauskas, et al., *RNA* **2012**, *18*, 1687.

[177] G. Lahoud, S. Goto-Ito, K. Yoshida, T. Ito, S. Yokoyama, Y.-M. Hou, *RNA* **2011**, *17*, 1236.

[178] M. Naghavi, S. E. Vollset, K. S. Ikuta, L. R. Swetschinski, A. P. Gray, E. E. Wool, et al., *The Lancet* **2024**, *404*, 1199.

[179] P. A. Elkins, J. M. Watts, M. Zalacain, A. van Thiel, P. R. Vitazka, M. Redlak, et al., *J. Mol. Biol.* **2003**, *333*, 931.

[180] T. Christian, R. Sakaguchi, A. P. Perlinska, G. Lahoud, T. Ito, E. A. Taylor, et al., *Nat. Struct. Mol. Biol.* **2016**, *23*, 941.

[181] R. Sakaguchi, G. Lahoud, T. Christian, H. Gamper, Y.-M. Hou, *Chem. Biol.* **2014**, *21*, 1351.

[182] P. J. Hill, A. Abibi, R. Albert, B. Andrews, M. M. Gagnon, N. Gao, et al., *J. Med. Chem.* **2013**, *56*, 7278.

[183] W. Zhong, K. K. Pasunooti, S. Balamkundu, Y. H. Wong, Q. Nah, V. Gadi, et al., *J. Med. Chem.* **2019**, *62*, 7788.

[184] A. J. Whitehouse, S. E. Thomas, K. P. Brown, A. Fanourakis, D. S.-H. Chan, M. D. J. Libardo, et al., *J. Med. Chem.* **2019**, *62*, 7210.

[185] S. E. Thomas, A. J. Whitehouse, K. Brown, S. Burbaud, J. M. Belardinelli, J. Sangen, et al., *Nucleic Acids Res.* **2020**, *48*, 8099.

[186] A. J. Wilkinson, N. Ooi, J. Finlayson, V. E. Lee, D. Lyth, K. S. Maskew, et al., *Bioorg. Med. Chem. Lett.* **2023**, *90*, 129331.

[187] R. S. W. Tsang, Y. A. Li, A. Mullen, M. Baikie, K. Whyte, M. Shuel, et al., *Int. J. Circumpolar Health* **2016**, *75*, 29798.

[188] S. Sethi, N. Evans, B. J. B. Grant, T. F. Murphy, *N. Engl. J. Med.* **2002**, *347*, 465.

[189] F. Sánchez, J. Mensa, J. A. Martínez, J. Angrill, M. A. Marcos, F. Marco, et al., *Rev. Esp. Quimioter.* **1999**, *12*, 369.

[190] H. Nikaido, D. G. Thanassi, *Antimicrob. Agents Chemother.* **1993**, *37*, 1393.

[191] A. R. Spaulding, E. A. Satterwhite, Y.-C. Lin, O. N. Chuang-Smith, K. L. Frank, J. A. Merriman, et al., *Front. Cell. Infect. Microbiol.* **2012**, *2*, 18.

[192] S. Y. C. Tong, J. S. Davis, E. Eichenberger, T. L. Holland, V. G. Fowler, *Clin. Microbiol. Rev.* **2015**, *28*, 603.

[193] S. S. Huang, V. L. Hinrichsen, R. Datta, L. Spurchise, I. Miroshnik, K. Nelson, et al., *PLoS One* **2011**, *6*, e24340.

[194] M. G. Goll, F. Kirpekar, K. A. Maggert, J. A. Yoder, C.-L. Hsieh, X. Zhang, et al., *Science (1979).* **2006**, *311*, 395.

[195] A. Jeltsch, A. Ehrenhofer-Murray, T. P. Jurkowski, F. Lyko, G. Reuter, S. Ankri, et al., *RNA Biol.* **2017**, *14*, 1108.

[196] H. Li, D. Zhu, J. Wu, Y. Ma, C. Cai, Y. Chen, et al., *RNA Biol.* **2021**, *18*, 2531.

[197] M. Becker, S. Müller, W. Nellen, T. P. Jurkowski, A. Jeltsch, A. E. Ehrenhofer-Murray, *Nucleic Acids Res.* **2012**, *40*, 11648.

[198] M. Schaefer, T. Pollex, K. Hanna, F. Tuorto, M. Meusburger, M. Helm, et al., *Genes Dev.* **2010**, *24*, 1590.

[199] S. Muller, I. M. Windhof, V. Maximov, T. Jurkowski, A. Jeltsch, K. U. Forstner, et al., *Nucleic Acids Res.* **2013**, *41*, 8615.

[200] I. Van den Wyngaert, J. Sprengel, S. U. Kass, W. H. M. L. Luyten, *FEBS Lett.* **1998**, *426*, 283.

[201] J. Yoder, *Hum. Mol. Genet.* **1998**, *7*, 279.

[202] G. Raddatz, P. M. Guzzardo, N. Olova, M. R. Fantappié, M. Rampp, M. Schaefer, et al., *PNAS* **2013**, *110*, 8627.

[203] M. Schaefer, F. Lyko, *Nat. Genet.* **2010**, *42*, 920.

[204] A. Zemach, I. E. McDaniel, P. Silva, D. Zilberman, *Science (1979).* **2010**, *328*, 916.

[205] H. Khalil, M. Tazi, K. Caution, A. Ahmed, A. Kanneganti, K. Assani, et al., *Epigenetics* **2016**, *11*, 381.

[206] A. Salzberg, O. Fisher, R. Siman-Tov, S. Ankri, *Biochem. Biophys. Res. Commun.* **2004**, *322*, 465.

[207] M. Kuhlmann, *Nucleic Acids Res.* **2005**, *33*, 6405.

[208] N. Kunert, J. Marhold, J. Stanke, D. Stach, F. Lyko, *Development* **2003**, *130*, 5083.

[209] F. Claudio-Piedras, B. Recio-Tótoro, R. Condé, J. M. Hernández-Tablas, G. Hurtado-Sil, H. Lanz-Mendoza, *Front. Immunol.* **2019**, *10*, 3025.

[210] S. Xue, H. Xu, Z. Sun, H. Shen, S. Chen, J. Ouyang, et al., *Biochem. Biophys. Res. Commun.* **2019**, *520*, 60.

[211] Y. Zhang, X. Zhang, J. Shi, F. Tuorto, X. Li, Y. Liu, et al., *Nat. Cell Biol.* **2018**, *20*, 535.

[212] J. Kiani, V. Grandjean, R. Liebers, F. Tuorto, H. Ghanbarian, F. Lyko, et al., *PLoS Genet.* **2013**, *9*, e1003498.

[213] H. Chen, H. Yang, X. Zhu, T. Yadav, J. Ouyang, S. S. Truesdell, et al., *Nat. Commun.* **2020**, *11*, 2834.

[214] K. Rai, S. Chidester, C. V. Zavala, E. J. Manos, S. R. James, A. R. Karpf, et al., *Genes Dev.* **2007**, *21*, 261.

[215] M. Schaefer, J. P. Steringer, F. Lyko, *PLoS One* **2008**, *3*, e1414.

[216] H. Li, H. Liu, D. Zhu, C. Dou, B. Gang, M. Zhang, et al., *Pharmacol. Res.* **2024**, *205*, 107222.

[217] F. Tuorto, F. Herbst, N. Alerasool, S. Bender, O. Popp, G. Federico, et al., *EMBO J.* **2015**, *34*, 2350.

[218] F. Tuorto, R. Liebers, T. Musch, M. Schaefer, S. Hofmann, S. Kellner, et al., *Nat. Struct. Mol. Biol.* **2012**, *19*, 900.

[219] T. Zabek, T. Szmatola, J. Adamczyk-Grochala, A. Lewinska, M. Wnuk, *J. Neurooncol.* **2023**, *163*, 61.

[220] J. Adamczyk-Grochala, D. Bloniarz, K. Zielinska, A. Lewinska, M. Wnuk, *Apoptosis* **2023**, *28*, 166.

[221] A. Lewinska, J. Adamczyk-Grochala, M. Wnuk, *Biochim. Biophys. Acta - Rev. Cancer.* **2023**, *1878*, 188964.

[222] Z. Durdevic, K. Hanna, B. Gold, T. Pollex, S. Cherry, F. Lyko, et al., *EMBO Rep.* **2013**, *14*, 269.

[223] R. R. Dev, R. Ganji, S. P. Singh, S. Mahalingam, S. Banerjee, S. Khosla, *Biochem. J.* **2017**, *474*, 2009.

[224] D. Thiagarajan, R. R. Dev, S. Khosla, *Epigenetics* **2011**, *6*, 103.

[225] S. Johannsson, P. Neumann, A. Wulf, L. M. Welp, H.-D. Gerber, M. Krull, et al., *Sci. Rep.* **2018**, *8*, 8880.

[226] E. C. Schulz, H. M. Roth, S. Ankri, R. Ficner, *PLoS One* **2012**, *7*, e38728.

[227] S. Li, J. Du, H. Yang, J. Yin, J. Ding, J. Zhong, *J. Mol. Cell Biol.* **2013**, *5*, 64.

[228] A. Dong, *Nucleic Acids Res.* **2001**, *29*, 439.

[229] A. Jeltsch, *ChemBioChem* **2002**, *3*, 274.

[230] T. P. Jurkowski, M. Meusburger, S. Phalke, M. Helm, W. Nellen, G. Reuter, et al., *RNA* **2008**, *14*, 1663.

[231] T. P. Jurkowski, R. Shanmugam, M. Helm, A. Jeltsch, *Biochemistry* **2012**, *51*, 4438.

[232] V. Khoddami, B. R. Cairns, *Nat. Biotechnol.* **2013**, *31*, 458.

[233] M. Schaefer, S. Hagemann, K. Hanna, F. Lyko, *Cancer Res.* **2009**, *69*, 8127.

[234] H. Abdulhaq, J. M. Rossetti, *Expert Opin. Investig. Drugs* **2007**, *16*, 1967.

[235] V. Khoddami, B. R. Cairns, *Nat. Protoc.* **2014**, *9*, 337.

[236] M. Schwickert, T. R. Fischer, R. A. Zimmermann, S. N. Hoba, J. L. Meidner, M. Weber, et al., *J. Med. Chem.* **2022**, *65*, 9750.

[237] L. Halby, N. Marechal, D. Pechalrieu, V. Cura, D.-M. Franchini, C. Faux, et al., *Phil. Trans. R. Soc. B.* **2018**, *373*, 20170072.

[238] M. Schwickert, R. A. Zimmermann, T. Habeck, S. N. Hoba, Z. Nidoieva, T. R. Fischer, et al., *ACS Med. Chem. Lett.* **2023**, *14*, 777.

[239] R. A. Zimmermann, T. R. Fischer, M. Schwickert, Z. Nidoieva, T. Schirmeister, C. Kersten, *Int. J. Mol. Sci.* **2023**, *24*, 6109.

[240] Z. Hu, C. M. Crews, *ChemBioChem* **2022**, *23*, e202100270.

[241] M. Békés, D. R. Langley, C. M. Crews, *Nat. Rev. Drug Discov.* **2022**, *21*, 181.

[242] M. Pettersson, C. M. Crews, *Drug Discov. Today Technol.* **2019**, *31*, 15.

[243] K. Li, C. M. Crews, *Chem. Soc. Rev.* **2022**, *51*, 5214.

[244] N. Kim, K. E. Lukong, *Oncol. Rev.* **2025**, *19*, 1564642.

[245] N. Bhatia, S. Hazra, S. Thareja, *Eur. J. Med. Chem.* **2023**, *256*, 115422.

[246] K. M. Sakamoto, K. B. Kim, A. Kumagai, F. Mercurio, C. M. Crews, R. J. Deshaies, *PNAS* **2001**, *98*, 8554.

[247] A. Ciechanover, A. Orian, A. L. Schwartz, *BioEssays* **2000**, *22*, 442.

[248] K. Breitschopf, E. Bengal, T. Ziv, A. Admon, A. Ciechanover, *EMBO J.* **1998**, *17*, 5964.

[249] A. R. Schneekloth, M. Pucheault, H. S. Tae, C. M. Crews, *Bioorg. Med. Chem. Lett.* **2008**, *18*, 5904.

[250] J. Hines, J. D. Gough, T. W. Corson, C. M. Crews, *PNAS* **2013**, *110*, 8942.

[251] M. S. Gadd, A. Testa, X. Lucas, K.-H. Chan, W. Chen, D. J. Lamont, et al., *Nat. Chem. Biol.* **2017**, *13*, 514.

[252] Y. Zhong, F. Chi, H. Wu, Y. Liu, Z. Xie, W. Huang, et al., *Eur. J. Med. Chem.* **2022**, *231*, 114142.

[253] Y. Ding, Y. Fei, B. Lu, *Trends Pharmacol. Sci.* **2020**, *41*, 464.

[254] X. Liu, A. Ciulli, *ACS Cent. Sci.* **2023**, *9*, 1269.

[255] S. L. Schreiber, G. R. Crabtree, *Immunol. Today* **1992**, *13*, 136.

[256] J. M. Sasso, R. Tenchov, D. Wang, L. S. Johnson, X. Wang, Q. A. Zhou, *Biochemistry* **2023**, *62*, 601.

[257] S. M. Banik, K. Pedram, S. Wisnovsky, G. Ahn, N. M. Riley, C. R. Bertozzi, *Nature* **2020**, *584*, 291.

[258] K. Raina, C. D. Forbes, R. Stronk, J. P. Rappi, K. J. Eastman, N. Zaware, et al., *Cell Chem. Biol.* **2024**, *31*, 1490.

[259] *Johnson & Johnson*, Johnson & Johnson completes acquisition of Halda Therapeutics and its novel platform to revolutionize cancer treatment and enable next-generation oral therapies. [online] https://www.jnj.com/media-center/press-releases/johnson-johnson-completes-acquisition-of-halda-therapeutics-and-its-novel-platform-to-revolutionize-cancer-treatment-and-enable-next-generation-oral-therapies. Accessed: 12.01.2026

[260] D. P. Bondeson, A. Mares, I. E. D. Smith, E. Ko, S. Campos, A. H. Miah, et al., *Nat. Chem. Biol.* **2015**, *11*, 611.

[261] E. F. Douglass, C. J. Miller, G. Sparer, H. Shapiro, D. A. Spiegel, *J. Am. Chem. Soc.* **2013**, *135*, 6092.

[262] Y. Zhang, C. Loh, J. Chen, N. Mainolfi, *Drug Discov. Today Technol.* **2019**, *31*, 53.

[263] S. J. Hughes, A. Ciulli, *Essays Biochem.* **2017**, *61*, 505.

[264] L. E. M. Miles, *Ric. Clin. Lab.* **1975**, *5*, 59.

[265] R. D. Roy, C. Rosenmund, M. I. Stefan, *BMC Syst. Biol.* **2017**, *11*, 74.

[266] D. P. Bondeson, B. E. Smith, G. M. Burslem, A. D. Buhimschi, J. Hines, S. Jaime-Figueroa, et al., *Cell Chem. Biol.* **2018**, *25*, 78.

[267] K.-H. Chan, M. Zengerle, A. Testa, A. Ciulli, *J. Med. Chem.* **2018**, *61*, 504.

[268] V. Zoppi, S. J. Hughes, C. Maniaci, A. Testa, T. Gmaschitz, C. Wieshofer, et al., *J. Med. Chem.* **2019**, *62*, 699.

[269] M. J. Roy, S. Winkler, S. J. Hughes, C. Whitworth, M. Galant, W. Farnaby, et al., *ACS Chem. Biol.* **2019**, *14*, 361.

[270] R. P. Nowak, S. L. DeAngelo, D. Buckley, Z. He, K. A. Donovan, J. An, et al., *Nat. Chem. Biol.* **2018**, *14*, 706.

[271] W. Farnaby, M. Koegl, M. J. Roy, C. Whitworth, E. Diers, N. Trainor, et al., *Nat. Chem. Biol.* **2019**, *15*, 672.

[272] A. Zorba, C. Nguyen, Y. Xu, J. Starr, K. Borzilleri, J. Smith, et al., *PNAS* **2018**, *115*, E7285.

[273] A. P. Crew, K. Raina, H. Dong, Y. Qian, J. Wang, D. Vigil, et al., *J. Med. Chem.* **2018**, *61*, 583.

[274] K. M. Riching, S. Mahan, C. R. Corona, M. McDougall, J. D. Vasta, M. B. Robers, et al., *ACS Chem. Biol.* **2018**, *13*, 2758.

[275] H. Zhao, *ChemMedChem* **2024**, *19*, e202400171.

[276] K. M. Riching, E. A. Caine, M. Urh, D. L. Daniels, *Chem. Soc. Rev.* **2022**, *51*, 6210.

[277] C. Crowe, M. A. Nakasone, S. Chandler, C. Craigon, G. Sathe, M. H. Tatham, et al., *Sci. Adv.* **2024**, *10*, eado6492.

[278] M. Li, Y. Zhi, B. Liu, Q. Yao, *J. Med. Chem.* **2023**, *66*, 2308.

[279] A. Rodríguez-Gimeno, C. Galdeano, *ChemBioChem* **2025**, *26*, e202400656.

[280] M. J. Clague, C. Heride, S. Urbé, *Trends Cell Biol.* **2015**, *25*, 417.

[281] G. Weng, C. Shen, D. Cao, J. Gao, X. Dong, Q. He, et al., *Nucleic Acids Res.* **2021**, *49*, D1381.

[282] T. Ishida, A. Ciulli, *SLAS Discovery* **2021**, *26*, 484.

[283] J. S. Schneekloth, F. N. Fonseca, M. Koldobskiy, A. Mandal, R. Deshaies, K. Sakamoto, et al., *J. Am. Chem. Soc.* **2004**, *126*, 3748.

[284] A. Klepach, H. Tran, F. Ahmad Mohammed, M. E. H. ElSayed, *Adv. Drug Deliv. Rev.* **2022**, *186*, 114322.

[285] C. E. Stebbins, W. G. Kaelin, N. P. Pavletich, *Science (1979).* **1999**, *284*, 455.

[286] T. Kamura, D. M. Koepp, M. N. Conrad, D. Skowyra, R. J. Moreland, O. Iliopoulos, et al., *Science (1979).* **1999**, *284*, 657.

[287] T. A. F. Cardote, M. S. Gadd, A. Ciulli, *Structure* **2017**, *25*, 901.

[288] P. H. Maxwell, M. S. Wiesener, G.-W. Chang, S. C. Clifford, E. C. Vaux, M. E. Cockman, et al., *Nature* **1999**, *399*, 271.

[289] P. Soares, M. S. Gadd, J. Frost, C. Galdeano, L. Ellis, O. Epemolu, et al., *J. Med. Chem.* **2018**, *61*, 599.

[290] C. Galdeano, M. S. Gadd, P. Soares, S. Scaffidi, I. Van Molle, I. Birced, et al., *J. Med. Chem.* **2014**, *57*, 8657.

[291] I. Van Molle, A. Thomann, D. L. Buckley, E. C. So, S. Lang, C. M. Crews, et al., *Chem. Biol.* **2012**, *19*, 1300.

[292] D. L. Buckley, J. L. Gustafson, I. Van Molle, A. G. Roth, H. S. Tae, P. C. Gareiss, et al., *Angew. Chem. Int. Ed.* **2012**, *51*, 11463.

[293] D. L. Buckley, I. Van Molle, P. C. Gareiss, H. S. Tae, J. Michel, D. J. Noblin, et al., *J. Am. Chem. Soc.* **2012**, *134*, 4465.

[294] M. Zengerle, K.-H. Chan, A. Ciulli, *ACS Chem. Biol.* **2015**, *10*, 1770.

[295] S. Angers, T. Li, X. Yi, M. J. MacCoss, R. T. Moon, N. Zheng, *Nature* **2006**, *443*, 590.

[296] W. Lenz, In *Problems of Birth Defects*, Springer Netherlands, Dordrecht, **1962**, pp. 199–199.

[297] T. Ito, H. Ando, T. Suzuki, T. Ogura, K. Hotta, Y. Imamura, et al., *Science (1979).* **2010**, *327*, 1345.

[298] P. S. M. Clark, P. A. Steinbach, P. B. A. B. Clemmons, *J. Adv. Pract. Oncol.* **2014**, *5*, 51.

[299] M. Cives, V. Simone, O. Brunetti, V. Longo, F. Silvestris, *Crit. Rev. Oncol. Hematol.* **2013**, *85*, 9.

[300] S. Singhal, J. Mehta, R. Desikan, D. Ayers, P. Roberson, P. Eddlemon, et al., *N. Engl. J. Med.* **1999**, *341*, 1565.

[301] G. Lu, R. E. Middleton, H. Sun, M. Naniong, C. J. Ott, C. S. Mitsiades, et al., *Science (1979).* **2014**, *343*, 305.

[302] J. Krönke, N. D. Udeshi, A. Narla, P. Grauman, S. N. Hurst, M. McConkey, et al., *Science (1979).* **2014**, *343*, 301.

[303] G. E. Winter, D. L. Buckley, J. Paulk, J. M. Roberts, A. Souza, S. Dhe-Paganon, et al., *Science (1979).* **2015**, *348*, 1376.

[304] J. Lu, Y. Qian, M. Altieri, H. Dong, J. Wang, K. Raina, et al., *Chem. Biol.* **2015**, *22*, 755.

[305] P. P. Chamberlain, A. Lopez-Girona, K. Miller, G. Carmel, B. Pagarigan, B. Chie-Leon, et al., *Nat. Struct. Mol. Biol.* **2014**, *21*, 803.

[306] E. S. Fischer, K. Böhm, J. R. Lydeard, H. Yang, M. B. Stadler, S. Cavadini, et al., *Nature* **2014**, *512*, 49.

[307] C. J. Diehl, A. Ciulli, *Chem. Soc. Rev.* **2022**, *51*, 8216.

[308] C. Pacini, J. M. Dempster, I. Boyle, E. Gonçalves, H. Najgebauer, E. Karakoc, et al., *Nat. Commun.* **2021**, *12*, 1661.

[309] L. Zhang, B. Riley-Gillis, P. Vijay, Y. Shen, *Mol. Cancer Ther.* **2019**, *18*, 1302.

[310] R. Shirasaki, G. M. Matthews, S. Gandolfi, R. de Matos Simoes, D. L. Buckley, J. Raja Vora, et al., *Cell Rep.* **2021**, *34*, 108532.

[311] J. S. Scott, I. N. Michaelides, M. Schade, *RSC Med. Chem.* **2025**, *16*, 449.

[312] B. E. Smith, S. L. Wang, S. Jaime-Figueroa, A. Harbin, J. Wang, B. D. Hamman, et al., *Nat. Commun.* **2019**, *10*, 131.

[313] G. M. Burslem, B. E. Smith, A. C. Lai, S. Jaime-Figueroa, D. C. McQuaid, D. P. Bondeson, et al., *Cell Chem. Biol.* **2018**, *25*, 67.

[314] X. Han, C. Wang, C. Qin, W. Xiang, E. Fernandez-Salas, C.-Y. Yang, et al., *J. Med. Chem.* **2019**, *62*, 941.

[315] D. Vemula, P. Jayasurya, V. Sushmitha, Y. N. Kumar, V. Bhandari, *Eur. J. Pharm. Sci.* **2023**, *181*, 106324.

[316] N. Bai, S. A. Miller, G. V. Andrianov, M. Yates, P. Kirubakaran, J. Karanicolas, *J. Chem. Inf. Model.* **2021**, *61*, 1368.

[317] G. Weng, D. Li, Y. Kang, T. Hou, *J. Med. Chem.* **2021**, *64*, 16271.

[318] D. Zaidman, J. Prilusky, N. London, *J. Chem. Inf. Model.* **2020**, *60*, 4894.

[319] M. L. Drummond, A. Henry, H. Li, C. I. Williams, *J. Chem. Inf. Model.* **2020**, *60*, 5234.

[320] W. Li, J. Zhang, L. Guo, Q. Wang, *J. Chem. Inf. Model.* **2022**, *62*, 523.

[321] K. Xu, Z. Wang, S. Xiang, R. Tang, Q. Deng, J. Ge, et al., *J. Chem. Inf. Model.* **2024**, *64*, 7666.

[322] E. Rovers, M. Schapira, *J. Chem. Inf. Model.* **2024**, *64*, 6162.

[323] J. Zattoni, P. Vottero, G. Carena, C. Uliveto, G. Pozzati, B. Morabito, et al., *Comput. Methods Programs Biomed.* **2025**, *264*, 108687.

[324] N. Bai, K. M. Riching, A. Makaju, H. Wu, T. M. Acker, S.-C. Ou, et al., *J. Biol. Chem.* **2022**, *298*, 101653.

[325] T. Dixon, D. MacPherson, B. Mostofian, T. Dauzhenka, S. Lotz, D. McGee, et al., *Nat. Commun.* **2022**, *13*, 5884.

[326] H. Yokoo, N. Shibata, A. Endo, T. Ito, Y. Yanase, Y. Murakami, et al., *J. Med. Chem.* **2021**, *64*, 15868.

[327] R. Krishna, J. Wang, W. Ahern, P. Sturmfels, P. Venkatesh, I. Kalvet, et al., *Science (1979).* **2024**, *384*, eadl2528.

[328] J. Abramson, J. Adler, J. Dunger, R. Evans, T. Green, A. Pritzel, et al., *Nature* **2024**, *630*, 493.

[329] R. Vannam, J. Sayilgan, S. Ojeda, B. Karakyriakou, E. Hu, J. Kreuzer, et al., *Cell Chem. Biol.* **2021**, *28*, 503.

[330] B. Jiang, Y. Gao, J. Che, W. Lu, I. H. Kaltheuner, R. Dries, et al., *Nat. Chem. Biol.* **2021**, *17*, 675.

[331] G. Luo, Z. Li, X. Lin, X. Li, Y. Chen, K. Xi, et al., *Acta Pharm. Sin. B* **2021**, *11*, 1300.

[332] C. A. Lipinski, F. Lombardo, B. W. Dominy, P. J. Feeney, *Adv. Drug Deliv. Rev.* **1997**, *23*, 3.

[333] A. Pike, B. Williamson, S. Harlfinger, S. Martin, D. F. McGinnity, *Drug Discov. Today* **2020**, *25*, 1793.

[334] L. P. Volak, H. M. Duevel, S. Humphreys, D. Nettleton, C. Phipps, A. Pike, et al., *Drug Metab. Dispos.* **2023**, *51*, 792.

[335] Y. Atilaw, V. Poongavanam, C. Svensson Nilsson, D. Nguyen, A. Giese, D. Meibom, et al., *ACS Med. Chem. Lett.* **2021**, *12*, 107.

[336] L. Goracci, J. Desantis, A. Valeri, B. Castellani, M. Eleuteri, G. Cruciani, *J. Med. Chem.* **2020**, *63*, 11615.

[337] M. Schneider, C. J. Radoux, A. Hercules, D. Ochoa, I. Dunham, L.-P. Zalmas, et al., *Nat. Rev. Drug Discov.* **2021**, *20*, 789.

[338] P. M. Cromm, K. T. G. Samarasinghe, J. Hines, C. M. Crews, *J. Am. Chem. Soc.* **2018**, *140*, 17019.

[339] J. Salami, S. Alabi, R. R. Willard, N. J. Vitale, J. Wang, H. Dong, et al., *Commun. Biol.* **2018**, *1*, 100.

[340] S. Khan, X. Zhang, D. Lv, Q. Zhang, Y. He, P. Zhang, et al., *Nat. Med.* **2019**, *25*, 1938.

[341] M. Guharoy, P. Bhowmick, M. Sallam, P. Tompa, *Nat. Commun.* **2016**, *7*, 10239.

[342] I. Churcher, *J. Med. Chem.* **2018**, *61*, 444.

[343] A. Mares, A. H. Miah, I. E. D. Smith, M. Rackham, A. R. Thawani, J. Cryan, et al., *Commun. Biol.* **2020**, *3*, 140.

[344] T. Mathieson, H. Franken, J. Kosinski, N. Kurzawa, N. Zinn, G. Sweetman, et al., *Nat. Commun.* **2018**, *9*, 689.

[345] R. P. Law, J. Nunes, C. Chung, M. Bantscheff, K. Buda, H. Dai, et al., *Angew. Chem. Int. Ed* **2021**, *60*, 23327.

[346] M. Hemkens, K. Stamp, L. I. Loberg, K. Moreau, T. Hart, *Drug Discov. Today* **2023**, *28*, 103643.

[347] G. Fan, S. Chen, Q. Zhang, N. Yu, Z. Shen, Z. Liu, et al., *MedComm (Beijing).* **2025**, *6*, e70401.

[348] Pfizer, A Study to Learn About a New Medicine Called Vepdegestrant (ARV-471, PF-07850327) in People Who Have Advanced Metastatic Breast Cancer (VERITAC-2), 2023. *Bethesda (MD): National Library of Medicine (US), ClinicalTrials.gov [Internet], ID: NCT05654623*.

[349] Celgene, A Study to Compare the Efficacy and Safety of BMS-986365 Versus the Investigator's Choice of Therapy in Participants With Metastatic Castration-resistant Prostate Cancer (rechARge), **2025**. *Bethesda (MD): National Library of Medicine (US), ClinicalTrials.gov [Internet], ID: NCT06764485*.

[350] BeOne Medicines, A Study of BGB-16673 Compared to Investigator's Choice in Participants With Chronic Lymphocytic Leukemia or Small Lymphocytic Lymphoma Previously Exposed to Both Bruton Tyrosine Kinase (BTK) and B-cell Leukemia/Lymphoma 2 Protein (BCL2) Inhibitors (CaDAnCe-302), **2025**. *Bethesda (MD): National Library of Medicine (US), ClinicalTrials.gov [Internet], ID: NCT06846671*.

[351] Novartis Pharmaceuticals, A Study of ARV-766 Given by Mouth in Men With Metastatic Prostate Cancer, **2021**. *Bethesda (MD): National Library of Medicine (US), ClinicalTrials.gov [Internet], ID: NCT05067140*.

[352] Bristol-Myers Squibb, A Study to Assess BMS-986458 Alone and in Combination With Anti-lymphoma Agents in Relapsed/Refractory Non-Hodgkin Lymphomas, **2023**. *Bethesda (MD): National Library of Medicine (US), ClinicalTrials.gov [Internet], ID: NCT06090539*.

[353] Children's Oncology Group, Testing the Addition of an Anti-cancer Drug, DT2216, to the Usual Chemotherapy Treatment for Relapsed or Refractory Solid Tumors and Fibrolamellar Carcinoma, **2025**. *Bethesda (MD): National Library of Medicine (US), ClinicalTrials.gov [Internet], ID: NCT06620302*.

[354] Ltd. Jiangsu HengRui Medicine Co., A Study of HRS-5041 Tablets Combined With Antitumor Therapy in Subjects With Advanced Prostate Cancer, **2024**. *Bethesda (MD): National Library of Medicine (US), ClinicalTrials.gov [Internet], ID: NCT06568094*.

[355] Henan Cancer Hospital, SHR2554 Combined With Endocrine Therapy in Advanced Breast Cancer, **2025**. *Bethesda (MD): National Library of Medicine (US), ClinicalTrials.gov [Internet], ID: NCT07125950*.

[356] Suzhou Kintor Pharmaceutical Inc, To Evaluate the Efficacy and Safety of GT20029 Solution in the Treatment of Androgenetic Alopecia (AGA) in Chinese Adult Males, **2023**. *Bethesda (MD): National Library of Medicine (US), ClinicalTrials.gov [Internet], ID: NCT06692465*.

[357] Inc. Tanabe Pharma America, A Study of MT-4561 in Patients With Various Advanced Solid Tumors, **2025**. *Bethesda (MD): National Library of Medicine (US), ClinicalTrials.gov [Internet], ID: NCT06943521*.

[358] Prelude Therapeutics, A Study of PRT3789 in Combination With Pembrolizumab in Patients With Advanced or Metastatic Solid Tumors With a SMARCA4 Mutation, **2025**. *Bethesda (MD): National Library of Medicine (US), ClinicalTrials.gov [Internet], ID: NCT06682806*.

[359] K. Fujita, N. Nonomura, *World J. Mens Health* **2019**, *37*, 288.

[360] T. Neklesa, L. B. Snyder, R. R. Willard, N. Vitale, K. Raina, J. Pizzano, et al., *Cancer Res.* **2018**, *78*, 5236.

[361] L. B. Snyder, T. K. Neklesa, R. R. Willard, D. A. Gordon, J. Pizzano, N. Vitale, et al., *Mol. Cancer Ther.* **2025**, *24*, 511.

[362] X. Gao, H. A. Burris III, J. Vuky, R. Dreicer, A. O. Sartor, C. N. Sternberg, et al., *J. Clin. Oncol.* **2022**, *40*, 17.

[363] L. Gennari, *Curr. Opin. Investig. Drugs* **2005**, *6*, 1067.

[364] S. M. Gough, J. J. Flanagan, J. Teh, M. Andreoli, E. Rousseau, M. Pannone, et al., *Clin. Cancer Res.* **2024**, *30*, 3549.

[365] Y. Li, D. Yang, X. Yin, X. Zhang, J. Huang, Y. Wu, et al., *JAMA Netw. Open* **2020**, *3*, e1918160.

[366] E. P. Hamilton, C. Ma, M. De Laurentiis, H. Iwata, S. A. Hurvitz, S. A. Wander, et al., *Future Oncol.* **2024**, *20*, 2447.

[367] Avirnas, Arvinas Announces Submission of New Drug Application to U.S. FDA for Vepdegestrant for Patients with ESR1-Mutated ER+/HER2- Advanced or Metastatic Breast Cancer. [online] Arvinas Announces Submission of New Drug Application to U.S. FDA for Vepdegestrant for Patients with ESR1-Mutated ER+/HER2- Advanced or Metastatic Breast Cancer | Arvinas. Accessed: 12.01.2026

[368] S. Nayak, J. D. Norris, M. Ammirante, E. Rychak, S. E. Wardell, D. Liao, et al., *Clin. Cancer Res* **2025**, *32*, 224.

[369] H. Wang, B. Lei, C. Huo, D. Sun, J. Chen, Z. Wang, et al., *WIPO - World Intellectual Property Organization* **2021** Degradation of bruton's tyrosine kinase (btk) by conjugation of btk inhibitors with e3 ligase ligand and methods of use. WO2021219070A1.

[370] M. C. Thompson, R. D. Parrondo, A. M. Frustaci, J. N. Allan, P. Ghia, I. Mocanu, et al., *Blood* **2024**, *144*, 885.

[371] D. E. Rathkopf, M. R. Patel, A. D. Choudhury, D. Rasco, N. Lakhani, J. E. Hawley, et al., *Ann. Oncol.* **2025**, *36*, 76.

[372] M. A. Clark, R. A. Acharya, C. C. Arico-Muendel, S. L. Belyanskaya, D. R. Benjamin, N. R. Carlson, et al., *Nat. Chem. Biol.* **2009**, *5*, 647.

[373] S. Brenner, R. A. Lerner, *PNAS* **1992**, *89*, 5381.

[374] P. Ma, S. Zhang, Q. Huang, Y. Gu, Z. Zhou, W. Hou, et al., *Acta Pharm. Sin. B* **2024**, *14*, 492.

[375] A. A. Peterson, D. R. Liu, *Nat. Rev. Drug Discov.* **2023**, *22*, 699.

[376] A. Gironda-Martínez, E. J. Donckele, F. Samain, D. Neri, *ACS Pharmacol. Transl. Sci.* **2021**, *4*, 1265.

[377] S. L. Belyanskaya, Y. Ding, J. F. Callahan, A. L. Lazaar, D. I. Israel, *ChemBioChem* **2017**, *18*, 837.

[378] P. A. Harris, S. B. Berger, J. U. Jeong, R. Nagilla, D. Bandyopadhyay, N. Campobasso, et al., *J. Med. Chem.* **2017**, *60*, 1247.

[379] A. J. Kennedy, L. Sundström, S. Geschwindner, E. K. Y. Poon, Y. Jiang, R. Chen, et al., *Commun. Biol.* **2020**, *3*, 782.

[380] C. K. Chana, P. Maisonneuve, G. Posternak, N. G. A. Grinberg, J. Poirson, S. M. Ona, et al., *J. Med. Chem.* **2022**, *65*, 12725.

[381] Q. Chen, C. Liu, W. Wang, X. Meng, X. Cheng, X. Li, et al., *ACS Chem. Biol.* **2023**, *18*, 25.

[382] J. W. Mason, Y. T. Chow, L. Hudson, A. Tutter, G. Michaud, M. V. Westphal, et al., *Nat. Chem. Biol.* **2024**, *20*, 170.

[383] J. S. Disch, J. M. Duffy, E. C. Y. Lee, D. Gikunju, B. Chan, B. Levin, et al., *J. Med. Chem.* **2021**, *64*, 5049.

[384] N. J. Gesmundo, B. Sauvagnat, P. J. Curran, M. P. Richards, C. L. Andrews, P. J. Dandliker, et al., *Nature* **2018**, *557*, 228.

[385] R. P. Thomas, R. E. Heap, F. Zappacosta, E. K. Grant, P. Pogány, S. Besley, et al., *Chem. Sci.* **2021**, *12*, 12098.

[386] H. Wilders, G. Biggs, S. M. Rowe, E. E. Cawood, I. G. Riziotis, A. R. Rendina, et al., *Angew. Chem. Int. Ed* **2025**, *64*, e202418314.

[387] B. Mahjour, R. Zhang, Y. Shen, A. McGrath, R. Zhao, O. G. Mohamed, et al., *Nat. Commun.* **2023**, *14*, 3924.

[388] S. Chen, Z. Wang, J. Gao, Y. Wang, J. Liang, Y. Zhu, et al., *J. Med. Chem.* **2025**, *68*, 13609.

[389] B. L. Roberts, Z.-X. Ma, A. Gao, E. D. Leisten, D. Yin, W. Xu, et al., *ACS Chem. Biol.* **2020**, *15*, 1487.

[390] M. P. Plesniak, E. K. Taylor, F. Eisele, C. M. B. K. Kourra, I. N. Michaelides, A. Oram, et al., *ACS Med. Chem. Lett.* **2023**, *14*, 1882.

[391] L. Guo, Y. Zhou, X. Nie, Z. Zhang, Z. Zhang, C. Li, et al., *Eur. J. Med. Chem.* **2022**, *236*, 114317.

[392] R. Stevens, E. Bendito-Moll, D. J. Battersby, A. H. Miah, N. Wellaway, R. P. Law, et al., *J. Med. Chem.* **2023**, *66*, 15437.

[393] C. E. Hendrick, J. R. Jorgensen, C. Chaudhry, I. I. Strambeanu, J.-F. Brazeau, J. Schiffer, et al., *ACS Med. Chem. Lett.* **2022**, *13*, 1182.

[394] R. Stevens, H. J. Shrives, J. Cryan, D. Klimaszewska, P. Stacey, G. A. Burley, et al., *RSC Med. Chem.* **2025**, *16*, 1141.

[395] R. D. Cummings, R. P. McEver, In *Essentials of Glycobiology*, Cold Spring Harbor (NY): Cold Spring Harbor Laboratory Press, **2009**.

[396] G. D. Brown, J. A. Willment, L. Whitehead, *Nat. Rev. Immunol.* **2018**, *18*, 374.

[397] T. B. H. Geijtenbeek, S. I. Gringhuis, *Nat. Rev. Immunol.* **2009**, *9*, 465.

[398] M. E. Taylor, K. Drickamer, *Curr. Opin. Cell Biol.* **2007**, *19*, 572.

[399] Kurt Drickamer, In *Progress in Nucleic Acid Research and Molecular Biology*, **1993**, Vol. 45, pp. 207–232.

[400] A. N. Zelensky, J. E. Gready, *FEBS J.* **2005**, *272*, 6179.

[401] K. Drickamer, *Journal of Biological Chemistry* **1988**, *263*, 9557.

[402] K. DRICKAMER, *Biochem. Soc. Trans.* **1989**, *17*, 13.

[403] W. I. Weis, R. Kahn, R. Fourme, K. Drickamer, W. A. Hendrickson, *Science (1979).* **1991**, *254*, 1608.

[404] K. Drickamer, *Nature* **1992**, *360*, 183.

[405] Y. Guo, H. Feinberg, E. Conroy, D. A. Mitchell, R. Alvarez, O. Blixt, et al., *Nat. Struct. Mol. Biol.* **2004**, *11*, 591.

[406] D. A. Mitchell, A. J. Fadden, K. Drickamer, *J. Biol. Chem.* **2001**, *276*, 28939.

[407] H. Feinberg, S. A. F. Jégouzo, Y. Lasanajak, D. F. Smith, K. Drickamer, W. I. Weis, et al., *J. J. Biol. Chem.* **2021**, *296*, 100368.

[408] R. T. Lee, Y. C. Lee, *Glycoconj. J.* **2000**, *17*, 543.

[409] S. Cabani, V. Mollica, L. Lepori, *J. Chem. Soc., Faraday Trans. 1* **1978**, *74*, 2667.

[410] S. Leusmann, P. Ménová, E. Shanin, A. Titz, C. Rademacher, *Chem. Soc. Rev.* **2023**, *52*, 3663.

[411] B. Ernst, J. L. Magnani, *Nat. Rev. Drug Discov.* **2009**, *8*, 661.

[412] C. B. Carlson, P. Mowery, R. M. Owen, E. C. Dykhuizen, L. L. Kiessling, *ACS Chem. Biol.* **2007**, *2*, 119.

[413] M. Mammen, S.-K. Choi, G. M. Whitesides, *Angew. Chem. Int. Ed.* **1998**, *37*, 2754.

[414] G. Vauquelin, S. J. Charlton, *Br. J. Pharmacol.* **2013**, *168*, 1771.

[415] N. J. Overeem, P. H. (Erik) Hamming, M. Tieke, E. van der Vries, J. Huskens, *ACS Nano* **2021**, *15*, 8525.

[416] A. Bernardi, J. Jiménez-Barbero, A. Casnati, C. De Castro, T. Darbre, F. Fieschi, et al., *Chem. Soc. Rev.* **2013**, *42*, 4709.

[417] T. K. Dam, C. F. Brewer, In *Adv Carbohydr Chem Biochem*, **2010**, pp. 139–164.

[418] K. Drickamer, *Nat. Struct. Mol. Biol.* **1995**, *2*, 437.

[419] C. Müller, G. Despras, T. K. Lindhorst, *Chem. Soc. Rev.* **2016**, *45*, 3275.

[420] L. Kiessling, *Curr. Opin. Chem. Biol.* **2000**, *4*, 696.

[421] V. Porkolab, C. Pifferi, I. Sutkeviciute, S. Ordanini, M. Taouai, M. Thépaut, et al., *Org. Biomol. Chem.* **2020**, *18*, 4763.

[422] S. Cecioni, A. Imberty, S. Vidal, *Chem. Rev.* **2015**, *115*, 525.

[423] V. Porkolab, M. Lepšík, S. Ordanini, A. St John, A. Le Roy, M. Thépaut, et al., *ACS Cent. Sci.* **2023**, *9*, 709.

[424] G. Bachem, E. Wamhoff, K. Silberreis, D. Kim, H. Baukmann, F. Fuchsberger, et al., *Angew. Chem. Int. Ed* **2020**, *59*, 21016.

[425] J. Ramos-Soriano, J. J. Reina, B. M. Illescas, N. de la Cruz, L. Rodríguez-Pérez, F. Lasala, et al., *J. Am. Chem. Soc.* **2019**, *141*, 15403.

[426] V. M. Krishnamurthy, V. Semetey, P. J. Bracher, N. Shen, G. M. Whitesides, *J. Am. Chem. Soc.* **2007**, *129*, 1312.

[427] S. Ordanini, N. Varga, V. Porkolab, M. Thépaut, L. Belvisi, A. Bertaglia, et al., *Chem. Commun.* **2015**, *51*, 3816.

[428] S. Wang, L. Dupin, M. Noël, C. J. Carroux, L. Renaud, T. Géhin, et al., *Chemistry – A European Journal* **2016**, *22*, 11785.

[429] T. K. Dam, T. A. Gerken, C. F. Brewer, *Biochemistry* **2009**, *48*, 3822.

[430] T. K. Dam, C. F. Brewer, *Biochemistry* **2008**, *47*, 8470.

[431] C. Chaipan, E. J. Soilleux, P. Simpson, H. Hofmann, T. Gramberg, A. Marzi, et al., *J. Virol.* **2006**, *80*, 8951.

[432] Y. van Kooyk, T. B. H. Geijtenbeek, *Nat. Rev. Immunol.* **2003**, *3*, 697.

[433] G. Tabarani, M. Thépaut, D. Stroebel, C. Ebel, C. Vivès, P. Vachette, et al., J. Biol. Chem. **2009**, *284*, 21229.

[434] A. Engering, T. B. H. Geijtenbeek, S. J. van Vliet, M. Wijers, E. van Liempt, N. Demaurex, et al., *J. Immunol.* **2002**, *168*, 2118.

[435] T. B. H. Geijtenbeek, R. Torensma, S. J. van Vliet, G. C. F. van Duijnhoven, G. J. Adema, Y. van Kooyk, et al., *Cell* **2000**, *100*, 575.

[436] B. J. Appelmelk, I. van Die, S. J. van Vliet, C. M. J. E. Vandenbroucke-Grauls, T. B. H. Geijtenbeek, Y. van Kooyk, *J. Immunol* **2003**, *170*, 1635.

[437] T. B. H. Geijtenbeek, D. J. E. B. Krooshoop, D. A. Bleijs, S. J. van Vliet, G. C. F. van Duijnhoven, V. Grabovsky, et al., *Nat. Immunol.* **2000**, *1*, 353.

[438] T. B. H. Geijtenbeek, D. S. Kwon, R. Torensma, S. J. van Vliet, G. C. F. van Duijnhoven, J. Middel, et al., *Cell* **2000**, *100*, 587.

[439] Y. van Kooyk, B. Appelmelk, T. B. H. Geijtenbeek, *Trends Mol. Med.* **2003**, *9*, 153.

[440] T. B. H. Geijtenbeek, S. J. van Vliet, E. A. Koppel, M. Sanchez-Hernandez, C. M. J. E. Vandenbroucke-Grauls, B. Appelmelk, et al., *J. Exp. Med.* **2003**, *197*, 7.

[441] N. Varga, I. Sutkeviciute, R. Ribeiro-Viana, A. Berzi, R. Ramdasi, A. Daghetti, et al., *Biomaterials* **2014**, *35*, 4175.

[442] M. Taouai, V. Porkolab, K. Chakroun, C. Cheneau, J. Luczkowiak, R. Abidi, et al., *Bioconjug. Chem.* **2019**, *30*, 1114.

[443] A. J. Engering, M. Cella, D. Fluitsma, M. Brockhaus, E. C. M. Hoefsmit, A. Lanzavecchia, et al., *Eur. J. Immunol.* **1997**, *27*, 2417.

[444] K. Takahashi, M. J. Donovan, R. A. Rogers, R. A. B. Ezekowitz, *Cell Tissue Res.* **1998**, *292*, 311.

[445] H. Macedo-Ramos, A. F. Batista, A. Carrier-Ruiz, L. Alves, S. Allodi, V. T. Ribeiro-Resende, et al., *BMC Microbiol.* **2014**, *14*, 211.

[446] J. Lubow, M. C. Virgilio, M. Merlino, D. R. Collins, M. Mashiba, B. G. Peterson, et al., *Elife* **2020**, *9*, e51035.

[447] P. D. Stahl, R. A. B. Ezekowitz, *Curr. Opin. Immunol.* **1998**, *10*, 50.

[448] P. B. Kang, A. K. Azad, J. B. Torrelles, T. M. Kaufman, A. Beharka, E. Tibesar, et al., *J. Exp. Med.* **2005**, *202*, 987.

[449] L. Martinez-Pomares, S. A. Linehan, P. R. Taylor, S. Gordon, *Immunobiology* **2001**, *204*, 527.

[450] P. Allavena, M. Chieppa, P. Monti, L. Piemonti, *Crit. Rev. Immunol.* **2004**, *24*, 179.

[451] S. J. Lee, S. Evers, D. Roeder, A. F. Parlow, J. Risteli, L. Risteli, et al., *Science (1979).* **2002**, *295*, 1898.

[452] M. E. Taylor, K. Drickamer, *J. Biol. Chem.* **1993**, *268*, 399.

[453] M. E. Taylor, K. Bezouska, K. Drickamer, *J. Biol. Chem.* **1992**, *267*, 1719.

[454] D. J. Fiete, M. C. Beranek, J. U. Baenziger, *PNAS* **1998**, *95*, 2089.

[455] C. E. Napper, K. Drickamer, M. E. Taylor, *Biochem. J* **2006**, *395*, 579.

[456] T. Frenz, E. Grabski, V. Durán, C. Hozsa, A. Stępczyńska, M. Furch, et al., *Eur. J. Pharm. Biopharm* **2015**, *95*, 13.

[457] T. S. Patil, A. S. Deshpande, *J. Control. Release* **2020**, *320*, 239.

[458] S. M. Van Patten, H. Hughes, M. R. Huff, P. A. Piepenhagen, J. Waire, H. Qiu, et al., *Glycobiology* **2007**, *17*, 467.

[459] R. O. Brady, G. J. Murray, N. W. Barton, *J. Inherit. Metab. Dis.* **1994**, *17*, 510.

[460] K. Prabahar, Z. Alanazi, M. Qushawy, *Indian J. Pharm. Educ. Res.* **2021**, *55*, 346.

[461] X. Feng, W. Xu, Z. Li, W. Song, J. Ding, X. Chen, *Advanced Science* **2019**, *6*, 1900101.

[462] K. R. Peterson, M. A. Cottam, A. J. Kennedy, A. H. Hasty, *Trends Pharmacol. Sci.* **2018**, *39*, 536.

[463] S. D. Steichen, M. Caldorera-Moore, N. A. Peppas, *Eur. J. Pharm. Sci.* **2013**, *48*, 416.

[464] M. Paurević, M. Šrajer Gajdošik, R. Ribić, *Int. J. Mol. Sci.* **2024**, *25*, 1370.

[465] A. Sato, S. Kawakami, M. Yamada, F. Yamashita, M. Hashida, *J. Drug Target.* **2001**, *9*, 201.

[466] O. V. Markov, N. L. Mironova, E. V. Shmendel, R. N. Serikov, N. G. Morozova, M. A. Maslov, et al., *J. Control. Release* **2015**, *213*, 45.

[467] K. Sheng, M. Kalkanidis, D. S. Pouniotis, S. Esparon, C. K. Tang, V. Apostolopoulos, et al., *Eur. J. Immunol.* **2008**, *38*, 424.

[468] J. J. García-Vallejo, W. W. J. Unger, H. Kalay, Y. van Kooyk, *Oncoimmunology* **2013**, *2*, e23040.

[469] W. W. J. Unger, A. J. van Beelen, S. C. Bruijns, M. Joshi, C. M. Fehres, L. van Bloois, et al., *J. Control. Release* **2012**, *160*, 88.

[470] J. Chae, S. H. Kang, J. Kim, Y. Choi, S. H. Kang, J. Choi, *Nanoscale Adv.* **2023**, *5*, 4536.

[471] C. Li, D. Zhang, Y. Pan, B. Chen, *Polymers (Basel).* **2023**, *15*, 3354.

[472] Y. Mizuta, H. Maeda, Y. Ishima, Y. Minayoshi, S. Ichimizu, R. Kinoshita, et al., *Adv. Funct. Mater.* **2021**, *31*, 2104136.

[473] K. Hirata, T. Maruyama, H. Watanabe, H. Maeda, K. Nakajou, Y. Iwao, et al., *J. Control. Release* **2010**, *145*, 9.

[474] B. Lantzberg, Y. Zeyn, R. Forster, L. Jian, D. Schauenburg, C. Hieber, et al., *J. Control. Release* **2025**, *382*, 113705.

[475] K. C. Tjandra, P. Thordarson, *Bioconjug. Chem.* **2019**, *30*, 503.

[476] O. Zimmer, A. Goepferich, *Eur. J. Pharm. Biopharm.* **2024**, *198*, 114240.

[477] A. M. Alkilany, L. Zhu, H. Weller, A. Mews, W. J. Parak, M. Barz, et al., *Adv. Drug Deliv. Rev.* **2019**, *143*, 22.

[478] S. Maslanka Figueroa, D. Fleischmann, S. Beck, A. Goepferich, *Macromol. Biosci.* **2020**, *20*, e1900427.

[479] D. R. Elias, A. Poloukhtine, V. Popik, A. Tsourkas, *Nanomedicine* **2013**, *9*, 194.

[480] F. Errani, A. Invernizzi, M. Herok, E. Bochenkova, F. Stamm, I. Corbeski, et al., *JACS Au* **2024**, *4*, 713.

[481] K. Hwang, J. Bae, Y.-L. Jhe, J. Kim, J.-H. Cheong, H.-S. Choi, et al., *Eur. J. Med. Chem.* **2024**, *279*, 116843.

[482] J. Cramer, A. Lakkaichi, B. Aliu, R. P. Jakob, S. Klein, I. Cattaneo, et al., *J. Am. Chem. Soc.* **2021**, *143*, 17465.

[483] I. Sutkeviciute, M. Thépaut, S. Sattin, A. Berzi, J. McGeagh, S. Grudinin, et al., *ACS Chem. Biol.* **2014**, *9*, 1377.

[484] R. Nar, Z. Wu, Y. Li, A. Smith, Y. Zhang, J. Wang, et al., *Genes Dis.* **2025**, *12*, 101452.

[485] W. Du, Y. Huang, X. Chen, Y. Deng, Y. Sun, H. Yang, et al., *Cell Chem. Biol.* **2024**, *31*, 177.

[486] B. Jubeh, Z. Breijyeh, R. Karaman, *Molecules* **2020**, *25*, 1543.

[487] P. Storck, F. Umstätter, S. Wohlfart, C. Domhan, C. Kleist, J. Werner, et al., *Antibiotics* **2020**, *9*, 844.

[488] H. Chung, J. Y. Park, K. Kim, R. J. Yoo, M. Suh, G. J. Gu, et al., *ACS Nano* **2022**, *16*, 12262.

[489] R.-J. E. Li, T. P. Hogervorst, S. Achilli, S. C. Bruijns, T. Arnoldus, C. Vivès, et al., *Front. Chem.* **2019**, *7*, 650.

[490] M. Meta, C. Zimmer, N. Fuchs, M. J. Zecher, A. Lahu, T. Schirmeister, *ACS Med. Chem. Lett.* **2024**, *15*, 837.

8 Appendix

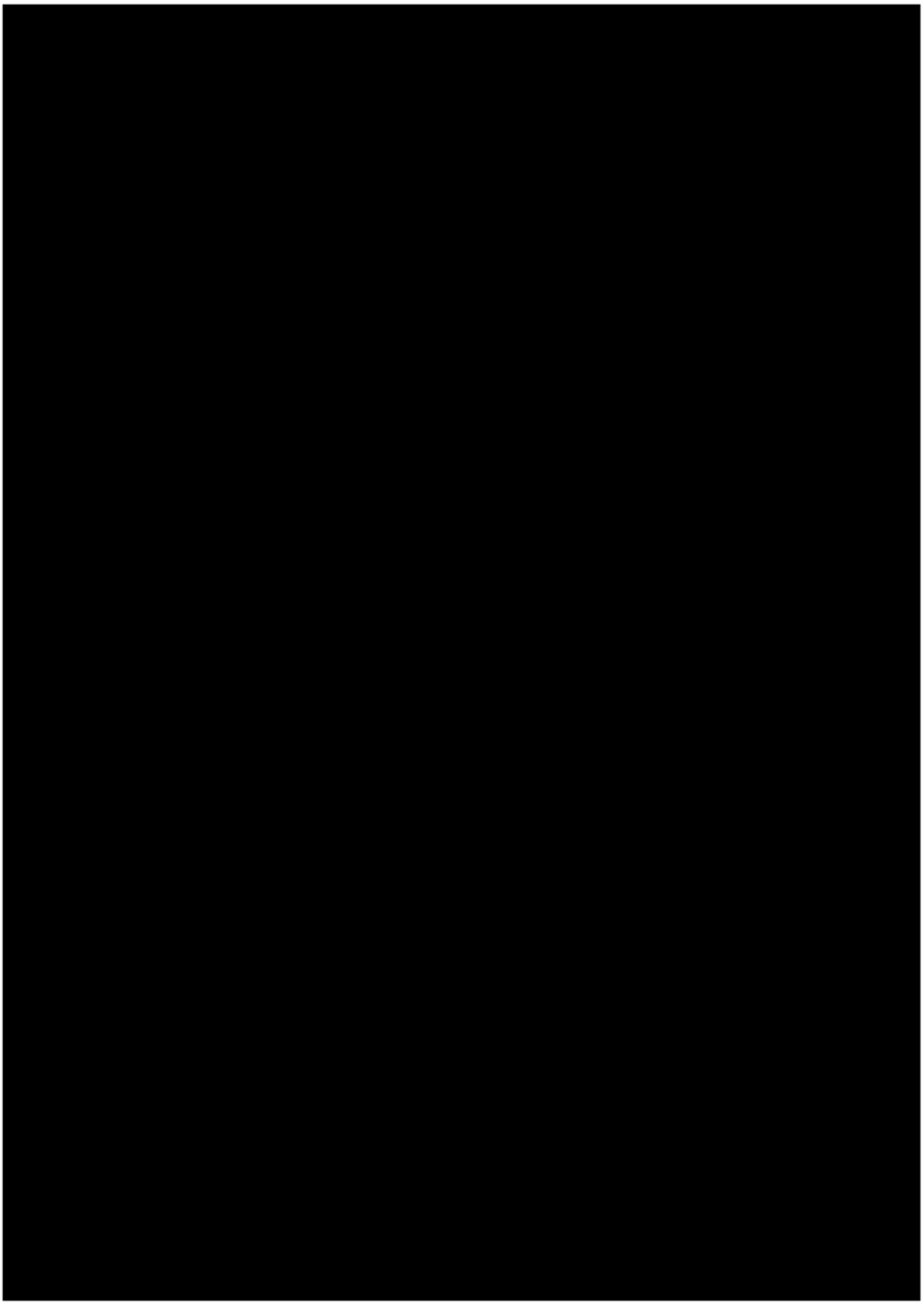
8.1 Usage of AI tools

AI-Tool	Used for	Why	Where
DeepL Translate	Single word translation	Better understanding of English texts	Literature research and selection
ChatGPT	Condensation of my draft texts. Correction of grammar, syntax, and spelling. Finding synonyms	Improved readability through increased precision and stylistic refinement	Throughout the entire thesis
Microsoft Word (integrated spelling and grammar correction)	Correction of grammar and spelling	Improved readability	Throughout the entire thesis

8.2 Nutzung KI-Tools

KI-Tool	Genutzt für	Warum	Wann
DeepL Translate	Übersetzung einzelner wörter	Hilfe zum Verständnis	Literaturrecherche und Auswahl
ChatGPT	Kürzung meiner Textentwürfe. Korrektur von Grammatik, Syntax und Rechtschreibung. Synonym Findung	Bessere Lesbarkeit durch Präzisierung und Stilglättung	Über die gesamte Arbeit hinweg
Microsoft Word (integrierte Rechtschreib- und Grammatikorrektur)	Korrektur von Grammatik und Rechtschreibung	Bessere Lesbarkeit	Über die gesamte Arbeit hinweg

9 Curriculum Vitae



Mainz, January 2026

Annabelle Carolin Weldert